Valley dynamics controlled by ferroelectric switching in monolayer In2Se3

Zhaorui Xia[1], Weibin Chu[2], Qijing Zheng[1*] and Jin Zhao[1,3,4*]

[1]Department of Physics, University of Science and Technology of China, Hefei, Anhui 230026, China
[2]Key Laboratory of Computational Physical Sciences (Ministry of Education), Institute of Computational Physical Sciences, Fudan University, Shanghai, 200433, China
[3]Department of Physics and Astronomy, University of Pittsburgh, Pittsburgh PA 15260, United States
[4]CAS Center for Excellence in Quantum Information and Quantum Physics, University of Science and Technology of China, Hefei, Anhui 230026, China

I. Abstract

Ferroelectricity, a property of materials associated with the emergence of spontaneous electric polarization, has been receiving much interest because their underlying physics and device application. However, how the ferroelectric switching influenced excited states molecular dynamics is still unclear. Here we used the time-domain ab initio nonadiabatic molecular dynamics (NAMD) to investigated the monolayer In_2Se_3 ferroelectric switching processes. Our research reveal that band crossing among Γ valley and M valley occur in momentum space due to their peculiar reverse pathway. While ferroelectric switching happen, excited electron transition take place between those two valleys. Both phonon and flip velocity plays crucial characters in this dynamics.

II. Introduction

Original 2D van der Waals ferroelectric material: In_2Se_3

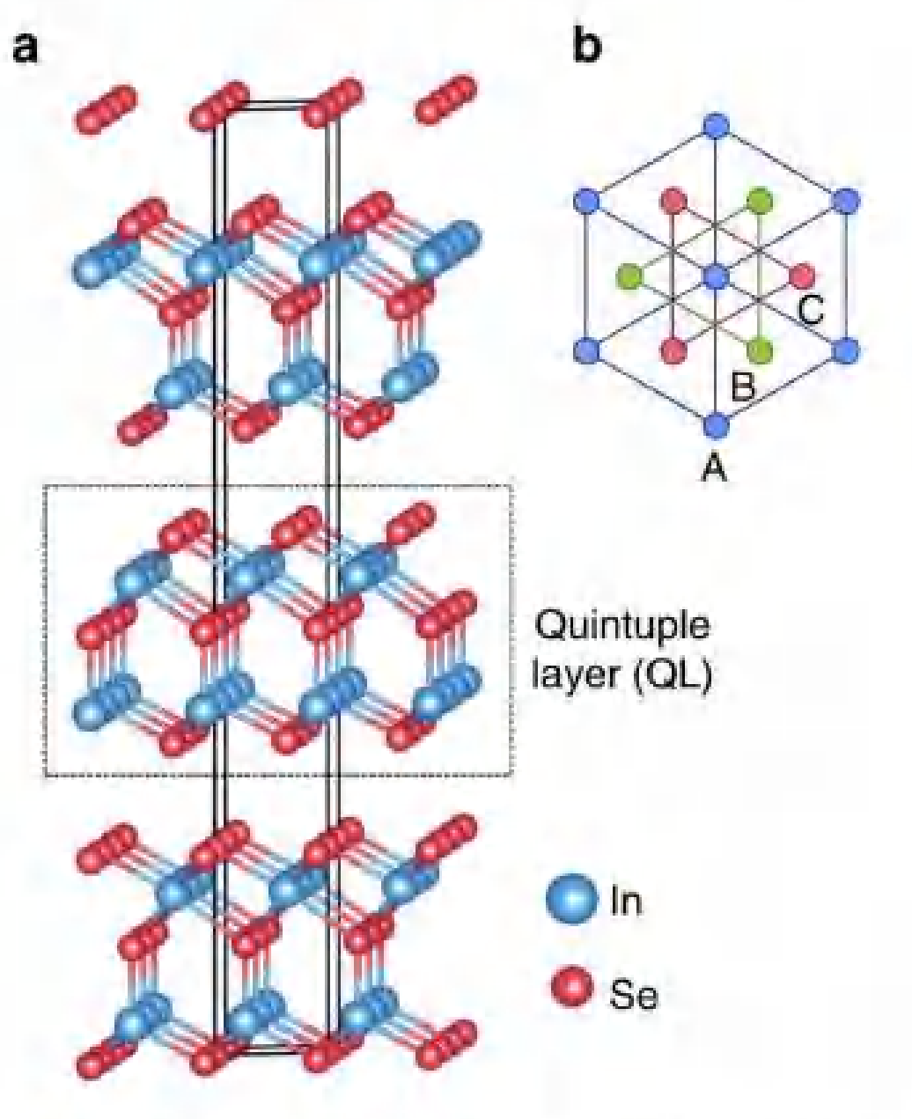

Nat.Commun. 8: 14956 (2017)

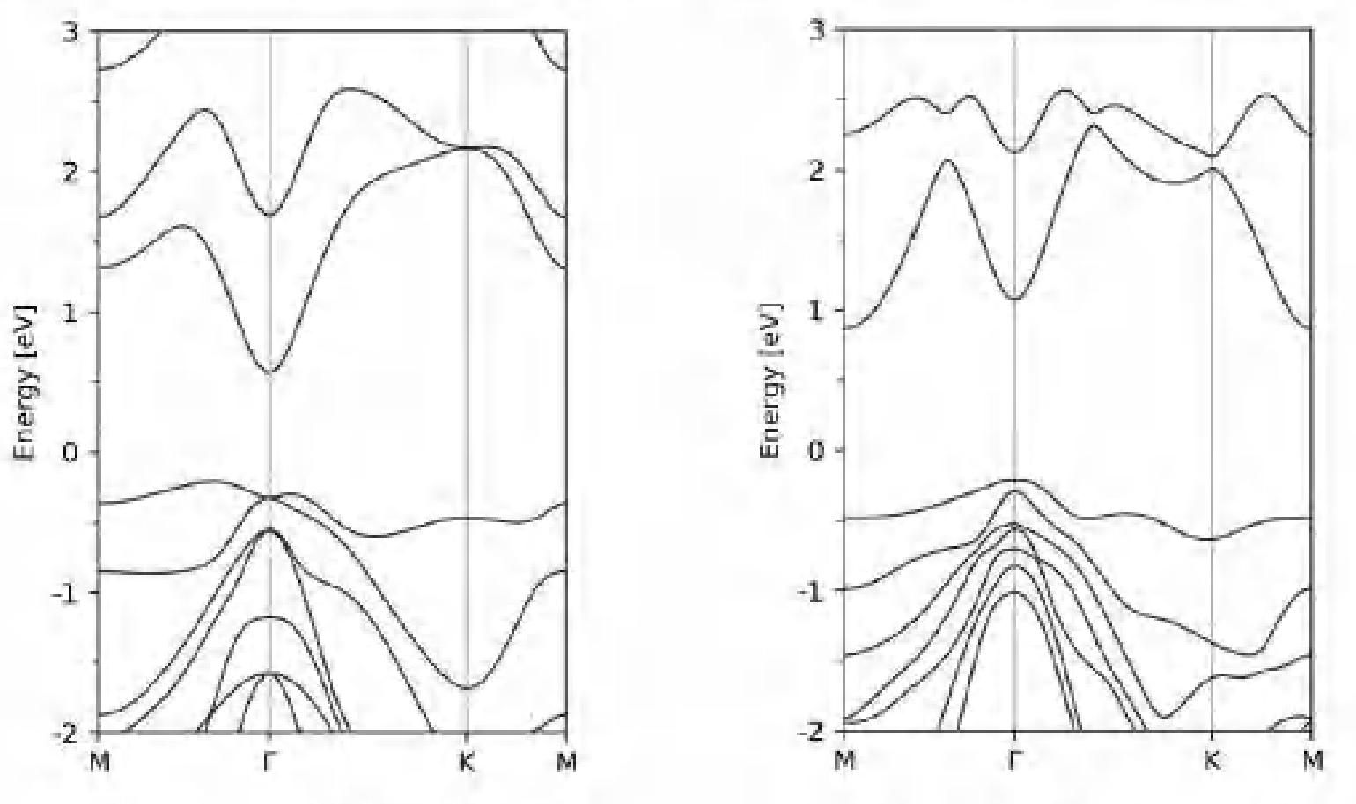

Initial and final state FE-ZB'

Intermediate state fcc'

The ferroelectric ground state FE-ZB' and metastable state fcc' are two key structures in polarization reversal.

III. Method

TDDFT + FSSH

Time-domain density functional theory (TDDFT) with fewest switches surface hopping (FSSH).

In TDDFT, the time-dependent KS orbitals $\psi_e(\mathbf{r},t)$ are expanded in the basis of instantaneous adiabatic KS orbitals $\phi_j(\mathbf{r},\mathbf{R}(t))$:

$$\Psi_e(\mathbf{r},t)=\sum_j c_j(t)\phi_j(\mathbf{r},\mathbf{R}(t))$$

By inserting this expansion into the TDKS equation, we get the equations of coefficients:

$$i\hbar\frac{\partial}{\partial t}c_j(t)=\sum_k c_k(t)\left[\varepsilon_k\delta_{jk}-i\hbar\mathbf{d}_{jk}(t)\right]$$

Where $\mathbf{d}_{\mathrm{jk}}$ is the nonadiabatic couplings (NACs) between KS state j and k. NACs can be written as:

$$\mathbf{d}_{jk}=\left\langle\phi_j\left|\frac{\partial}{\partial t}\right|\phi_k\right\rangle=\sum_I\frac{\langle\phi_j|\nabla_{\mathbf{R}_I}\mathcal{H}|\phi_k\rangle}{\varepsilon_k-\varepsilon_j}\cdot\dot{\mathbf{R}}_I$$

Using FSSH, hopping probabilities between the adiabatic KS states can be written as:

$$P_{j\rightarrow k}(t,\Delta t)=\frac{2\Re[c_j^*c_k\mathbf{d}_{jk}]\Delta t}{c_j^*c_j}$$

NA/AD Contribution

The time-dependent photocarrier transition information can be divided into two parts:

$$\frac{d\rho(\mathbf{r},t)}{dt}=\sum_j\left[\frac{d}{dt}c_j^*(t)c_j(t)\right]\phi_j^*(\mathbf{r},\mathbf{R}(t))\phi_j(\mathbf{r},\mathbf{R}(t))$$
$$+c_j^*(t)c_j(t)\left[\frac{d}{dt}\phi_j^*(\mathbf{r},\mathbf{R}(t))\phi_j(\mathbf{r},\mathbf{R}(t))\right]$$

The first part is the variation of KS states population, which denoted as nonadiabatic (NA) contribution, the second is the change of adiabatic KS orbitals, which denoted as adiabatic (AD) contribution.

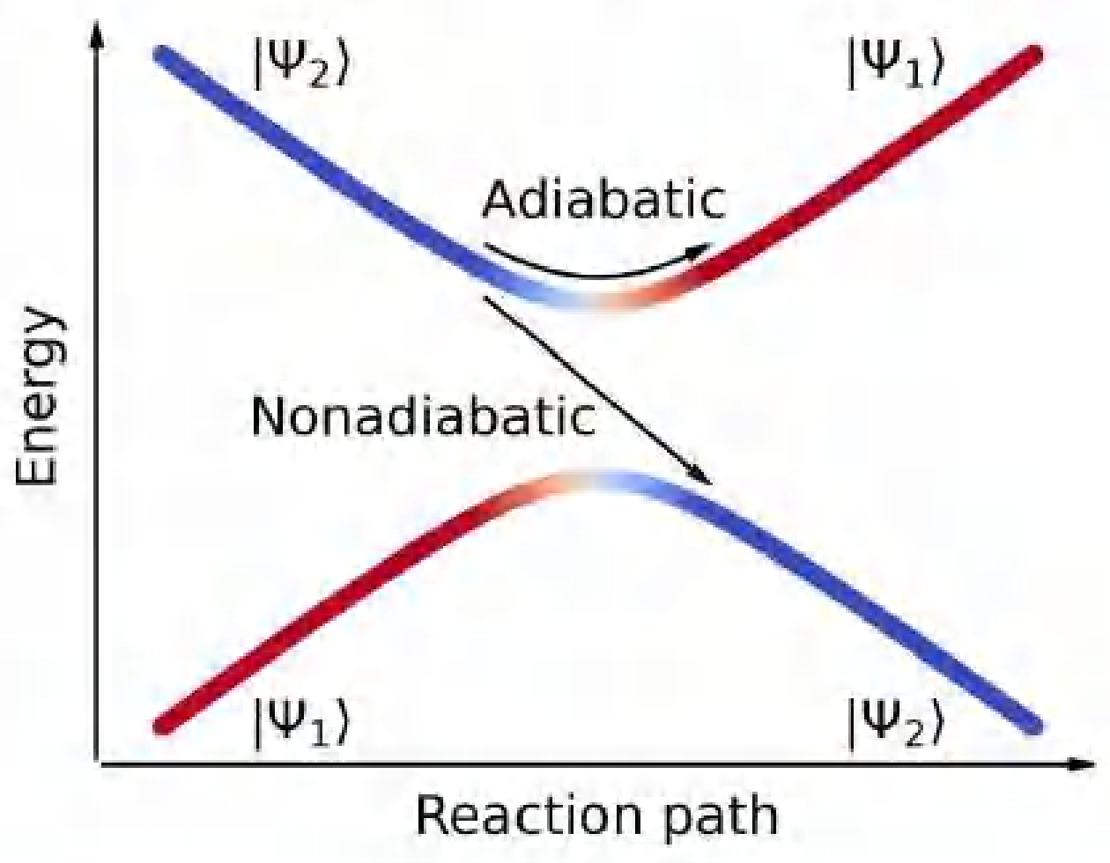

IV. Ferroelectric Switching Dynamics

Three-step concerted reversal mechanism

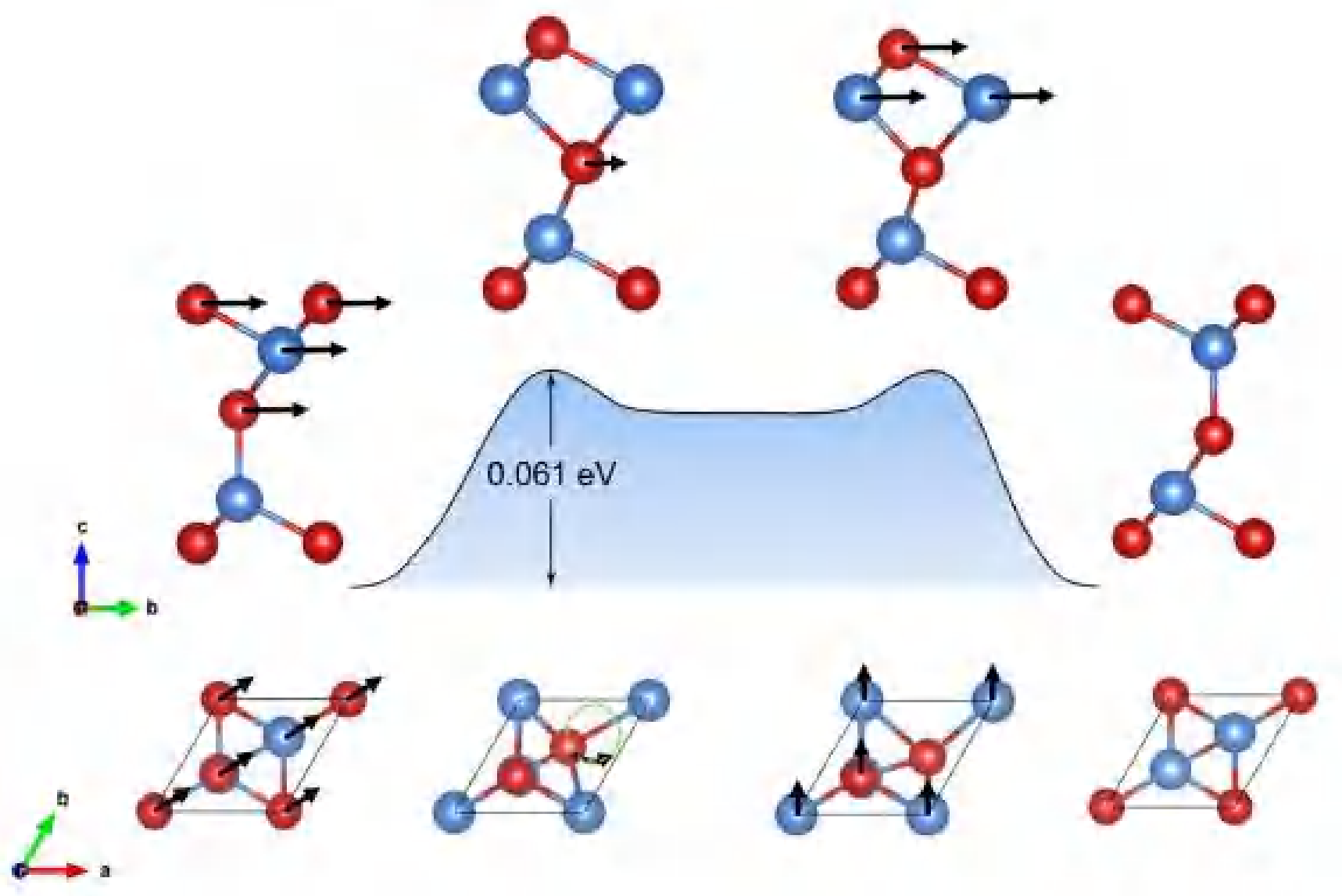

The ferroelectric polarization reverses via an intermediate state, fcc', causing CBM switches from Γ valley to M valley and then return to Γ valley.

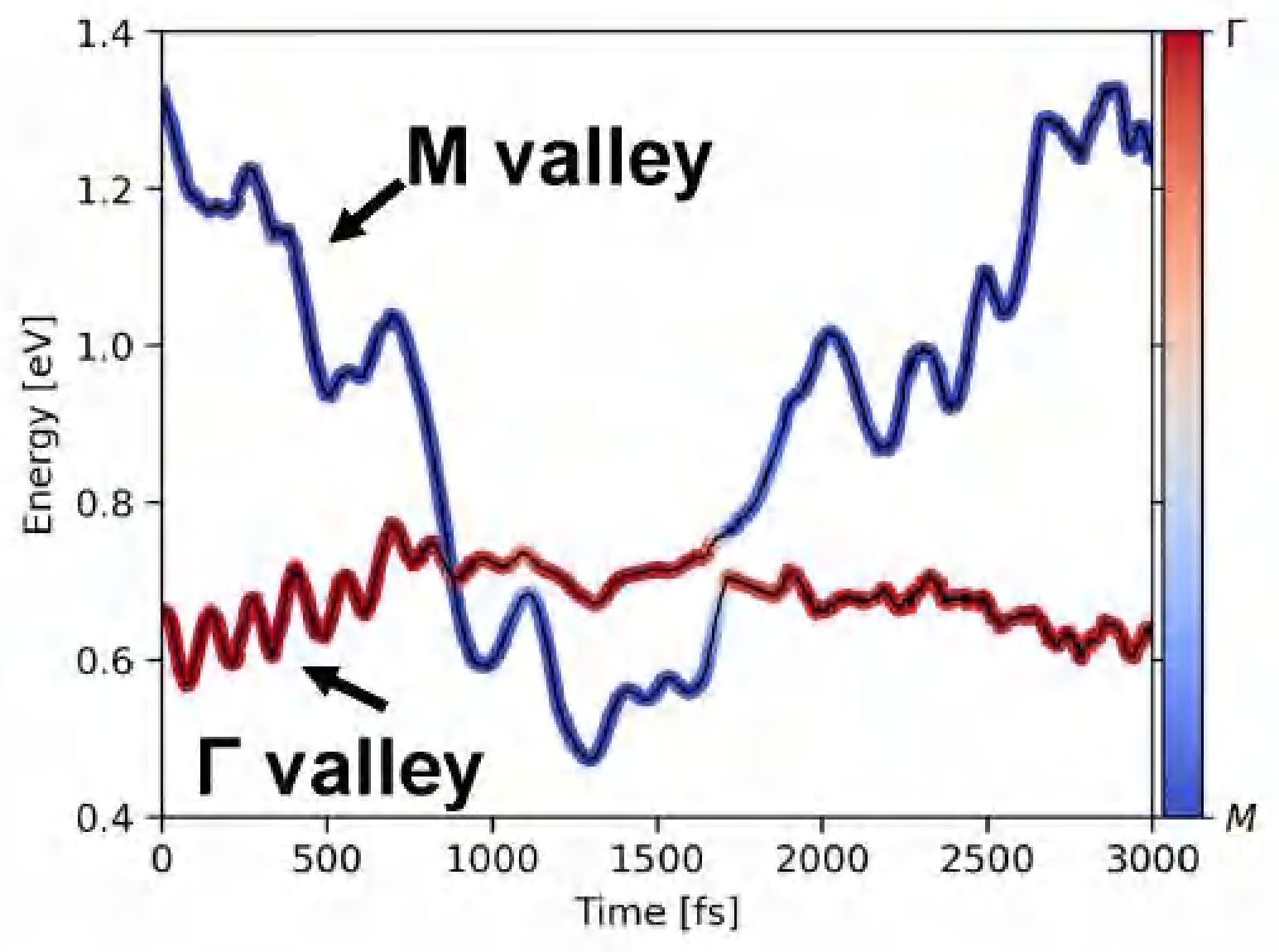

Time-dependent Kohn-Sham orbitals in a polarization reversal process. The red and blue lines denote the momentum space constitution in energy levels near the CBM. There are two crossings in reversal MD.

V. NAMD Results

Time-dependent electron energy change and momentum change

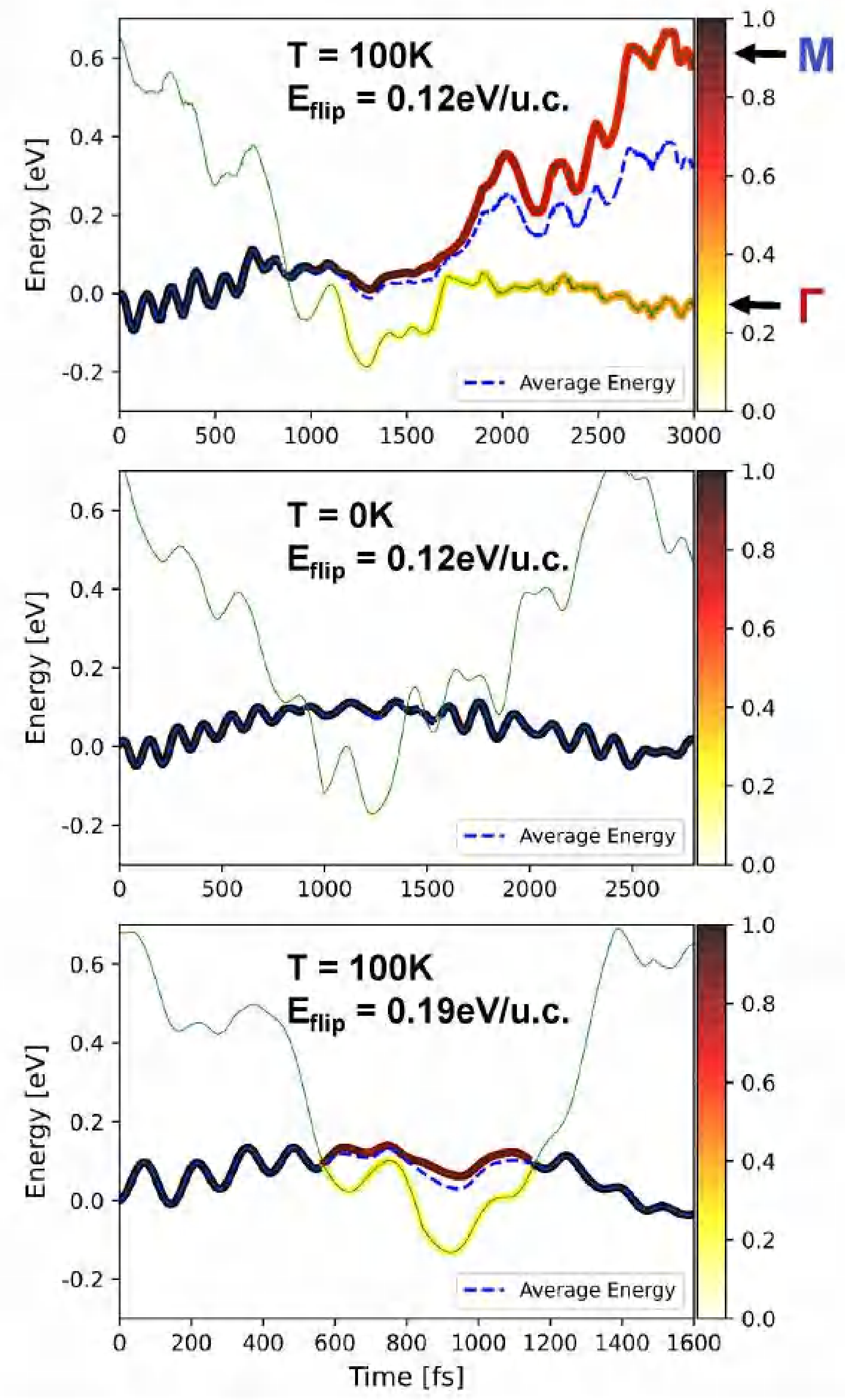

- Initially the electron set to Γ valley band. Due to the large interaction between two valleys, the energy degeneracy in second crossing point broken, leading to electron transition to M valley band, mainly induced by AD contribution.
- In zero-temperature reversal simulation, electron transition to M valley is forbidden in second crossing by lack of electron-phonon coupling (EPC), reveal that EPC is fundamentally for valley transfer dynamics.
- When apply larger flip velocity, the energy split in second crossing point decreased. The electron transition near the second crossing point mainly controlled by NA contribution, electron will stay at Γ valley. Thus the flip velocity also influences the valley transfer dynamics.

VI. Conclusion

- The monolayer In_2Se_3 CBM perform a Γ-M-Γ valley shift during the ferroelectric switching.
- The electron in the two valleys would relax to each other due to the adiabatic contribution at the second crossing.
- The intensity of EPC and flip velocity are two key factors that determine the extent of carrier transfer.

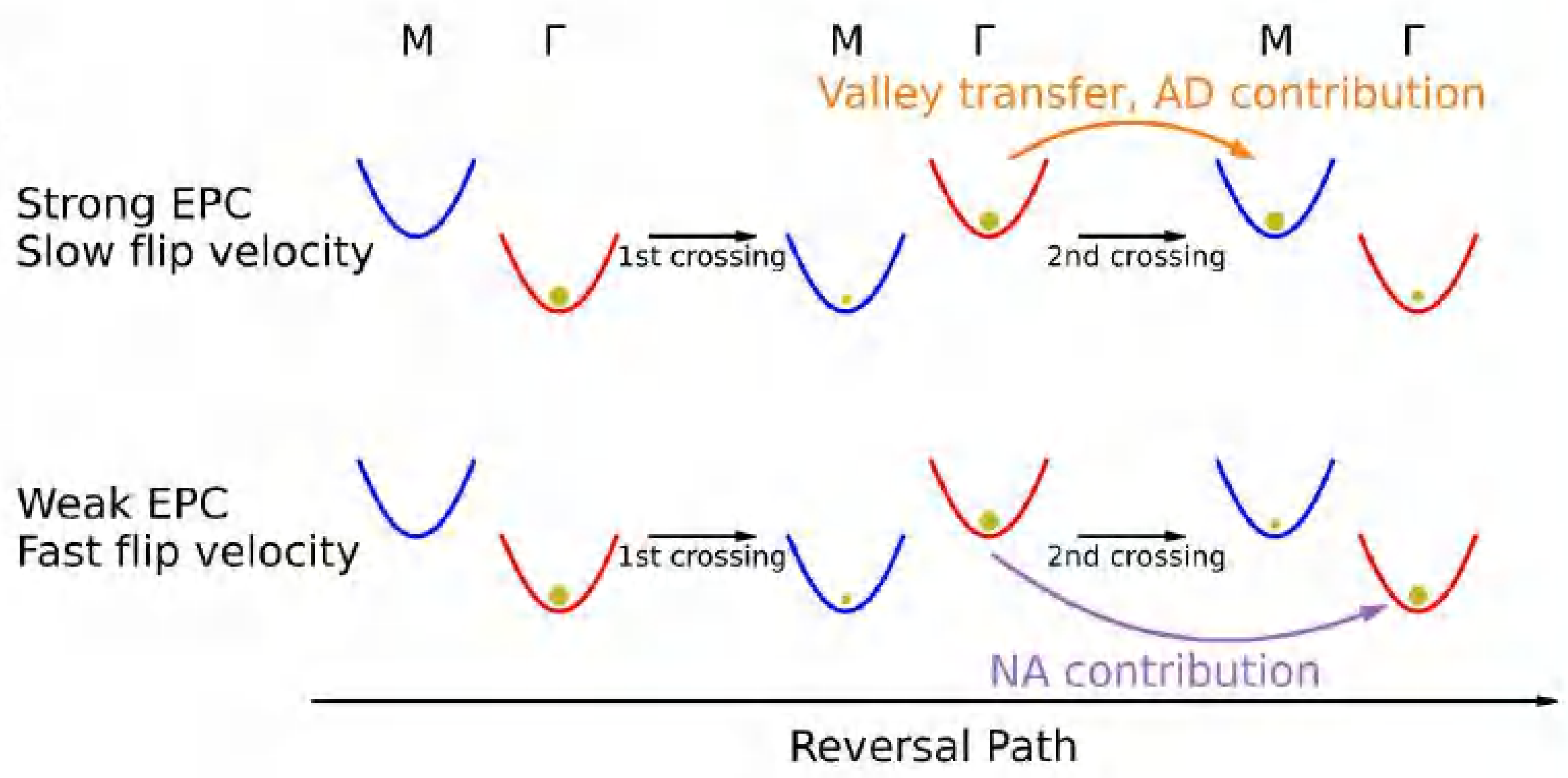

2022材料多尺度计算模拟国际会议

Tuning photoelectron dynamic behavior of thiolate-protected MAu24 nanoclusters via heteroatom substitution

Xueke Yu (于雪克), Yan Su (苏艳), Jijun Zhao (赵纪军)

Key Laboratory of Materials Modification by Laser, Ion and Electron Beams (Dalian University of Technology), Ministry of Education, 116024

E-mail: yxk@mail.dlut.edu.cn, su.yan@dlut.edu.cn

Abstract

Heteroatom substitution of gold nanoclusters enables precise tuning of their physicochemical properties at single-atom level, which has importance impact on the applications related to excited states including photovoltaic, photocatalysis and photo-luminescence. To this end, understanding the effect of metal exchange on the structures, electronic properties and photoexcited dynamic behavior of nanoclusters is imperative. Combining density functional theory with time-domain nonadiabatic molecular dynamics simulation, herein we explored the effect of metal replacement on electronic and vibrational properties as well as excited-state dynamics of ligand-protected $MAu_{24}(SR)_{18}$ (M = Pd, Pt, Cd, and Hg) nanoclusters. At atomistic level, we elucidate hot carrier relaxation and recombination dynamic behavior with various doping atoms. Such distinct excited-state behavior of $MAu_{24}(SR)_{18}$ nanoclusters is attributed to different energy gaps and electron–phonon coupling between the donor and acceptor energy levels, owing to the perturbation of nanocluster by single foreign atom. The specific phonon modes involved in excited-state dynamics have been identified, which are associated with the MAu_{12} core and ligand rings. This time-dependent excited-state dynamic study fills the gap between structure/composition and excited-state dynamic behavior of $MAu_{24}(SR)_{18}$ nanoclusters, which would stimulate the exploration of their applications involving photoenergy storage and conversion.

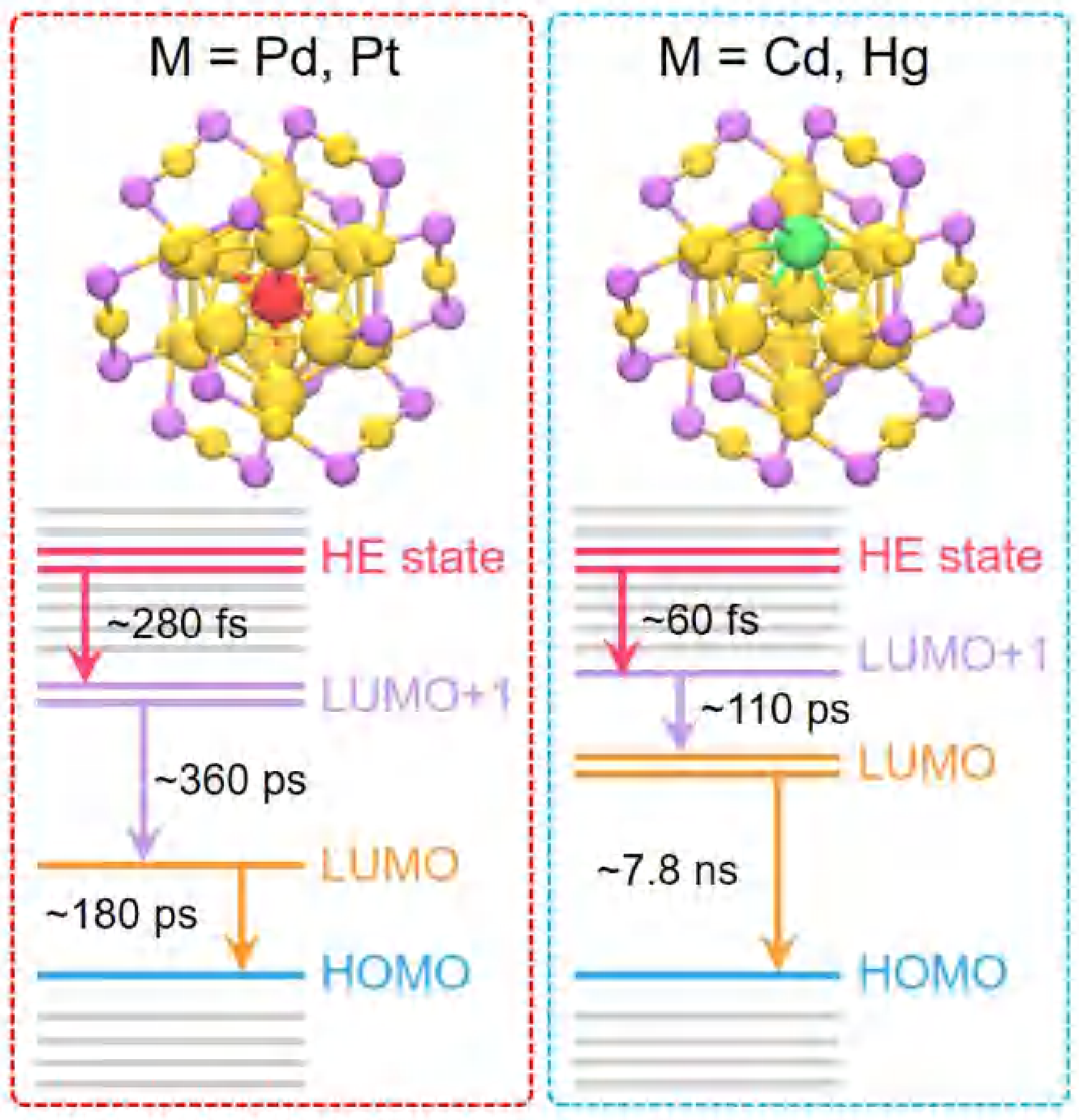

Fig. 1 Schematic illustration of photoexcited carrier dynamics of $MAu_{24}(SR)_{18}$ nanoclusters.

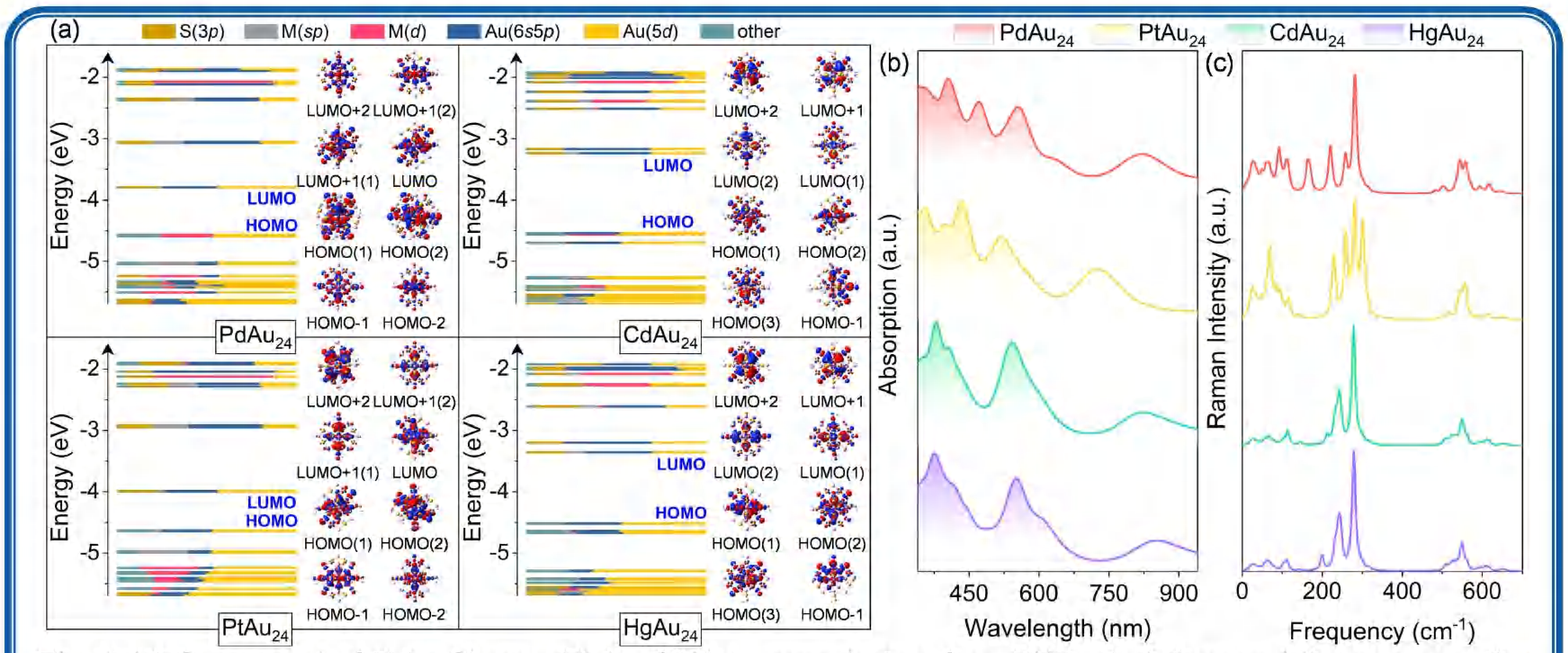

Fig. 2 (a) Component of Kohn-Sham orbitals of MAu_{24} nanoclusters from DFT calculations and the corresponding charge density distributions in range of HOMO–3 to LUMO+3. (b) The absorption spectra of MAu_{24} (M = Pd, Pt, Cd, and Hg) nanoclusters. (c) Raman spectra of MAu_{24} nanoclusters from DFT calculations.

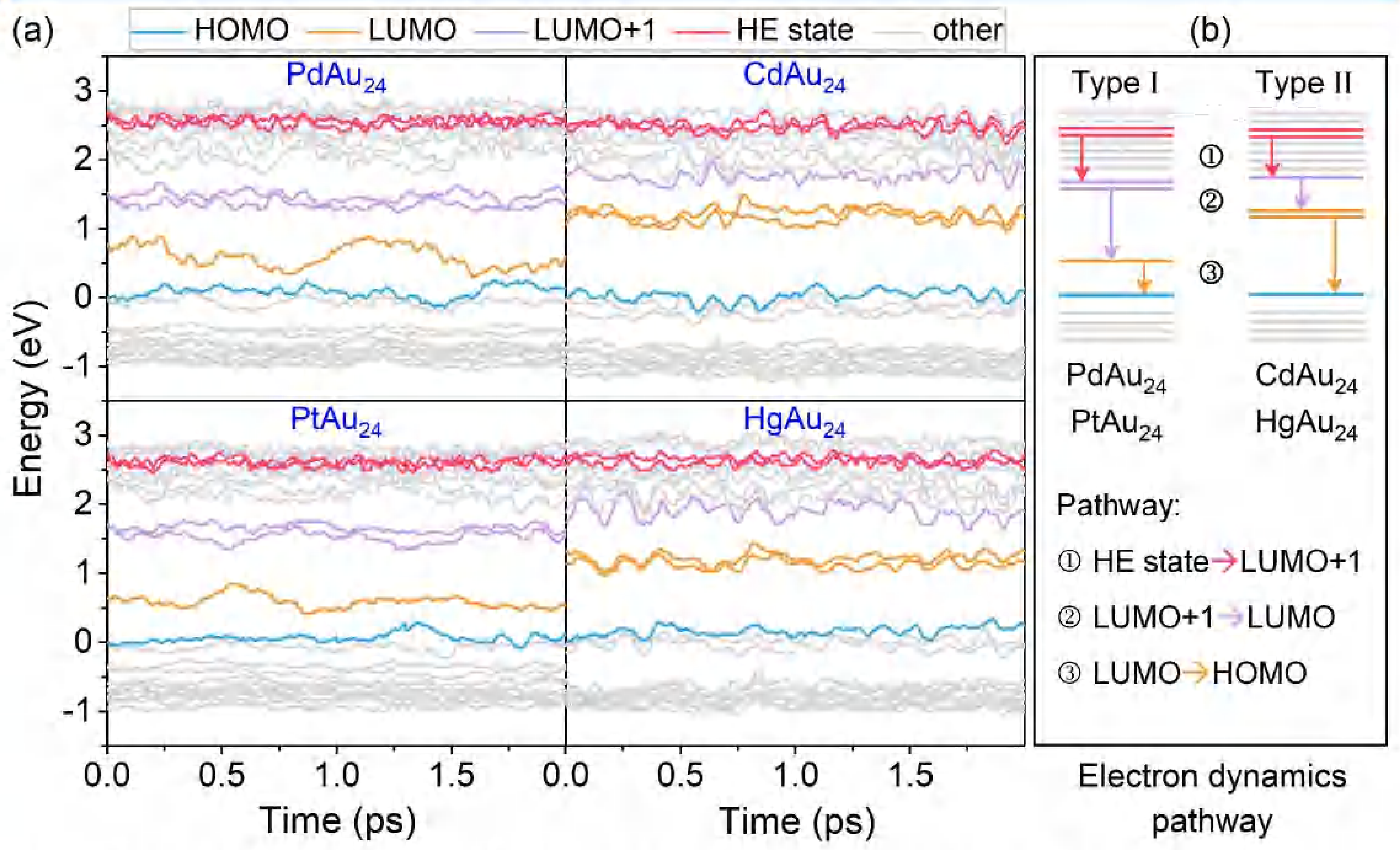

Fig. 3 The time evolution of key states for MAu_{24} nanoclusters. (b) Schematic diagram depicting the excited electron relaxation dynamics in MAu_{24} nanoclusters.

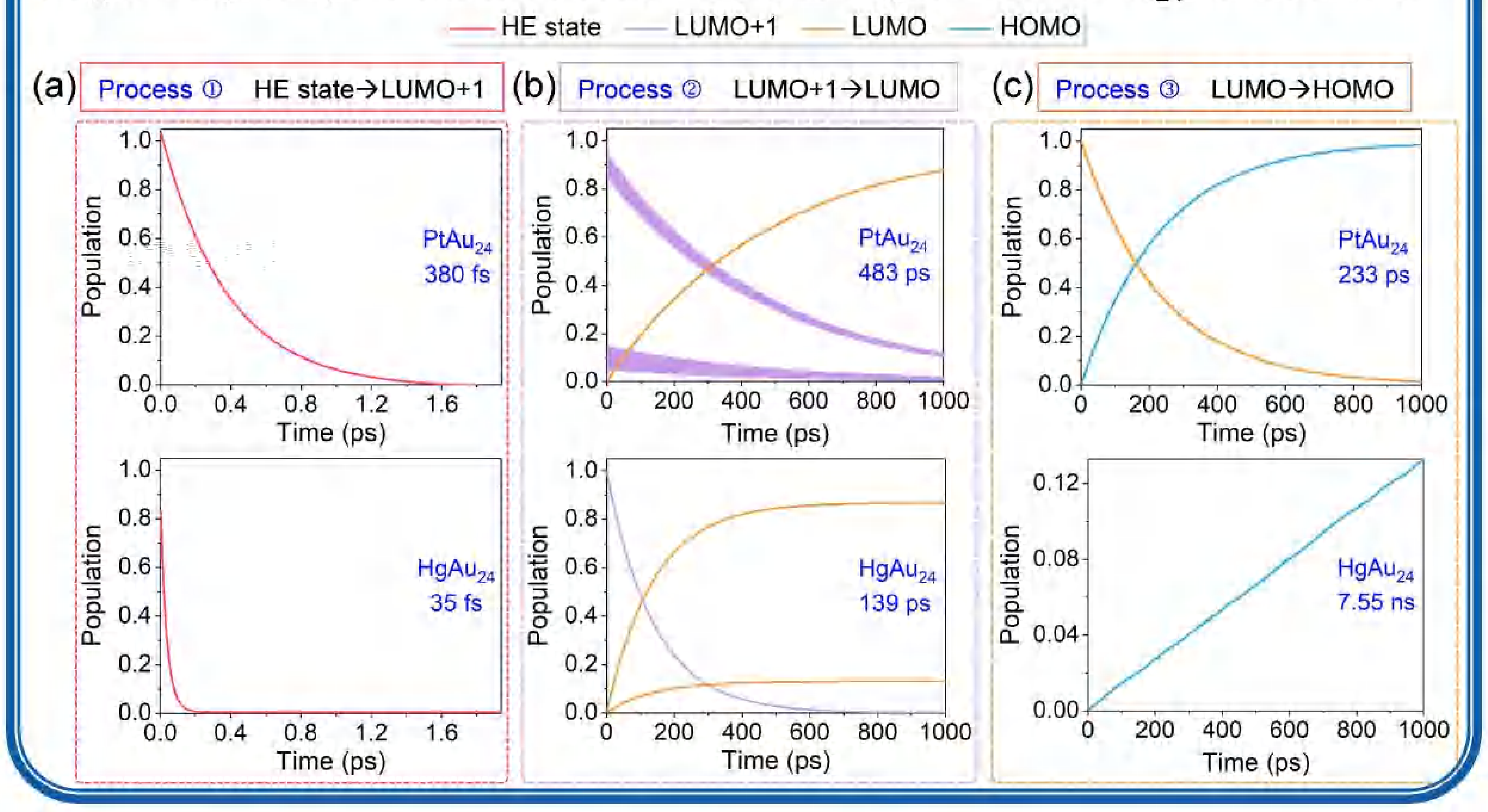

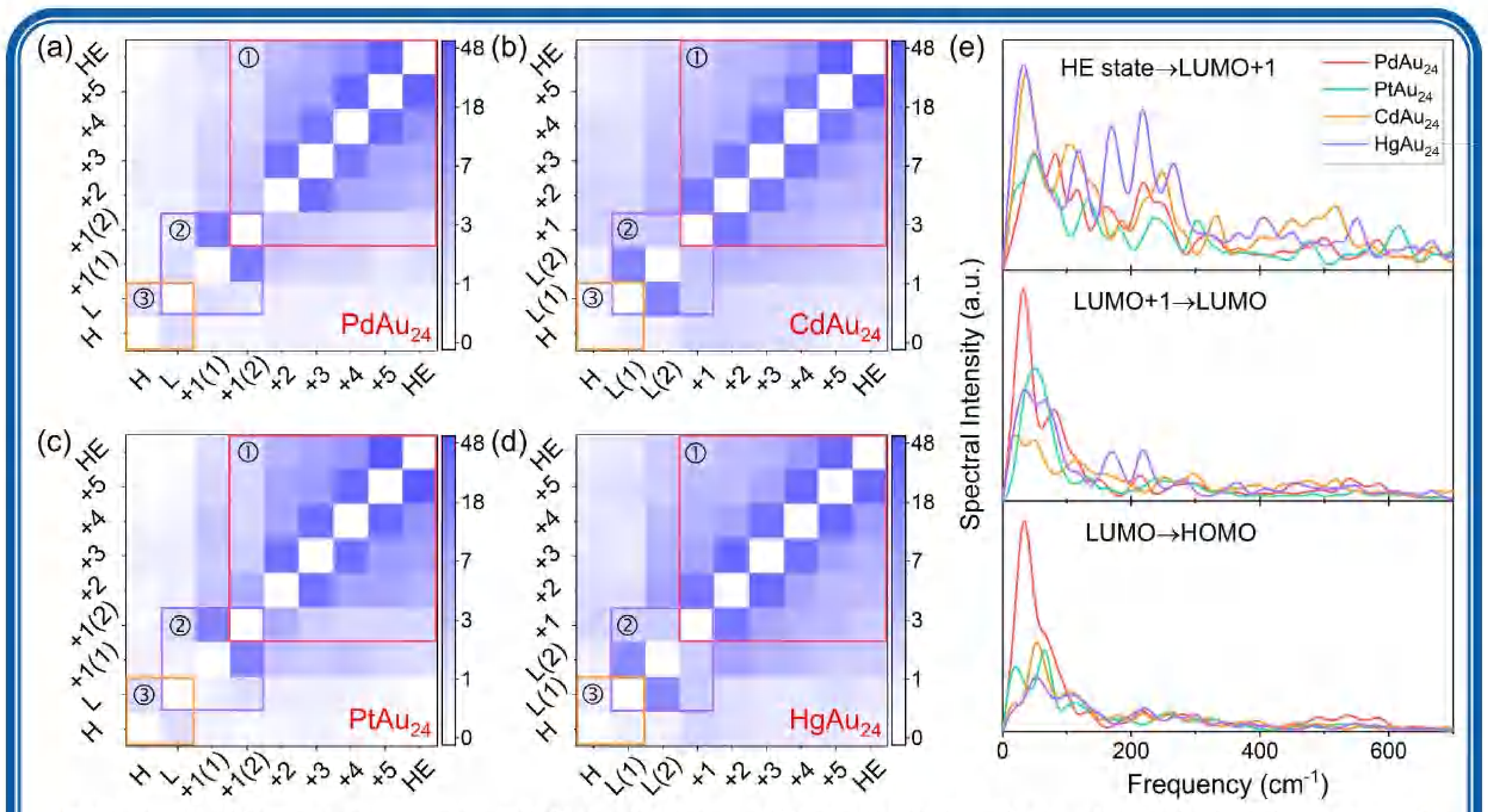

Fig. 4 (a-d) The average NAC between different states from HE states to HOMO. (e) Fourier transforms of the energy gap fluctuations of three processes.

Conclusion

✧The $MAu_{24}(SR)_{18}$ nanoclusters exhibit alterable energy gaps owing to the different strengths of *d-d* hybridization between Au and M dopants.

✧The incorporation of single foreign atom facilitates distinct excited-state behavior of $MAu_{24}(SR)_{18}$, which is ascribed to synergistic effect of energy gap, electron-phonon coupling, and decoherence time.

✧Vibrations of the MAu_{12} core and ligand rings are identified to be the dominant phonon modes involved in photocarrier dynamics.

✧For the electron-hole recombination dynamics, the difference of HOMO-LUMO gaps and MAu_{12} vibrations lead to nearly 100-fold difference in the carrier lifetimes of $MAu_{24}(SR)_{18}$ nanoclusters.

International Conference of Multi-scale Modeling and Simulation of MATERIALS(icm^3-2022)

Stochastic Artificial Synapses Made of Magnetic Domain Walls

Cen Wang[a)], Kuan Wang[a)], Xinyu Wen, Yuhui He*, Yue Zhang*
School of Optical and Electronic Information, Huazhong University of Science and Technology

Abstract

An artificial synapse hardware based on silicon complementary metal oxide semiconductor in spiking neural network (SNN) always needs complex device structure to realize multi resistance states, which requires a large area and a high power. How to adjust more states with fewer devices is challenging. This paper proposes a stochastic synapse hardware based on probabilistic generation and deterministic motion of magnetic domain walls driven by spin currents. The probabilistic generation of the DWs updates the weight stochastically. And the deterministic DW motion brings about multi states. The proposed structure could use fewer devices to implement more resistance states, which improves the flexibility of weight adjustment at a fixed device size. As an example, we show that a SNN based on this stochastic synapse could classify the breast cancer data with a high accuracy of 95.76%.

Introduction and motivation

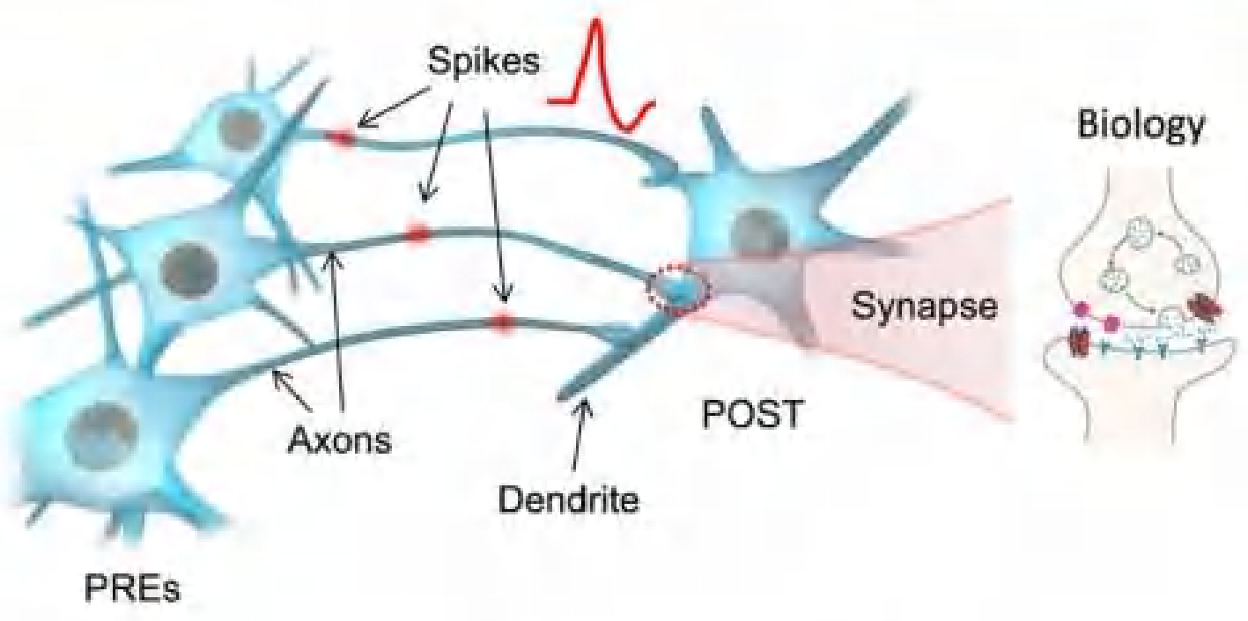

Science advances, 2018, 4(9): eaat4752.

Spiking Neural Network (SNN)

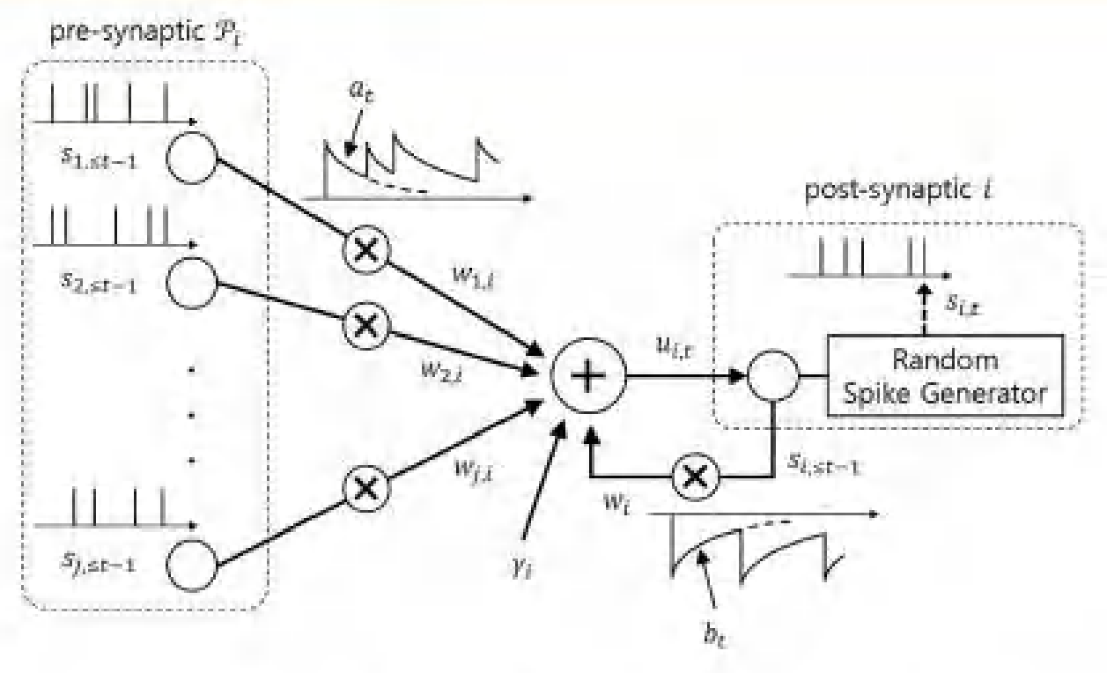

IEEE Signal Processing Magazine, 2019, 36(6): 64-77.

Stochastic neuron in SNN

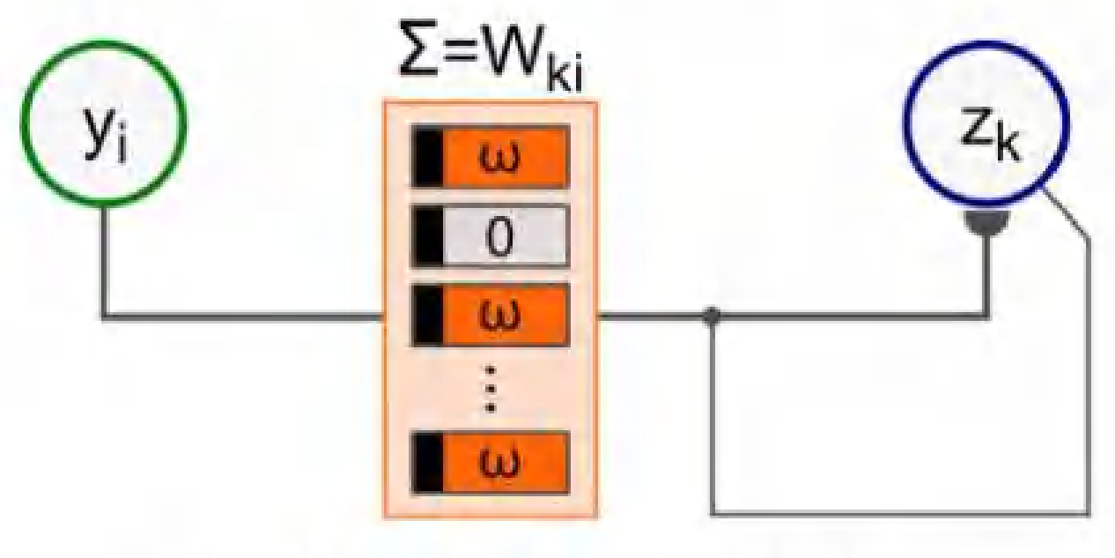

Frontiers in neuroscience, 2014, 8: 412.

Stochastic synapse in SNN

A synapse made of M memristors		
Memristor	Number of states	States
Deterministic binary	2	0, $M \times \omega$
Stochastic binary	M+1	0, ω, 2ω, … $M \times \omega$
Stochastic multiple (X)	**$M \times X$+1**	**0,…, X,…, $M \times X$**

More adjustable states in a stochastic multi-state memristor!

Models and methods

A stochastic DW memristor model

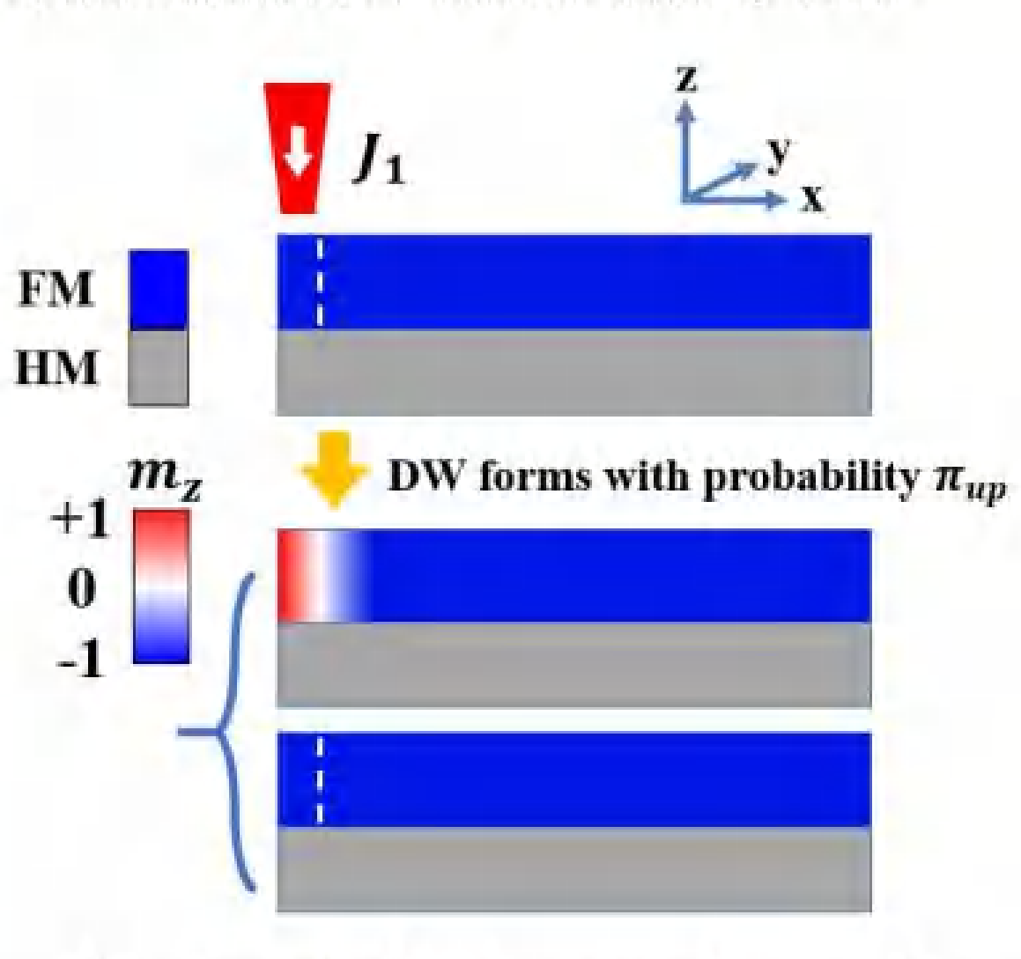

Stochastic DW generation under spin transfer torque (STT)

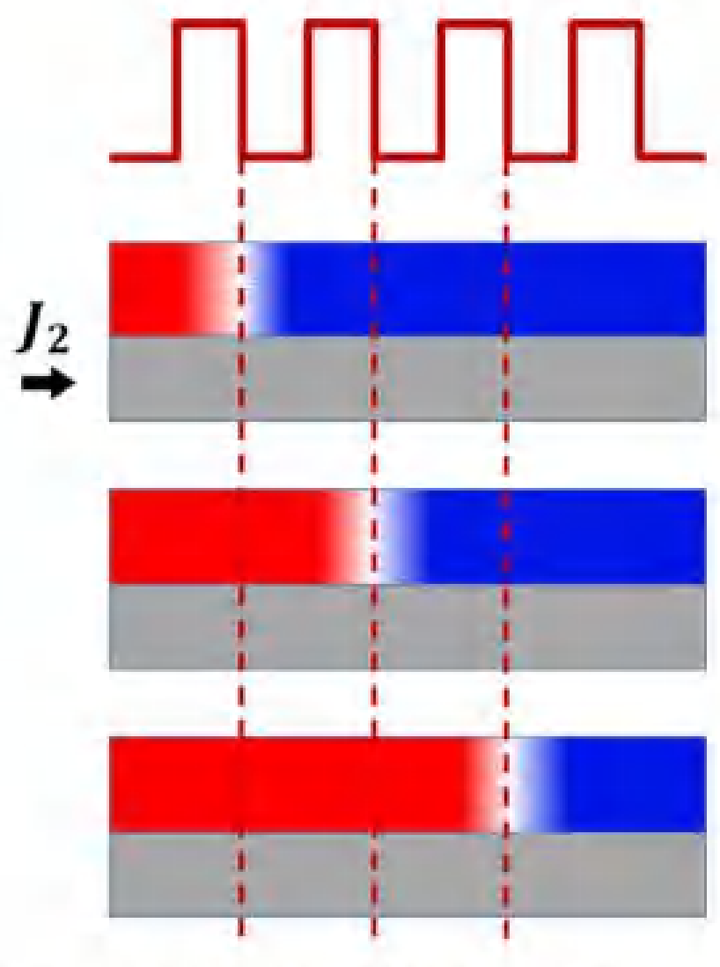

Deterministic DW motion under spin orbit torque (SOT)

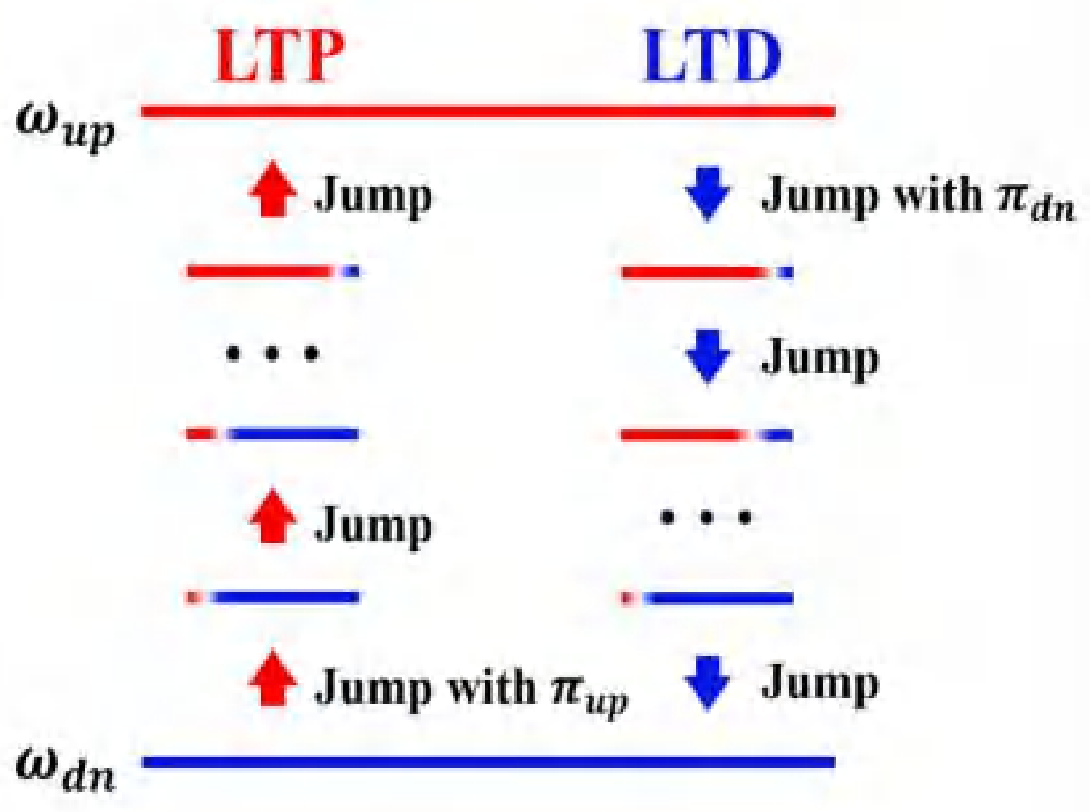

Weight adjustment

Software: Object Oriented Micro–Magnetic Framework with a code of thermal fluctuation

Method: Numerically solving the stochastic Landau–Lifshitz–Gilbert equation:

$$\frac{d\vec{m}}{dt} = -\gamma_0 \vec{m} \times \vec{H}_{eff} + \alpha\left(\vec{m} \times \frac{d\vec{m}}{dt}\right) + \vec{\tau}_{STT} + \vec{\tau}_{SOT}$$

$\vec{H}_{eff}$: Exchange, Demagnetization, Anisotropy, Dzyaloshinskii-Moriya interaction, Thermal fluctuation

Parameters	values
Damping constant α	0.27
Spin polarization P	0.4
Spin hall angle θ_{SH}	0.4
Saturation magnetization M_S	9.1×10^5 A/m
Exchange constant A	2×10^{-11} J/m
Magnetic anisotropy constant K	2×10^6 J/m^{-3}
DM interaction constant D	1.5 mJ/m^{-2}

Stochastic DW generation and deterministic DW motion

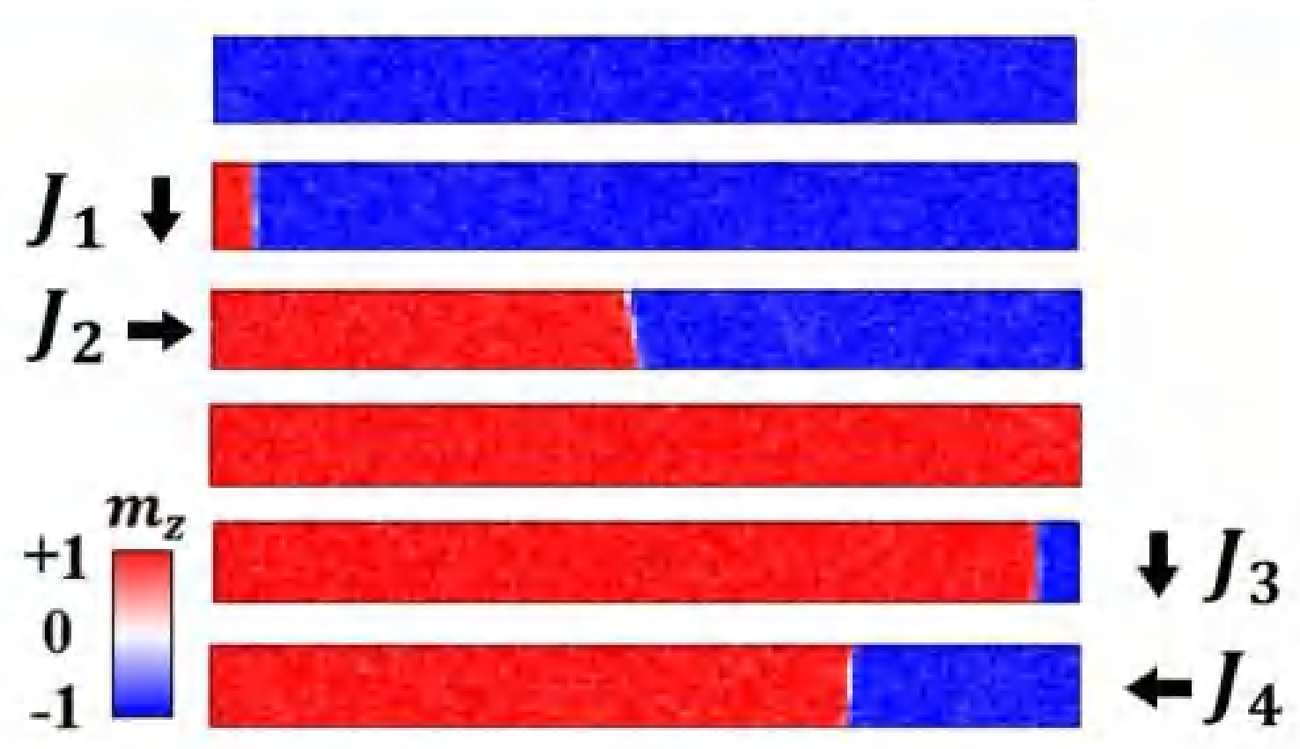

Snapshots of DW generation and motion

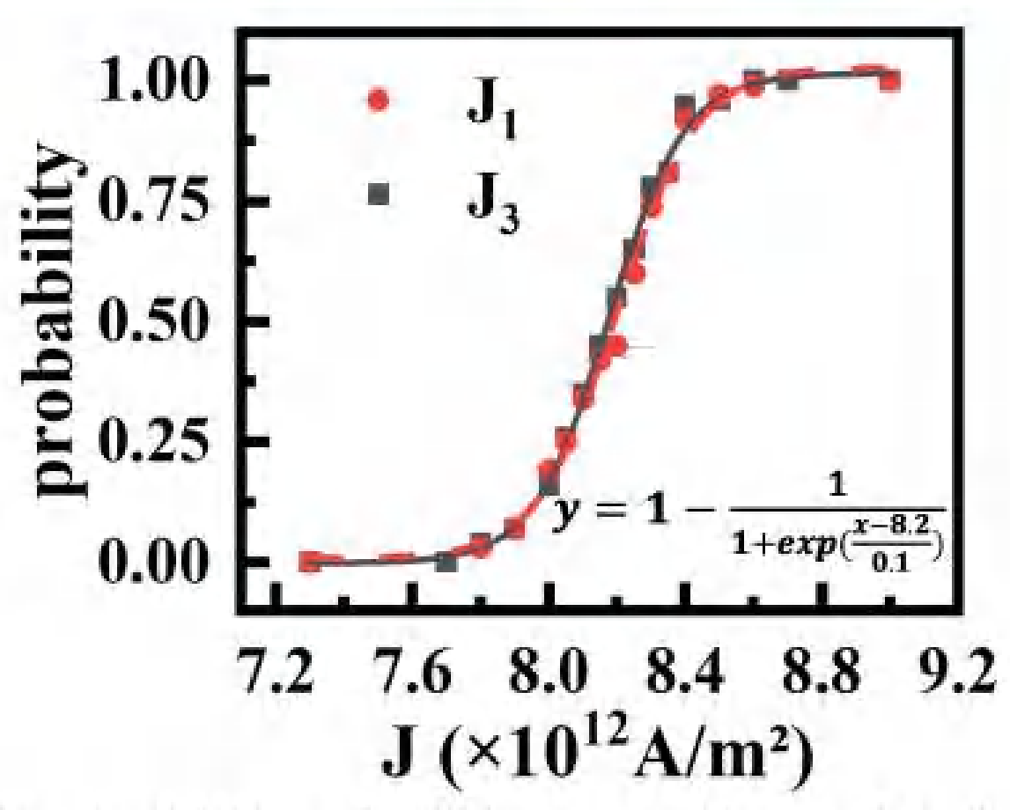

Probability of DW generation with J_1 and J_3

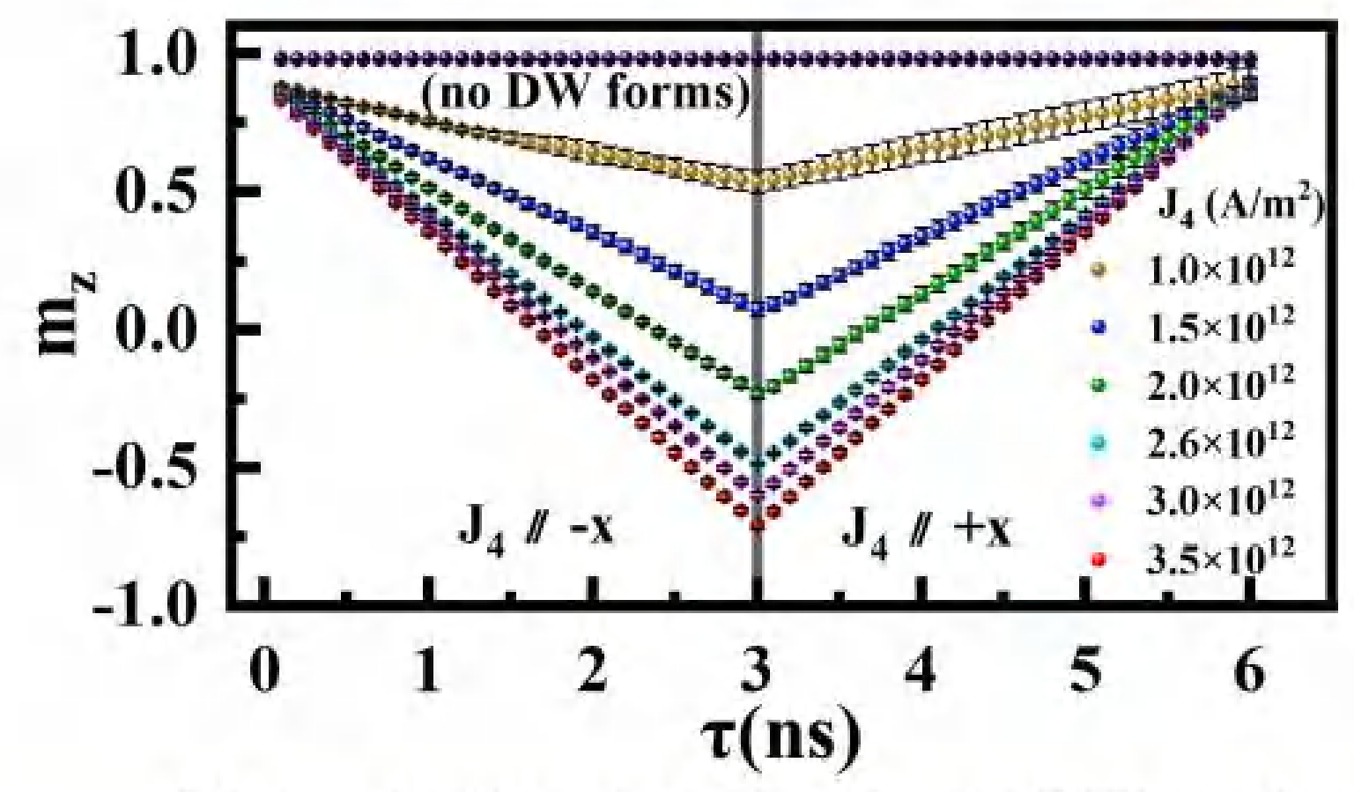

Magnetization changing due to DW motion

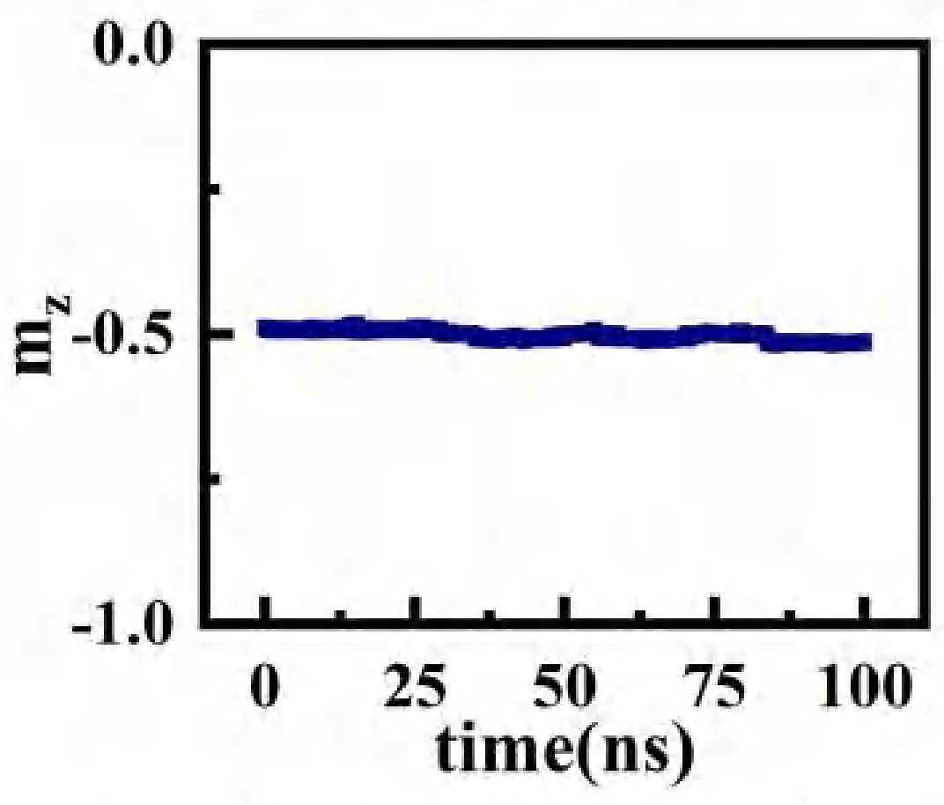

Nonvolatility of a DW memristor

Weight adjustment in a single synapse

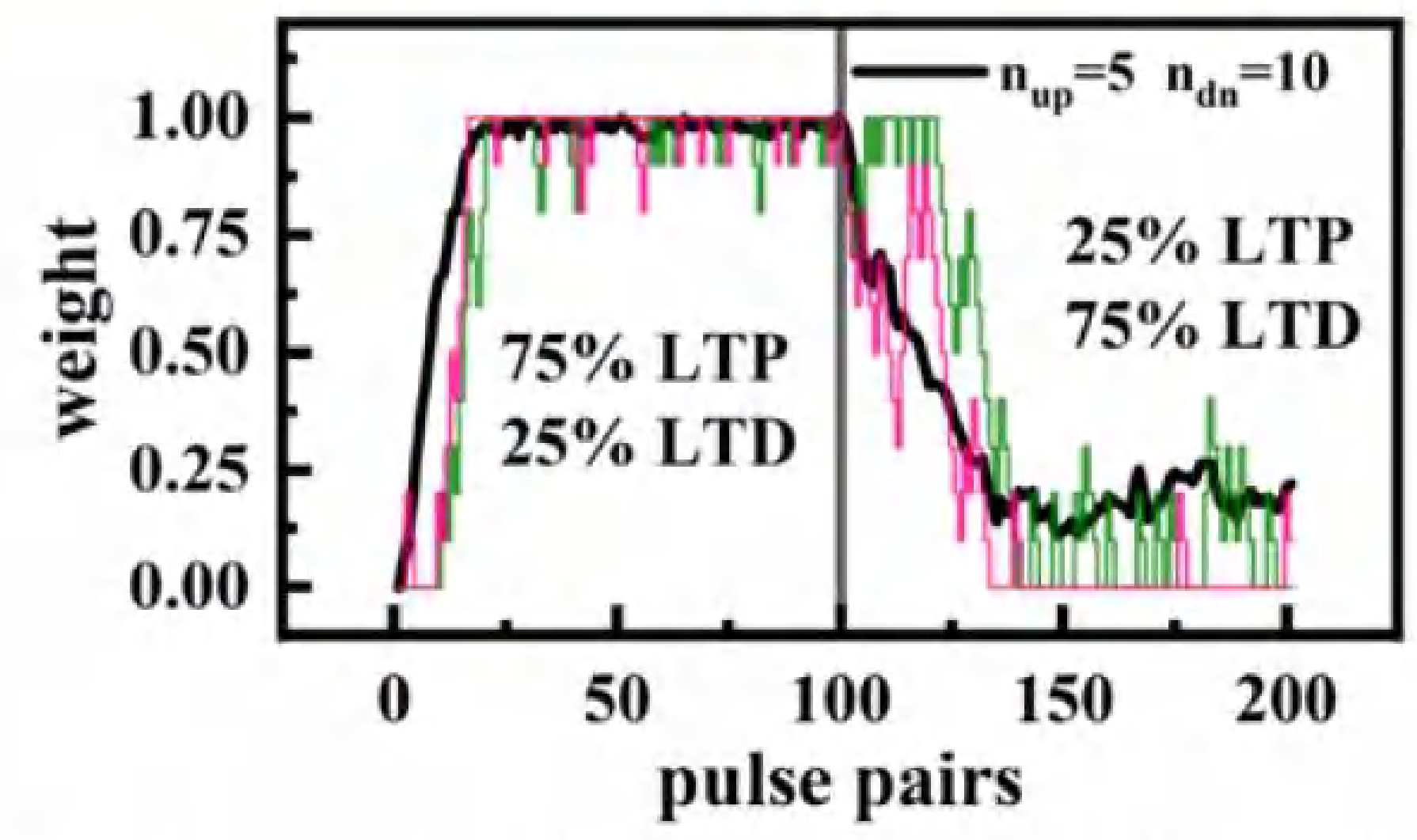

n_{up}=5: 5 weights in LTP
n_{up} =10: 10 weights in LTD
Software: Python3.10.0
Black line: Average weight over 20 runs
Pink and green lines: Two examples

Training for weight adjustment of a single stochastic DW synapse

SNN made of stochastic DW synapses and its application

A stochastic synapse based on *M* DW memristors

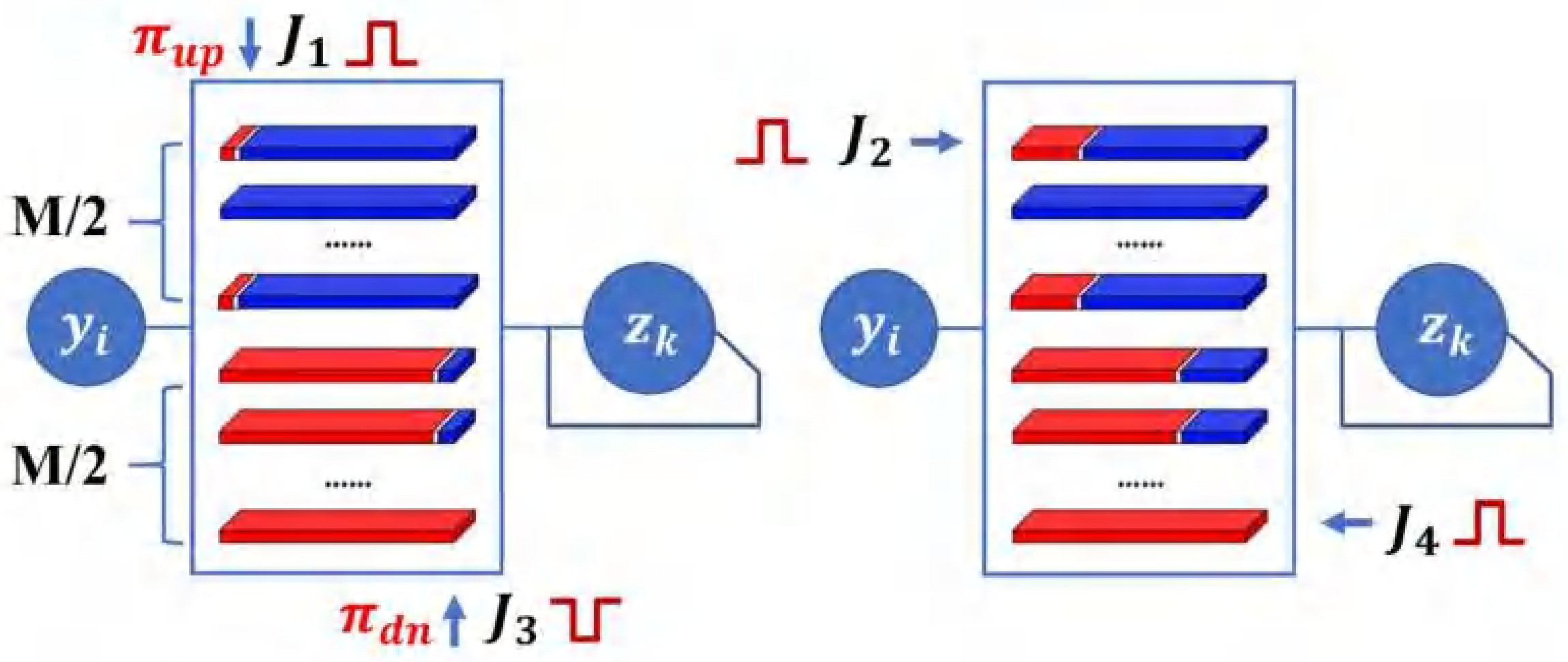

Long term potentiation (LTP): $\Delta W_{LTP} = \sum_{j=1}^{n_{up}} \Delta W_j$

weight	0	$\Delta\omega/n_{up}$	$2\times\Delta\omega/n_{up}$	…	$n_{up}\times\Delta\omega/n_{up}$
label (j)	0	1	2	…	n_{up}
number(m_j)	m_0	m_1	m_2	…	$m_{n_{up}}$

j	ΔW_1
1	$(m_0\pi_{up} - m_1)\Delta\omega/n_{up}$
(1, n_{up})	$(m_{j-1} - m_j)j\Delta\omega/n_{up}$
n_{up}	$m_{n_{up}}\Delta\omega$

m_z = –1: ω_{dn}
m_z = +1: ω_{up}
$\Delta\omega$: ω_{up} –ω_{dn}

$$\frac{d}{dt}W_{ki} = s_k(t)[m_P \times T_P \times \omega_P \times y_i(t) + m_D \times T_D \times \omega_D \times \left(1 - y_i(t)\right)\boxtimes$$

$$\text{LTP: } m_P = [m_0 \quad \cdots \quad m_j \quad \cdots \quad m_{n_{up}}];\ T_P = \begin{bmatrix} -\pi_{up} & \pi_{up} & 0 & 0 & \cdots & 0 \\ 0 & -1 & 1 & 0 & \cdots & 0 \\ 0 & 0 & -1 & 1 & \cdots & 0 \\ \vdots & \ddots & \ddots & \ddots & \ddots & \vdots \\ \vdots & \ddots & \ddots & \ddots & \ddots & 1 \\ 0 & 0 & \cdots & \cdots & \cdots & 0 \end{bmatrix};\ \omega_P = \begin{bmatrix} 0 \\ \Delta\omega/n_{up} \\ 2 \times \Delta\omega/n_{up} \\ \vdots \\ n_{up} \times \Delta\omega/n_{up} \end{bmatrix}$$

$$\text{LTD: } m_D = [m_0 \quad \cdots \quad m_j \quad \cdots \quad m_{n_{dn}}];\ T_D = \begin{bmatrix} 0 & 0 & 0 & 0 & \cdots & 0 \\ 1 & -1 & 0 & 0 & \cdots & 0 \\ 0 & 1 & -1 & 0 & \cdots & 0 \\ \vdots & \ddots & \ddots & \ddots & \ddots & \vdots \\ \vdots & \ddots & \ddots & \ddots & -1 & 0 \\ 0 & 0 & \cdots & \cdots & \pi_{dn} & -\pi_{dn} \end{bmatrix};\ \omega_D = \begin{bmatrix} 0 \\ \Delta\omega/n_{dn} \\ 2 \times \Delta\omega/n_{dn} \\ \vdots \\ n_{dn} \times \Delta\omega/n_{dn} \end{bmatrix}$$

- $\pi = \pi_{up} = \pi_{dn} = 0$: $m_P = [M/2 \quad 0 \quad \cdots \quad 0]$, $m_P \times T_P = [0 \quad \cdots \quad 0]$
  $m_D = [0 \quad \cdots \quad 0 \quad M/2]$, $m_D \times T_D = [0 \quad \cdots \quad 0]$

  No DW forms, and the weight doesn't update.

- $\pi = \pi_{up} = \pi_{dn} = 1$: $\frac{d}{dt}W_{ki} = N_m \Delta\omega s_k(t) \boxtimes \frac{y_i(t)}{n_{up}} + \frac{[1-y_i(t)]}{n_{dn}} \boxtimes$

  Introducing the probability improves the flexibility of the weight manipulation.

SNN made of stochastic DW synapses for classifying a breast cancer

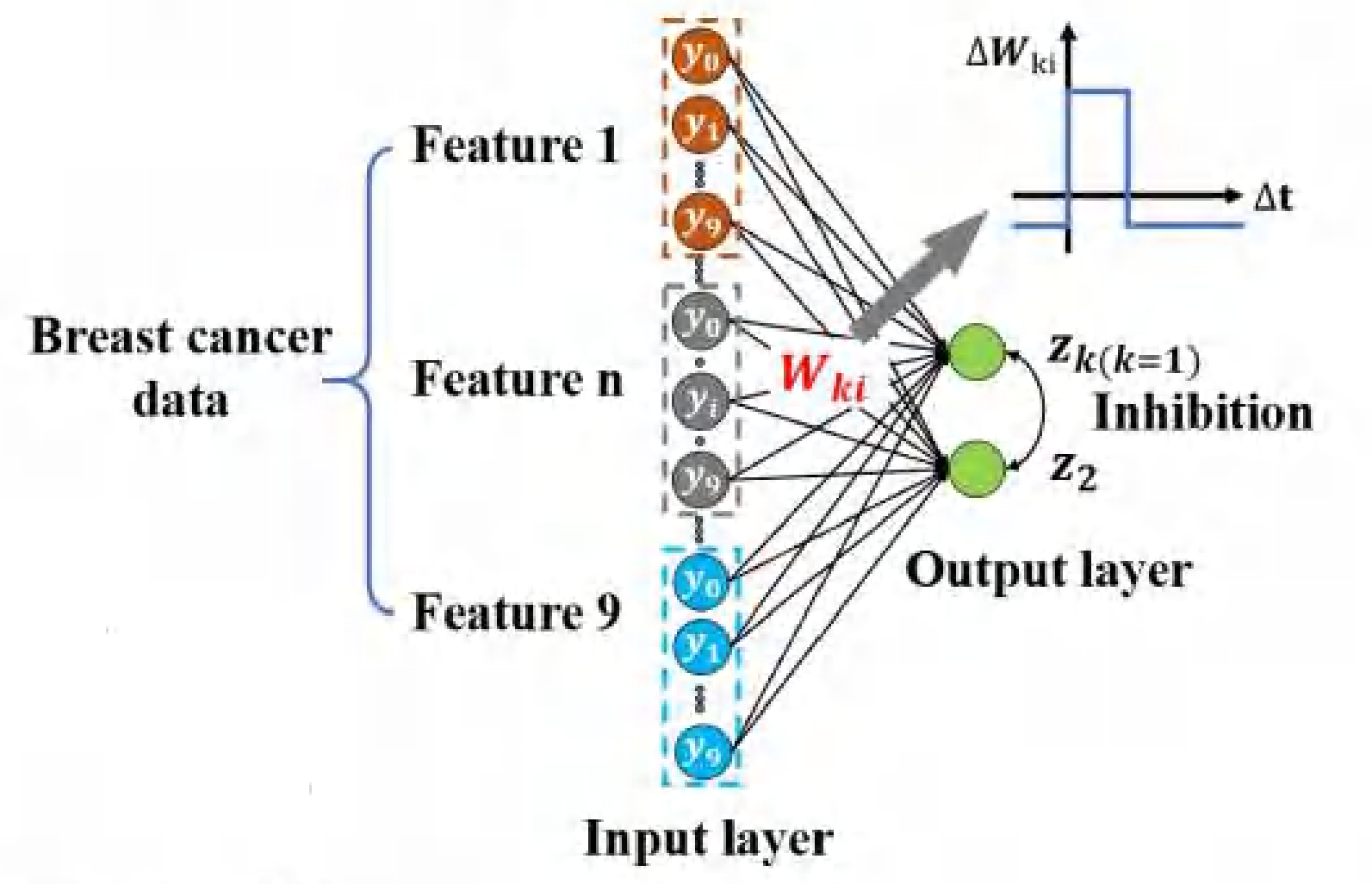

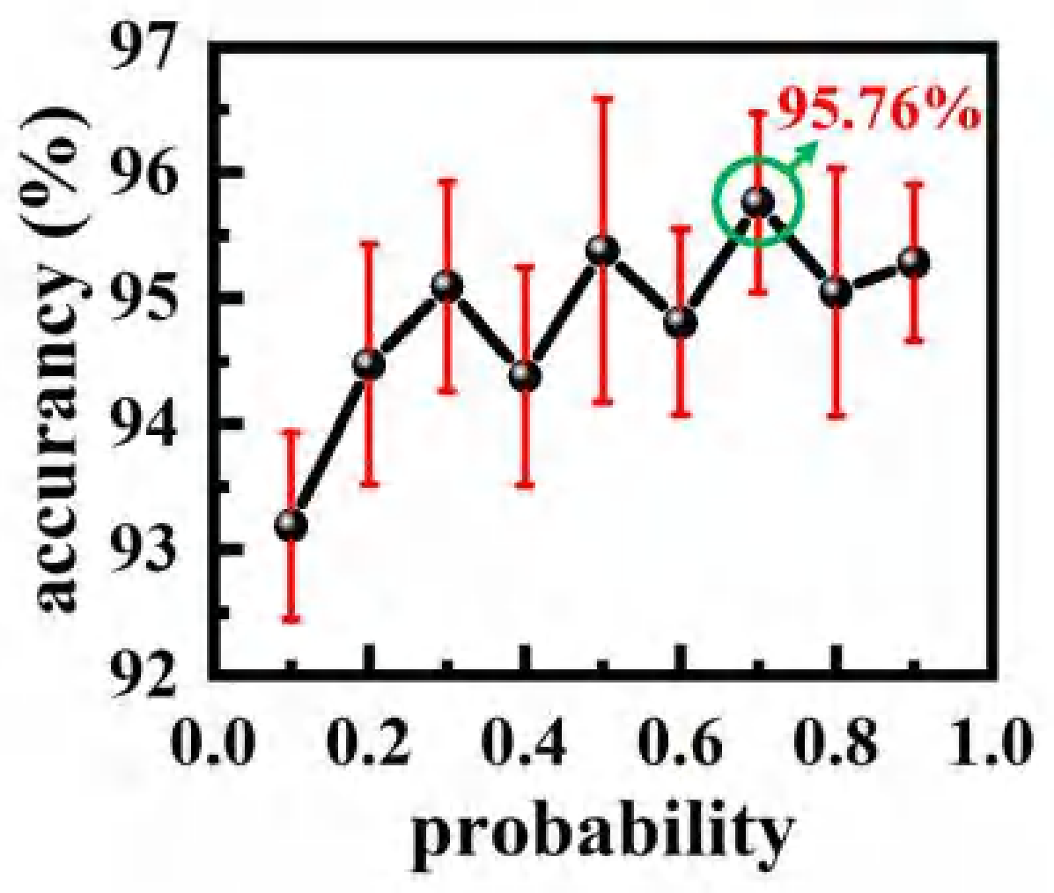

$\pi = \pi_{up} = \pi_{dn} = 1$:

No difference between two outputs for the same inputs and two identical deterministic synapses

Conclusion

We proposed a multi-state nonvolatile artificial synapse based on probabilistic generation and deterministic motion of magnetic DWs under spin current. Because of the stochastic DW generation at 300 K, the weight could be adjusted in a wide range with very few memristors. As a typical example for application, this stochastic synapse model was used in an SNN to classify the breast cancer, and the highest accuracy reached 95.76%.

Contact information

*Email: yue-zhang@hust.edu.cn<Yue Zhang>; heyuhui@hust.edu.cn <Yuhui He>
a) Cen Wang and Kuan Wang contributed equally to this work

23th International Conference of
Multi-scale Modeling and Simulation of Materials
Junly 4-8, 2022, Chengdu, China

Study on the conformation, spectrum, and properties of Paxlovid in different solvents: Part I, Nirmatrelvir

Yunlu Li [a,b,*], **Wenwu Shi**[a,b], **Zhenlong Tu**[a,b], **Bangjin Sun**[a,b], **Mei Xue**[c,*], **Xinzhong Wang**[a,*]

a Department of Electronic Communication and Technology, Shenzhen Institute of Information Technolog, Shenzhen, 518172, China
b School of materials and Energy, University of Electronic Science and Technology of China, Chengdu, 610054, China
c Shool of Materials Science & Engineering, Beijing Institute of Technology, Beijing, 100081, China

Introduction

- As COVID-19 spread around the world, it is urgent to develop oral coronavirus drugs.
- Pfizer's oral antiviral drug Paxlovid (Nirmatrelvir/ritonavir) has a cure rate of 89%, but there is no message about structure, confomation, and physical chemical information about it.
- In this work, the conformation of Nirmatrelvir in gas and different solvents were searched.
- Orbital, spectra (IR, Raman, ROA, ECD, UV-vis), reactivity, and intramolecular interaction was analyzed.

Methods

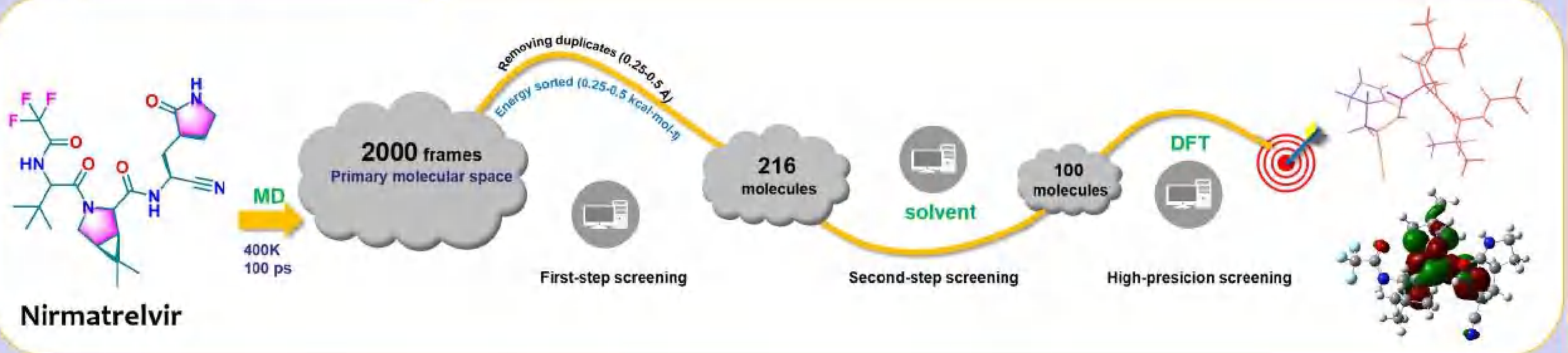

Nirmatrelvir

- Initial MD simulation (GNF0-xTB) using XTB package.
- Coarse-grained optimization (GNF0-xTB) using XTB package.
- Middle-level optimization (GNF2-xTB) using XTB package.
- Precise optimization (B3LYP-D3(BJ)/6-31G* using Gaussian 16 package.
- TD-DFT (PBE1PBE/TZVP) using Gaussian 16 package.
- Energy calculation (PWB95-D3(BJ)/def2-QZVPP) using ORCA 5.02 package.

Conformation

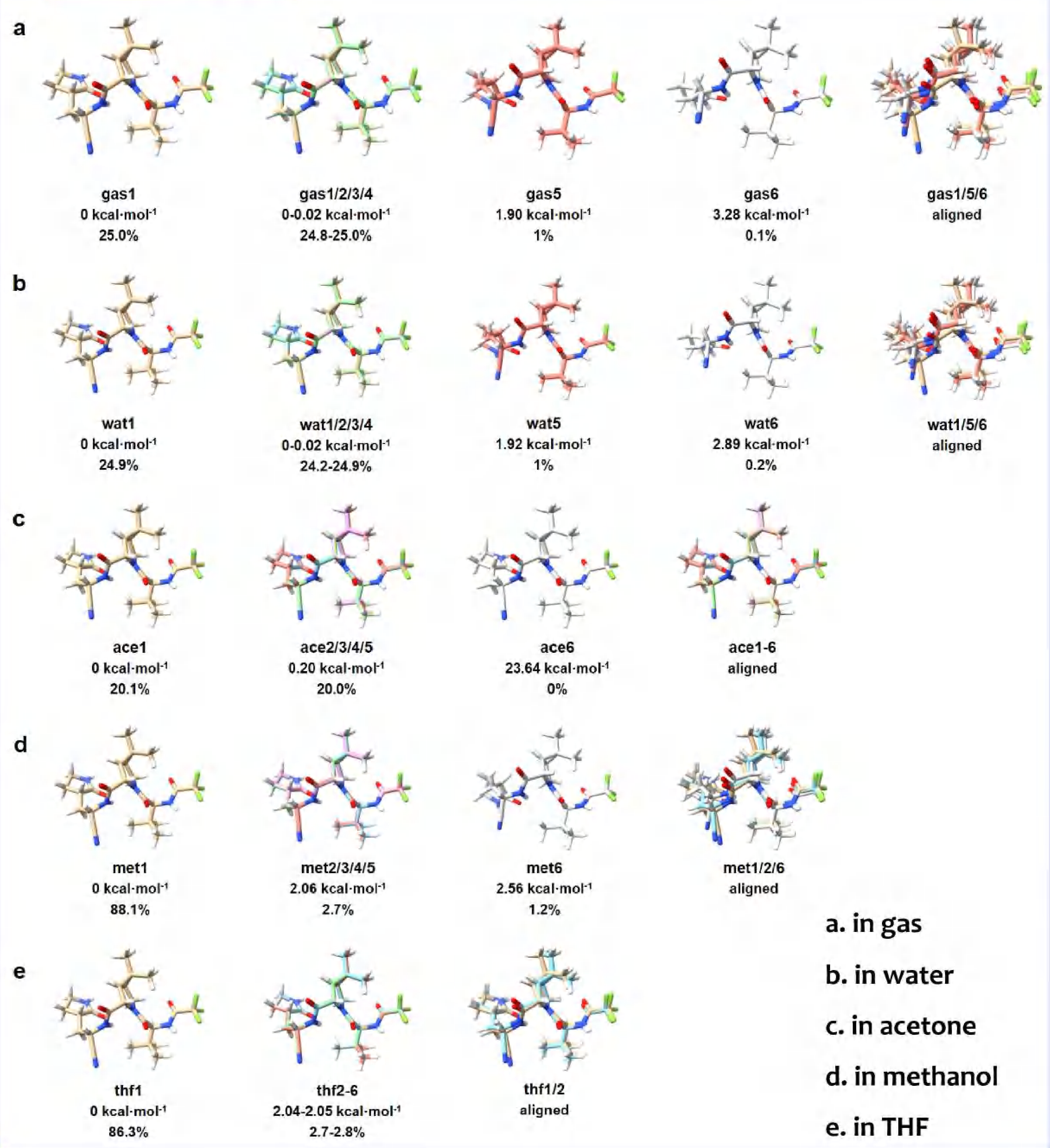

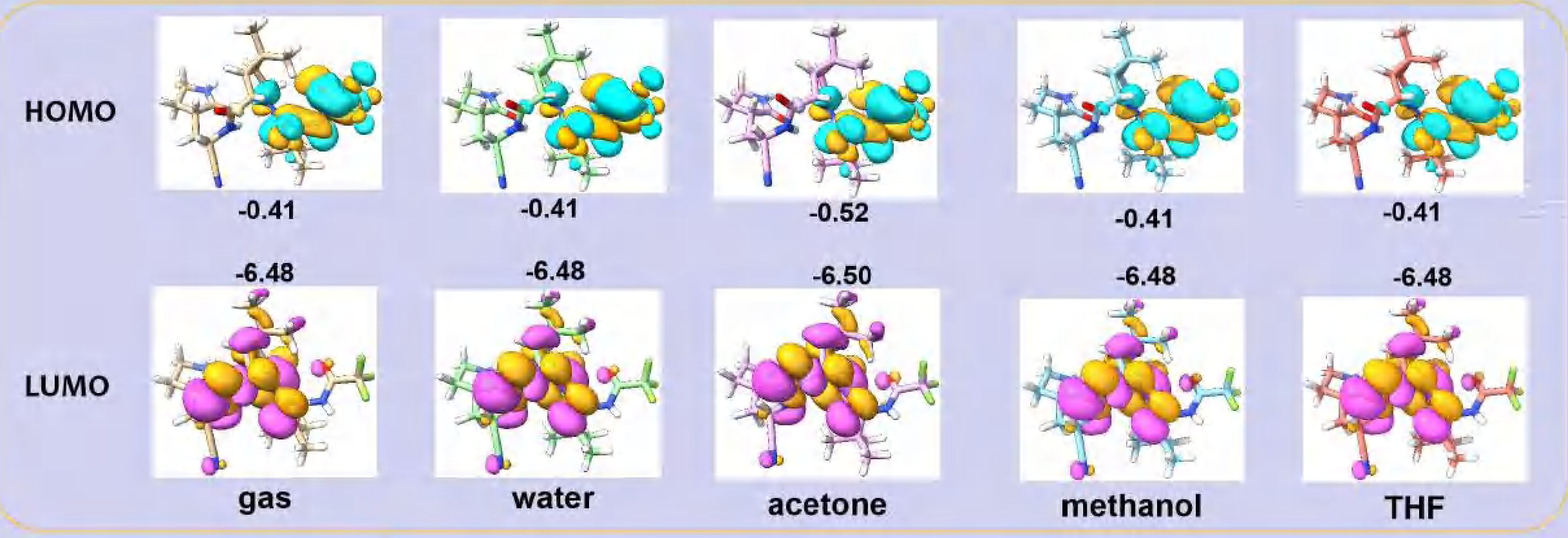

Vibration

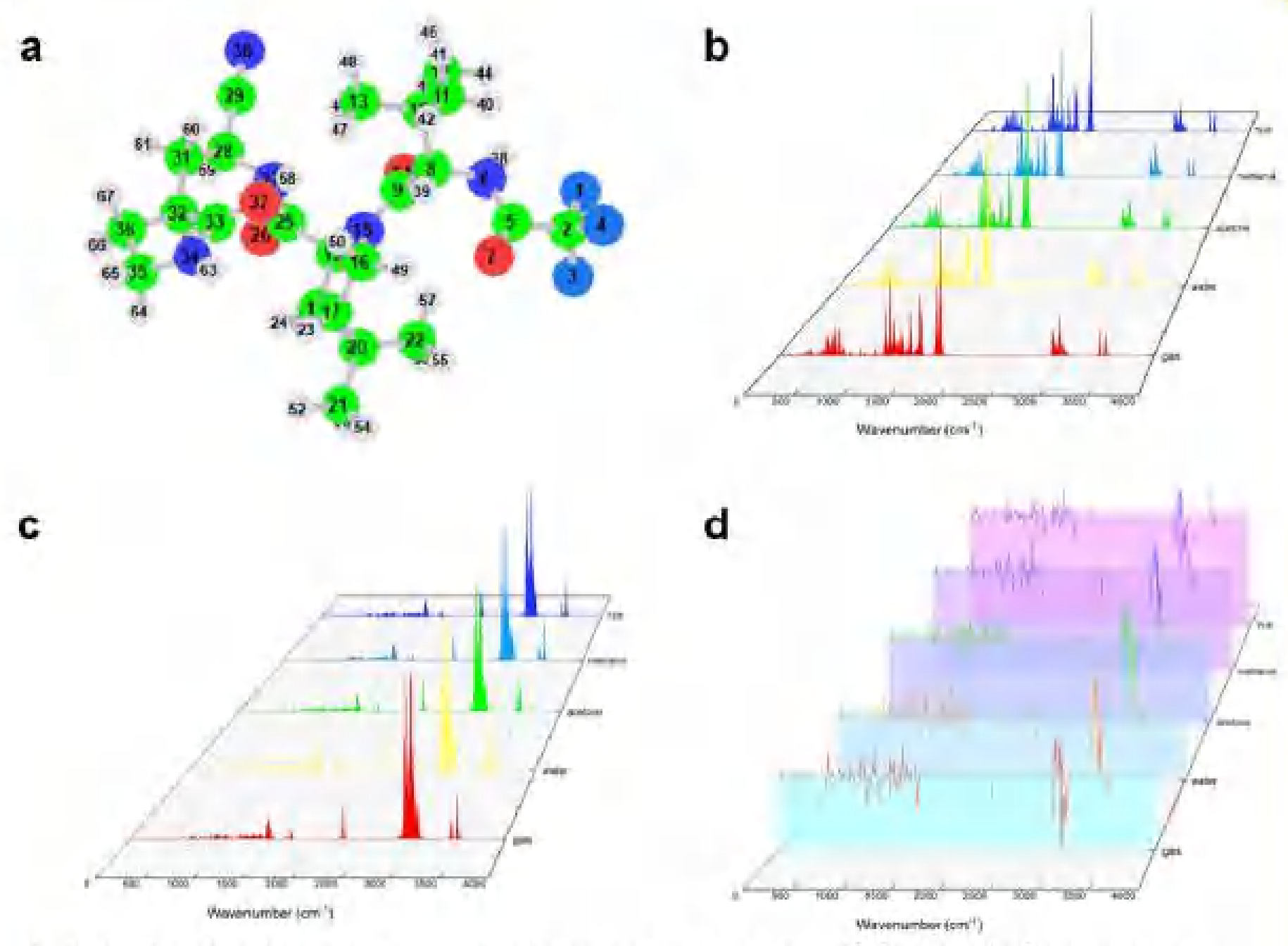

(a) Labeled structure of nirmatrelvir, (b) IR, (c) Raman (532nm), (d) ROA.

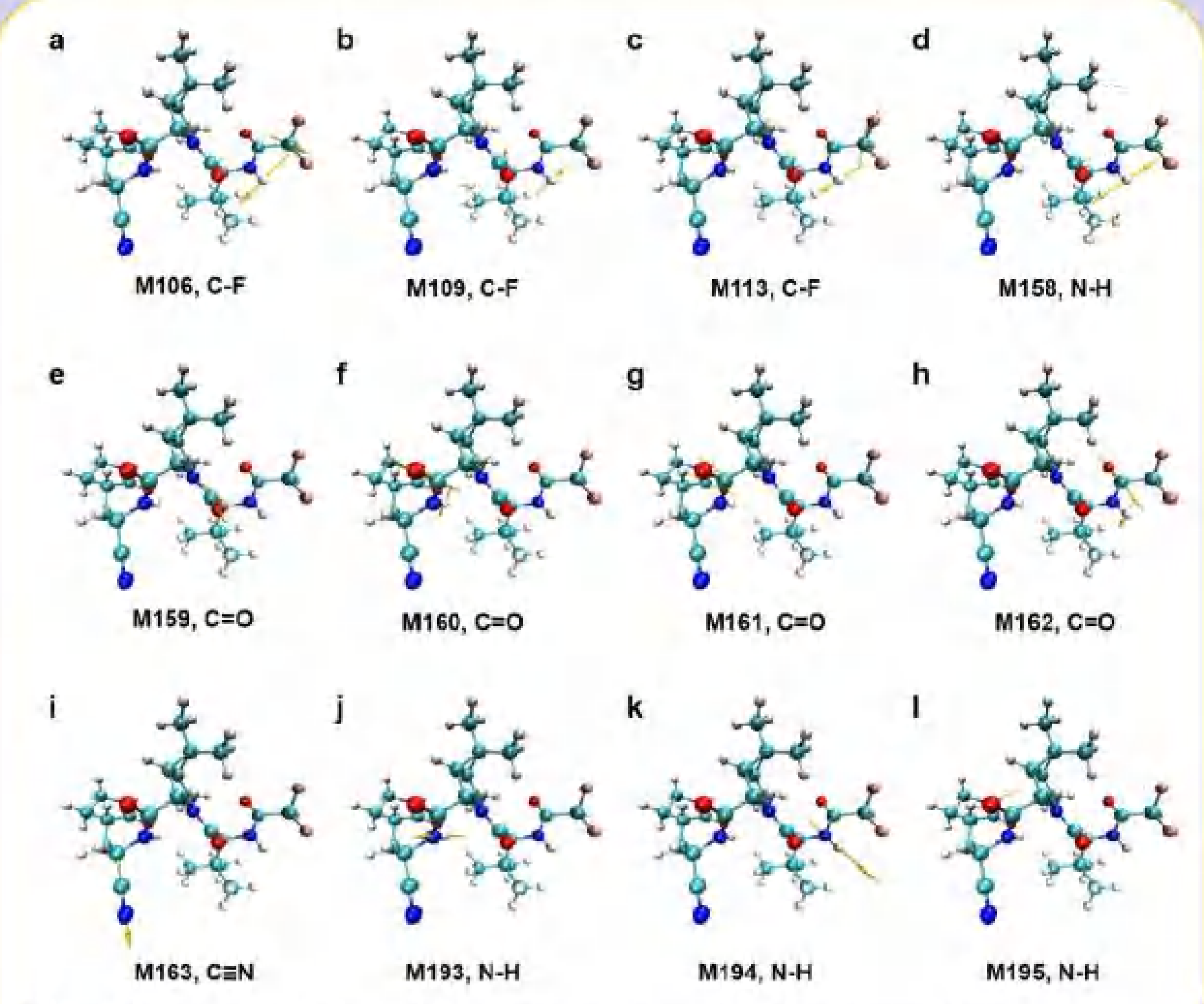

The characteristic vibration vector in the gas phase.

Excitation

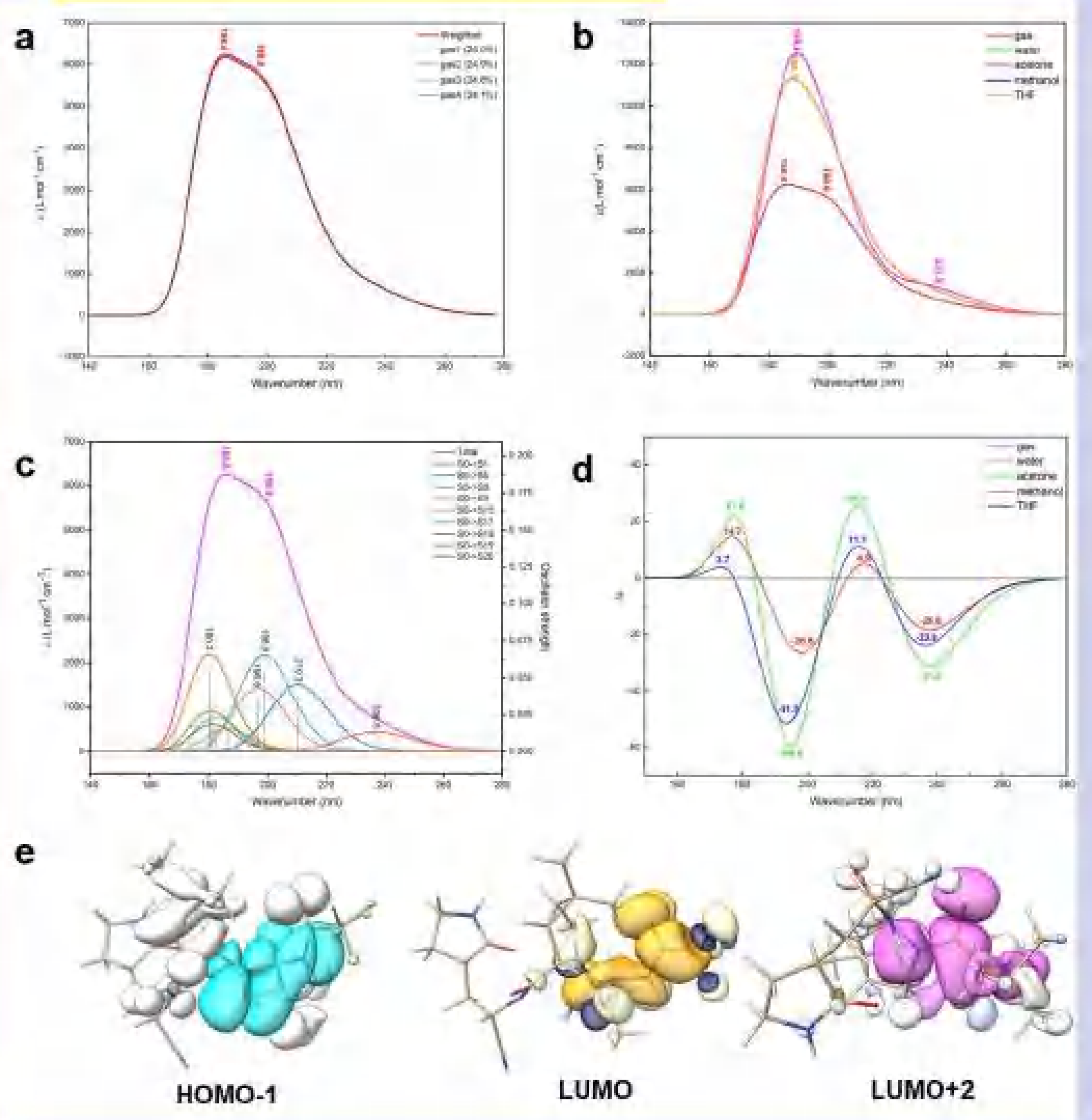

Excited state	Excited energy /eV	Wavenumber /nm	oscillator strength	Main contribution
So->S1	5.2330	236.93	0.0109	H-1 -> L 42.7%, H-1 -> L+2 35.7%
So->S6	5.8965	210.27	0.0375	H-1 -> L 52.2%, H-1 -> L+2 25.9%
So->S8	6.2340	198.88	0.0538	H -> L+2 49.2%, H-2 -> L 40.1%
So->S9	6.2986	196.84	0.0353	H-2 -> L 51.9%, H -> L+2 38.2%
So->S15	6.6435	186.62	0.0128	H-2 -> L+3 23.5%, H-1 -> L+3 22.1%
So->S17	6.7849	182.74	0.0194	H-2 -> L+2 29.0%, H-9 -> L 13.0%
So->S18	6.8335	181.44	0.0153	H-4 -> L 82.8%
So->S19	6.8588	180.77	0.0227	H -> L+5 22.4%, H-2 -> L+2 20.3%
So->S20	6.8751	180.34	0.0543	H-2 -> L+2 19.5%, H -> L+5 18.2%, H-3 -> L+3 18.1%

(a) UV-vis of different conformation in the gas phase, (b) UV-vis in gas, water, acetone, methanol, and THF, (c) Attribution of excited states corresponding to UV-vis, (d) ECD in gas, water, acetone, methanol, and THF, (e) Corresponding main orbital (HOMO-1, LUMO, and LUMO+2) of So -> S1 transition in the gas phase.

Reactivity and interaction

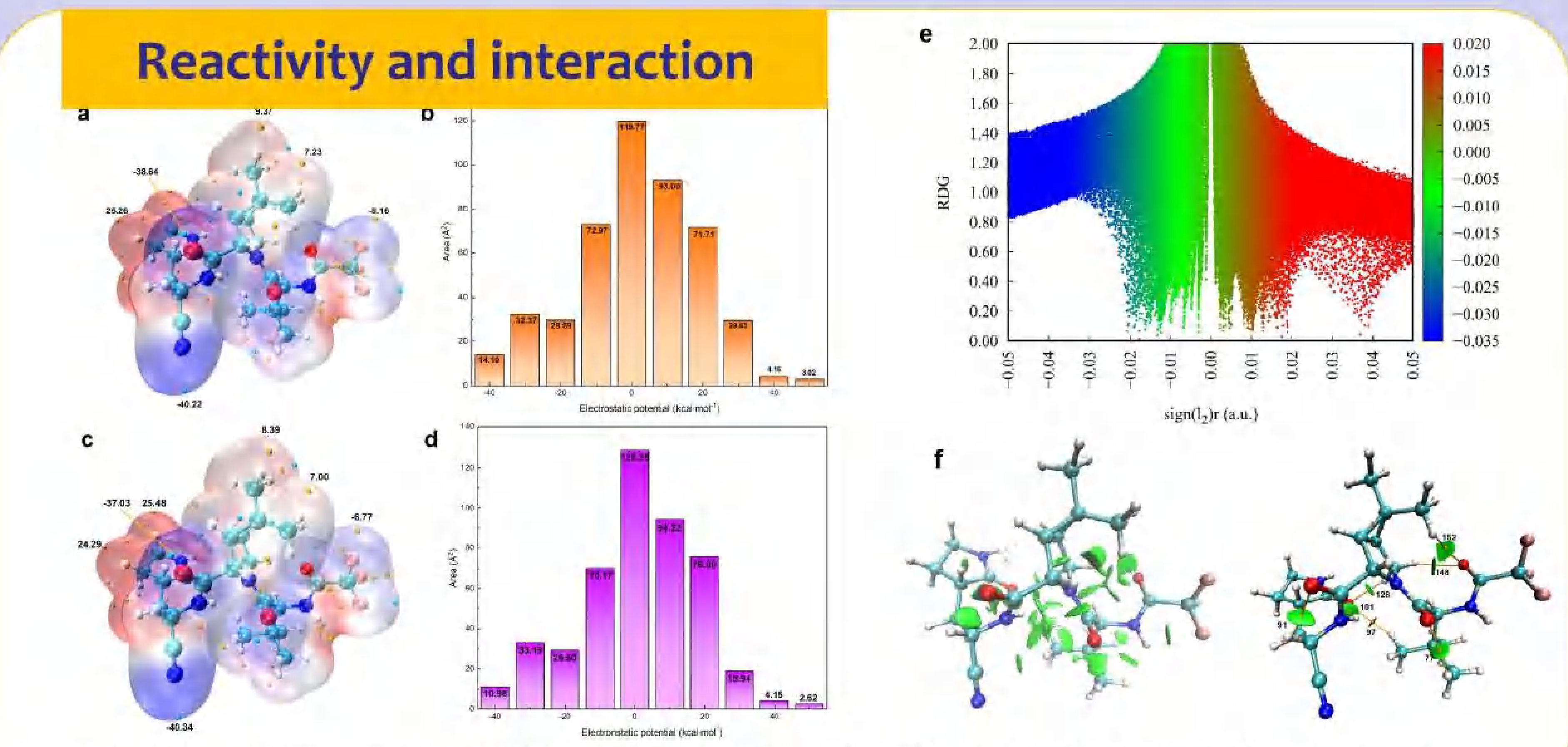

ESP and its distribution interval statistics. (a) and (b) in the gas phase, (c) and (d) in acetone. (e) RGD in gas, (f) BCP, path, and RGD.

Conclusion

- Using DFT method, the Nitrmatrelvir's conformation, spectrum and properties were probed in gas and solvent.
- A thermodynamic stable conformation can be found and the structure is almost identical.
- The solvent environment has a little effect on the vibration spectrum, but in acetone, the LUMO has a great decrease to -0.52 eV, with a gap of 5.99 eV.
- The UV-vis and ECD spectrum have an obvious response in acetone than in gas and other solvents.
- The charge distribution of the molecule in the gas and solvent and other descriptors were studied to evaluate its reactivity.
- The intramolecular interactions were studied from topological analysis, AIM analysis, and RDG illustration, this chemical information helps us to have a deeper understanding of its structure and properties.

Interfacial interactions of O_2 and H_2O molecules with PuH_2 (110) and (111) surfaces from first-principles calculations

Jingli Shi[a], Runyu Zhou[a], Gan Li[b], Lei Wan[c], Tao Gao[a]*, Wenhua Luo[b]

[a] *Institute of Atomic and Molecular Physics, Sichuan University, Chengdu 610065, China*
[b] *China Academy of Engineering Physics, Mianyang 621900, China*
[c] *School of Materials Science and Engineering, Lanzhou University of Technology, Lanzhou 730050, China*

Abstract

The interfacial reaction of highly active plutonium hydride in humid circumstance is of great interest in nuclear safe handling and storage, but it is poorly understood so far. We first studied the O_2 adsorption on (110) and (111) surfaces of PuH_2 by first-principles DFT+*U* method. We found that there were dissociative and non-dissociative adsorptions of oxygen on surfaces. The interactions between H_2O and oxygen adsorption structures were explored. This work could provide new insights into the adsorption morphology of oxygen on hydride surface and the interaction between oxide/hydride interface and water.

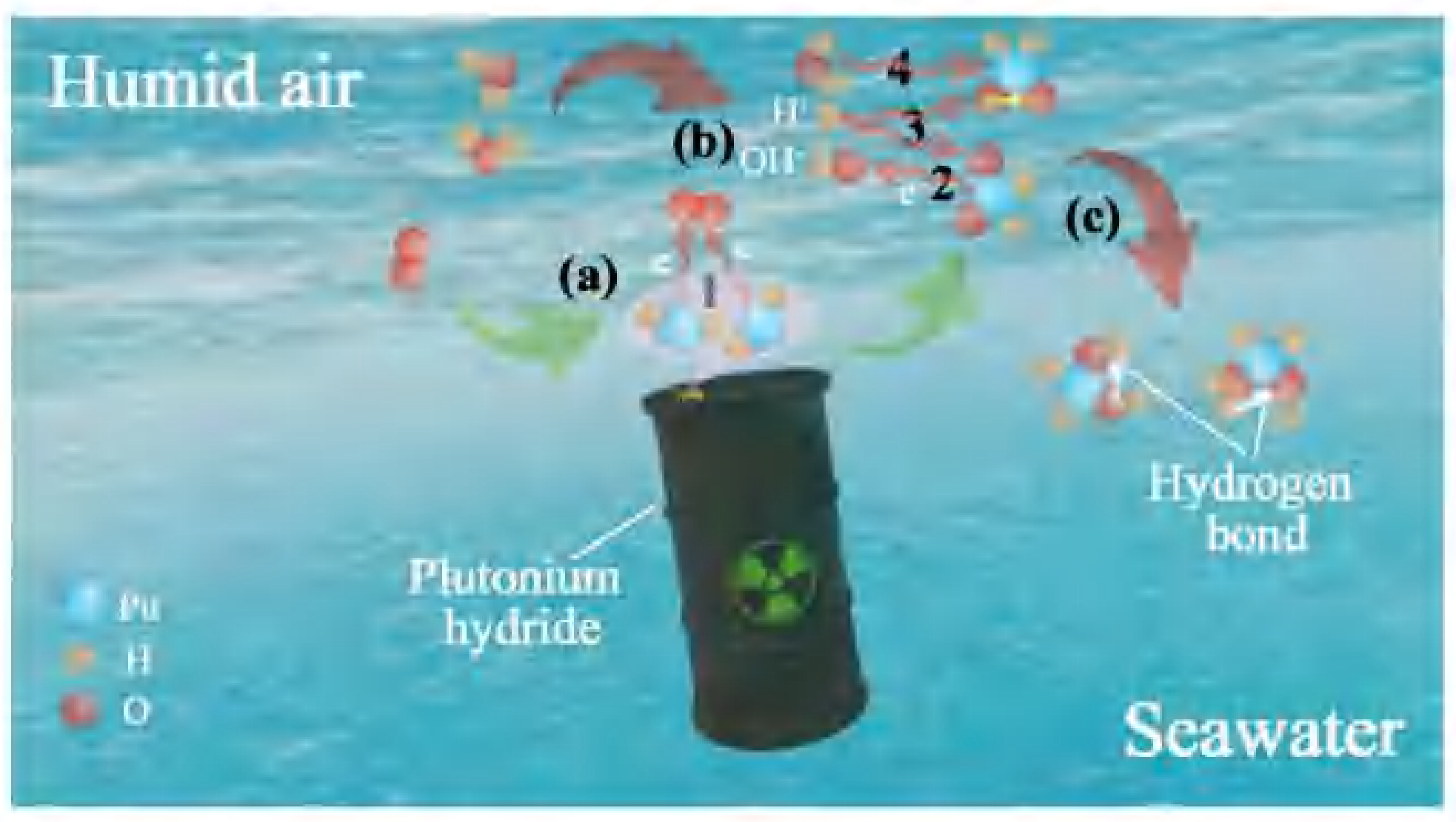

Fig. 1. Interfacial interaction of O_2 and H_2O molecules with PuH_2 {110} and {111} surfaces. (a) O_2 reacts with the surface of PuH_2 to form oxides. (b) H_2O molecules interact with the oxide/hydride interface. (c) The OH groups or a mixed adsorption state of OH groups and H_2O molecule appear on surfaces.

Introduction

Plutonium chemistry has received widespread concern because of its important role in the safe disposal of nuclear waste and environmental proliferation risk. When plutonium comes into contact with water or air, it is easy to hydrogenate to form highly reactive plutonium hydride [1-4]. It will give rise to a series of subtle reactions with water and oxygen from the environmental atmosphere. The impact of nuclear waste disposal on the environment, such as the Fukushima nuclear accident, has always been a matter of great concern to researchers [5]. Therefore, the study of the potential interfacial reaction behavior and surface corrosion products of plutonium hydride in moist air is necessary to strengthen nuclear security.

Methodology

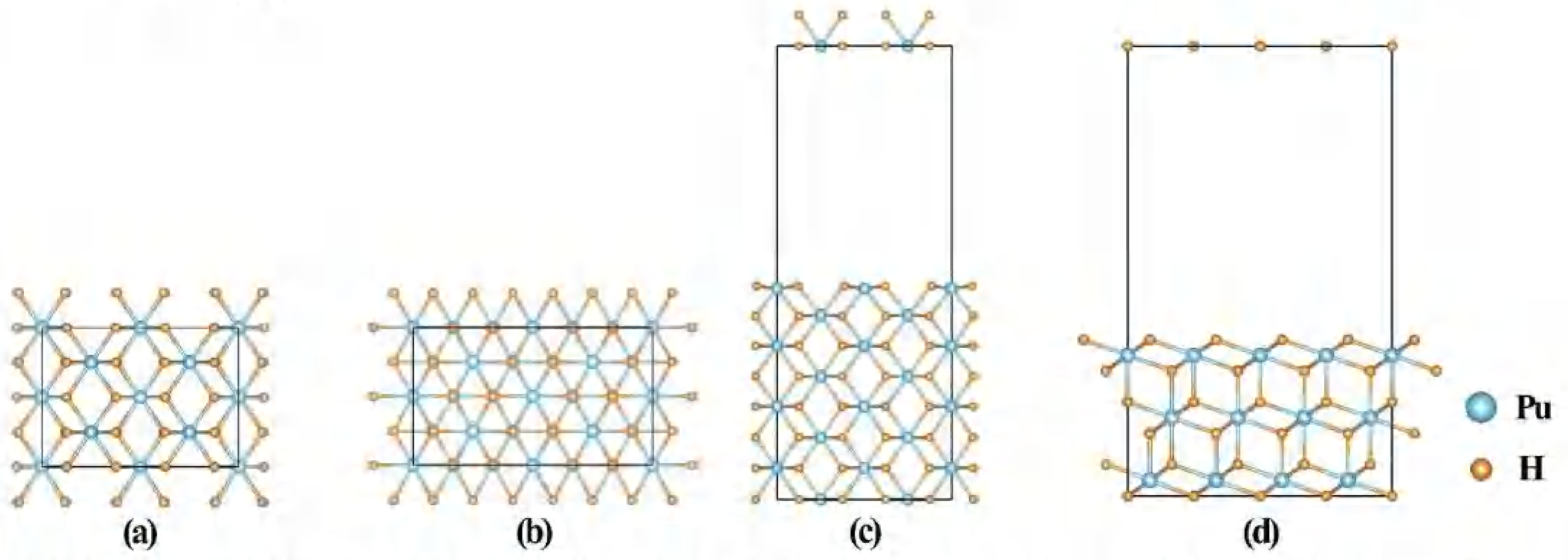

Fig. 2. Top ((a) and (b), respectively) and side ((c) and (d), respectively) views of stoichiometric PuH_2 (110) and (111) surfaces. Blue and orange spheres respectively represent plutonium and hydrogen atoms.

DFT+*U* calculations were performed using Vienna *Ab-initio* Simulation Package [6]. The adsorption energies (E_{ads}) of adsorbate on surface are defined as E_{ads}=$E_{slab+adsorbate}$-E_{slab}-$E_{adsorbate}$[7]. The work function (Φ) can be expressed as Φ=E_{vac}-E_F.

Results and discussions

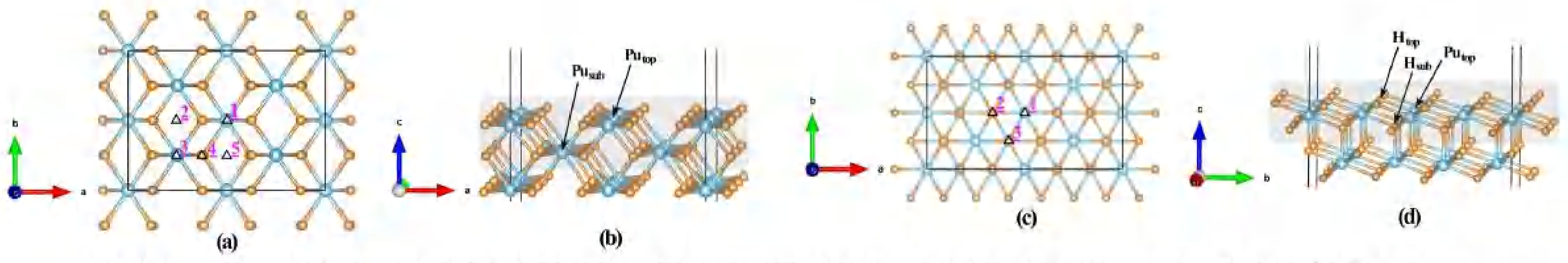

Fig. 3. Top ((a) and (c), respectively) and side ((b) and (d), respectively) views of adsorption sites on PuH_2 (110) and (111) surfaces.

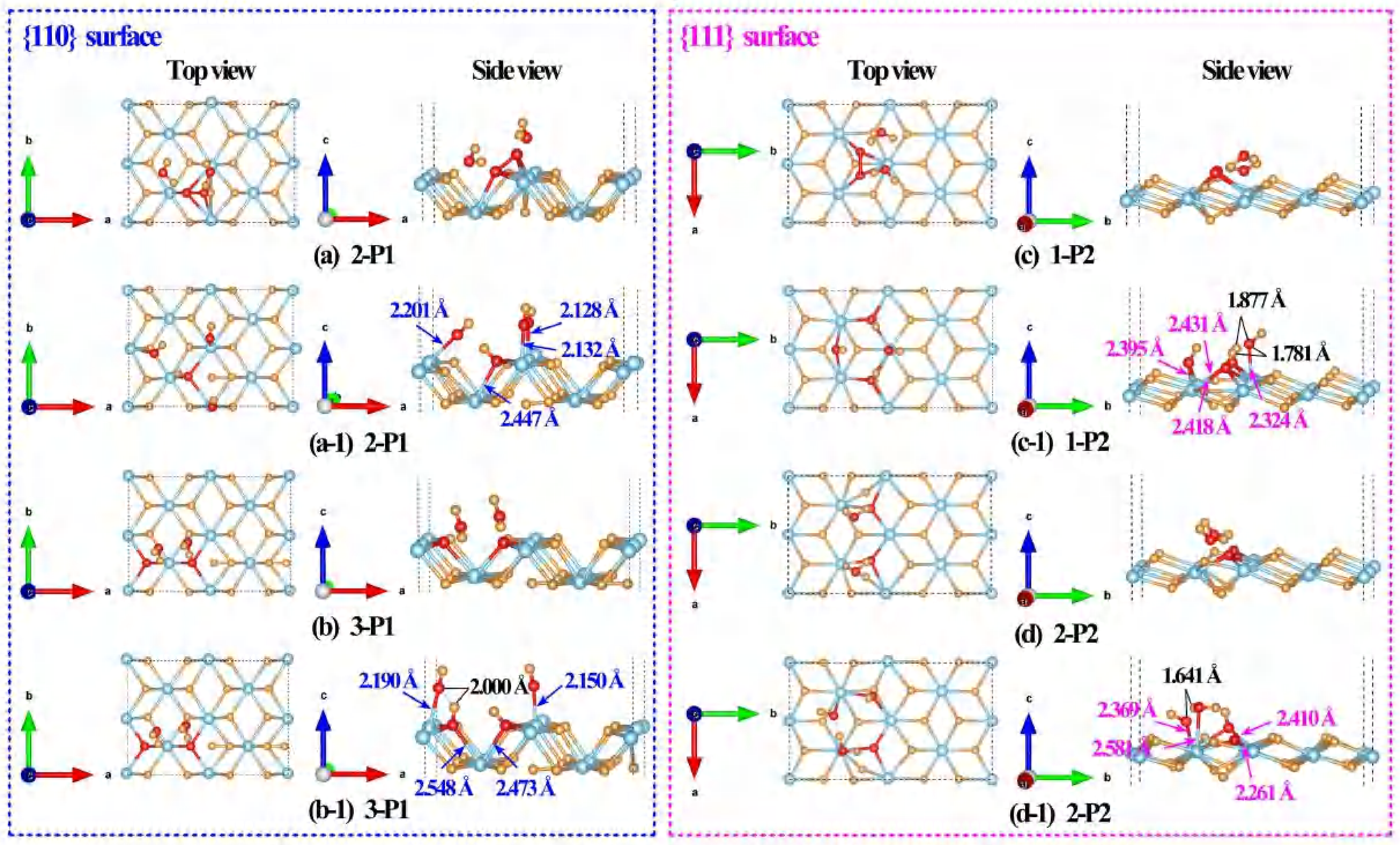

Fig. 4. H_2O molecules interact with the O_2/slab systems. (a), (b), (c), and (d) denote the initial configurations, while (a-1), (b-1), (c-1), and (d-1) represent the final configurations.

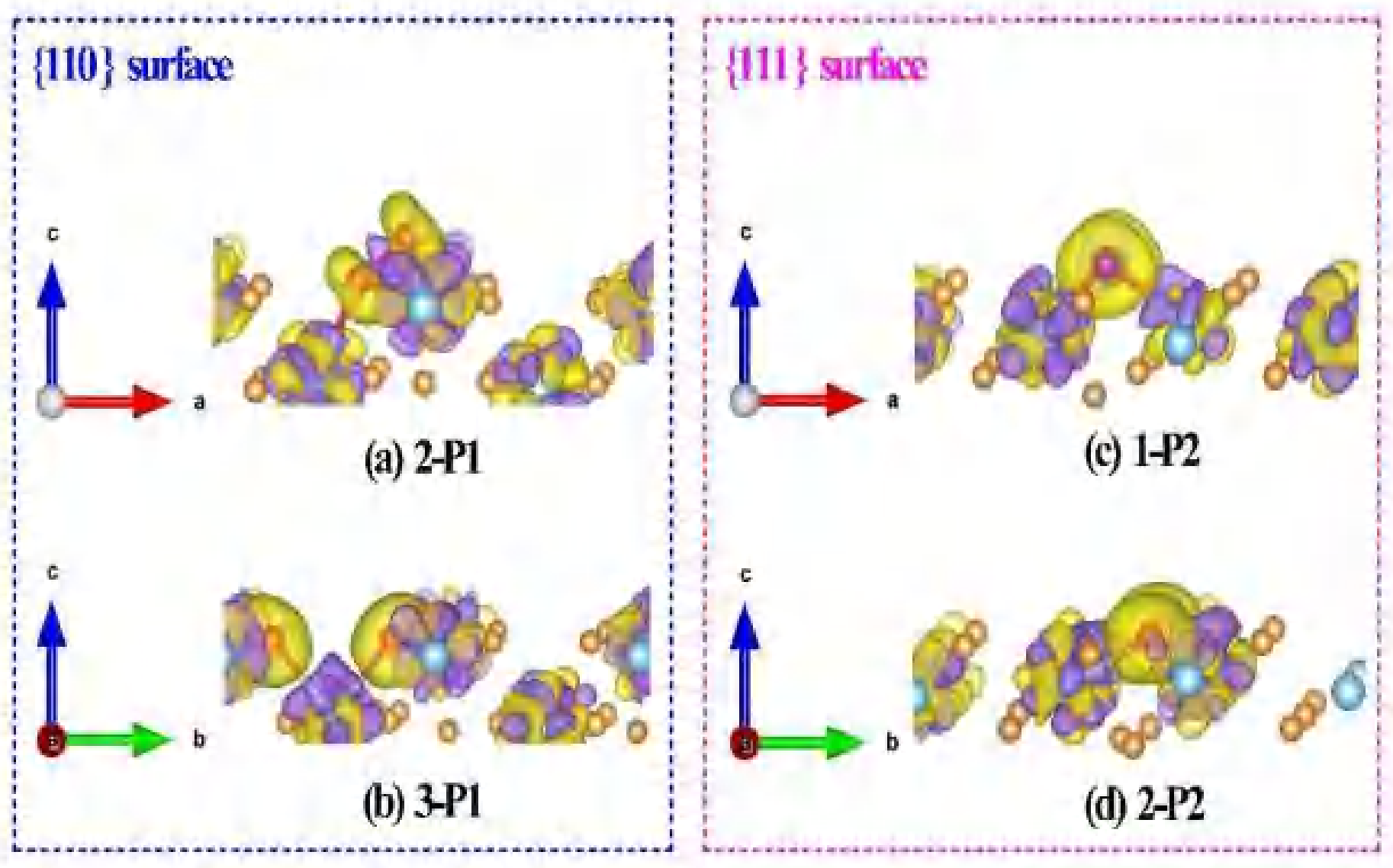

Fig. 5. Differential charge density of O_2/slab adsorption systems. Yellow regions mean charge aggregation, purple regions represent charge depletion. The isosurface value is set to 0.005 e/Å^3.

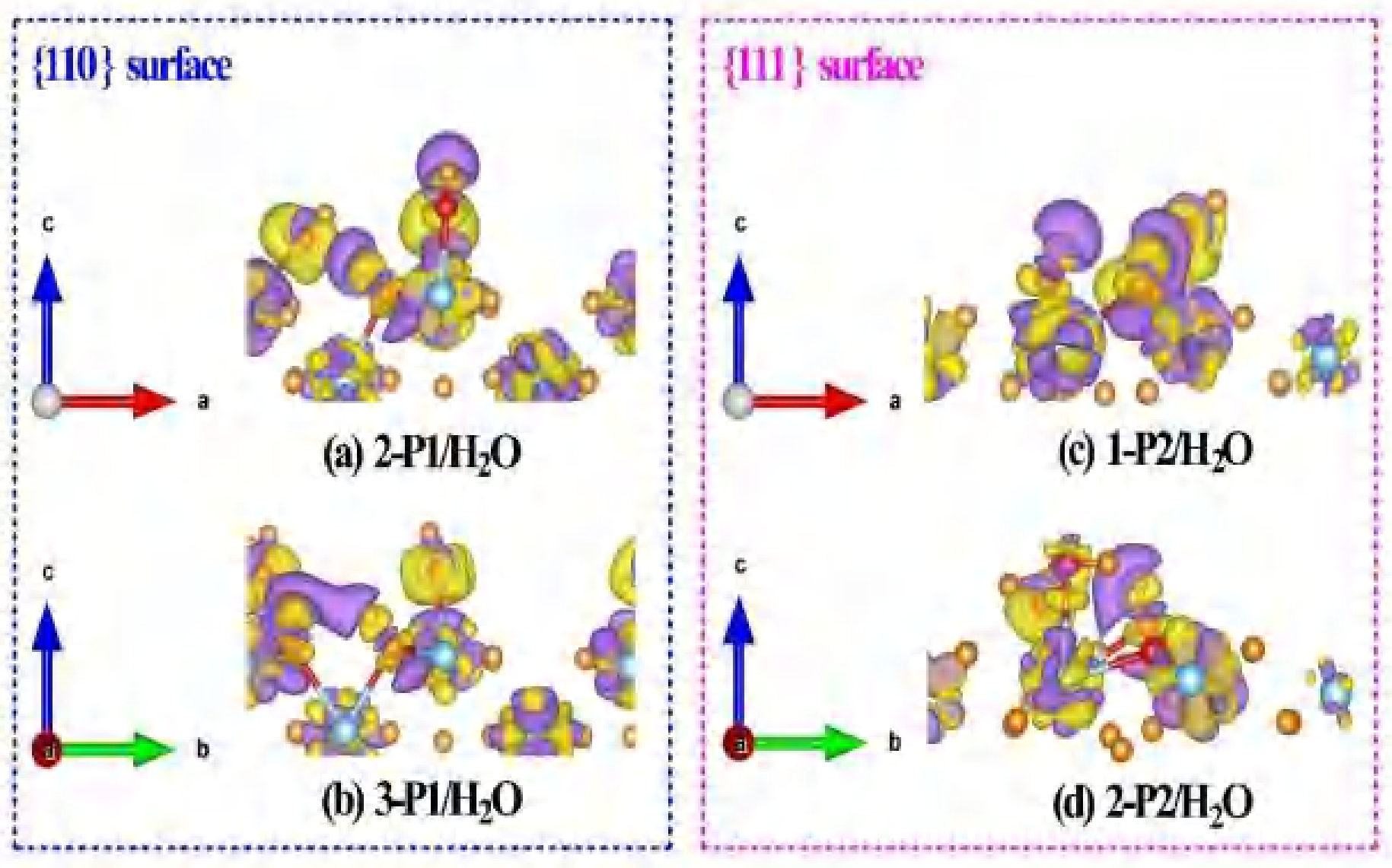

Fig. 6. Differential charge density of H_2O-O_2/slab adsorption systems. Yellow regions mean charge aggregation, purple regions represent charge depletion. The isosurface value is set to 0.005 e/Å^3.

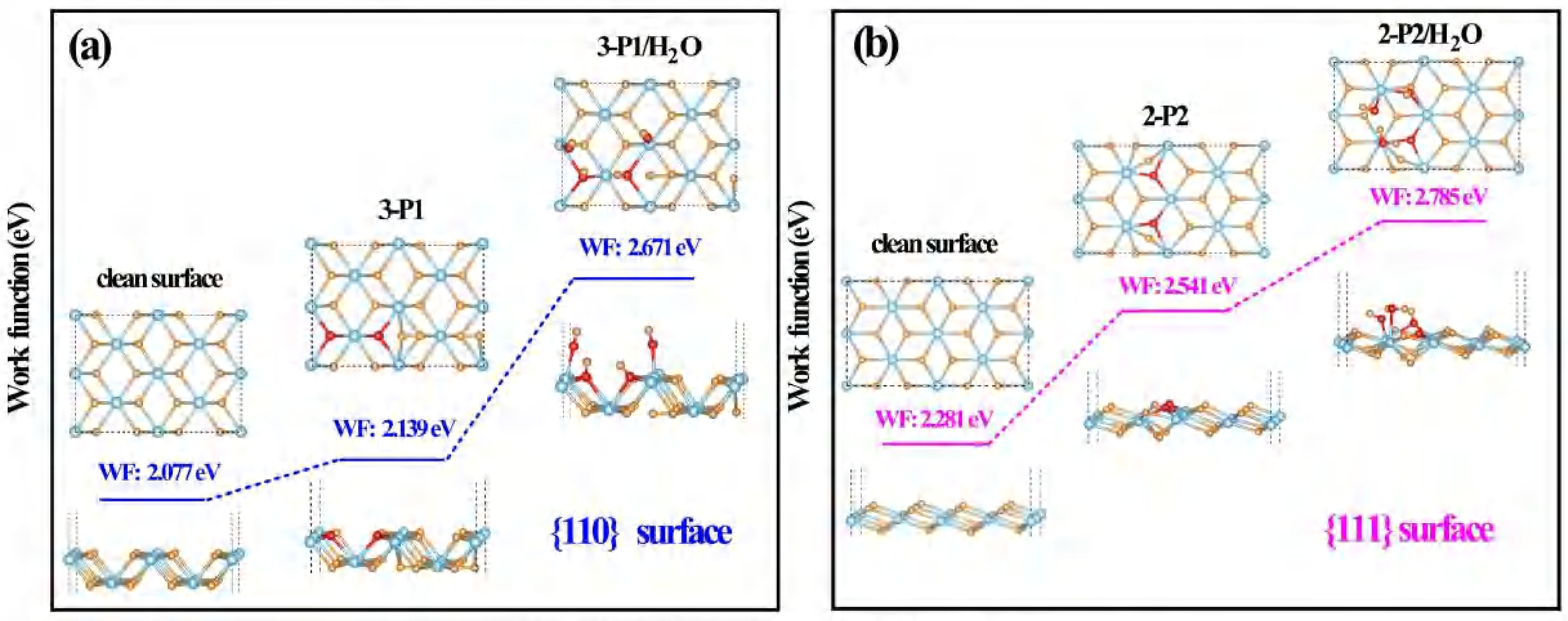

Fig. 7. Work function for clean and different adsorbed systems.

The H_2O molecules can dissociate into OH groups and H atoms when it interacts with the oxygen adsorption structures, then they are captured to create Pu-O and H-O bonds. The local work function increase.

Conclusions

The first-principles DFT+*U* calculations were performed to study the interfacial reaction mechanism among O_2 and H_2O molecules with the (110) and (111) surfaces of PuH_2. The results suggests that there are dissociative and non-dissociative adsorptions of oxygen. The H_2O molecules can be dissociated into OH groups and H atoms, then they are caught to generate Pu-O and H-O bonds. The OH groups or a mixed adsorption state of OH groups and H_2O molecule will appear on surfaces, and hydrogen bonding interactions occur among them.

Acknowledgement

This work is supported by the SPC-Lab Research Fund (No.WDZC2020 01).

References

[1] Haschke JM, Dinh LN. J. Alloys Compd 2017; 698:44-48.
[2] Haschke JM, Allen TH, Los Alamos Sci 2000; 26:252-273.
[3] Haschke JM, Stakebake JL. Springer, Dordrecht, 2006, pp. 3199-3272.
[4] Brierley M, Knowles JP, Sherry A, Preuss M. J. Nucl. Mater 2016; 469:145-152.
[5] Donald SB, Stanford JA, Haschke JM, Ashley DD, Talbot WA. Corros Sci 2021; 187:109527.
[6] Blöchl PE. Projector Augmented-Wave Method. Phys. Rev. B 1994; 50:17953-17979.
[7] Bengtsson L. Dipole correction for surface supercell calculations. Phys. Rev. B 1999; 59:12301-12304.

Interfacial corrosion behavior between O atoms and alloy elements at iron-liquid LBE interface by first-principles molecular dynamics

Runyu Zhou[a], Jingli Shi[a], Ruijie Zhang[a], Tao Gao[a*], Changan Chen[b]**

[a] *Institute of Atomic and Molecular Physics, Sichuan University, Chengdu 610065, China*
[b] *Key Laboratory of Surface Physics and Chemistry, China Academy of Engineering Physics, Mianyang 621907, China*

Abstract

The interfacial corrosion behavior between LBE adding O atoms and Fe substrate surface containing alloy elements (Cr, Ni, Al, Si) has been studied by first-principles molecular dynamics simulations. Theoretical calculations show that the O atoms in LBE could form the protective oxide layer with the alloy elements (Cr, Al, Si) on the Fe substrate surface at the iron-liquid LBE interface, in which slows down the corrosion process. This work is instructive for a deeper understanding of corrosion mechanism and provides valuable information for the performance evaluation and material design of the steel under reactor conditions.

Introduction

Nuclear energy is considered as a highly efficient, economical, clean, and sustainable energy [1,2]. Vigorously developing the nuclear energy market and industry will help solve the problem of energy shortage. The lead-cooled fast reactor system is one of the main types of the fourth-generation reactor. In this system, the liquid lead or Pb-Bi eutectic (LBE) is generally used as a heat exchange medium for the heat from the inside of the reactor when it flows out through the coolant [3]. Due to the excellent properties of liquid Pb-Bi eutectic (LBE), such as high thermal conductivity, low melting point, high boiling point, good chemical inertness, and low neutron absorption cross section [4], it is considered as an excellent lead-cooled fast reactor coolant material with great development potential. However, as a heavy liquid metal material, the high corrosion of LBE to the container material will cause safety problems and economic losses of the reactor [5-7]. Therefore, exploring the conditions that could effectively slow down the corrosion process becomes one of the key problems in the development of the lead-based nuclear systems.

Analysis technology

Radial distribution function: $g_{AB}(r) = \frac{V}{N_A N_B}\langle\frac{\sum_{i=1}^{N_A} n_{iB}(r, \Delta r)}{4\pi r^2 \Delta r}\rangle$

Estimated mean effective potential energy: $V(r) = -RTln\big(g(r)\big)$

Mean square displacement: $\langle\Delta r_A(t)^2\rangle = \frac{1}{N_A}\langle\sum_{i=1}^{N_A}|\overrightarrow{r_{Ai}}(t+t_0) - \overrightarrow{r_{Ai}}(t_0)|^2\rangle$

Diffusion coefficient based on Einstein's relation: $D_A = \lim_{t\to\infty}\frac{\langle\Delta r_A(t)^2\rangle}{6t}$

Methodology

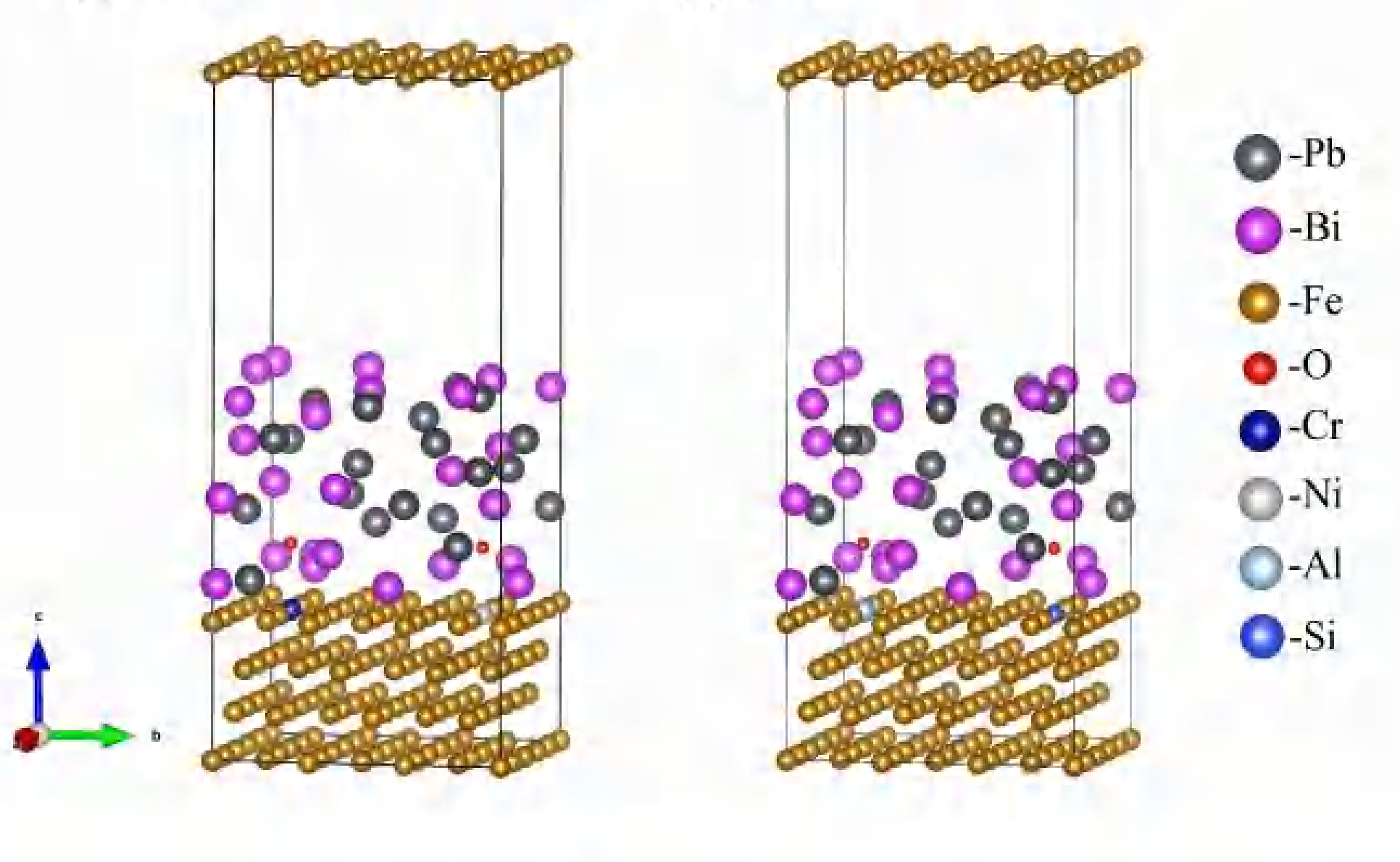
(a) case 1: (b) case 2:

Fig. 1. The models used for calculation, (a) for case 1; (b) for case 2.

Results and discussions

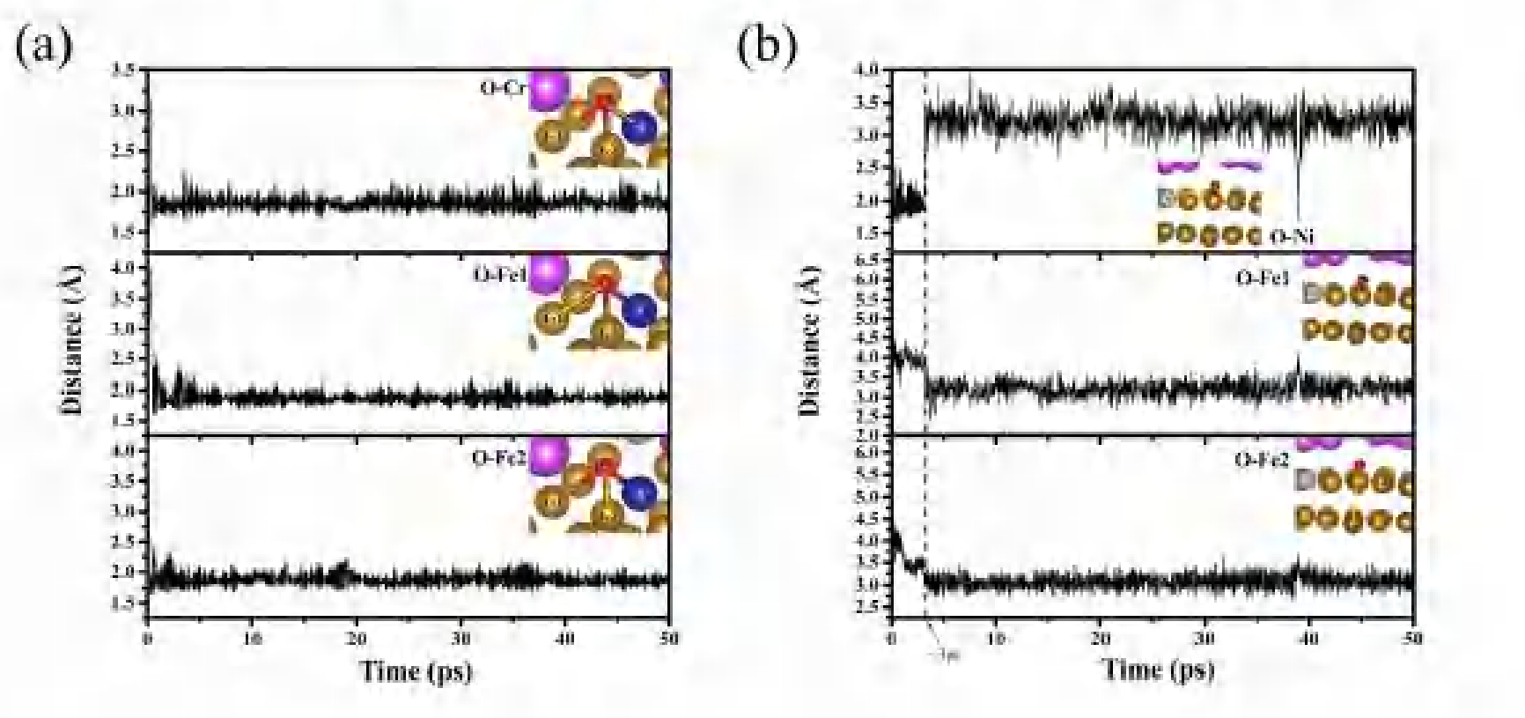

Fig. 2. The calculated bond lengths between (a) the O^{Cr} atom and its neighboring atoms; (b) the O^{Ni} atom and its nearby atoms.

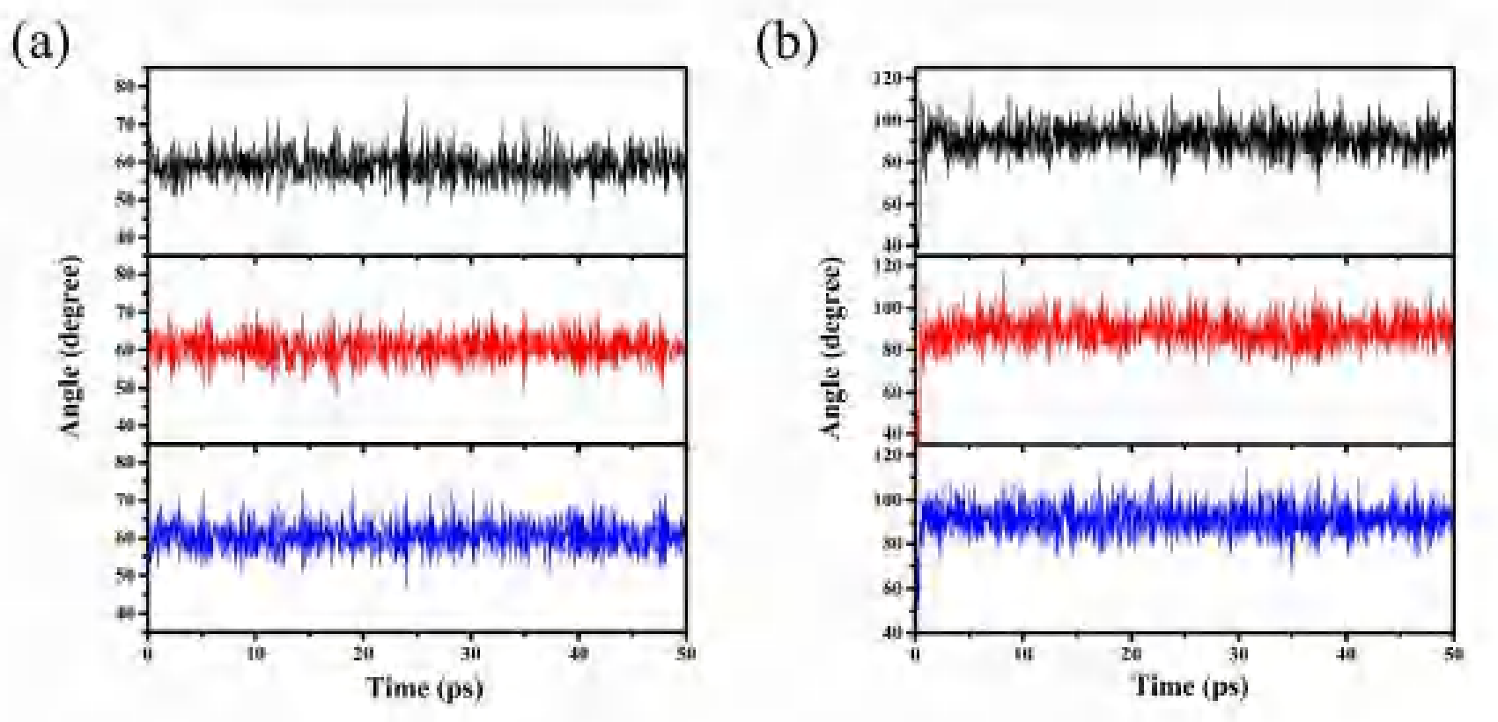

Fig. 3. Degrees of (a) the three interior angles in the bottom triangle and (b) the three top angles in the three side triangles of the O^{Cr}-complex.

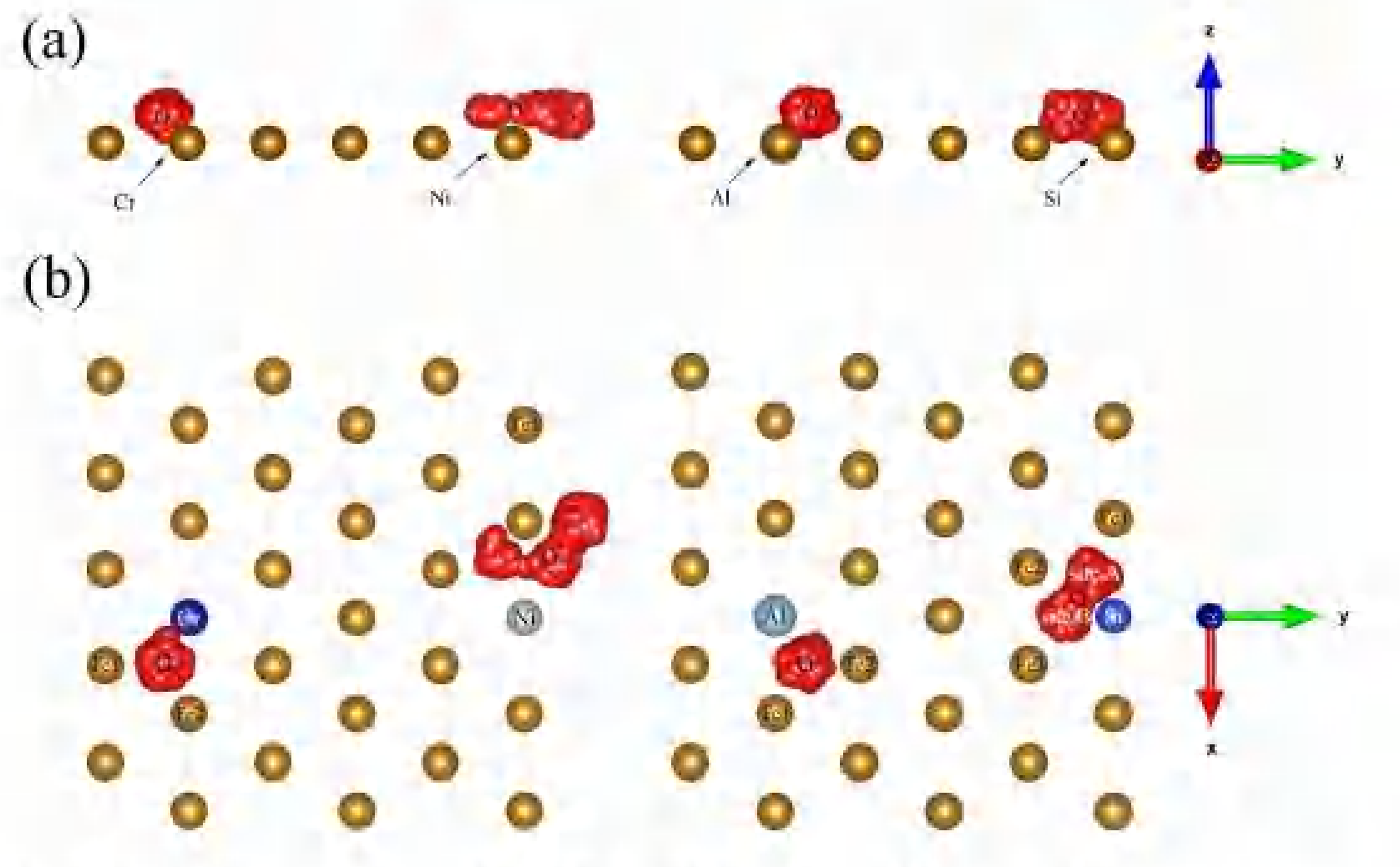

Fig. 4. The motion trajectories of the O^{Cr}, O^{Ni}, O^{Al}, and O^{Si} atoms in case 1 and case 2 from (a) the front view and (b) the top view.

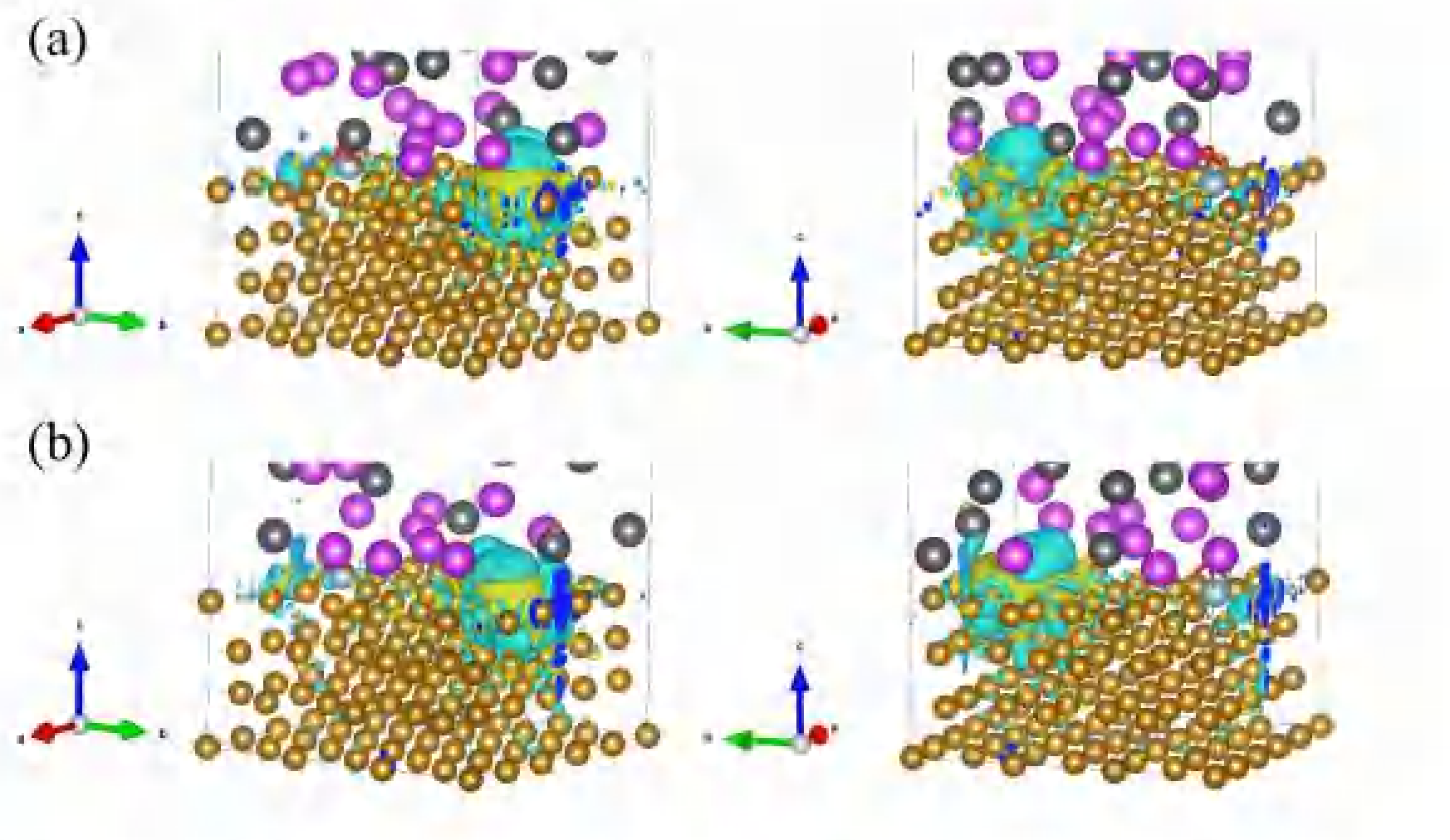

Fig. 5. The differential charge density maps in (a) site A and (b) site B from the front view and the back view. The blue surface represents the charge exhaustion, while the yellow surface represents the charge accumulation.

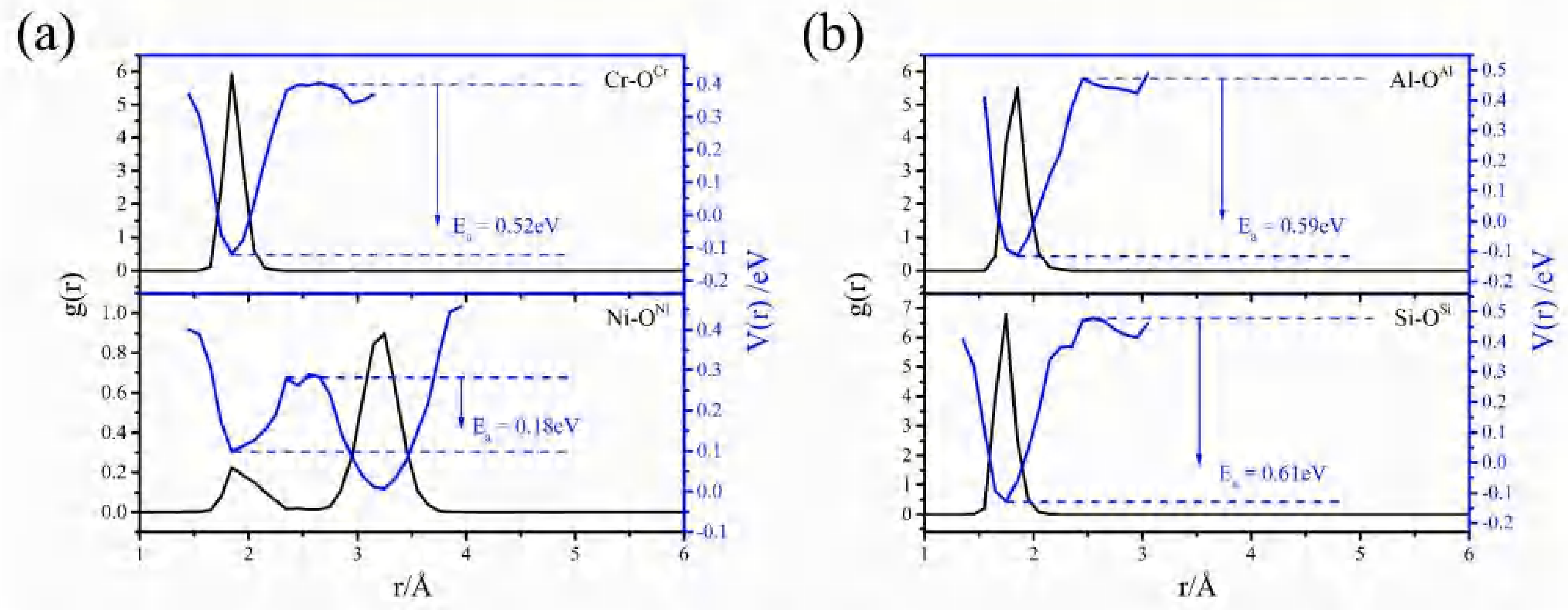

Fig. 6. The radial distribution functions and the estimated mean effective potential energy paths between the alloy elements (Cr, Ni, Al, Si) and the O atoms in case 1 and case 2.

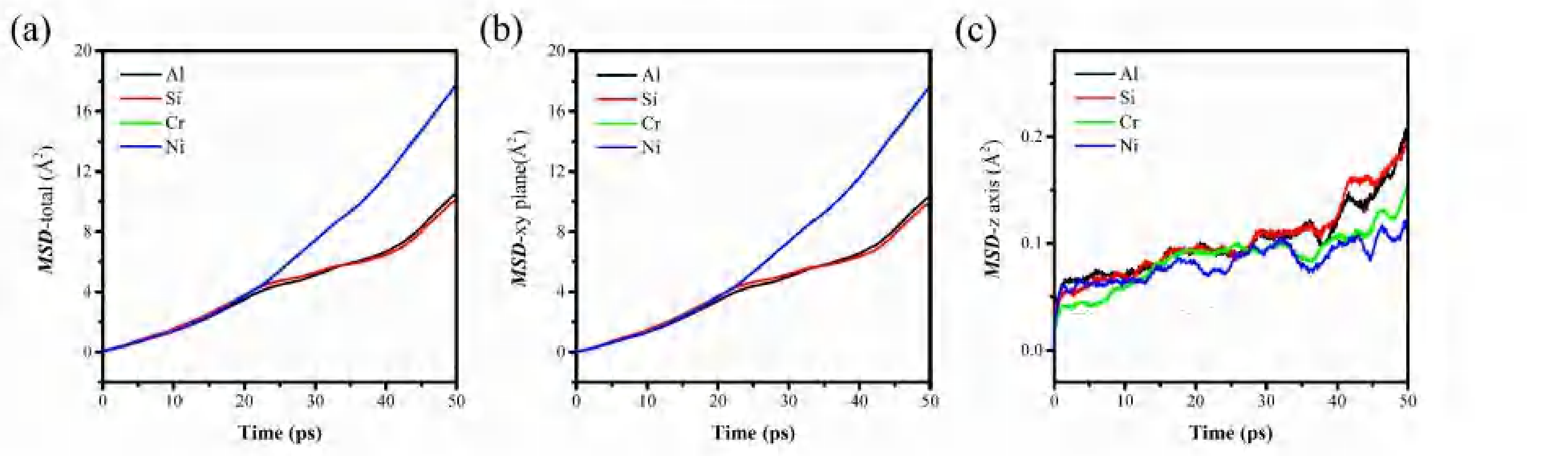

Fig. 7. The mean square displacement (MSD) values of the four alloy elements. (a) the total MSD values; (b) the MSD values in the xy plane; (c) the MSD values along the z axis.

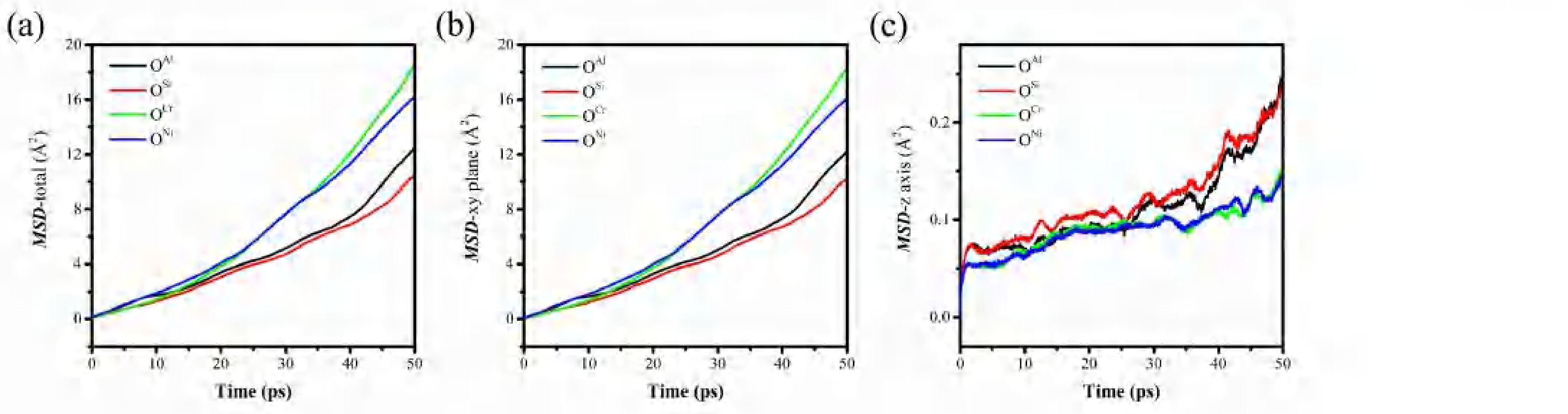

Fig. 8. The mean square displacement (MSD) values of the four O atoms. (a) the total MSD values; (b) the MSD values in the xy plane; (c) the MSD values along the z axis.

Conclusions

In a word, the interfacial corrosion behavior between O atoms in LBE and alloy elements (Cr, Ni, Al, Si) on Fe substrate surface has been studied by first-principles molecular dynamics simulations. The bond length and angle analysis show that the O atoms are more likely to form tetrahedral-like O-complexes with Al, Si and Cr atoms compared with Ni atom. Furthermore, the mean square displacement indicates that the alloy elements are less likely to separate from the iron substrate surface. Based on the calculation of diffusion coefficient, the Si atom has the lowest value while the highest value is Ni. Therefore, the Ni atoms are more likely to enter the LBE compared with the other elements (Cr, Al, Si). Overall, doped Si and Al atoms can effectively slow down the corrosion process of the steel. This work could provide the guidelines for the further design of high-performance corrosion-resistant materials.

Acknowledgements

This work was supported by the National Natural Science Foundation of China (NO. U20B2009).

References

[1] S.J. Zinkle, G.S. Was, Acta Mater. 1 (3) (2013) 735-758.
[2] A.J. Koning, D. Rochman, Ann Nucl Energy. 35 (11) (2008) 2024-2030.
[3] J.J. Park, D.P. Butt, C.A. Beard, Nucl Eng Des. 196 (3) (2000) 315-325.
[4] S. Malang, R. Mattas, Fusion Eng Des. 27 (1995) 399-406.[4] Brierley M, Knowles JP, Sherry A, Preuss M. J. Nucl. Mater 2016; 469:145-152.
[5] R.G. Ballinger, J. Lim, Nucl Technol. 147 (3) (2004) 418-435.
[6] F. Barbier, G. Benamati, C. Fazio, A. Rusanov, J Nucl Mater. 295 (2-3) (2001) 149-156.
[7] F. Barbier, A. Rusanov, J Nucl Mater. 296 (1-3) (2001) 231-236.

Two Dimensional MOene: from Superconductors to Direct Semiconductors and Weyl Fermions

燕罗[1]，褚维斌[2]，王保田[3]，周柳江[1,4]*
1. 电子科技大学物理学院 ，成都610054.
2. 复旦大学计算物理科学研究所计算物理科学重点实验室(教育部)，上海200433.
3. 中国科学院高能物理研究所，北京10049.
4. 电子科技大学长江三角洲地区研究所(湖州)，湖州313001.

研究背景

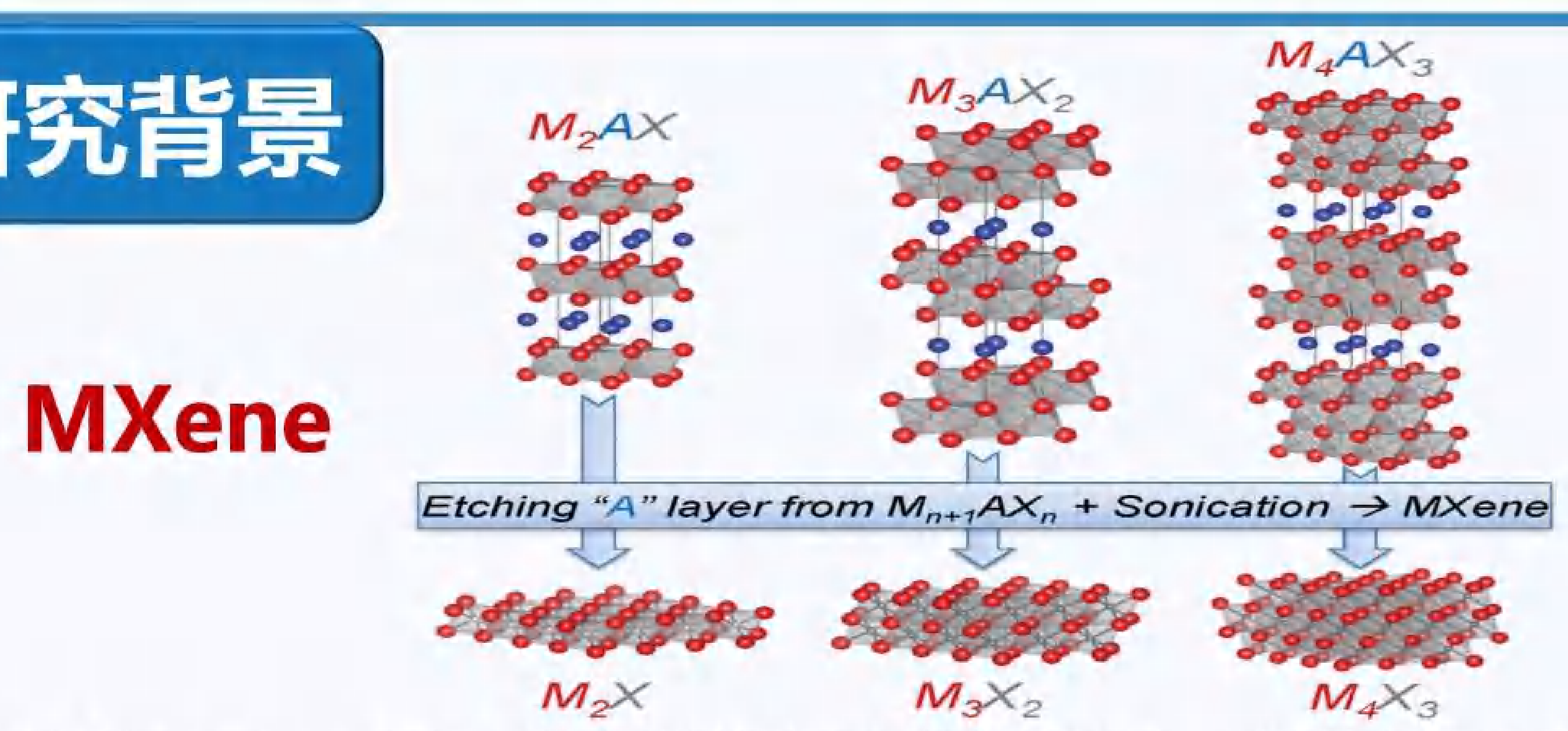

- ◆ 传统MXene具有丰富的物理和化学性质，广泛应用于能量捕获与存储，电子，催化，生物医学，传感等领域。
- ◆ 直接带隙半导体的MXene却十分稀少，仅仅只有$Sc_2C(OH)_2$, $Y_2C(OH)_2$, 和$Cr_2TiC_2(OH)_2$被报道，限制其在光电领域应用。
- ◆ 二维Tl_2O是具有高载流子迁移率的直接半导体，但是Tl元素的有毒性和稀缺性限制它的广泛应用。
- ◆ 地球含量丰富且对环境友好的Ti元素，其中1T-Ti_2O的体相早在1970年就已经被合成，最近通过熔盐法和脉冲激光沉积技术也得到了具有高导电性的1T-Ti_2O金属薄膜。

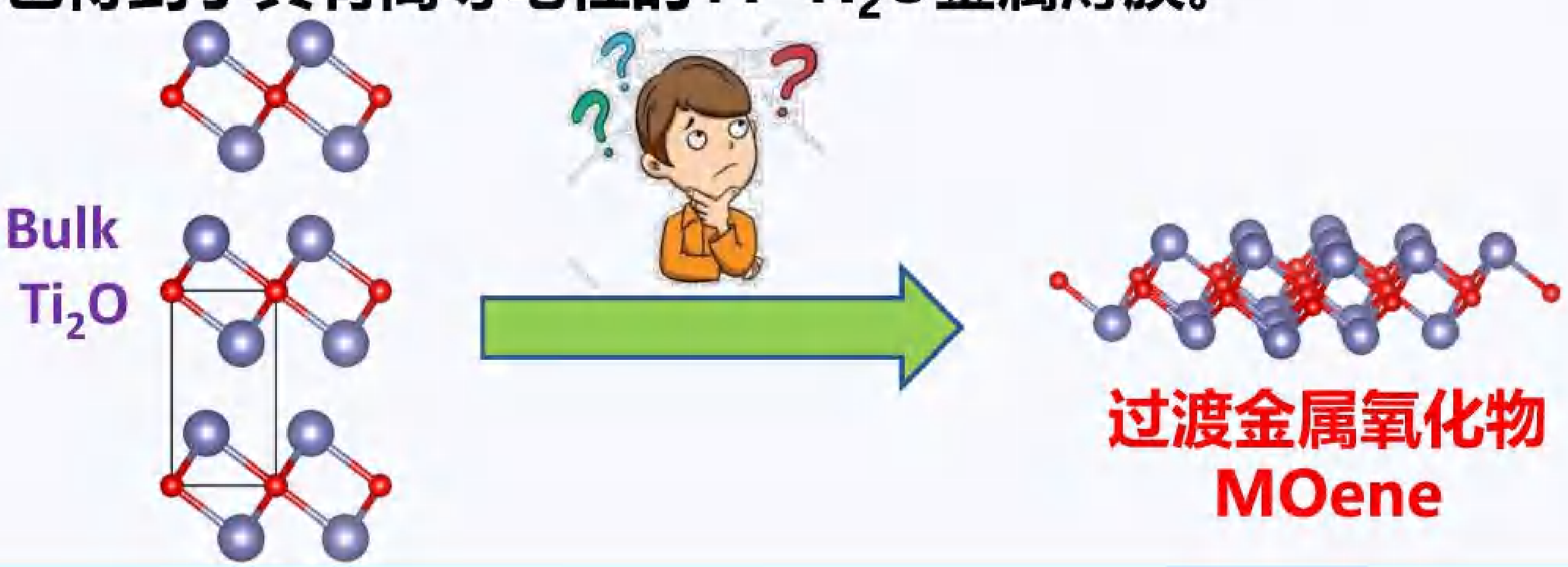

研究方法

➢密度泛函理论

力、电子、跃迁矩阵元、光、分子动力学

➢含时密度泛函，多体微扰理论(GW+BSE)

光吸收、激子效应

➢Bardeen–Cooper–Schrieffer超导理论

超导电性

➢非绝热分子动力学：表面态跃迁理论

Hefei-NAMD

光动力学、光生载流子转移、复合等

MOene的晶体结构

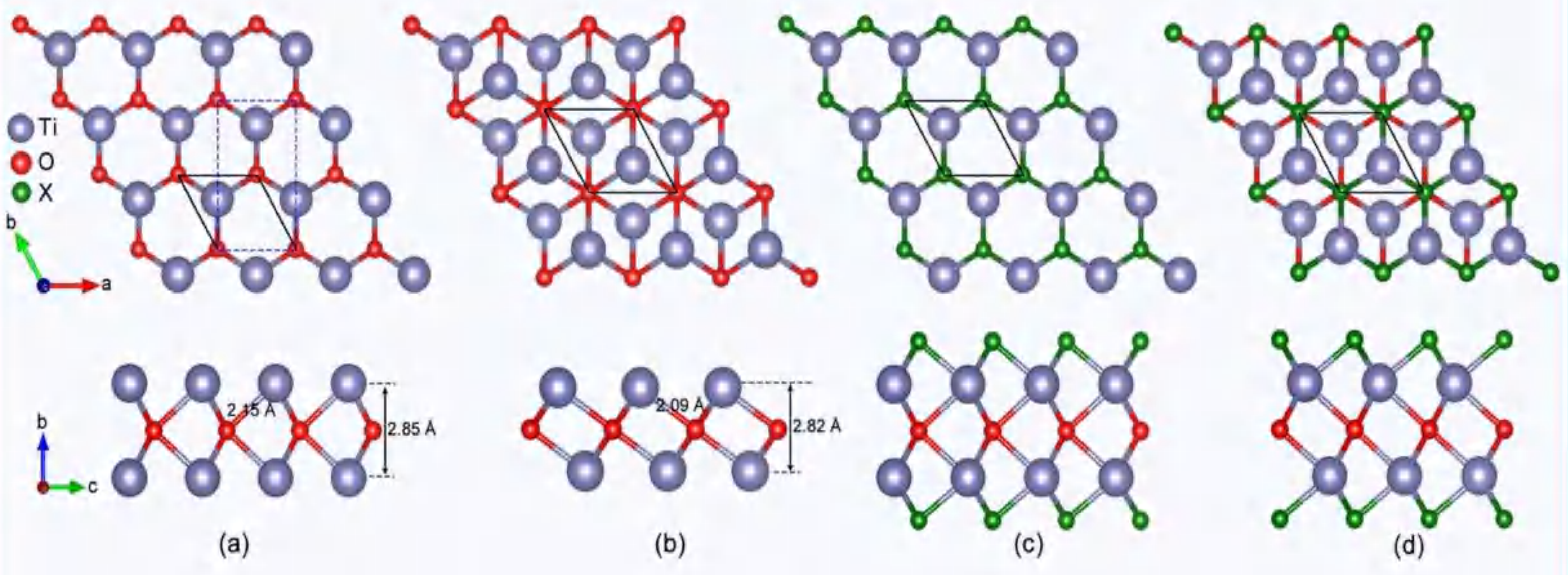

将传统MXene扩展到过渡金属氧化物MOene, 分子式为$M_{n+1}O_nT_x$，M为过渡金属，T为表面官能团 (-F、-O、-H、-OH)。

MOene的性质

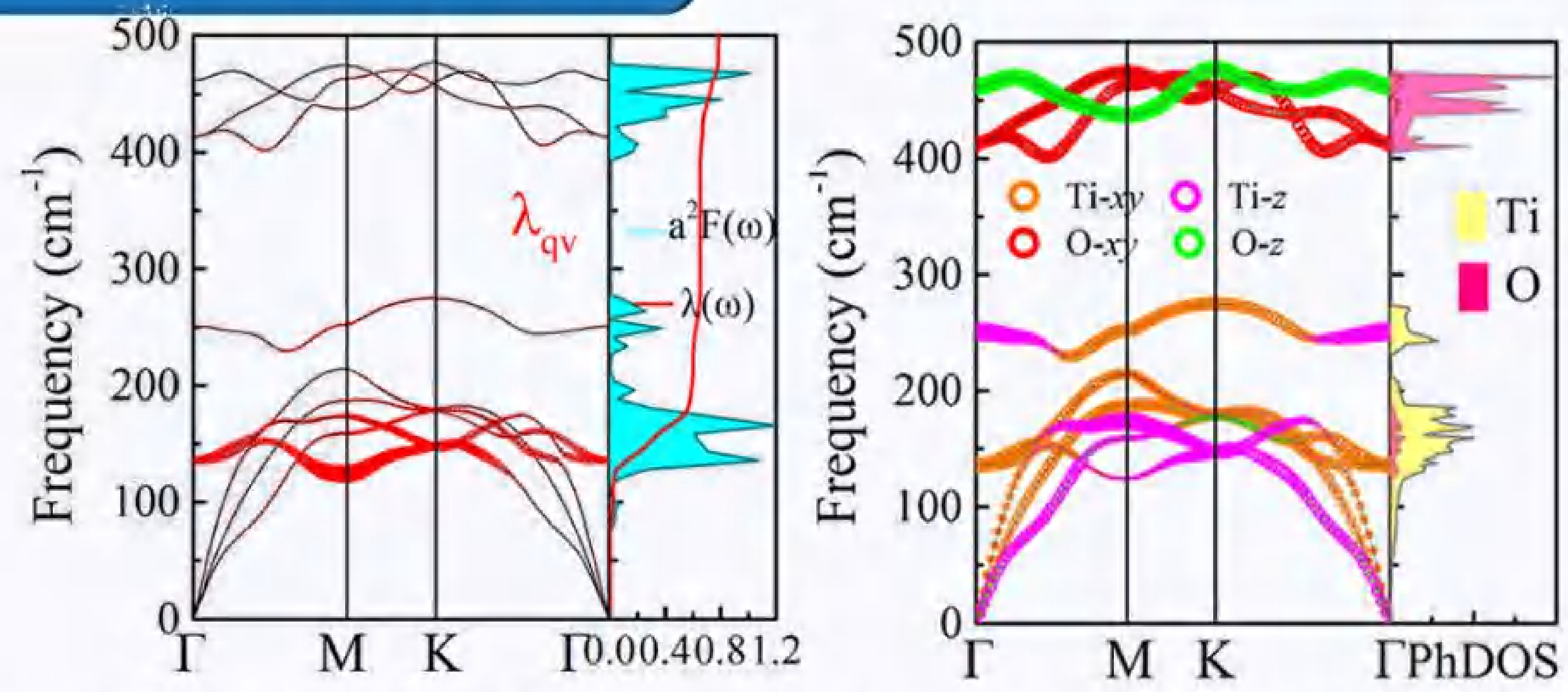

Ti_2O为本征超导体，超导温度超过大部分已报道的MXene超导体。

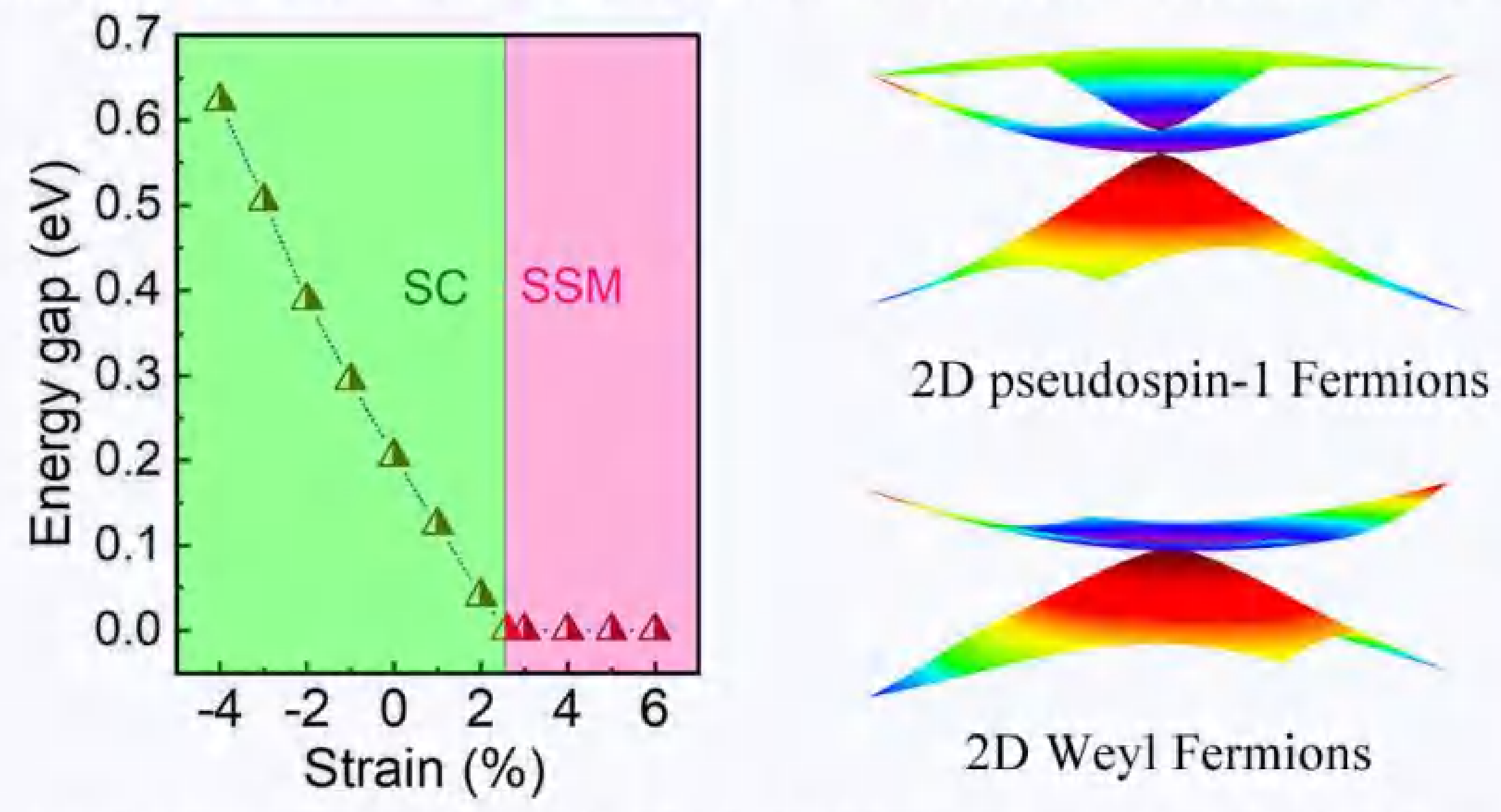

应力工程产生量子相变：在拉应力的作用下产生新颖的二维费米子。

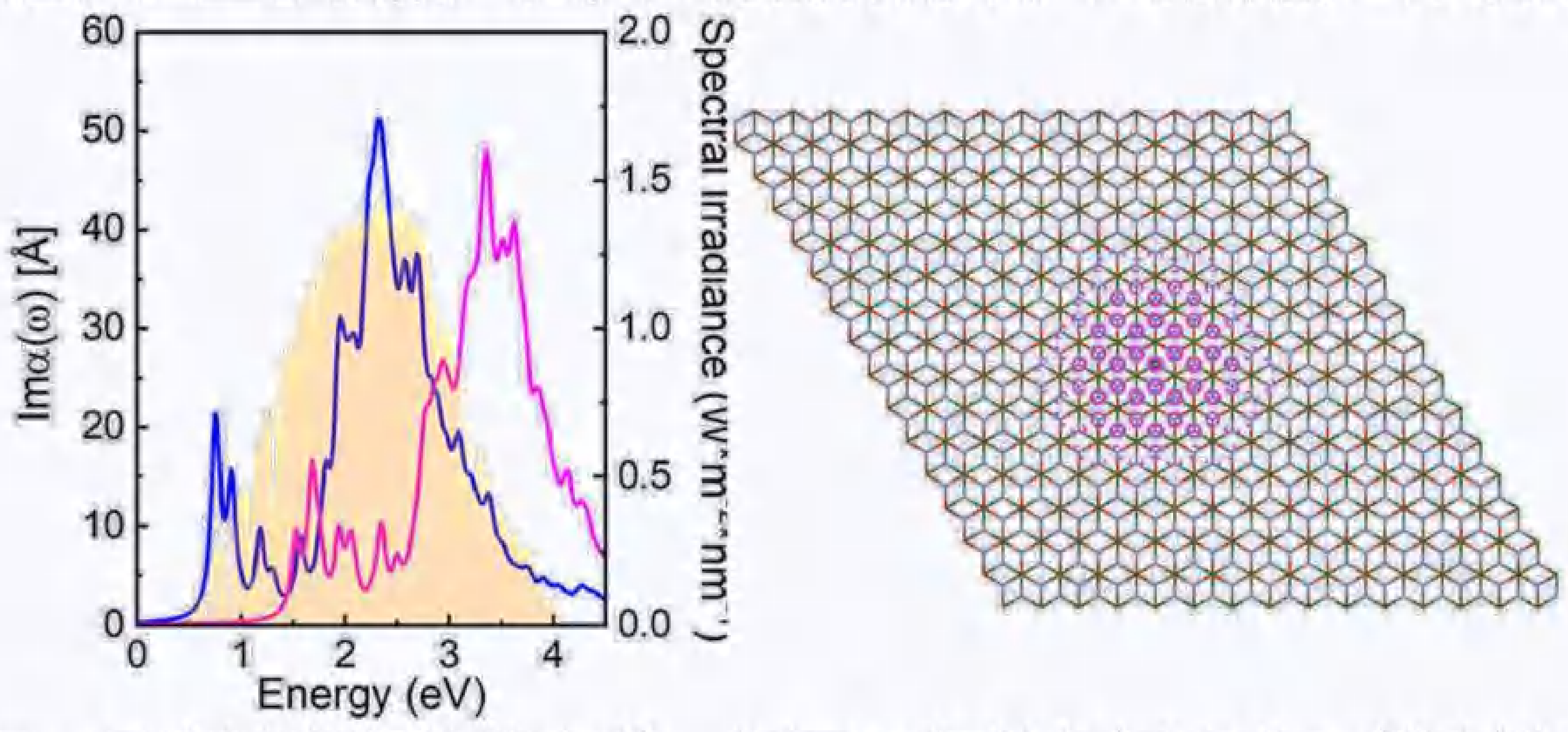

红外和可见光波段强的光吸收，适用于红外探测和太阳能电池材料。

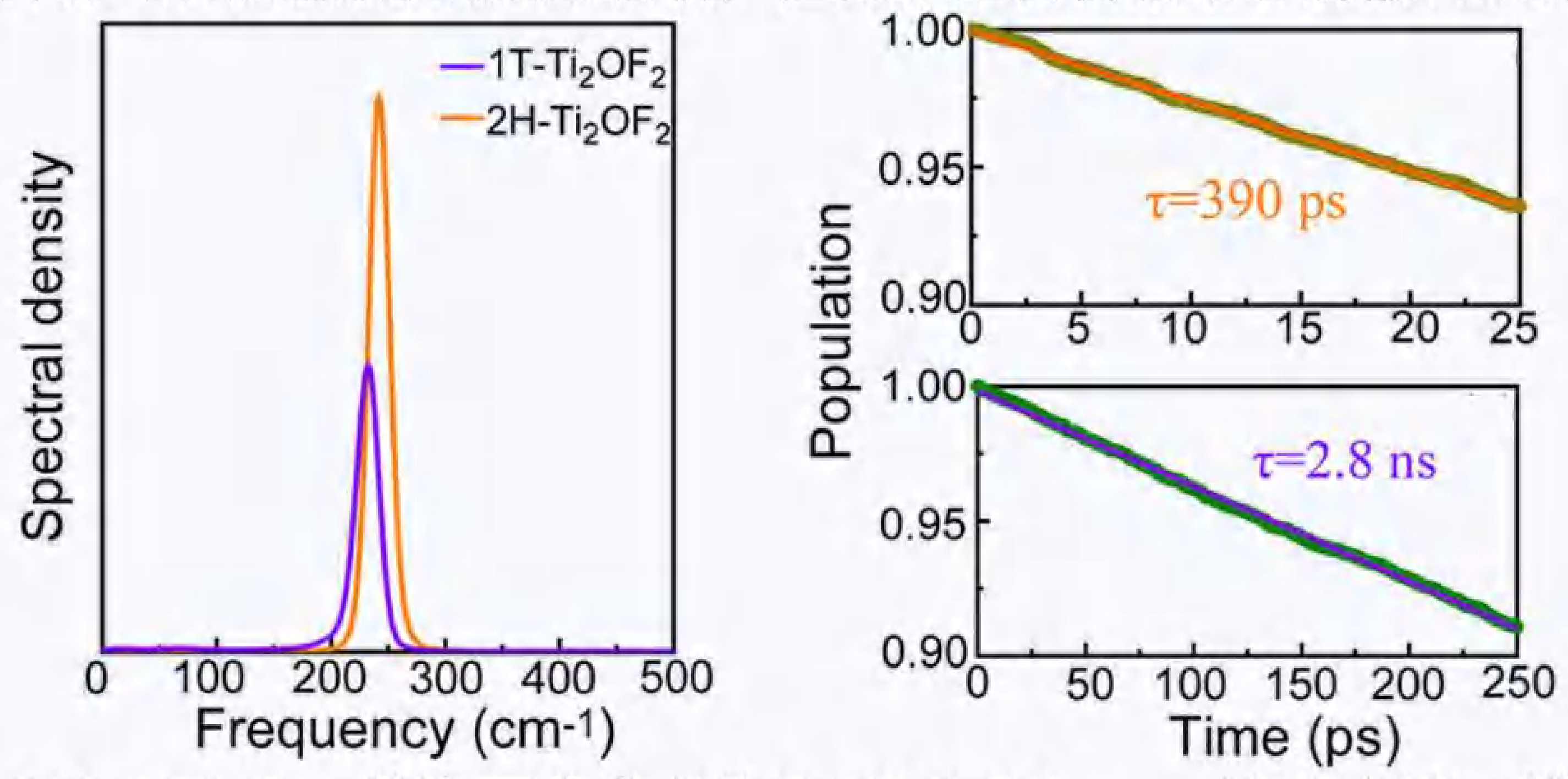

2H-和1T-Ti_2OF_2载流子寿命分为0.39 和2.8 ns，比肩主流二维半导体。

结论

- ➢ 扩展传统MXene到过渡金属氧化物，命名为MOene。
- ➢ 表面卤化可实现本征超导到半导体的转变，可用于光电器件。
- ➢ 应力工程可诱导量子相变，形成新颖的二维费米子。
- ➢ 在红外和可见光波段有不错的光吸收，可用于红外探测与太阳能电池。
- ➢ 大的带隙，弱的非绝热耦合，短的退相干实间 → 长的载流子寿命。

参考文献

1. Kornilov, II et al., *Metall. Mater. Trans. B, 1970, 1, 2569.*
2. Wang, Ruxing et al., *J. Alloys Compd, 2019, 786, 607.*
3. Fan, Yunjie et al., *Mater. Sci. Eng. B, 2004, 371, 103.*
4. Yan, Luo; Zhou, Liujiang; et al., *J. Phys. Chem. Lett. 2020, 12, 494–500.*
5. Yan, Luo; Zhou, Liujiang; et al., *Nano Lett. 2022. Accepted.*
https://doi.org/10.1021/acs.nanolett.2c01914

ISE, CAEP **ICM^3 - 2022**

Numerical simulation of plastic bonded explosive by three-body potential peridynamics model

Xiaolong Li, Zhiming Hao

Institute of Systems Engineering, China Academy of Engineering Physics, Mianyang 621999, China

Email：lixiaolong20@gscaep.ac.cn

Introduction/Highlight

As well known, there exists Poisson's ratio limitation issue in classical bond based peridynamic (BB-PD) model. In contrast, the formulated three-body potential PD model can solve this issue effectively due to considering three-body interaction micro-potential between material points within PD framework. In present study, combined with bond stretch based failure criterion, some numerical specimens of plastic bonded like materials are simulated associating with quasi-static elastic brittle mixed mode fracture behaviors. The performance of the proposed PD model is validated by the results.

Methods

1.0 Three-body potential PD model

Different from the central pair-wise potential used in BB-PD model, the modified micro-potential, i.e., three-body potential, takes the form as

$$w_{ij} = \frac{1}{2} c_{\mathrm{s}} s^2 \left|\xi_{ij}\right| + \int_{H_i} \frac{1}{4} c_{\mathrm{t}} \left|\xi_{ij}\right| \left|\xi_{ik}\right| \left(\cos\theta_{jik} - \cos\theta_{jik0}\right)^2 dV_k \quad (1)$$

Its physical meaning is illustrated in Fig. 1.

And the PD strain density energy (SED) is defined as.

$$W\left(\underline{\mathbf{Y}}\right) = \frac{1}{2}\int_{H_i} w_{ij} \mathrm{d}V_j \quad (2)$$

As the procedures provided by Silling et al. (2007), taking Frechet derivative of PD SED given in Eq. (2), we can get the three-body potential PD force function as

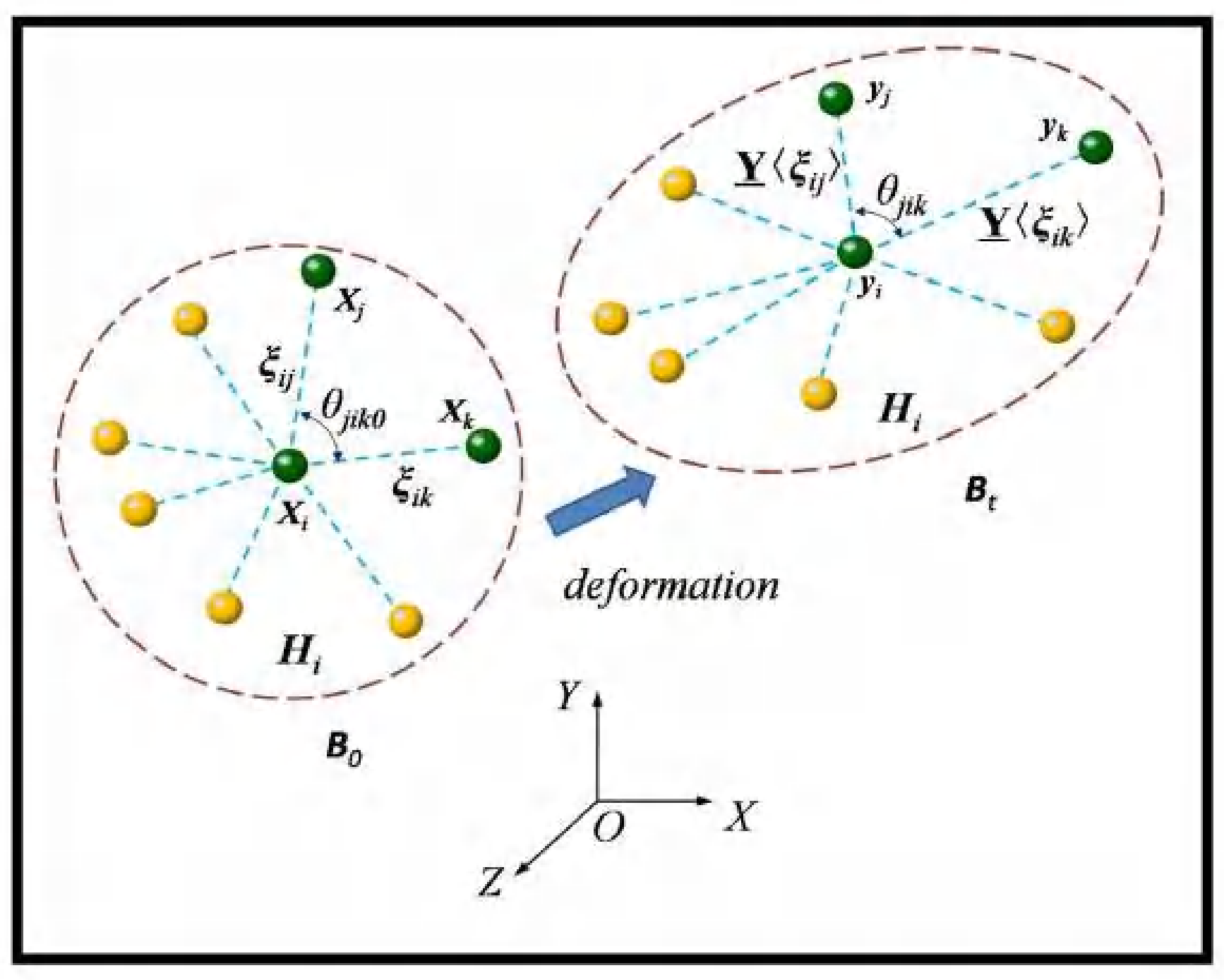

Fig. 1 Schematic of three-body micro-potential.

$$\begin{aligned} \underline{\mathbf{T}}\left(\underline{\mathbf{Y}}\right)\left\langle\xi_{ij}\right\rangle = & \frac{1}{2} c_{\mathrm{s}} s \frac{\xi_{ij}+\boldsymbol{\eta}_{ij}}{\left|\xi_{ij}+\boldsymbol{\eta}_{ij}\right|} \\ & + \frac{1}{2}\int_{H_i}\left\{\frac{c_{\mathrm{t}}\left|\xi_{ij}\right|\left|\xi_{ik}\right|\left(\cos\theta_{jik}-\cos\theta_{jik0}\right)}{\left|\underline{\mathbf{Y}}\left\langle\xi_{ij}\right\rangle\right|}\mathbf{e}_{\mathrm{t}}\left(\underline{\mathbf{Y}}\left\langle\xi_{ij}\right\rangle, \underline{\mathbf{Y}}\left\langle\xi_{ik}\right\rangle\right)\right\}\mathrm{dV}_k \end{aligned} \quad (3)$$

with

$$\mathbf{e}_{\mathrm{t}}\left(\underline{\mathbf{Y}}\left\langle\xi_{ij}\right\rangle, \underline{\mathbf{Y}}\left\langle\xi_{ik}\right\rangle\right) = \frac{\underline{\mathbf{Y}}\left\langle\xi_{ik}\right\rangle}{\left|\underline{\mathbf{Y}}\left\langle\xi_{ik}\right\rangle\right|} - \cos\theta_{jik}\frac{\underline{\mathbf{Y}}\left\langle\xi_{ij}\right\rangle}{\left|\underline{\mathbf{Y}}\left\langle\xi_{ij}\right\rangle\right|} \quad (4)$$

Therefore, the PD force density between two material points is

$$\mathbf{f}_{ij} = \underline{\mathbf{T}}\left(\underline{\mathbf{Y}}\right)\left\langle\xi_{ij}\right\rangle - \underline{\mathbf{T}}\left(\underline{\mathbf{Y}}\right)\left\langle-\xi_{ij}\right\rangle \quad (5)$$

Based on SED equalization, the conversion relations between PD material parameters and elastic constants are listed in Table 1.

Table 1 PD material parameters c_{s}, c_{t} for the proposed PD model

		c_{s}	c_{t}
3D		$\frac{30Ev}{\pi\delta^4(1+v)(1-2v)}$	$\frac{9E(1-4v)}{\pi^2\delta^8(1+v)(1-2v)}$
2D	Plane stress	$\frac{24Ev}{\pi\delta^3(1-v^2)}$	$\frac{9E(1-3v)}{\pi^2\delta^6(1-v^2)}$
	Plane strain	$\frac{24Ev}{\pi\delta^3(1+v)(1-2v)}$	$\frac{9E(1-4v)}{\pi^2\delta^6(1+v)(1-2v)}$

2.0 Failure criterion

Bond stretch based failure criterion is used in present study, as

$$\mu\left(\xi_{ij}, t\right) = \begin{cases} 1, & s < s_c \\ 0, & s \geq s_c \end{cases} \quad (6)$$

And the damage degree index for a point at time t is a scalar value function defined by Silling et al. (2005).

Results/Discussion

Polymer square plate subjected to mixed-mode loads

A pre-cracked square-plate subjected to quasi-static diagonal loads is used to test the ability of the proposed PD model as shown in Fig. 2. A series of numerical specimens with different inclinations of the initial crack are simulated. The predicted final crack growth paths indicated by damage maps are in good agreement with corresponding experimental results as shown in Fig. 3.

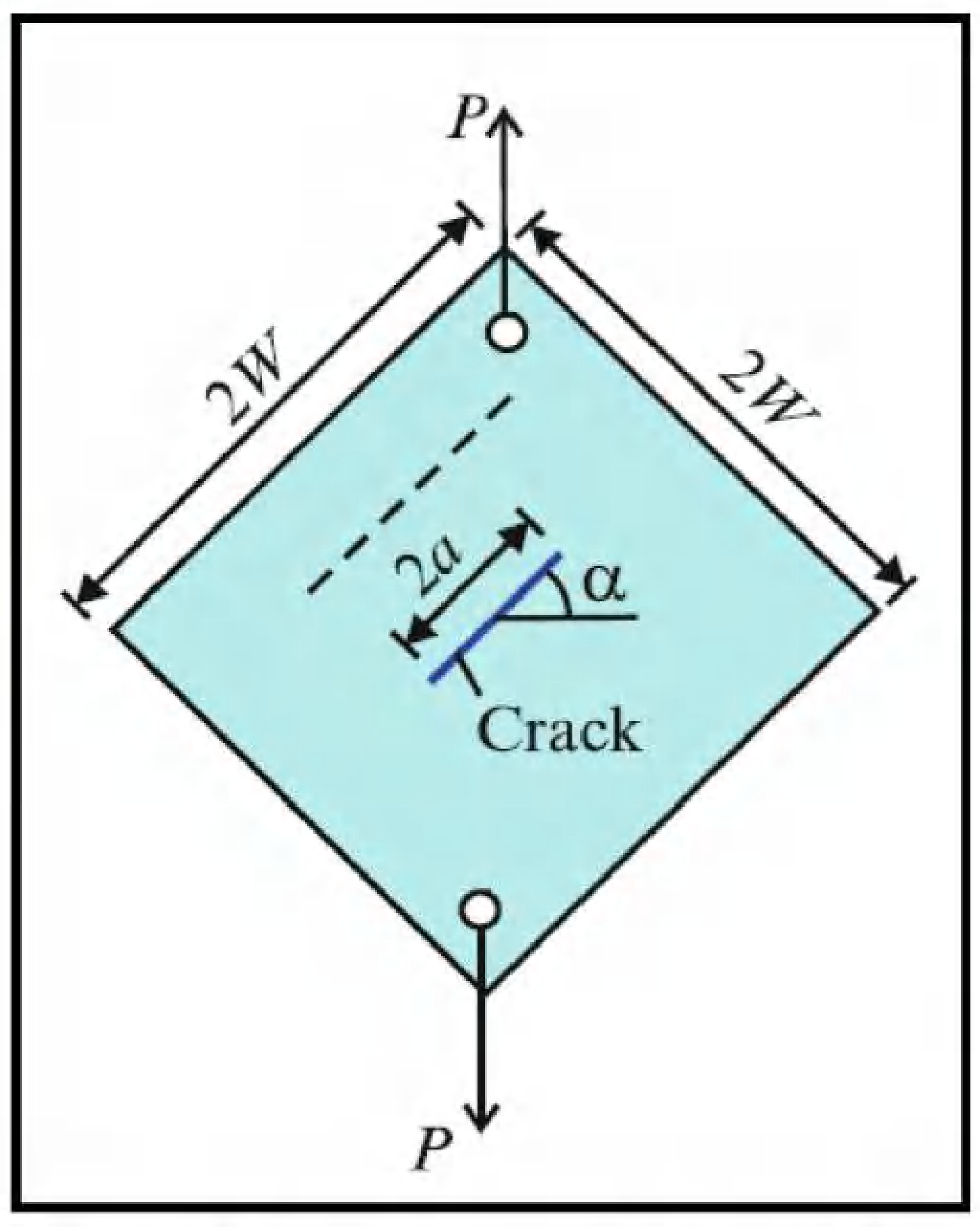

Fig.2 Dimensions of diagonally loaded square plate

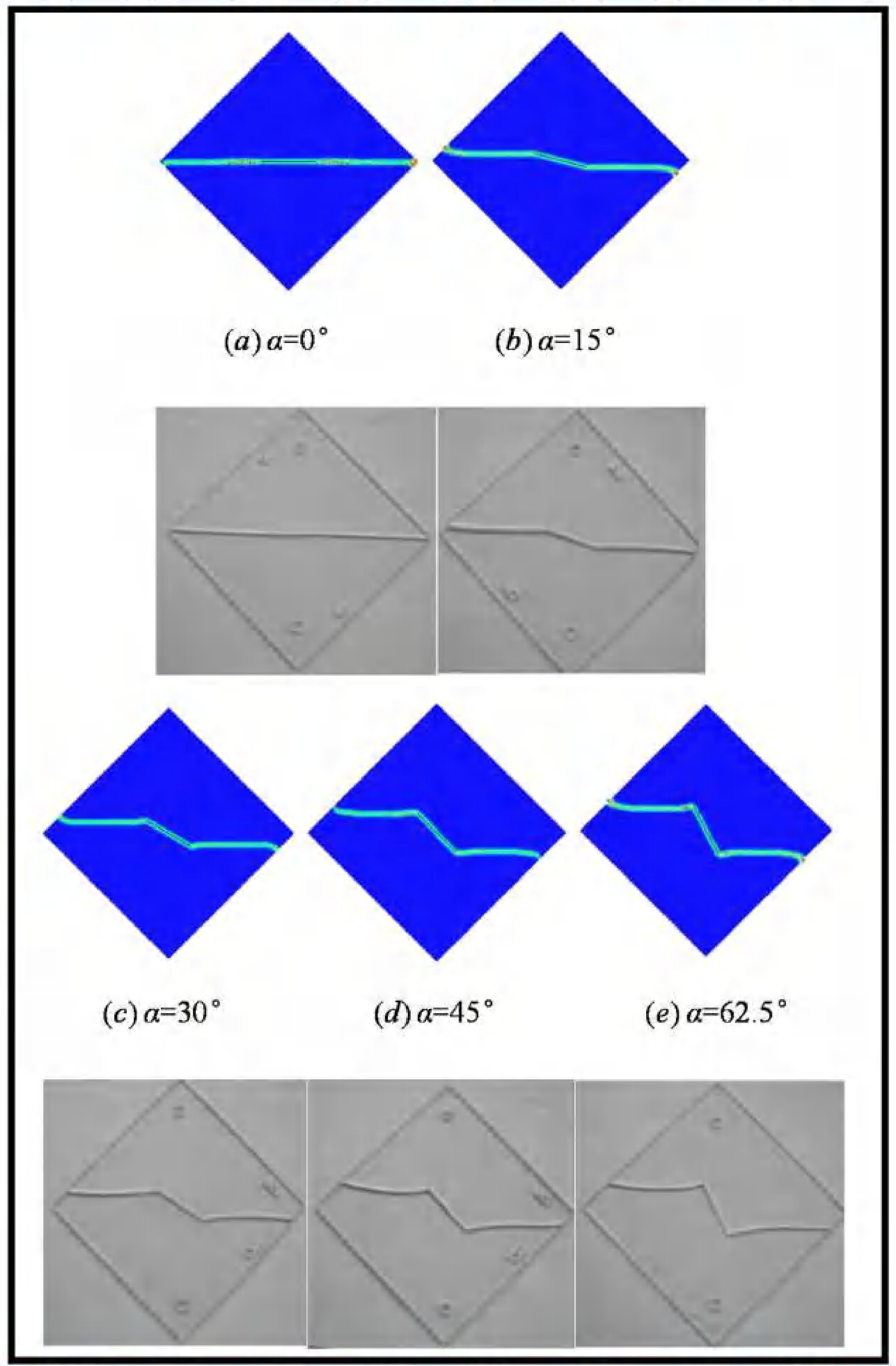
(a) α=0° (b) α=15°

(c) α=30° (d) α=45° (e) α=62.5°

Fig. 3 Comparison of final crack growth paths

Conclusions

(1) The formulated three-body potential PD model contains two material parameters. Therefore, it owns the ability of eliminating restriction on values of Poisson' ratio;

(2) Combining with bond stretch failure criterion, the proposed numerical method can capture the fracture behaviors effectively for elastic brittle materials under quasi-static loading condition.

湖南師範大學 · 物理与电子科学学院
HUNAN NORMAL UNIVERSITY SCHOOL OF PHYSICS AND ELECTRONICS

First Principles Study of WS_2 Moiré Superlattice Electron Structure

Shengguo Yang,[1] Mingxing Chen [1,*]
[1]Key Laboratory for Matter Microstructure and Function of Hunan Province, Key Laboratory of Low-Dimensional Quantum Structures and Quantum Control of Ministry of Education, School of Physics and Electronics, Hunan Normal University, Changsha 410081, China

Twisted bilayer transition metal dichalcogenides as a platform to explore moiré physics. We investigate electronic structures of a series of twisted bilayers WS_2 using first-principles. We find that moiré potential modulates the band structure of TMD, which result intervalley scattering between the Γ and K valleys. As a result, new quasi-particle pattern obtained, which was not seen in the monolayers and bilayers.

A. WS_2 Moiré Superlattice

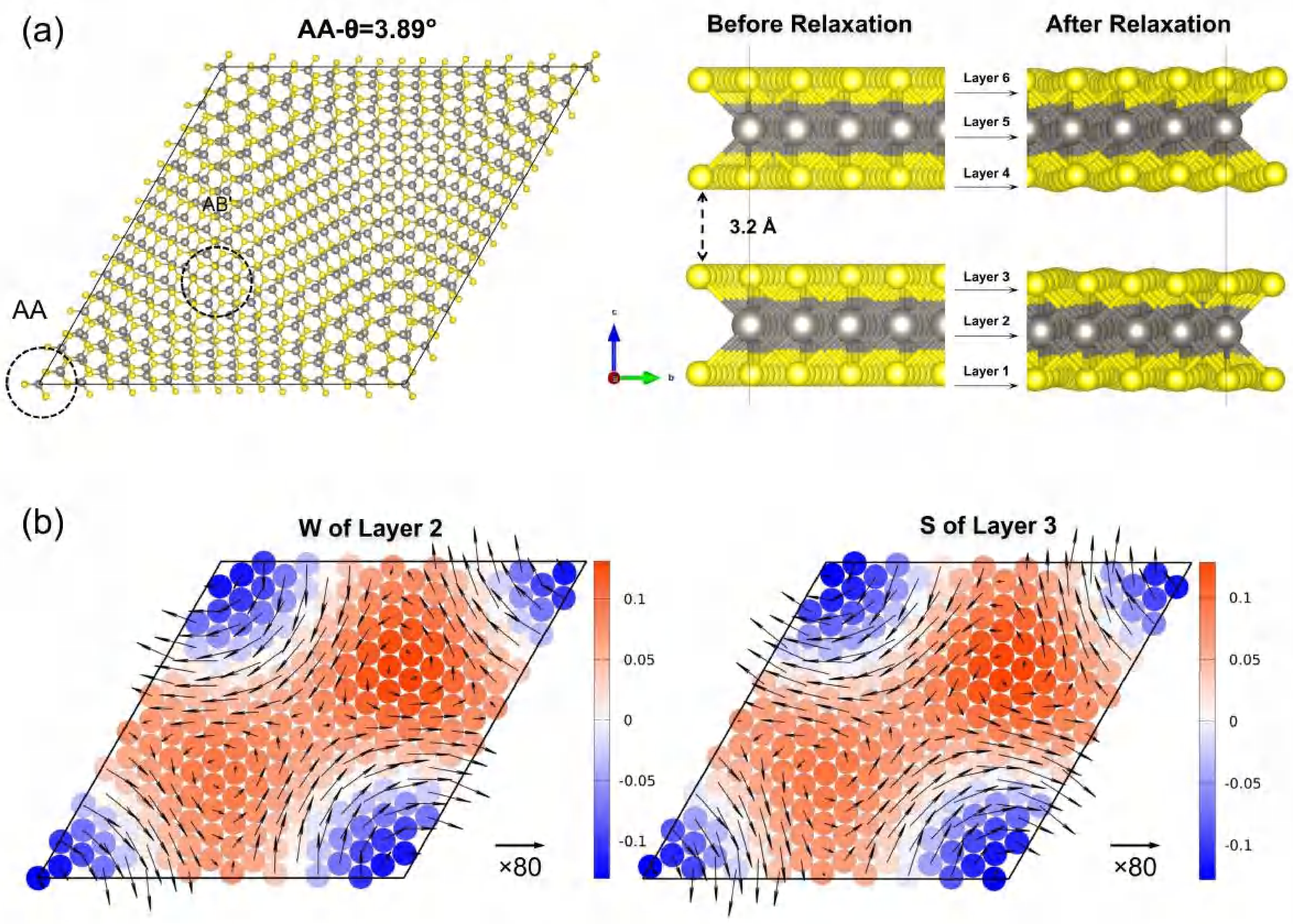

Figure 1. Strong structural reconstruction in in-plane (arrows) and out-of-plane (red and blue) induced by moiré potential.

B. Brillouin Zone and Flat Band Structure

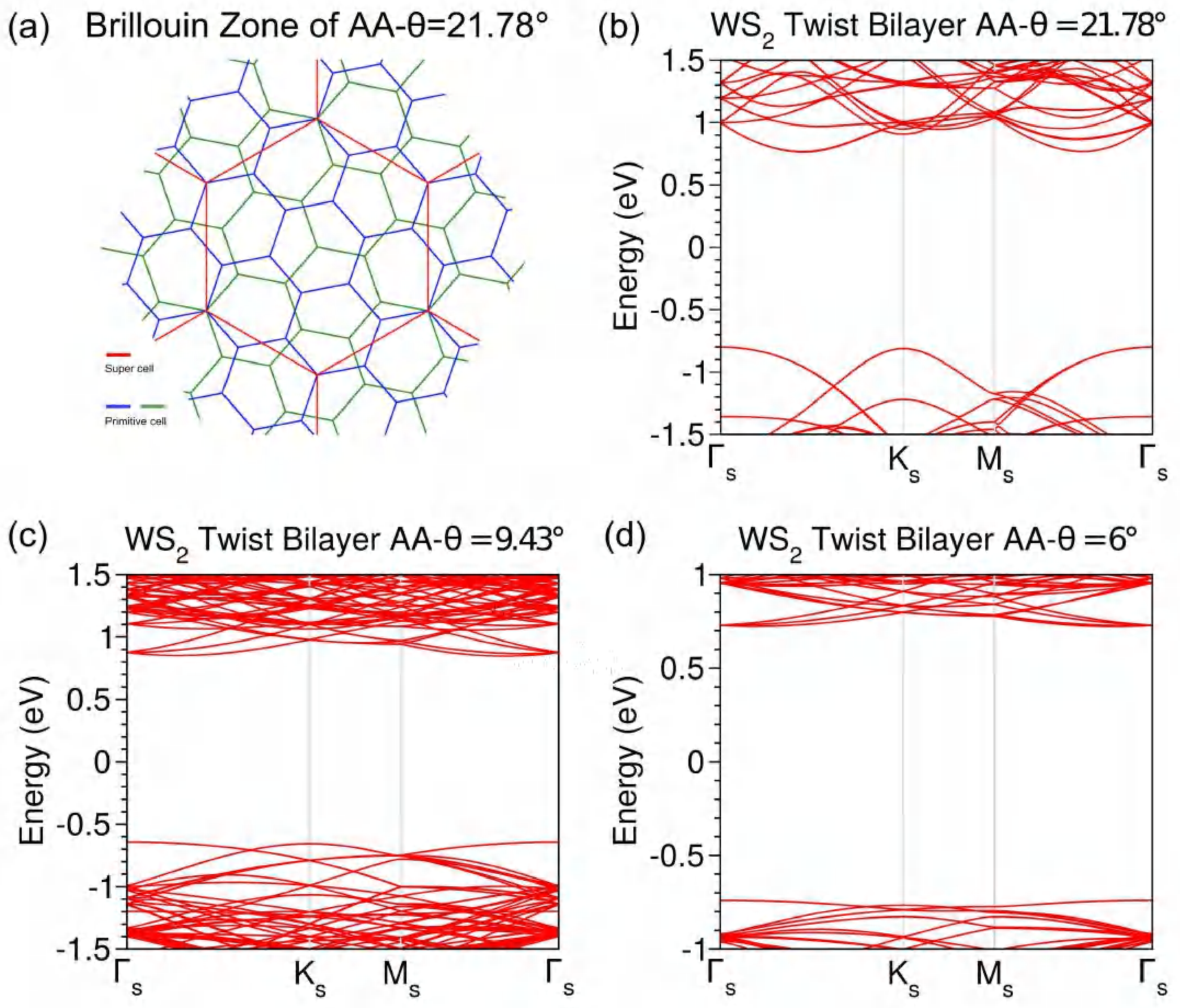

Figure 2. The emergence of flat bands in WS_2 moiré superlattice.

C. Unfolded Band Structure

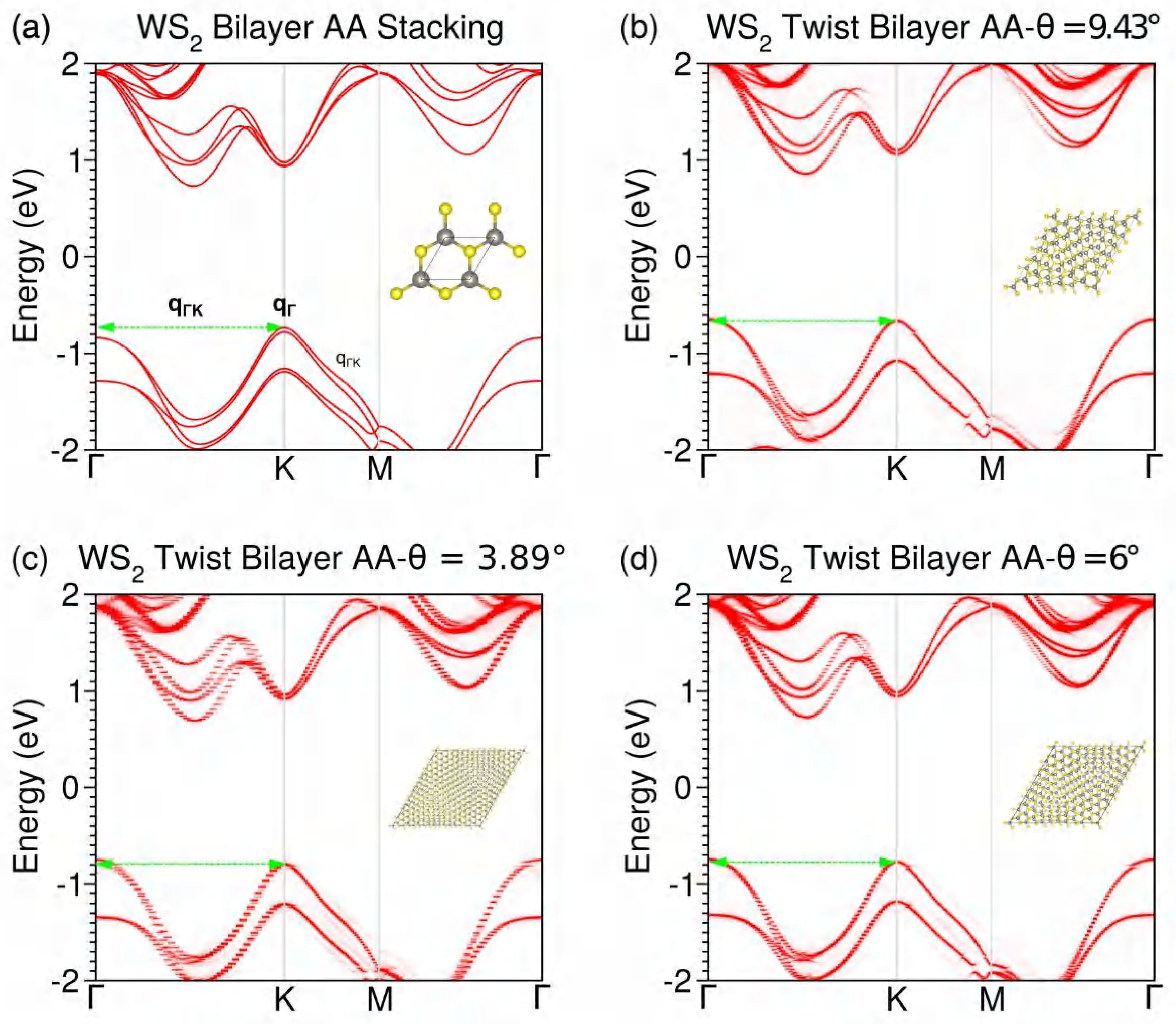

Figure 3. Relative shifting of Γ and K valleys is modulated by moiré potential.

D. Quantum quasi-particle interference of WS_2

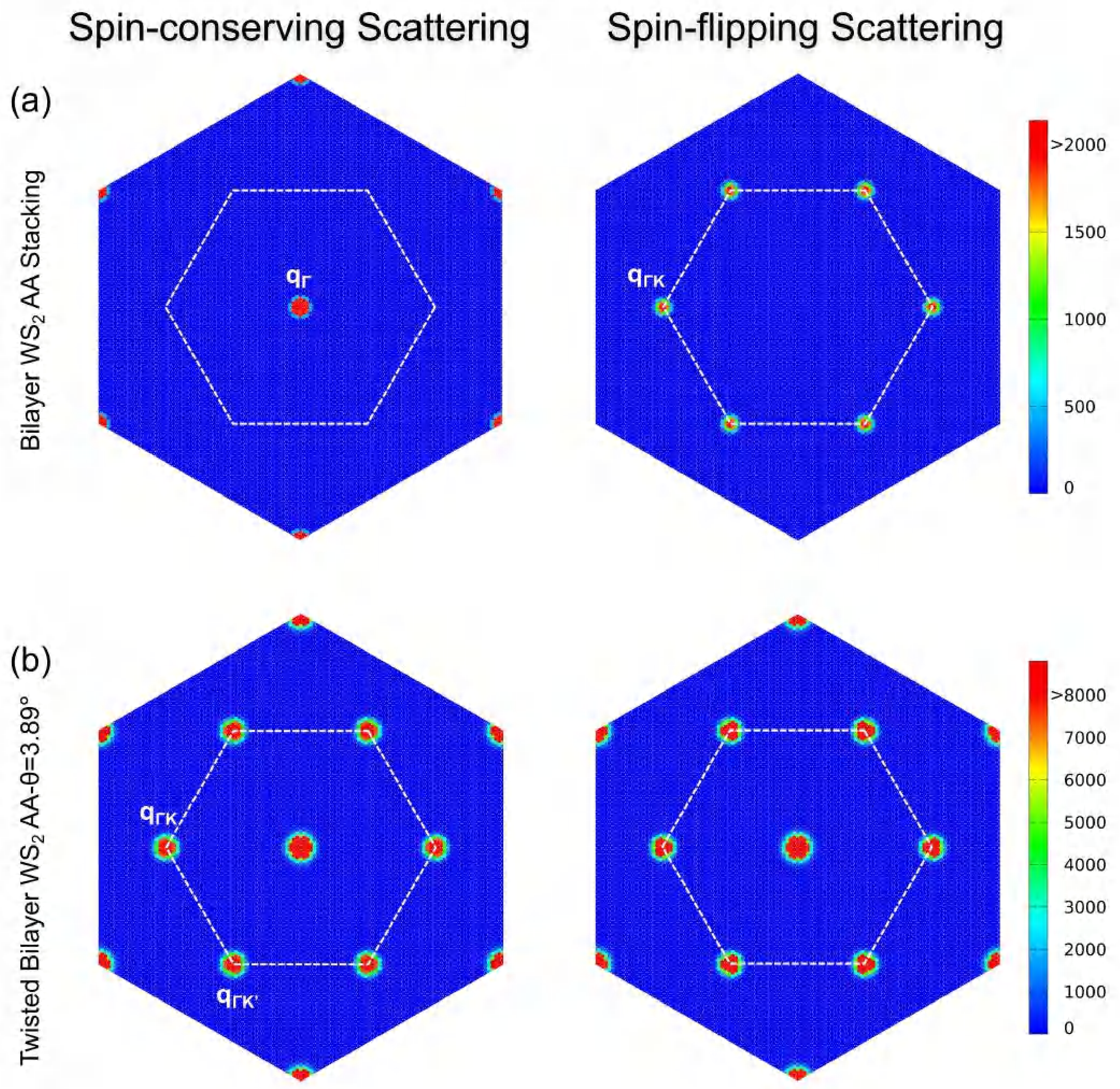

Figure 4. Intervalley scattering for twisted bilayer WS_2 at same the energy as in Fig. 3a arising from moiré potential.

E. Conclusions

- The emergence of flat bands in WS_2 moiré superlattice.
- Relative shifting of Γ and K valleys modulated by the moiré potential.
- New quantum quasi-particle interference due to intervalley scattering arising from moiré potential.

F. Acknowledgment

This work was supported by the National Natural Science Foundation of China (Grants No. 11774084, No. 12174098, No. U19A2090, and No. 91833302).

Email: sgyang@hunnu.edu.cn; mxcheng@hunnu.edu.cn

2022材料多尺度计算模拟国际会议
International Conference of Multi-scale Modeling and Simulation of Materials (ICM^3-2022)
2022年7月4-8日 | 四川·成都 4-8th July，2022 | Chengdu·China

Valence Oscillation of Transition Metals in Oxygen Evolution Reactions via Ligand Modification

Pai Wang, Yanning Zhang*
Institute of Fundamental and Frontier Sciences, University of Electronic Science and Technology of China,
Pai Wang: hanjiang_wang777@std.uestc.edu.cn *Yanning Zhang: yanningz@uestc.edu.cn

Introduction

Decorating the organic ligands becomes the powerful technique to achieve control of the environment surrounding the active site. Here, a coordination compound which includes 1,10-phenanthroline (phen) ligand and cobalt oxide is fabricated. Therefore, we demonstrate the prominent roles played by ligands in tuning electrocatalysis through modulating the valence of activity site. Our calculations elaborate the valence oscillation mechanism and offer a new dimension to engineer and optimize the electrocatalytic performance for various TMs and beyond.

Results

◆Ligand-directed modulation for enhanced oxygen reduction

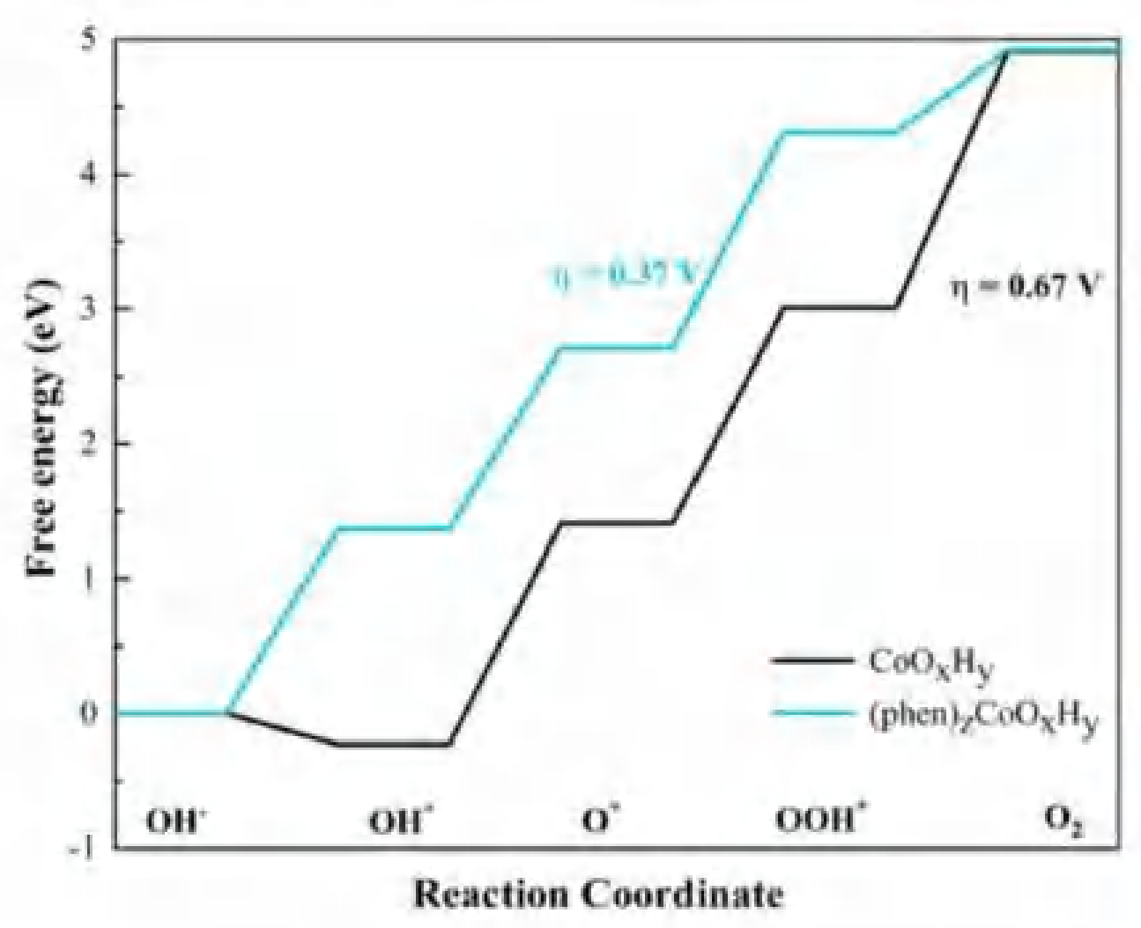

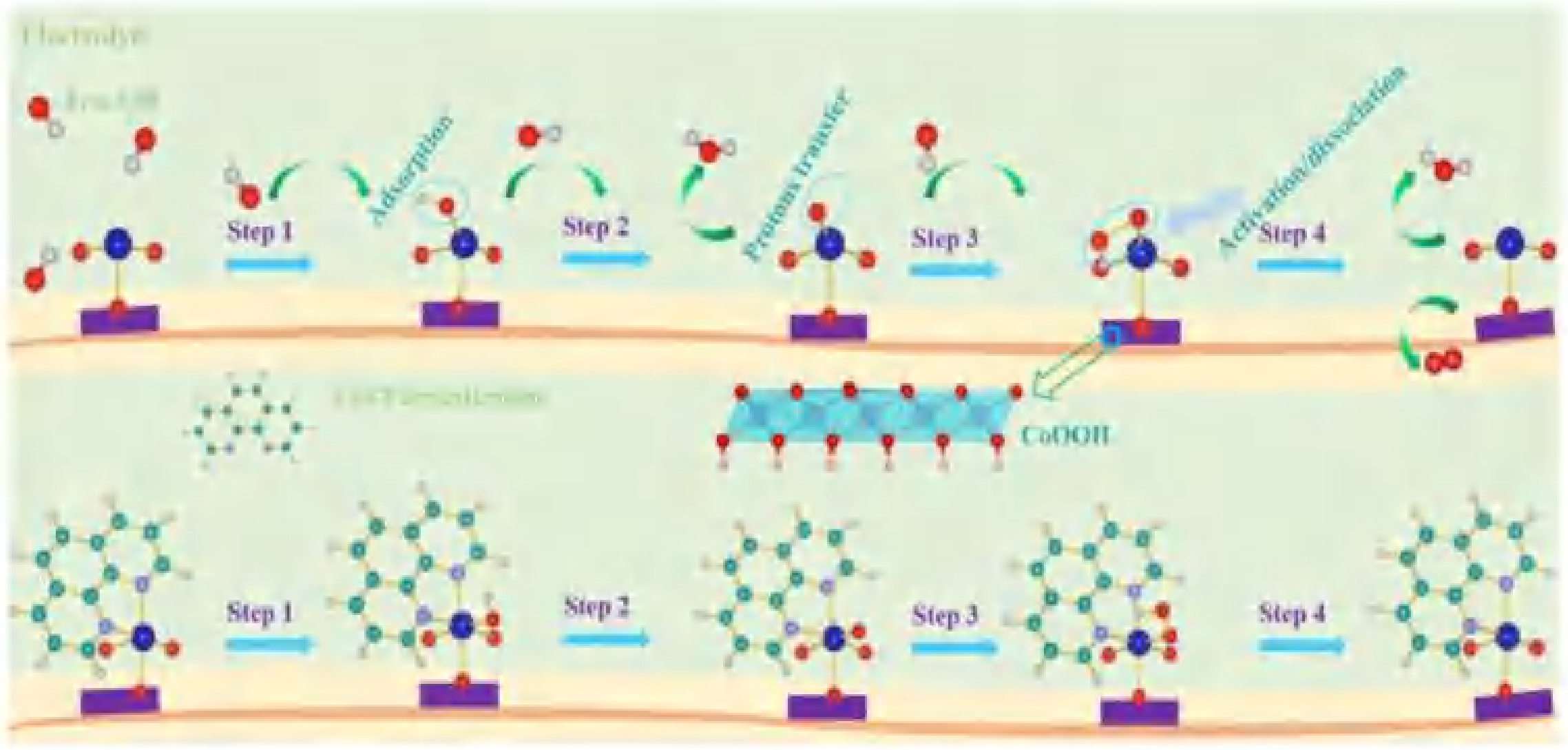

- ➢ The phen ligand highly improves catalytic activity for Cobalt sites by tuning its coordination environment.

◆Valence oscillation of activity sites for oxygen evolution

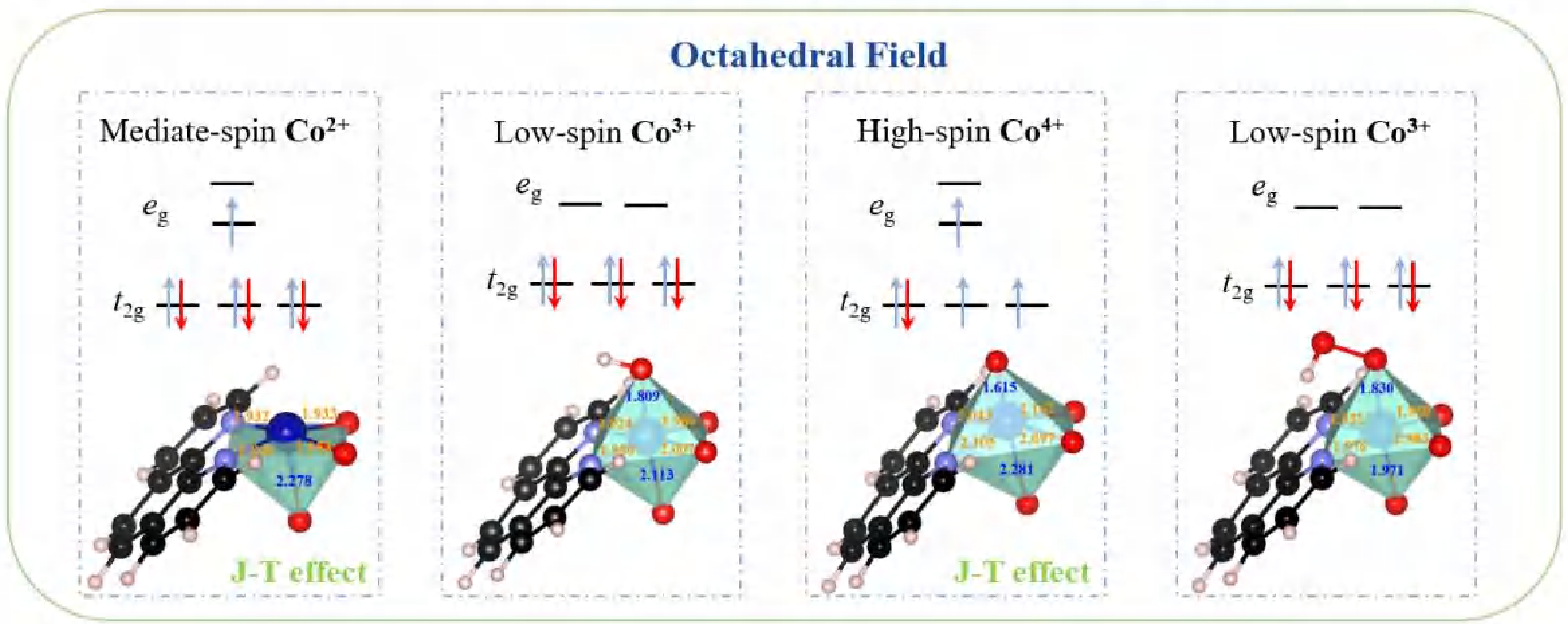

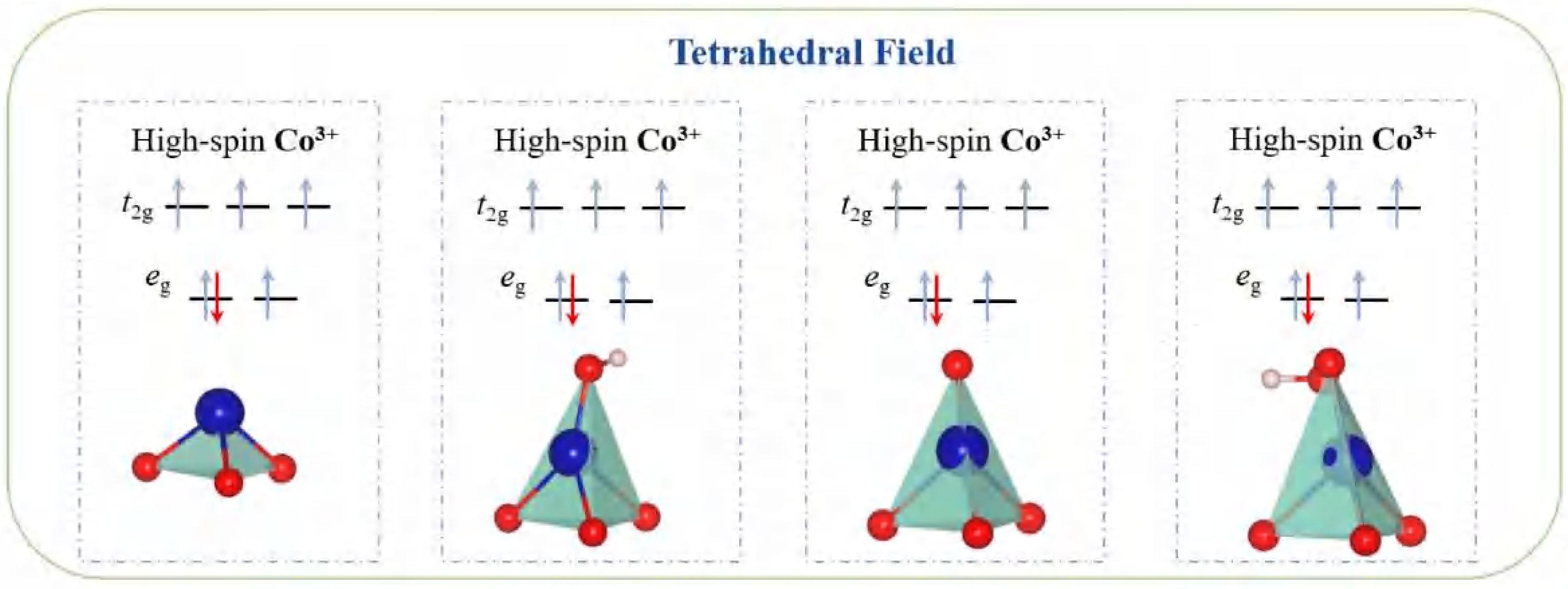

- ➢ The ligand can change the crystal field of the adsorption site, and some structures show the Jahn-Teller effect, resulting in different electron arrangements to produce Co with several valence states during oxygen evolution process.

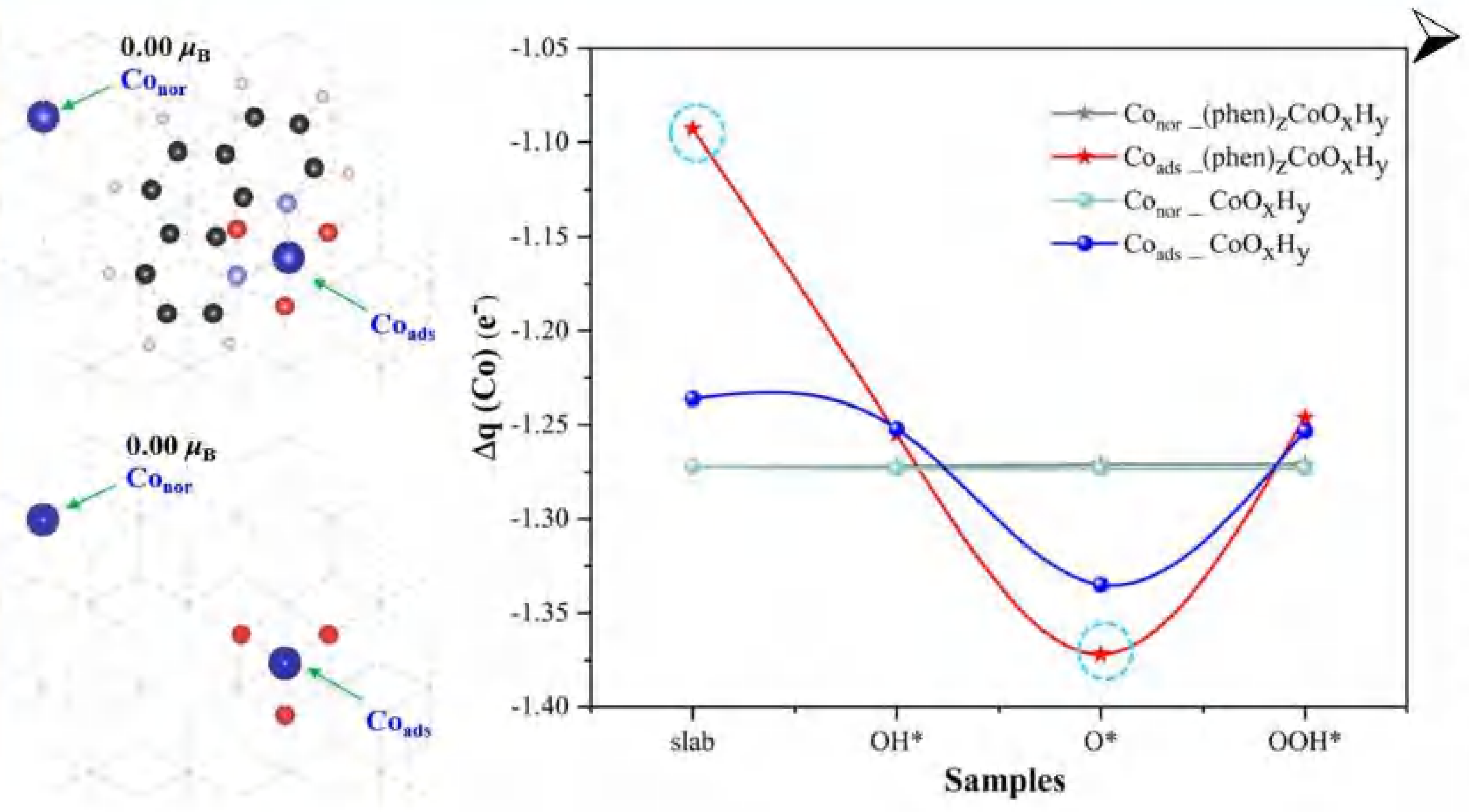

- ➢ The comparison of charge transfer between the active site and the normal Co confirms the phenomenon of valence oscillation in the system;

◆Strong interactions during oxygen evolution

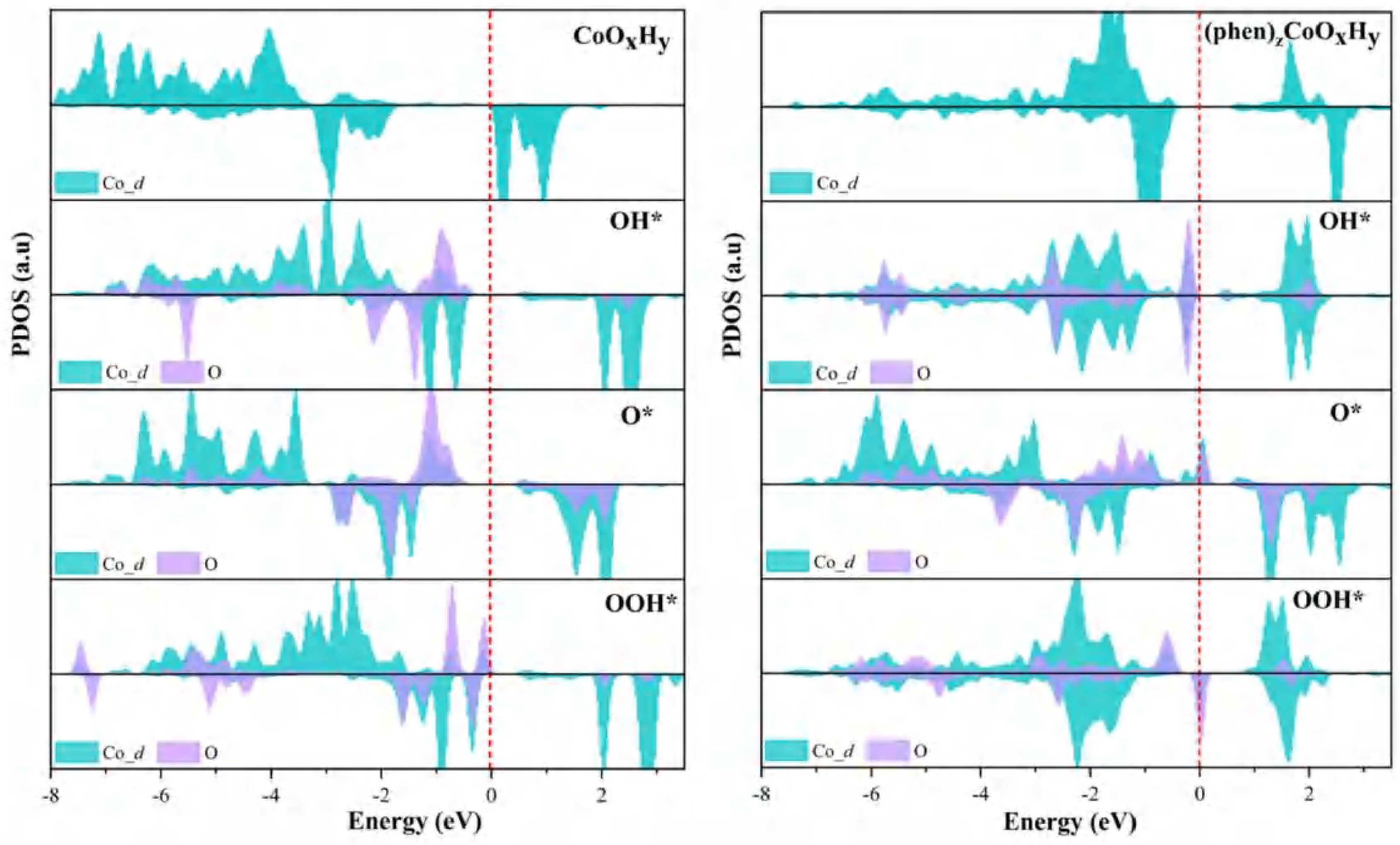

- ➢ Adjustment of the coordination environment enables strong interactions between adsorption sites and adsorbed groups.

◆Implicit solvation model for corroboration

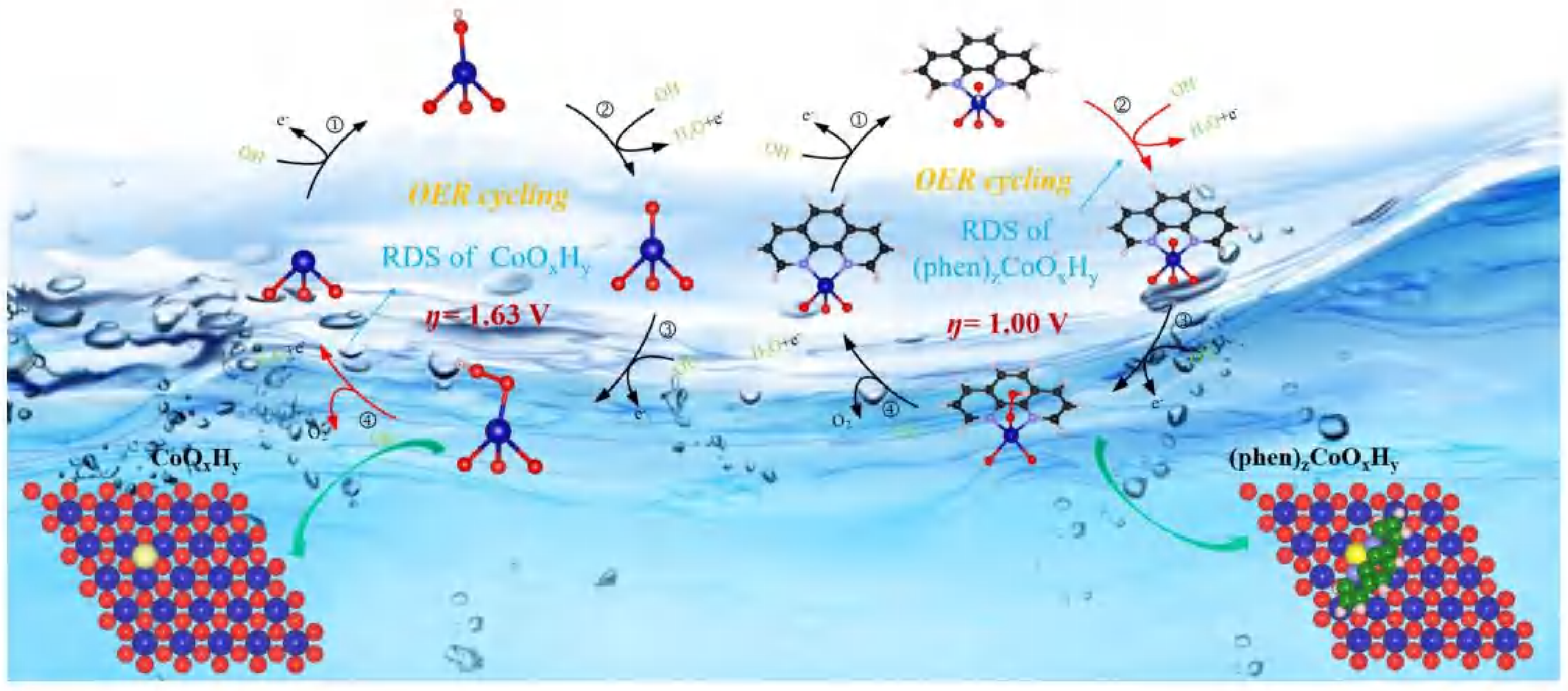

- ➢ Implicit solvation effects also confirm that phen ligand enhances the activity of Co sites.

Conclusions

The phen ligand can effectively adjust the coordination environment of Co site and cause its valence to oscillate, finally improving its catalytic performance. This work provides a detailed theoretical mechanism by which the coordination environment enhances oxygen evolution proceedings.

References

- *Nat. Catal.*, 2021, **4**, 1050–1058
- *Chem. Sci.*, 2019, **10**, 3340–3345
- *ACS Appl, Mater, Interfaces*, 2021, **13**, 48661−48668

Contact

http://msdlab.uestc.edu.cn
Materials Calculation and Design Lab

Computation and data driven discovery of topological phononic materials

Jiaxi Liu[1,2], Jiangxu Li[1,2], Stanley A. Baronett[3], Mingfeng Liu[1,2], Lei Wang[1,2], Ronghan Li[1,2], Yun Chen[1,2], Dianzhong Li[1], Qiang Zhu[3], and Xing-Qiu Chen,[1,2‡]

1 Shenyang National Laboratory for Materials Science, Institute of Metal Research, Chinese Academy of Sciences, Shenyang, Liaoning, China
2 School of Materials Science and Engineering, University of Science and Technology of China, Shenyang, Liaoning, China
3 Department of Physics and Astronomy, University of Nevada, Las Vegas, NV, USA.

Abstract

The discovery of topological quantum states marks a new chapter in condensed matter physics and materials science. Analogous to electronic system, topological concepts have been extended into phonons, boosting the birth of topological phononics (TPs). We present a high-throughput screening and data-driven approach to compute and evaluate TPs among over 10,000 real materials. We have discovered 5014 TP materials and grouped them into two main classes of Weyl and nodal-line (ring) TPs. We have clarified the physical mechanism for the occurrence of single Weyl, high degenerate Weyl, individual nodal-line (ring), nodal-link, nodal-chain, and nodal-net TPs in various materials. Among the phononic systems, we have predicted the hourglass nodal net TPs in TeO_3. In addition, we found that different types of TPs can coexist in many materials (ScZn). Their potential applications and experimental detections have been discussed. This work substantially increases the amount of TP materials, which enables an in-depth investigation of their structure-property relations and opens new avenues for future device design related to TPs.

Schematic flowchart

Workflow for high-throughput screening of topological phonons

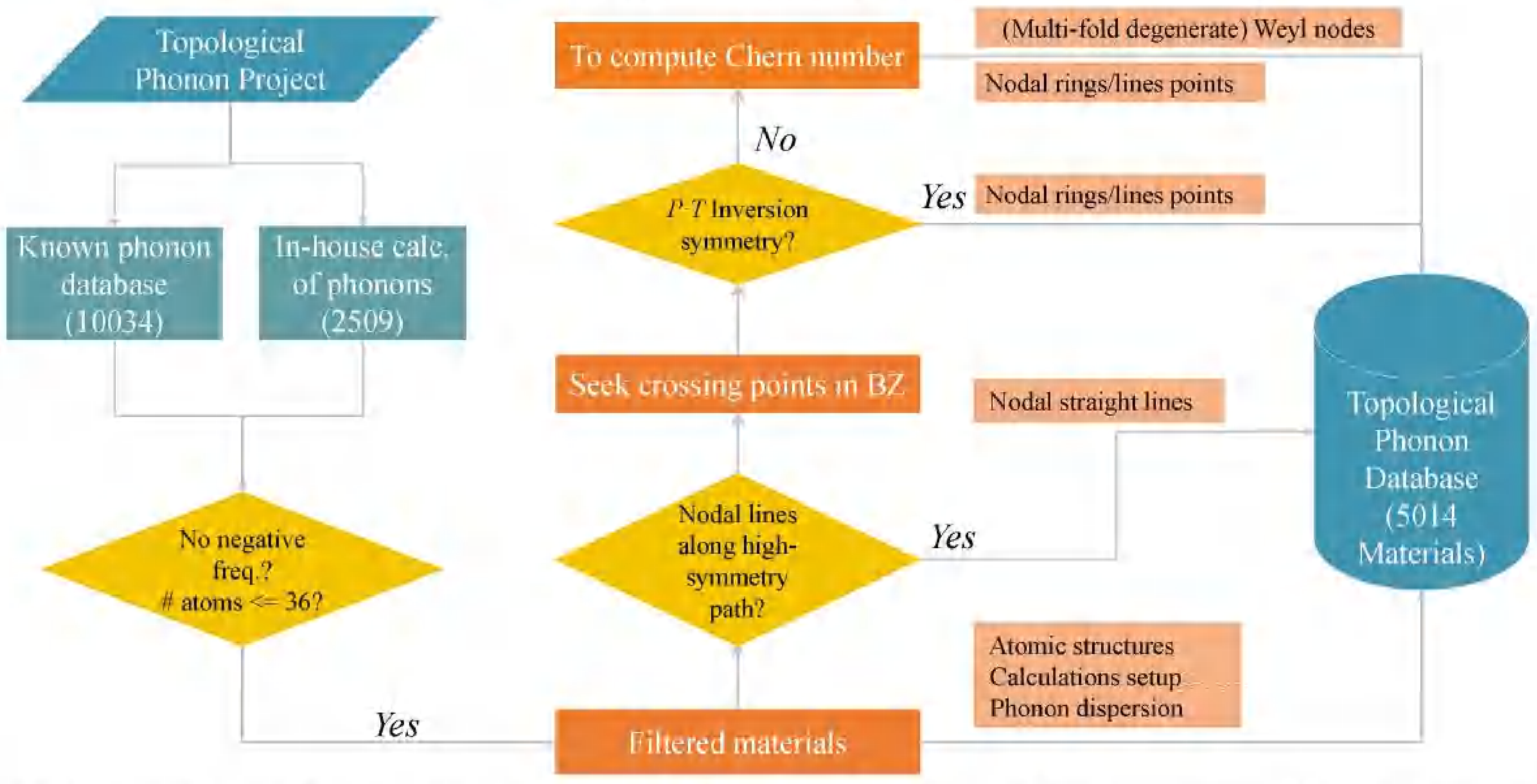
Topological Phonon Project

Known phonon database (10034)

In-house calc. of phonons (2509)

No negative freq.? # atoms <= 36?

Yes

Filtered materials

Atomic structures
Calculations setup
Phonon dispersion

Nodal lines along high-symmetry path?

Yes

Nodal straight lines

Seek crossing points in BZ

P·T Inversion symmetry?

Yes

Nodal rings/lines points

No

To compute Chern number

(Multi-fold degenerate) Weyl nodes

Nodal rings/lines points

Topological Phonon Database (5014 Materials)

This workflow is capable of identifying the features of TPs, elucidating details of topology and constructing TPs database by computing and collecting phonons of a variety of solid materials in an automatic manner.

Nodal-line (ring) TPs in ScZn

Nodal-line (ring) TPs formed by continuous phononic band crossings. We introduce ScZn (B2 lattice structure) with the PT symmetries, that hosts both nodal-ring and straight line TPs.

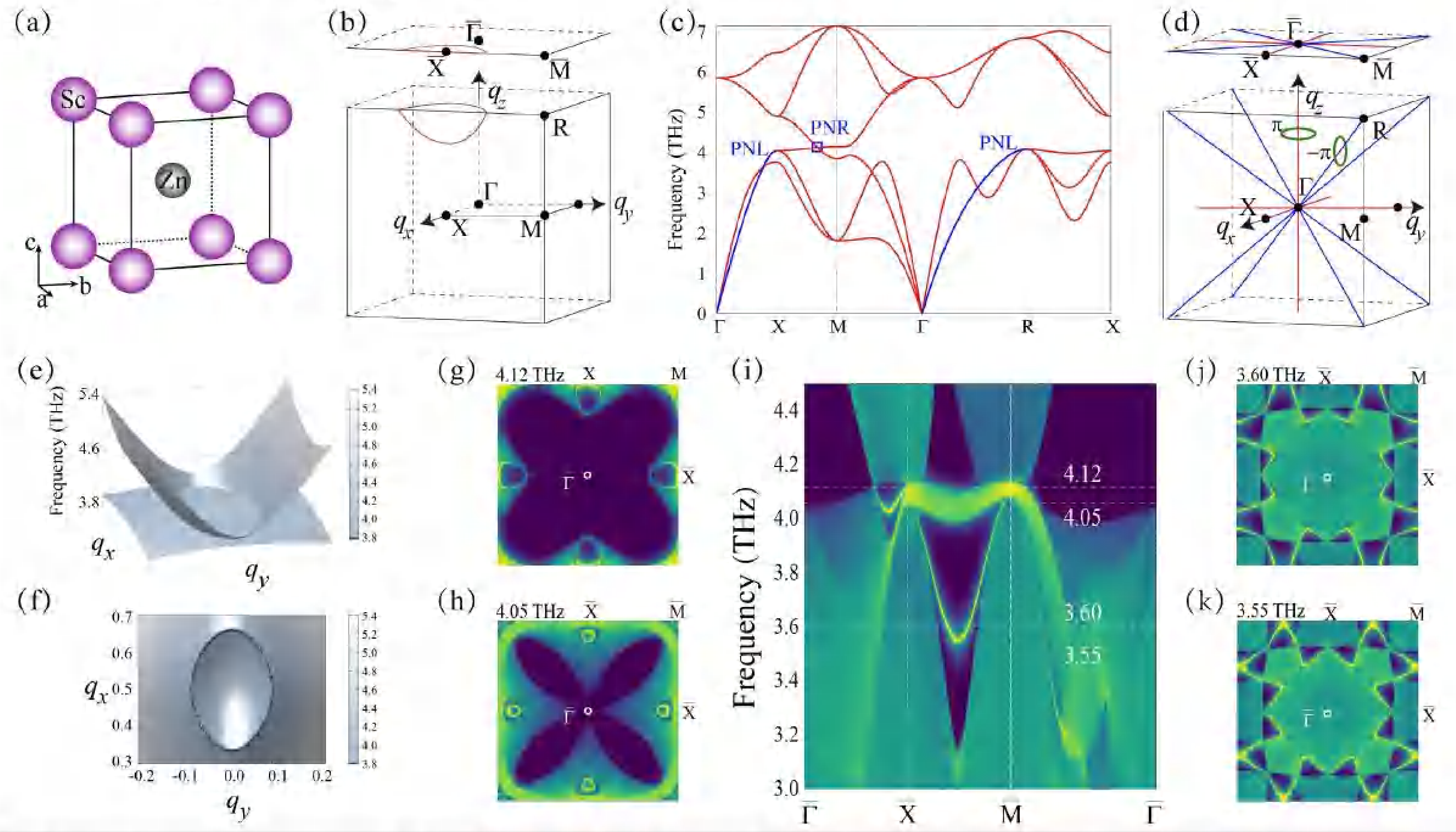

FIG.2. a Crystal structure of ScZn (Pm-3m 221). b BZ of ScZn and the illustration of the nodal-ring TPs. c Phonon spectrum of ScZn. d The illustrations of the straight nodal-line TPs along the Γ–R and Γ–X lines. e, f 3D phonon bands around the nodal-line TPs surrounding the M point. g, h The derived phononic surface states at 4.12 and 4.05 THz, respectively, of the (001) surface BZ (as defined in b). i The surface phononic spectrum of the (001) surface. j, k Phononic surface states at 3.60 and 3.55 THz, respectively.

Hourglass nodal-net of TeO_3

Besides nodal-line (ring) TPs associated with the symmorphic symmetries, nonsymmorphic space groups can produce the symmetry-enforced nodal-line (ring) TPs. Nonsymmorphic symmetries are formed by combining the operations of the point group and translations by fraction.

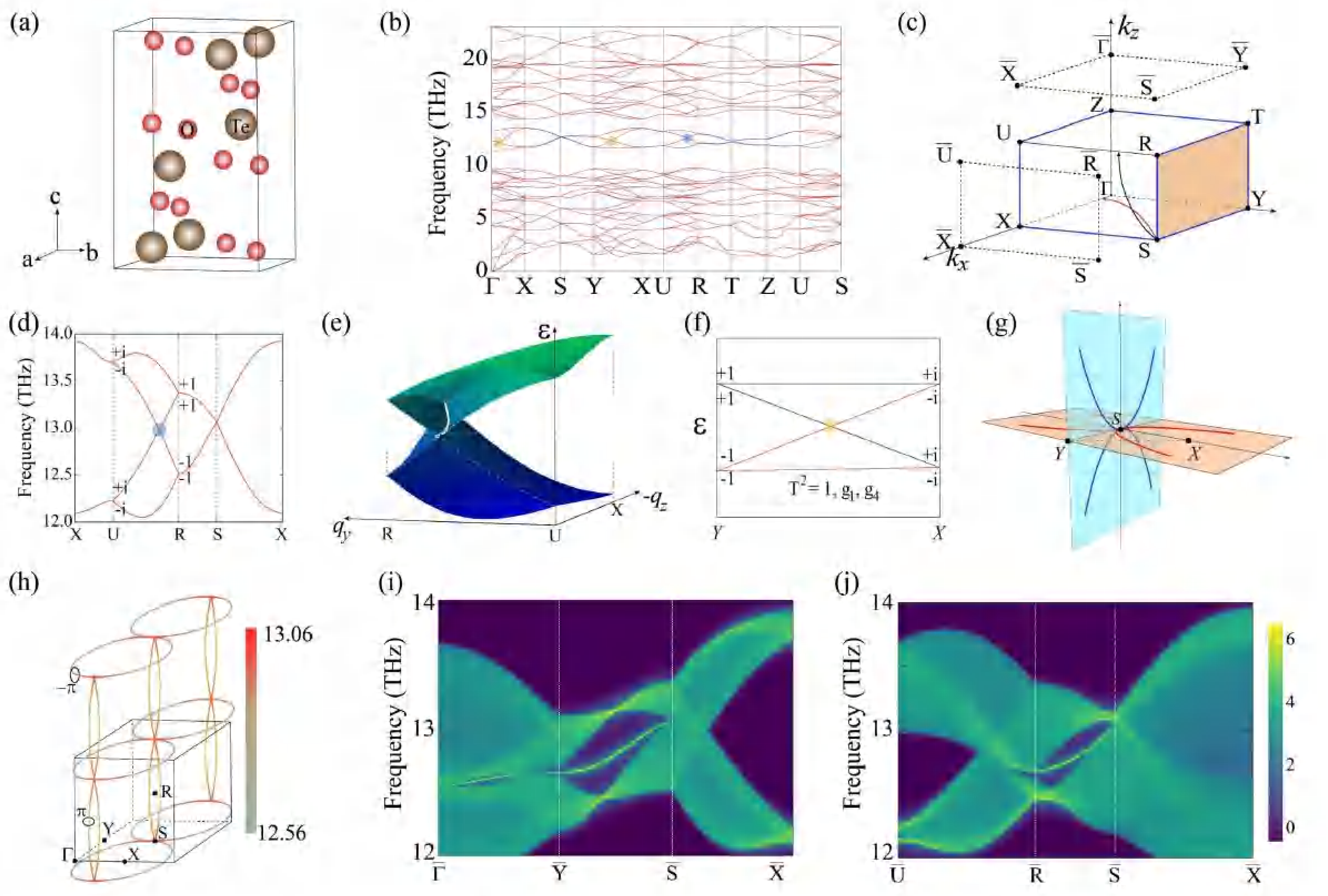

FIG. 3. a The unit cell of TeO_3 (SG Pnna 52). b Phonon dispersion of TeO_3. c Bulk BZ and the (001) and (100) surface BZs. The red and black arrows denote the hourglass nodal-line TPs, blue lines along the BZ boundary represent the twofold degenerate nodal-line TPs. All points on the $q_y = \pi$ plane are twofold degenerate nodal points (nodal surface), as shown in the yellow plane. d The phonon spectrum along X–U–R–S–X at the q_{yz} plane. The eigenvalues of {Mx | b/2 + c/2} are given at both U and R points. e 3D phonon dispersions at the q_{yz} plane. The solid white line represents the hourglass nodal line on which any point represents a hourglass nodal point. f The phononic hourglass nodal dispersions protected by g1 and g4. g Hourglass nodal chains (HNCs) at the q_{xy} and q_{yz} plane. h The shape of the Hourglass nodal new in the 3D view. Two black circles are used to calculate the Berry phase of the HNCs and the color represents the energy dispersion of the HNN in THz. i, j The phononic surface states along the high-symmetry lines for the (001) and (100) surfaces, respectively.

Different types of TPs

Due to the diversity of g and M symmetries, more interesting and nontrivial TPs forming by nodal-line (ring) TPs can be discovered.

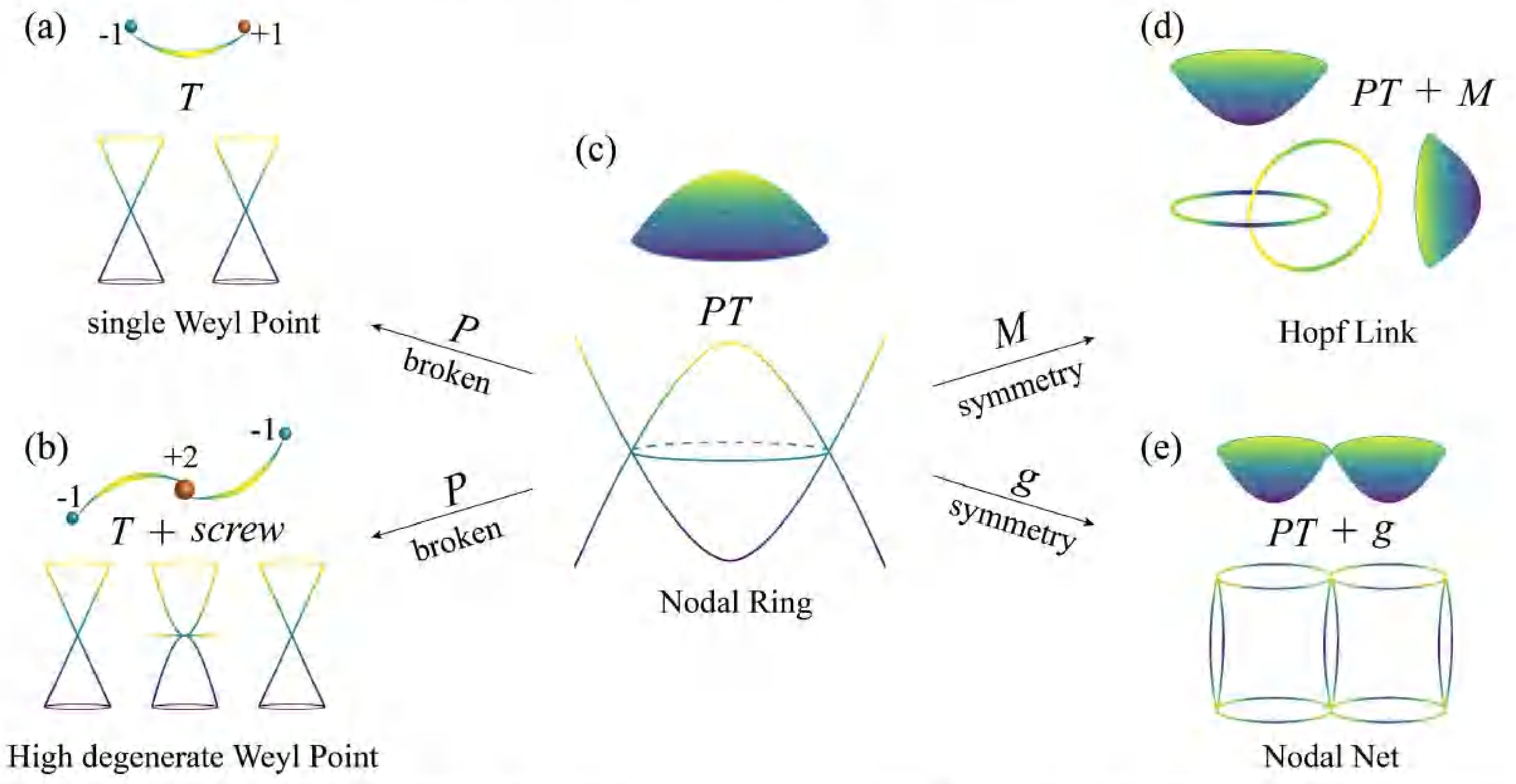

FIG. 4. The schematic relations between different types of TPs. a Single Weyl TPs in the open arc states. b High degenerate Weyl TPs in the arc surface states. c Nodal-ring (line) TPs in drumhead-like surface states. d Hopf-link TPs in nontrivial surface states. e Nodal-net TPs (e.g., HNN) and their corresponding drumhead-like surface states

When a large set of TP materials data is available, one can expect a variety of new phenomena by manipulating chemistry and structure. Therefore, the researches on topological phonons certainly deserve to be exploited further.

Conclusion

Acknowledgement /

National Science Fund for Distinguished Young Scholars (51725103) / National Natural Science Foundation of China (Grant Nos.51671193) / Science Challenging Project (Grant Nos. TZ2016004) / Major research project 2018ZX06002004

We have developed a HT and data-driven approach to evaluate the TPs in over 10,000 materials, using the existing phononic database and our in-house calculations. Our screening suggests that TP states are universally present, highlighting extensive possibilities for realizing TPs in a variety of materials toward different potential applications. We expect more topological bulk phonons and nontrivial edge states to be detected by experiments in near future. As such, many exciting phenomena, such as topological superconductivity and high thermoelectricity, may be realized by utilizing the topological phonons in those identified TP materials.

First-principles study on the properties of $MoSi_2N_4$ adsorbed with noble metals

Jing Xu [a,b], Yu-mei Zhang [b], Wei-bin Zhang [a,b]*
a. Physics and Optoelectronic Engineering, Yangtze University, Jingzhou, P.R. China
b. School of Physics and Electronic Information, Yunnan Normal University, Kunming, P.R. China

Background

- Nitric oxide(NO) pollution is currently a serious problem
- Many experiments have demonstrated the outstanding performance of two-dimensional materials in NO removal.
- The recently emerged two-dimensional material $MoSi_2N_4$ has the same superior properties and can enhance the removal efficiency with the adsorption of noble metals.

Computational details

- The first-principles calculations performed in this paper are based on the framework of density function theory (DFT)
- The climbing image nudged elastic band (CI-NEB) method was conducted to investigate the reaction coordinates from their initial states (IS) to their final states (FS), which also located the transition states (TS).

Result and discussion

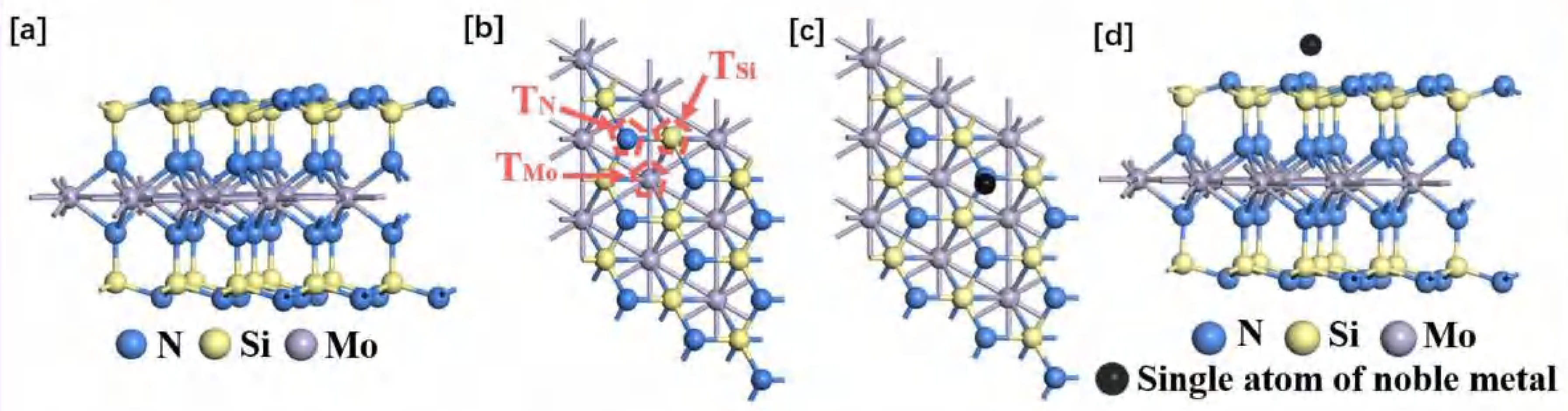

- The structure also does not change.
- A sandwich structure consisting of a Mo-N layer and two Si-N layers is presented.

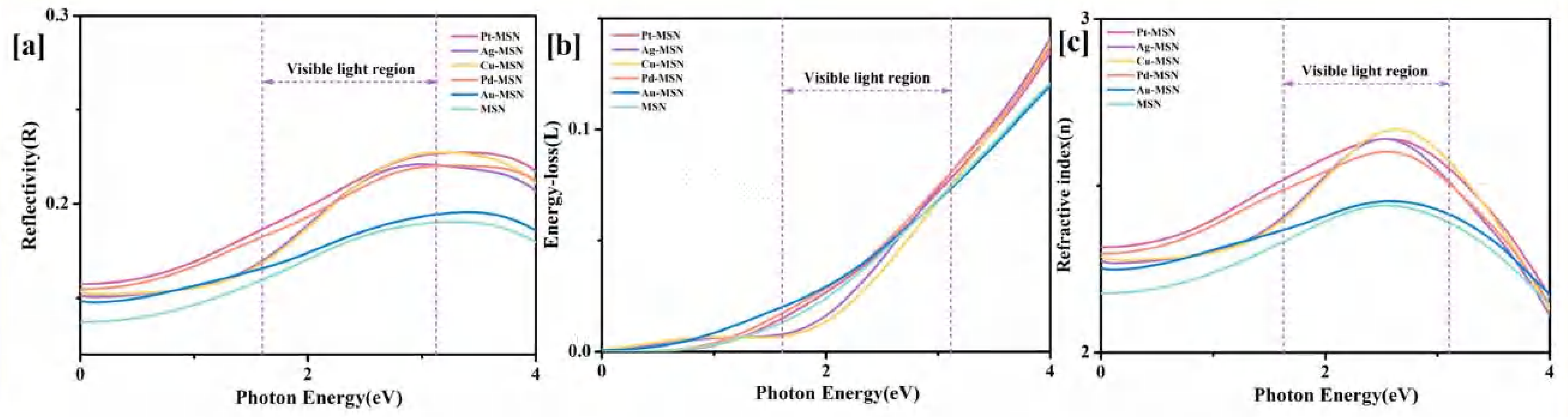

- The reflectance, refractive index, and energy loss of the materials do not show a significant increase.

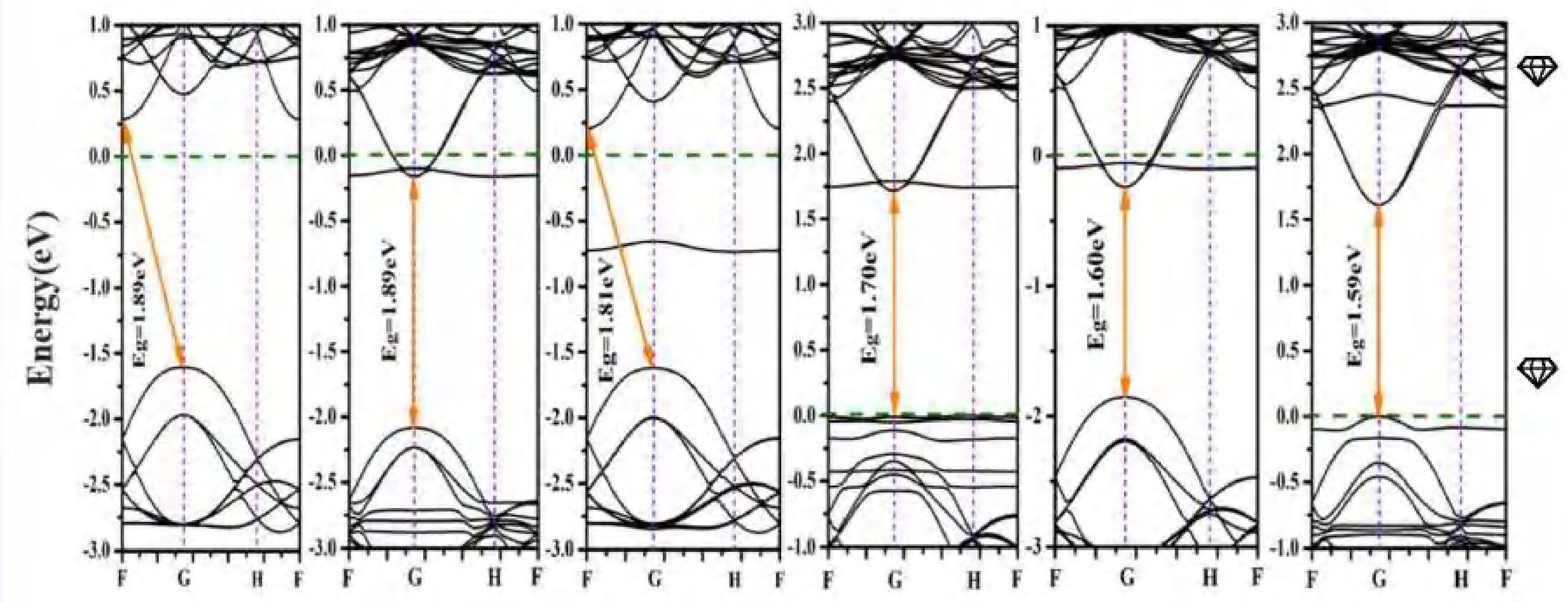

- The structure from an indirect bandgap to a direct bandgap.
- The bandgap of MSN-Pd has the largest change.

- The smaller the potential distance between VBE and O_2/H_2O redox line, the easier it is for hole to interact with O_2.

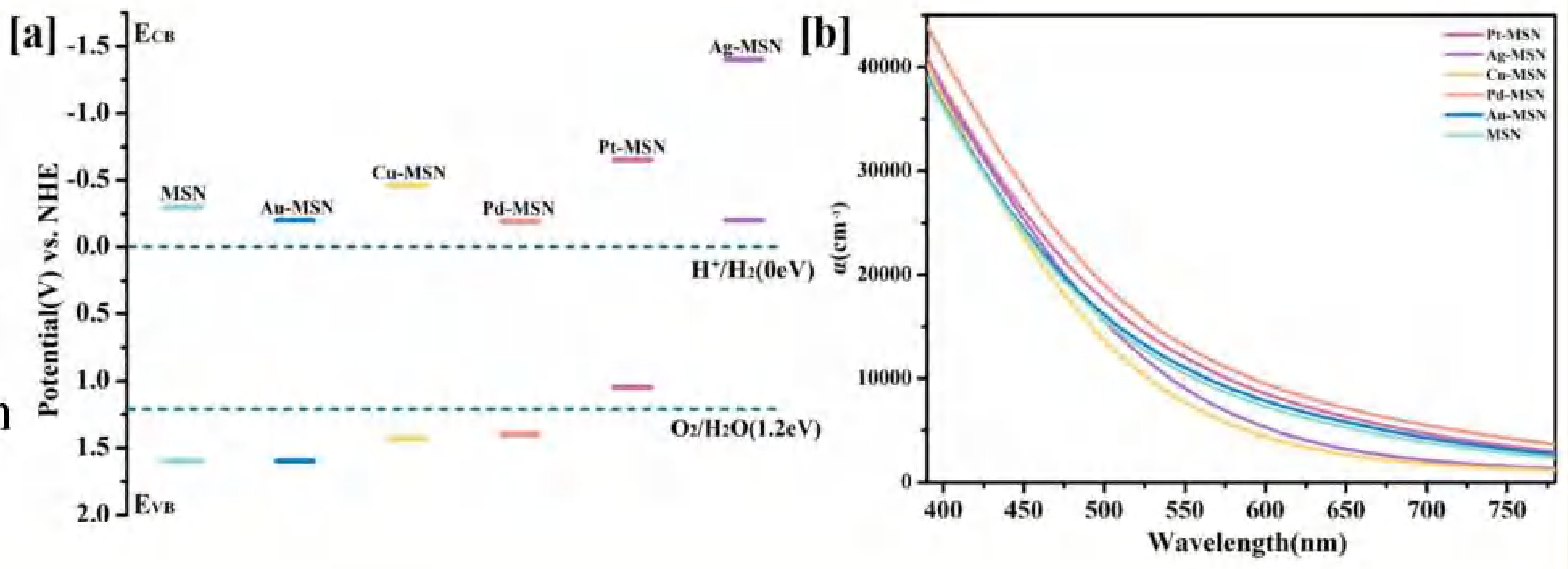

- The adsorption of single atoms of noble metals can effectively modulate band gap size.

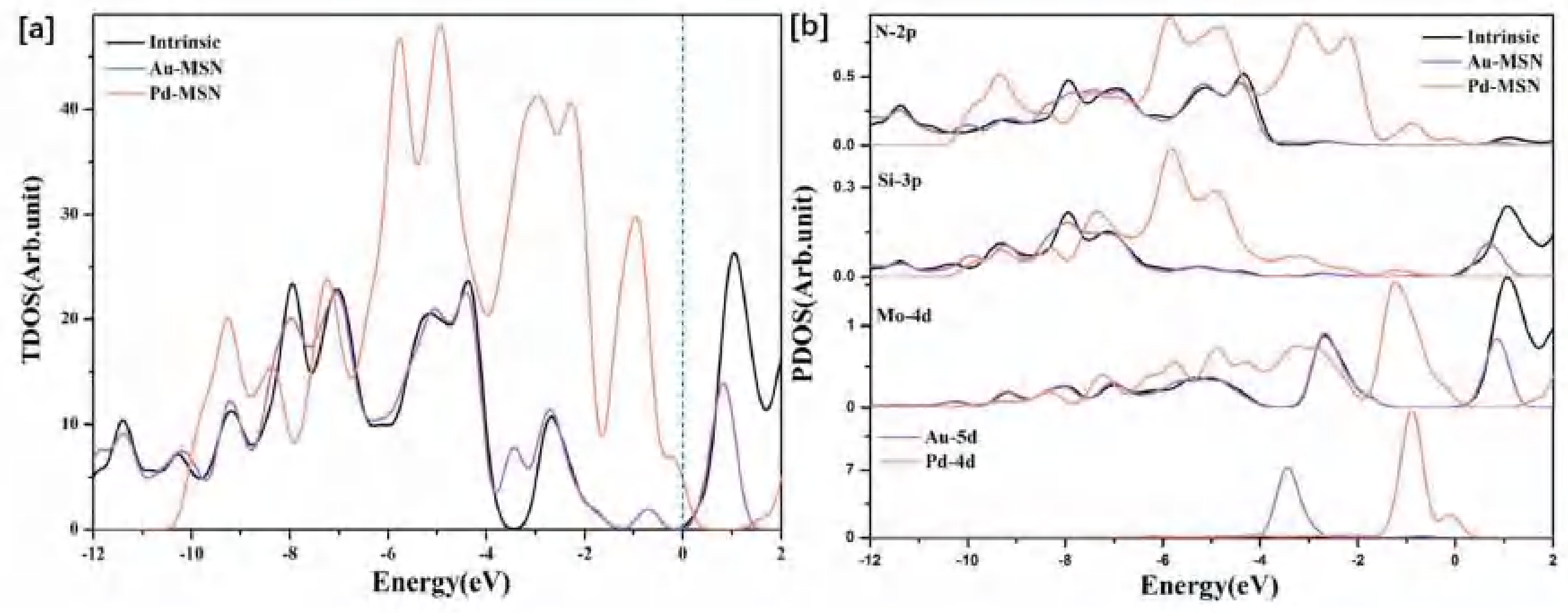

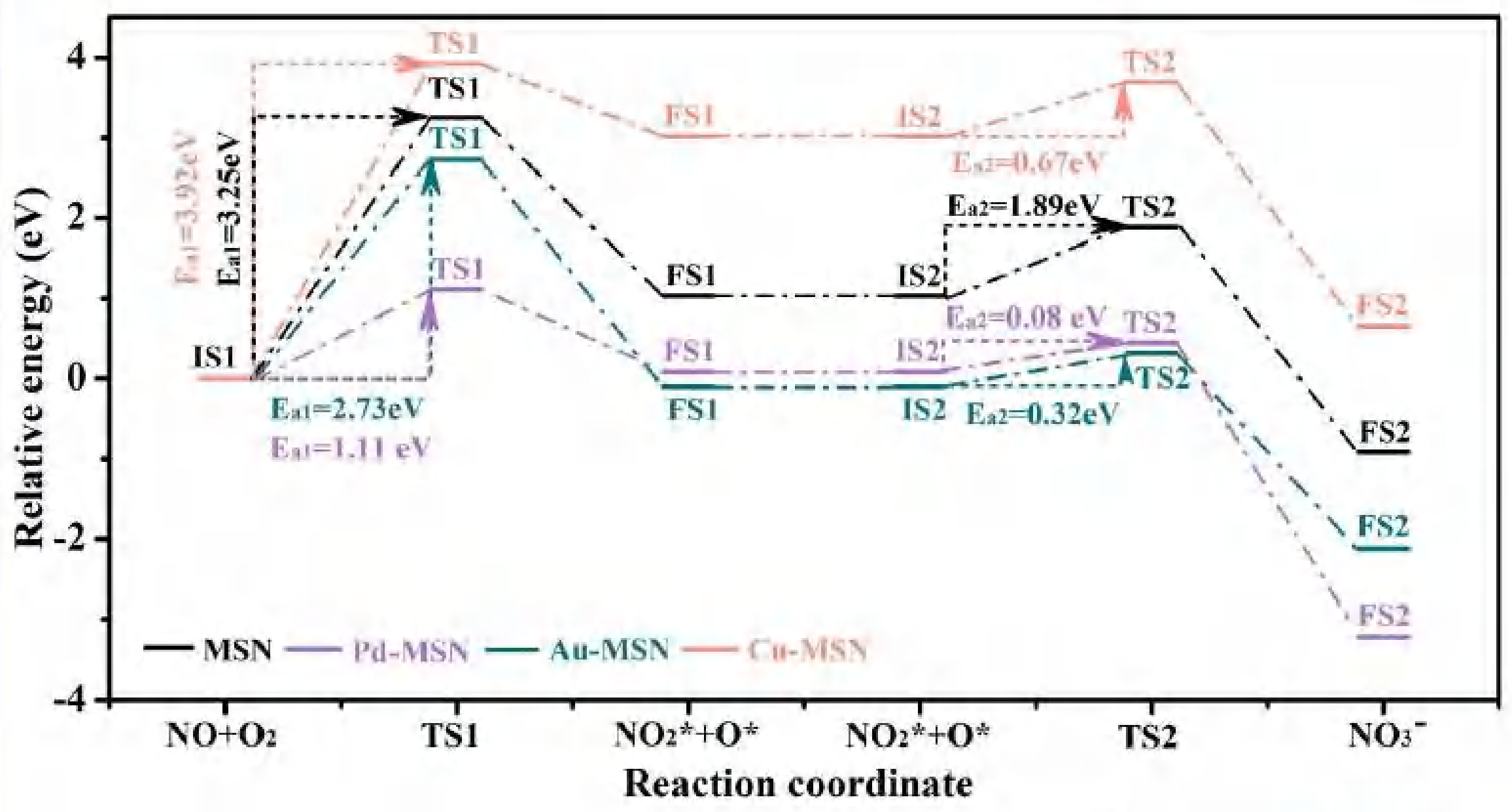

- The desorption energy of the intrinsic MSN is 1.09 eV, indicating that NO_2 is easily desorbed from the surface.

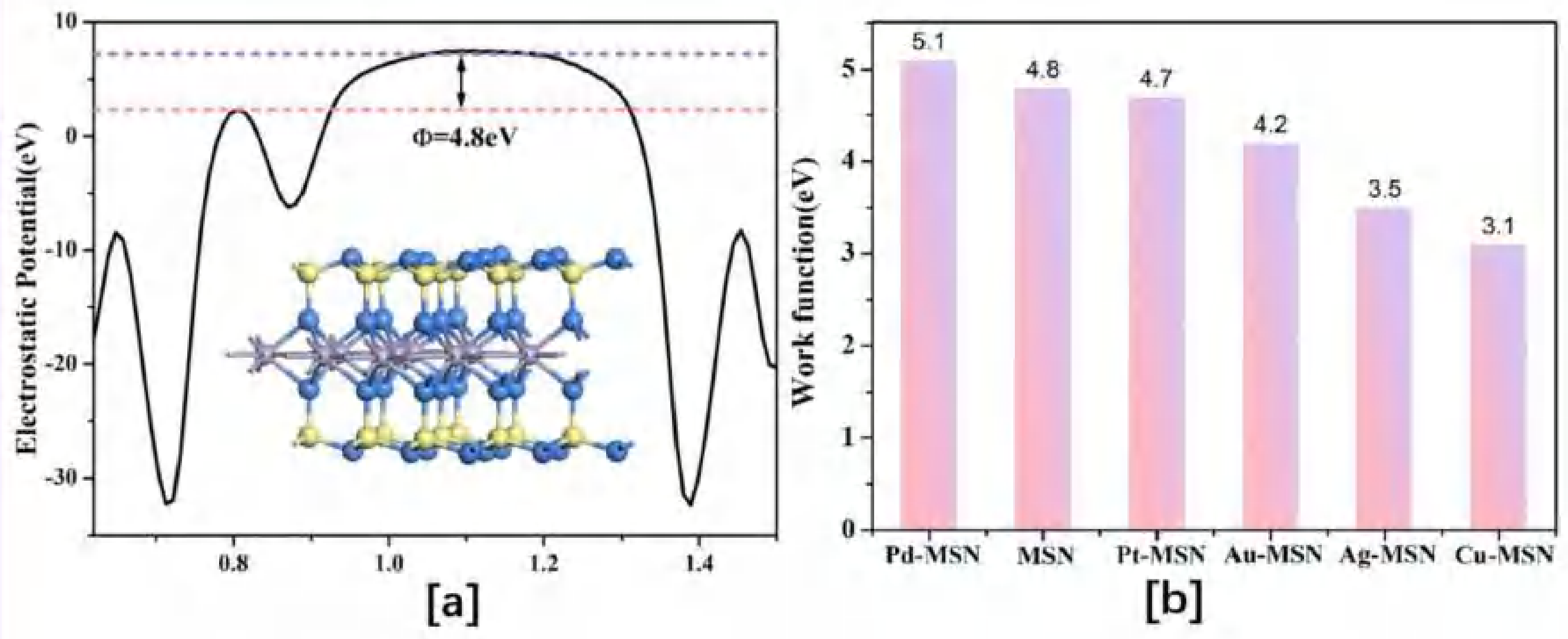

- We can obtain the Fermi levels and band edges, which will be discussed as follows.

- In summary, whether it is a indirect oxidation process or a direct oxidation process, Pd-MSN has minimal activation energy.

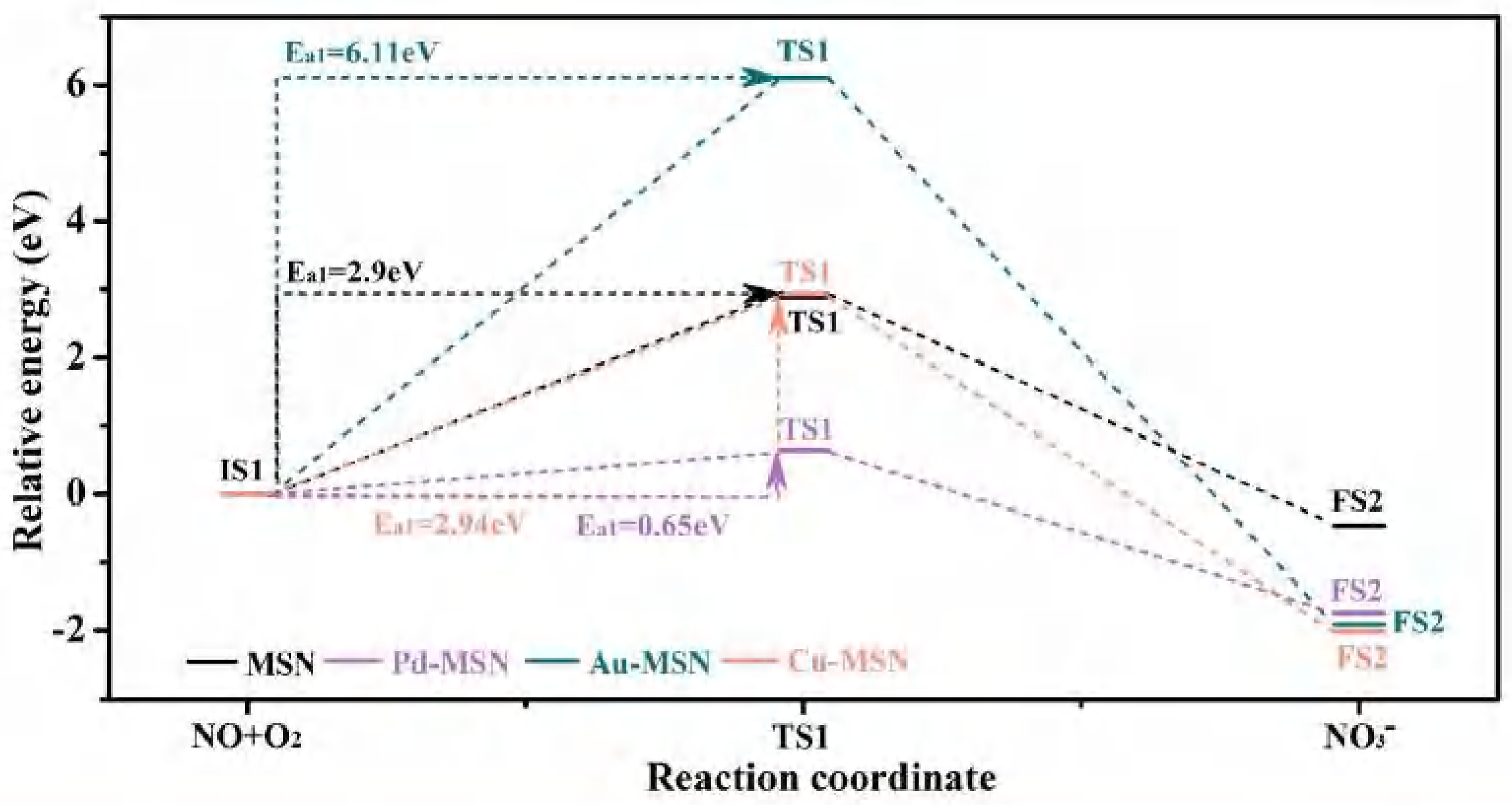

Conclusion

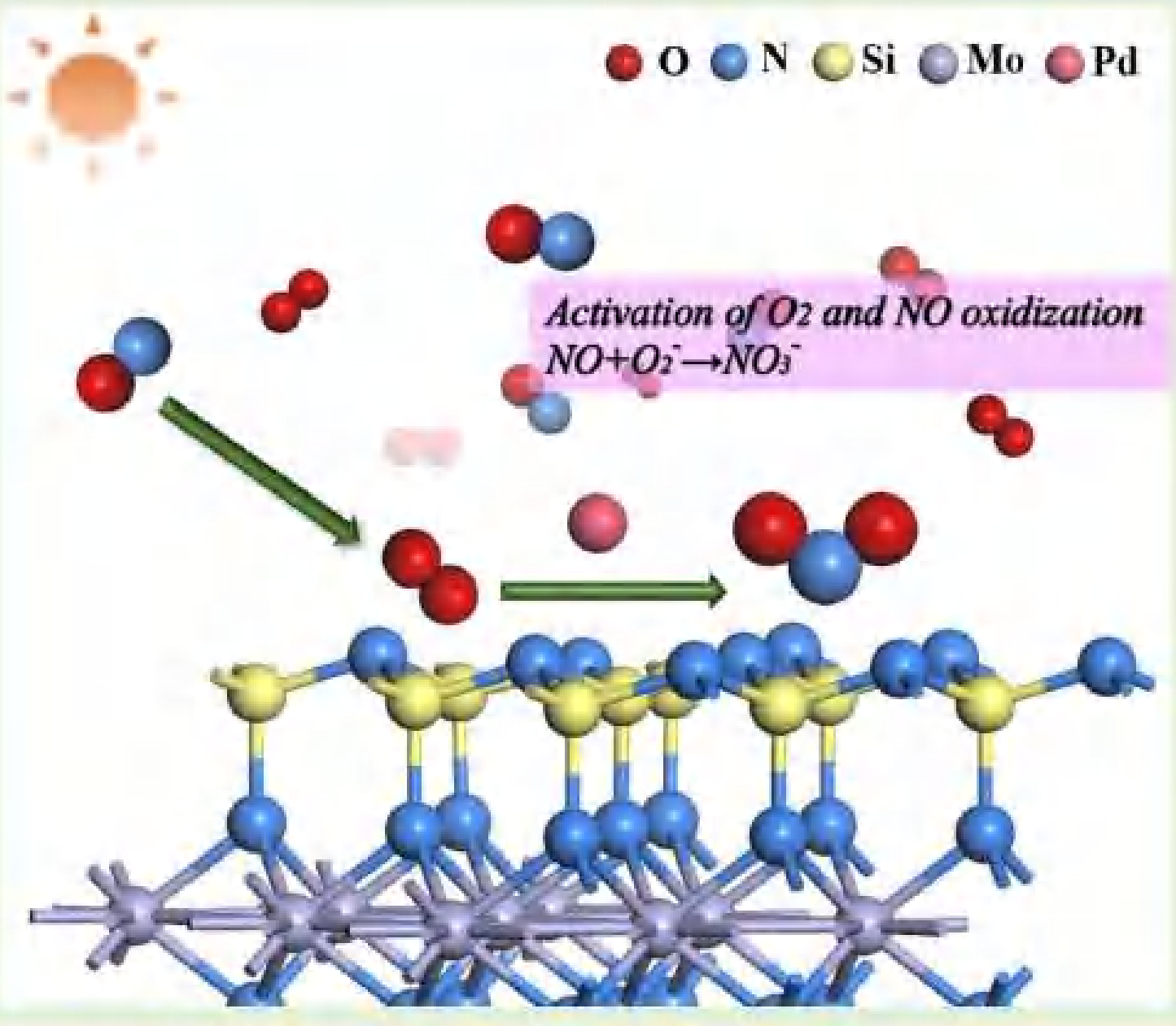

- The band gap of MSN changes significantly after the adsorption of single noble metals
- The most significant increase in the optical absorption coefficient is Pd-MSN.
- The most suitable band edge position of Pd-MSN
- The potential barriers were reduced on the surface of Pd-MSN for NO removal.
- All the above conclusions indicate that Pd-MSN is a promising NO oxide material.

References

Yi-Lun Hong, et al. "Chemical vapor deposition of layered two-dimensional MoSi2N4 materials." Science 369.6504 (2020): 670-674.
Weibin Zhang, et al. "Photocatalytic improvement of Mn-adsorbed g-C3N4." *Applied Catalysis B: Environmental* 206 (2017): 271-281.
Yuehan Cao, et al. "The role of potassium in the activation of oxygen to promote nitric oxide oxidation on honeycomb-like h-BN (001) surfaces." *Physical Chemistry Chemical Physics* 20.41 (2018): 26777-26785.

Hot Carrier Dynamics in Silicon from Ab Initio Nonadiabatic Molecular Dynamics Simulation in Momentum Space

Zhenyu Wang[1], Qijing Zheng[1], Zhenfa Zheng[1*] and Jin Zhao[1,2*]

[1]ICQD/Hefei National Laboratory for Physical Sciences at Microscale, CAS Key Laboratory of Strongly-Coupled Quantum Matter Physics,
and Department of Physics, University of Science and Technology of China, Hefei, Anhui 230026, China.
[2]Department of Physics and Astronomy, University of Pittsburgh, Pittsburgh, Pennsylvania 15260, USA

ABSTRACT

Relaxation of hot electron in Si is studied using Molecular dynamics simulation which includes electron-phonon coupling. We have simulated some relaxation processes with different initial energy and momentum and focus on the processes whose initial state is at or L point. Our calculations show that during the relaxation, the hot electrons will redistribute in brillouin zone within donzens of femtosecond, and then relax to CBM as a whole. This two-step relaxation is consistent with experiments.

INTRODUCTION

Recently, the processes of hot-electron relaxation in Si have been studied theoretically and experimentally. Previous researches have shown that the relaxation of hot electrons can be considered as a two-step process consists of momentum relaxation and energy relaxation.

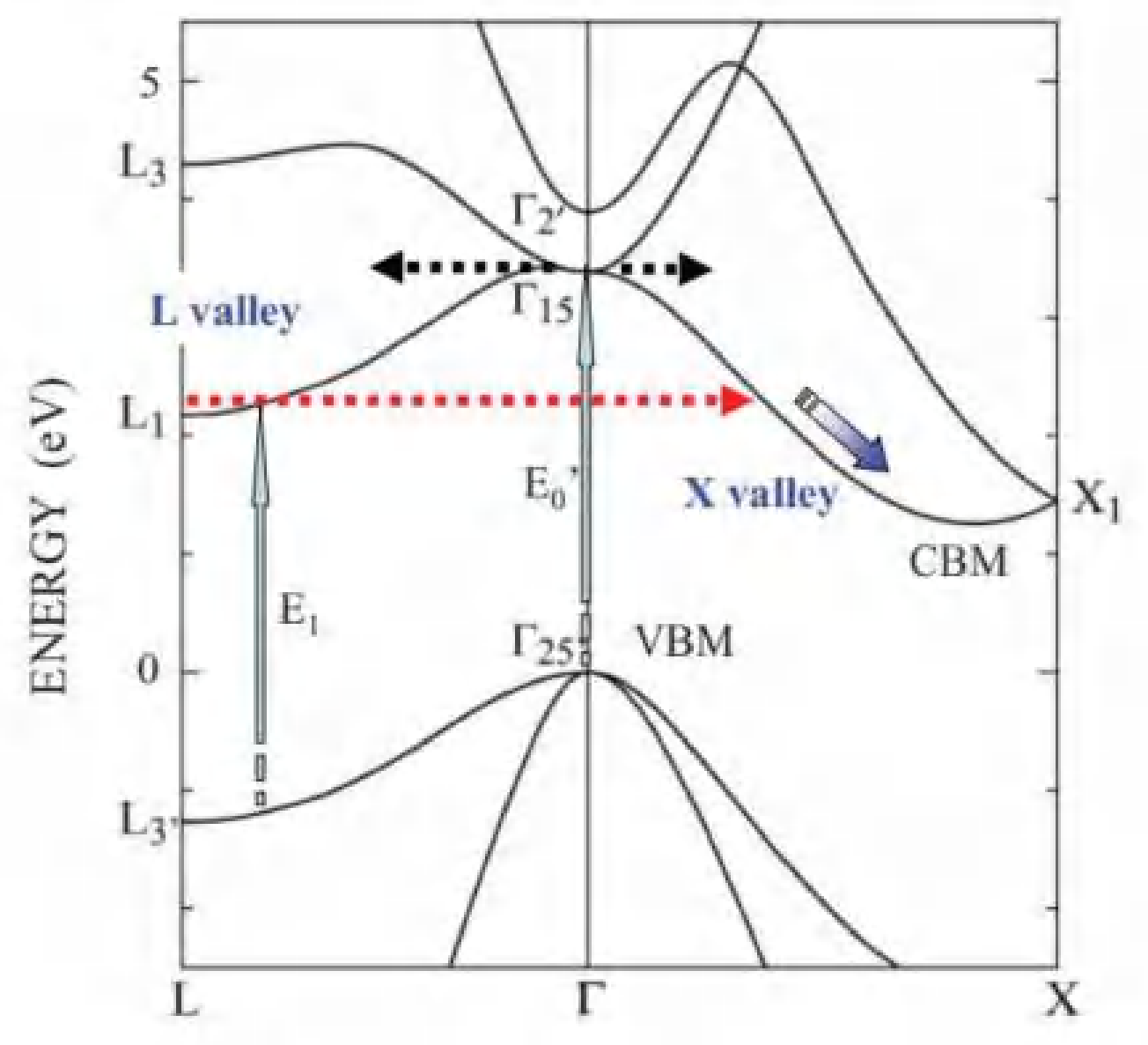

*Phys.Rev.B.*84,235210-235221(2011)

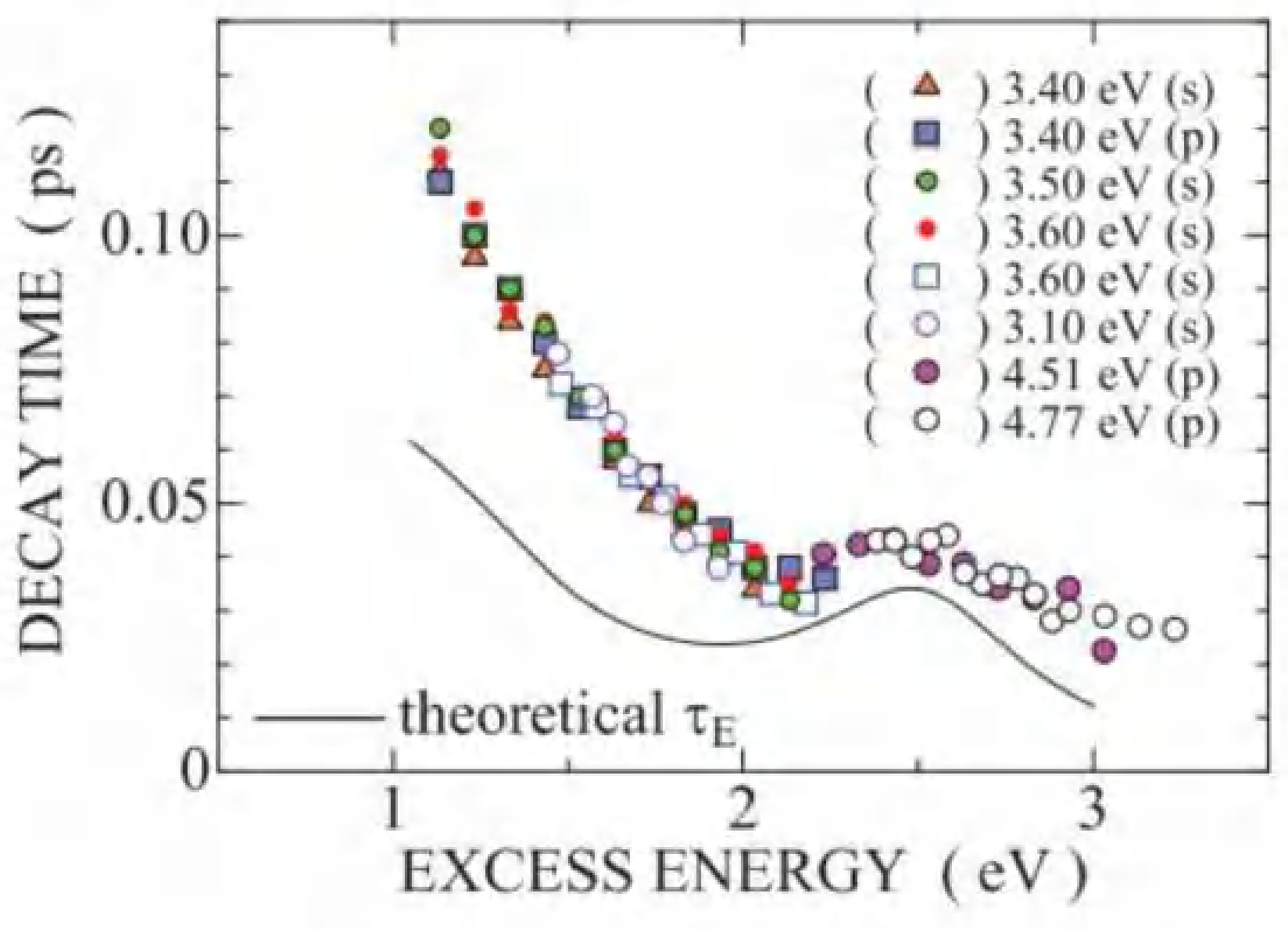

*Phys.Rev.B.*100, 035201-035214 (2019)

During the momentum scattering, hot electrons in Si are quasi-equilibrated in the momentum space, forming the hot-electron ensembles.

RESULT

hot electron

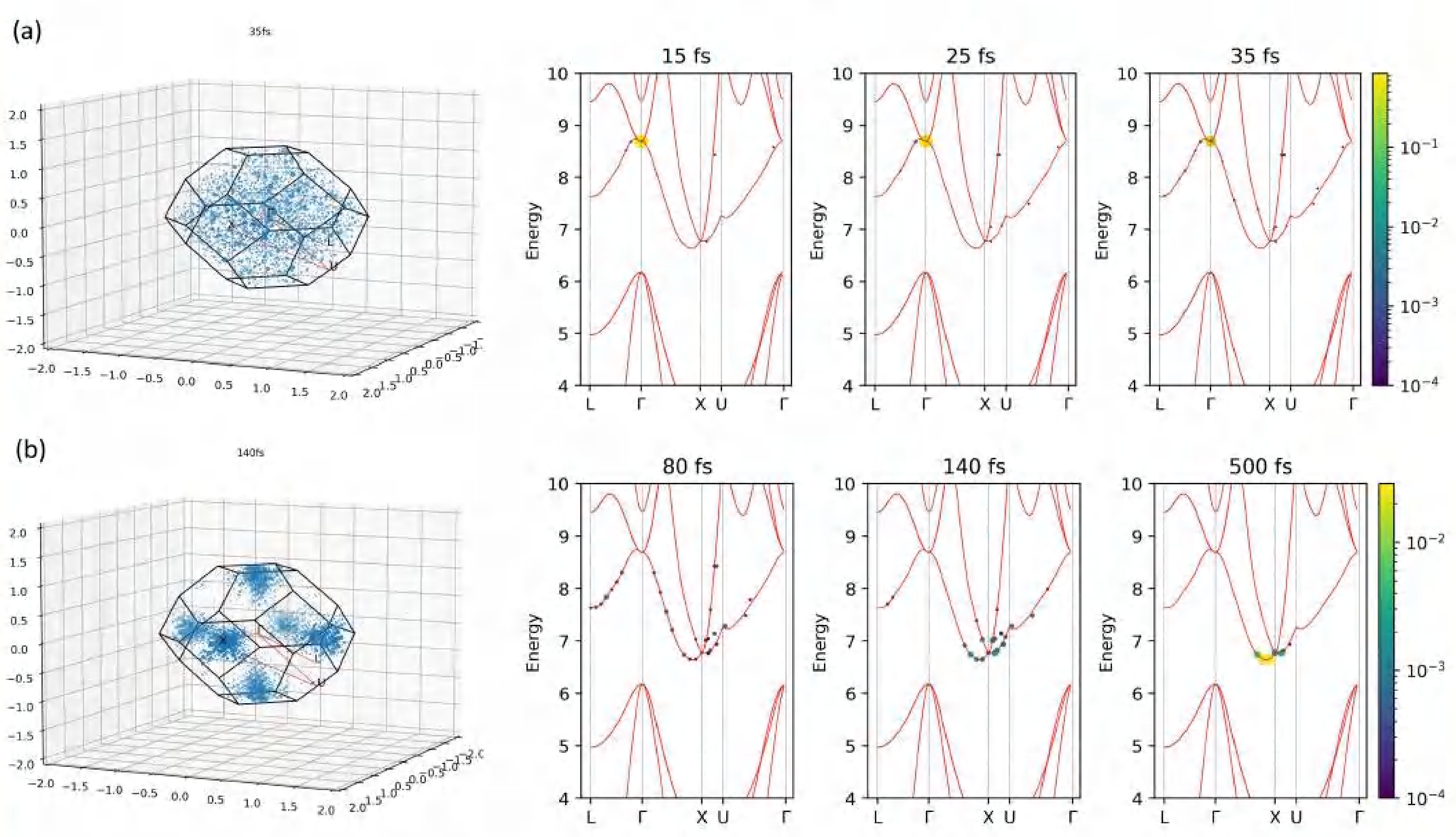

For an excitation at , in the first few tens of femtoseconds, the ultrafast momentum scattering processes transfer hot electrons to other points of the BZ. And then the hot electrons relax to CBM as a whole.

RESULT

phonon

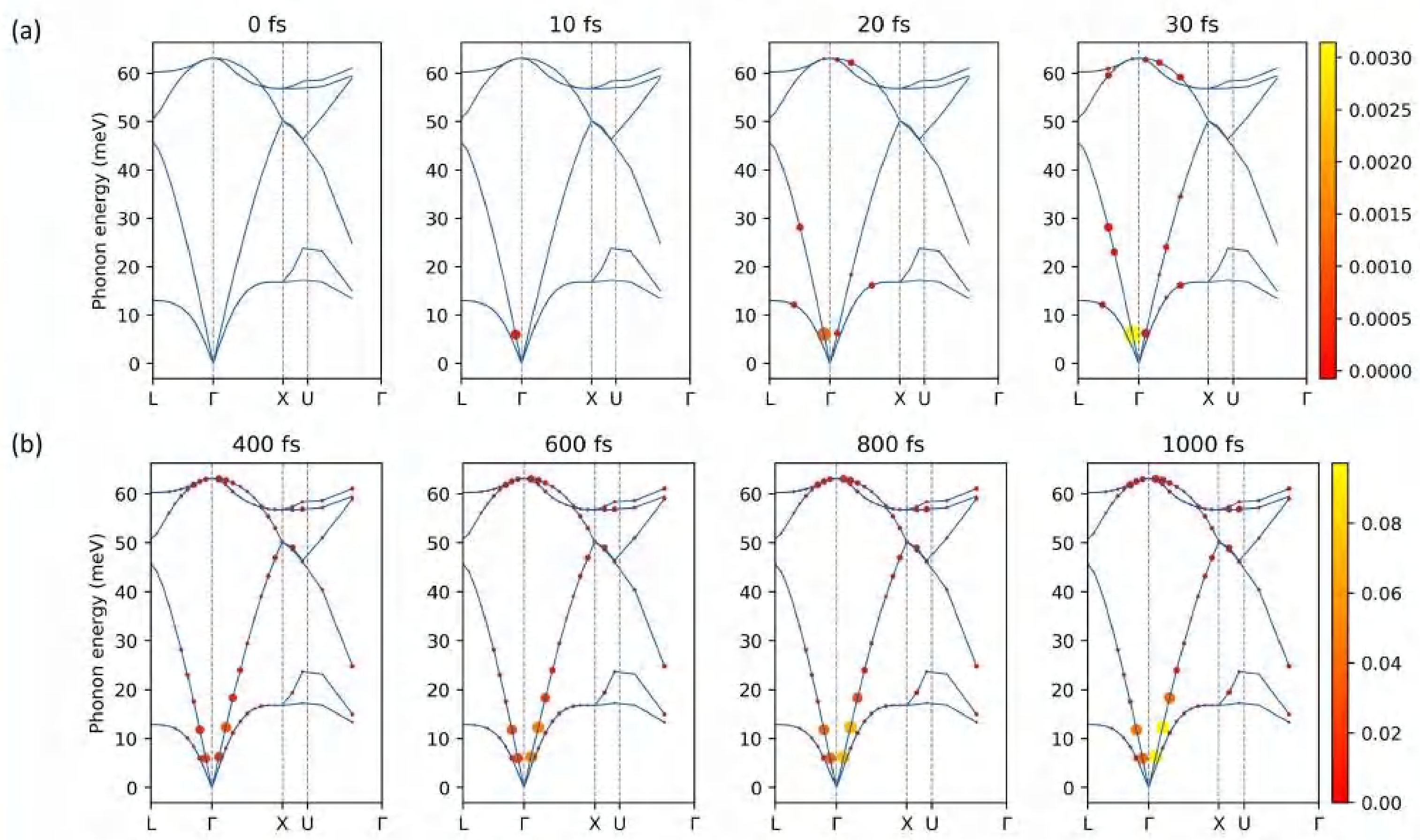

The corresponding evolution of phonons show that at the beginning of the relaxation what dominants the energy transfer from hot electrons to lattice is acoustic phonons. This agrees with the statement that electrons lose a large proportion of energy to acoustic phonons reported before.

RESULT

characteristics

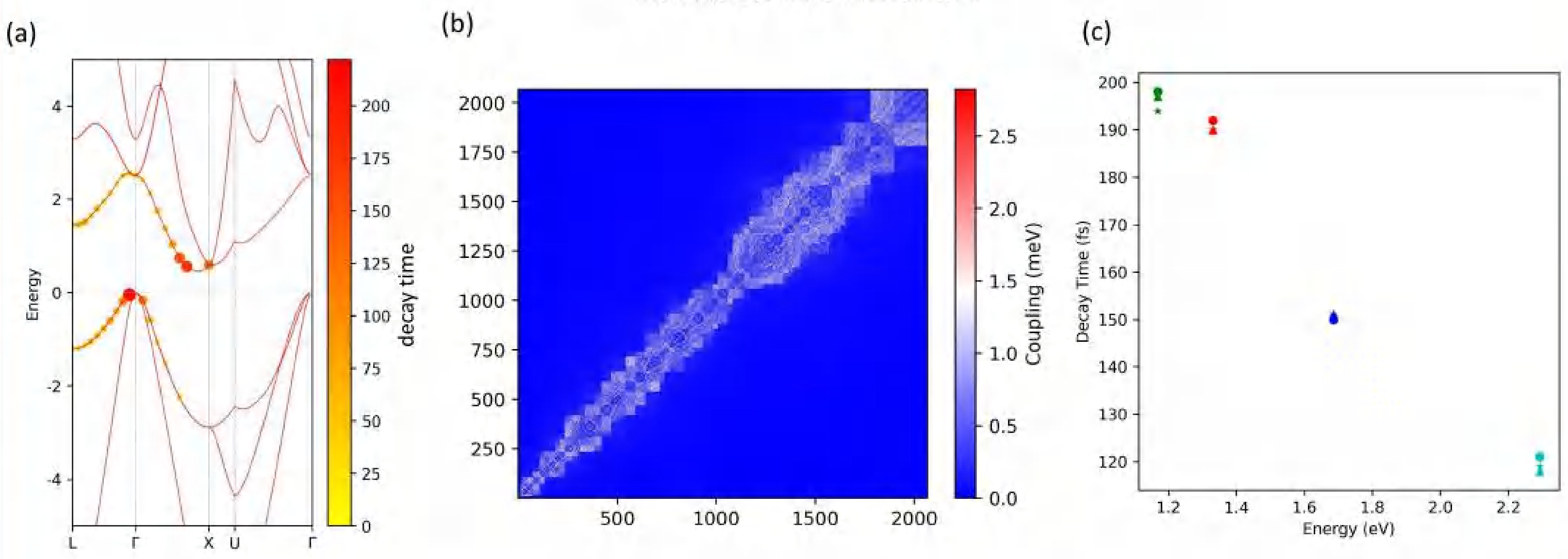

Besides, there are two main characteristics of the hot electrons relaxation, one of which is that the decay time[fig.(a)] of states with different initial energy (Ei) is proportional to their Ei and stay in step with the EPC strength[fig.(b)]. The other one is that decay times of hot electrons have been determined as a function of excess energy E_{ex} no matter the initial k point is, as shown in [fig.(c)].

CONCLUSION

In conclusion, there are two main characteristics in this dynamic process: 1) the decay time is proportional to E_{ex} indicating the relaxation processes is governed by e-ph interactions, and 2) the decay time is determined as a function of excess energy E_{ex}.

MORE

Corresponding Author:

E-mail: wangzhenyu@mail.ustc.edu.cn

Ultrafast Dynamics of Photogenerated Carriers at O_2/TiO_2 Interface

Jinhong Xu[1], Weibin Chu[2], Qijing Zheng[1*] and Jin Zhao[1,3,4*]

[1]Department of Physics, University of Science and Technology of China, Hefei, Anhui 230026, China
[2]Key Laboratory of Computational Physical Sciences (Ministry of Education), Institute of Computational Physical Sciences, Fudan University, Shanghai, 200433, China
[3]Department of Physics and Astronomy, University of Pittsburgh, Pittsburgh PA 15260, United States
[4]CAS Center for Excellence in Quantum Information and Quantum Physics, University of Science and Technology of China, Hefei, Anhui 230026, China

I. Abstract

Past studies indicated that O_2 is the electron scavenger on TiO_2 surface, which can trap the photoexcited electrons and make them separated from the excited holes, increasing the lifetime of excited state carriers. we have studied the excited carrier dynamics at O_2/TiO_2 interface by ab initio NAMD simulation. DFT calculations verify that the energy level of O_2 is in the middle of the band gap of TiO_2, suggesting that O_2 can trap electrons. Then we performed NAMD calculations on the electron trapping process. The results show that the electron trapping happens on the order of hundreds of femtoseconds, and the mechanism of electron migration is mainly a non-adiabatic process. O_2 has a strong ability to trap the electrons, which can capture about 60% of the electrons. Moreover, we found that the higher the temperature, the higher the initial energy of the electrons, the faster the migration of the electrons. Our study provides useful insight into understanding the photocatalytic mechanism on TiO_2 surface.

II. Introduction

CH_3OH can trap hole and O_2 can trap electron

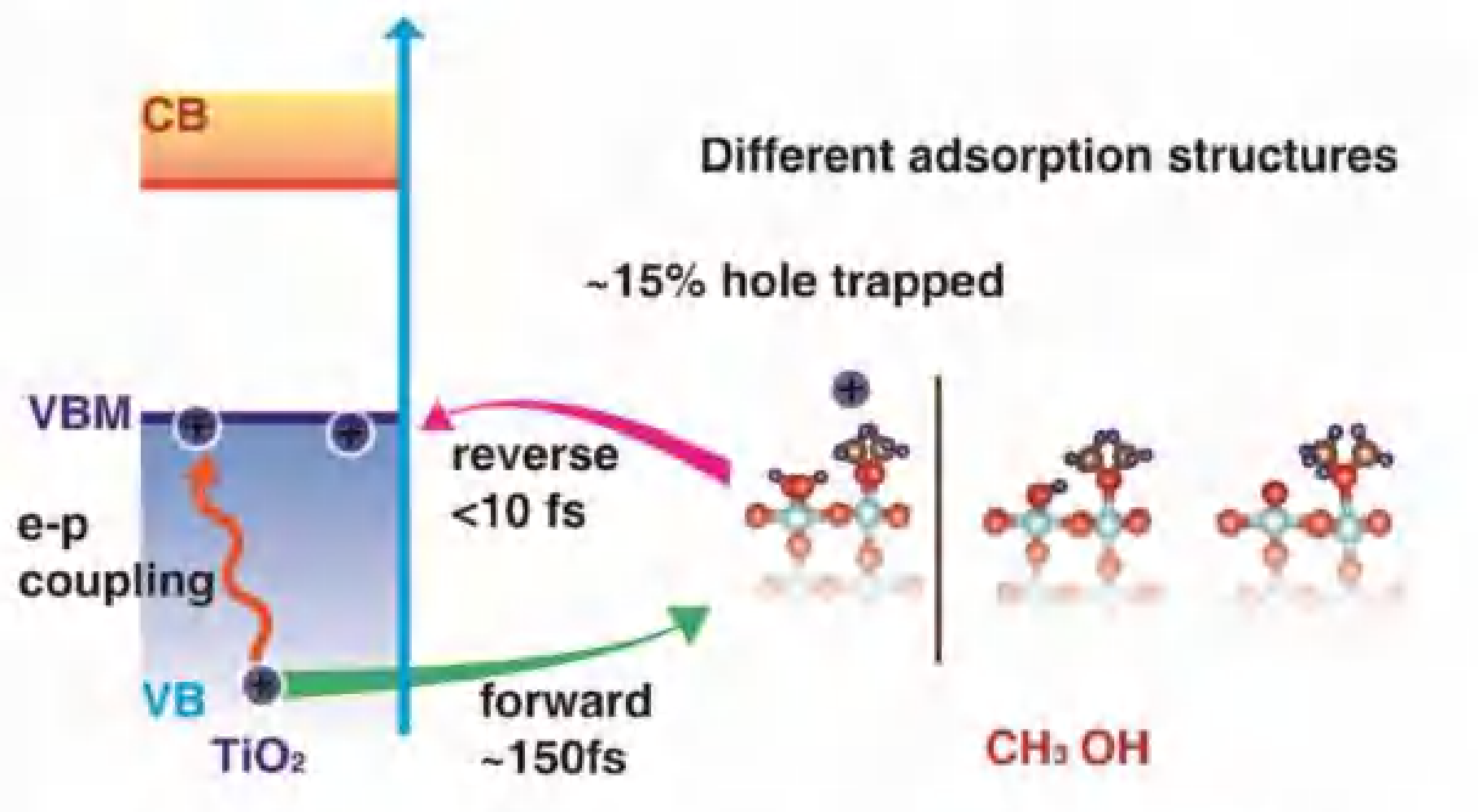

W. Chu et al. *J. Am. Chem. Soc.*, 138, 13740–13749(2016)

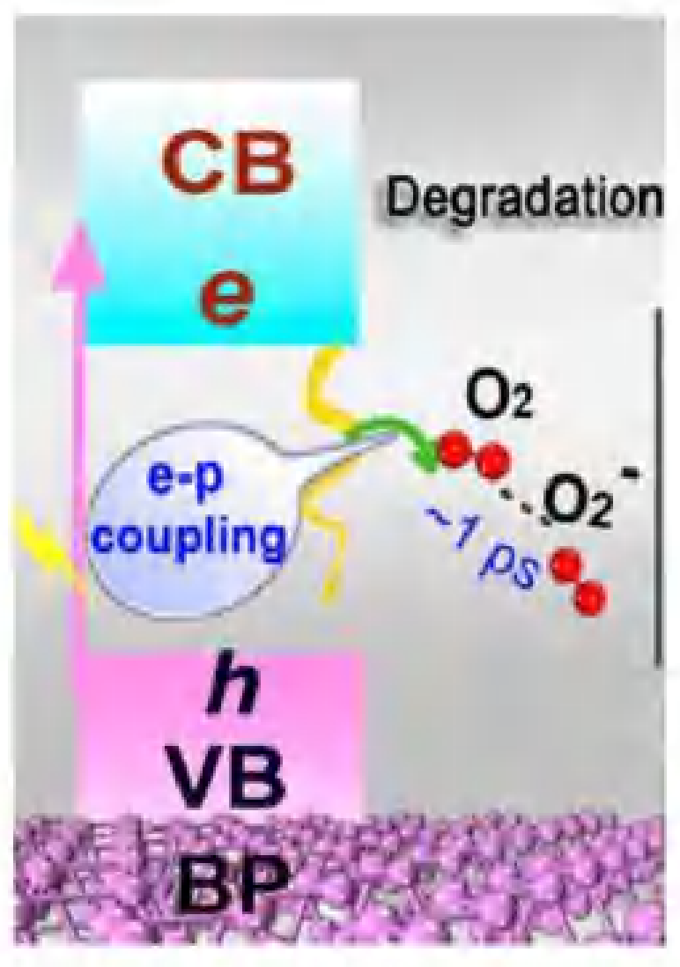

X.Niu et al. *J. Phys. Chem. Lett.*, 9, 5034-5039(2018)

III. Method

TDDFT + FSSH ➡ Heifei NAMD

Time-domain density functional theory (TDDFT) with fewest switches surface hopping (FSSH).

In TDDFT, the time-dependent Kohn-Sham (KS) orbitals $\psi_P(\boldsymbol{r},t)$ are expanded in the basis of instantaneous adiabatic KS orbitals $\phi_j(\boldsymbol{r},\boldsymbol{R}(t))$.

$$\Psi_P(\boldsymbol{r},t)=\sum_j c_j(t)\phi_j(\boldsymbol{r},\boldsymbol{R}(t))$$

In FSSH, Classical approximation of atomic nuclei, electrons adopt quantum evolution on the potential energy surface.

$$\begin{cases} i\hbar\dfrac{\partial\psi_p(\boldsymbol{r},\boldsymbol{R},t)}{\partial t}=\hat{H}_{el}(\boldsymbol{r},\boldsymbol{R})\psi_p(\boldsymbol{r},\boldsymbol{R},t) \\ M_\alpha\ddot{\boldsymbol{R}}_{\boldsymbol{\alpha}}=-\nabla_{\boldsymbol{\alpha}}E_K^{el}(\boldsymbol{R}) \end{cases}$$

Using the previous three equations, we can obtain the evolution equation of the coefficients.

$$i\hbar\frac{\partial}{\partial t}c_j(t)=\sum_k c_k(t)\left[\varepsilon_k\delta_{jk}-i\hbar\mathbf{d}_{jk}(t)\right]$$

$$\boldsymbol{d}_{jk}=\left\langle\phi_j\middle|\frac{\partial}{\partial t}\middle|\phi_k\right\rangle=\sum_\alpha\frac{\langle\phi_j|\nabla_{\mathbf{R}_\alpha}\mathcal{H}|\phi_k\rangle}{\varepsilon_k-\varepsilon_j}\cdot\dot{\boldsymbol{R}}_\alpha$$

$\boldsymbol{d}_{\mathrm{jk}}$ is the nonadiabatic couplings (NACs) between KS state j and k.

Using FSSH, hopping probabilities between the adiabatic KS states can be written as:

$$P_{j\to k}=\max\left\{\frac{2\Re\left[C_j^*C_k d_{jk}\cdot\dot{\boldsymbol{R}}\right]\Delta t}{C_j^*C_j},0\right\}$$

None-adiabatic (NA) and Adiabatic (AD) Contribution

The time-dependent photocarrier transition information can be divided into two parts:

$$\frac{d\rho(\mathbf{r},t)}{dt}=\sum_{ij}\left\{\left[\frac{d}{dt}c_i^*(t)c_j(t)\right]\phi_i^*(\mathbf{r},\mathbf{R})\phi_j(\mathbf{r},\mathbf{R})+c_i^*(t)c_j(t)\left[\frac{d}{dt}\phi_i^*(\mathbf{r},\mathbf{R})\phi_j(\mathbf{r},\mathbf{R})\right]\right\}$$

The first part is Non-adiabatic Term, the variation of KS states population, which denoted as nonadiabatic contribution, due to change of the state occupation.

The second is the change of adiabatic KS orbitals, which denoted as adiabatic contribution, due to change of state localization.

IV. Electronic Structure Results

O_2/TiO_2 DOS and process of O_2 traping electron from TiO_2

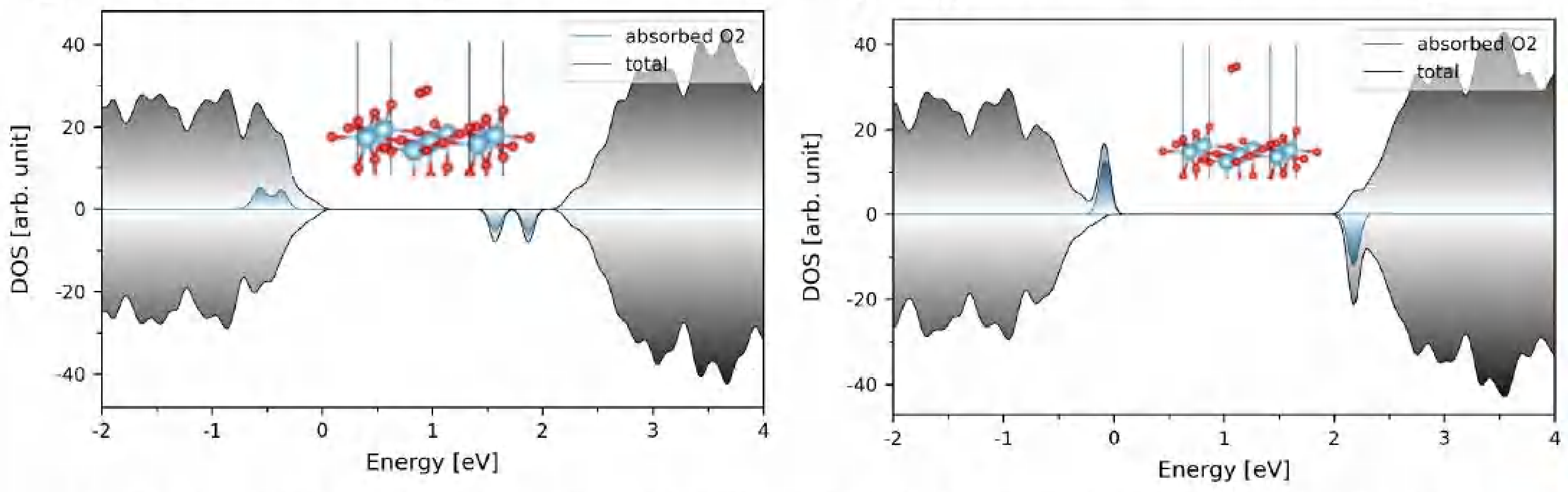

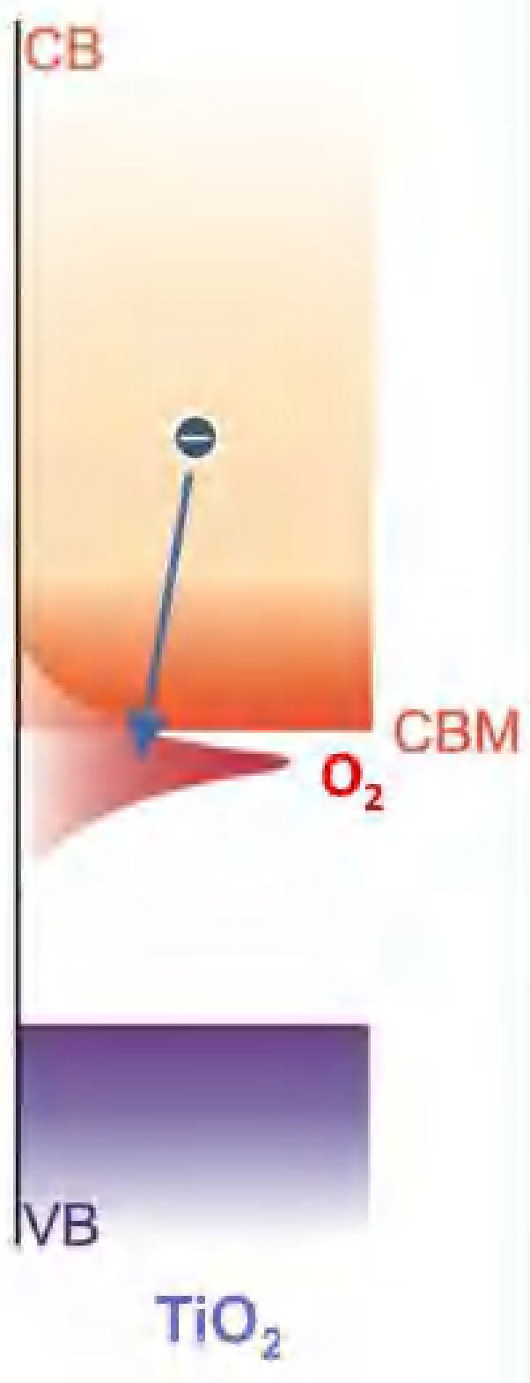

- In the DOS diagram, the LUMO orbital of O_2 is in the middle of the band gap of TiO_2, corresponding to the two degenerate 2p orbitals and closing to the CBM of TiO_2. It proves that O_2 can capture electrons from TiO_2
- If we move the position of O_2 away from the TiO_2 surface, the two 2p orbitals are degenerate due to the weakening of the surface interaction At the same time, the energy moves up.

V. NAMD Results

Diadiabatic Molecular Dynamics at O2/TiO2 Interface

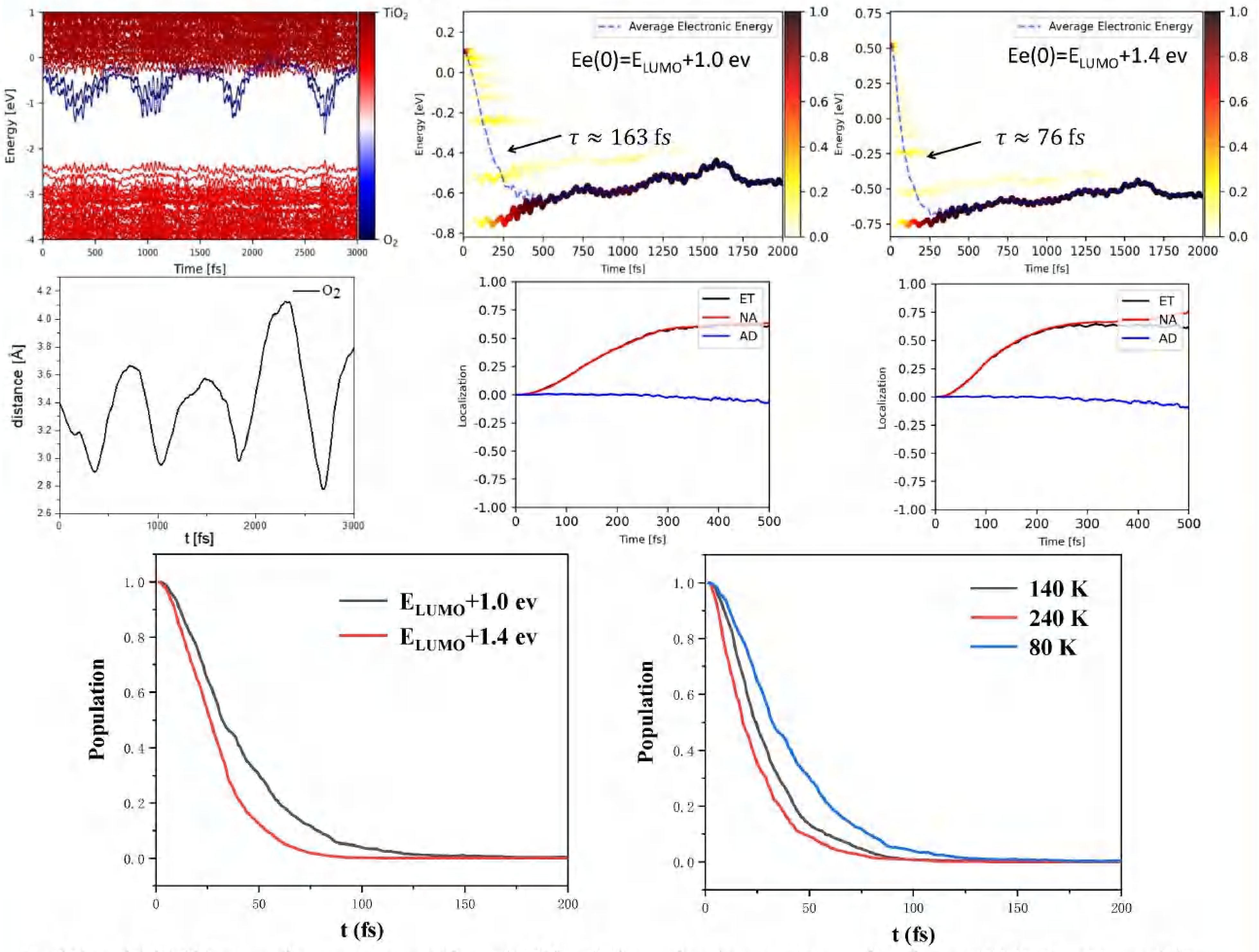

- The NAMD results suggest that 60% of the electrons transfer from TiO_2 to O_2, while the charge transfer was mainly due to the NA contribution, with little AD contribution.
- the higher the temperature, the higher the electron initial energy, the faster the electron transfer from TiO_2 to O_2.

VI. Conclusion

- O_2 can capture about 60% of the electrons from TiO_2. Here the LUMO energy level of O_2 hardly crosses the conduction band of TiO_2, so the charge transfer is basically NA contribution.
- The higher the initial energy of electrons, the more intermediate energy levels meaning more channels, the faster the electron migration. The higher the temperature, the more phonons, and the movement speed of the nucleus are affected, thereby NACs changes.

KRPOJ A Band Unfolding Program

for Phononic and Electronic Band Structures

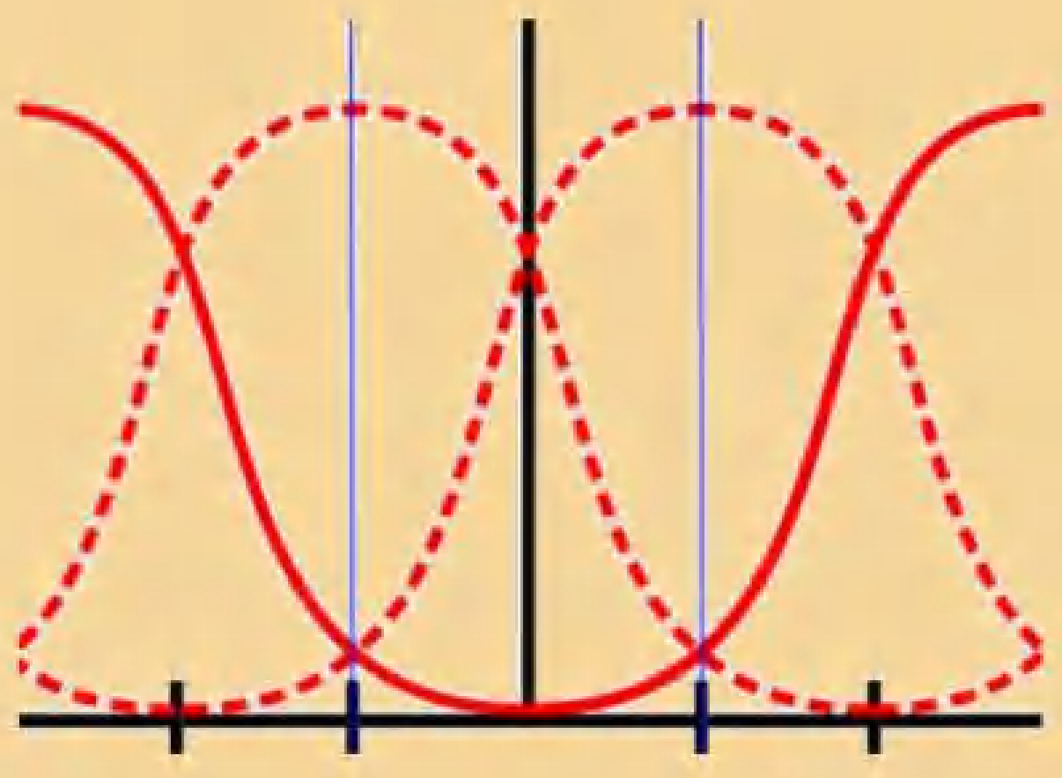

Abstract

KPROJ is a band unfolding program that can perform band unfolding calculation for bulk and interface systems from supercell calculations. Here, we present our recent advances in developing the KPROJ program. We have implemented a new Fast Fourier transform algorithm to significantly speed up the partial layer integration of wavefunctions. We have developed new interfaces of the program to the linear combination of atomic orbitals method and phonon calculations. A few applications of the program are given.

Keyword ： band unfolding , layer projection , plane waves , lcao , phonon

1. Band folding phenomenon arising from the use of supercells :

Translation symmetry: $E(k+G)=E(k)$

Translation symmetry: $E(k+G')=E(k)$ $G'=\frac{1}{2}G$

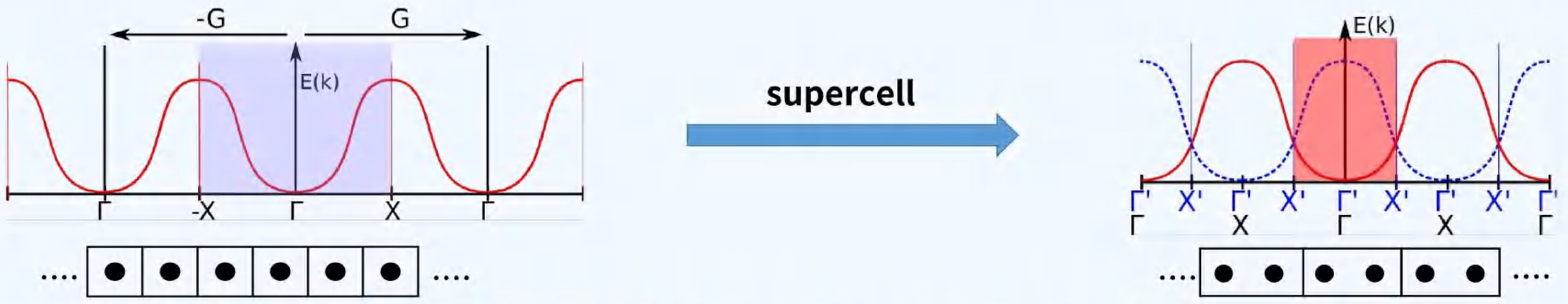

3. Moire-Graphene θ = 9.43° （Plane waves method）

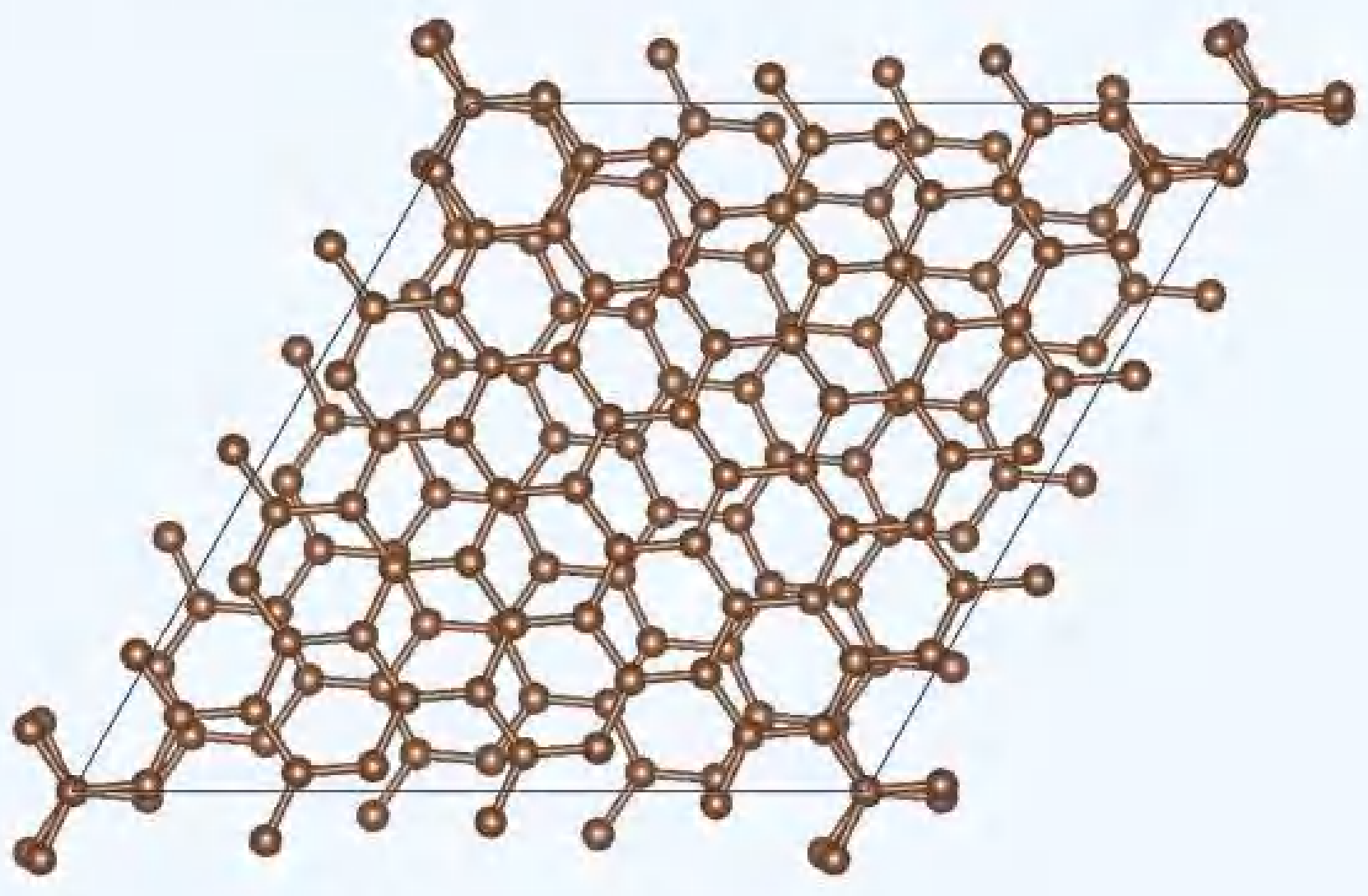

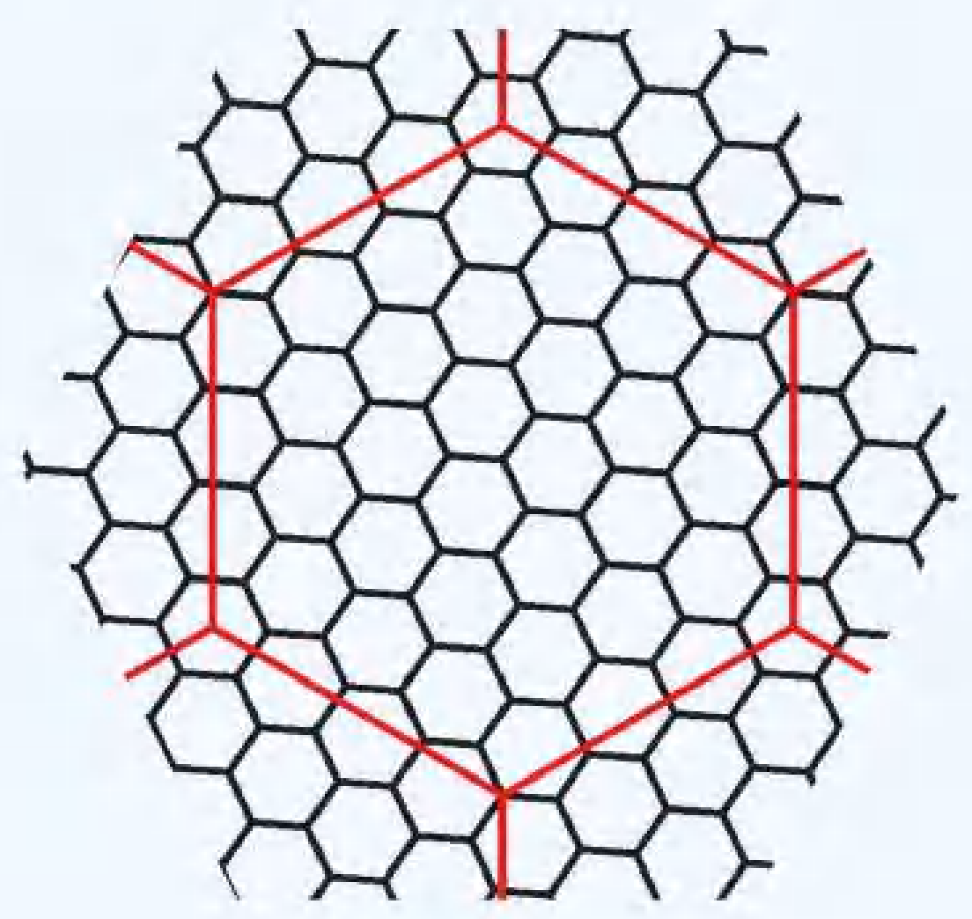

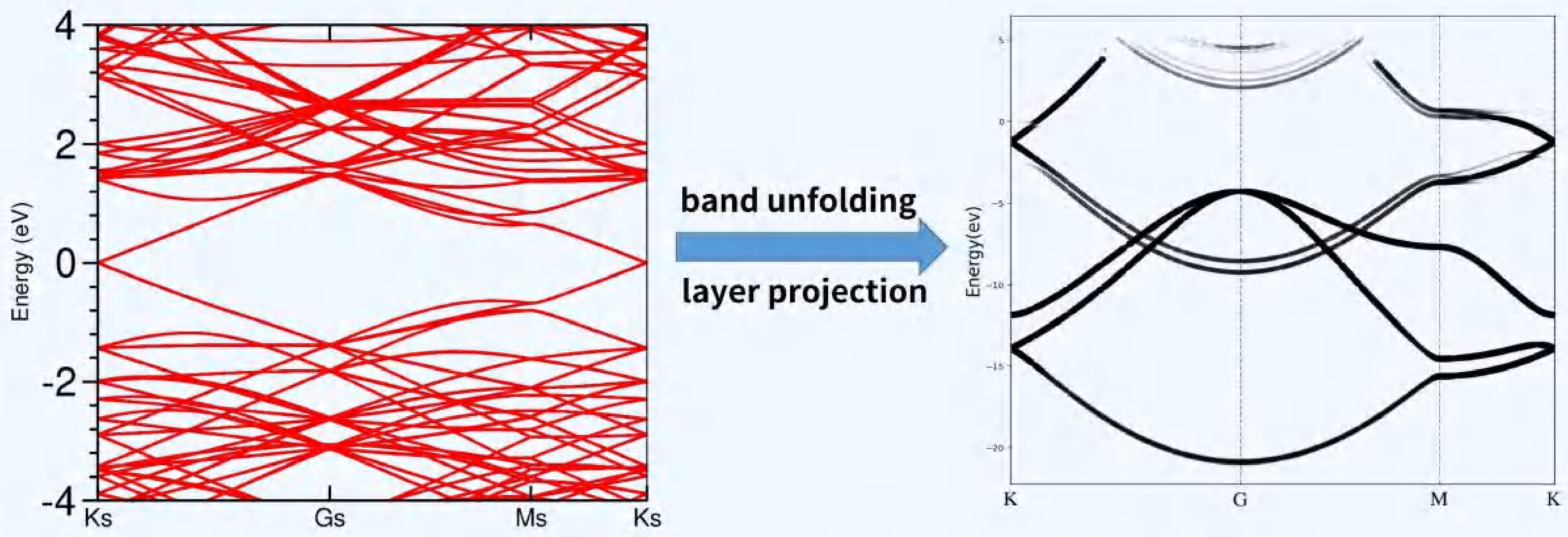

(1) Band structure of Moire-Graphene (left) along supercell BZs and band structure after band unfolding (right) along primitive cell BZs

2. Moire-WS$_2$ θ = 9.43° （LCAO method）

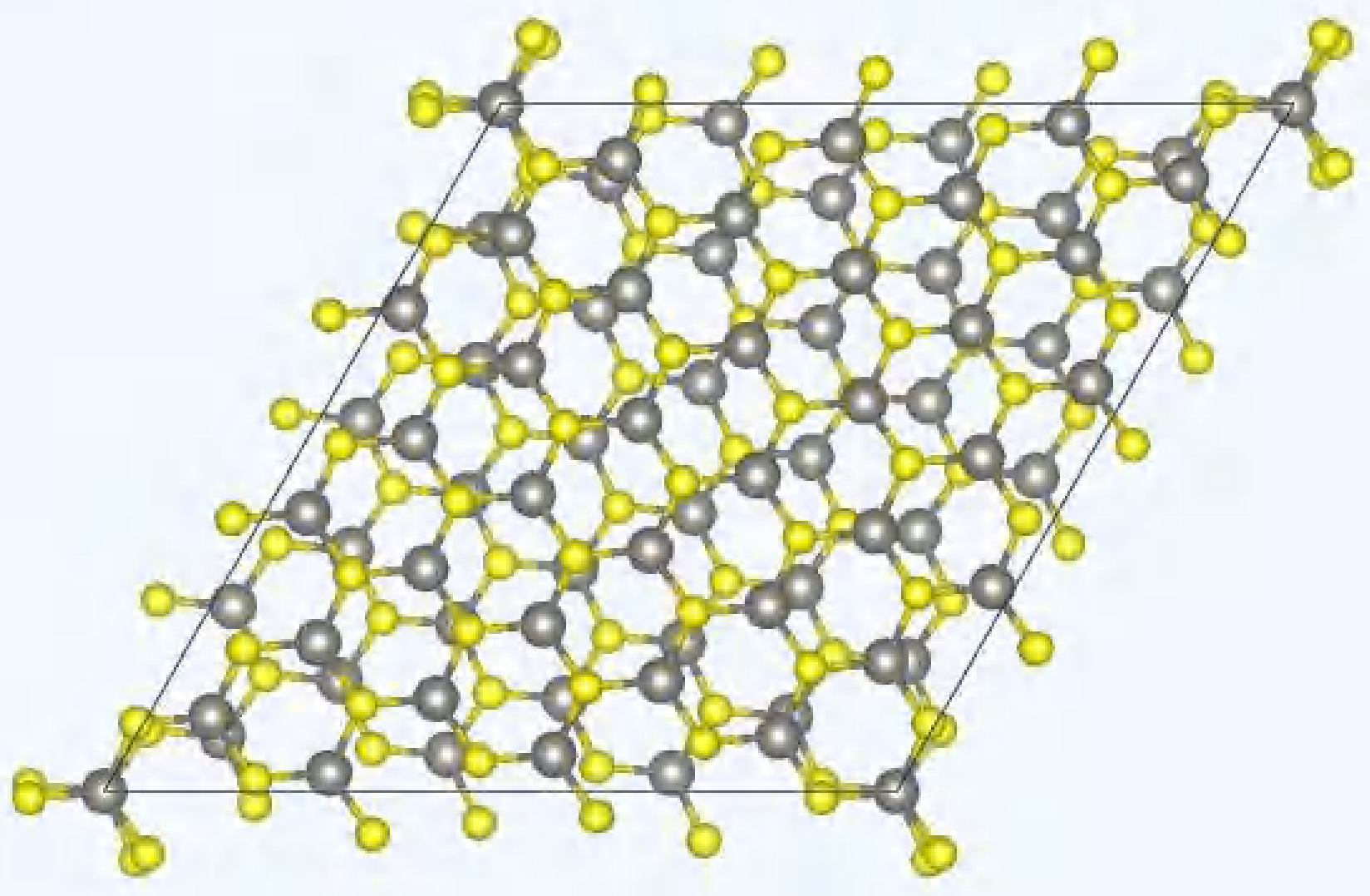

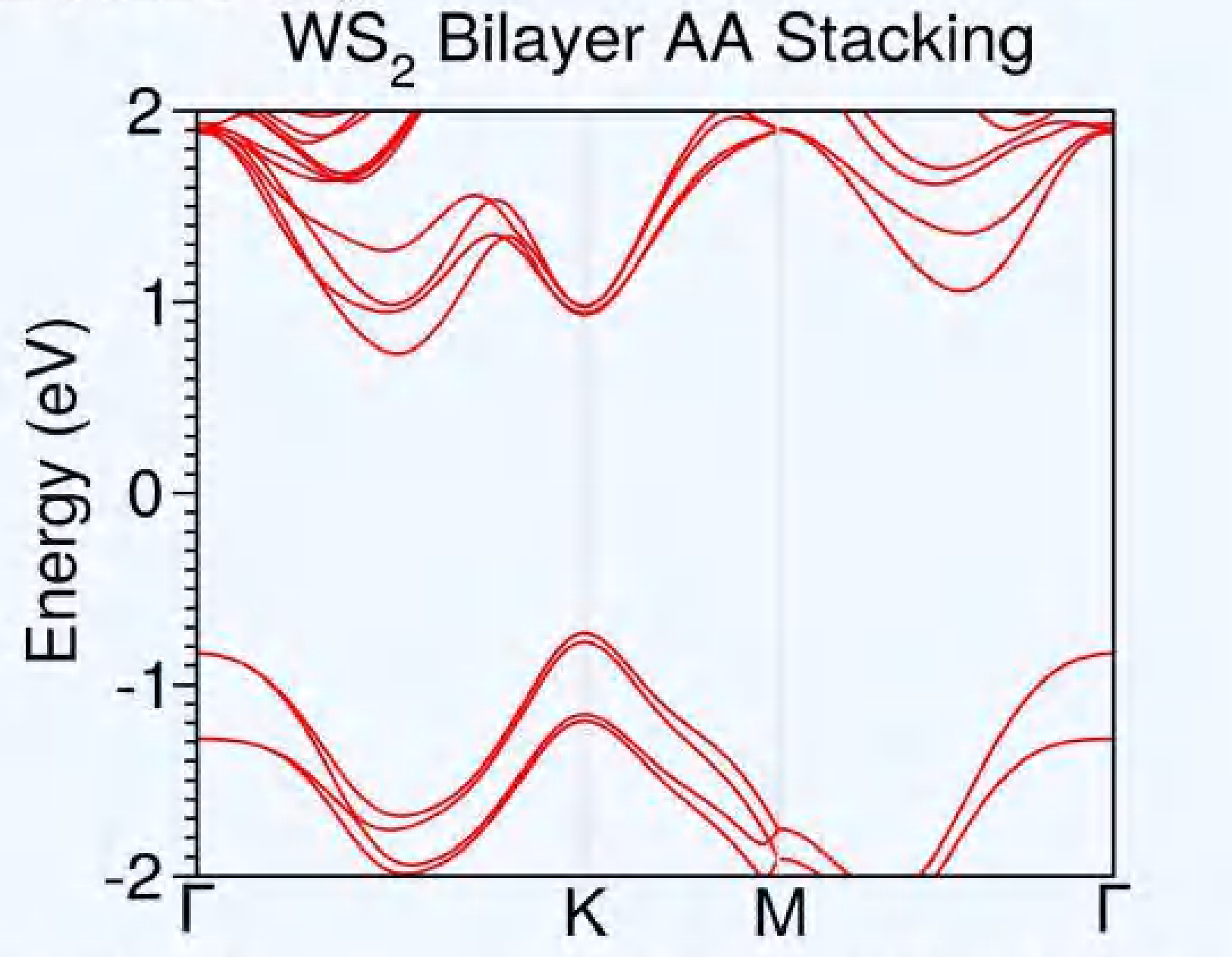

(1) Band structure of bilayer WS$_2$ with soc

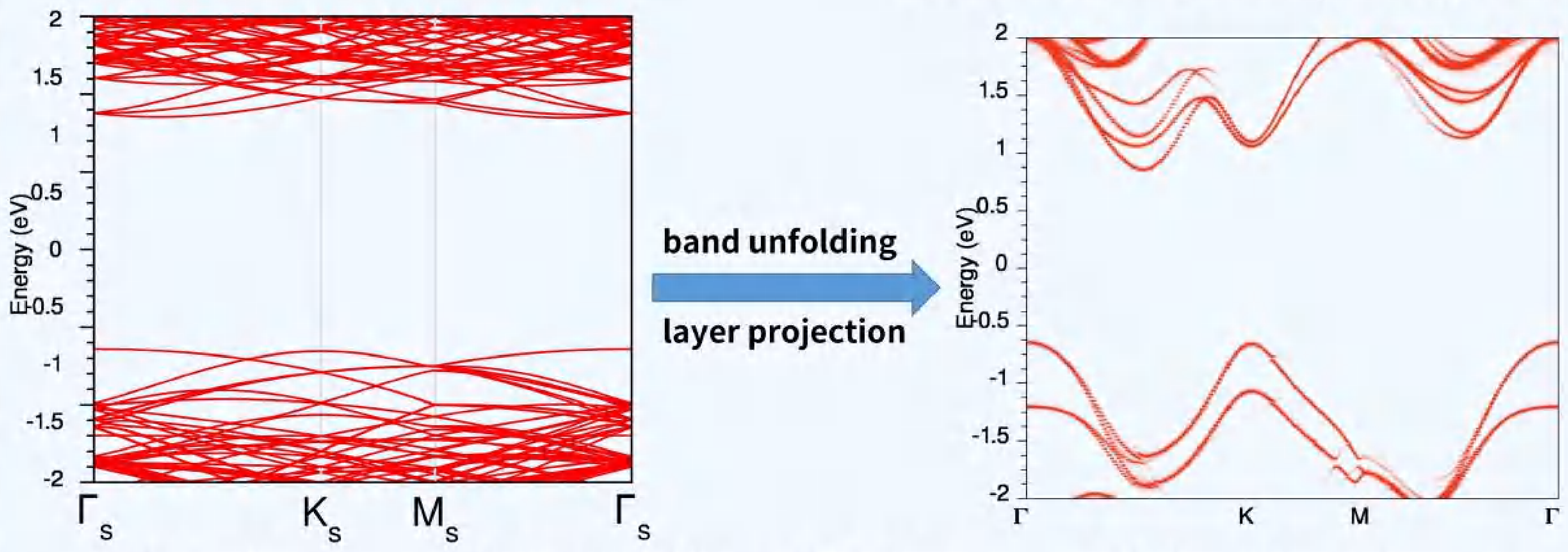

(2) Band structure of Moire-WS$_2$ with soc(left) along supercell BZs and band structure after baunfolding (right) along primitive cell BZs

4. Moire Graphene θ = 9.43° （Phonon）

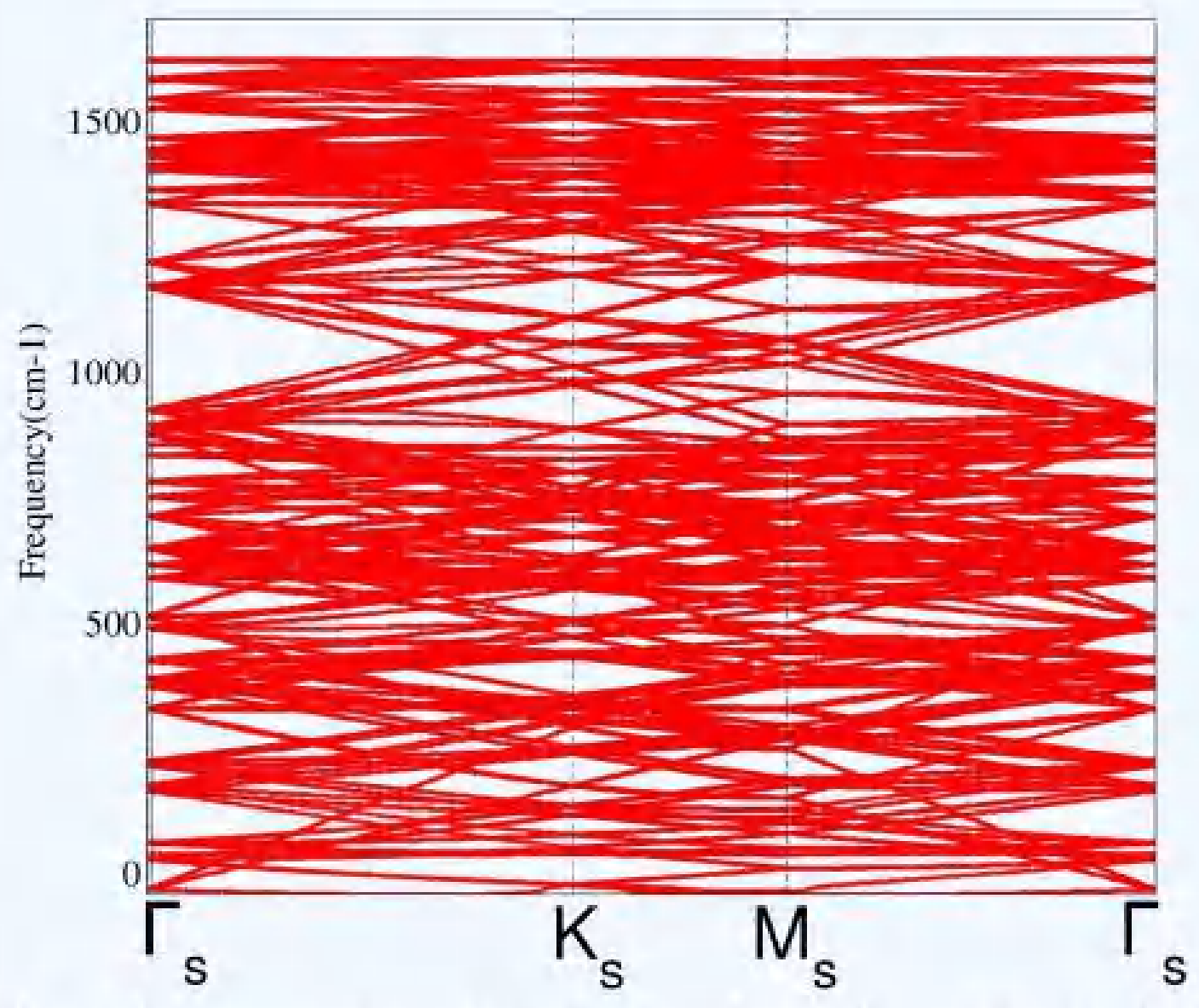

(1) Phonon spectrum of Moire-Graphene along super cell BZs

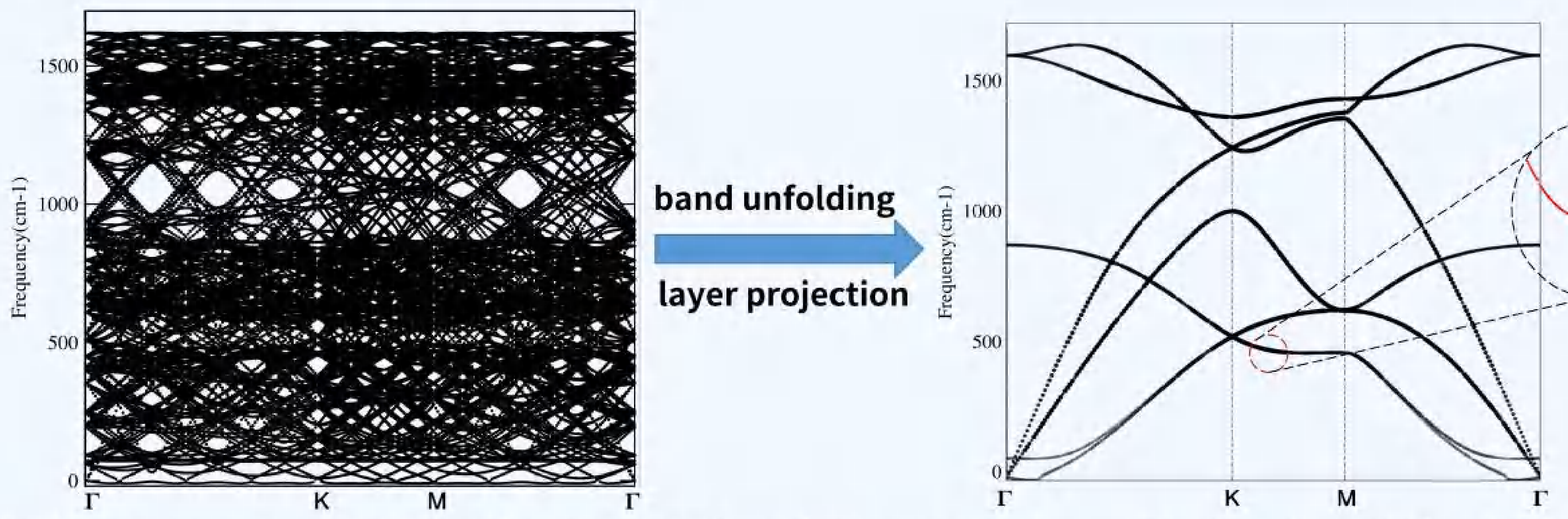

(2) Phonon spectrum of Moire-Graphene(left) and phonon spectrum after band unfolding (right) along primitive cell BZs

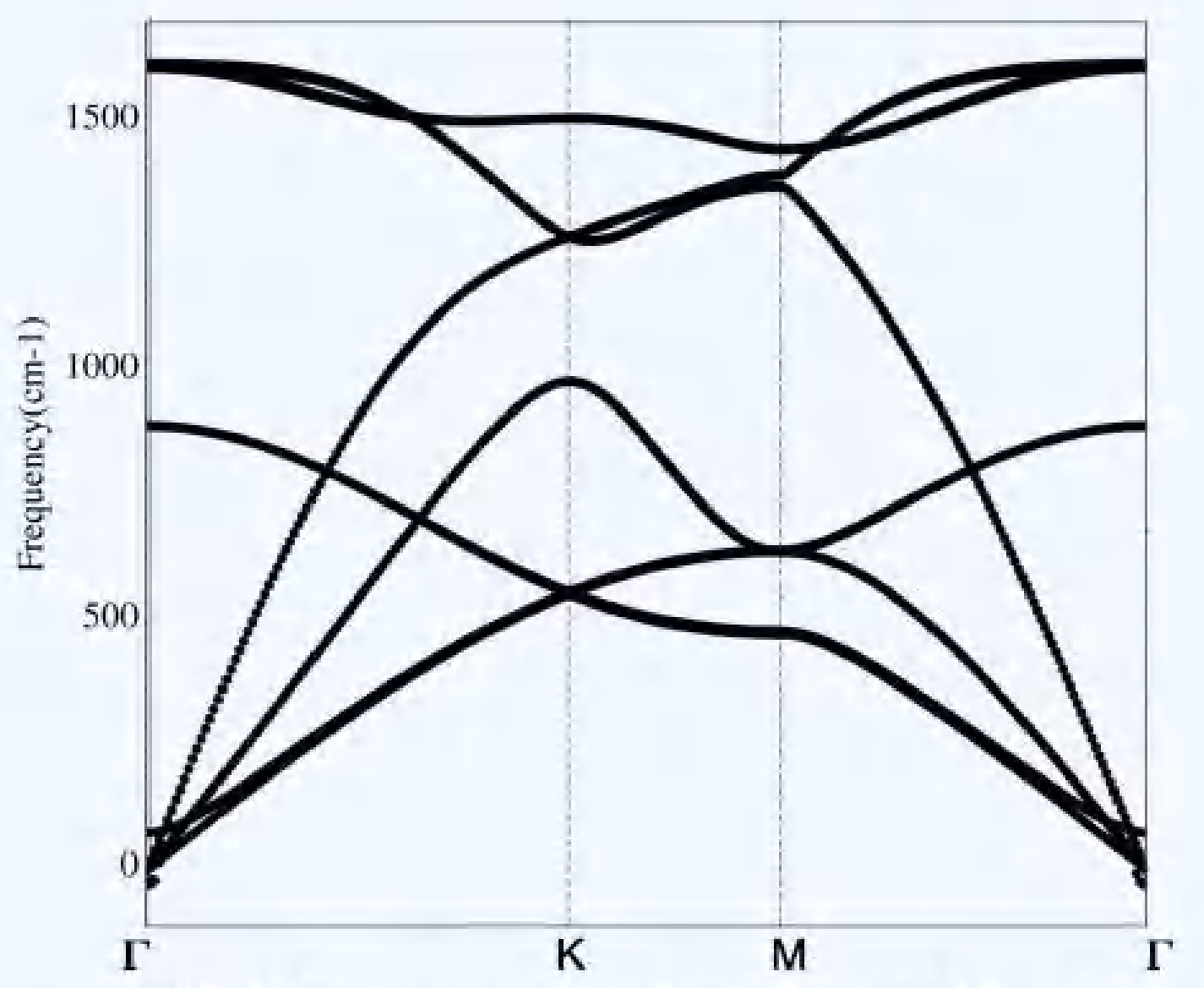

(2) Phonon spectrum of bilayer AA-stacking graphene

Conclusion :

1. New interfaces to KPROJ have been developed.
2. New FFT algorithm has been implemented.
3. Moire effects on the electronic and phononic band structures are revealed using the program.

KPROJ have interfaced to VASP, Quantum ESPRESSO, Abinit, ABACUS and Phononpy

Code address：https://github.com/mxchen-2020/kproj

Contact:
Mingxing Chen (mxchen@hunnu.edu.cn),
School of Physics and Electronics, Hunan Normal University .
Jiaxin Chen (chenjiaxin@hunnu.edu.cn),
School of Physics and Electronics, Hunan Normal University .

Ultrafast Magnetization Dynamics Controlled by Photo-Excitation in VSe_2 Monolayer from Ab Initio Nonadiabatic Molecular Dynamics

Linjie Chen [1] Zhenfa Zheng [2] Qijing Zheng [2*] Qunxiang Li [1*] Jin Zhao [2*]

[1]Department of Chemical Physics, USTC [2]Department of Physics, USTC

Abstract

Magnetism in 2D materials has attracted broad interest in spintronics, which makes 2D magnet a promising next-generation information technology. In this work, we use time-domain ab initio non-adiabatic molecular dynamics (NAMD) to study spin dynamics in a 2D magnet, monolayer VSe_2 at 300K. During the relaxation, the spin-minority electron tends to flip the spin due to spin-orbit coupling (SOC), whereas the spin-majority electron preserves due to stronger electron-phonon coupling (EPC). With more electrons excited, the system's magnetic moment would first increase, then decrease to 50% and finally return to a high level. This prediction provides theoretical fundamentals of controlling the magnetization of 2D materials.

Introduction

Monolayer VSe_2 has been predicted and reported as one of the first room-temperature 2D ferromagnets. Ma et al.[1] calculated the electronic structure by DFT and predict it a metallic 2D ferromagnet. Bonilla et al.[2] synthesized single and few layer VSe_2 sheets on HOPG and MoS_2 substrates using MBE and performed magnetic characterization, and confirmed the room-temperature magnetism.

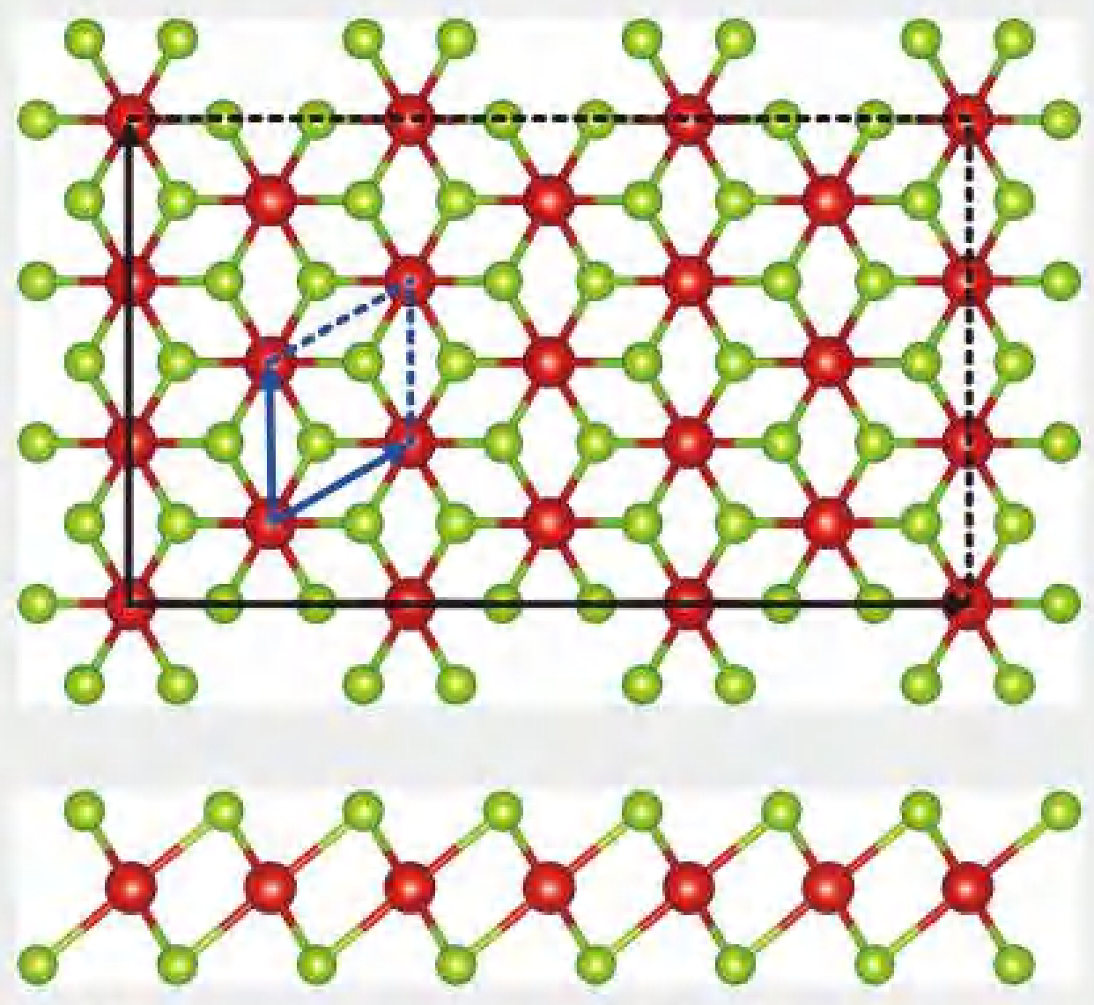

(a) Geometry structure of 1T VSe_2 monolayer

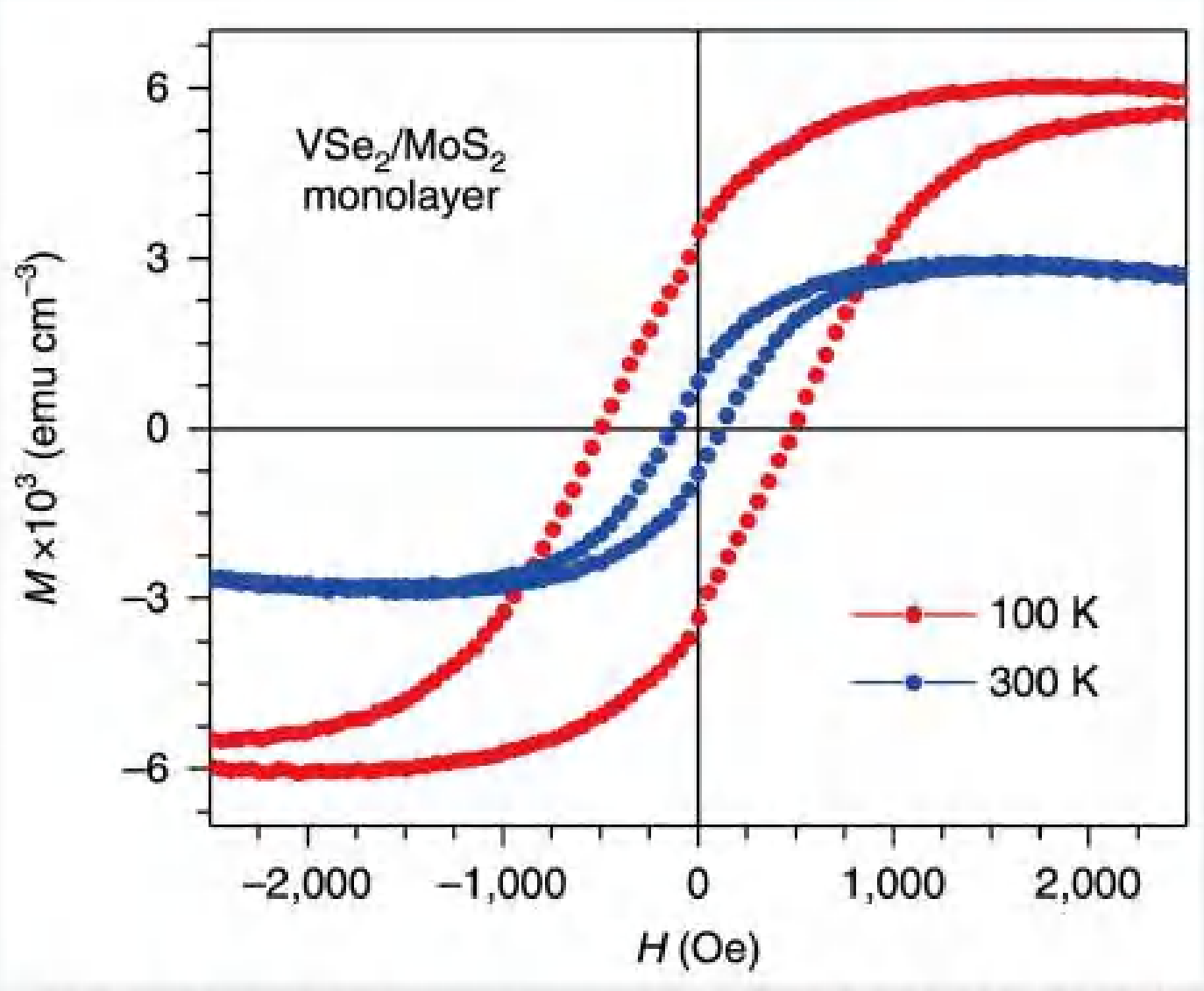

(b) *Nature Nanotechnology* 13, 289–293 (2018)

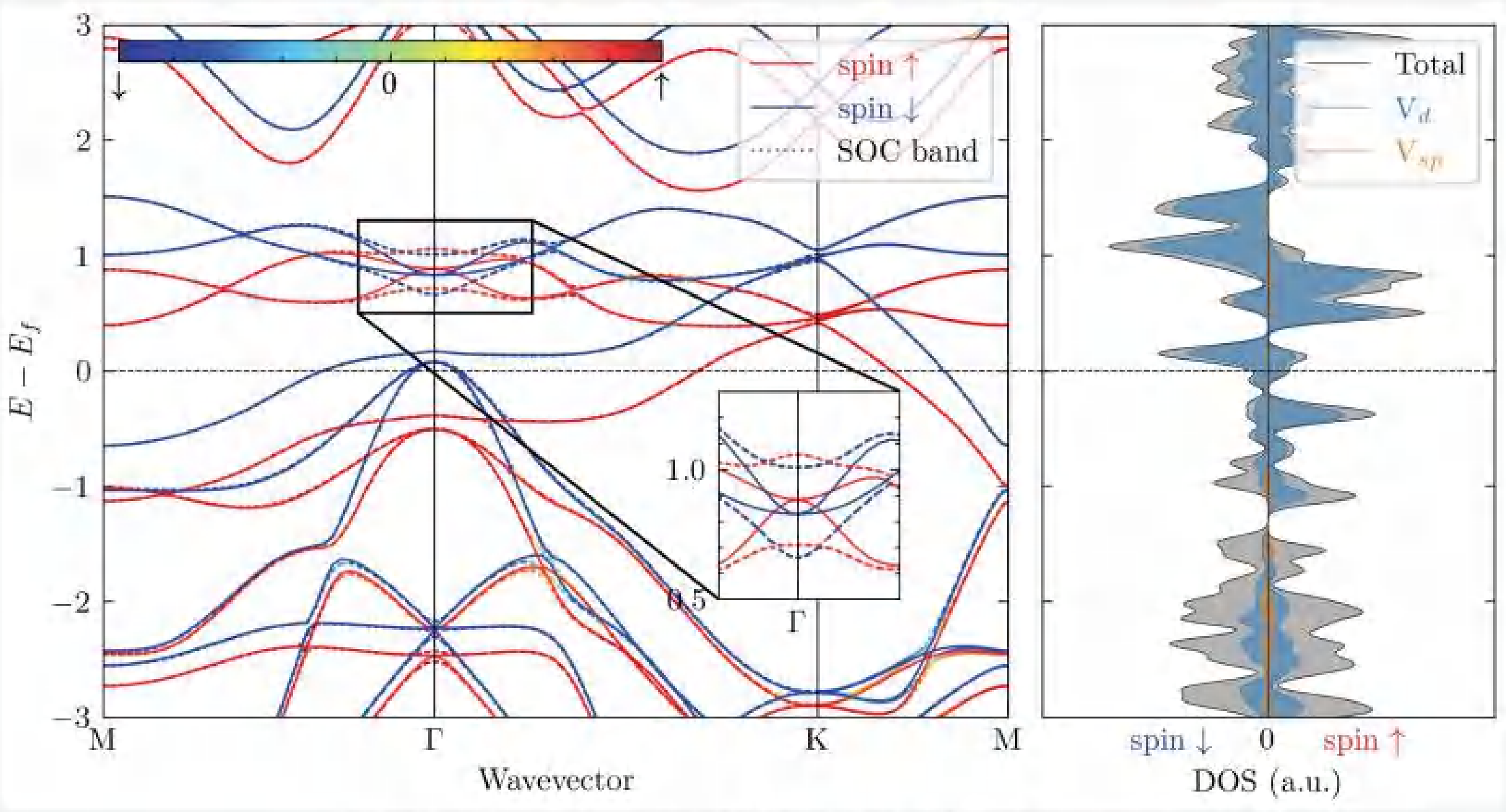

(c) Bandstructure and DOS of 1T VSe_2 monolayer

The calculated bandstructure and DOS indicates the VSe_2 monolayer is both metallic and ferromagnetic. The magnetism is mainly contributed by *d* electron of V atoms. Also, the considerable splitting of SOC bands near 1eV means the SOC effect cannot be ignored. These electronic structure features are crucial to the magnetization change.

SOC-included NAMD Methodology [3]

The time-dependent Schrödinger equation

$$i\hbar\frac{\partial|\Psi(\mathbf{r},\mathbf{R}(t),\mathbf{s},t)\rangle}{\partial t} = \mathcal{H}^{\mathrm{tot}}(\mathbf{r},\mathbf{R}(t),\mathbf{s})\,|\Psi(\mathbf{r},\mathbf{R}(t),\mathbf{s},t)\rangle \tag{1}$$

where the total Hamiltonian is given by

$$\mathcal{H}^{\mathrm{tot}}(\mathbf{r},\mathbf{R}(t),\mathbf{s}) = \mathcal{H}^{0}(\mathbf{r},\mathbf{R}(t)) + \mathcal{H}^{\mathrm{SOC}}(\mathbf{r},\mathbf{R}(t),\mathbf{s}) \tag{2}$$

by expanding the wavefunction with a *basis set* $\{|\psi_i\rangle\}$ or *represenation*

$$|\Psi\rangle = \sum_i |\psi_i\rangle\langle\psi_i|\Psi\rangle = \sum_i c_i|\psi_i\rangle \tag{3}$$

and substituting eq (3) into eq(1), we have

$$\begin{aligned}\frac{\partial c_j(t)}{\partial t} &= -\sum_i\left[\frac{i}{\hbar}\langle\psi_j|\mathcal{H}^{\mathrm{tot}}|\psi_i\rangle + \langle\psi_j|\frac{d}{dt}|\psi_i\rangle\right]c_i(t)\\ &= -\sum_i\left[\frac{i}{\hbar}\langle\psi_j|\mathcal{H}^{0}|\psi_i\rangle + \frac{i}{\hbar}\langle\psi_j|\mathcal{H}^{\mathrm{SOC}}|\psi_i\rangle + \langle\psi_j|\frac{d}{dt}|\psi_i\rangle\right]c_i(t)\\ &= -\sum_i(i\hbar^{-1}H^0_{ji} + i\hbar^{-1}H^{SOC}_{ji} + T_{ji})c_i(t)\end{aligned} \tag{4}$$

The red part and blue part correspond to SOC and EPC, respectively.
In NAMD, the wavefunction is propagated by updating the coefficients $c_i(t)$, and the time-dependent population is defined as $\rho_i(t) = |c_i(t)|^2$. All the information related to the dynamics are within the time-dependent population.

SOC Included Spin Dynamics

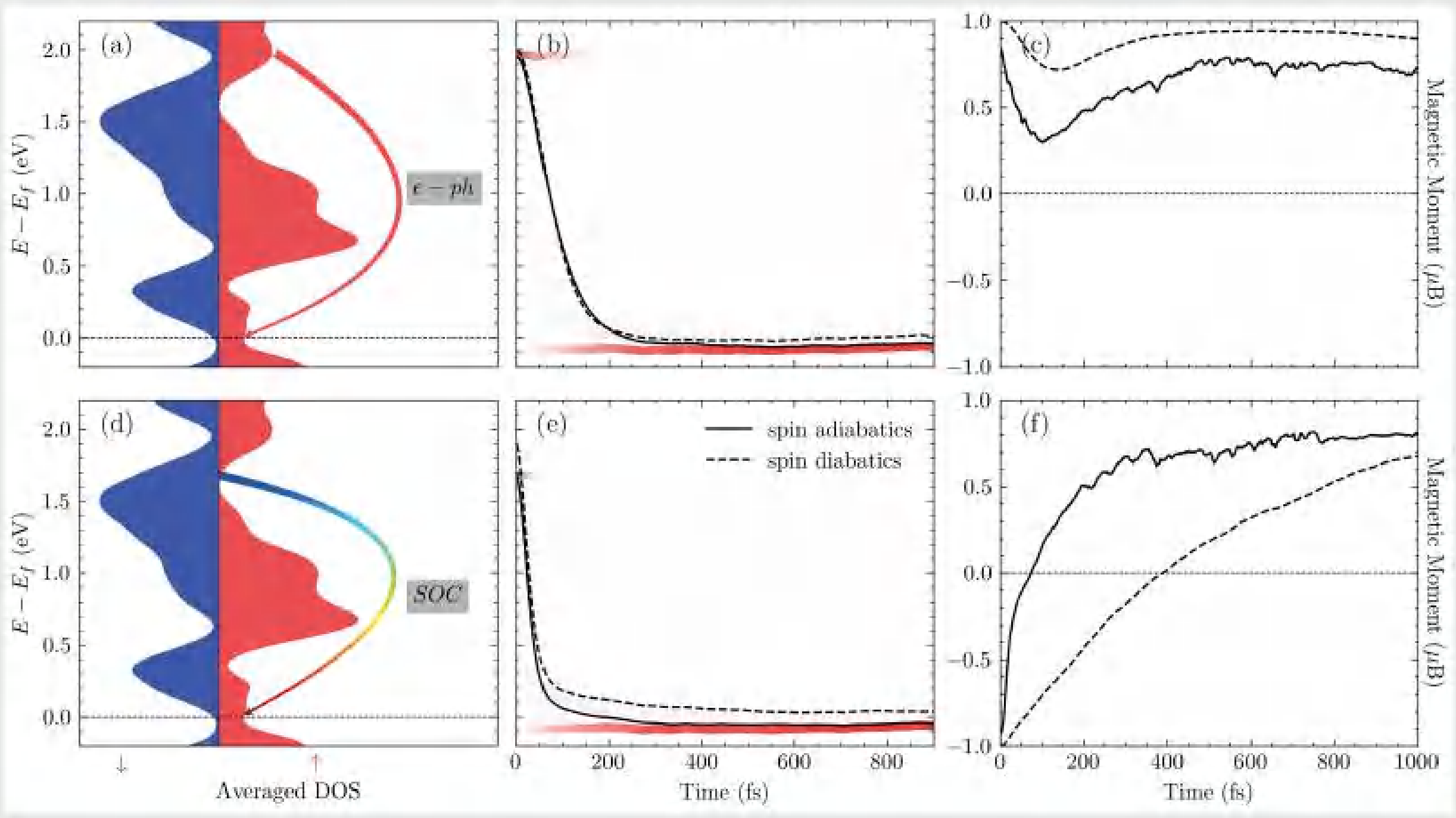

Given that spin majority is spin up, the spin up electrons stick to be spin up through EPC, while the spin down electrons turn into spin down through smaller SOC.

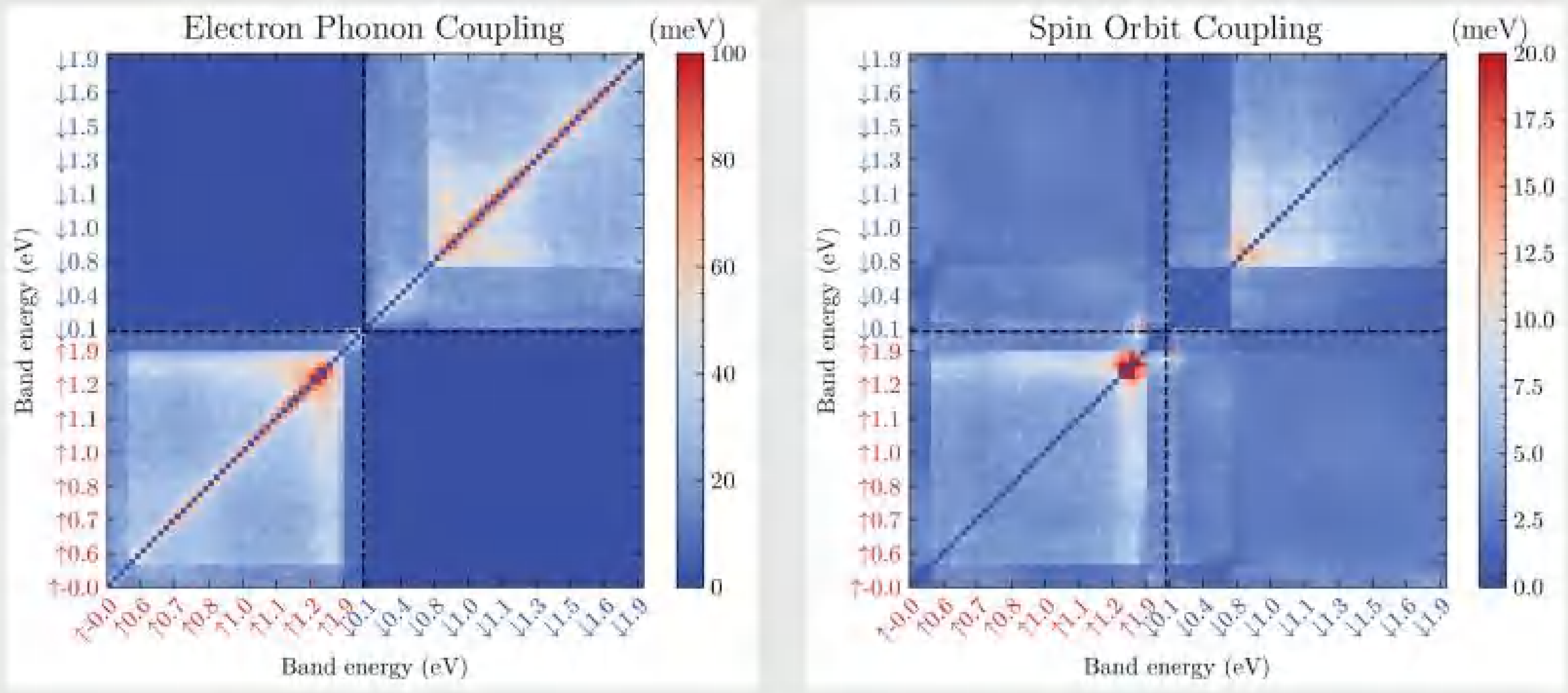

EPC makes electron decay among the states in same spin while SOC provides the channels to make electron flip the spin. The spin-diabatic picture shows that when SOC is smaller than EPC by alomost an order of magnitude, which makes spin flip process slower than EPC induced transition.

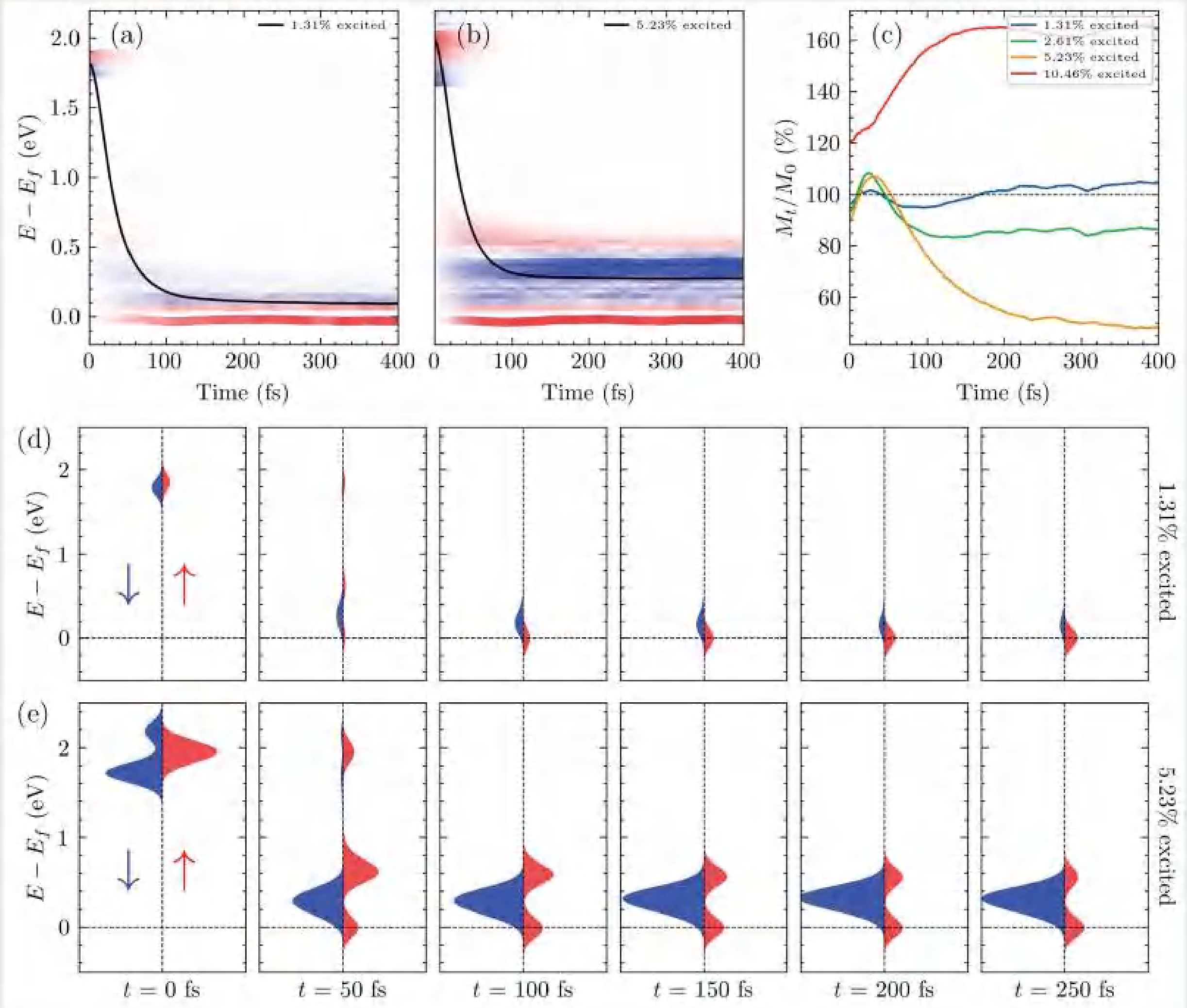

The magnetization change depends on the photo-excitation ratio. This phenomenon originates from the special band spin distribution above the Fermi level: the spin down bands are sandwiched by spin up bands around Fermi level and ∼0.6eV.

References

- Yandong Ma et al. "Evidence of the existence of magnetism in pristine VX2 monolayers (X= S, Se) and their strain-induced tunable magnetic properties". In: *ACS nano* 6.2 (2012), pp. 1695–1701.
- Manuel Bonilla et al. "Strong room-temperature ferromagnetism in VSe2 monolayers on van der Waals substrates". In: *Nature nanotechnology* 13.4 (2018), pp. 289–293.
- Zhenfa Zheng, Qijing Zheng, and Jin Zhao. "Spin-orbit coupling induced demagnetization in Ni: Ab initio nonadiabatic molecular dynamics perspective". In: *Physical Review B* 105.8 (2022), p. 085142.

Layer-dependent magnetic phase diagram in Fe_nGeTe_2 ($3 \leq n \leq 7$) ultrathin films: coexistence of localized and itinerant electronic states of Fe with variable valence

Qinxi Liu[1], Jianpei Xing[1], Zhou Jiang[1], Yu Guo[1], Xue Jiang[1]*, Yan Qi[2,1]*, Jijun Zhao[1]

[1]*Key Laboratory of Materials Modification by Laser, Ion and Electron Beams (Ministry of Education), Dalian University of Technology, Dalian 116024, China*
[2]*School of Physics and Materials Engineering, Dalian Minzu University, Dalian 116600, China*

ABSTRACT

Two-dimensional (2D) ferromagnets with high Curie temperature (T_C) are highly desirable due to their potential applications in spintronic devices. However, they are rarely obtained in experiments mainly due to the challenge of synthesizing high-quality 2D crystals, and their T_C values are below the room temperature. By first-principles calculations, herein we design a family of stable 2D Fe_nGeTe_2 ($4 \leq n \leq 7$) ultrathin films that are similar to the reported Fe_3GeTe_2, which exhibit coexistence of itinerant and localized magnetism. The coexistence of itinerant and localized magnetism could distinguished by their a_1 and e_1/e_2 electrons. Among them, 2D Fe_3GeTe_2 and Fe_4GeTe_2 are ferromagnetic metals with T_C of 138 K and 68 K, respectively; 2D Fe_5GeTe_2, Fe_6GeTe_2 and Fe_7GeTe_2 ultrathin films are Néel's P-types, R-type, R-type ferrimagnetic metals with T_C of 320 K, 450 K and 570 K, respectively.

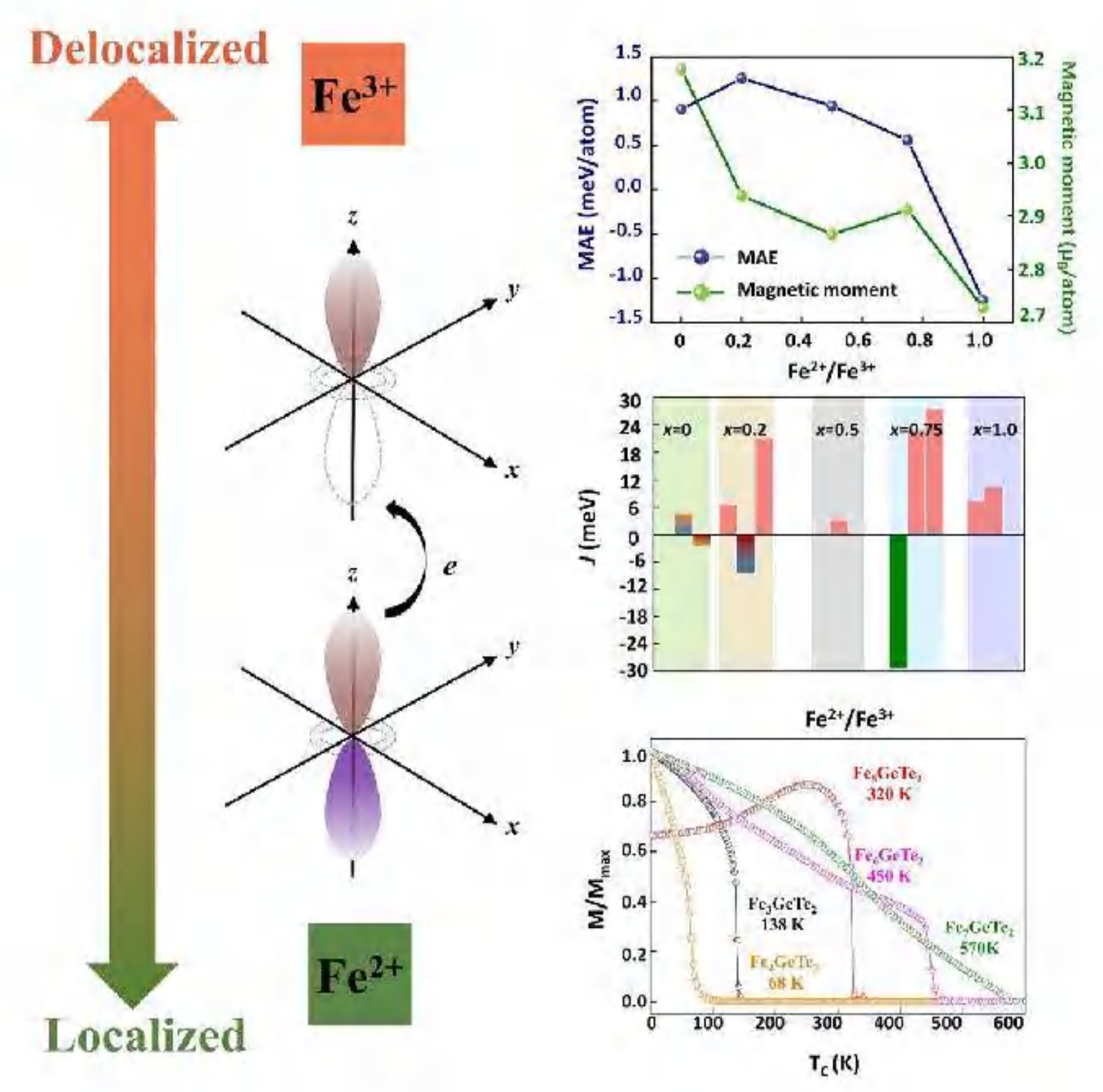

Co-existence of localized and delocalized magnetism

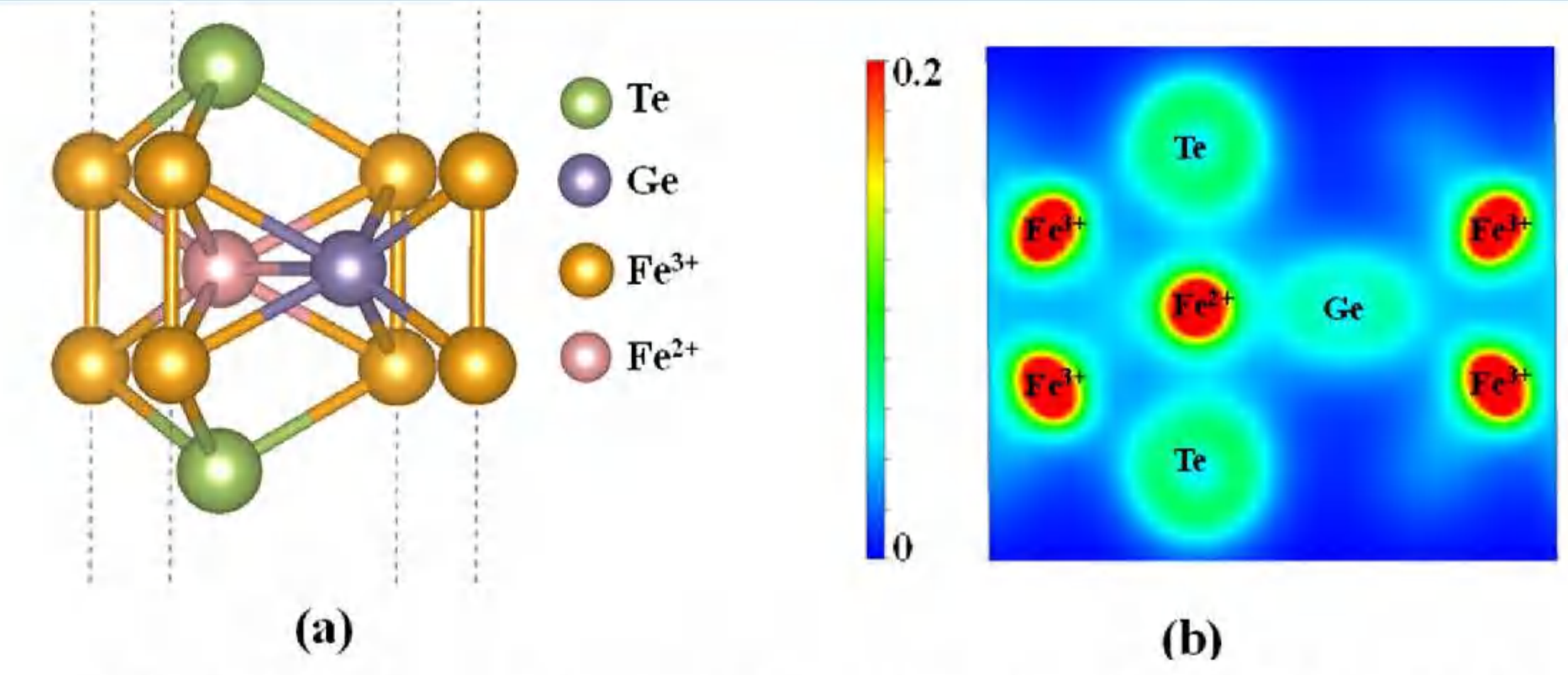

Fig. 1 (a) The structure and (b) charge density of 2D Fe_3GeTe_2

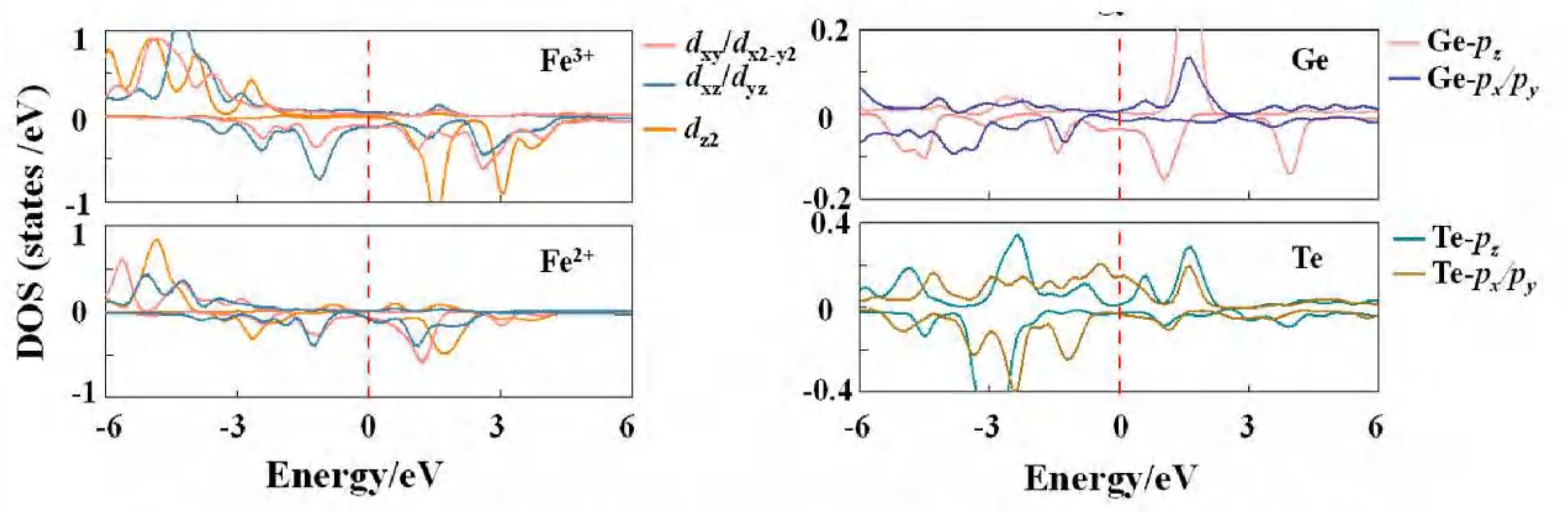

Fig. 2 The orbital-projected density of states for 2D Fe_3GeTe_2.

Magnetic coupling mechanism in Fe_3GeTe_2

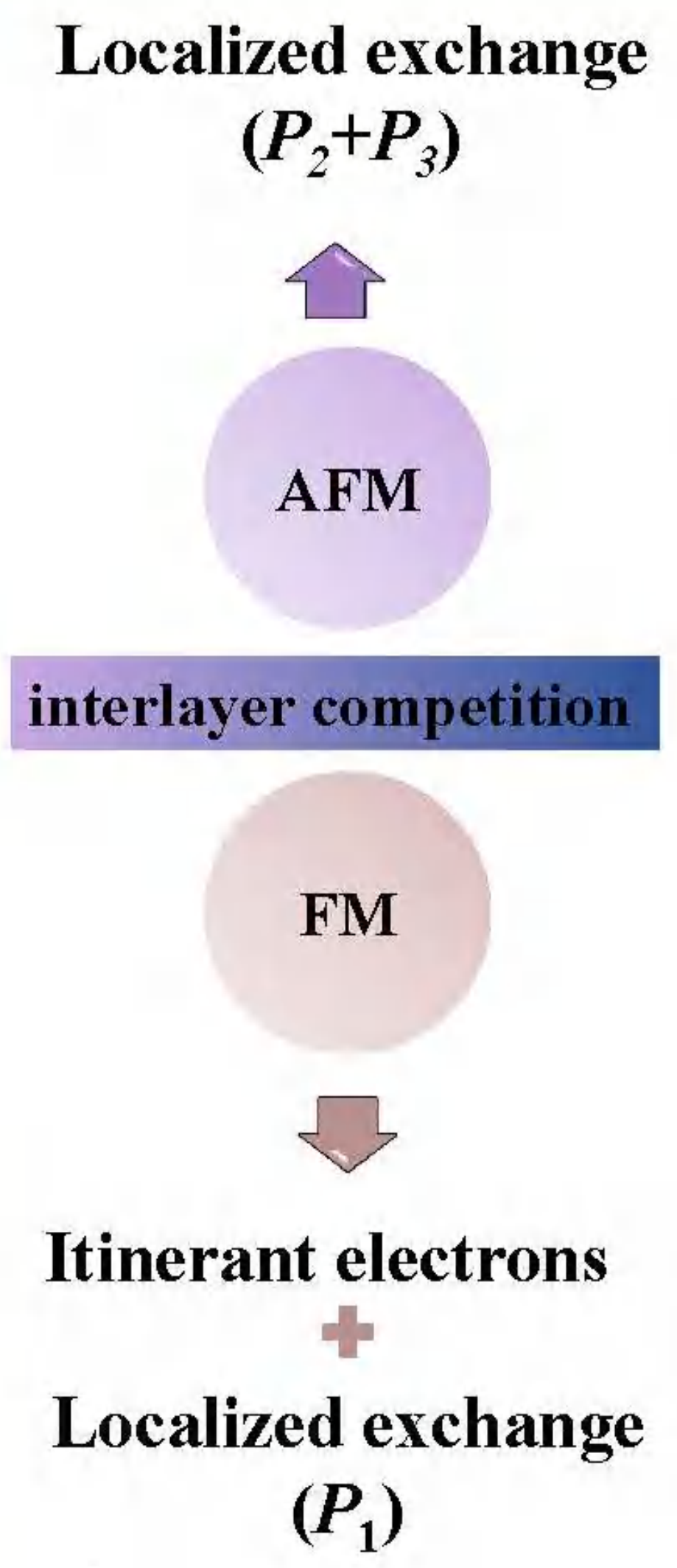

Localized exchange (P_2+P_3)

AFM

interlayer competition

FM

Itinerant electrons

+

Localized exchange (P_1)

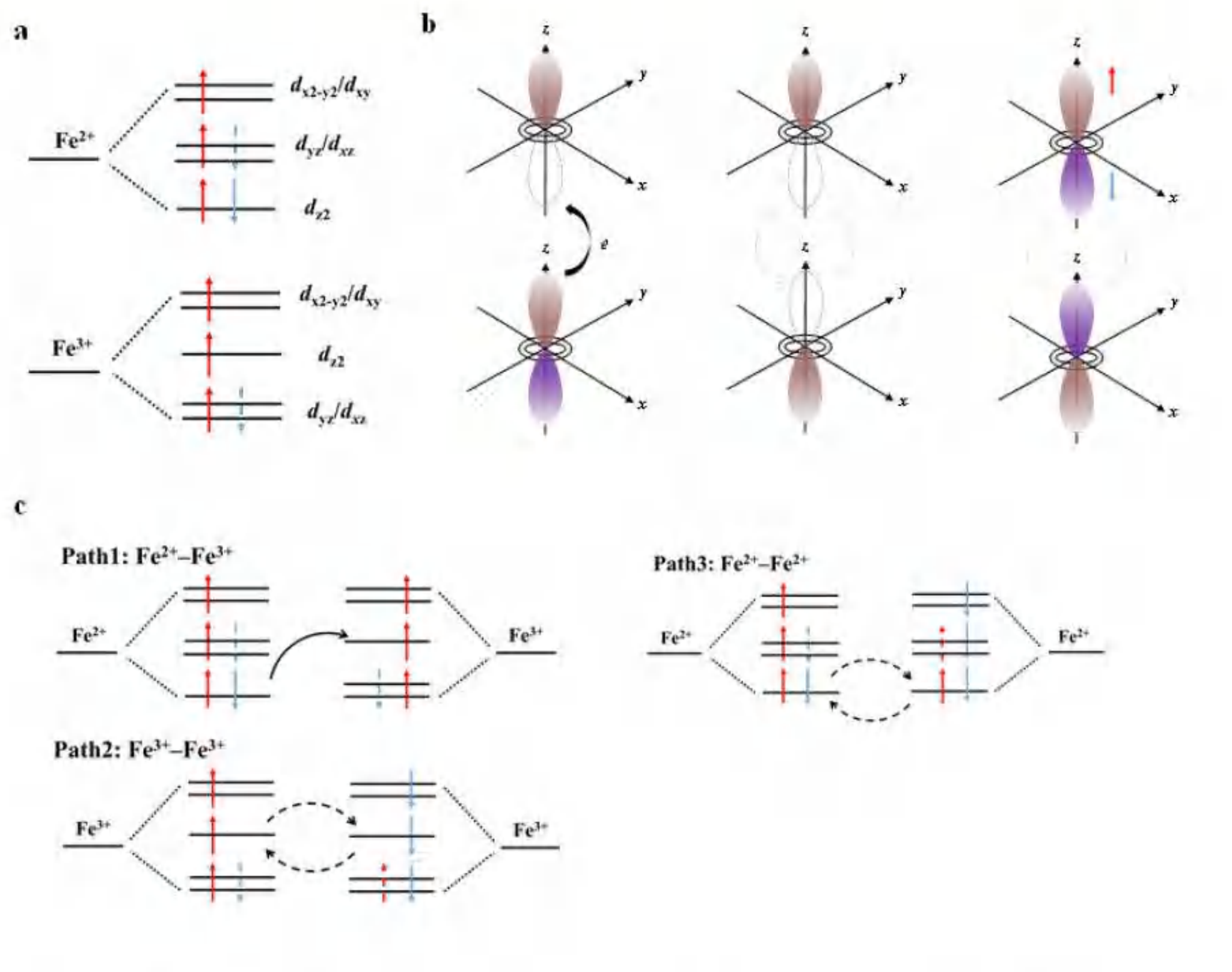

Fig. 3 (a)The schematic representation of splitting d orbital in Fe^{2+} and Fe^{3+} ions, respectively. (b) Three possible process of the exchange between localized d_{z^2} orbital. (c) Three possible Fe-Fe exchange paths.

Magnetic behavior of Fe_nGeTe_2 ultrathin films

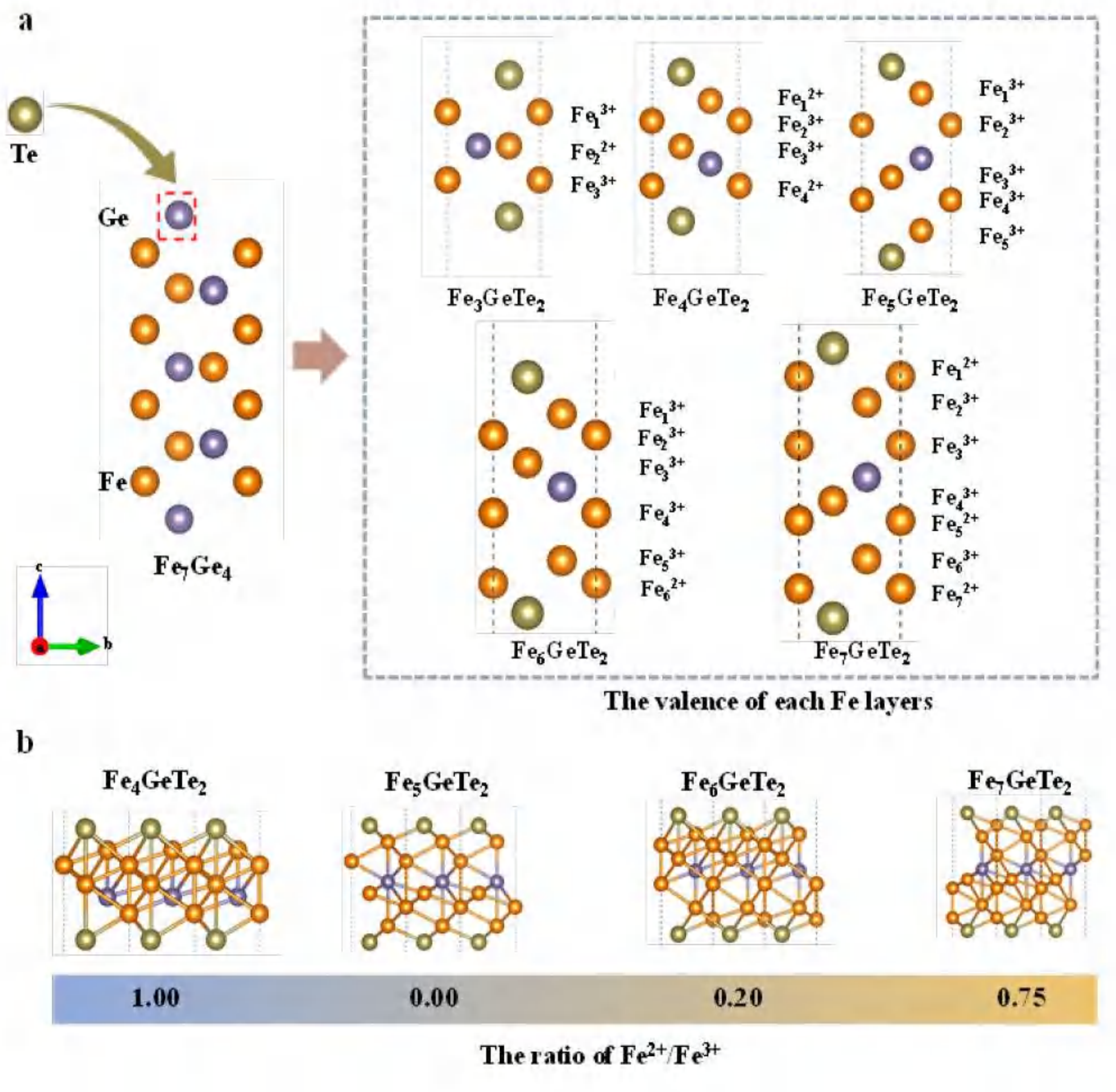

Fig. 4 Schematic illustration of Te-substituted Fe_7Ge_4 crystal and constituted five structures in the series of Fe_nGeTe_2

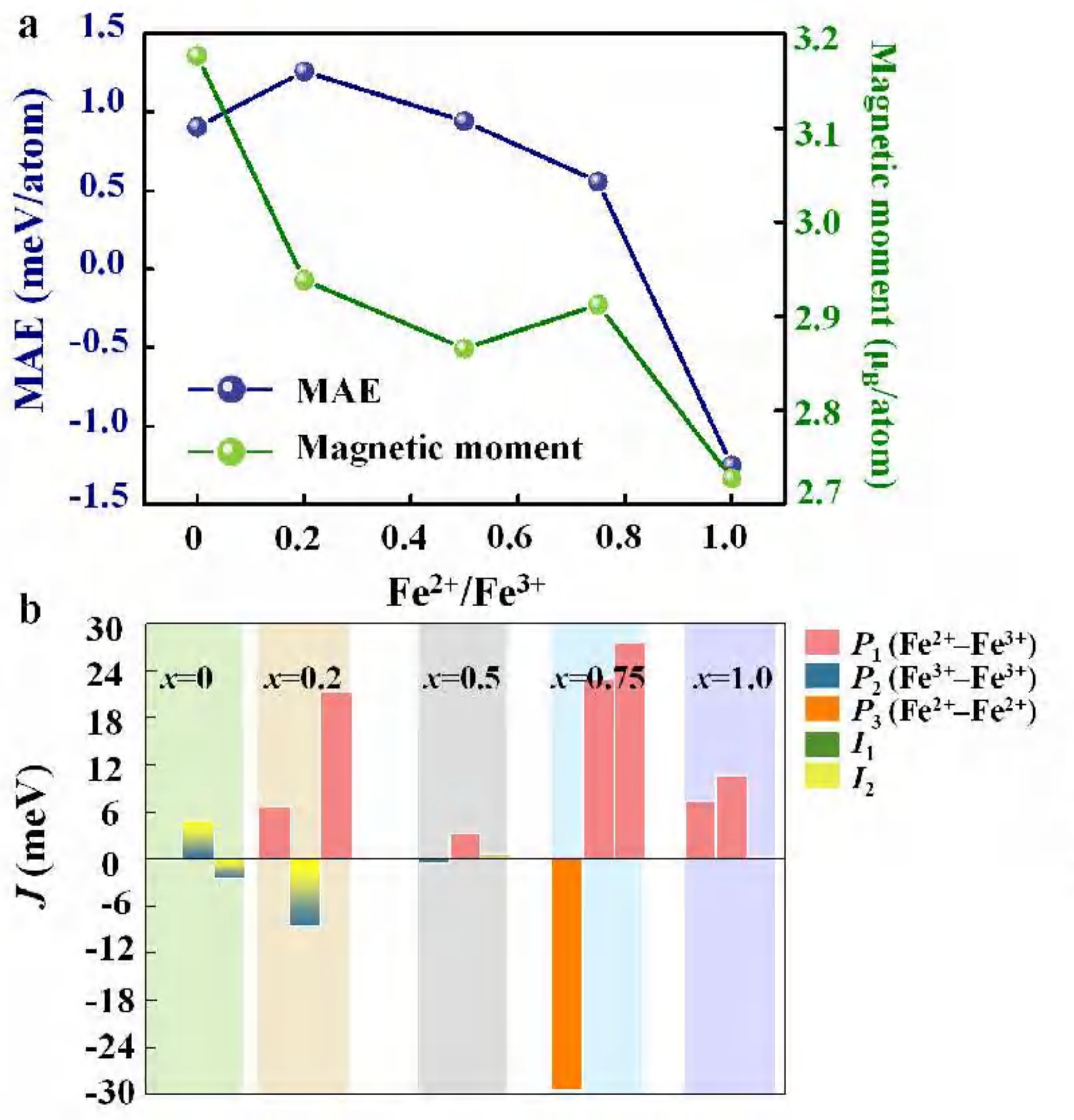

Fig. 5 The ratio of Fe^{2+}/Fe^{3+} (x) in multilayer Fe_nGeTe_2 as a function of (a) MAE and magnetic moment per atom and (b) exchange parameters.

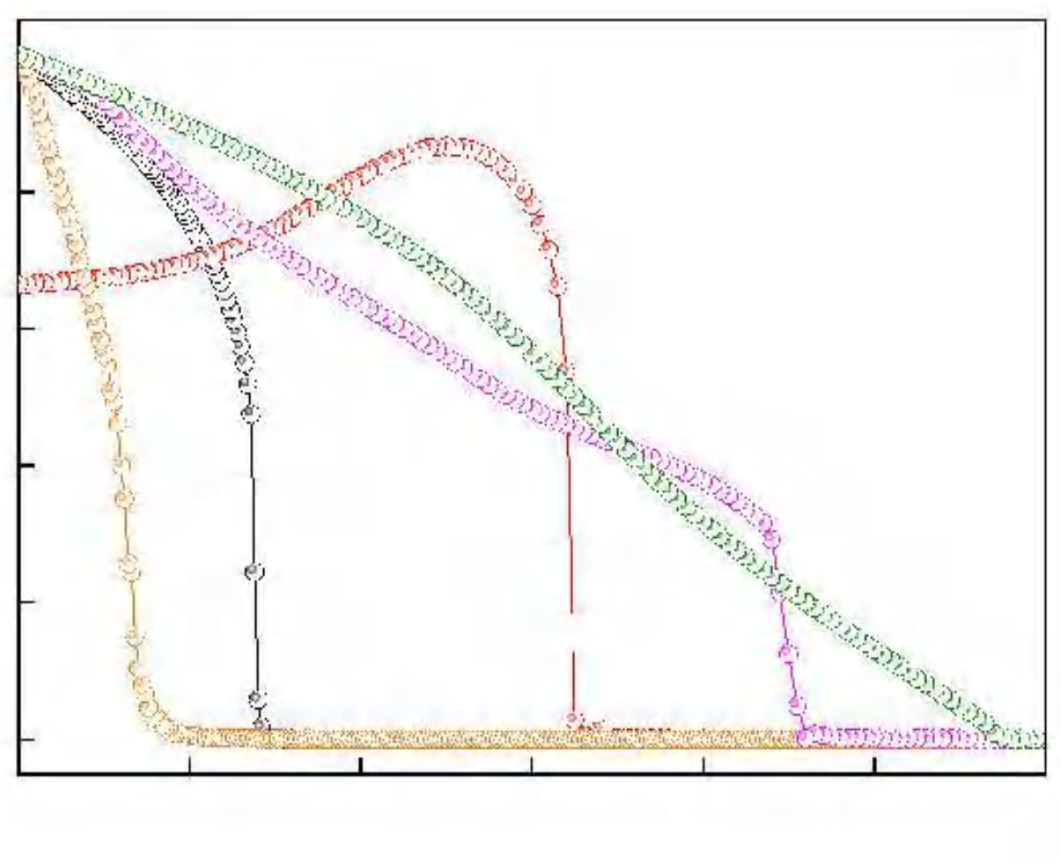

Fig. 6 Normalized magnetization of Fe atoms in Fe_nGeTe_2 as a function of temperature.

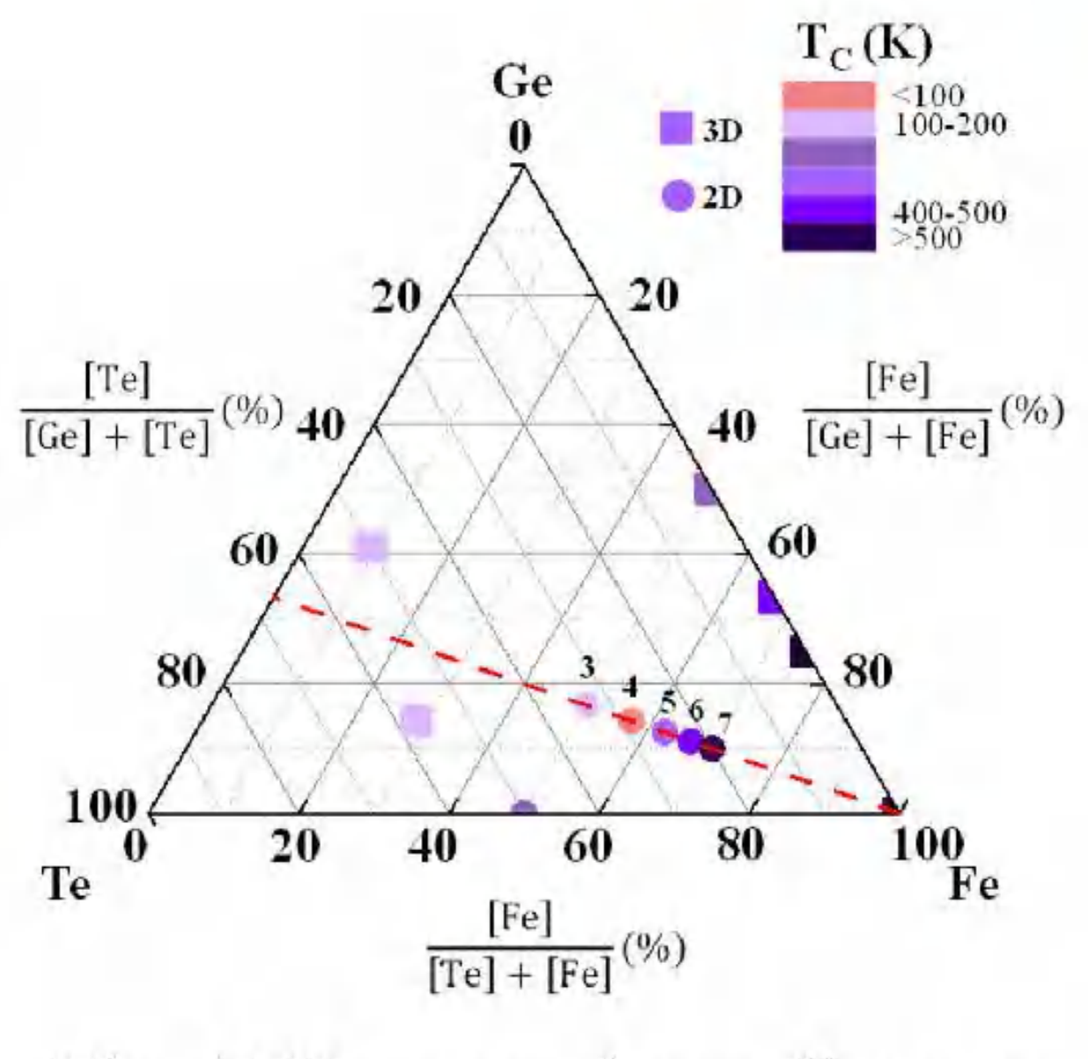

Fig. 7 Ternary phase diagram of various Fe-rich compositions.

Table 1. The corresponding magnetic parameter for Fe_nGeTe_2

	x	Thickness (Å)	E_{form} (eV/atom)	M (μ_B)	MAE (meV)	T_C (K)	Exchange parameter (meV)		
							J_1	J_2	J_3
Fe_3GeTe_2	0.5	8.61	−0.08	2.87	2.83	138	−0.44	3.27	0.47
Fe_4GeTe_2	1.0	9.10	−0.03	2.73	−5.01	68	7.40	10.50	0.10
Fe_5GeTe_2	0	10.95	−0.11	3.18	4.53	320	−0.20	4.70	−2.60
Fe_6GeTe_2	0.2	11.03	−0.05	2.94	6.31	450	6.60	−8.60	21.20
Fe_7GeTe_2	0.75	12.21	−0.01	2.91	3.91	570	−29.40	23.00	27.50

Conclusion

- **The coexistence states exhibited in Fe_nGeTe_2 family**
- **Localized exchange play an important role in metallic Fe_nGeTe_2 films**
- **Metallic Fe_nGeTe_2 films are potential room-temperature ferromagnets/ferrimagnets.**

DOI: https://doi.org/10.1038/s42005-022-00921-3

Alloying Two-Dimensional $NbSi_2N_4$: A New Strategy to Realize Half-Metallic Antiferromagnets

Yanxia Wang, Xue Jiang*, Yi Wang and Jijun Zhao

Key Laboratory of Material Modification by Laser, Ion and Electron Beams, Dalian University of Technology, Ministry of Education, Dalian 116024, China

E-mail: wangyanxia@mail.dlut.edu.cn, jiangx@dlut.edu.cn

Abstract: Finding two-dimensional (2D) materials with both **100% spin polarization** and **zero net magnetic moment** is essential for next-generation spintronics. **Half-metallic antiferromagnets (HMAFs)** are ideal materials to satisfy these exigent needs, but such a system has **never** been found among 2D inorganic materials. In this paper, we theoretically demonstrate that intrinsic 2D HMAFs can be realized by alloying Nb with Mn in 2D septuple-atomic-layer $NbSi_2N_4$. By continuously incorporating Mn, stronger Mn-N hybridization relative to Nb-N induces **metal** to **half-metal** to **semiconductor transition**. The competitive coupling between Nb-*d* itinerant electron spin and Nb-Mn *d-d* direct interaction drives the **ferromagnetic** to **antiferromagnetic** phase transition. For **the first time** in 2D inorganic materials, the exact cancellation of the local magnetic moments and band gap opening in one spin channel is obtained simultaneously at the Nb/Mn ratio of 3:1, as demonstrated by our first-principles calculations. The present results would not only inspire materials design of more 2D HMAFs in the future but also impel the development of next-generation antiferromagnetic spintronic devices.

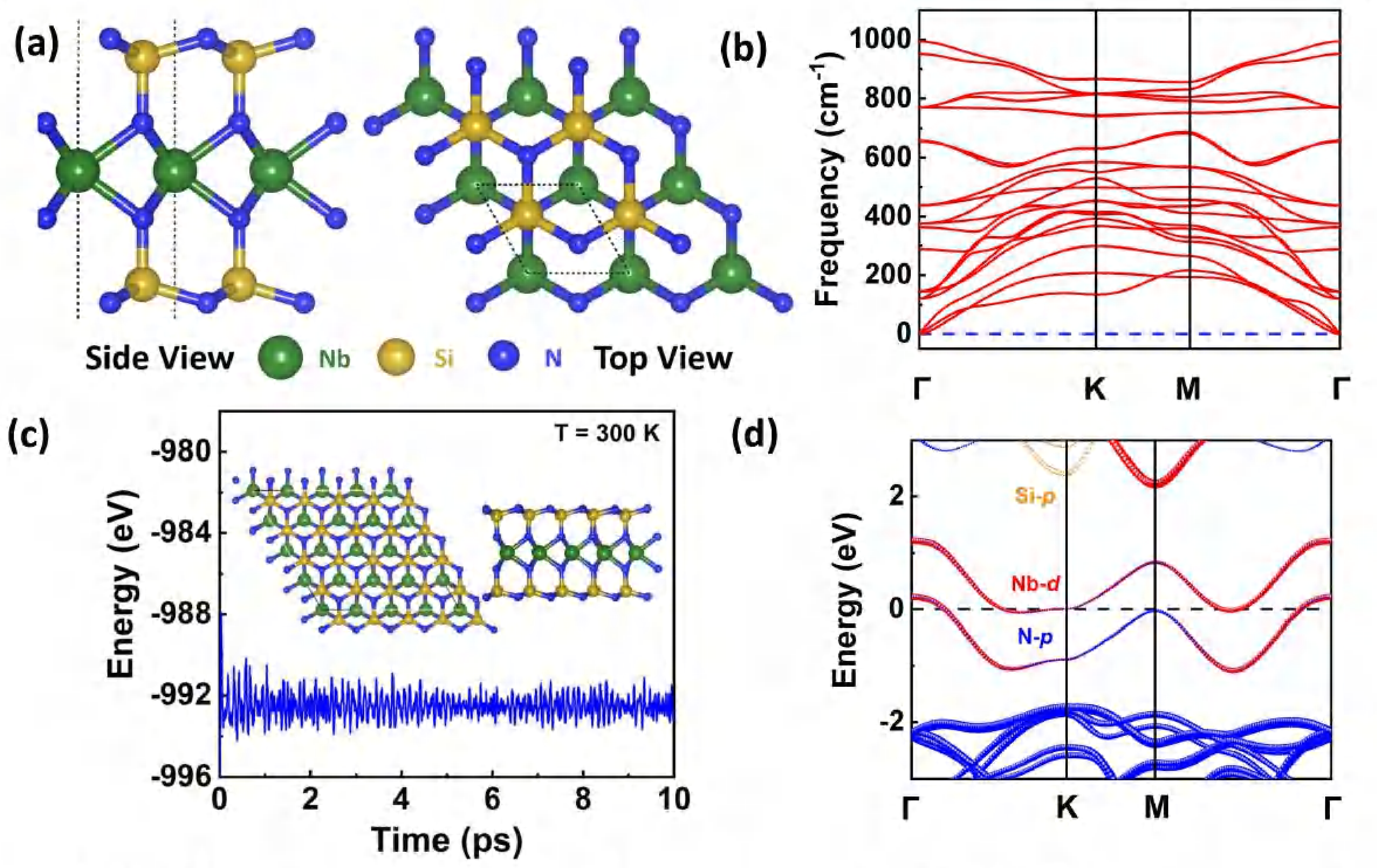

Fig. 1: (a) Top and Side view of the optimized 2D $NbSi_2N_4$ monolayer. (b) Phonon dispersion spectrum. (c) AIMD simulation of 2D $NbSi_2N_4$ monolayer at 300 K of 10 ps. (d) Atom-projected band structure of monolayer $NbSi_2N_4$..

◆ $NbSi_2N_4$ monolayer is a FM metal with excellent dynamic and thermodynamic stability. But the Tc (12 K) is very low.

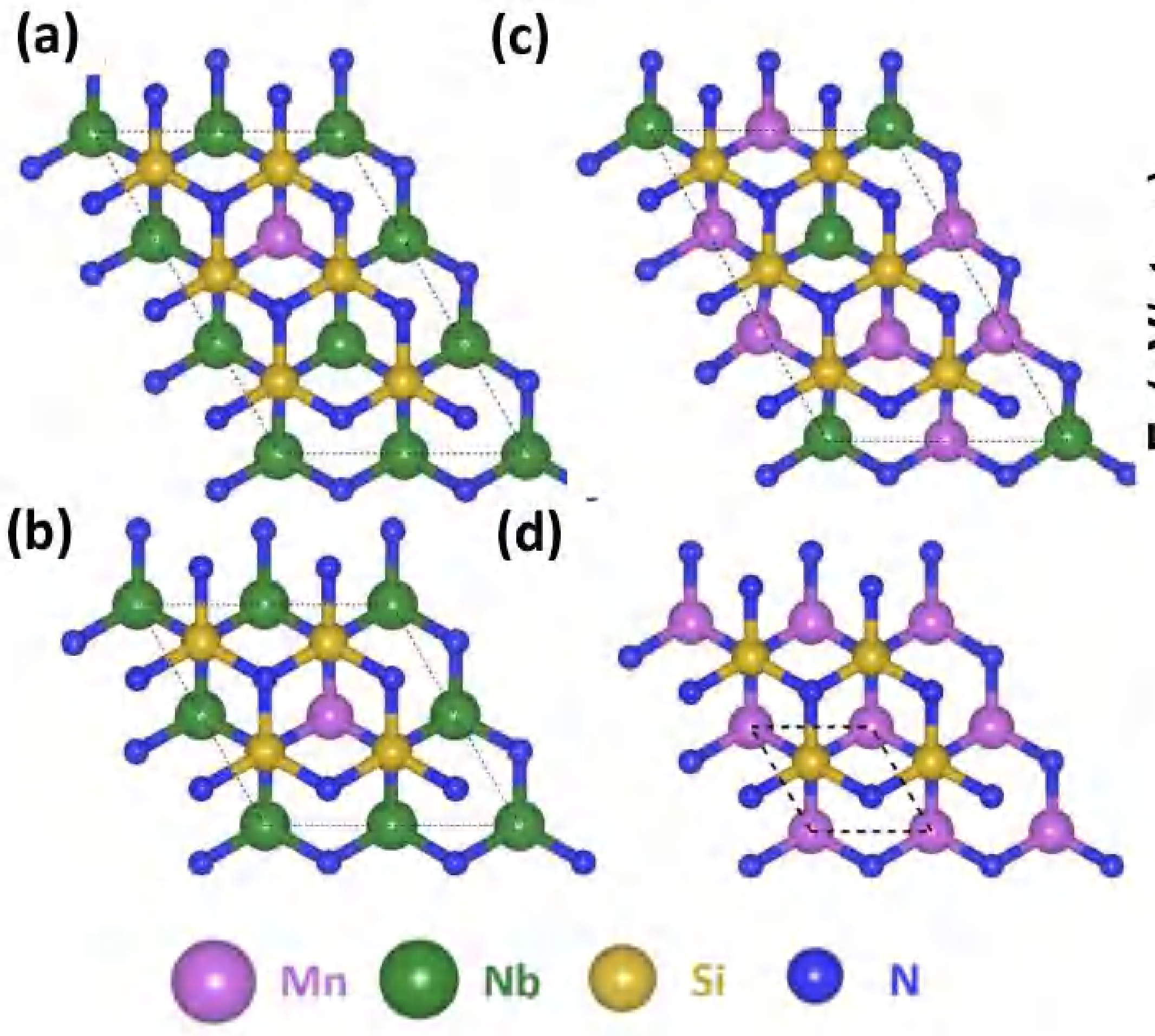

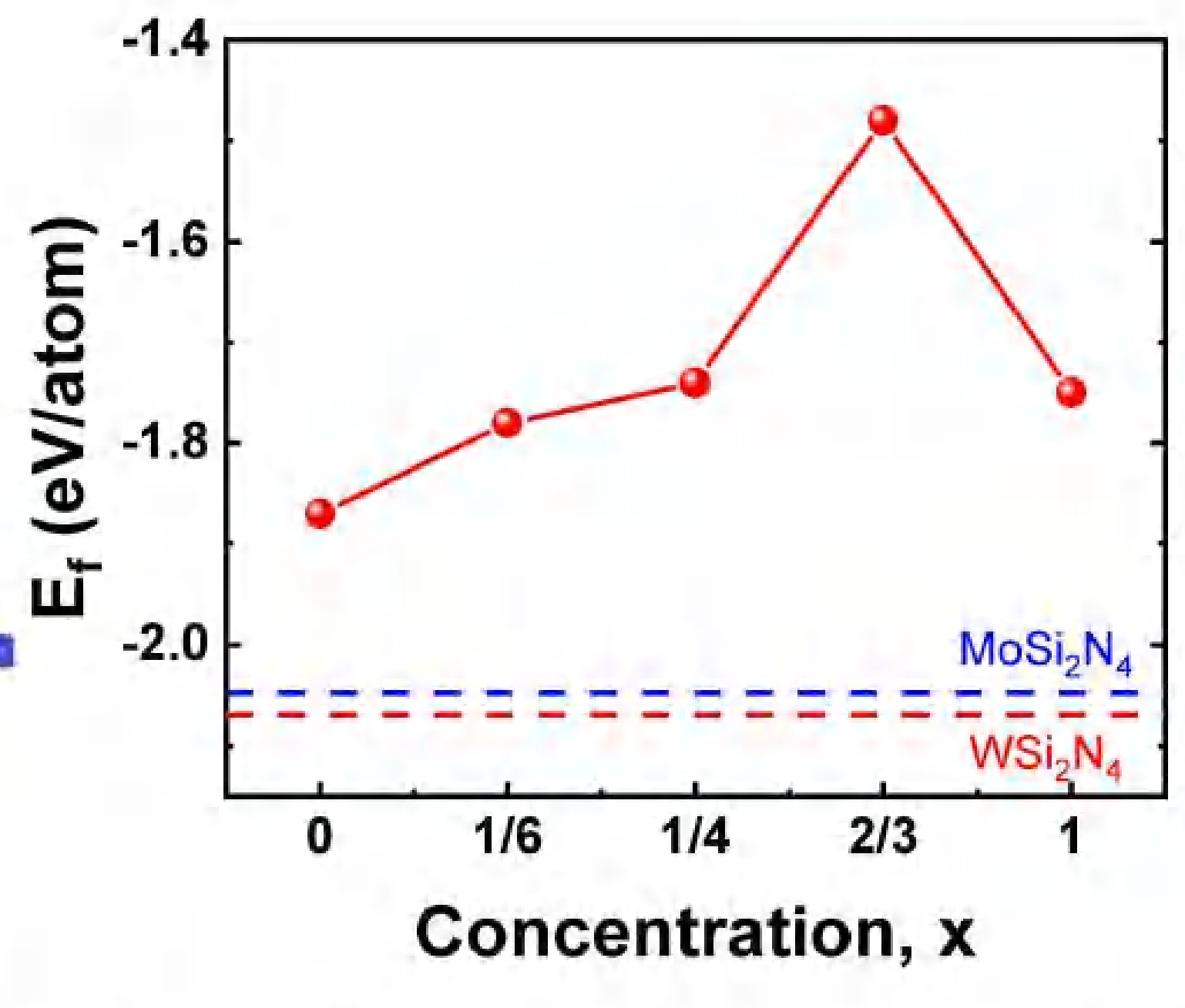

Fig. 3: The formation energy of $Nb_{1-x}Mn_xSi_2N_4$ (x=1/6, 1/4, 2/3, 1).

Fig. 2: The alloying structures of $Nb_{1-x}Mn_xSi_2N_4$. (a) x = 1/6, (b) x = 1/4, (c) x = 2/3, and (d) x = 1

◆ $Nb_{1-x}Mn_xSi_2N_4$ monolayer has high possibility of experimental synthesis

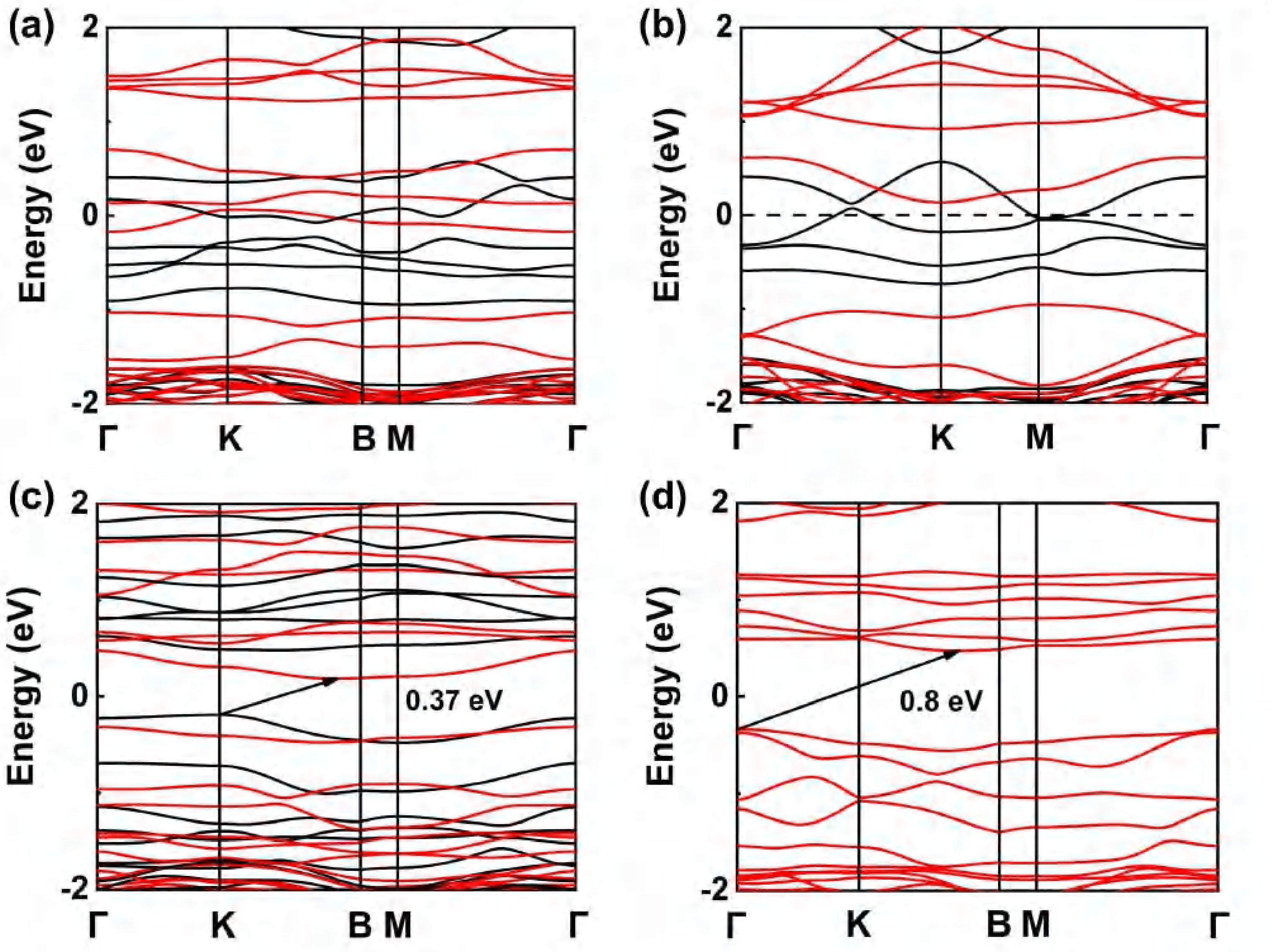

Fig. 4: Band structures of $Nb_{1-x}Mn_xSi_2N_4$. (a) x = 1/6, (b) x = 1/4, (c) x = 2/3, and (d) x = 1 monolayers.

◆ With the increase of Mn alloying content, the properties change from metal FM to metal FIM to HMAF to AFM semiconductor.

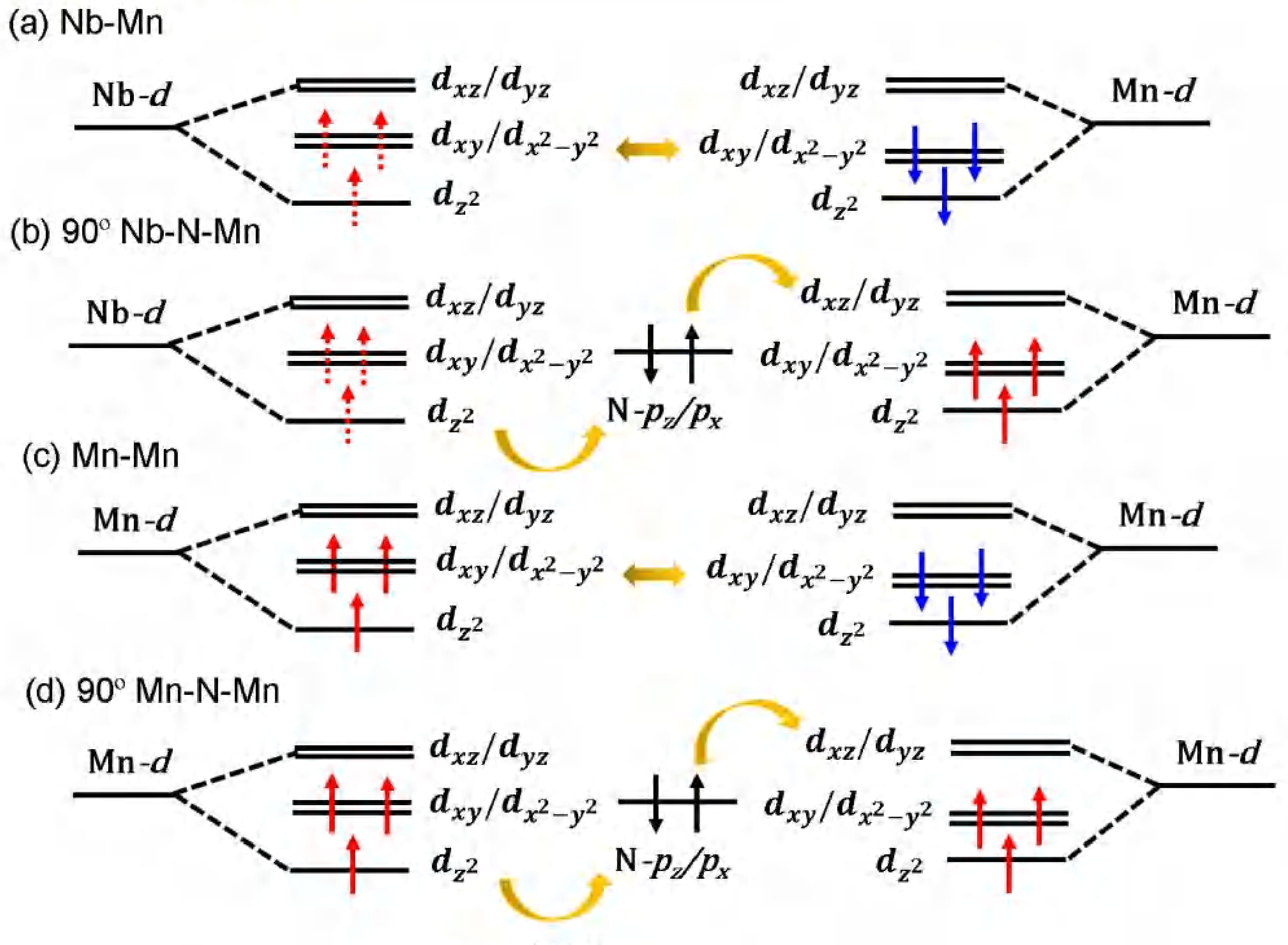

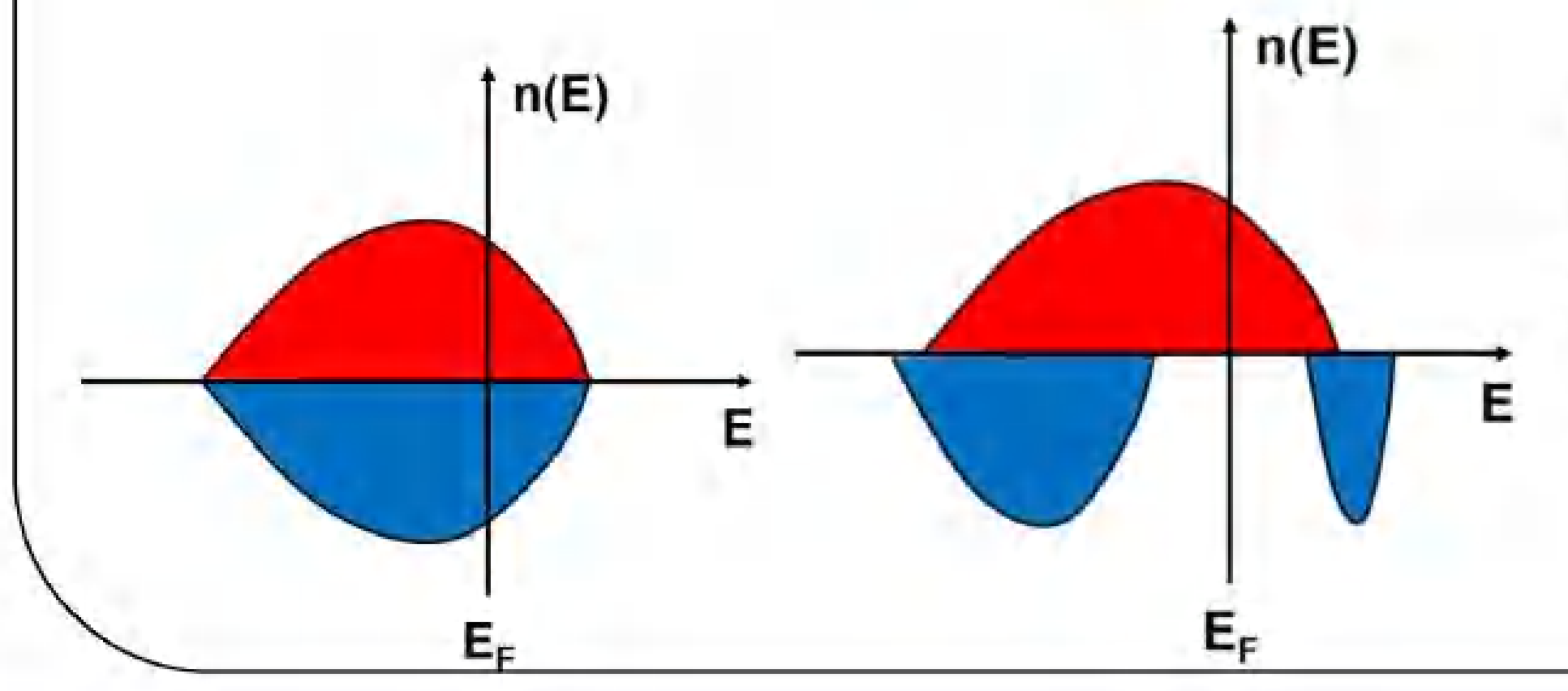

Fig. 5: Schematic diagram of conventional AFM and HMAF.

Conclusion:

✓By continuously incorporating Mn, stronger Mn-N hybridization relative to Nb-N induces metal to half-metal to semiconductor transition.

✓The competitive coupling between Nb-*d* itinerant electron and Nb-Mn *d-d* direct interaction in $Nb_{1-x}Mn_xSi_2N_4$ drives ferromagnetic to antiferromagnetic phase transition.

✓For the first time in 2D inorganic materials, a 2D intrinsic inorganic HMAF is obtained at Nb/Mn ratio of 3:1.

DOI: 10.1039/d2nr01728h

Structural phase transition and superconductivity of ytterbium under high pressure

Qingzhuo Duan,[1] Junyu Shen,[1] Xin Zhong,[2,*] Haiyan Lu,[3,*] and Cheng Lu[1,*]

[1]*School of Mathematics and Physics, China University of Geosciences (Wuhan), Wuhan 430074, China*

[2]*Key Laboratory of Functional Materials Physics and Chemistry of the Ministry of Education, College of Physics, and National Demonstration Center for Experimental Physics Education, Jilin Normal University, Changchun 130103, China*

[3]*Science and Technology on Surface Physics and Chemistry Laboratory, P.O. Box 9-35, Jiangyou 621908, China*

Recent advances in theory and experiment declare the rare earth (RE) hydrogen-rich compound LaH_{10} is a near room-temperature superconductor under high pressure. To understand the underlying mechanism of superconductivity and explore the crucial role of lanthanides in forming the RE-based polyhydrides, we here perform a theoretical study on the structural phase transition and superconductivity of late lanthanide ytterbium (Yb) metal under high pressure up to 240 GPa. Two new structures, $R\bar{3}m$ and $I4/mmm$ phases, of Yb are uncovered. Most interestingly, the $P6_3/mmc$ phase of Yb is serendipitously discovered to be a superior superconductor with T_c value of 19.5 K at 160 GPa, which is higher than other known RE elemental superconductors. The present findings establish new structural phase transition sequence of Yb, which offer insights for further understanding the vital physics mechanisms of lanthanide-based superconductor.

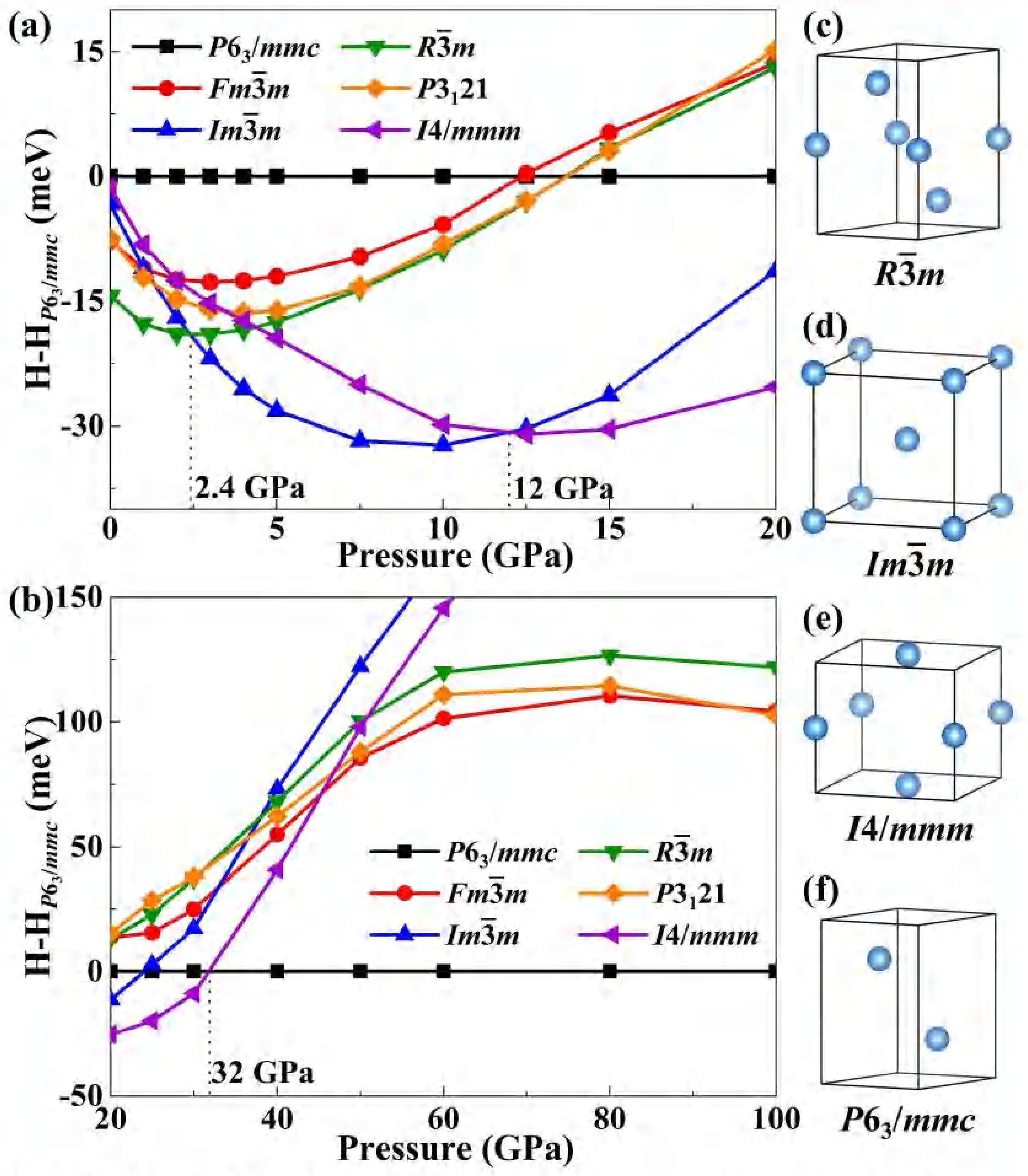

FIG 1. Calculated enthalpies per atom of various phases of Yb under different pressures.

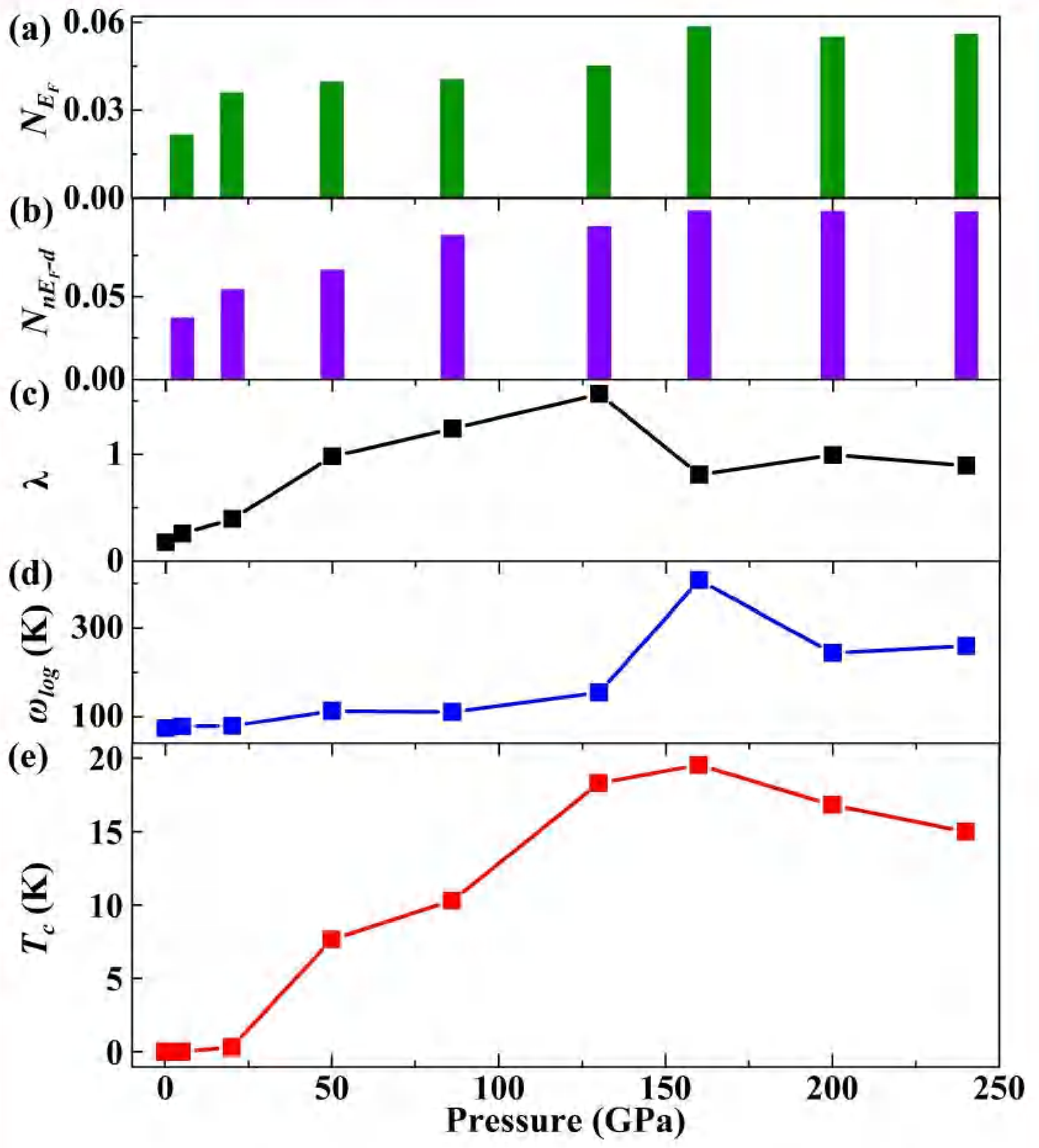

FIG 3. Calculated EPC parameters and *Tc* of Yb under different pressures.

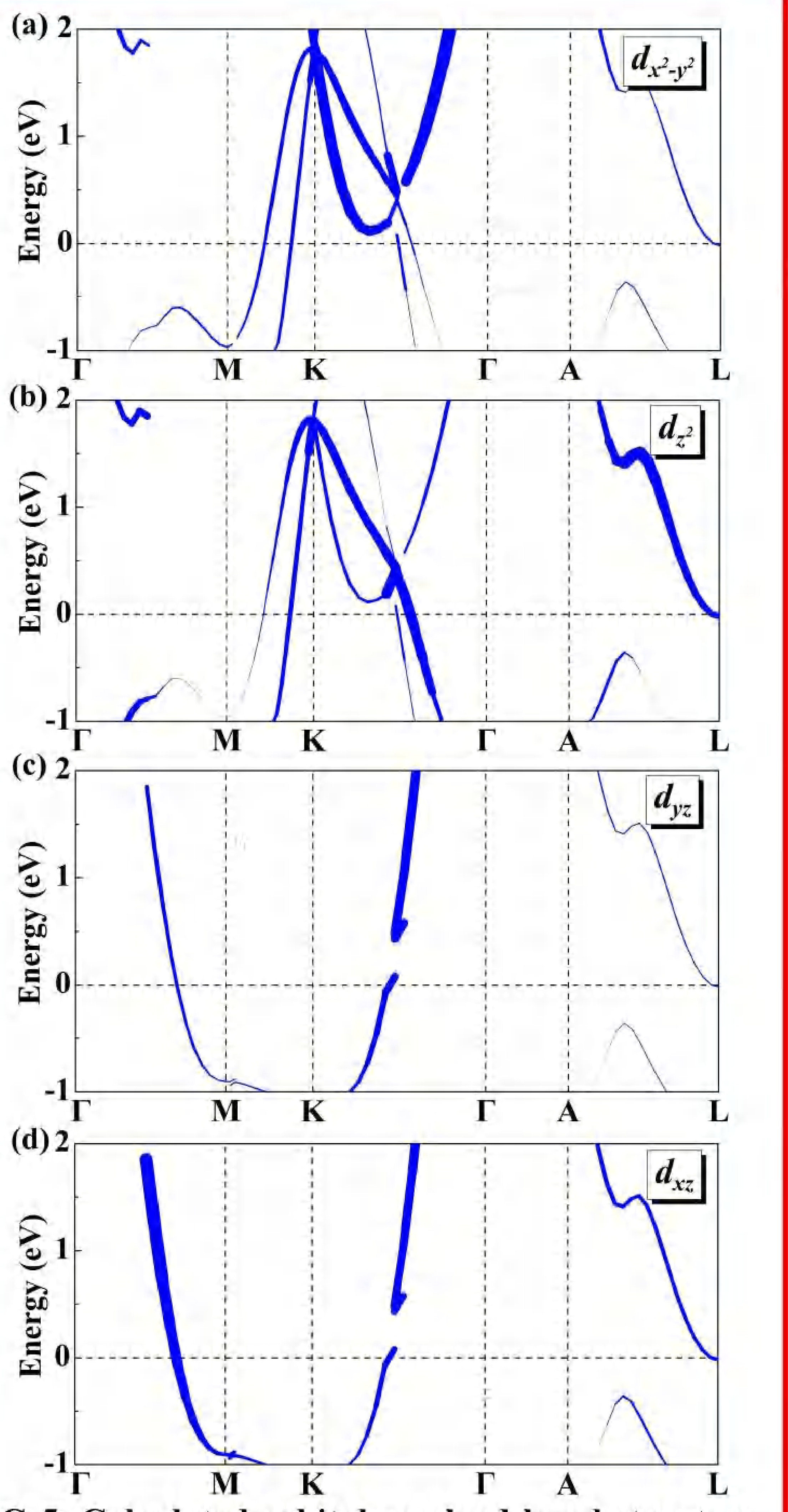

FIG 5. Calculated orbital-resolved band structures corresponding to different orbitals of $P6_3/mmc$ phase of Yb under 160 GPa.

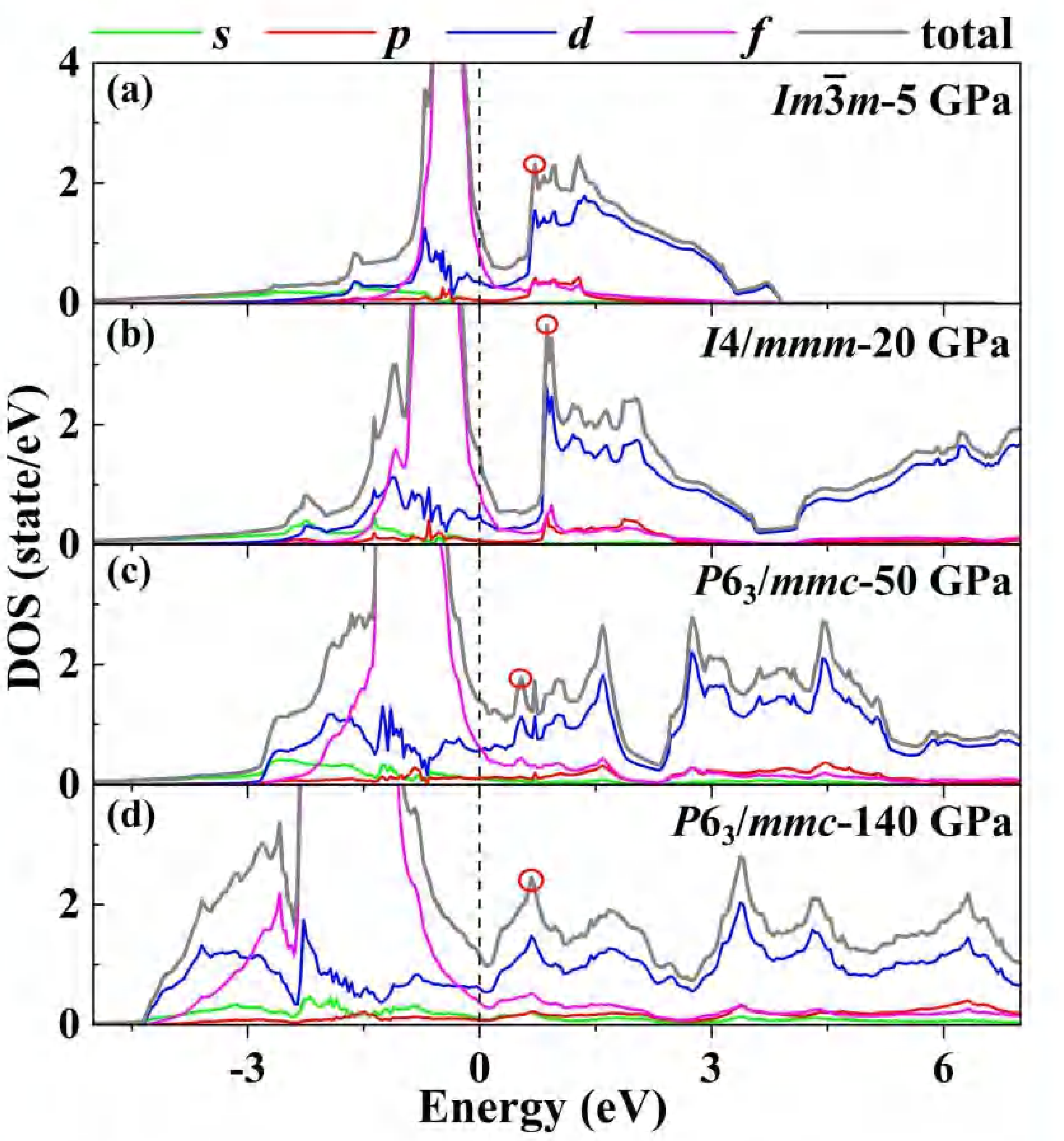

FIG 2. Calculated electronic density of states of Yb under different pressures. (a) $Im\bar{3}m$ at 5 GPa, (b) $I4/mmm$ at 20 GPa, (c) $P6_3/mmc$ at 50 GPa, and (d) $P6_3/mmc$ at 140 GPa.

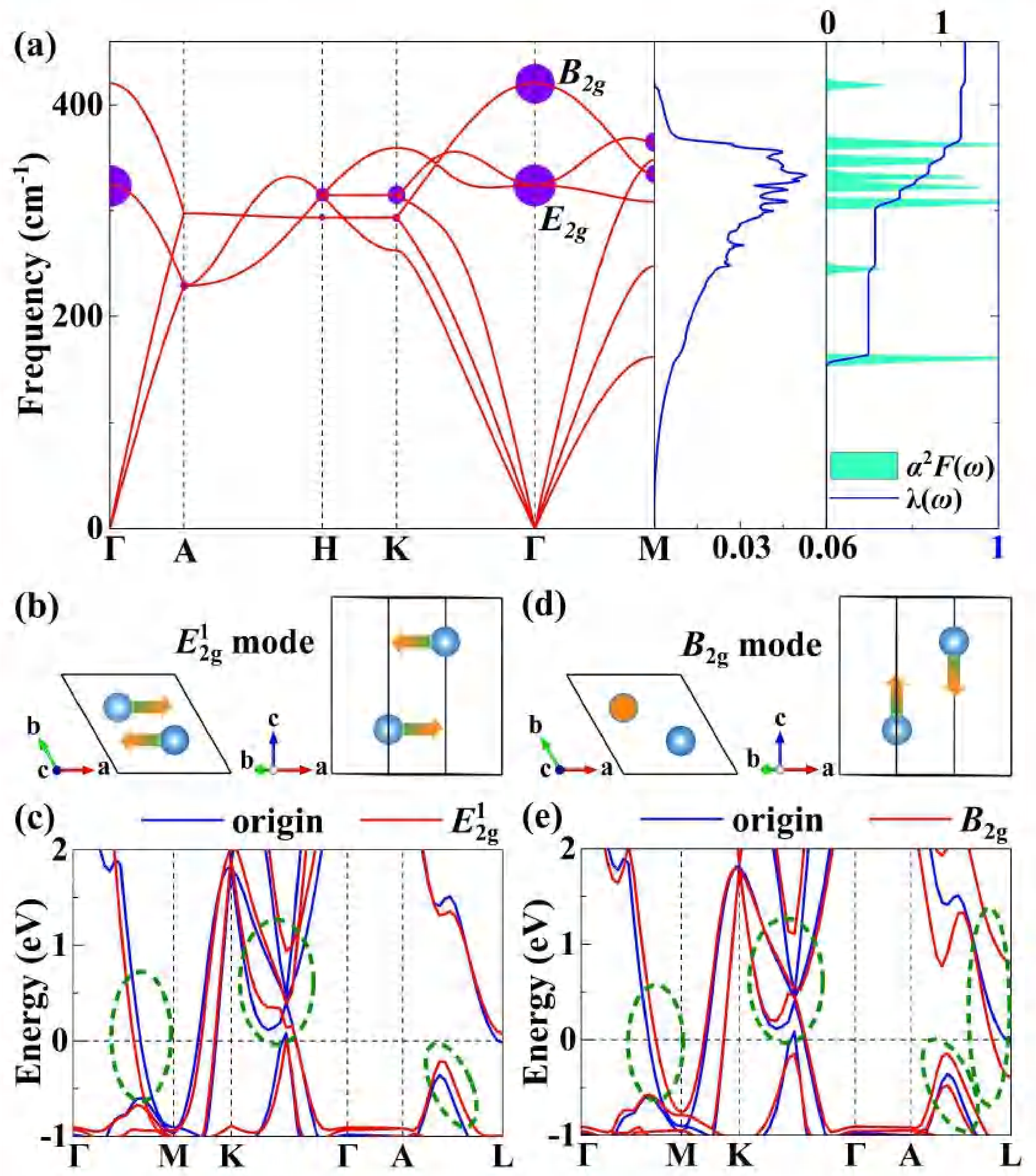

FIG 4. Calculated phonon dispersion curves, phonon density of states, and EPC parameters of the $P6_3/mmc$ phase of Yb under 160 GPa.

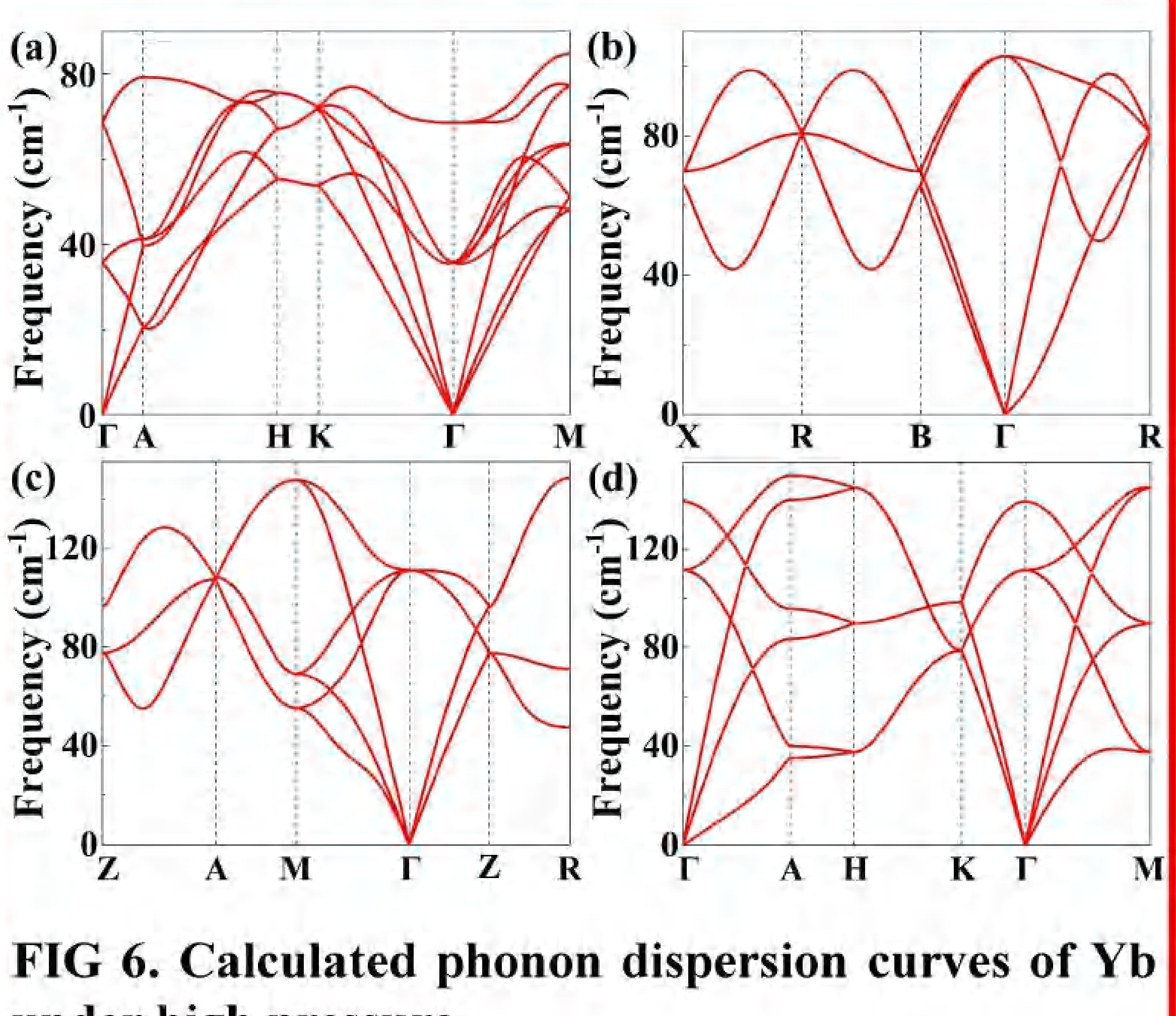

FIG 6. Calculated phonon dispersion curves of Yb under high pressure.

CONCLUSION

In summary, we carry out a theoretical study on the structural phase transition and superconductivity of Yb under high pressure by crystal structure prediction and first-principle calculations. Two novel structures of Yb with $R\bar{3}m$ and $I4/mmm$ symmetries are uncovered. The $R\bar{3}m$ structure possesses the semimetallic properties from ambient pressure to 2 GPa, and the $I4/mmm$ structure is a metallic phase stabilized from 11.8 GPa to 32 GPa. Most importantly, the $P6_3/mmc$ phase of Yb is found to be an outstanding superconductor with T_c value of 19.5 K at 160 GPa, which is the highest T_c for lanthanide superconductors. The high T_c of Yb under high pressure is attributed to the abundant 4*d* states and low 4*f* states at Fermi level. These findings establish new structural phase transition sequence of Yb under high pressure, which offer crucial insights for design of the more complex lanthanide-based superconductor.

Reference: Qingzhuo Duan, Junyu Shen, Xin Zhong,* Haiyan Lu,* and Cheng Lu,* Phys. Rev. B 105, 214503 (2022).

Electronic address: zhongxin@calypso.cn(Xin Zhong); hyluphys@163.com(Haiyan Lu); lucheng@calypso.cn(Cheng Lu).

Acknowledgements: This work was supported by the National Natural Science Foundation of China (Nos. 12111530103 and 12174352).

Growth mechanism of several metal electrodes on the surface of carbon nanotube FET

Weili Li , Yifan Liu, Yanning Zhang*, Zhiyong Zhang*,Chuanhong Jin*,
Institute of Fundamental and Frontier Sciences, University of Electronic Science and Technology of China,
Chengdu 610054, China
Key Laboratory for the Physics and Chemistry of Nanodevices and Center for Carbon based Electronics,
School of Electronics, Beijing 100871, China.
State Key Laboratory of Silicon Materials, School of Materials Science and Engineering, Zhejiang University,
Hangzhou, 310027, China
E-mail: yanningz@uestc.edu.cn

Introduction

- **Carrier transport through the valence and conduction bands of a high-quality semiconducting SWNT could be ballistic, presenting an opportunity to realize ballistic field-effect transistors (FETs) based on molecular electronic materials.[1]**
- **Top-gate field-effect transistors (FETs) fabricated on the CNT array show better performance than that of commercial silicon metal oxide semiconductor FETs with similar gate length.[2]**
- **The contact formation and scaling of top-gated CNT FETs, especially Sc-contacted or n-type CNT FETs, has rarely been investigated at an atomic scale.[3]**

1.Javey et al. Nature 424, 654-657 (2003)
2.Liu et al., Science 368, 850–856 (2020)
3.Qiu et al., Science 355, 271-276 (2017)

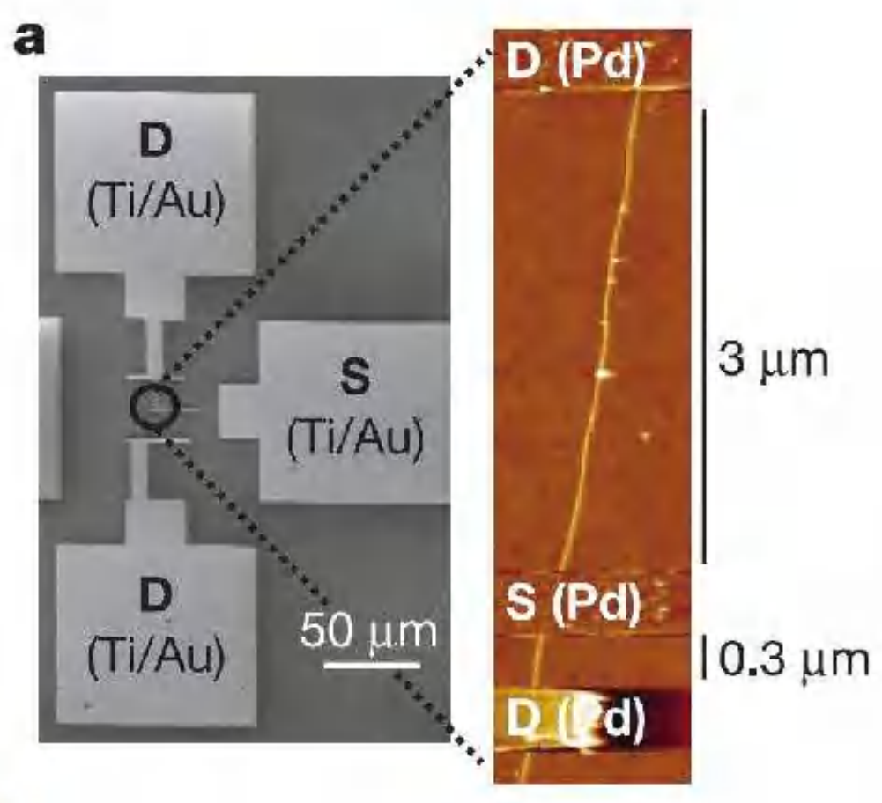

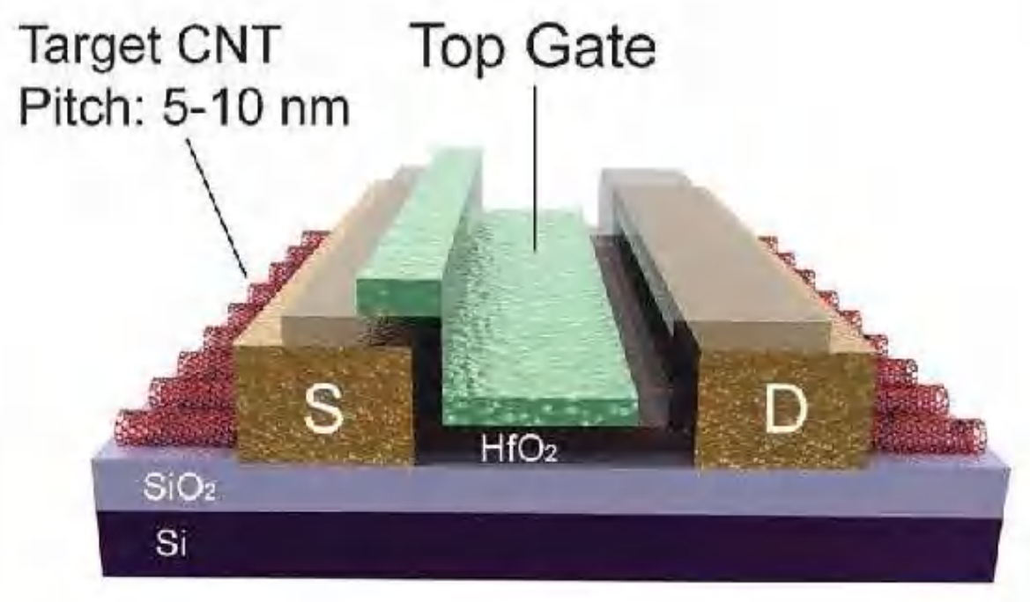

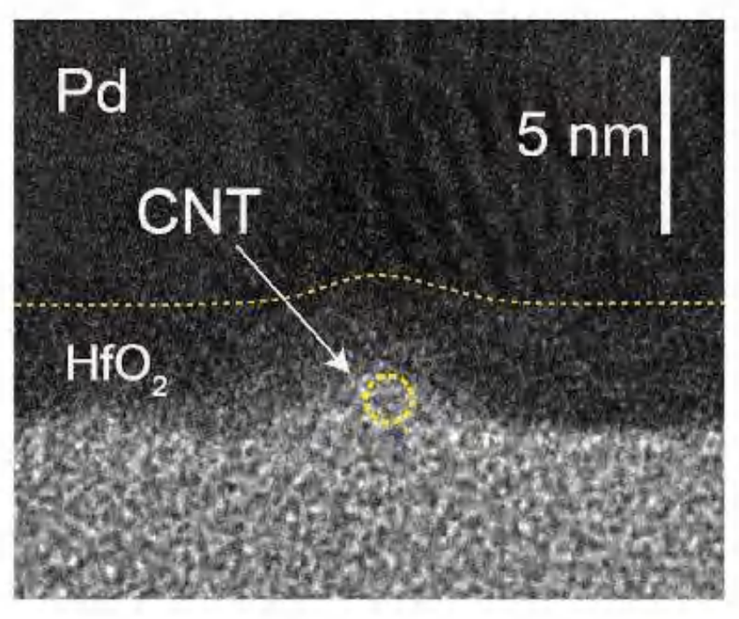

Experimental image

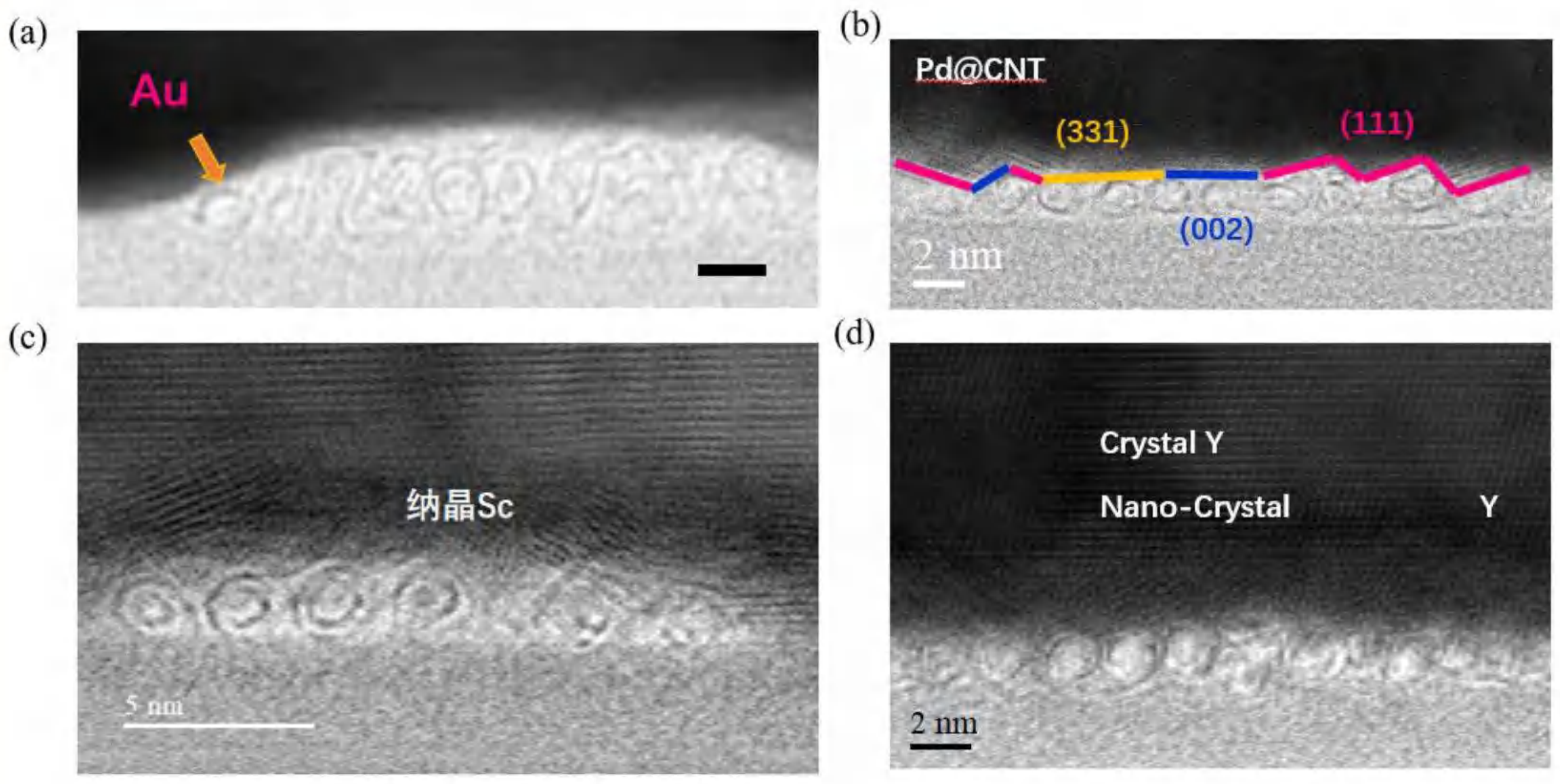

Cross-section STEM images of carbon nanotube surfaces grown with different metal electrodes of (a) Au, (b) Pd, (c) Sc (d) Y. The data consists of single-phase nanocrystalline, and polycrystalline phase with multiple Miller indices.

Atom Structure and of metals on CNT surface

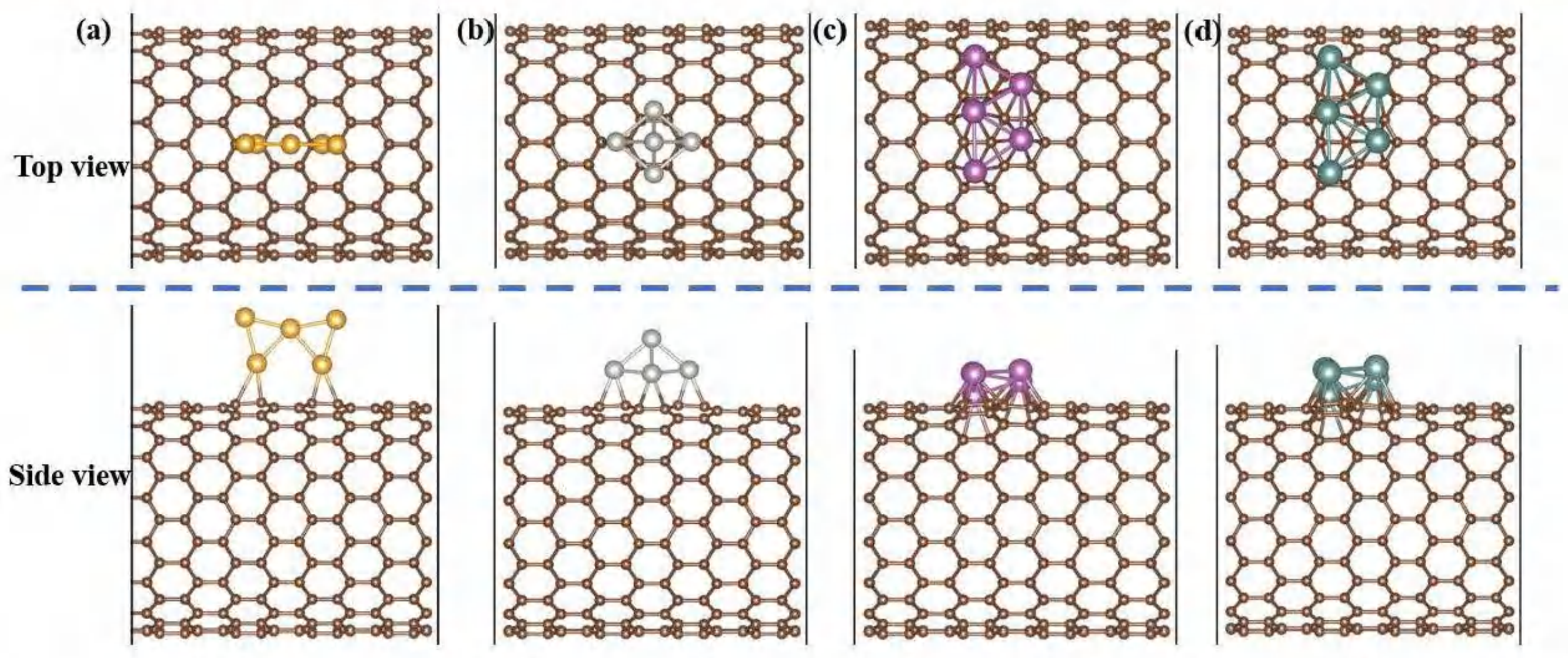

Initial structure of different metal electrodes growth on CNT surface: (a) Au, (b) Pd, (c)Sc, (d) Y. For (c) and (d), the planar structure is preferentially generated on CNT surface.

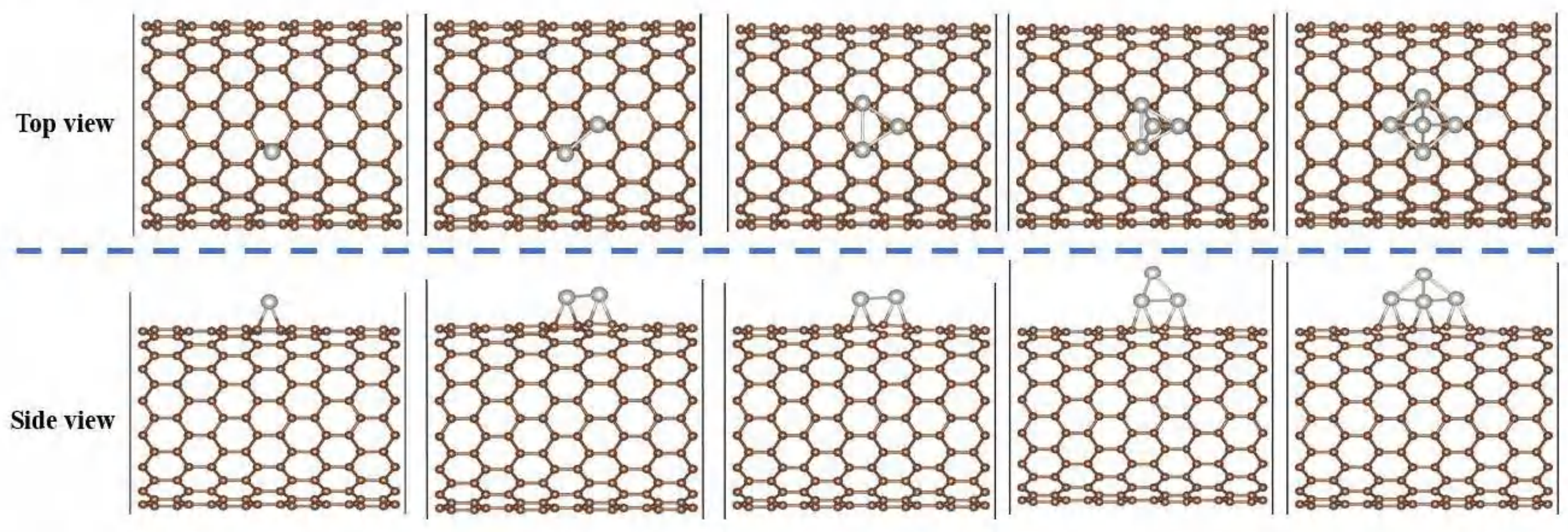

The growth structure of Pd on CNT surface, from one atom to five atoms. When the fourth Pd atom is on the surface, the structure shows a three-dimensional growth pattern.

Different Pd patterns at CNT

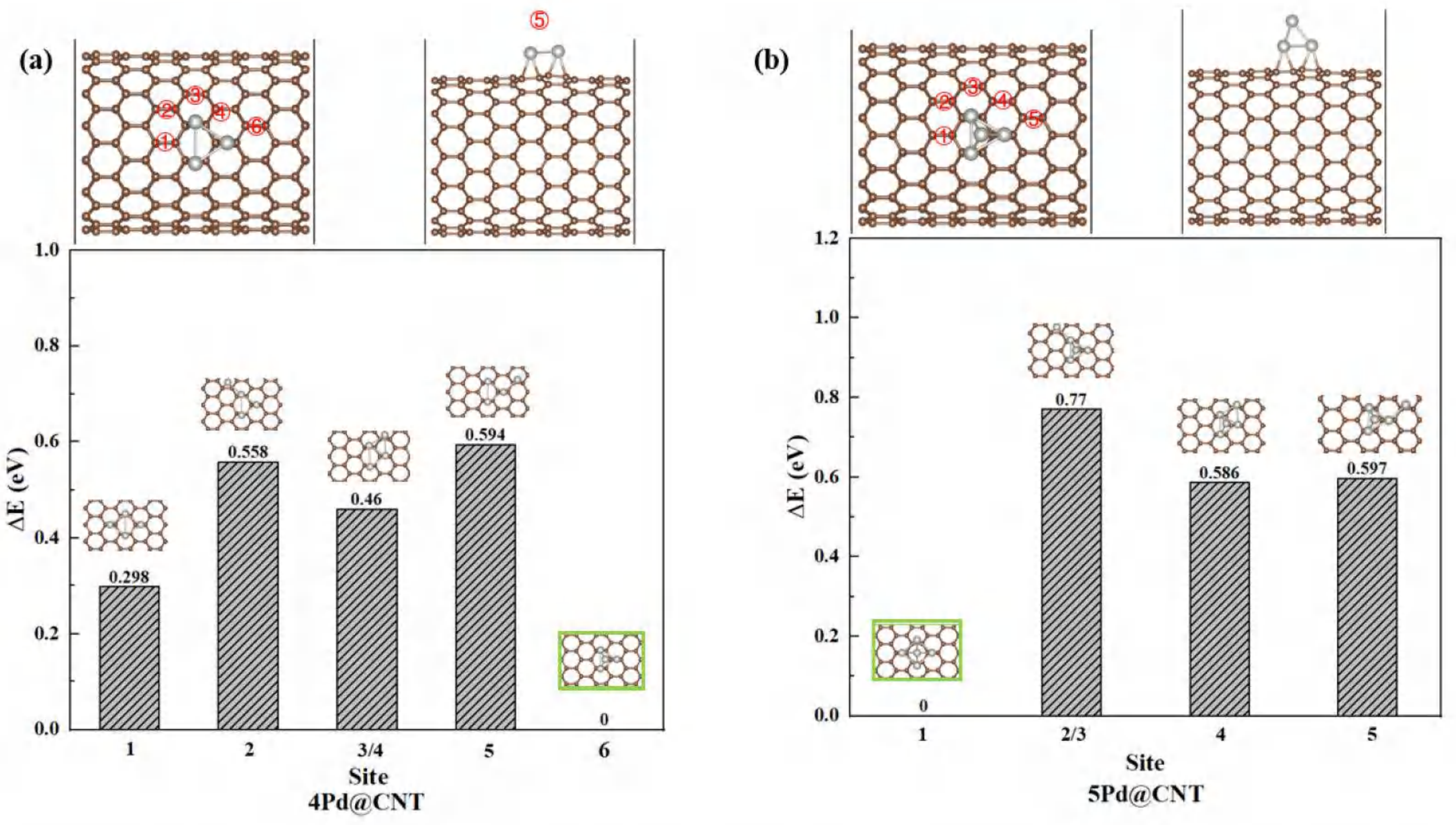

The structure and energy of (a) 4-atom, (b) 5-atom Pd patterns on CNT surface. It indicates as more Pd atoms are adsorbed on CNT surface, the strong force between Pd-Pd causes a preferred growth into independent island structures.

Energy evaluation of growth structures

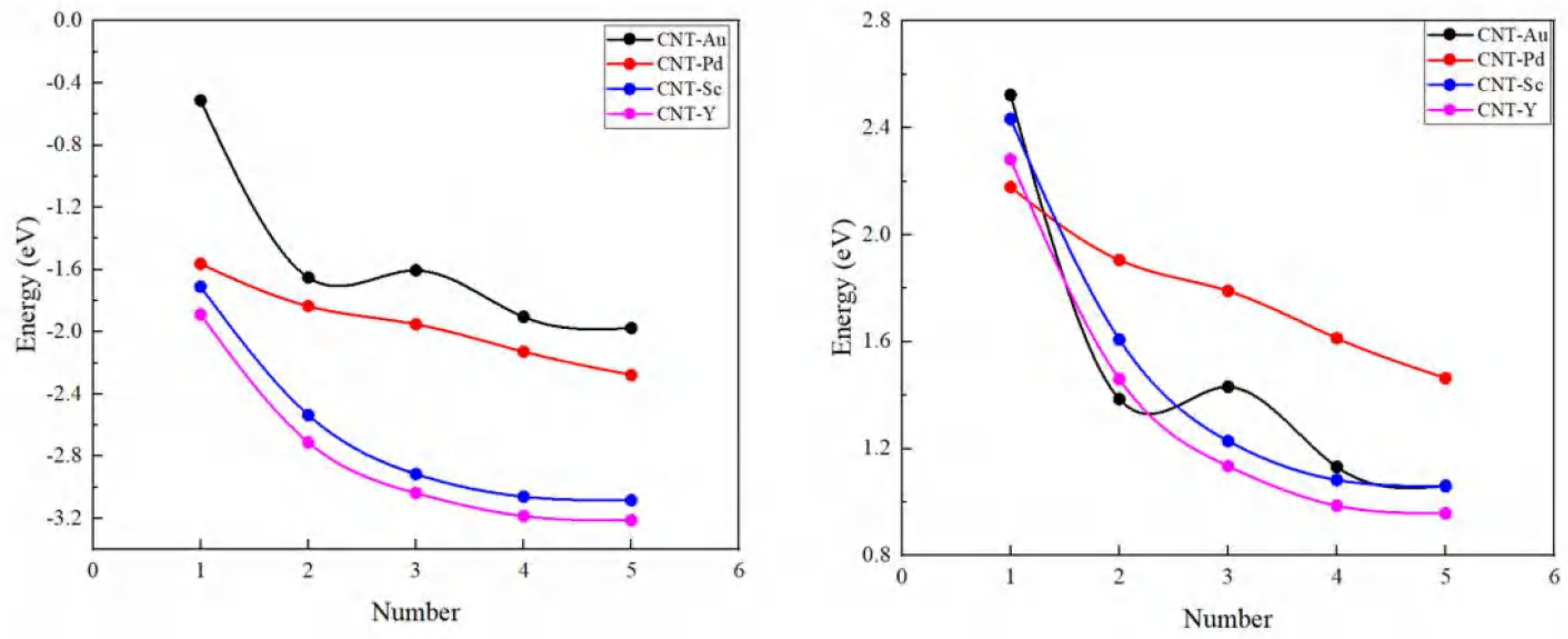

Average adsorption energies and average formation energies of different growth structures. Each energy profile converges with increased the number of atoms.

Conclusion

- ☐The growth primitives of Au, Pd, Sc and Y were formed in different growth modes at the initial growth stage on CNT surface.
- ☐Pd atoms will grow into a three-dimensional island structure, and then form tiny nanoisland, making the final structure present complex nanostructures with multiple Miller indices.
- ☐There are strong interactions between Sc or Y atoms and CNT surface. Sc and Y atoms preferentially cover the entire surface of CNT, forming regular nanocrystalline structure with low crystal Miller indices.

In the preparation

TC11钛合金氧化初期热力学研究

董自成，杨梦梦，王皞*（haowang7@usst.edu.cn）
上海理工大学，材料科学与工程学院/增材制造研究院

引言

TC11钛合金的名义成分为Ti-6.5Al-3.5Mo-1.5Zr-0.3Si，是一种α+β型双相高温钛合金。它具有比强度高，热加工工艺性能良好，且耐腐蚀性强、热膨胀系数低、热导率低等优异的综合性能。故常用于热等静压成型工艺制备航空发动机和飞机结构件。但在此成型工艺下，TC11钛合金粉末表面容易生成复杂的氧化膜，影响部件的性能。

钛合金材料的氧化对其加工和服役性能有重要影响，然而氧化是极其复杂的过程，实验上很难进行原位跟踪。并且目前对于钛合金氧化过程中氧化膜的形成与演化机制尚不完全清楚，其中最缺乏的是相应的氧化行为热力学信息。本工作在相图计算(calculation of phase diagrams, CALPHAD)技术的基础上，借助已有的PanTi高质量钛合金热力学数据库，结合成熟的计算相图软件Pandat，对TC11钛合金在不同温度下的初期氧化行为进行了热力学计算。

计算结果与讨论

借助前期积累的高质量PanTi热力学数据库，对TC11钛合金的初期氧化行为进行了计算，没有考虑Mo和Si对氧化行为的影响，计算条件：P:1 Bar、T:600℃-1200℃ 、 Al:6.5 wt％ 、 Zr:1.5 wt％ 、 O:0~50 wt％ 、 log10(P(O₂)):−38~−20 Pa。

图1所示为TC11钛合金在相应计算条件下的T和O wt%相图。由图可知，合金在O含量为10％以下时主要为BCC、HCP、Ti_3Al相，随着氧含量的增加，开始出现相应的金属氧化产物相。600~730℃左右最先出现Zr的氧化产物ZrO_2，合金元素出现氧化物的顺序为Zr、Al、Ti，而在此温度范围以上最先出现的是Al的氧化产物Al_2O_3，合金元素出现氧化物的顺序为Al、Zr、Ti。当氧含量在17％左右时开始依次出现一系列Ti的氧化物Ti_3O_2、A_TiO、$TiO_x(Ti^{2+},Ti^{3+})$。当温度在600~900℃左右，氧含量为21％左右时，HCP相消失，合金以完全氧化物相的形式存在，而在此温度范围以上HCP相的消失大概在氧含量27％左右。之后随着氧含量的增加开始发生$TiO_x(Ti^{2+},Ti^{3+})$向Ti_2O_3、Ti_2O_3向TiO_2的转变。最后氧化物相的存在形式为TiO_2、Al_2O_3、ZrO_2。

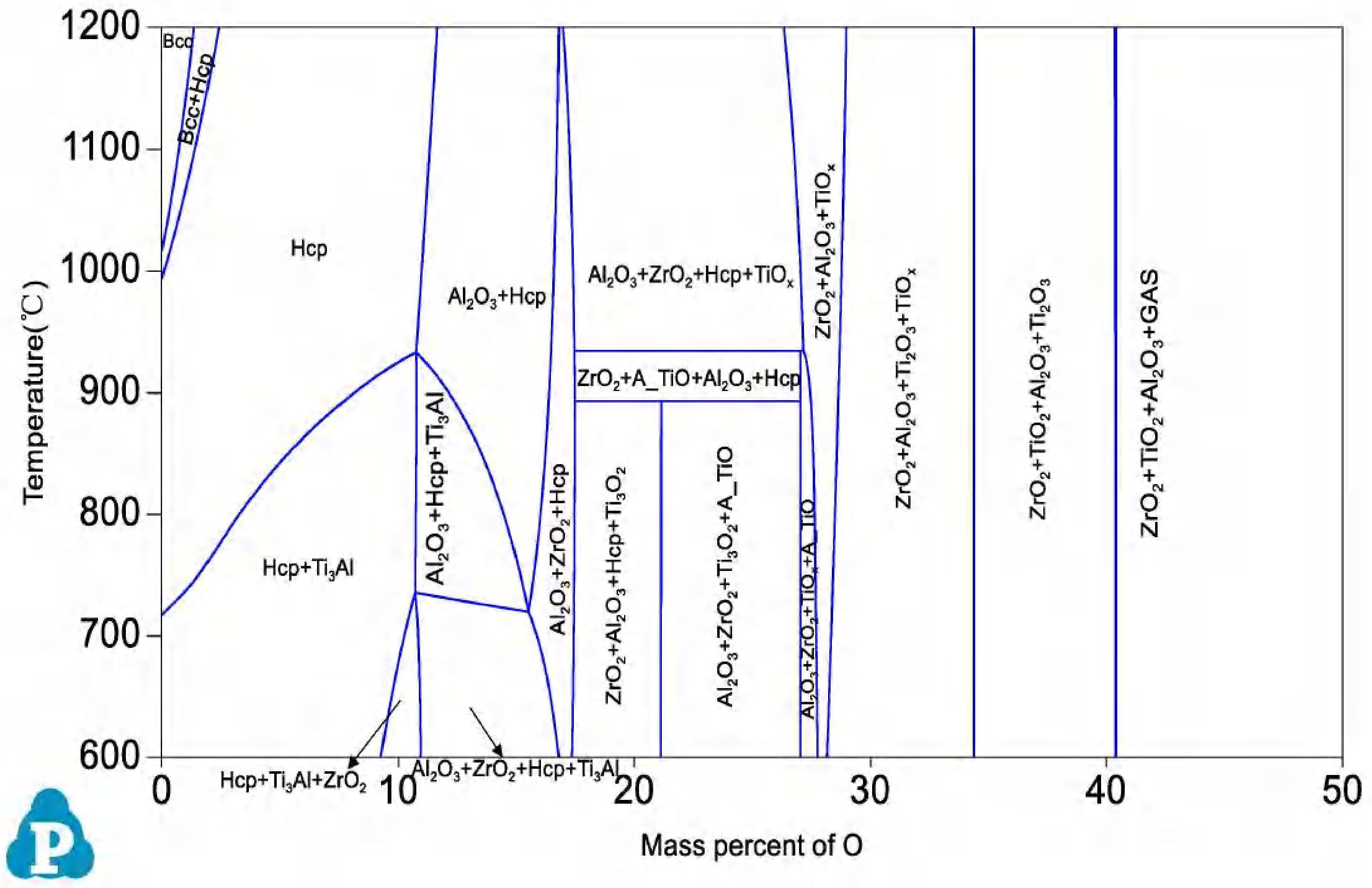

图1 Ti-6.5Al-1.5Zr计算成分下的T和O wt%相图

图2所示为相应计算条件下的T和log10(P(O₂))相图。分别以1100℃和700℃去分析。由图可知，1100℃，氧分压为-38~-30Pa时，合金为BCC单相，随氧分压的增大，BCC单相转变为HCP单相。当氧分压达到-25Pa左右时，合金开始氧化，为Al的氧化产物Al_2O_3。进一步增大氧分压至-23Pa左右时，出现Zr的氧化产物ZrO_2。随着氧分压的继续增大，HCP相随即消失，出现Ti的氧化产物Ti_2O_3 、$TiO_x(Ti^{2+},Ti^{3+})$，合金进入完全氧化状态。700℃，氧分压为-38~-20Pa时，合金已经进入完全氧化状态。随着氧分压的增加，依次出现一系列Ti的氧化产物的转变，从Ti_3O_2、A_TiO到$TiO_x(Ti^{2+},Ti^{3+})$、Ti_2O_3，再从Ti_2O_3到TiO_2。最后氧化产物的存在形式为TiO_2、Al_2O_3、ZrO_2。

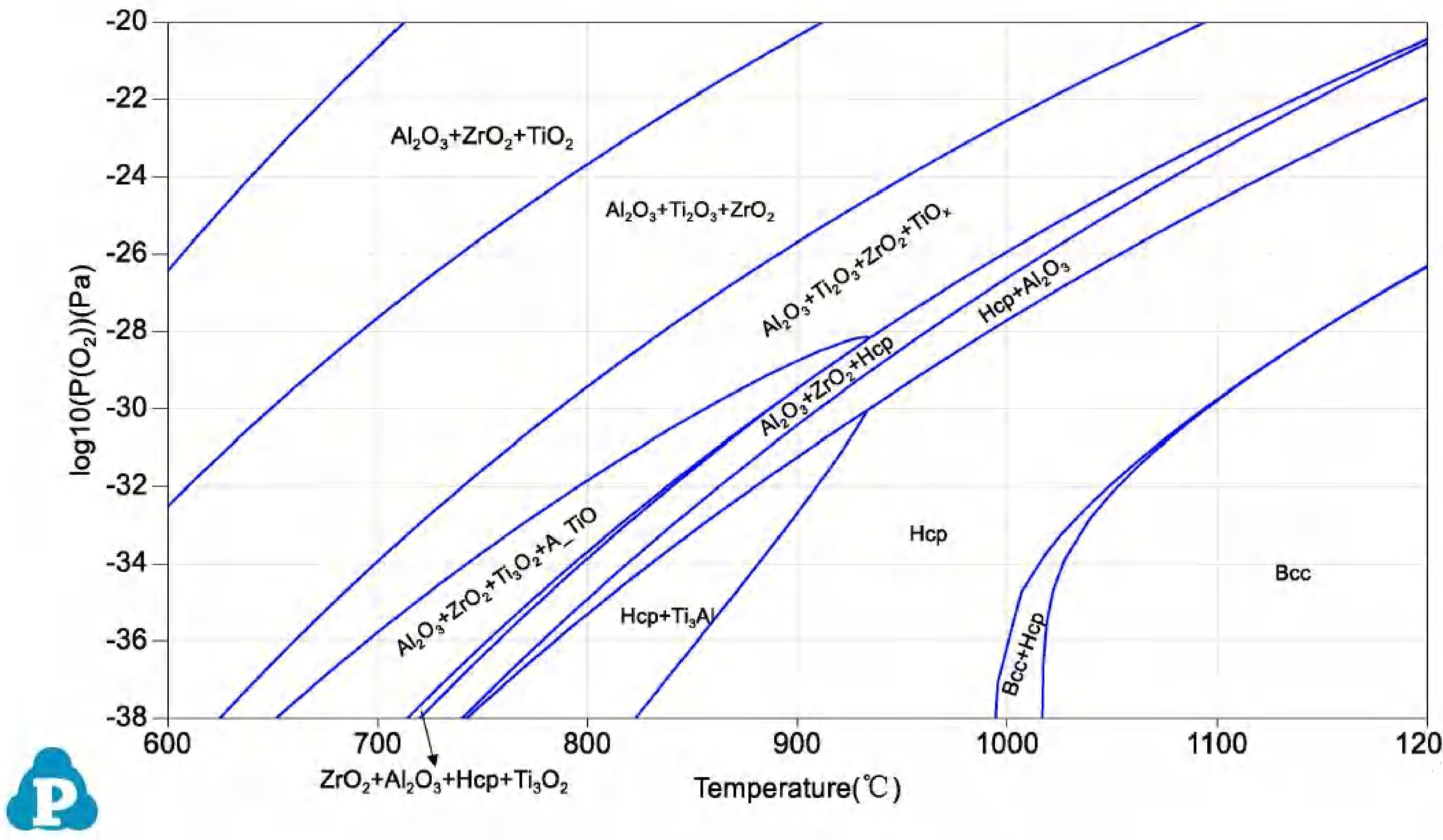

图2 Ti-6.5Al-1.5Zr计算成分下的T和log10(P(O₂))相图

进一步计算各氧化产物的摩尔分数随温度和氧分压的变化关系，结果如图3所示。由图可知，随着氧化的进行， Al_2O_3、 ZrO_2的摩尔分数基本不变，且 ZrO_2的摩尔分数很低，Ti的氧化产物出现形式依次为Ti_3O_2、A_TiO、$TiO_x(Ti^{2+},Ti^{3+})$、 Ti_2O_3、TiO_2且每个氧化产物的摩尔分数都有其对应的氧分压和温度范围。

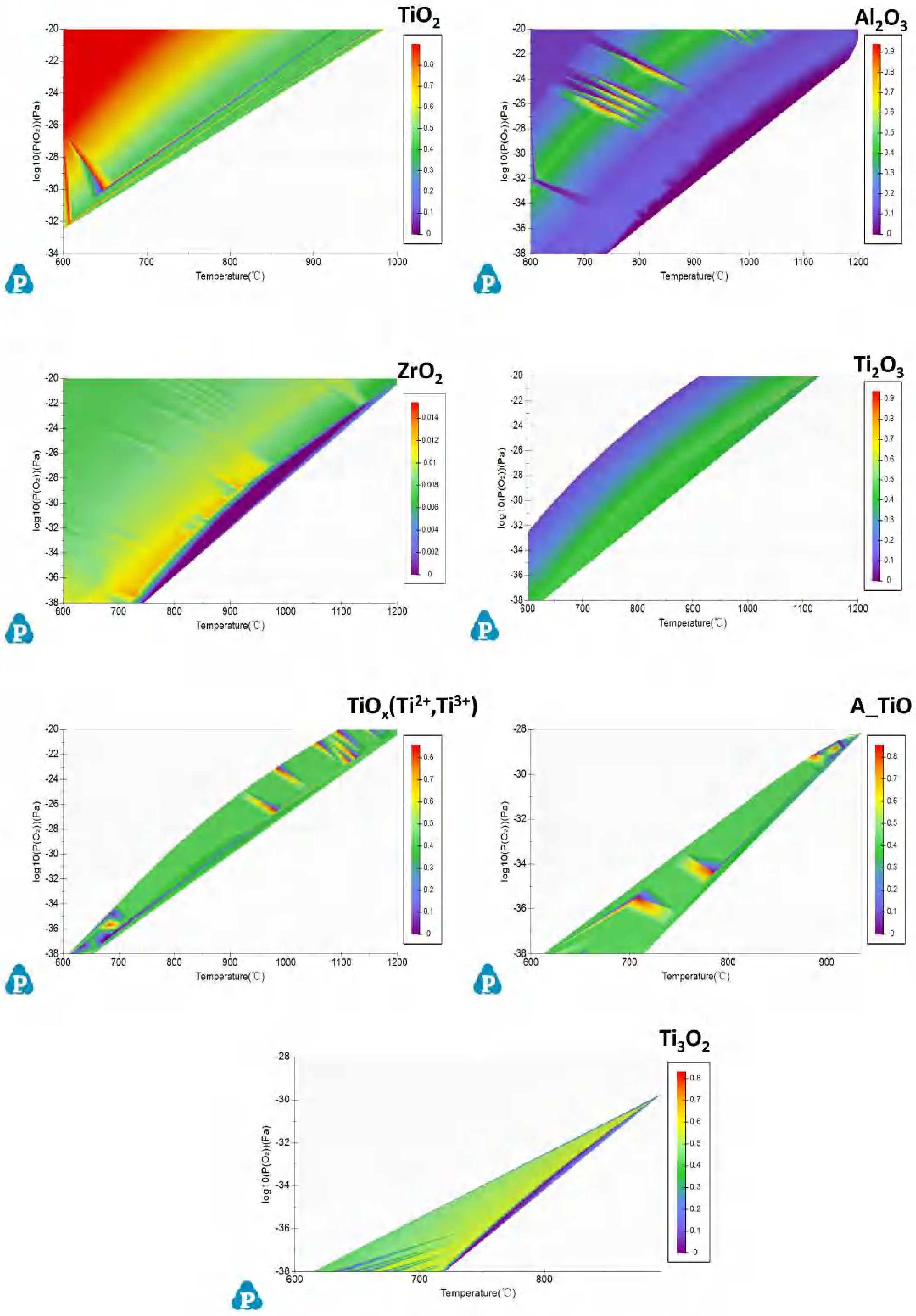

图3 各氧化产物的摩尔分数随温度和氧分压的变化

结论

基于上述计算结果，可得TC11钛合金在不同条件下的初期氧化行为，氧化产物有TiO_2、 Al_2O_3、 ZrO_2、 Ti_2O_3 、$TiO_x(Ti^{2+},Ti^{3+})$、 Ti_3O_2、A_TiO且分别对应的有其T和log10(P(O₂))及O wt%范围。

增材制造钛合金疲劳寿命预测

高帅龙[1]，王暤[1, *]（haowang7@usst.edu.cn）
上海理工大学，材料科学与化学学院/增材制造研究院

摘要

在当前的工艺条件下，增材制造钛合金难以避免孔洞等冶金缺陷，导致打印态材料和部件的疲劳性能明显低于铸造态和变形态，严重影响增材制造钛合金在航空航天等领域的应用。因此，阐明孔洞缺陷对材料和部件疲劳寿命的影响就显得至关重要。然而疲劳性能数据往往数据量小、分散度大，给寿命模型的建立带来困难。本工作借助对抗网络等机器学习方法，系统研究了缺陷尺寸和位置对旋弯疲劳最大循环周次的协同影响，实现疲劳寿命的准确预测。

解决思路

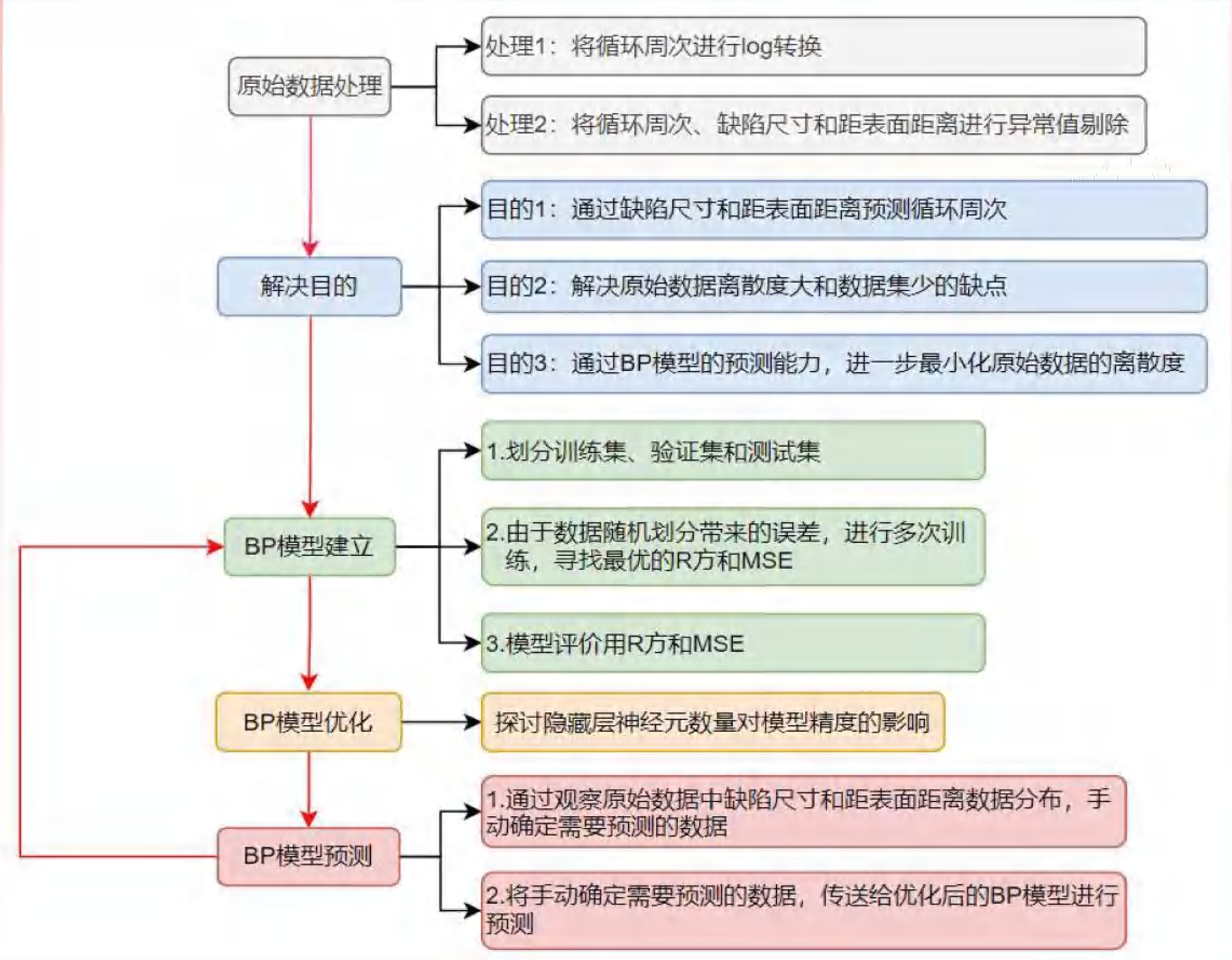

原始数据处理
- 处理1：将循环周次进行log转换
- 处理2：将循环周次、缺陷尺寸和距表面距离进行异常值剔除

解决目的
- 目的1：通过缺陷尺寸和距表面距离预测循环周次
- 目的2：解决原始数据离散度大和数据集少的缺点
- 目的3：通过BP模型的预测能力，进一步最小化原始数据的离散度

BP模型建立
- 1.划分训练集、验证集和测试集
- 2.由于数据随机划分带来的误差，进行多次训练，寻找最优的R方和MSE
- 3.模型评价用R方和MSE

BP模型优化
- 探讨隐藏层神经元数量对模型精度的影响

BP模型预测
- 1.通过观察原始数据中缺陷尺寸和距表面距离数据分布，手动确定需要预测的数据
- 2.将手动确定需要预测的数据，传送给优化后的BP模型进行预测

数据清洗

一：Log化

首先，将循环周次未Log化和缺陷尺寸进行多项式2阶和3阶数据拟合；其次，将循环周次Log化和缺陷尺寸进行多项式2阶和3阶数据拟合。R方依次如右图所示。

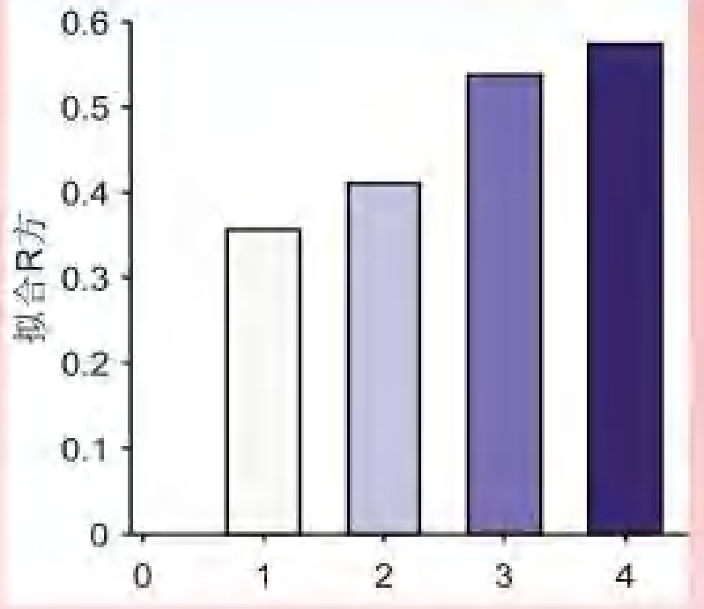

发现：3阶均比2阶拟合效果好；Log化均比未Log化拟合效果好；即转换后的数据与缺陷尺寸呈一定的相关性，便于模型训练时寻找潜在的关系。当拟合R方为最高0.574时，拟合效果如下图所示。

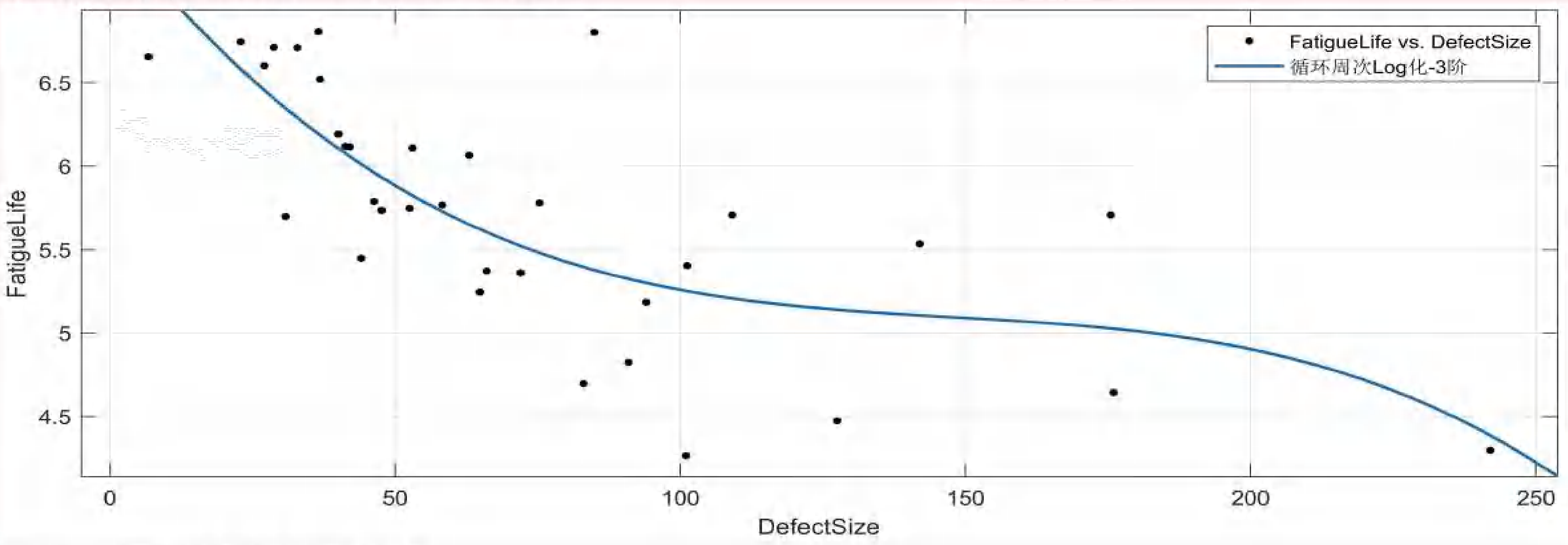

二：异常值剔除

数值不在区间【均值-2x标准差的，均值+2x标准差的】判定为异常值。

数值不在区间【下四中位-1.5x中位差，上四中位+1.5x中位差】判定为异常值。

模型结果

考虑到BP模型的超参数也会对预测能力产生一定的影响，所以仅对第一隐藏层神经元数量参数进行模型优化。分别建立了3次BP神经网络，神经元数量依次为3、4和5。并取3者中R方较高的模型，进行后续的数据预测。模型信息如下图所示。

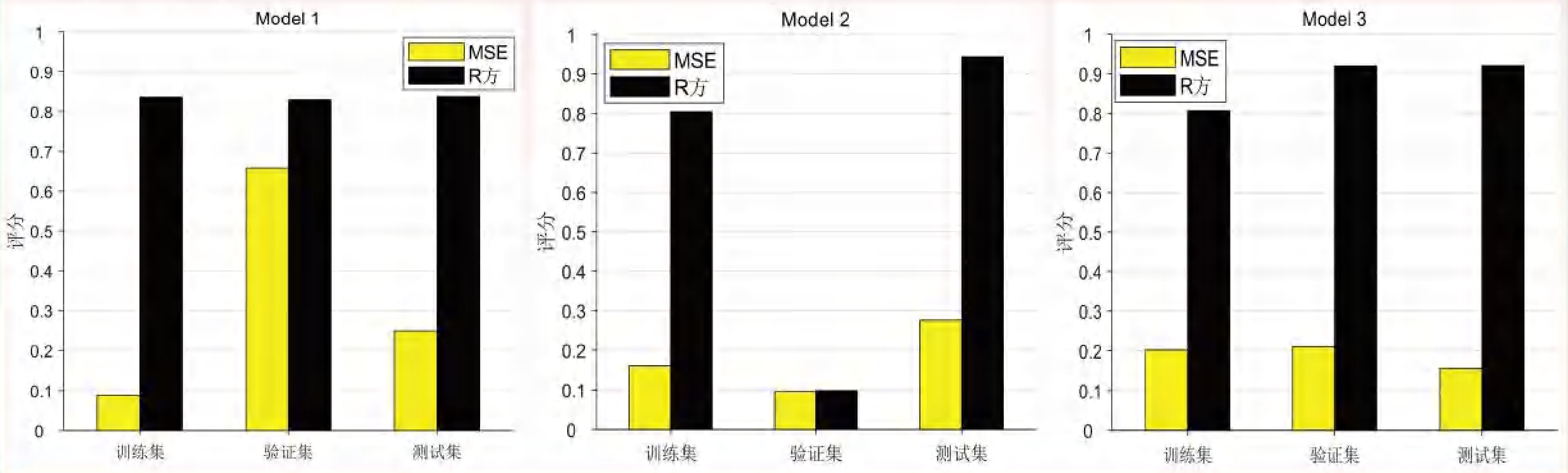

模型预测

第一步，通过对原始数据中缺陷尺寸观察，发现最小值6.7，最大值242；

第二步，通过对原始数据中距表面距离观察，发现最小值6，最大值377；

第三步，对缺陷尺寸以5-255，步长5；对距表面距离以5-385，步长10；

最终生成需要预测的1014组数据；预测效果下图所示；其中的红点数据是异常值剔除后得到的30组数据，曲面数据是预测的1014组数据。

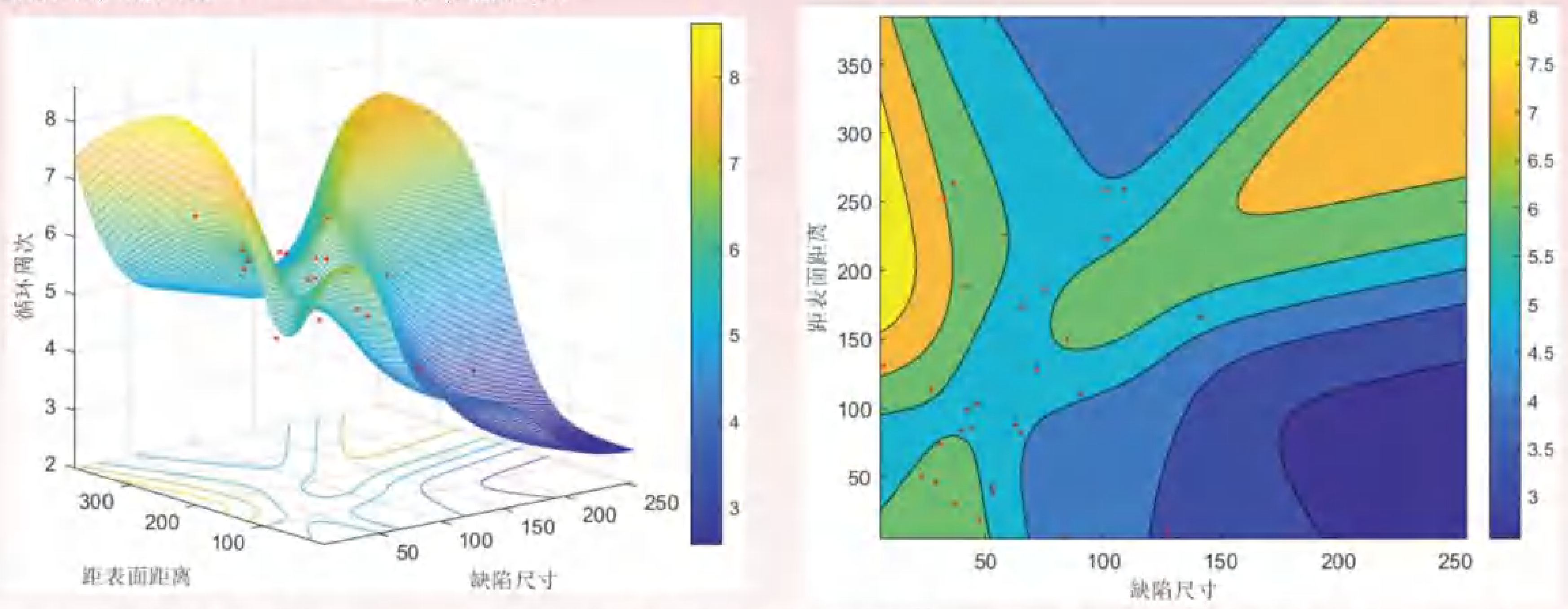

将预测得到的1014组数据画成三维散点图，并取缺陷尺寸和距表面距离视角，对比数据处理中循环周次Log化-3阶。发现预测数据和原始数据中，缺陷尺寸和循环周次走向一致。具体结果如下图所示。

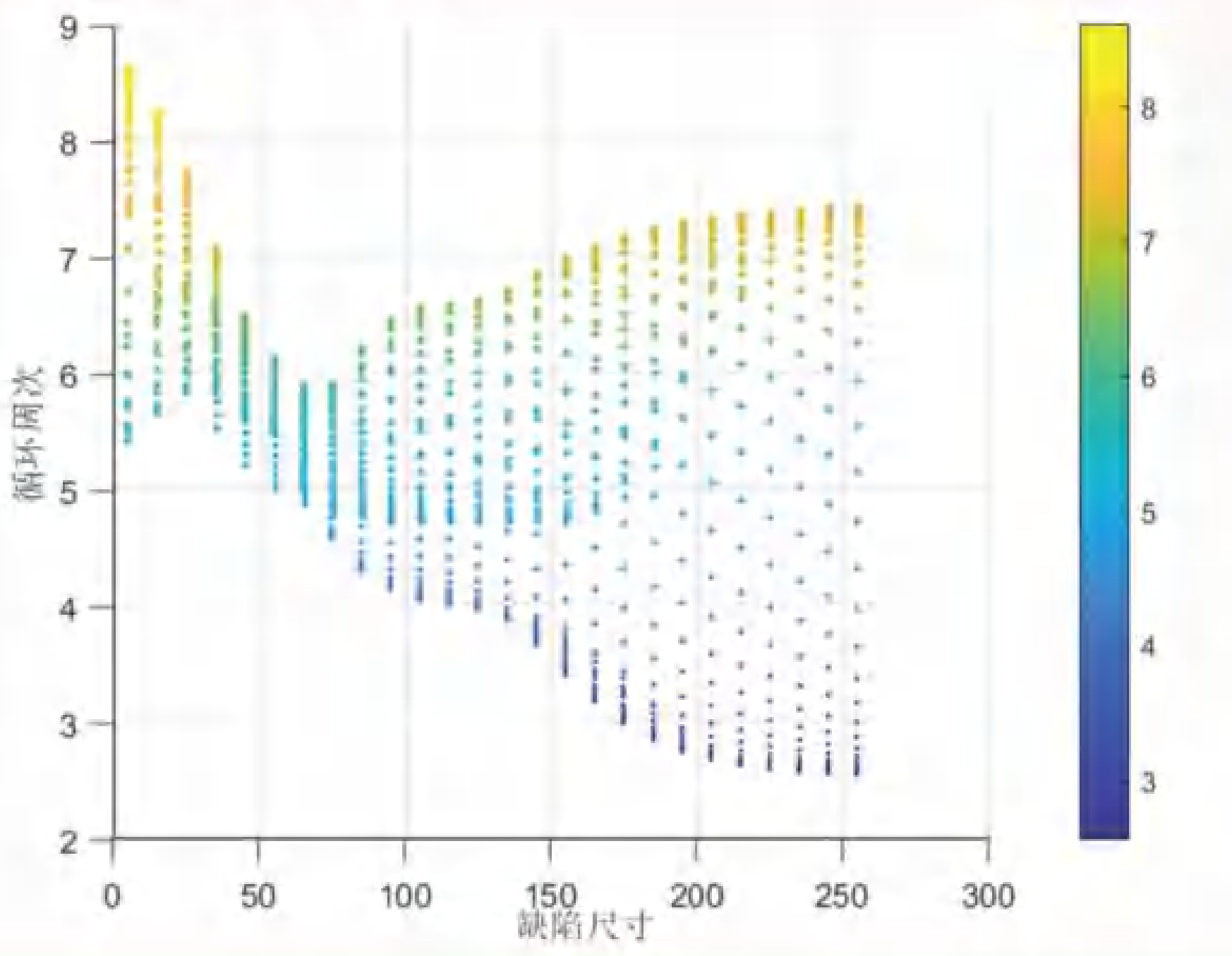

结论

1.通过研究BP模型第一隐藏层神经元数量对模型精度的影响，发现第一隐藏层神经元为4时，模型预测能力最好；

2.对循环周次数据进行Log化，可以找到循环周次和缺陷尺寸之间的相关性；也为找到循环周次、缺陷尺寸和距表面距离之间的相关性，提高可能性；

Significantly enhanced ferromagnetic coupling and Curie temperature in van der Waals CrSBr/MoTe$_2$ heterostructure

Yinlu Gao (高寅露), Qinxi Liu, Xue Jiang (蒋雪), Jijun Zhao (赵纪军)

Key Laboratory of Materials Modification by Laser, Ion and Electron Beams (Dalian University of Technology), Ministry of Education, Dalian 116024, China

Email:gaoyinlu@mail.dlut.edu.cn; *jiangx@dlut.deu.cn; zhaojj@dlut.edu.cn

Abstract CrSBr monolayer is a promising ferromagnetic (FM) semiconductor with stable magnetic ground state, large band gap and high carrier density. However, its Curie temperature (T_C) of about 146 K is still below room temperature. We explore the electronic and magnetic properties of the CrSBr/MoTe$_2$ heterostructure to boost the T_C via proximity effect using first-principles calculations. The long-range FM ordering in the CrSBr layer is enhanced both through a newly extra spin superexchange channel (Cr-Te-Cr) offered by MoTe$_2$ substrate and the reduced degeneracy t_{2g} orbitals of the Cr atoms. As a direct consequence of the enhanced FM coupling, T_C is increased to 225 K. The strong *p-d* hybridizations raise the interorbital hopping between the t_{2g} states through the Cr-Te-Cr superexchange channel. Since the hopping is related to the off-diagonal matrix element of the velocity operator, suggesting that is necessary not only for the increased T_C, but also for the nonzero Berry curvature. Additionally, the Fermi level (E_F) is pushed into higher energy levels with the electron-doped CrSBr layer due to the charge transfer. The synergic effect of the E_F shift from transferred electron filling and interorbital hopping from Cr-Te interaction brings nonzero anomalous Hall conductivity (AHC) in the heterostructure. Our work reveals that interface is an uplifting way to engineer the magnetic and transport properties of 2D magnets, which provides new opportunities for fantastic spintronic devices.

Introduction

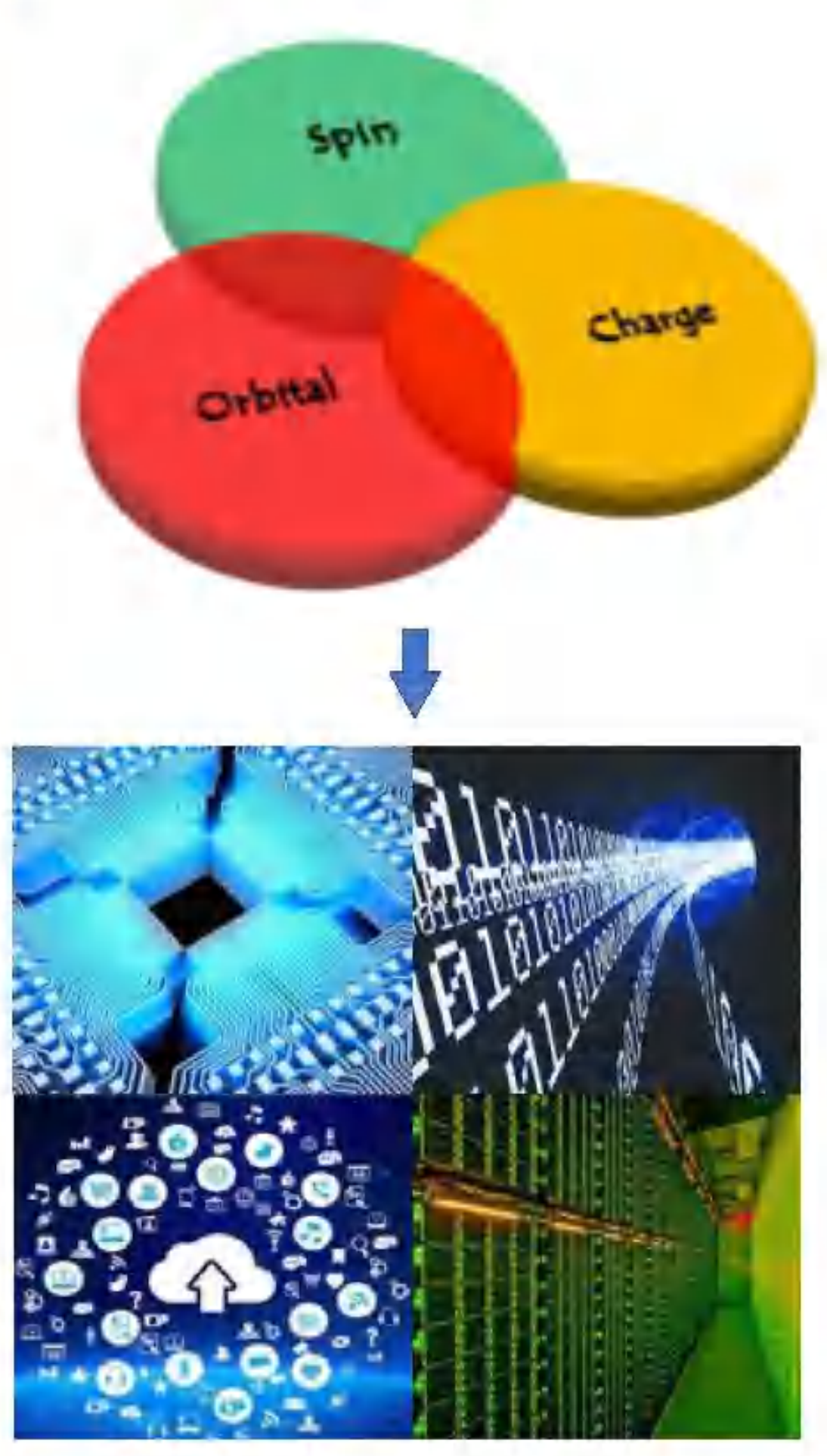

Bilayer Cr$_2$Ge$_2$Te$_6$, T_C = 28 K

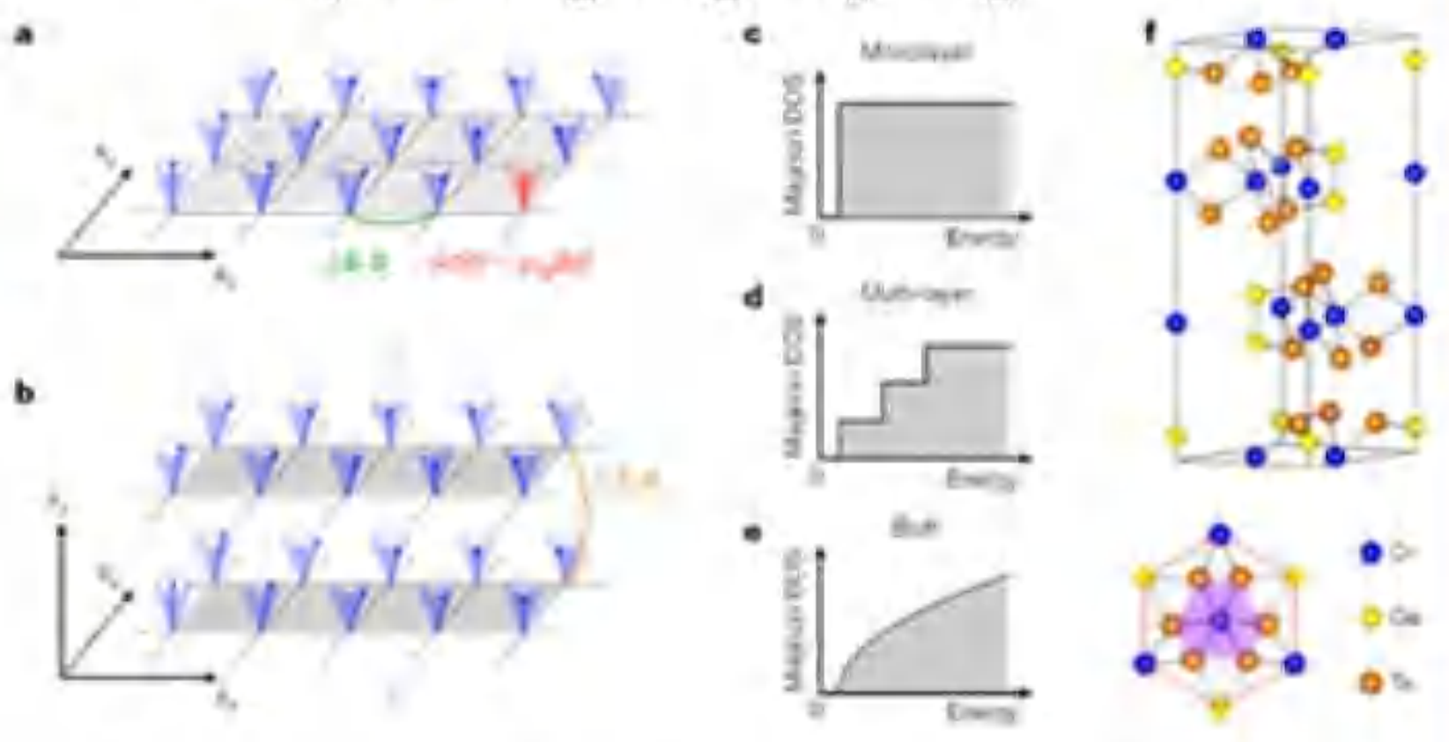

Monolayer CrI$_3$, T_C = 45 K

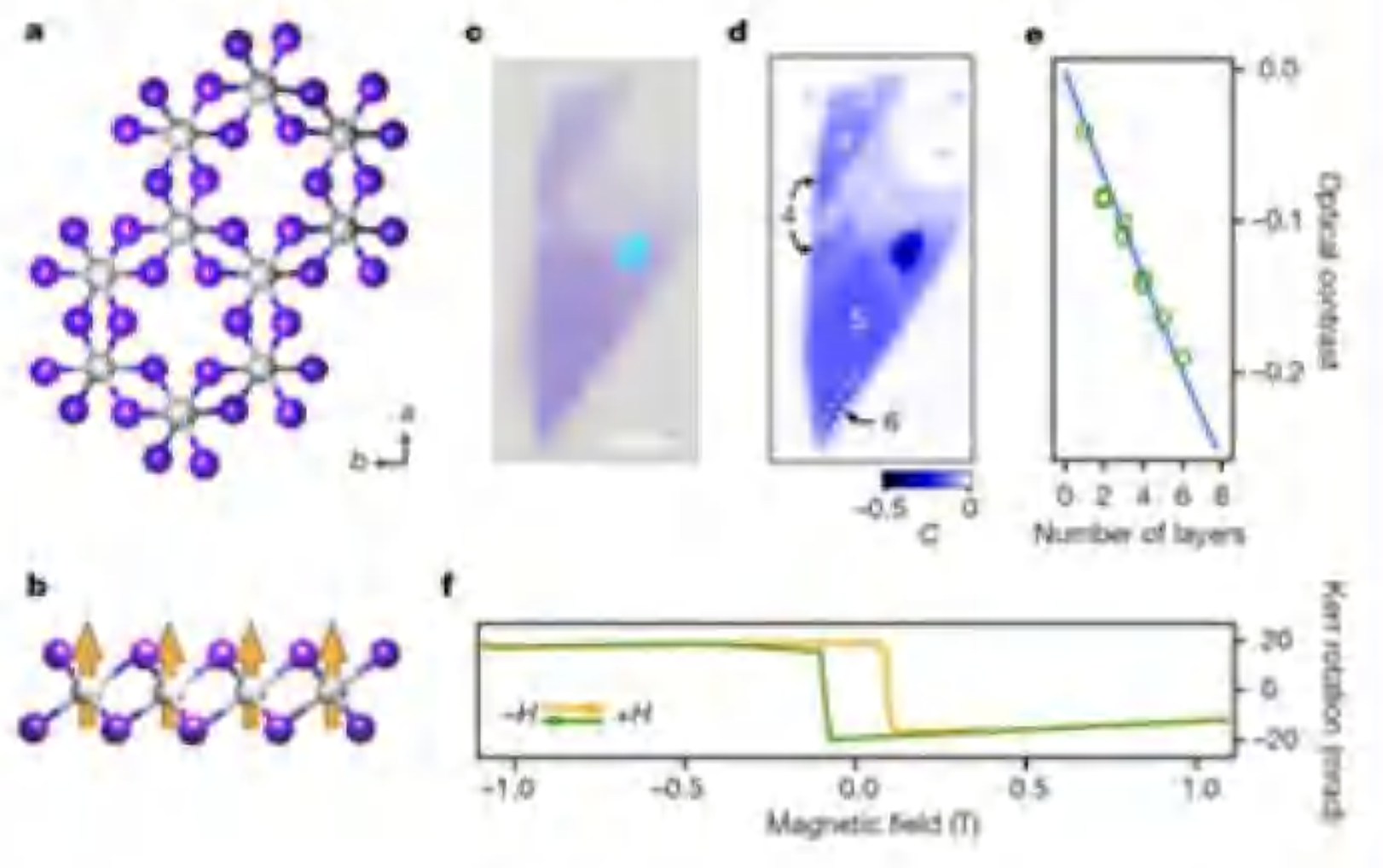

- low Curie temperature
- low carrier concentration

C. Gong, et al., *Nature* 546, 265 (2017)

B. Huang, et al., *Nature* 546, 270 (2017)

Results and discussion

Models

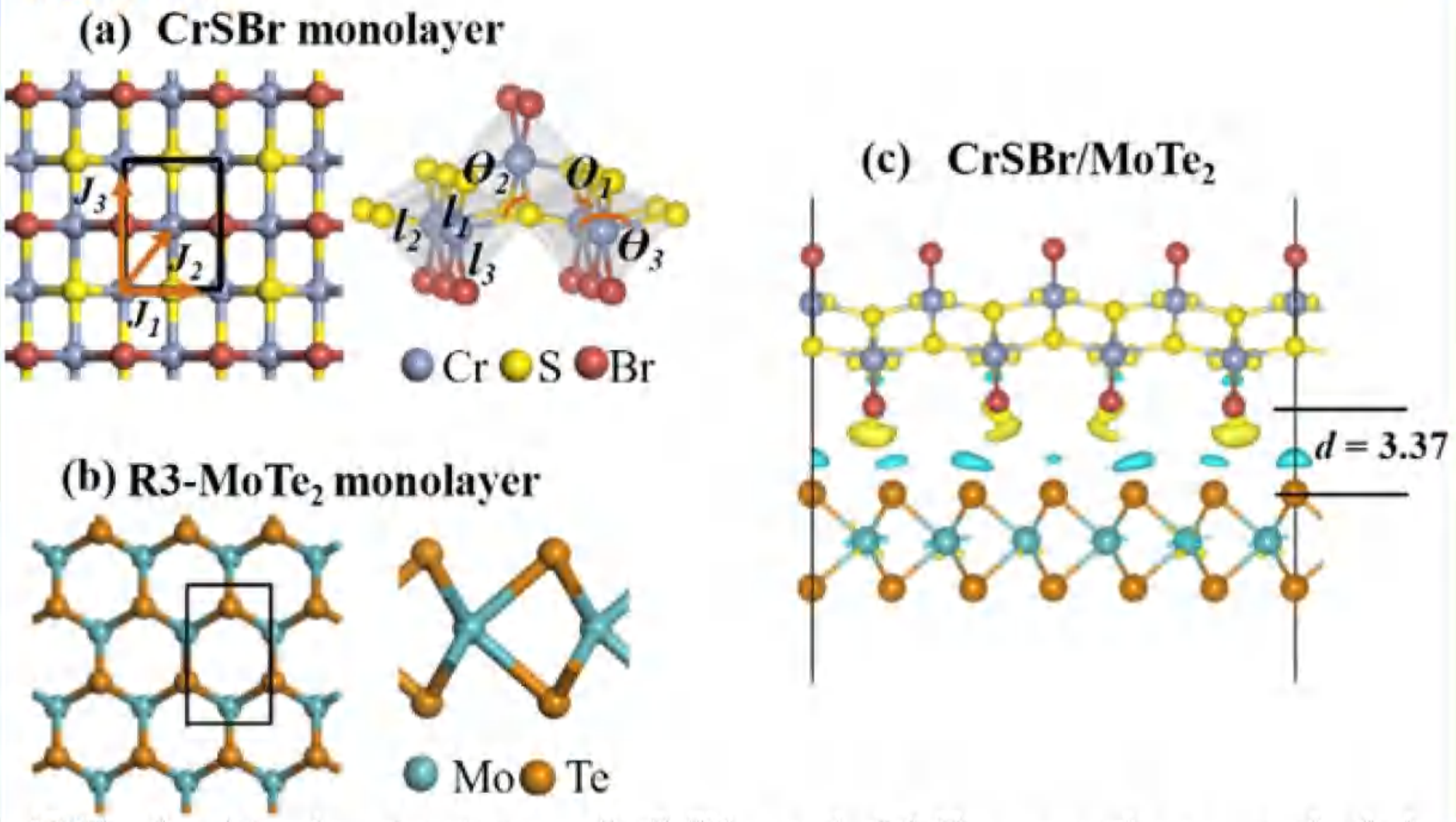

FIG. 1. Atomic structures of CrSBr and MoTe$_2$ monolayers and their heterostructure. (a) Top and side views of a CrSBr monolayer in the orthogonal structure. The intralayer parameters J_1, J_2 and J_3 between Cr site are represented with arrows. (b) Top and side views of 1×√3 unit cell of MoTe$_2$ monolayer. (c) Differential electronic charge density for CrSBr/MoTe$_2$ heterostructure (stack-A) with isosurface of 3×10^{-4} eV/Bohr^3. Yellow and cyan colors represent the charge accumulation and depletion regions, respectively. The blue balls are Cr atoms, yellow are S, red are Br, green are Mo and brown are Te atoms.

Spin orbital reconfiguration

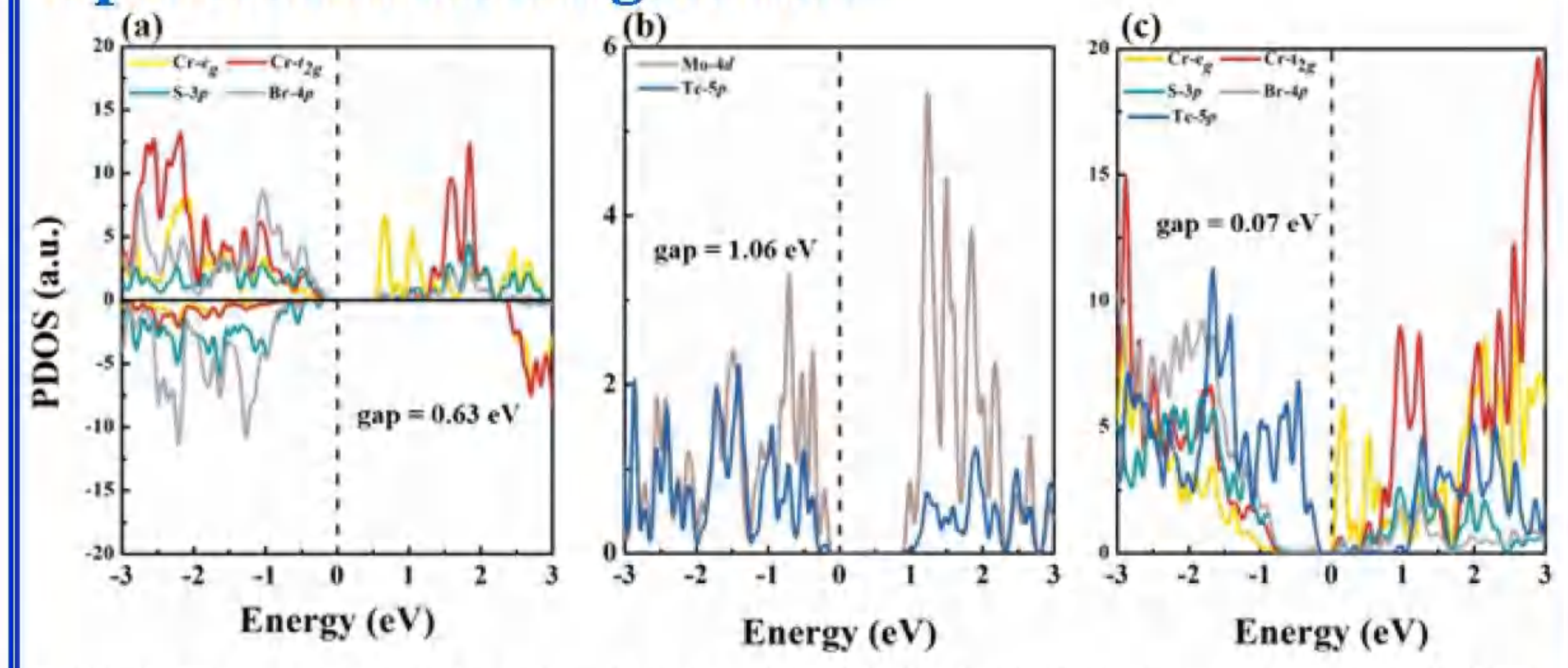

FIG. 2. The projected density of states (PDOSs) of (a) CrSBr monolayer, (b) WTe$_2$ monolayer and (c) CrSBr/MoTe$_2$ heterostructure. SOC effect was taken into account for the calculation in MoTe$_2$ monolayer and the heterostructure.

	ΔE_1	ΔE_2	ΔE_3	J_1	J_2	J_3	$E_{[100]}$	$E_{[010]}$	$E_{[001]}$	M	T_C
CrSBr	51.99	48.72	49.05	1.19	1.44	0.65	–18	75	0	3.25	168
CrSBr/MoTe$_2$	66.43	65.01	66.49	2.18	1.85	0.59	–12	56	0	3.28	225

Table 1. The energy difference ($\Delta E = E_{AFM} - E_{FM}$, meV/Cr) between the ferromagnetic states and the antiferromagnetic states, intralayer spin-exchange coupling parameters J_1, J_2, J_3 (meV), the magnetic anisotropy energy in different directions compared with the [001] direction (μeV/Cr), the magnetic moment (M, μ_B/Cr) and Curie temperatures (T_C, K) predicted using Heisenberg model for CrSBr monolayer and CrSBr/MoTe$_2$ heterostructure.

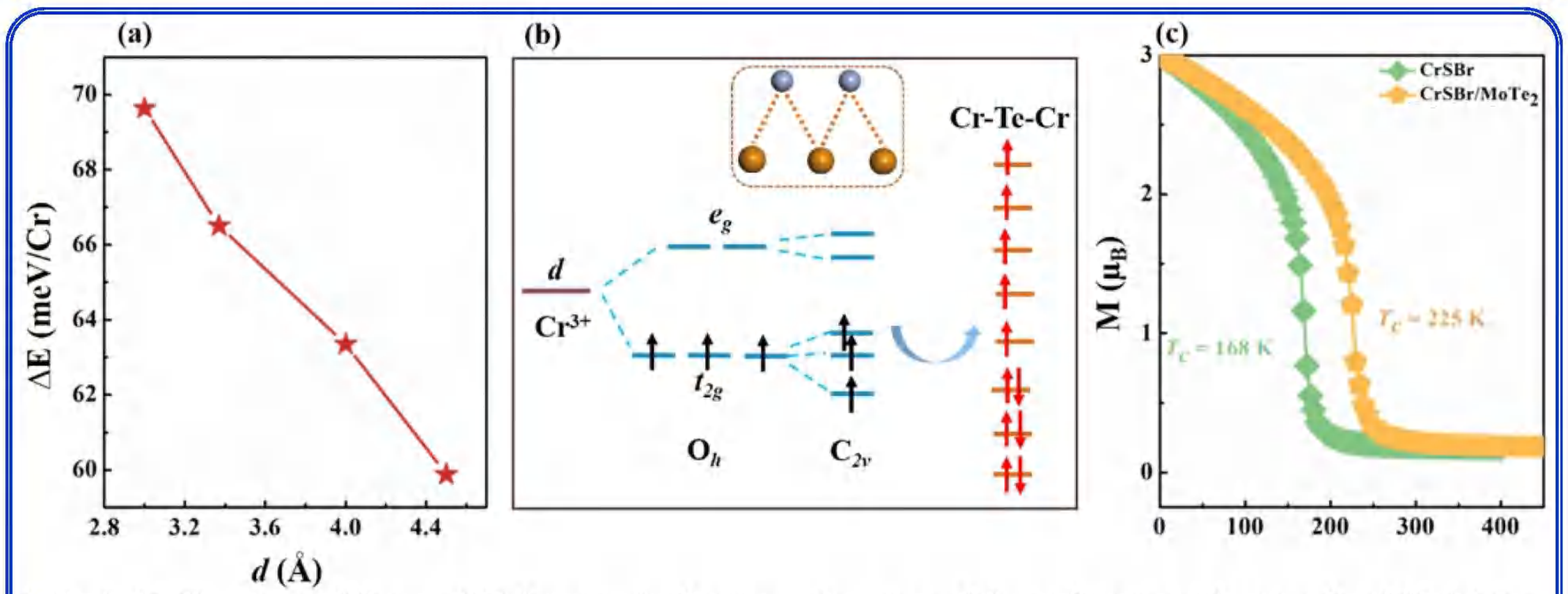

FIG. 3. (a) The energy difference (ΔE) between the ferromagnetic states and the antiferromagnetic states for CrSBr/MoTe$_2$ heterostructure as a function of the interlayer distance (*d*). (b) The crystal field splitting from an ideal octahedron with O_h symmetry to a distorted octahedron with C_{2v} symmetry and the schematic of extra Cr-Te-Cr superexchange coupling channel. The dotted rectangle represents the additional path between Cr and Te atoms. (c) Monte Carlo simulations of the magnetization for CrSBr monolayer and CrSBr/MoTe$_2$ heterostructure.

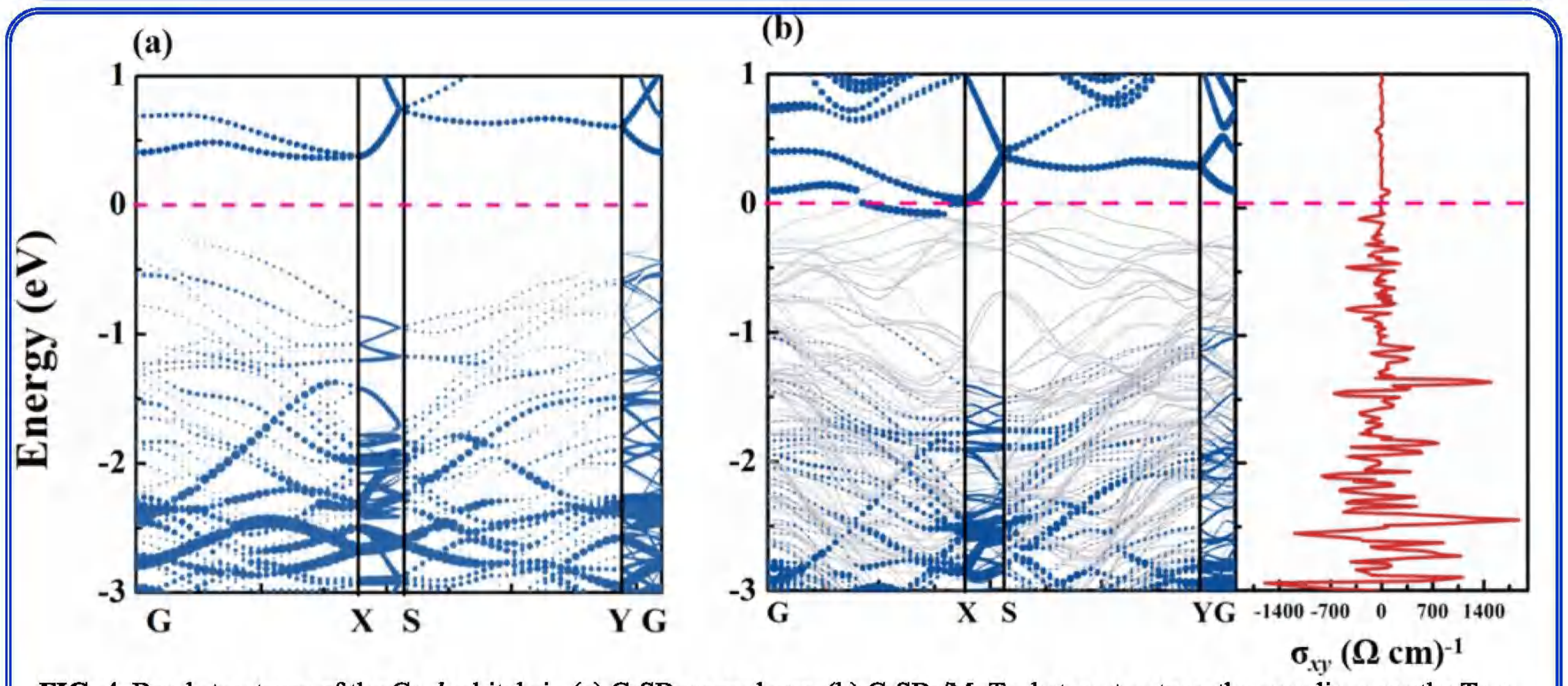

FIG. 4. Band structures of the Cr-*d* orbitals in (a) CrSBr monolayer, (b) CrSBr/MoTe$_2$ heterostructure, the grey lines are the Te-*p* orbitals. The right part is the anomalous Hall conductivity (AHC) as a function of Fermi energy in the CrSBr/MoTe$_2$ heterostructure.

Conclusion

☐ The long-range FM ordering in the CrSBr layer is enhanced both through a newly extra spin superexchange channel (Cr-Te-Cr) offered by MoTe$_2$ substrate and the reduced degeneracy t_{2g} orbitals of the Cr atoms;

☐ T_C is increased from 168 K to 225 K;

☐ The synergic effect of the E_F shift from transferred electron filling and interorbital hopping from Cr-Te interaction brings nonzero anomalous Hall conductivity (AHC) in the heterostructure.

Device Performance and Strain Effect of Sub-5 nm Monolayer InP Transistors

Linqiang Xu,[1] Jing Lu[1, 2, 3,*]
[1]State Key Laboratory for Mesoscopic Physics and Department of Physics, Peking University, Beijing 100871, P. R. China
[2]Collaborative Innovation Center of Quantum Matter, Beijing 100871, P. R. China
[3] Beijing Key Laboratory for Magnetoelectric Materials and Devices, Peking University, Beijing 100871, P. R. China

Introduction

Indium phosphide (InP) has higher electron mobility, electron saturation velocity, and drain current than silicon (Si), and the ultra-thin (UT) InP field-effect transistor (FET) probably possesses a better device performance than the UT Si counterpart. Recently, InP film has been successfully grown with a thickness down to 6.3 nm. We investigate the device performance of the *n*-type sub-5 nm monolayer (ML) InP (the limitation of UT InP film) FETs based on the *ab initio* quantum transport simulation. The on-state currents of the ML InP FETs fulfill the International Technology Roadmap for Semiconductors (ITRS) requirements for the high-performance (HP)/low-power (LP) devices when the gate lengths (L_g) are reduced to 2/4 nm. Besides, the intrinsic delay time of the 3-nm-L_g ML InP FETs and the power-delay product of the 1-nm-L_g ML InP FETs could meet both the HP and LP demands of the ITRS. Finally, we also study the effect of strain on the ML InP FETs. In a word, our results show that UT InP is a potential channel candidate for the next-generation FETs.

Results

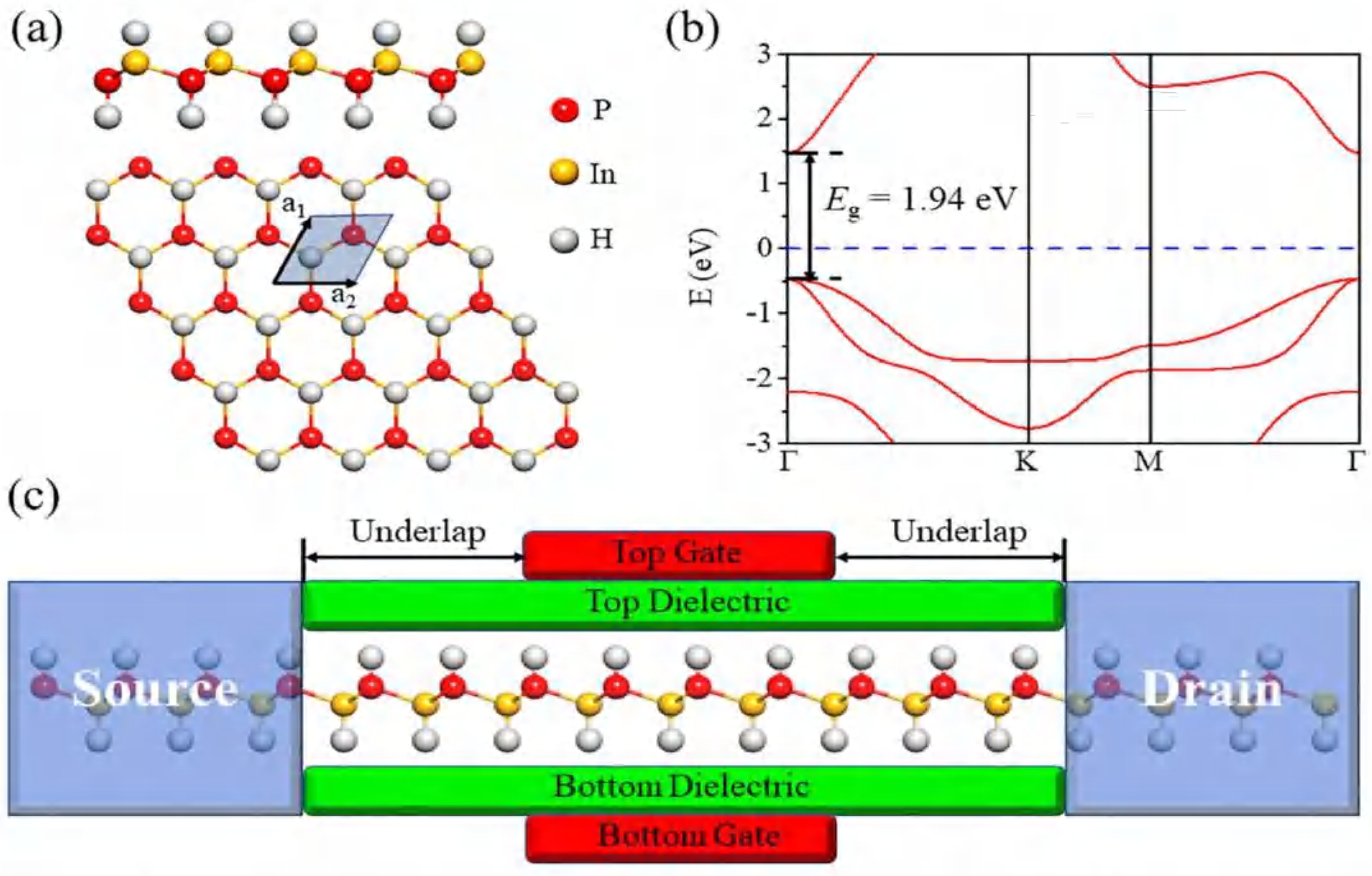

Figure 1. (a) Side and top view of the optimized ML InP structure. (b) Band structure of the ML InP. (c) Schematic diagram of the ML InP MOSFET.

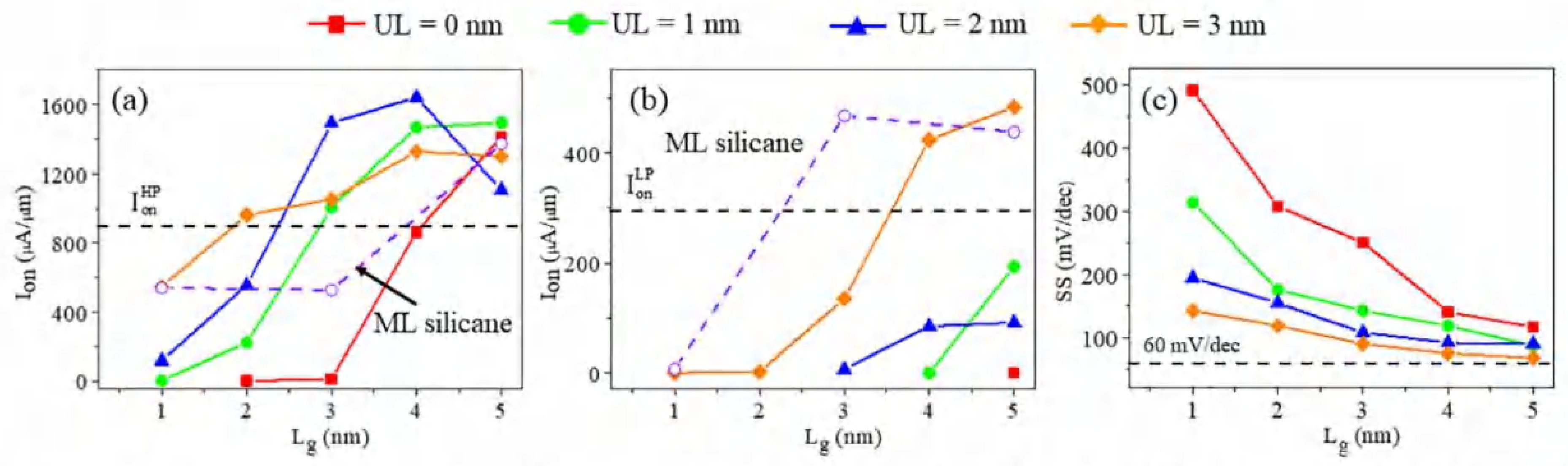

Figure 2. I_{on} as a function of L_g for the (a) HP and (b) LP applications in the ML InP MOSFETs with UL of 0-3 nm. (c) SS as a function of L_g in the ML InP MOSFETs with UL of 0-3 nm.

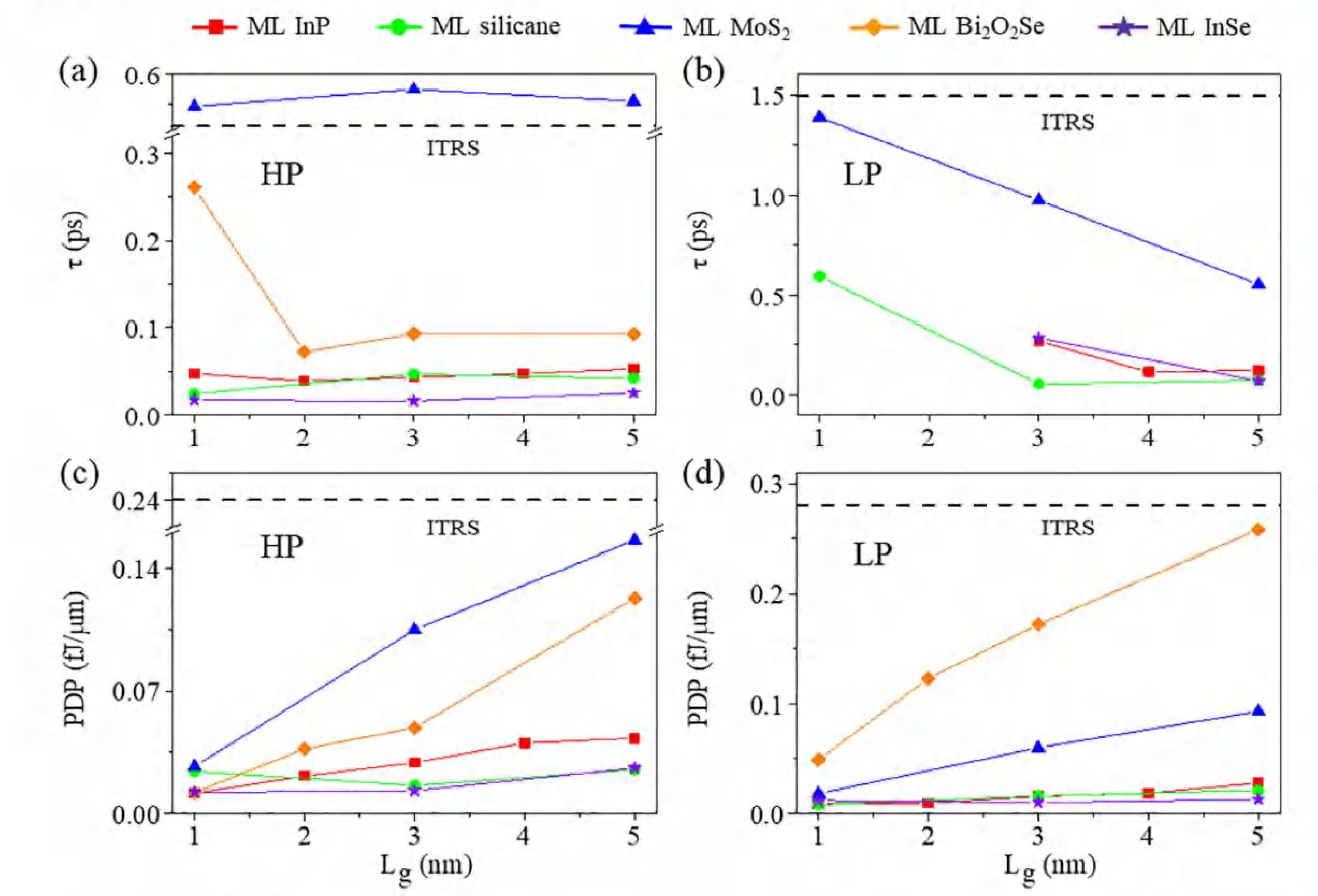

Figure 3. Optimal (a) HP τ, (b) LP τ, (c) HP PDP, and (d) LP PDP of the *n*-type 2D ML MOSFETs versus L_g.

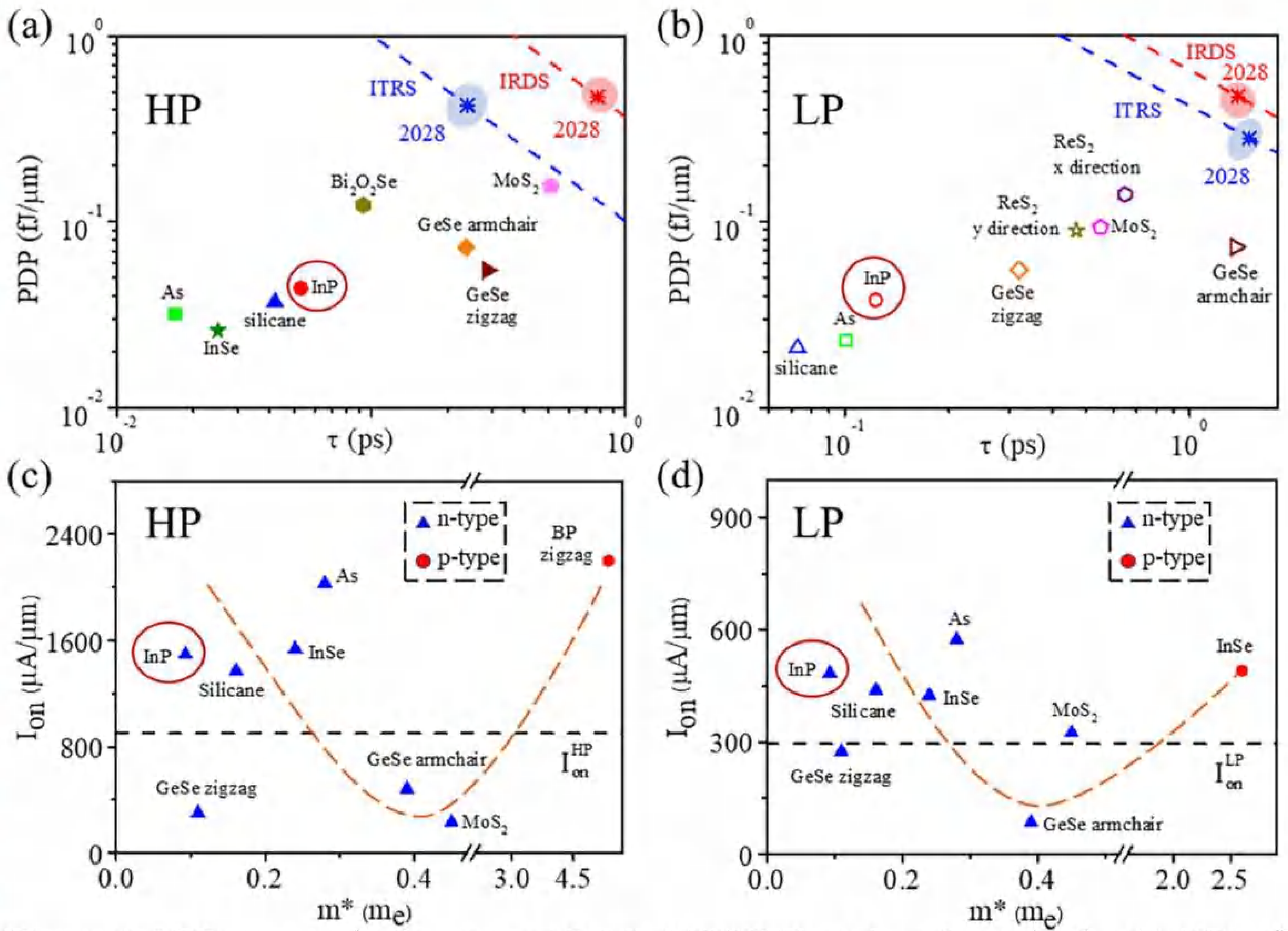

Figure 4. PDP versus τ in the *n*-type 2D ML MOSFETs at L_g = 5 nm for the (a) HP and (b) LP applications. (c) HP and (d) LP I_{on} of the *n*- and *p*-type MOSFETs at L_g = 5 nm versus *m** of the 2D semiconductors.

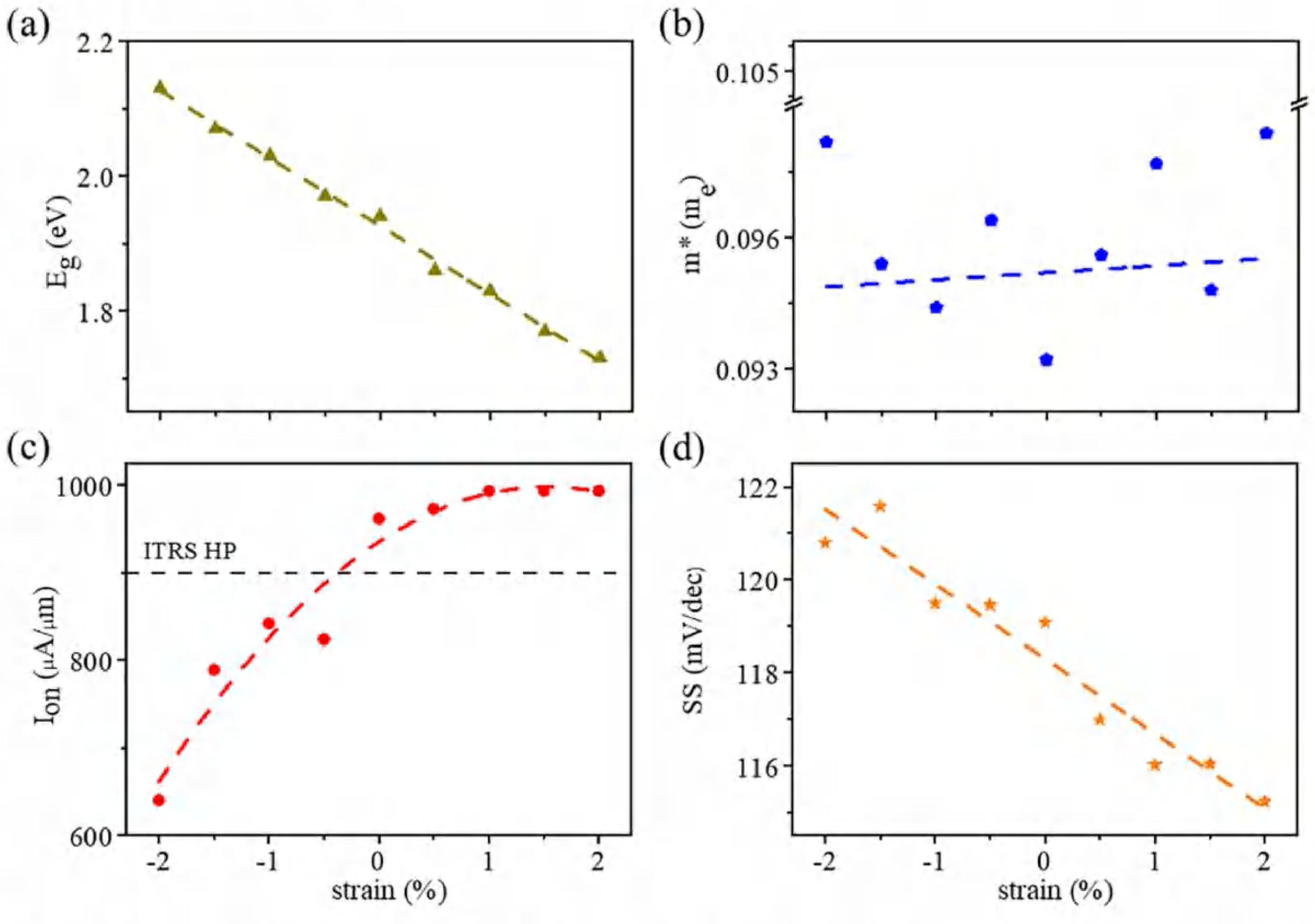

Figure 5. (a) E_g and (b) m^* of the ML InP as a function of the biaxial strain. (c) I_{on} and (d) SS of the ML InP MOSFETs at L_g = 2 nm and UL = 3 nm as a function of the biaxial strain.

Method

Density functional theory (DFT) coupled with the nonequilibrium Green's function (NEGF) formalism and Vienna *ab initio* simulation package in the form of projector augmented waves with the GGA-PBE exchange and correlation interaction are adopted.

Conclusion

I_{on} of the ML InP MOSFETs fulfills the HP and LP goals of the ITRS until L_g is decreased to 2 and 4 nm, respectively. As for τ and PDP, the 1-nm-L_g and 3-nm-L_g ML InP MOSFETs can well satisfy the ITRS requirements for the HP and LP devices, respectively. The effect of strain on the ML InP MOSFETs is also investigated. Unfortunately, we find that the strain is unable to significantly improve the corresponding device performance. Therefore, UT InP is a potential channel candidate to replace Si for extending Moore's law to the sub-5 nm region.

Linqiang Xu, Jing Lu*, et al. Device Performance and Strain Effect of Sub-5 nm Monolayer InP Transistors. *J. Mater. Chem. C*, 2022, 10, 2223.

Uranium phase transition predicted by a novel machine learning potential

Hongjian Chen[1], **Wangyu Hu***, **Dingwang Yuan**, **Bowen Huang**
College of Materials Science and Engineering, Hunan University, ChangSha, 410082, China

Abstract

The evolution of different phase structures (mainly α, β and bcc or γ) of uranium is of great significance for its application. A machine learning moment tensor potential (MTP) for uranium was developed based on active learning, from which the properties of statics and thermodynamics for α-U can be appropriately reproduced, and γ-U stabilizes only when it is greater than 25GPa at 0K. The β-U will first transform into the stable phase α-U, and then there is a phase transition of α↔γ around 1100K during the heating process. The pure α-U transforms into the γ-U at around 1050K, which is very close to the Experimental value(1045K). All of these provide theoretical guidance for the experimental study of the evolution mechanism of different phases of uranium.

Machine learning training workflow

Structure of Uranium

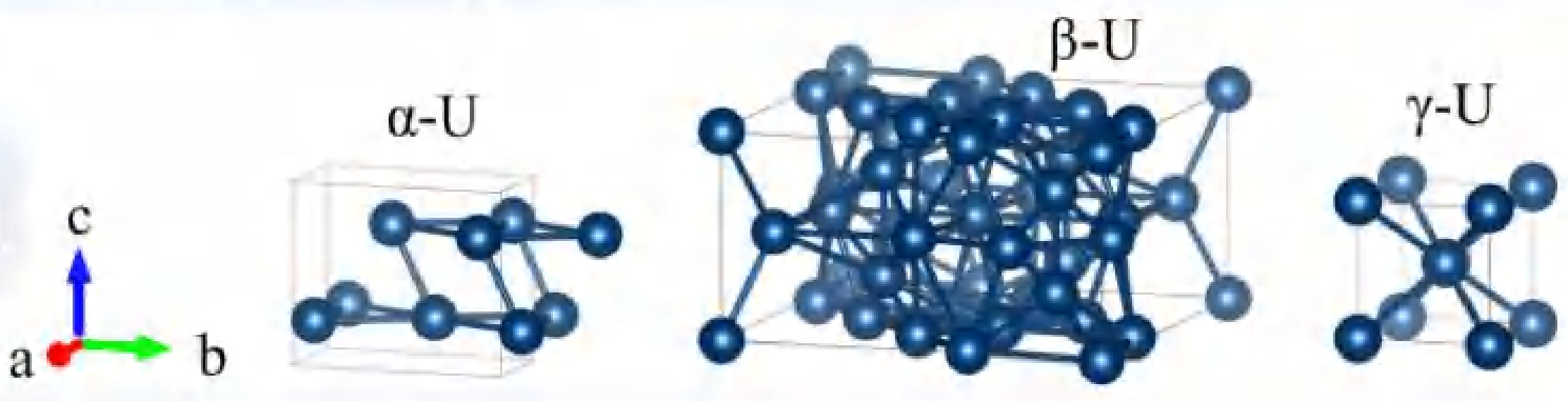

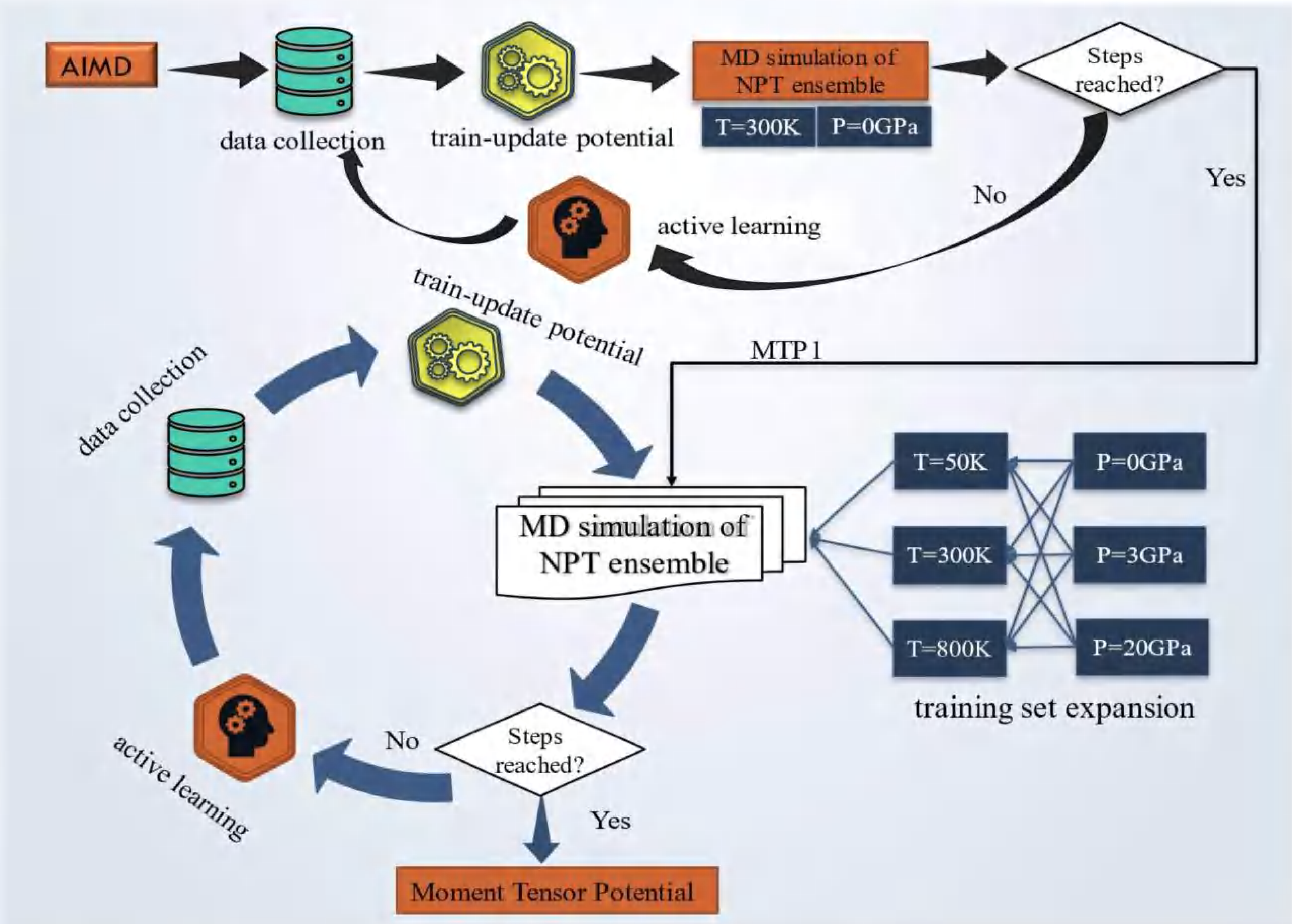

Experimental validation

☐ Accuracy of MTP model

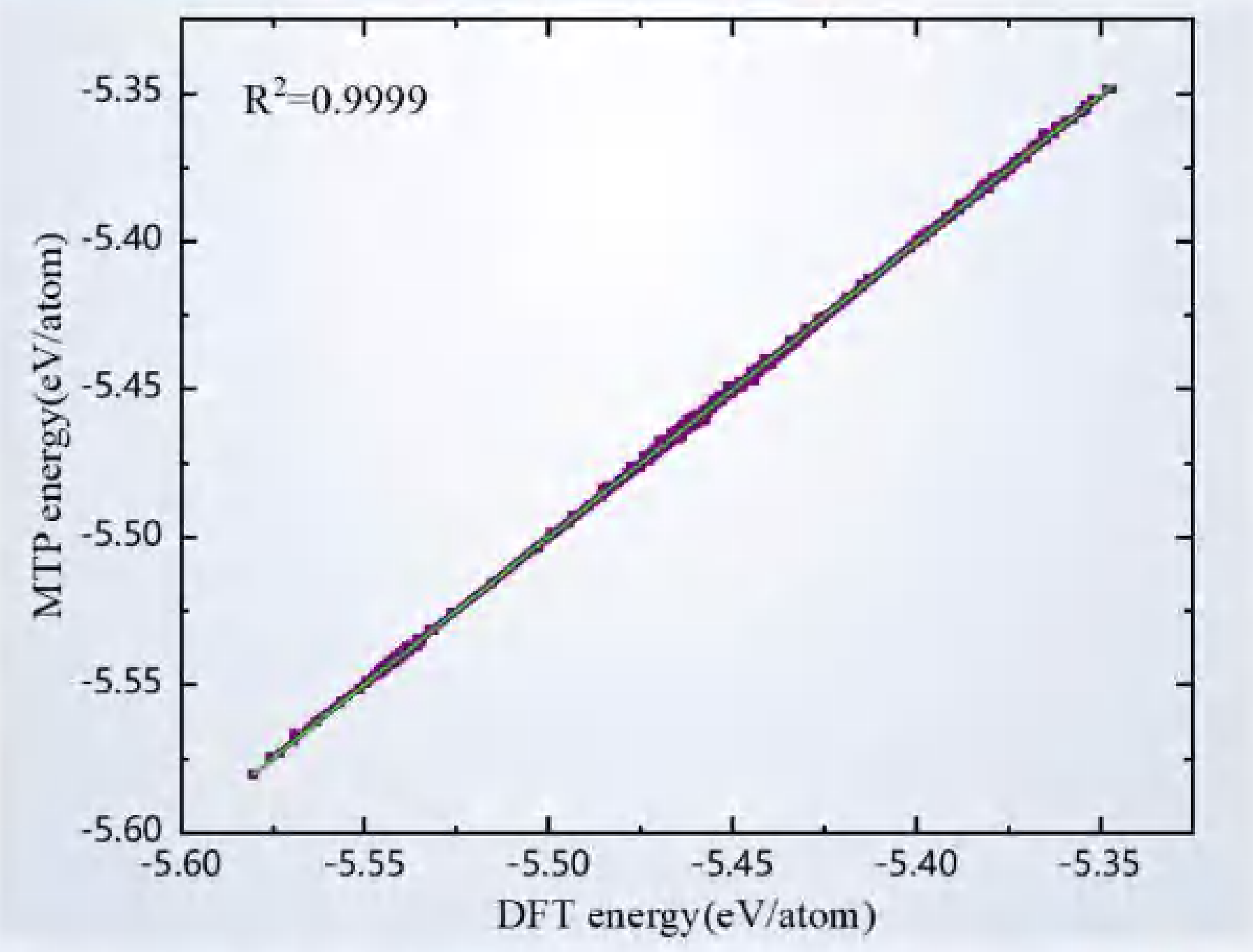

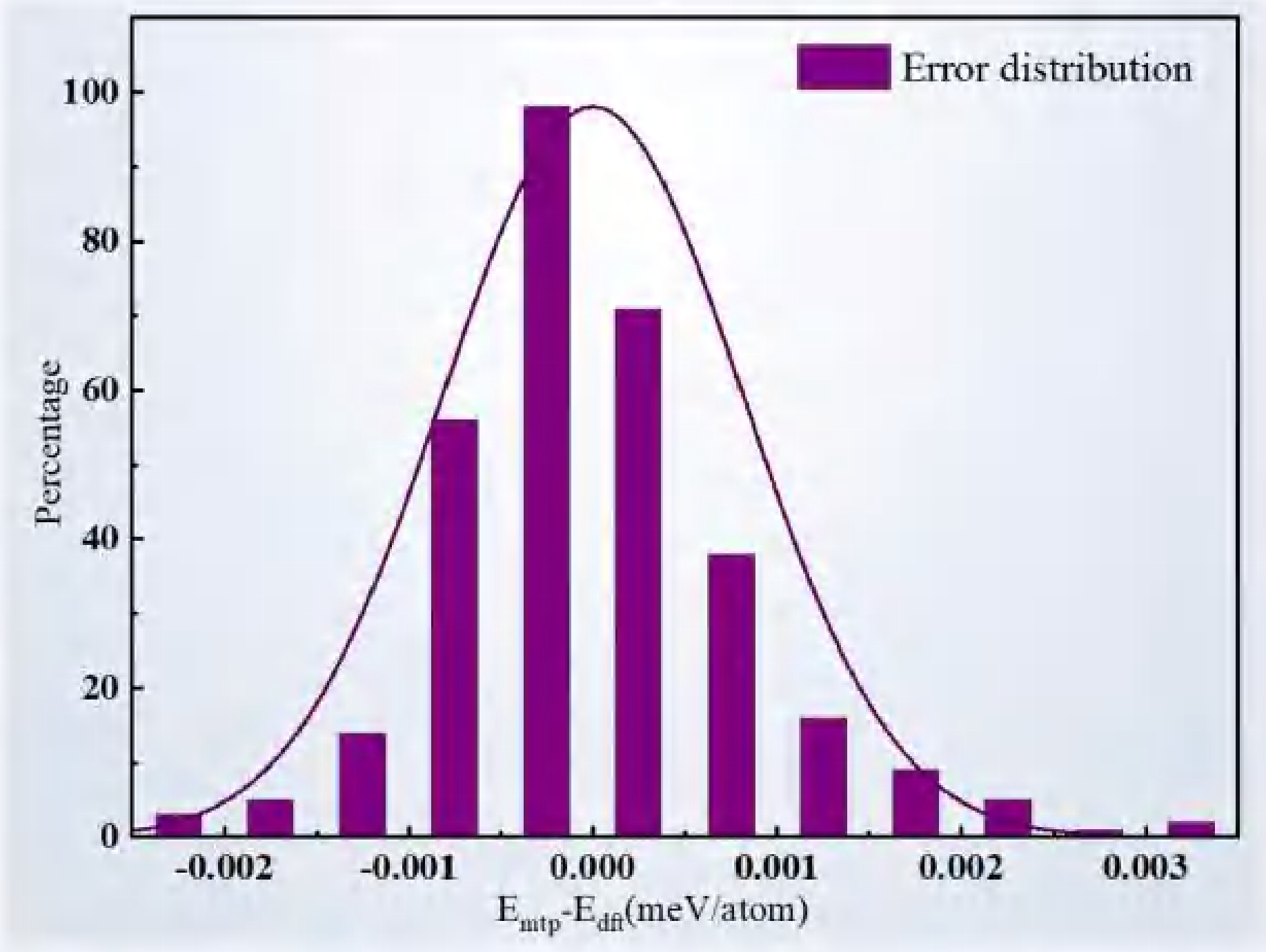

- Energies of atomic configurations in the **active learning datasets**(**left**). The straight **green** line represents the perfect fit. The error distributions (**right**) in the active learning datasets.

☐ Static properties

- MTP can better reproduce the experimental value of elastic modulus

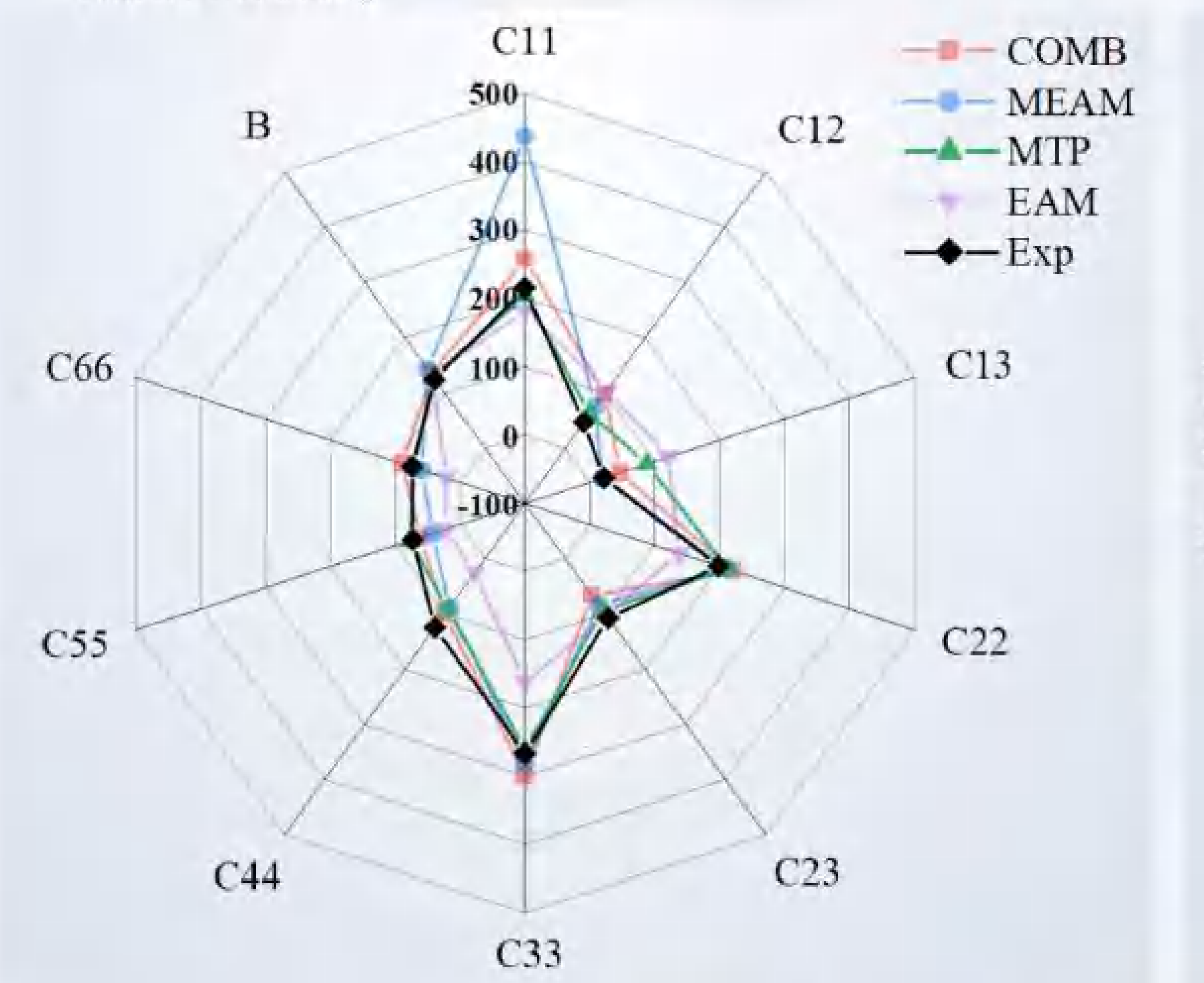

- MTP can get a better pressure to volume ratio curve

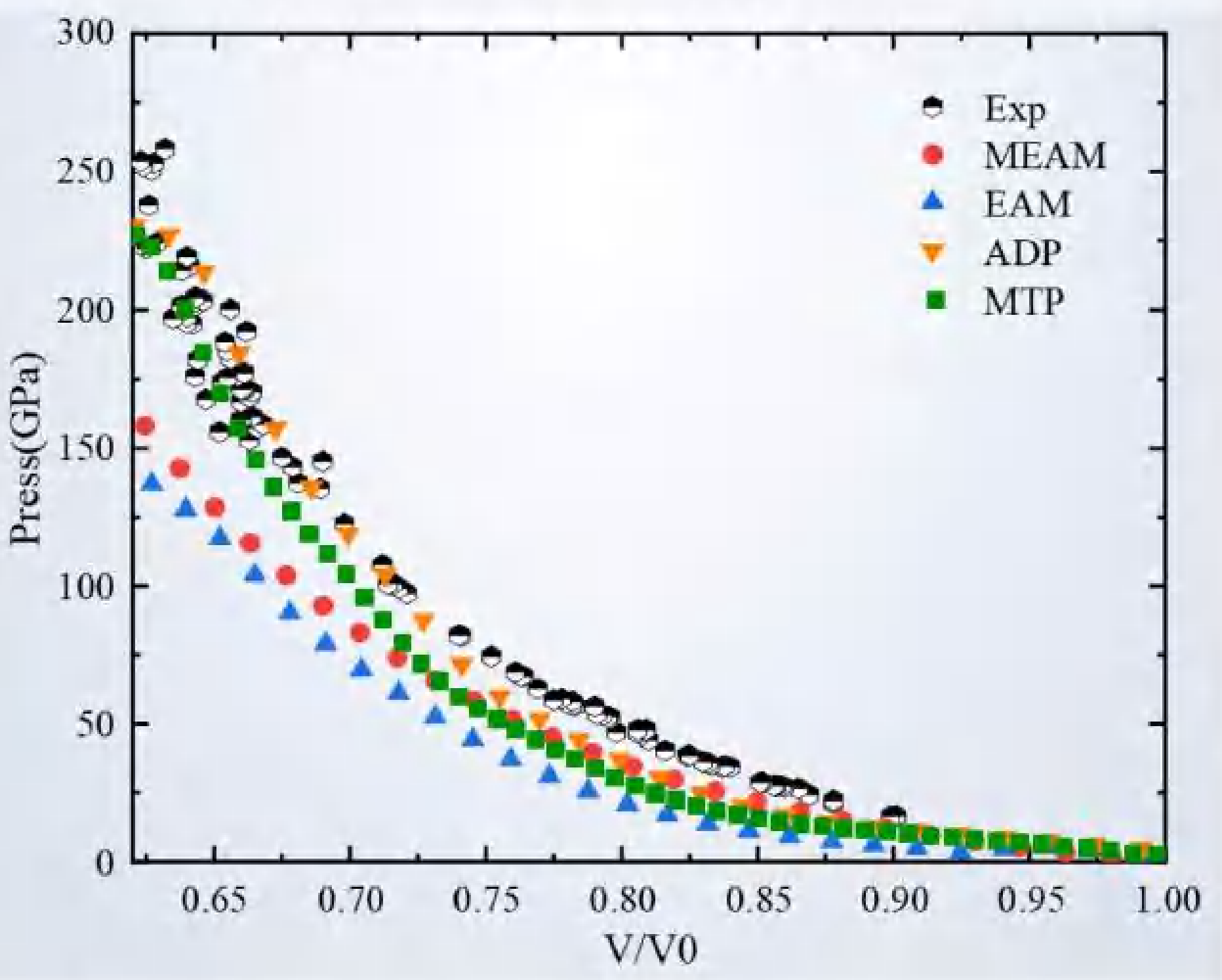

Ref. J.R. Fernández, M.I. Pascuet et al. Model. Simul. Mater. Sci. Eng. 22 (2014).

- The lattice constants of the different phases compare well with the DFT values.

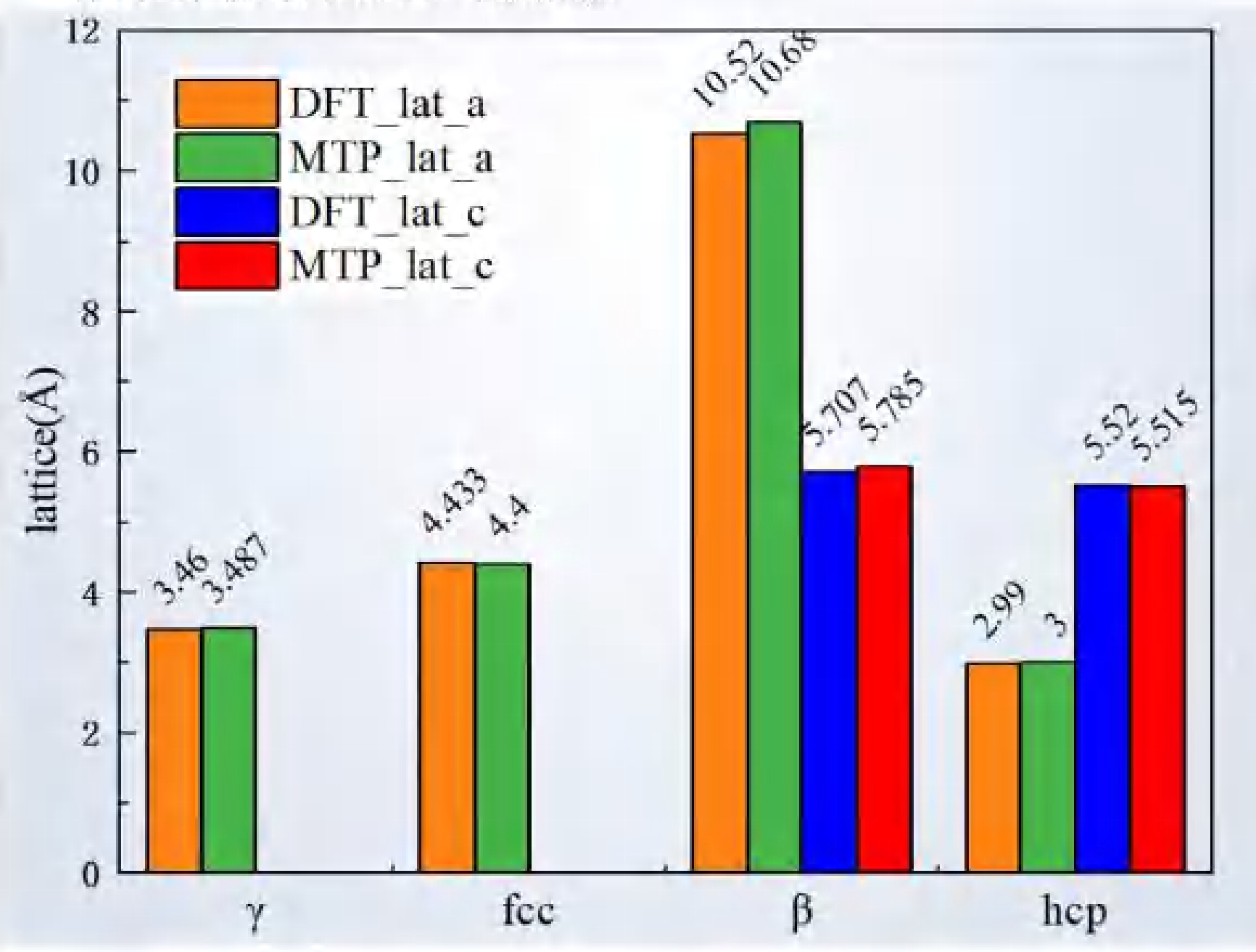

- γ-U instability at 0K begins to be suppressed after greater than 25 GPa.

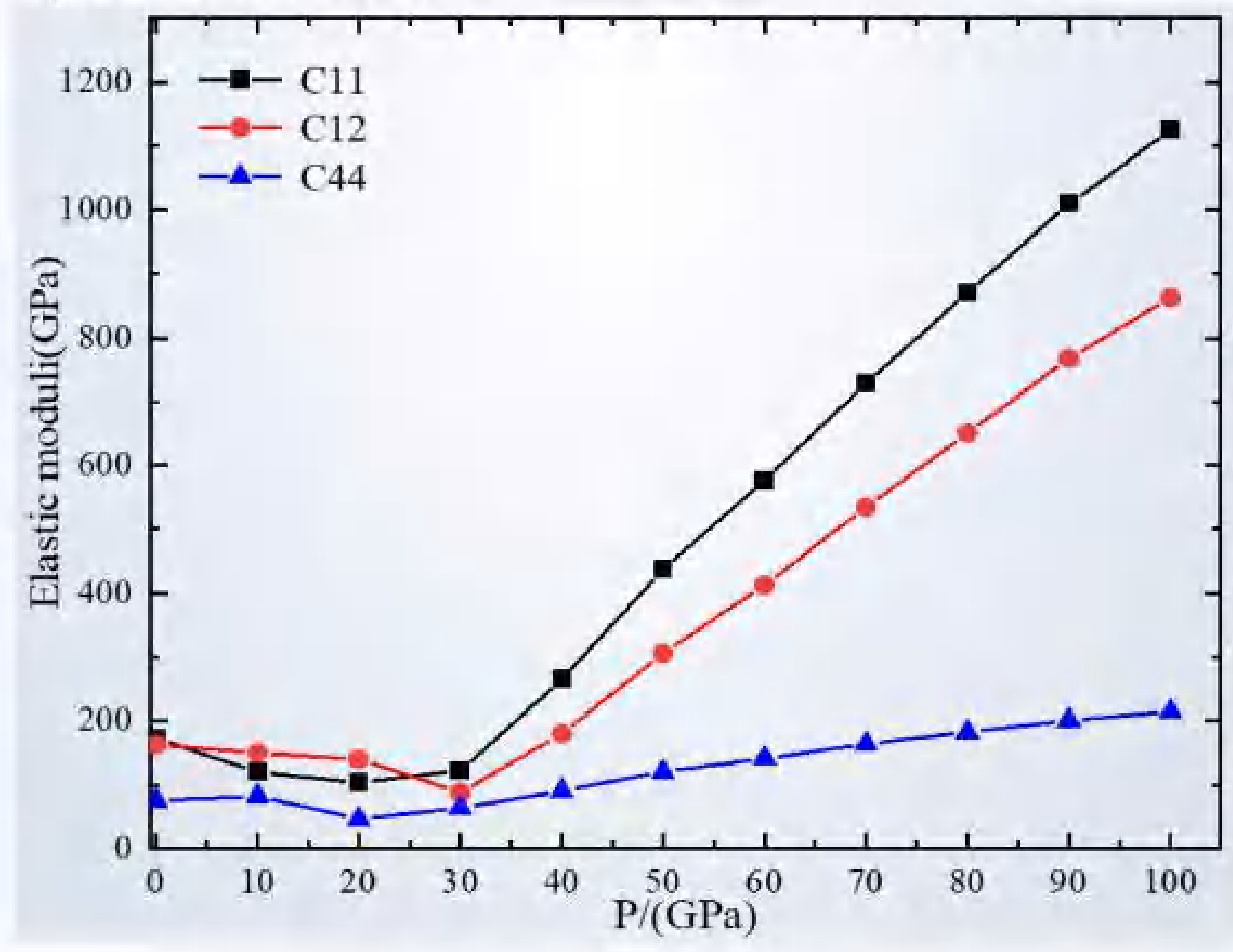

☐ Thermodynamic properties

- MTP can observe the temperature point corresponding to the jump of Cp value.

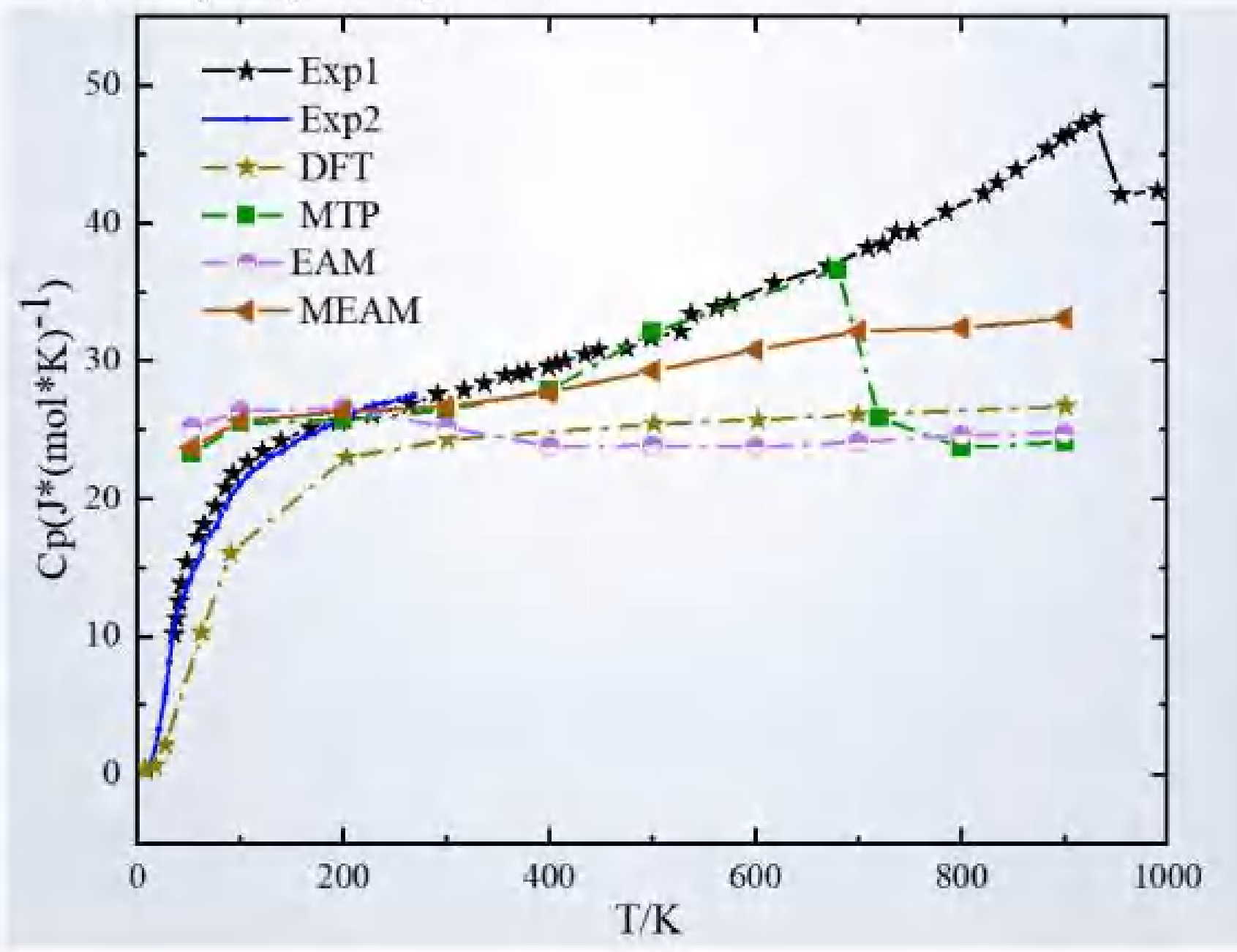

- MTP is closer to the thermal conductivity value of DFT than the traditional potentials.

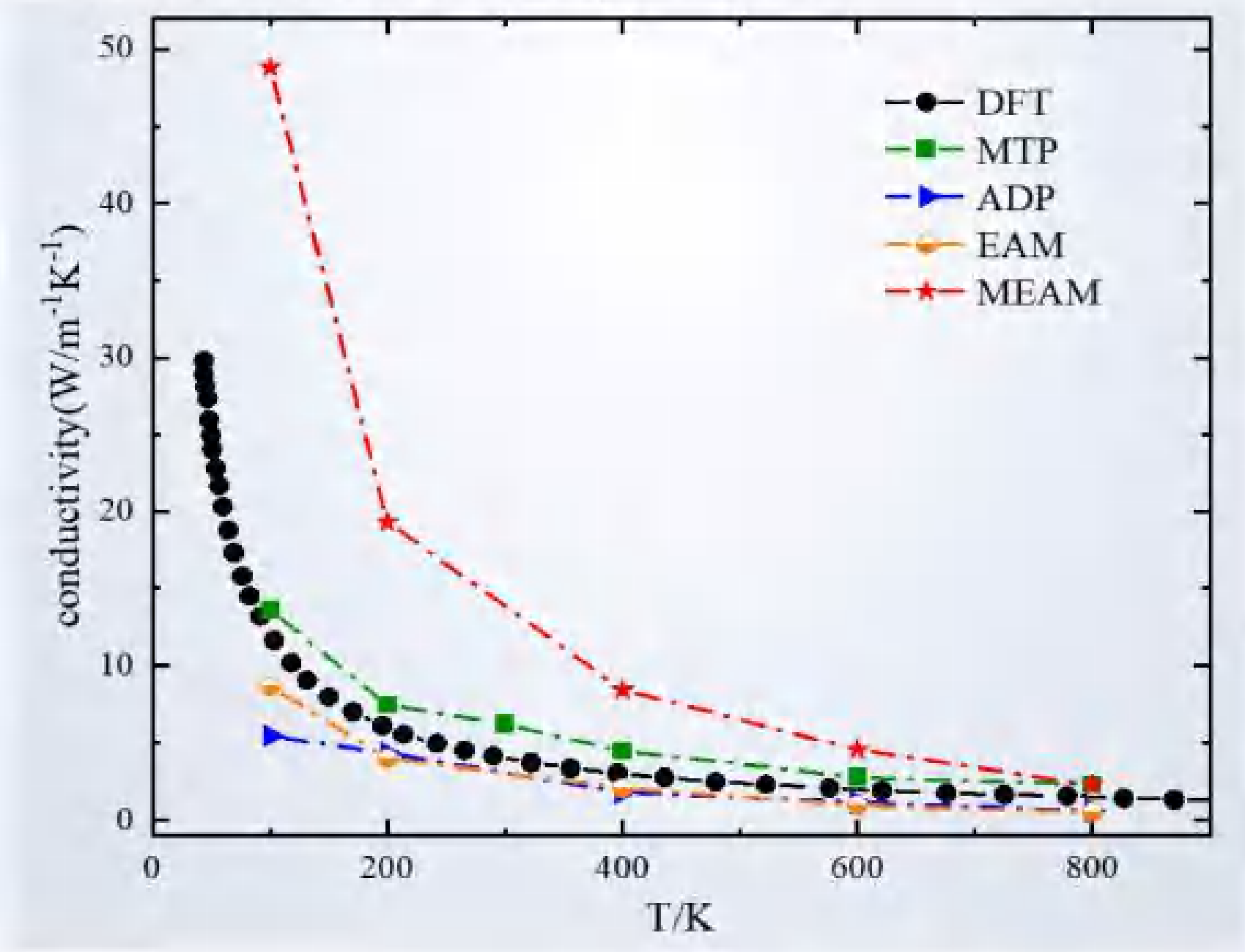

- The β-U first transforms into stable α phase and finally into high temperature γ-U with increasing temperature.

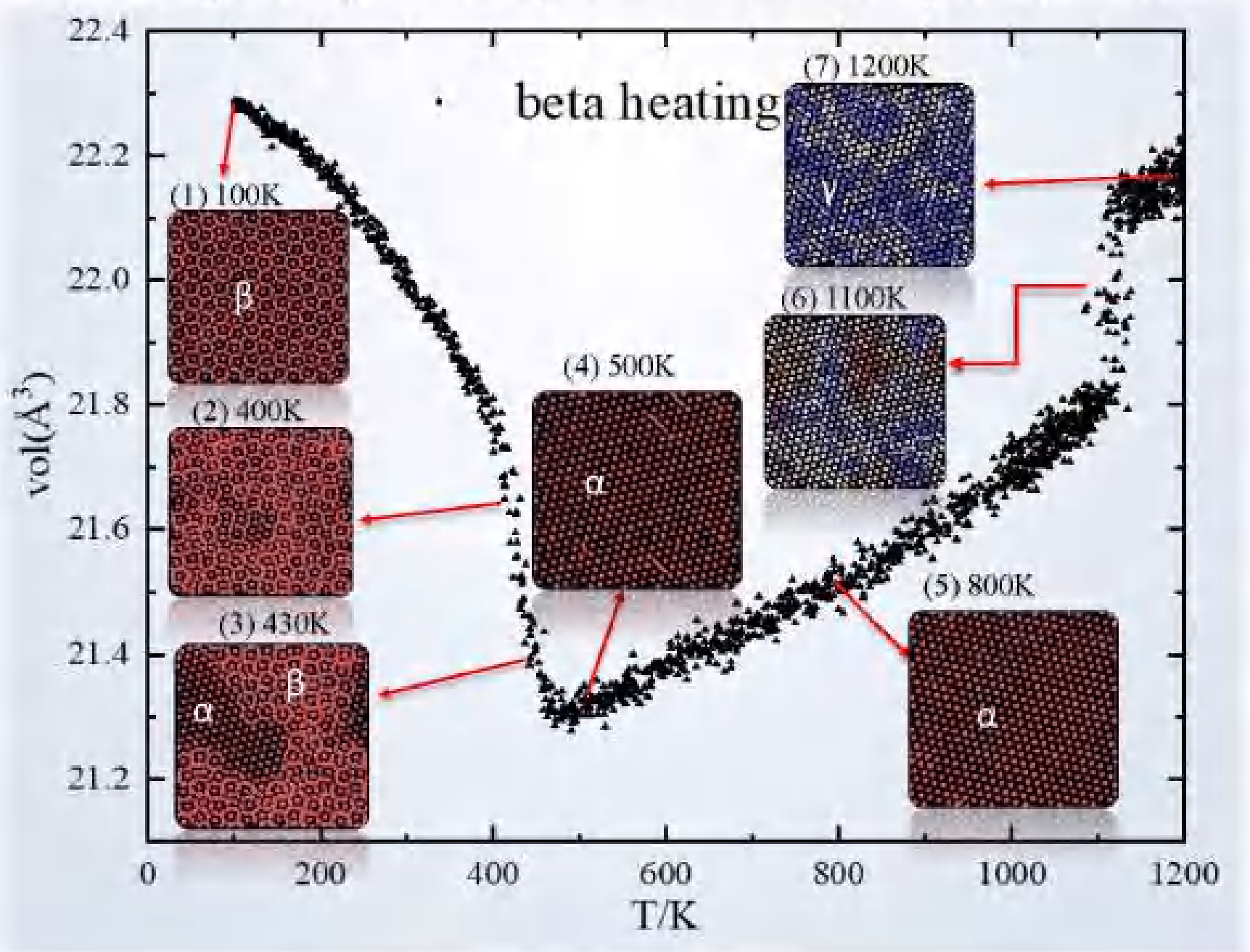

- Pure α-U undergoes α↔γ phase transition with increasing temperature.

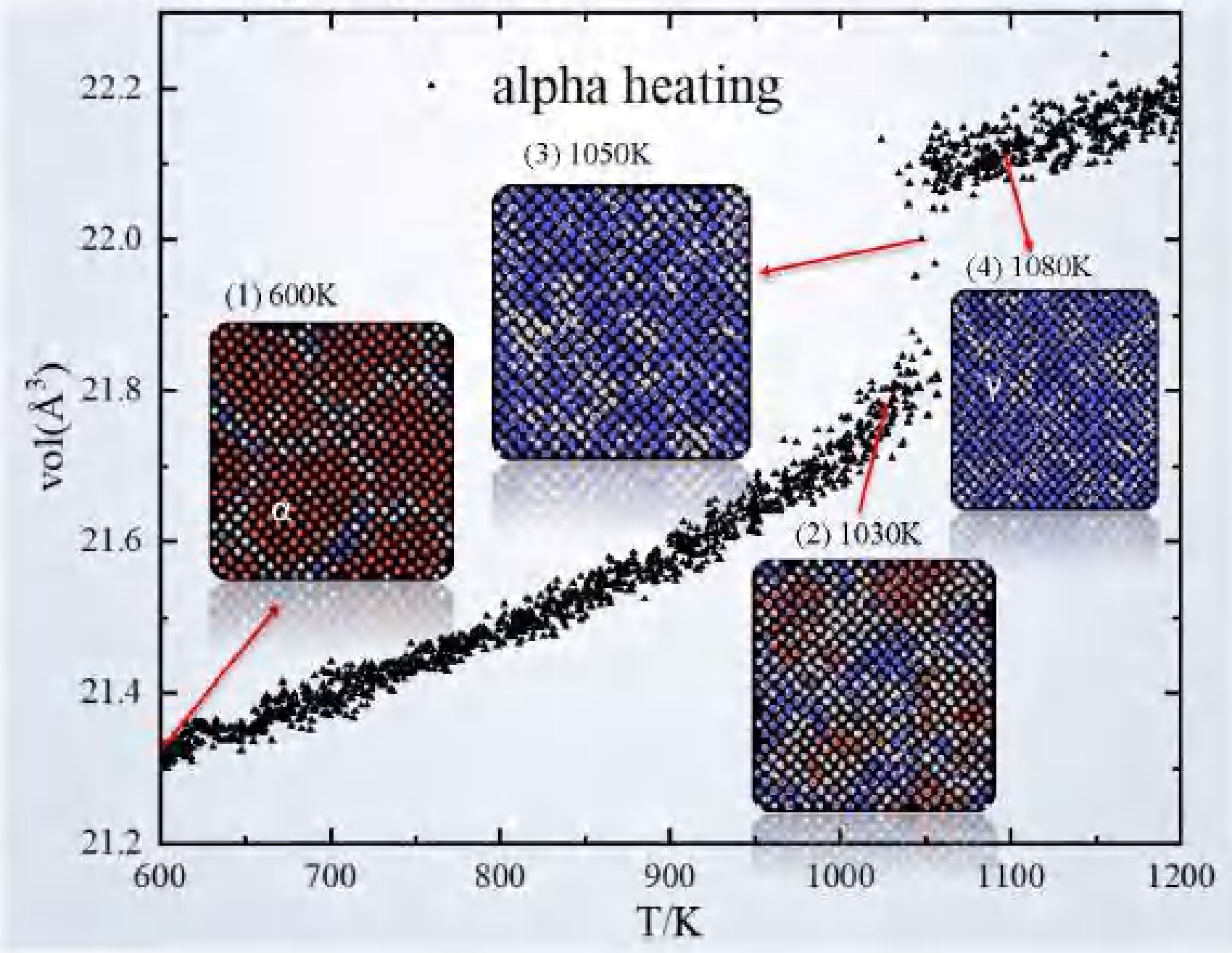

Conclusions

➢(1) The machine learning MTP of metallic uranium can well describe the static properties of α-U, β-U, γ-U, fcc-U and hcp-U.

➢(2) The curve of isobaric heat capacity of α-U calculated by MTP with temperature can show the jump point of heat capacity observed in the experiment, and the calculation result of thermal conductivity is also more reasonable.

➢(3) The β-U will transform into α-U and finally into γ-U with increasing temperature, and pure α-U undergoes α↔γ transition when the temperature increases, of which the phase transition temperature is 1050K.

Support by (National Key Research Project of China, Grant No. 2018YFB0704000)

Contact Me

Email: hjchen@hnu.edu.cn Mobile Phone: 18720988648

Stacking and spin-orbit coupling effects on electronic and excitonic structures of bilayer hexagonal GaTe

Jinsen Han and Jiayu Dai

Department of Physics, National University of Defense Technology, Changsha 410073

Introduction

Two-dimensional materials (2D materials), such as graphene-based materials[1] , transition metal dichalcogenide (TMD)[2] , as well as other Xenes[3] exhibit excellent electronic and optical properties, which provide huge potential applications in spintronics, valleytronics and optoelectronics. The stacking geometry of the multilayer 2D materials will tremendously influence the electronic properties which has been demonstrated by recently emerged twisted graphene candidates, whereby the hidden superconductivity state is revealed by band engineering with magic angle twisting[4]. Here in this poster, we study the geometry stacking effects on tuning the electronic properties of the bilayer hexagonal Gallium Telluride (*bh*-GaTe) based on *ab initio* Many-Body perturbation theory (*ab*MBPT), on this basis, the spin-orbital coupling (SOC) term will strongly influence the exciton behaviors reflected by optical absorption edge. We investigate that an intrinsic hybridized interlayer and intralayer exciton hopping between dark and light state can be tuned by SOC implementation, which results in a pre-edge peak for the absorption curve. This results depict the importance of geometry stacking effects together with SOC for designing the 2D few layer based optoelectronic devices in visible spectrum.

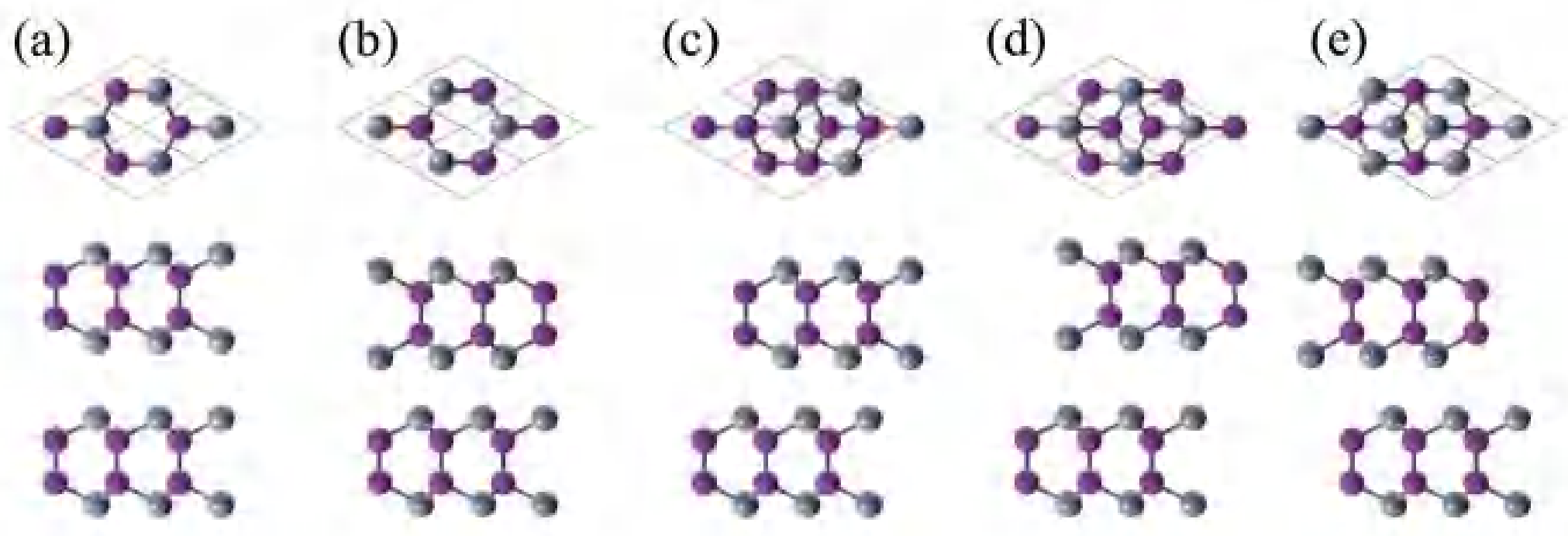

Fig. 1 The stable configurations of *bh*-GaTe. Gallium atoms are purple, and Tellurium are gray. Different stacking structures are shown as (a)-(e) named AA, AA', AB, AB' and AB" respectively. The upper pictures represent the top view and lower one represent the side view.

Method

Density Functional Theory (DFT): [5]

Kohn-Sham Equation

$$ {}_{\mathrm{KS}}[\;] = [\;] + {}_{\mathrm{H}}[\;] + {}_{\mathrm{ext}}[\;] + {}_{\mathrm{xc}}[\;] $$

Many-body Perturbation Theory (MBPT): [6]

Hedin Equation

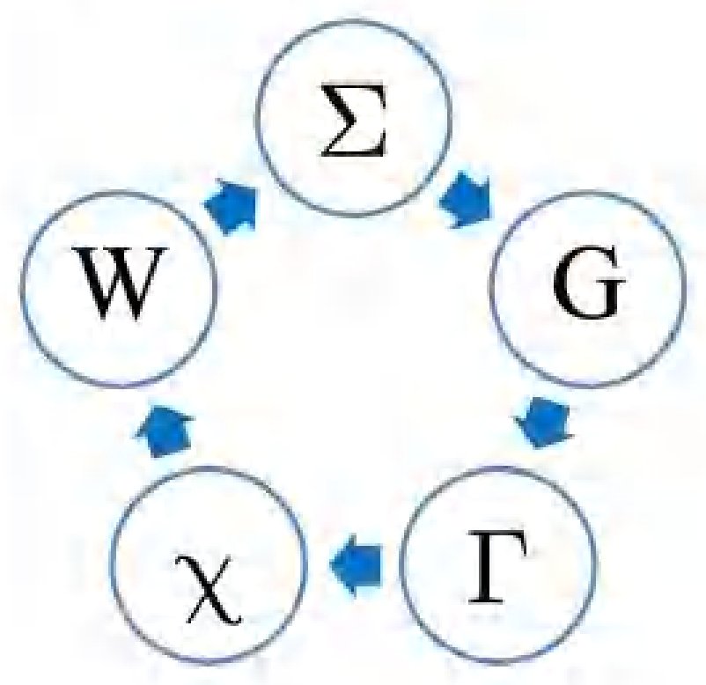

G_0W_0 Approximation

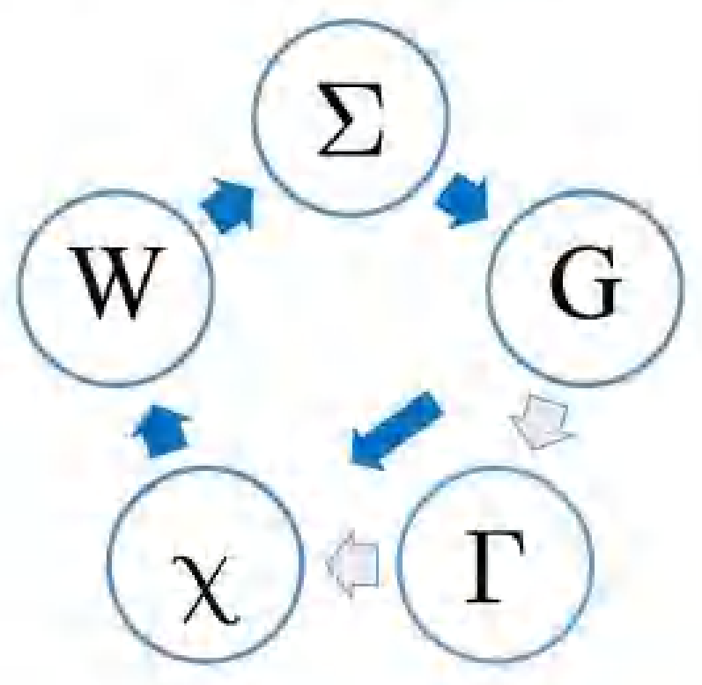

Bethe-Salpeter Equation

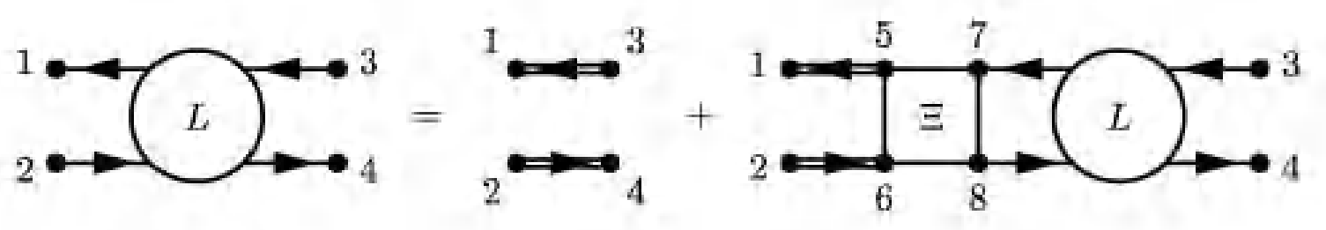

Results & Discussion

Electronic Structures

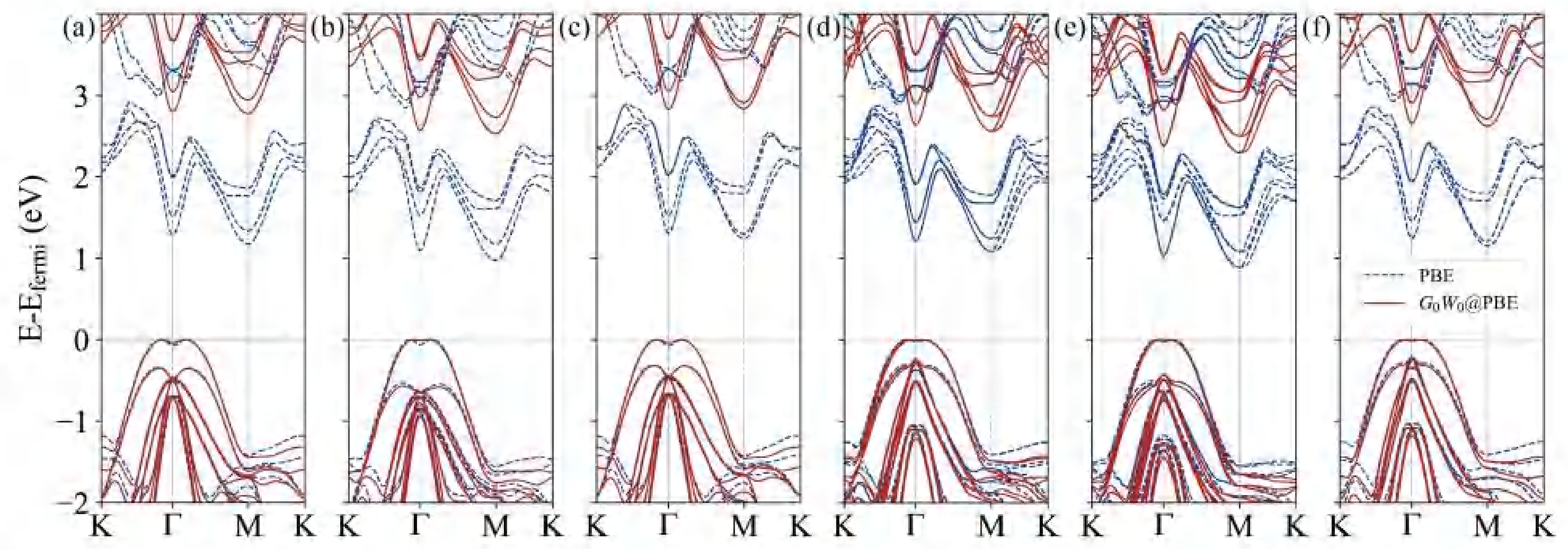

Fig. 2 Band structure of different stacked bilayer hexagonal GaTe, where the top of valance band was shifted at 0 eV, with (a)-(c) columns indicate AA, AB and AB' without SOC and (d)-(f) columns with SOC, respectively. The blue dash line represents the PBE results while the red solid line contains the G0W0 correction.

The electronic structure dependence of the stacking mode. When decreasing the layer distance, the band gap increases due to the increase of interlayer interaction. The DFT calculation underestimates the band gap for such 2D materials with strongly screening Coulomb interaction, however, the quasiparticle will compensate such effects by giving more accurate electronic structure. Because both Gallium and Tellurium have *d*-electrons, the SOC effects would reduce the band gap and change the energy degeneracy for those atomic configuration without spatial inversion symmetry. The SOC changes the shape of band structure, transferring it from indirect gap type to quasi-direct gap type, which is of vital importance to the optical and excitonic properties.

Optical and Excitonic Structures

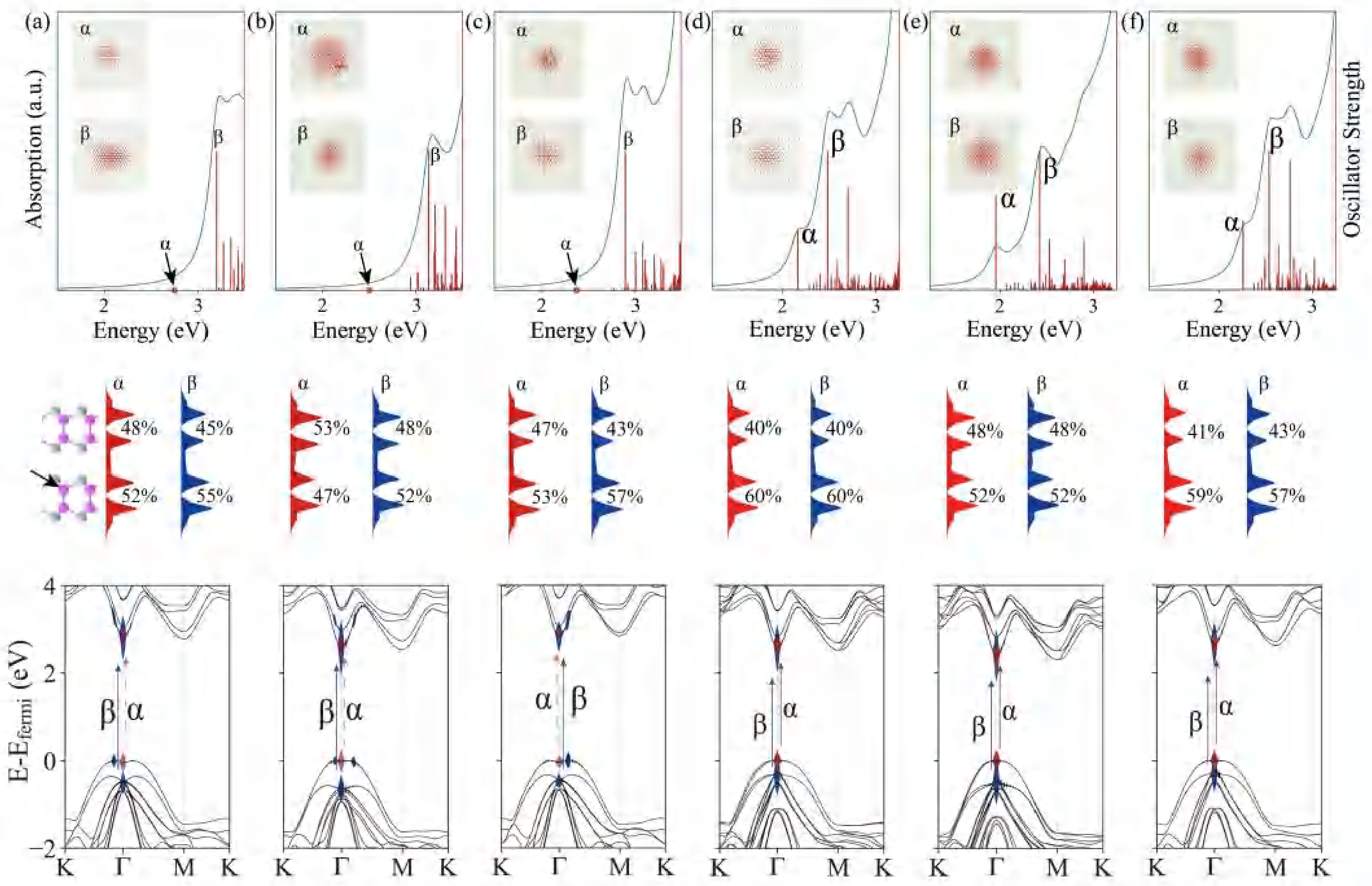

Fig. 3 The upper panel gives optical absorption (green curve) and excitonic oscillator strength (red lines) of different stacked *bh*-GaTe, where (a)-(c) indicate stacking modes AA, AB and AB' without SOC respectively and (d)-(f) indicate the same stacking mode with SOC. The top view of the first several bright exciton distributions in real space for each stacking is listed in subplot, where α (red circle) represents the first exciton and β represents the dominant exciton to the first absorption peak. The middle panel shows the layer distribution of α (red) and β (blue) exciton, where the arrow indicates the hole position located near the Gallium atom in the bottom layer. The bottom panel is the sketch of oscillator strength responsible for both α and β excitons from reciprocal space.

Different stacking modes lead to varied band structures, then different optical absorption spectra complied with electron excitation structures are naturally formed. We find the absorption edge features are closely related with different geometry structure of *bh*-GaTe, therefore can be utilized as an effective diagnosis for multilayer domains. Our calculation reveals that the first prominent excitons are intrinsic hybridized interlayer and intralayer excitons, which leads to a long lifetime of the excitons due to the less overlap of electron and hole wavefunctions. Furthermore, the spin-orbit interaction also plays a role in the redshift of the optical absorption as well as a pre-edge feature, since the transferring from dark state into bright state for the first exciton occurs. Specifically, for AA and AB stacking, the SOC also significantly enlarges the binding energy of first exciton.

Conclusion

We investigate the electronic and excitonic properties of five different type stacking mode *bh*-GaTe based on the first principle many-body perturbation theory. We find that the DFT calculation will underestimate the band gap for all five structures while quasiparticle will give about 1.45 eV energy correction. We find The the electronic structures heavily depend on the stacking mode, with the increase of band gap as the increase of interlayer interaction. Together with spin-orbit coupling, we find the energy-splitting along to K path due to a spatial inversion symmetry breaking for AA and AB stackings. Moreover, the SOC can induce the system from indirect band gap system into a quasi-direct band gap one. The SOC also makes contribution to the redshift of the absorption peak and transfer the first exciton from dark state into bright state. We also report The the geometry dependence of the optical absorption spectra, as well as the underlying excitonic structures. All the excitons near the first absorption peak are composed by intrinsic mixed interlayer and intralayer modes.

Reference

[1] Novoselov, K. S., *et al.*, *Science* **306**, 666–669 (2004).
[2] Mak, K. F., *et al.*, *Phys. Rev. Lett.* **105**, 136805 (2010).
[3] Huang, Z., *et al.*, *Nano Today* **35**, 100906 (2020).
[4] Cao, Y., *et al.*, *Nature* **556**, 43–50 (2018).
[5] Giannozzi, P. *et al.*, *J. Phys. Condens. Matter* **21**, 395502 (2009).
[6] Sangalli, D. *et al.*, *J. Phys. Condens. Matter* **31**, 325902 (2019).

Acknowledgement

Supported by

The National Key R&D Program of China No. 2017YFA0403200
The National NSFC No. 11774429 and No. 12047561
The NSAF No. U1830206
The Postgraduate Scientific Research Innovation Project of Hunan Province No. CX20200012

Contact Information

J. Han: hanjinsen12@nudt.edu.cn
J. Dai: jydai@nudt.edu.cn

Development of machine learning potential to predict grain boundary thermal conductivity

Shihui Ning[1], Hongjian Chen[2], Dingwang Yuan[3], Wangyu Hu[3], Bowen Huang*

College of Materials Science and Engineering, Hunan University, Changsha 410082, PR China

Abstract

We develop a machine learning potential which is based on the optimization of genetic algorithms. The machine learning potential is able to accurately describe the basic properties of thorium dioxide and predicts the thermal resistance of thorium dioxide grain boundaries. The prediction results for five grain boundaries show that the higher the grain boundary energy, the higher the thermal resistance. This work provides an important perspective for the design of thorium dioxide nuclear fuel.

Methods

◆Machine learning potential model and Algorithm

$$E_{\alpha\beta}(r_{ij}) = F_{\mathrm{C}}(r_{ij}) + F_{\mathrm{B}}(r_{ij}) + F_{\mathrm{M}}(r_{ij}) \quad ,F_{\mathrm{C}}(r_{ij}) = \frac{q_\alpha q_\beta}{4\pi\epsilon_0 r_{ij}}$$

$$F_{\mathrm{M}}(r_{ij}) = D_{\alpha\beta}\left[\exp\left(-2\gamma_{\alpha\beta}(r_{ij}-r_0)\right) - 2\exp\left(-\gamma_{\alpha\beta}(r_{ij}-r_0)\right)\right]$$

$$F_{\mathrm{B}}(r_{ij}) = A_{\alpha\beta}\exp\left(\frac{-r_{ij}}{\rho_{\alpha\beta}}\right) - \frac{C_{\alpha\beta}}{r_{ij}^6}$$

◆Algorithm and Optimization flow

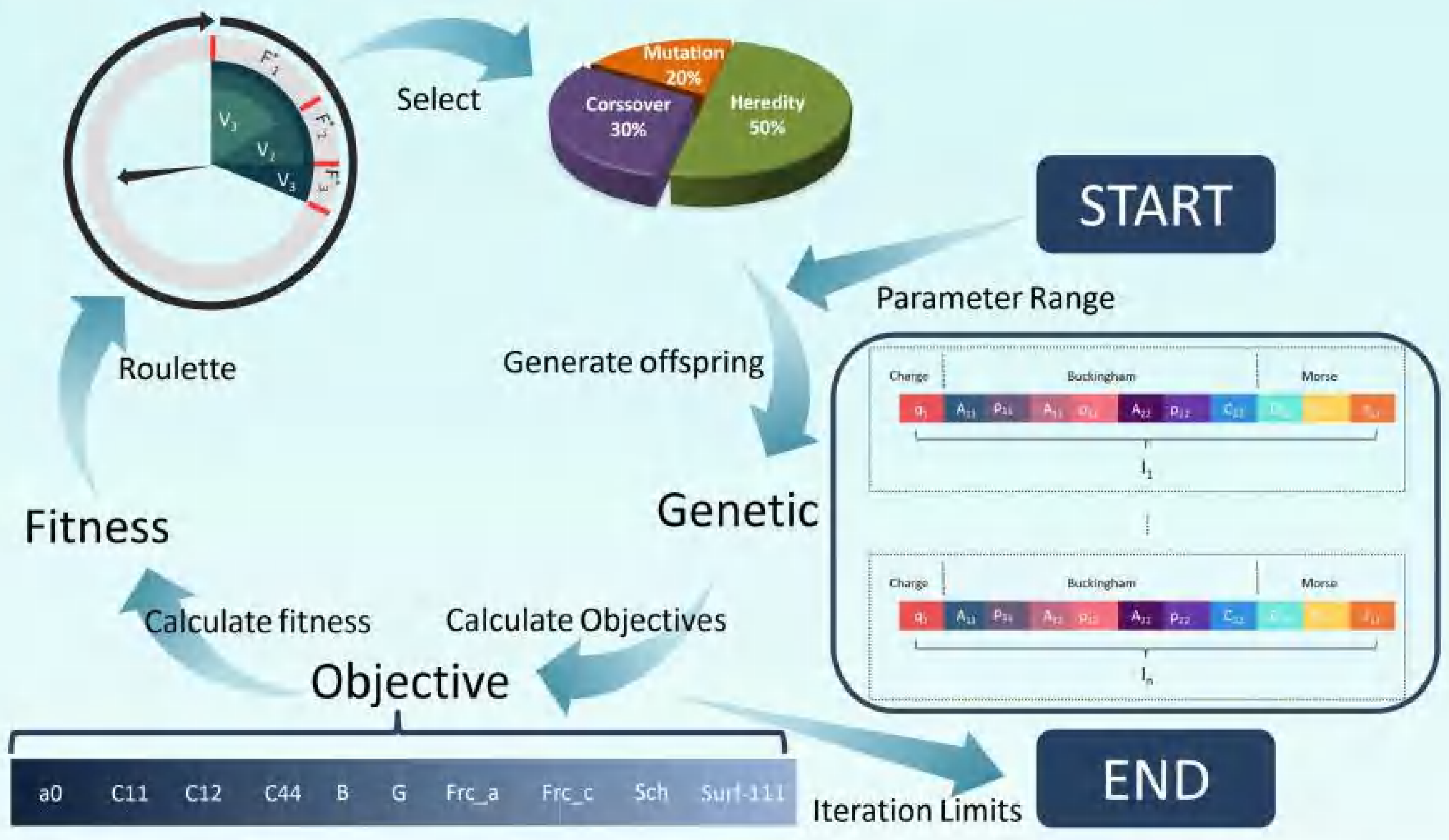

$F_{\mathrm{M}}(r_{ij})$ and $F_{\mathrm{B}}(r_{ij})$ are used to describe the short-range interactions and $F_{\mathrm{C}}(r_{ij})$ describes the long-range interactions, The initial parameters are obtained first, and then the parameter set is used to calculate the objective, to obtain the individual fitness, and then the genetic individual and type are determined.

◆Optimization results

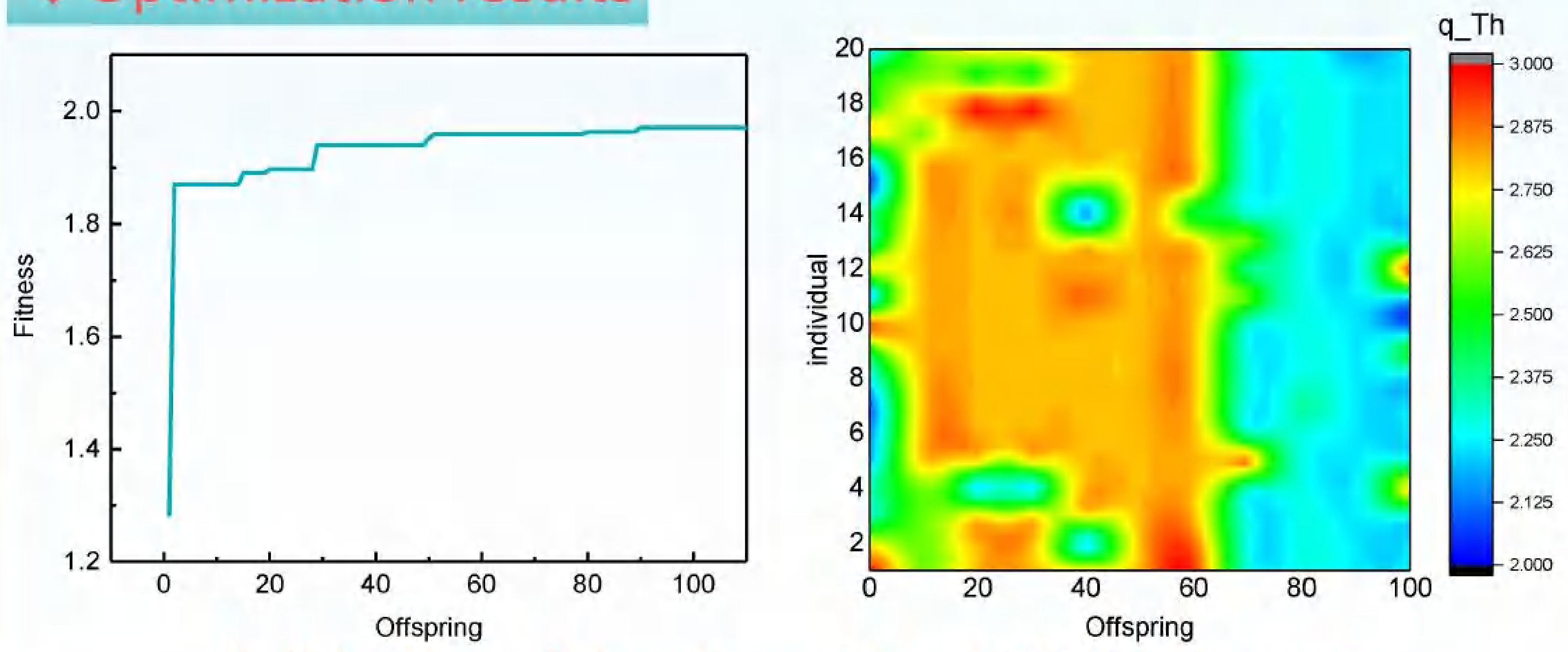

The higher Fitness, the lower the error. Automatic Optimized parameters

$F_{\mathrm{B}}(r_{ij})$	Th	Th	11499.19	0.169724	0
	Th	O	951.5263	0.328916	0
	O	O	1534.594	0.340045	3.381945
$F_{\mathrm{M}}(r_{ij})$	Th	O	1.085366	1.645179	2.352348

The most optimal Combination of potential parameters

fitness increases with iteration indicating that the computational error decreases. The optimization parameters tend to stabilize with iteration. The final optimization to get a combination of potential that less than the error range, and the next step is to talk about the potential to predict the thermal conductivity properties of thorium dioxide

prediction

◆Basic properties

Basic property calculation including lattice constant (a0), modulus of elasticity, point defect energy, surface energy

Objective	Exp[1]	DFT	MLP(this work)	CRG[2]	Nashk[3]	Oakuy[3]
a0(Å)	5.599	5.6	5.593	5.593	5.594	5.579
C11(GPa)	367	367	363	352	573	441
C12(GPa)	106	106	100	113	168	93
C44(GPa)	79	79	82	71	132	86
Bulk modulus(GPa)	195	195	188	193	303	209
Shear modulus(GPa)	96	96	101	90	157	115
Frenkel_O	-	4.2	5.82	5.03	6.6	7.64
Frenkel_Th	-	13.5	13.3	13.65	19.39	20.56
Sch	-	5.5	9.6	6.39	10.39	13.79
Surface_111	-	0.053	0.02	-	0.056	0.066

[1]LANG, S. M., & KNUDSEN, F. P. (1956). *Journal of the American Ceramic Society.*
[3]Cooper, M. W. D., Rushton, M. J. D., & Grimes, R. W. (2014). *Journal of Physics Condensed Matter*, *26*(10).
[3]Behera, R. K., & Deo, C. S. (2012). Journal of Physics Condensed Matter, 24(21).

◆Thermal conductivity prediction

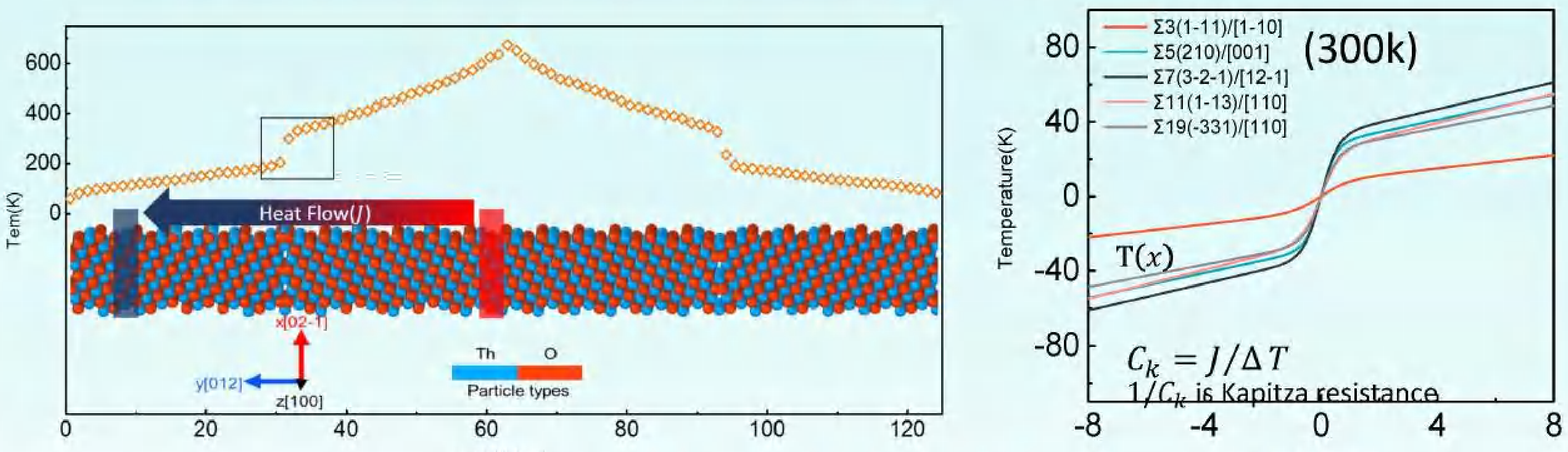

Non-equilibrium method of calculating thermal conductivity

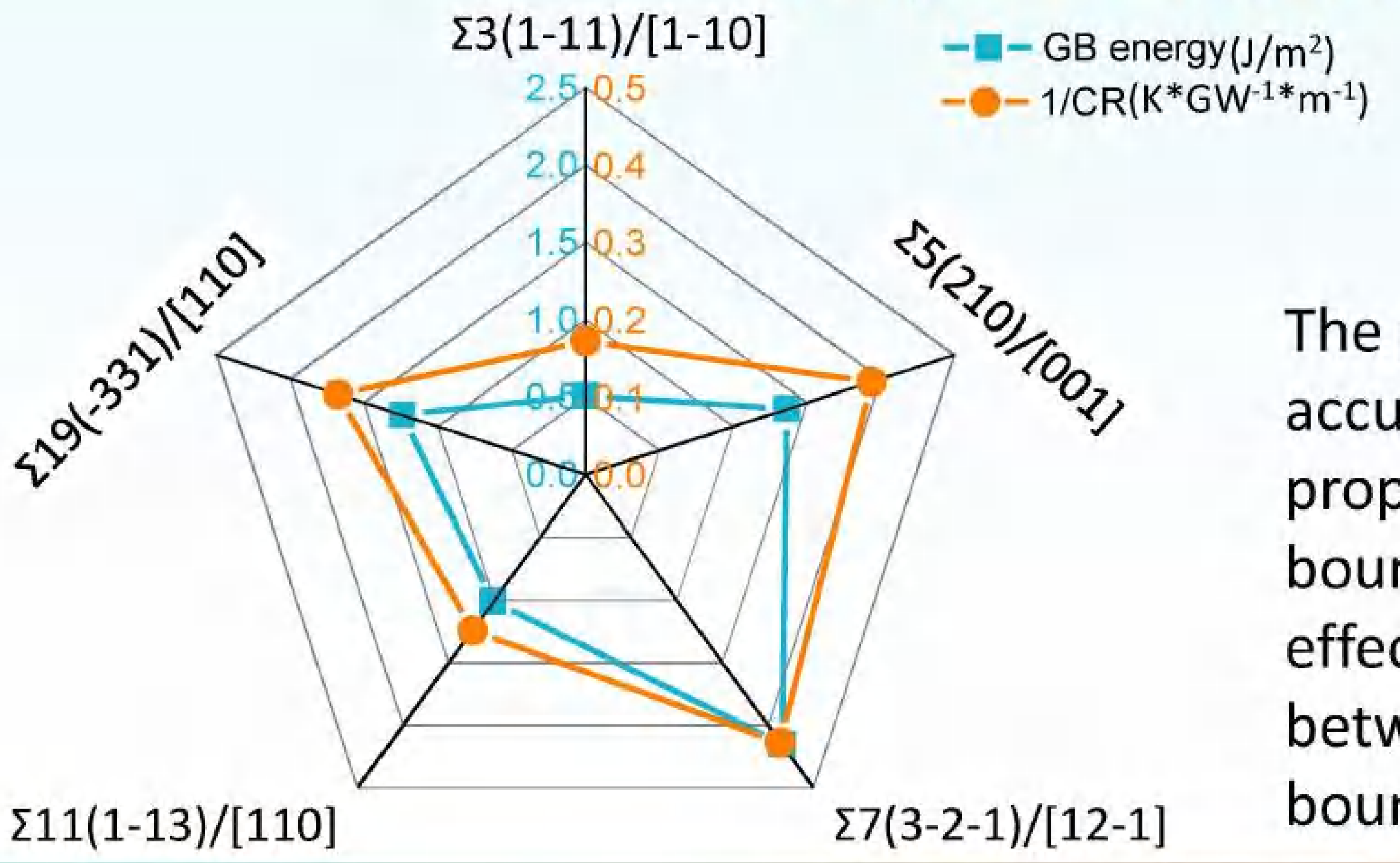

The potential of this work is able to accurately calculate the fundamental properties of thorium dioxide. All grain boundaries have thermal resistance effects and there is a strong correlation between thermal resistance and grain boundary energy.

Conclusion

- Provides an effective machine learning method for potential optimization
- The potential of this work can accurately predict properties of thorium dioxide

Acknowledgements (National Key Research Project of China, Grant No. 2018YFB0704000)

Spin Seebeck effect and magnetoresistance in zigzag antimony nanoribbons

Liyan Lin, Yandong Guo*, Hongli Zeng, Yue Jiang, Xiaohong Yan
College of Electronic and Optical Engineering, Nanjing University of Post
and Telecommunications, Nanjing 210046, China

Abstract

Due to their novel physical and chemical properties, two-dimensional (2D) materials have been widely investigated both theoretically and experimentally. We investigate the spin-dependent electric and thermoelectric properties of zigzag antimony nanoribbons using density-functional theory combined with non-equilibrium Green's function method. Spin Seebeck effect (SSE) and a large magnetoresistance are discovered in freestanding honeycomb antimoney nanoribbons with zigzag edge.

Background

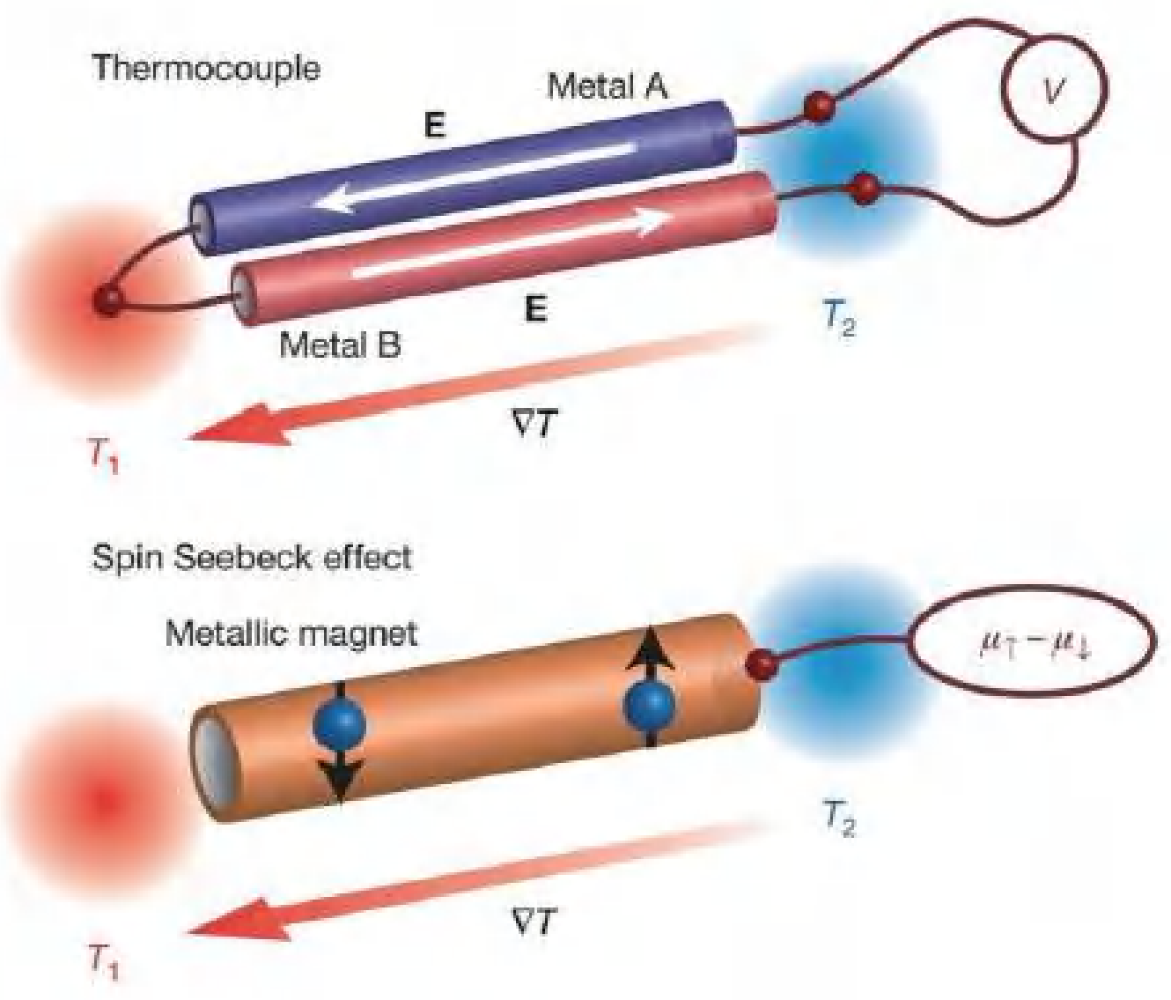

Illustration of a thermocouple and the spin Seebeck effect[1]

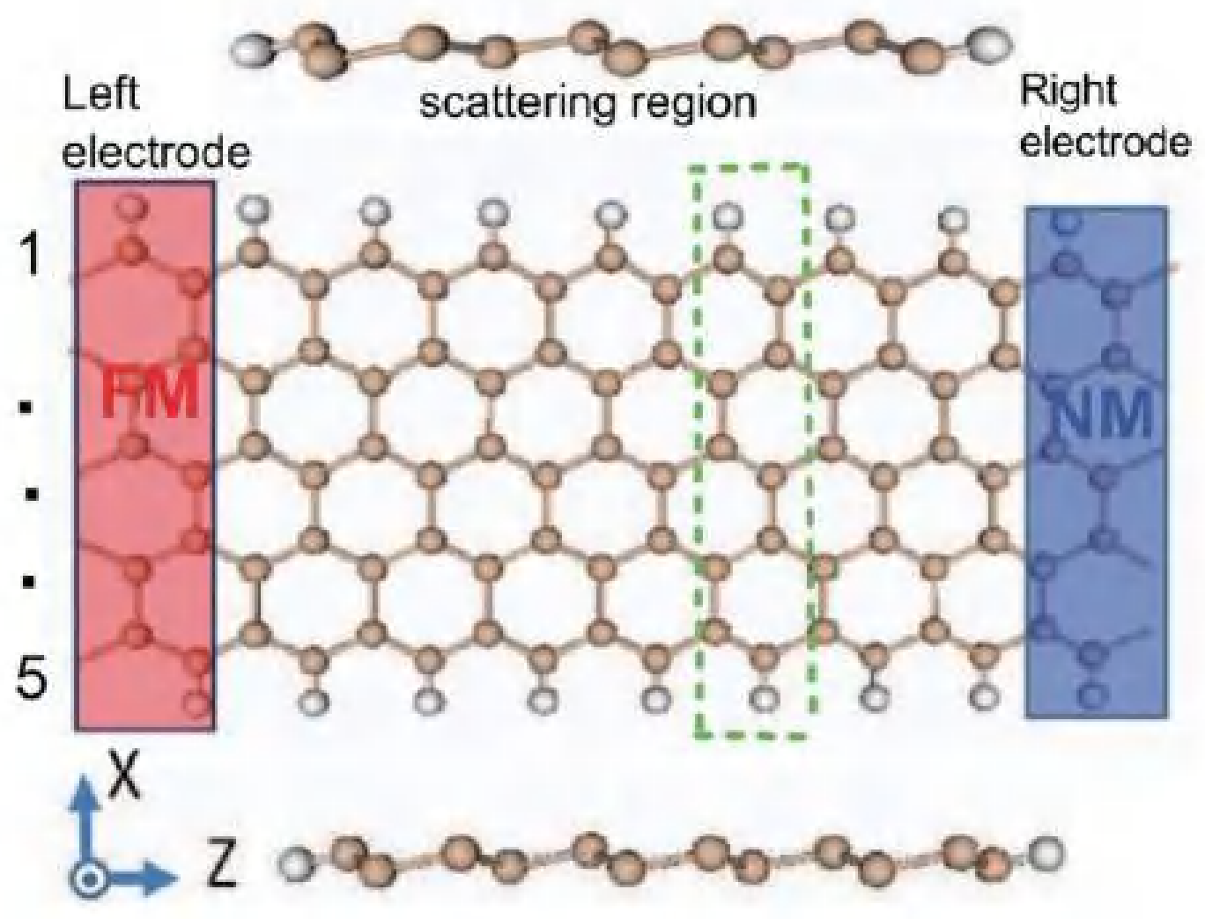

Illustration of the thermospin device based on a zigzag-edge silicene nanoribbons[2]

What about the zigzag antimony nanoribbons?

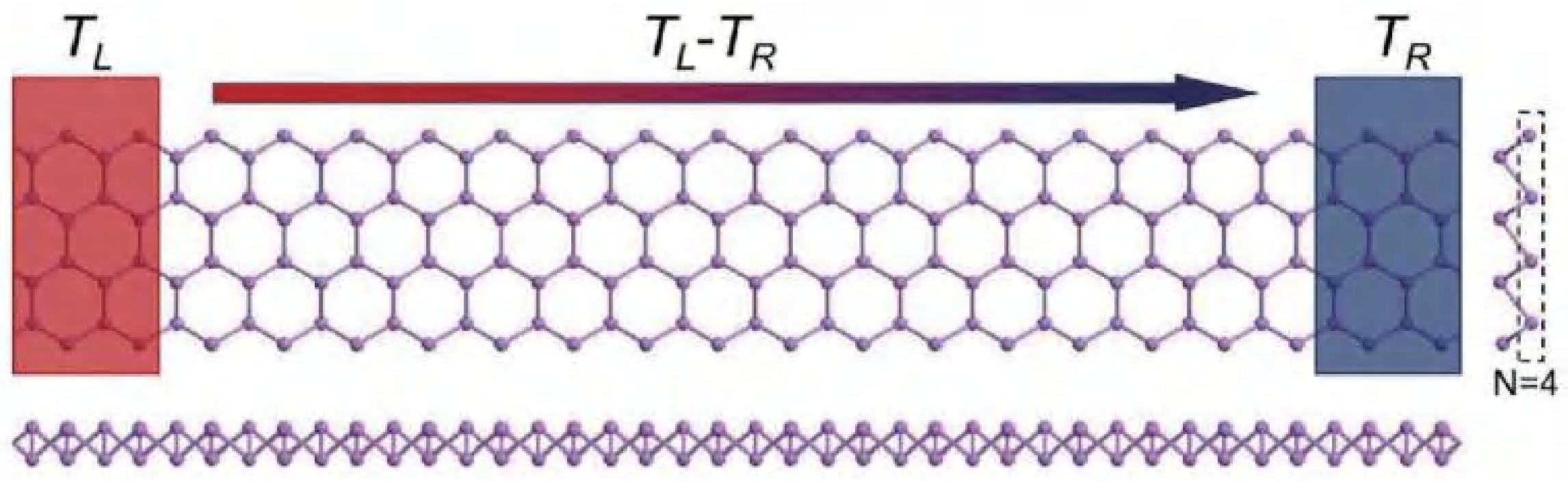

The schematic diagram of zigzag antimony nanoribbon-based thermal spin caloritonics device.

Results and discussion

Spin Seebeck effect in zigzag antimony nanoribbons

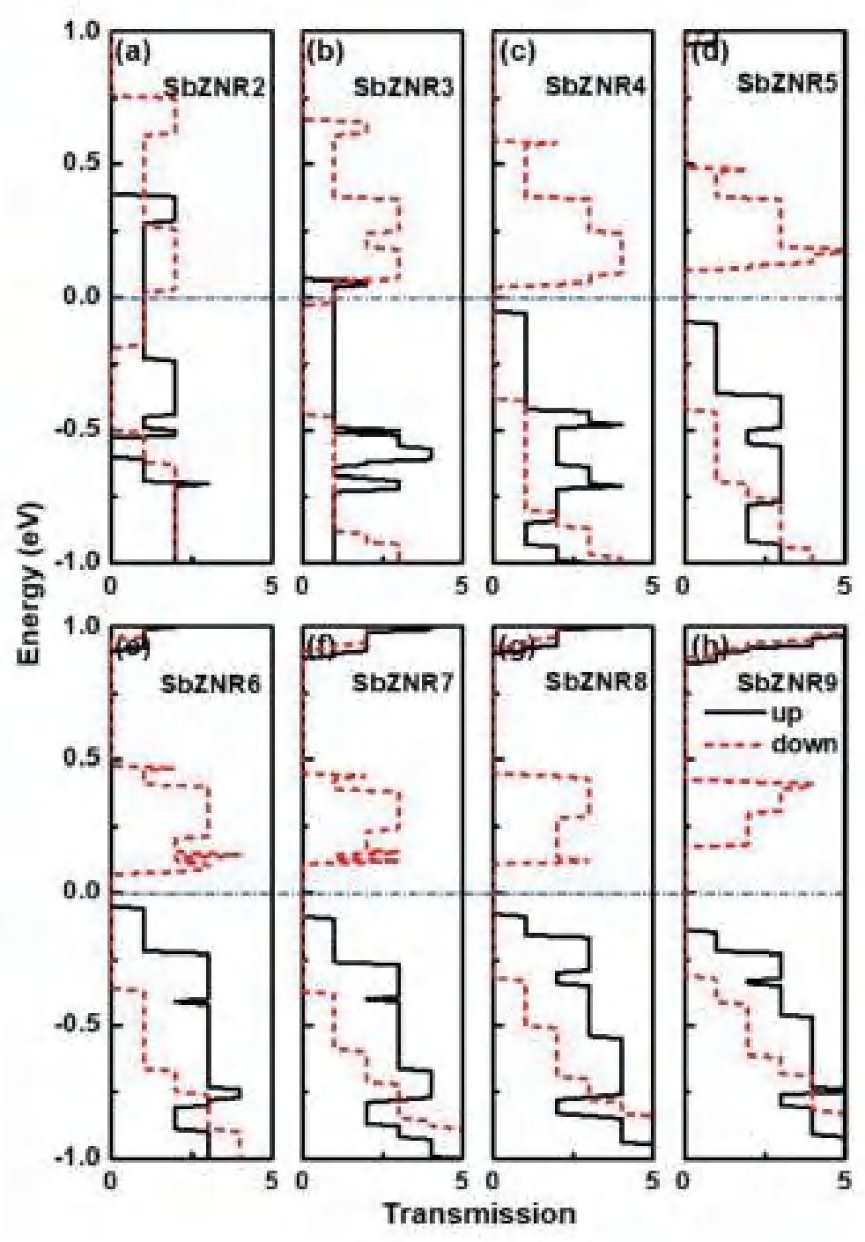

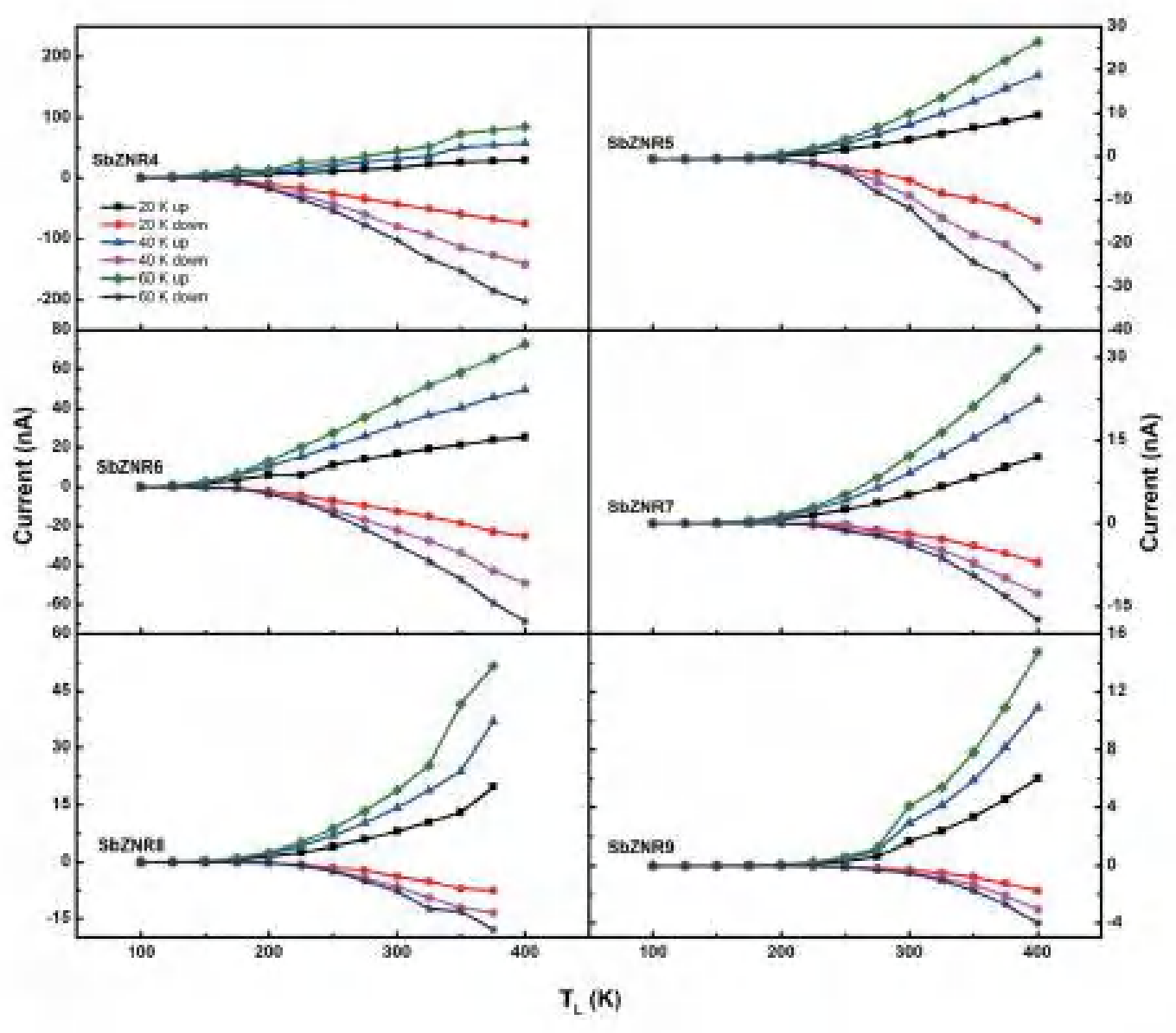

- The transmission of spin-up and o spin-down reside discretely on both sides of E_F.
- Spin-dependent current and temperature of the six structures by applaying a temperature gradient.

Magnetoresistance in zigzag antimony nanoribbons

- Magnetoresistance(MR)in the SBZNR2-SBZNR9 at zero bias.

Structure	$G^P(\mu s)$	$G^{AP}(\mu s)$	MR(%)	Structure	$G^P(\mu s)$	$G^{AP}(\mu s)$	MR(%)
SbZNR2	77.0	4.34×10^{-1}	1.76×10^4	SbZNR3	37.9	4.91×10^{-2}	7.70×10^4
SbZNR4	1.20×10^{-11}	2.13×10^{-13}	5.54×10^3	SbZNR5	5.69×10^{-13}	3.91×10^{-14}	1.35×10^3
SbZNR6	8.01×10^{-13}	4.37×10^{-14}	1.73×10^3	SbZNR7	2.58×10^{-13}	4.83×10^{-14}	4.34×10^2
SbZNR8	3.85×10^{-13}	7.01×10^{-14}	4.48×10^2	SbZNR9	2.71×10^{-13}	1.03×10^{-13}	1.63×10^2

Computational method

- **DFT & NEGF[3,4]**
- **PBE & GGA[5]**

Atomistix Toolkit package

References

[1]K. Uchida, S. Takahashi, K. Harii, et al., Nature, 2008, 455, 778–781.

[2] X. Yang , Y. Liu S , J. Feng, et al., Aip. Adv., 2014, 4, 261905.

[3] M. Brandbyge, J.-L. Mozos, P. Ordejón, et al., Phys. Rev. B: Condens. Matter Mater. Phys., 2002, 65, 165401.

[4]J. Taylor, H. Guo and J. Wang, Phys. Rev. B: Condens. Matter Mater. Phys., 2001, 63, 245407.

[5]J. P. Perdew, K. Burke and M. Ernzerhof, Phys. Rev. Lett., 1996, 77, 3865–3868.

Negative Poisson Ratio in Two-Dimensional Tungsten Nitride: Synergistic Effect from Electronic and Structural Properties

Wenyuan Jin,[†] Weiguo Sun,[†] Xiaoyu Kuang,[†,] Cheng Lu,[‡,*] Liangzhi Kou[‖,*]*

[†]Institute of Atomic and Molecular Physics, Sichuan University, Chengdu 610065, China
[‡]School of Mathematics and Physics, China University of Geosciences (Wuhan), Wuhan 430074, China
[‖]School of Mechanical, Medical and Process Engineering, Queensland University of Technology, Brisbane, Queensland 4001, Australia
Queensland 4001, Australia

ABSTRACT

Low-dimensional materials with high stabilities and outstanding mechanical properties are essential for next generation microelectromechanical systems (MEMS). The successful synthesis of two-dimensional (2D) tungsten nitride makes it a promising candidate for the MEMS application. Here, we have confirmed the existence of experimentally synthesized W_2N_3 and predicted three additional new 2D monolayer tungsten nitrides: WN_2,WN_4, and W_3N based on extensively structural searches by CALYPSO method and first-principle calculations. The calculations indicate that the nitrogen-rich WN_4 monolayer possesses large in-plane negative Poisson ratios $\nu_x = -0.103$ and $\nu_y = -0.113$, which are attributed to the 4-foldcoordinated WN_4 tetrahedron combined with the strong coupling between the 2p orbitals of N and 5d orbitals of W. Our findings not only enrich the family of 2D transition metal nitrides with excellent mechanical properties but also open avenues for design and synthesis of other novel 2D layered materials.

METHODS

First-principles calculation and Crystal structure prediction

The ground state structural searches of 2D tungsten nitrides are carried out by unbiased CALYPSO structural search method. The structural optimizations and energy calculations are performed by Vienna ab initio simulation package (VASP). All of the monolayer structures are separated by a vacuum space of at least 15 Å in the z direction to avoid the interactions between adjacent layers due to the periodicity.

RESULTS

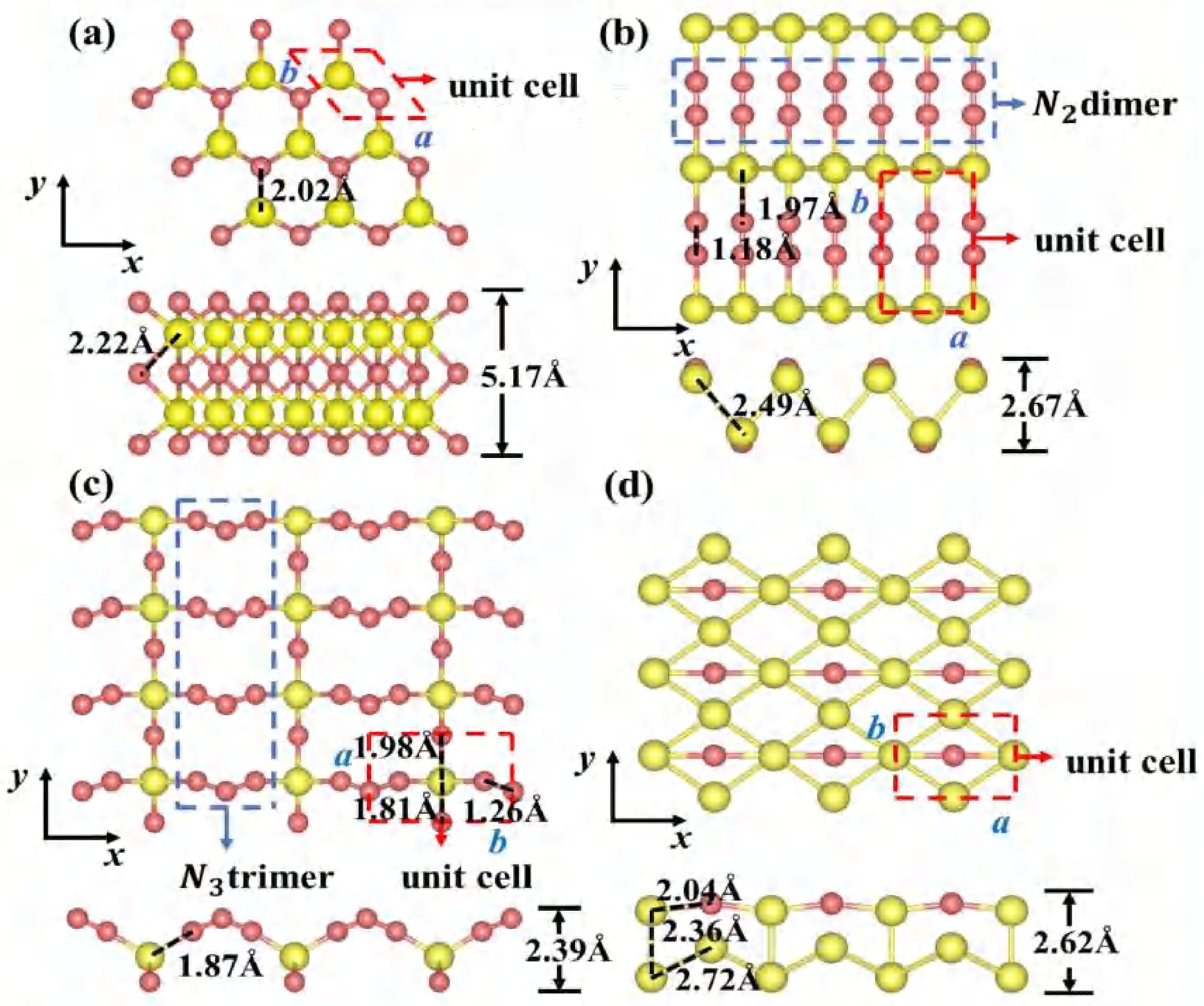

FIG 1. Top and side views of monolayer (a) W_2N_3 (b) WN_2, (c) WN_4, and (d) W_3N. W and N atoms are represented by yellow and pink spheres, respectively.

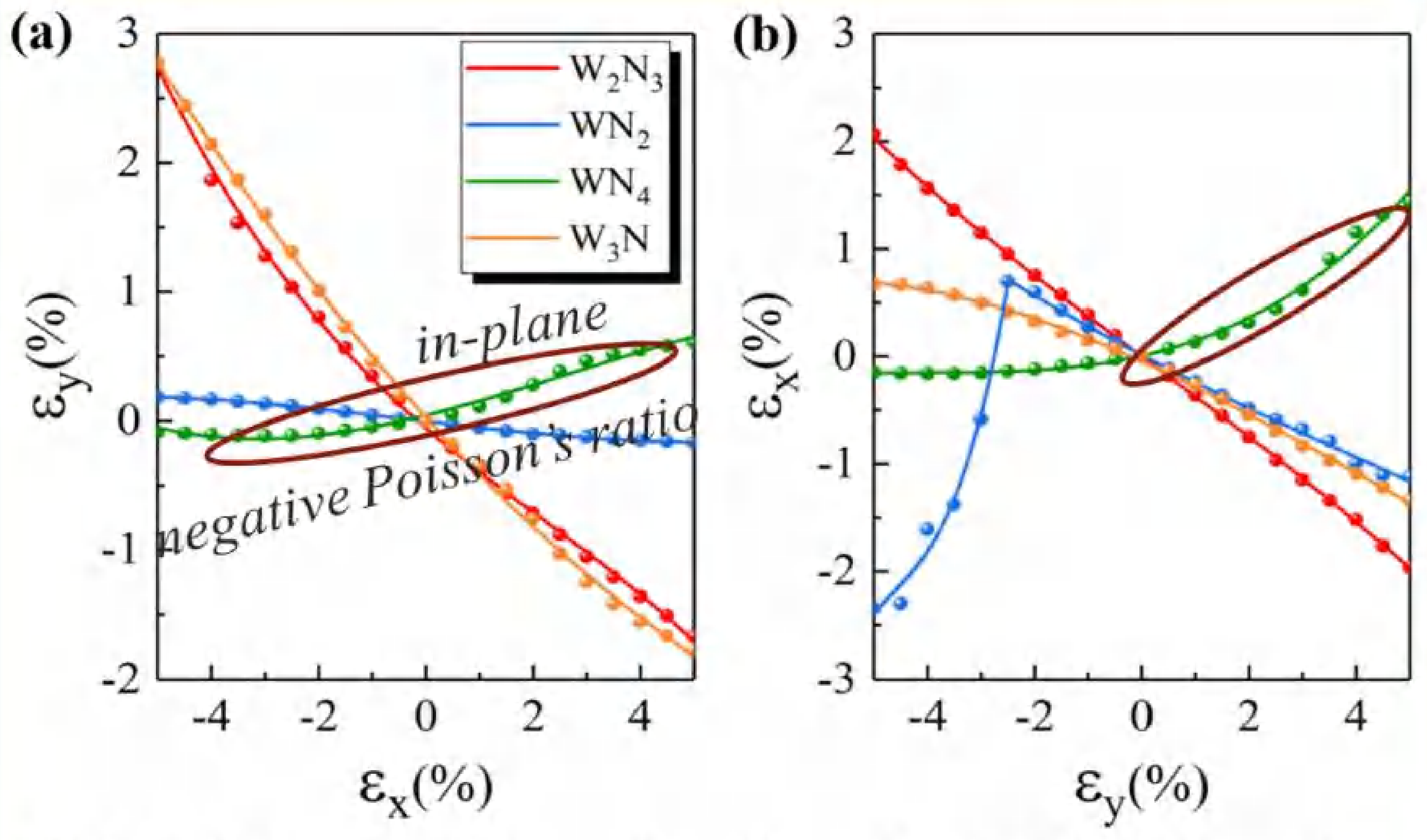

FIG 2. Poisson ratio as a function of uniaxial deformation of W_2N_3, WN_2,WN_4, and W_3N monolayers in the (a) x-axis and (b) y-axis.

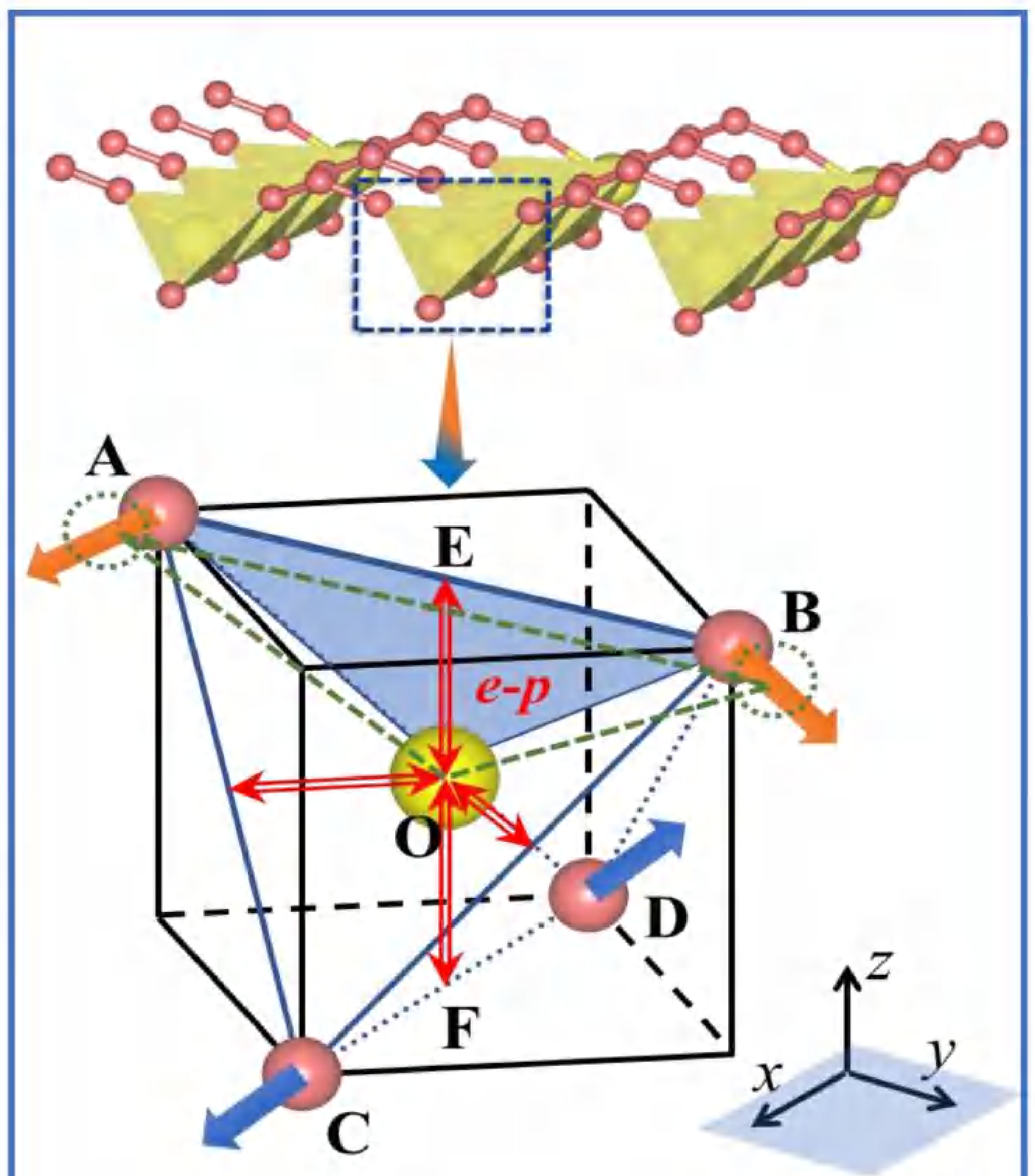

FIG 3. Explanation of the Poisson ratio for WN_4 monolayer. Each W atom is coordinated by four N atoms, forming a WN_4 tetrahedron. The force is applied along the x-axis. The red arrows indicate the direction of the e−p orbital interactions. The orange arrows show the resulting movement of the N atoms within the A−O−B plane.

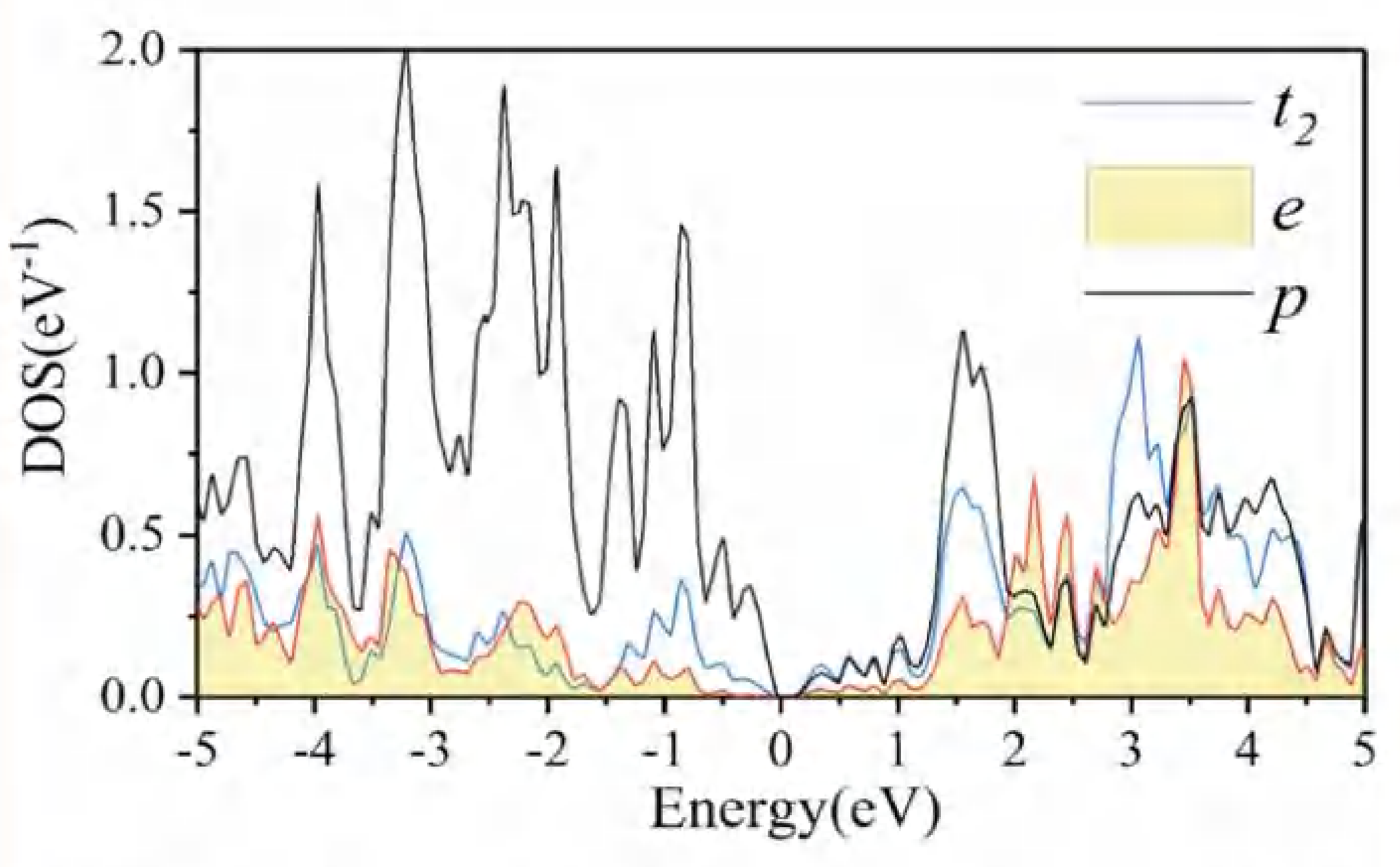

FIG 4. Partial DOS of WN_4 monolayer. The e−p orbital coupling manifests itself in the overlap of their DOS. The Fermi level is set to zero.

THEORY

Crystal field theory and Pauling's third rule

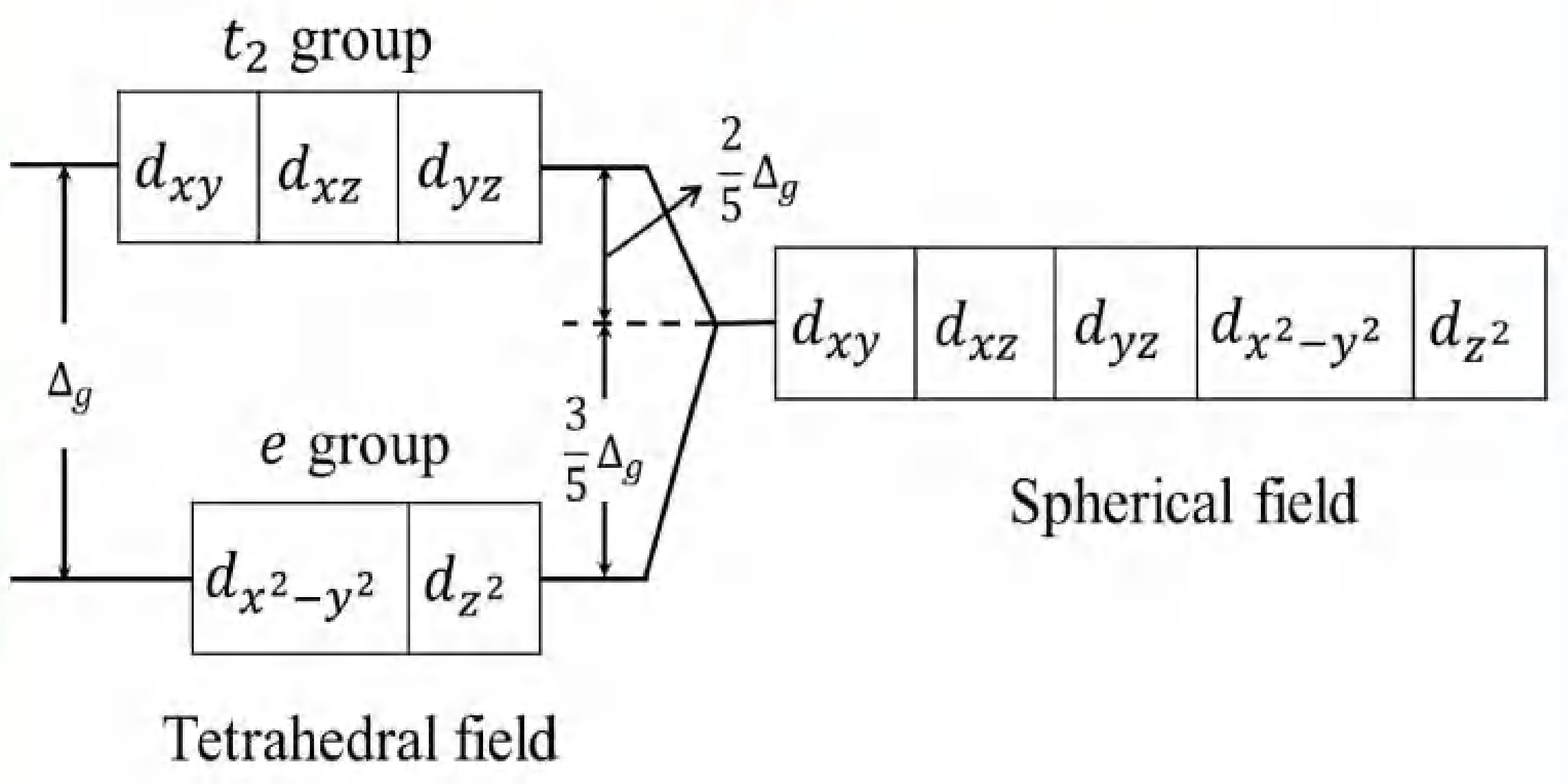

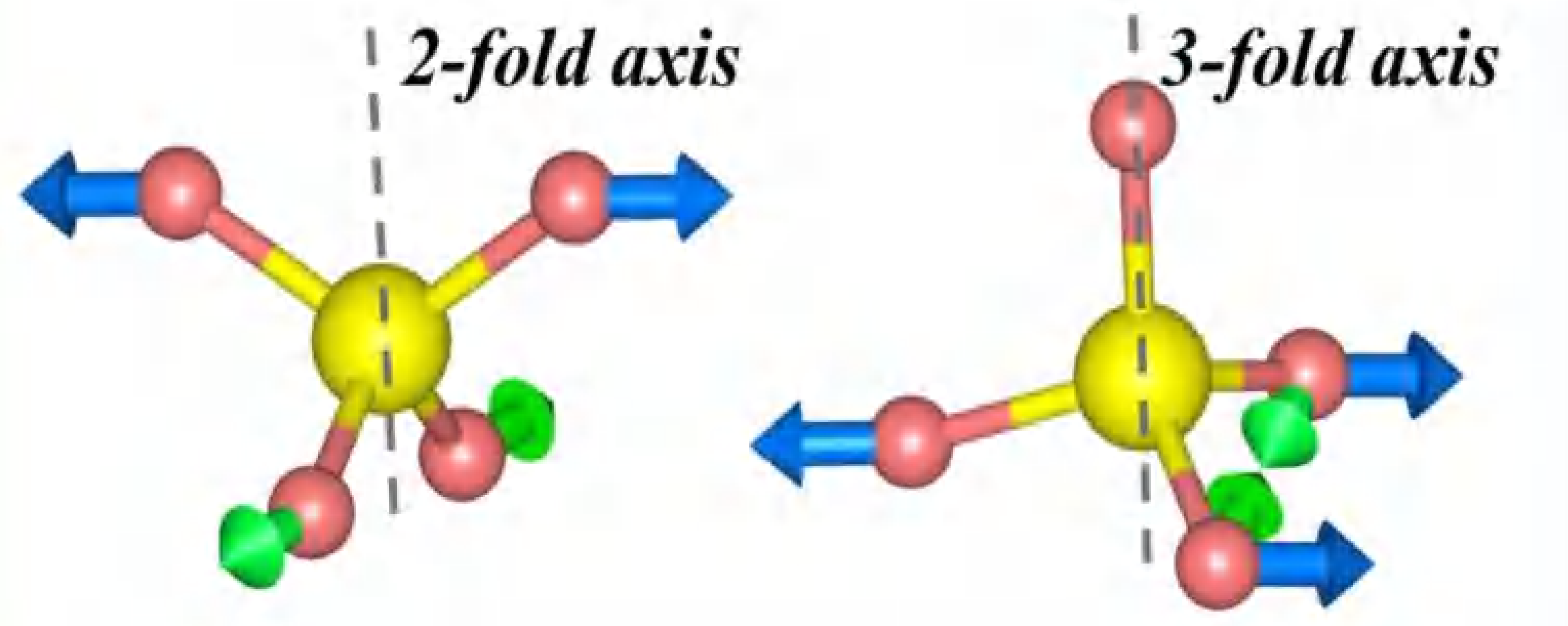

CONCLUSIONS

- **Found the first transition metal nitrides with large negative Poisson ratio (NPR)**
- **Propose a reasonable explanation about the mechanism of negative Poisson ratio**
- **Discovered the influence of low-dimensional and crystal fields effects on the mechanical properties of two-dimensional system**
- **Identified the synthesized 2D hexagonal-W_2N_3 and uncovered three new stable monolayers of WN_2,WN_4, and W_3N**

ACKNOWLEDGEMENT

This work is supported by National Natural Science Foundation of China (Nos. 12111530103, 12174352 and 11874043)

Reference: W. Jin, W. Sun, X. Kuang, C. Lu, L. Kou, J. Phys. Chem. Lett. 2020, 11, 9643−9648
Electronic address: [a] scu_kuang@163.com (Xiaoyu Kuang), [b] lucheng@ calypso.cn (Cheng Lu), [c] liangzhi.kou@qut.edu.au (Liangzhi Kou).

The Magnetic and Electronic Properties of Monolayer Transition Metal Silicides: First-principles Study

2022材料多尺度计算模拟国际会议

2022 ICM^3

宁波大学物理科学与技术学院

School of Physical Science and Technology

Xu-Xin Kang,[a] Jun Hu[a,b,*] and Xiang-Mei Duan[a,b,*]

[a] School of Physical Science and Technology, Ningbo University, Ningbo, P.R. China.

[b] Laboratory of Clean Energy Storage and Conversion, Ningbo University, Ningbo, P.R. China.

Introduction

- 2D magnetism materials have great potential for various applications;
- 2D FM materials such as CrI_3 and Fe_3GeTe_2 have been synthesized;
- We systematically studied the magnetic configuration and electronic properties of monolayer TM_2Si (M = Cr, Mo, W) with different U values;
- We also demonstrated that the oxygen functionalization and biaxial strain can effectively tune the electronic properties.

Methods

- Using Vienna Ab-initio Simulation Package(VASP);
- Spin-polarized calculations were adopted;
- The GGA in the form of the PBE function;
- GGA + U was used to examine the magnetic configuration;
- The effect of Spin-Orbit Coupling (SOC) was included in the electronic band structure calculations.

Results and Discussions

I) Structure and magnetic states of Cr_2Si

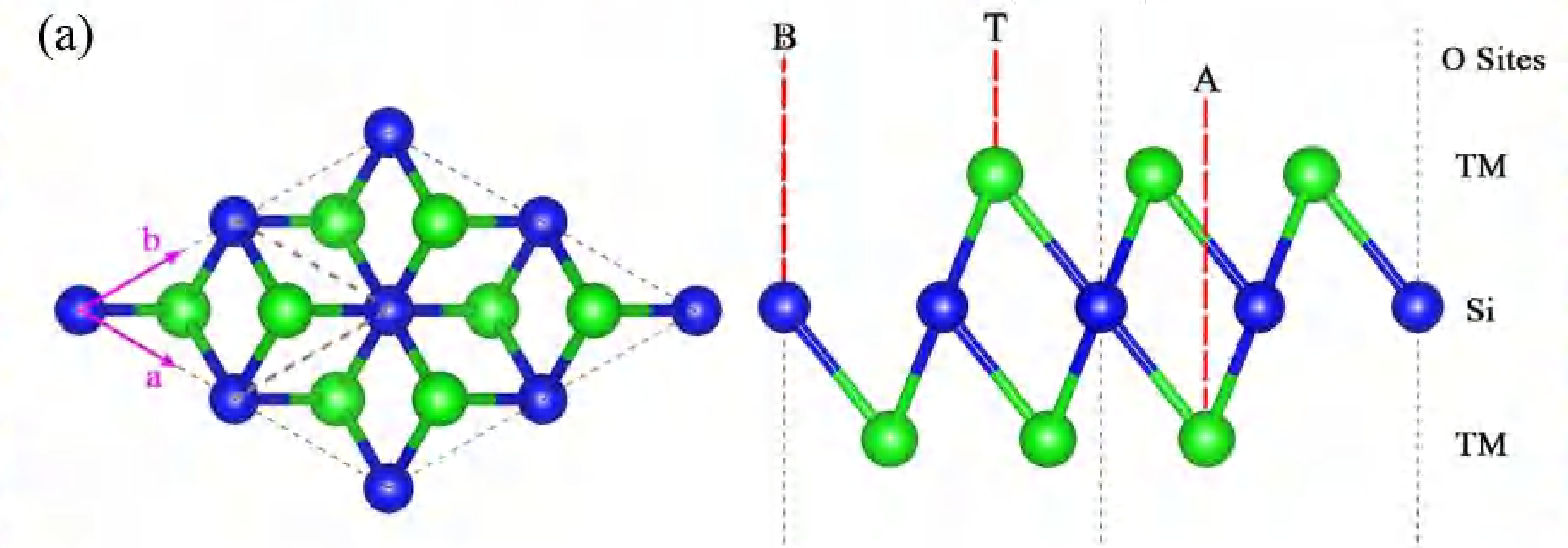

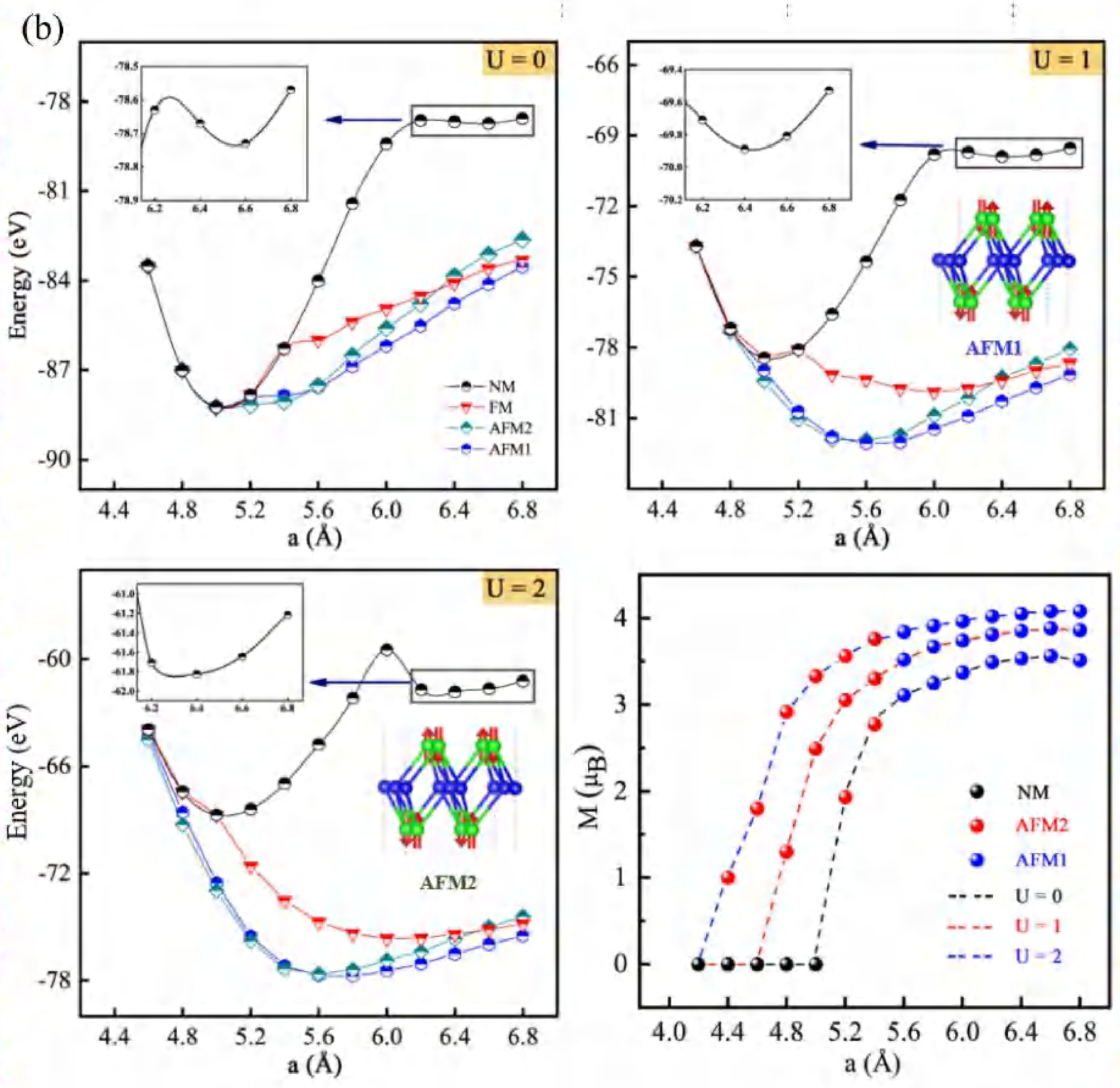

- ✓ The strong Coulombic interactions between Cr-3d electrons, ground state: **U = 0, NM; U = 1, AFM1; U = 2, AFM1**;
- ✓ a = 6.4 ~ 6.6 Å has the local minimum in NM configuration;
- ✓ As the U values increases, the energy difference between NM and magnetic configurations gradually increases;
- ✓ The magnetic moment increases gradually with the increase of the lattice.

II) Ground state and oxygen tuned energy band structures of Mo_2Si, W_2Si

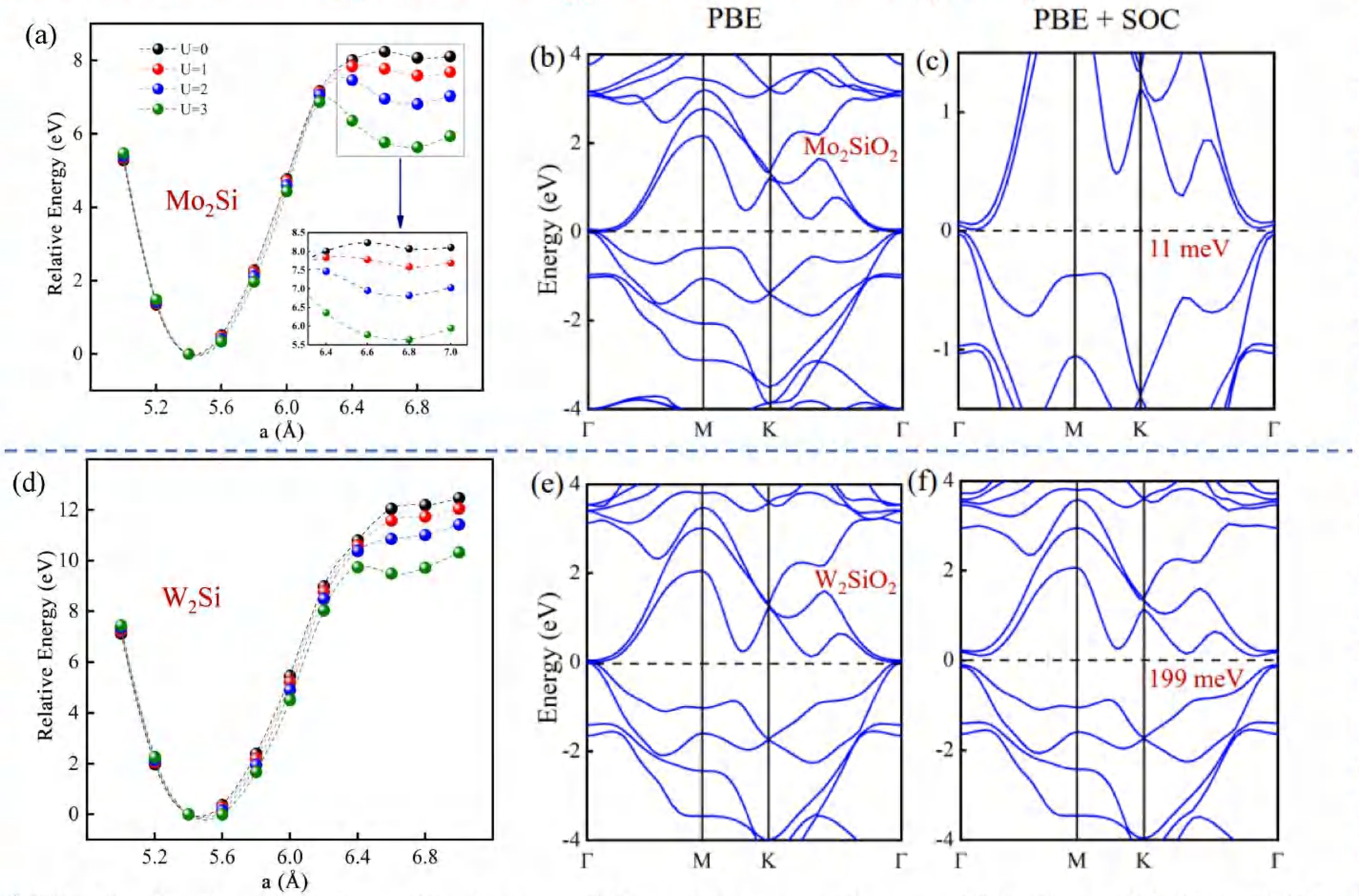

- ✓ The Coulomb correlation effect is negligible and the ground state of Mo_2Si and W_2Si are NM;
- ✓ There is a degenerate band touch point on the Fermi level of Mo_2SiO_2 and W_2SiO_2 without SOC, and the indirect band gap of W_2SiO_2 is as large as **199 meV** with SOC.

III) Biaxial strain tune the electronic properties of Mo_2SiO_2 and W_2SiO_2

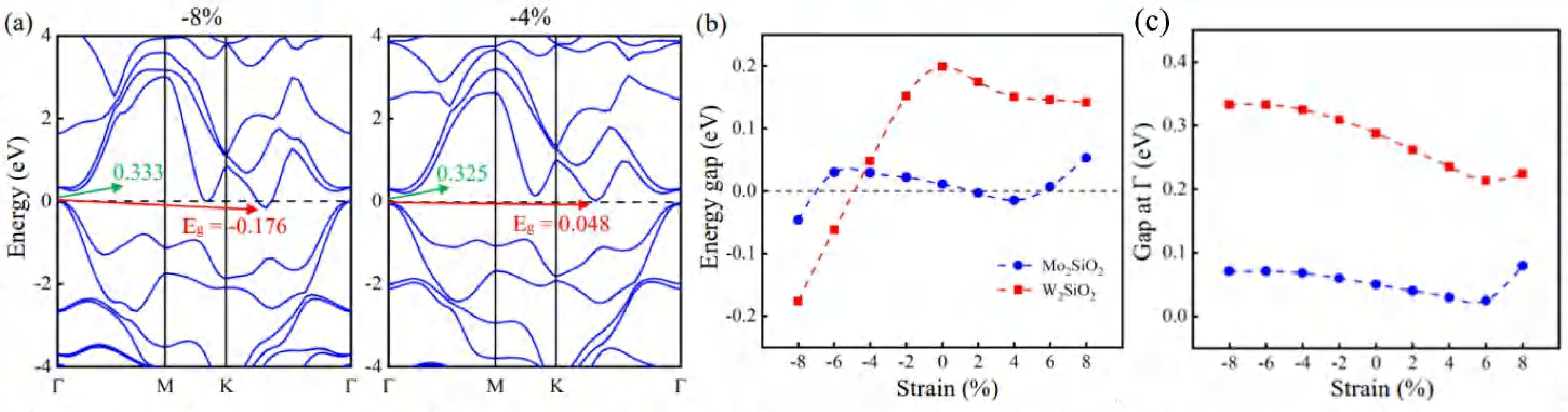

- ✓ For Mo_2SiO_2, a back and forth transition insulator-metal is achieved in range of -8~8%;
- ✓ For W_2SiO_2, the band gap gradually decreases with tensile strain increases, while compression strain achieves a transition from semiconductor to metal.

Conclusions

- The ground state of monolayer Cr_2Si is AFM1, while Mo_2Si and W_2Si are nonmagnetic;
- Coulomb U plays an important role in the Cr_2Si, but has almost no effect on Mo_2Si and W_2Si;
- Oxygen functionalization causes a transition from metal to half metal, and the SOC-induced band gap of W_2SiO_2 as large as 199 meV;
- Insulator-to-metal transition in Mo_2SiO_2 and W_2SiO_2 occurs when moderate biaxial strain is applied.

References

1. H. M. Weng et al., *Phys. Rev. B* 2015, **92**, 075436.
2. H. Hadipour and Y. Yekta, *Phys. Rev. B* 2019, **100**, 195118.
3. X. L. Lan and F. Y. Li et al., *Phys. Status Solidi RRL* 2021, **15**, 2100048.
4. E. German, R. Faccio et al., *J. Phys. Commun.* 2017, **1**, 055006.
5. Z. X. Shen and X. G. Wan et al., *Phys. Rev. B* 2021, **103**, 085102.

More information, please contact: Kangxuxin22@163.com

铌的机器学习势函数的构建

李帅航，宁世辉，袁定旺，黄博文，胡望宇*
湖南大学材料科学与工程学院

摘要 运用两种不同的机器学习方法，分别构建了有关Nb的机器学习势。第一个机器学习势，高维神经网络势（接下来用NNP代称）为基于Behler J团队开发的高维神经网络势框架拟合。第二个机器学习势，矩张量势（接下来用MLP代称）基于Shapeev, Alexander V等人开发矩张量势框架拟合。为了评估势模型的有效性，计算了这两个势模型的BCC-Nb的压力与体积比曲线，进一步检测了晶格常数，内聚能，弹性常数，结构稳定性，空位形成能，自间隙原子形成能等基础性质，还计算了势模型在高温高压下的性质，主要包括高压下力学与热力学检测。

构建流程

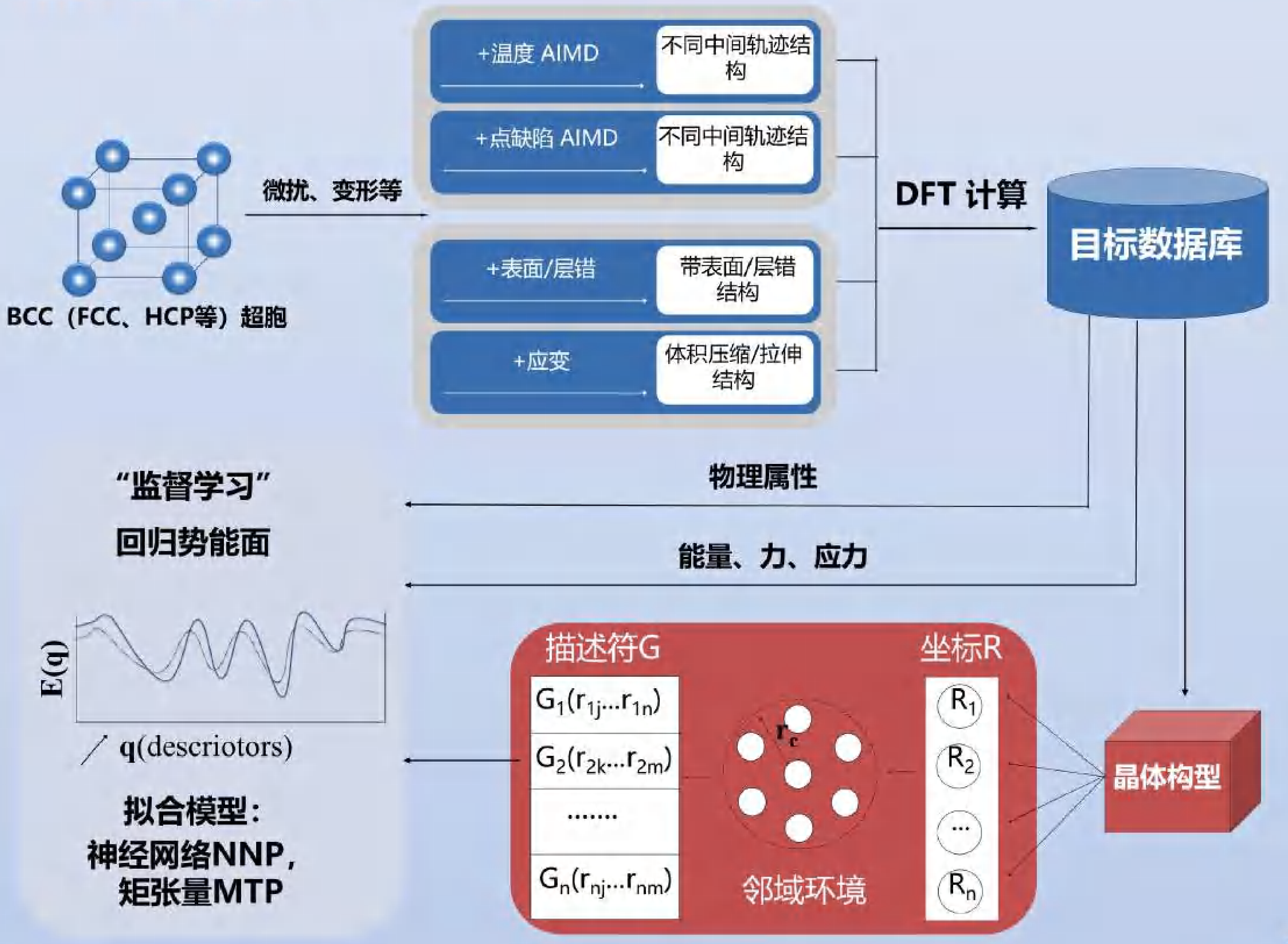

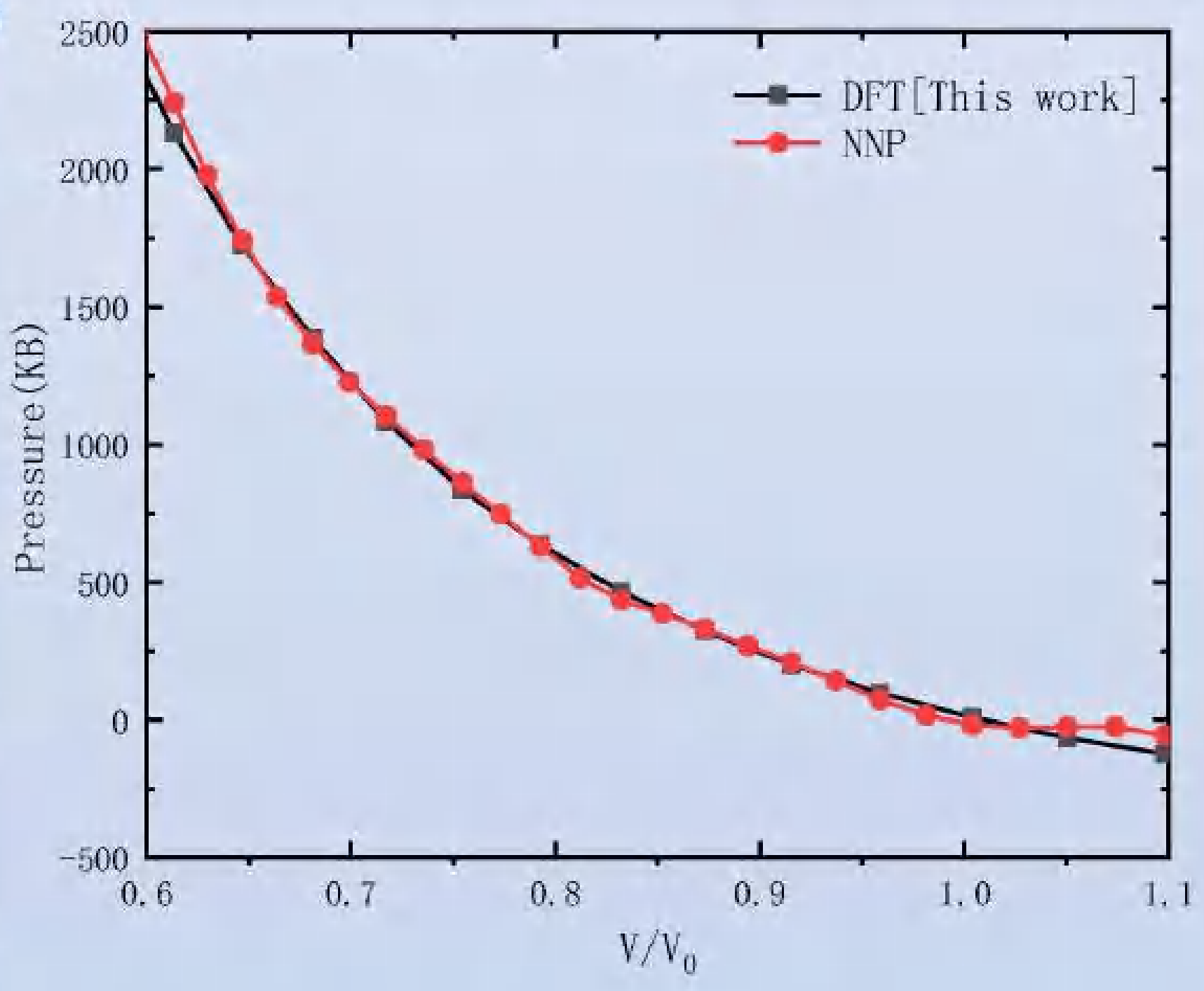

左图为NNP描述BCC-Nb的压力和体积比关系与DFT进行对比曲线。可见NNP的曲线与DFT值十分接近。右图是MTP计算Nb的熔点随压力变化与实验值进行对比曲线。MTP描述T-P较为接近实验值。

当前Nb势函数计算的部分性质与实验、第一性原理的比较

	DFT	EXP	NNP	MTP
		Lattice properties		
a_{bcc} (eV)	3.31	3.30	3.29	3.32
Ec(eV)	7.00	7.57	6.96	7.00
C_{11}(Gpa)	251	252.7	222.4	270
C_{12}(Gpa)	134	133.2	133.8	127
C_{44}(Gpa)	22	31	38.85	19
$\Delta E_{fcc-bcc}$	0.32	0.22	0.44	0.28
$\Delta E_{hcp-bcc}$	0.30		0.20	0.33
		Point defect(eV)		
E^f_v	2.72	2.6-3.1	2.98	2.27
E^f_i (d001)	5.95		6.04	6.33
E^f_i (d110)	5.60		5.31	6.31
E^f_i (d111)	5.25		5.27	5.11
E^f_i (Oct)	4.89		4.38	6.40
E^f_i (Tetr)	5.76		5.27	5.11
		Surface energy(J/m^2)		
E_{sf}100	2.34	2.39	2.396	2.01
E_{sf}110	1.98	1.86	2.01	1.70
E_{sf}111	2.30		2.62	2.1

总结 从表格可以看出，对于晶格常数，内聚能和弹性常数，我们拟合的势模型的计算值均接近第一性原理值。并且两个势模型计算显示，BCC-Nb结构是基态结构，与实际相符。

对于点缺陷，我们计算了单空位形成能以及五种典型自间隙原子组态（<111>哑铃、<110>哑铃、<100>哑铃、八面体间隙、四面体间隙）的形成能。NNP计算的空位形成能为2.98eV，与实验值接近。对于自间隙，NNP和MTP计算的能量最低构型是<111>哑铃，与DFT结果一致。

对于面缺陷，我们计算了三种典型低指数表面的形成能。当前势模型都预测得到（110）表面的形成能最低，与DFT结果一致。

两种势模型相比较，对于Nb的基态性质，两个模型的描述都符合实验值；对于缺陷性质，NNP比MTP更接近第一性原理值；对于高温高压下Nb的热力学性质，MTP计算比NNP计算结果跟接近实验值。

Electric-field-driven excitonic instability in an organometallic manganese-cyclopentadienyl wire

Jing Liu Yuanchang Li*

School of Physics, Beijing Institute of Technology, Beijing 100081, China

Abstract

Excitonic insulator is a macroscopic quantum system whose ground state consists of spontaneously formed and condensed excitons. While various excitonic insulators have been explored, they are almost exclusively characterized by the condensation of dark (optically inactive) excitons. Our first-principles *GW*–BSE calculations show that a transverse electric field will drive an organometallic manganese-cyclopentadienyl wire into a unique "bright" excitonic insulator phase, as the combined consequence of giant Stark effect and electric-field-induced symmetry breaking. Such bright excitonic insulators can be directly identified by experiment due to their coherent radiation. Our results are not only of scientific interest in electric-field control of exciton condensation, but may also open an opportunity to create a coherent light source based on the excitonic insulator.

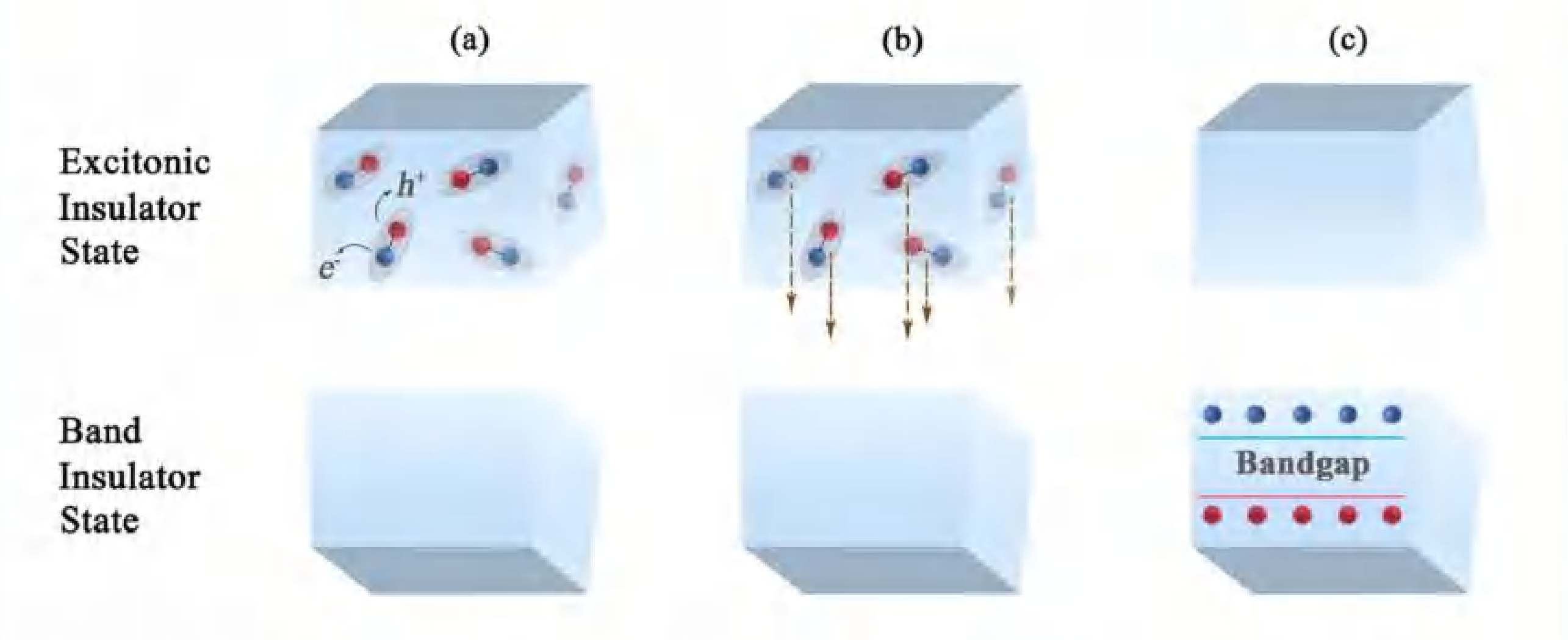

FIG. 1. Schematic illustration of distinguishing an excitonic insulator from a band insulator through the coherent radiation across an external field-induced phase transition.

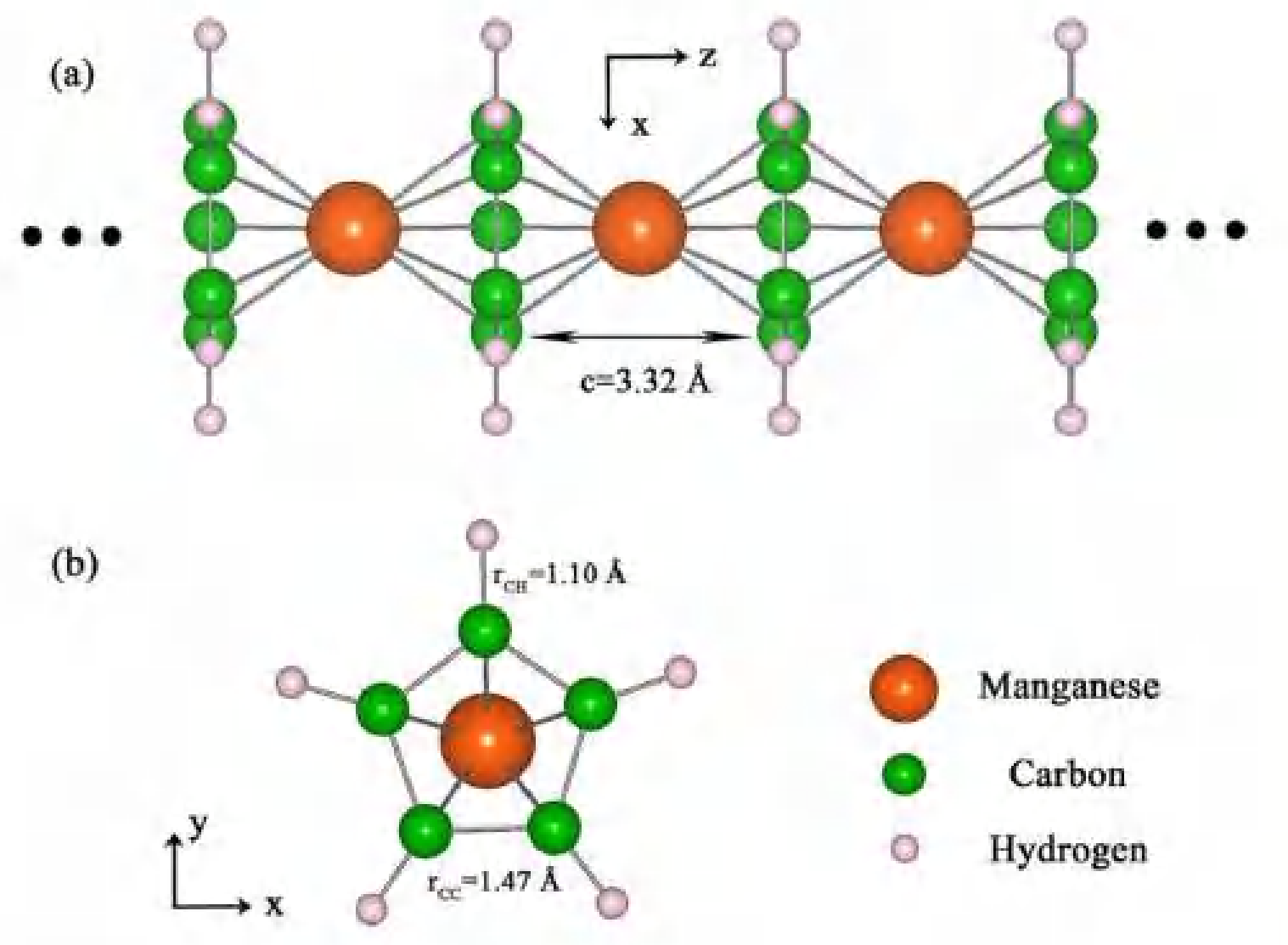

FIG. 2. (a) Side view and (b) top view of $(\mathrm{MnCp})_\infty$ wire.

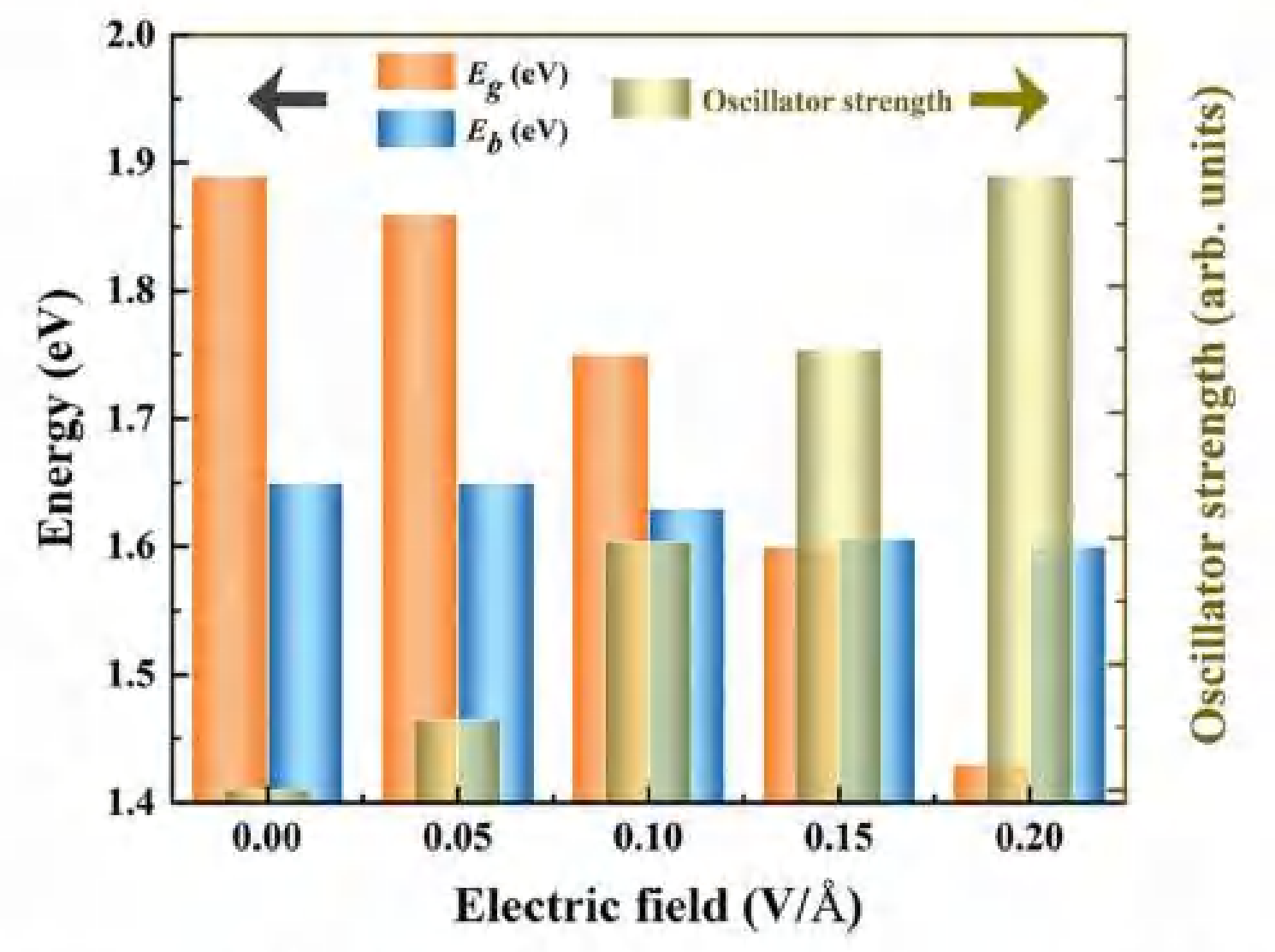

FIG. 4. Electric-field dependence of E_g, E_b, and oscillator strength of the ground-state X_1 exciton.

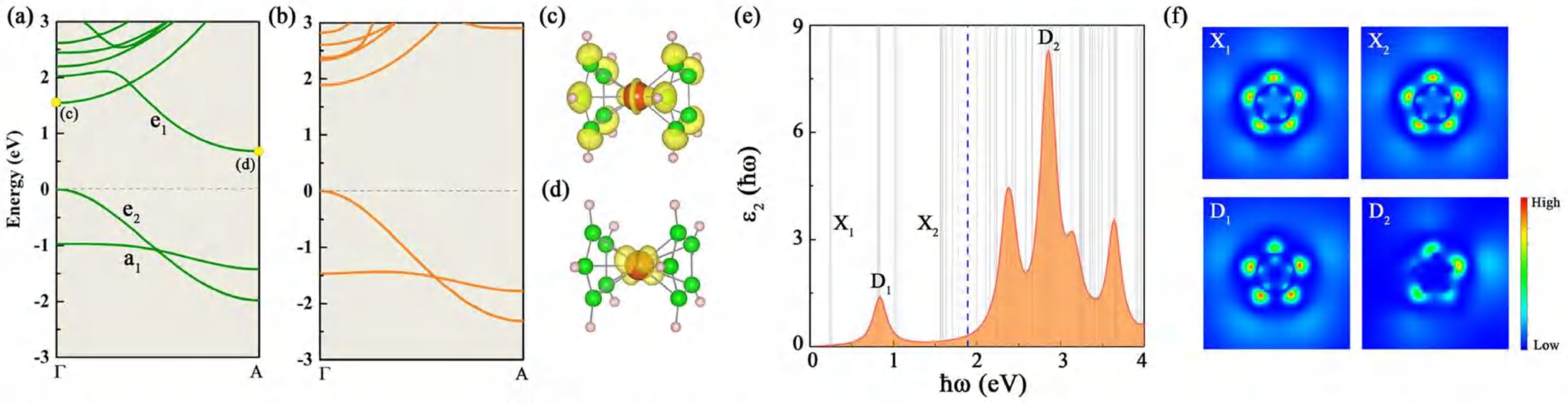

FIG. 3. Band structures respectively calculated by (a) PBE and (b) G_0W_0 methods. (c), (d) Decomposed charge densities corresponding to the states marked in (a) (yellow dots). (e) Exciton energies (gray vertical lines) superimposed on the imaginary part of the BSE dielectric function. (f) Two-dimensional cross section of the real space exciton wave functions for the states noted in (e).

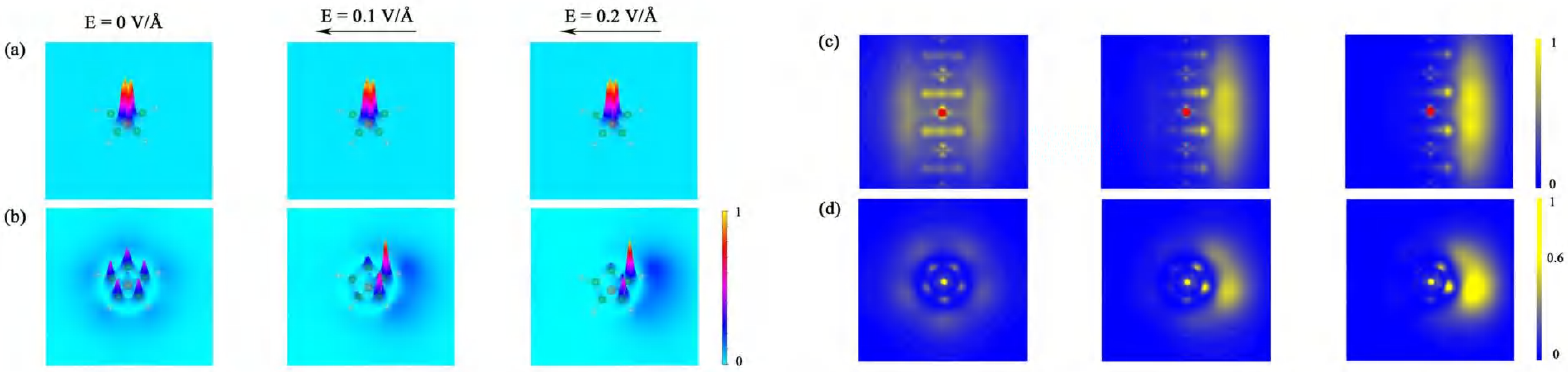

FIG. 5. Decomposed charge densities at the point for the (a) top valence band, and (b) bottom conduction band under zero, E = 0.1 V/Å and E = 0.2 V/Å electric field. (c) Side view and (d) top view of the real-space exciton wave functions for the X_1 under zero, E = 0.1 V/Å, and E = 0.2 V/Å electric field.

Conclusion

In conclusion, first-principles calculations using the prototype $(\mathrm{MnCp})_\infty$ show a new kind of bright excitonic insulators that have not yet been recognized by the research community. Its unique fingerprint is embodied in the electron-hole coherent radiation recombination across an excitonic-insulator–band-insulator phase transition, which therefore allows the experimental identification with certainty. By contrast, such coherent radiation does not exist in the dark excitonic insulator. A practical concern is which materials are suitable for tuning into the bright excitonic insulator via the mechanism proposed here. Of course, not any band insulator can serve this purpose, even if a giant Stark shift is achieved. Instead, ones need to focus on materials that break the synergy between E_g and E_b so that applying an external field can reverse the relative size of the two. Generally, such materials are characterized by the forbidden transitions between the bandedge states. Our work thus provides a prospect for exciton manipulation in low-dimensional systems, as well as construction of coherent optical devices based on the excitonic insulators.

PHYSICAL REVIEW B 104, 085150 (2021)

FOR MORE INFORMATION:

*** Corresponding author. E-mail address: yuancli@bit.edu.cn**

Jing Liu. Phone: 18515397566

Optical and electrical properties of van der Waals heterojunction Germanene/MoSSe

Yuan jun[1] Wang Fanfan[1] Zhou Jun*[1]

[1] Institute of Photonics, Faculty of Science, Ningbo University, Ningbo, Zhejiang, China

INTRODUCTION

Since the discovery of graphene, two-dimensional materials have received extensive research. Although single-layer two-dimensional structures have many advantages, it have some defects limit their applications. Building heterogeneous junctions is an excellent strategy to solve this problem.

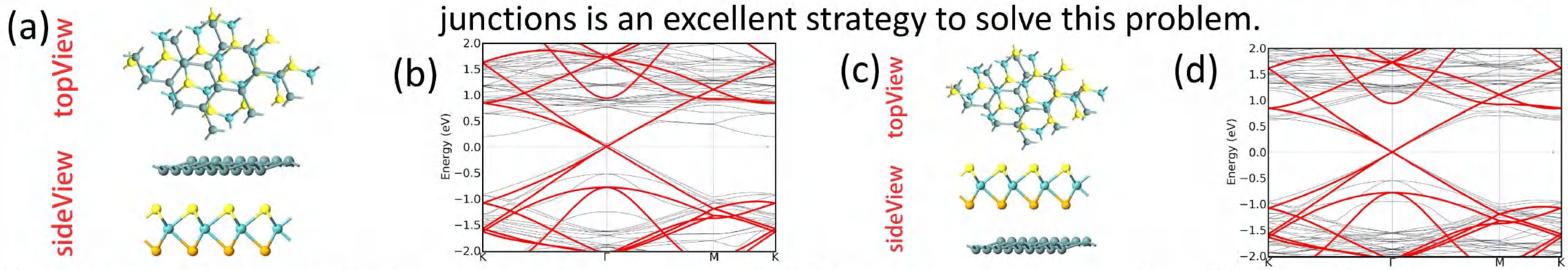

Fig.1 Relaxed geometric structures of germanene/MoSSe heterostructures for different stacking patterns: (a) germanene/SMoSe,(c)germanene/SeMoS. (b) and (d) band structures of the heterostructures, correspondingly.

OPTICAL PROPERTIES

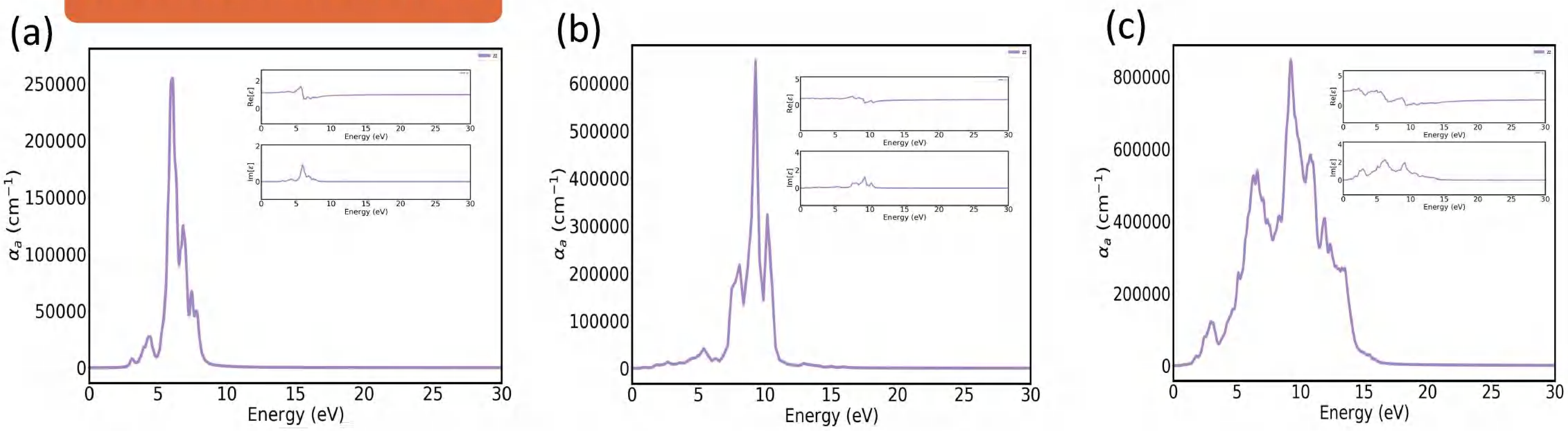

Fig.2 Optical absorption of the (a) MoSSe ,(b)germanene and (c) heterostructures, the tiny graphs in each plot are the corresponding dielectric functions.

ELECTRIC FIELD TUNABILITY

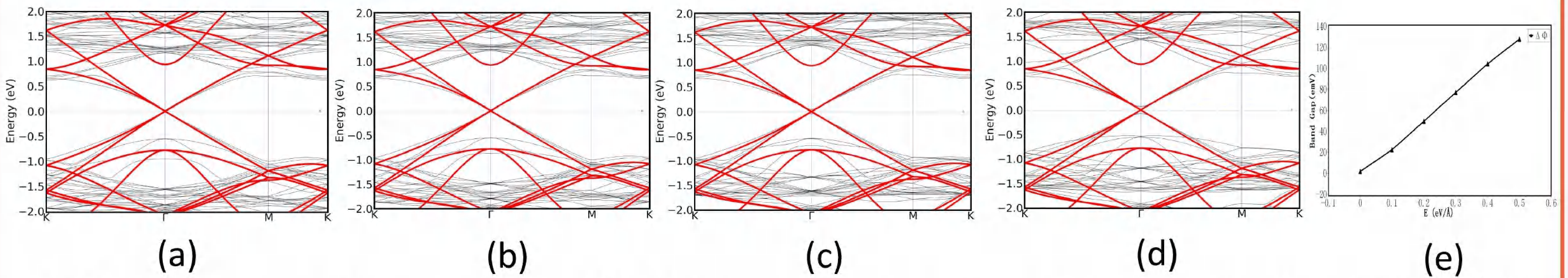

Fig.3 Bnad structures of the germanene/MoSSe heterostructure under positive electric gating of (a) 0 V/Å (b) 0.1 V/Å (c) 0.3 V/Å (d) 0.5 V/Å. (e)The variations of band gap as a function of electric gating.

CONCLUSION

In conclusion, by constructing heterojunctions, we can retain their advantages and present new physical properties. We applied the first principles to study the interface characteristics , electrical and optical performance of germanene/MoSSe. Compared with monolayers, heterostructures not only preserve monolayer properties, but also exhibit enhancement effect. In addition, the band gap also increases with the increase of the external electric field, and the MoSSe layer becomes an n-type semiconductor.

E-mail:zhoujun@nbu.edu.cn

Two-Dimensional Fe_8N Nanosheets: Ferromagnets and Nitrogen Diffusion

Jiafei Pang,[1] Wenyuan Jin,[1] Xiaoyu Kuang,[1, *] and Cheng Lu [2, *]

[1]*Institute of Atomic and Molecular Physics, Sichuan University, Chengdu 610065, China*
[2]*School of Mathematics and Physics, China University of Geosciences (Wuhan), Wuhan 430074, China*

ABSTRACT

We perform a first-principles study and identify two intriguing ferromagnets, hollow-Fe_8N (H-Fe_8N) and bridge-Fe_8N (B-Fe_8N) monolayers, by extensive structural searches. Both H-Fe_8N and B-Fe_8N nanosheets are buckled triangular lattices with a similar motif, but they are distinguishable by the positions of N atoms. The magnetic and electronic properties show that H-Fe_8N is a low-spin ferromagnet; in contrast, B-Fe_8N is a high-spin ferromagnet, which originates from the 3*d* orbital splitting of the Fe atom due to the low/high symmetric crystal field. Surprisingly, two stable Fe_8N monolayers can be transferred to each other by N atom diffusion from the bridge position to the hollow position with the migration energy barrier of 1.5 eV. The energy barrier is affected by introduced Fe defects and rare earth metal dopants. These findings introduce a new tactic to regulate the 2D Fe-nitride monolayers at the atomic scale.

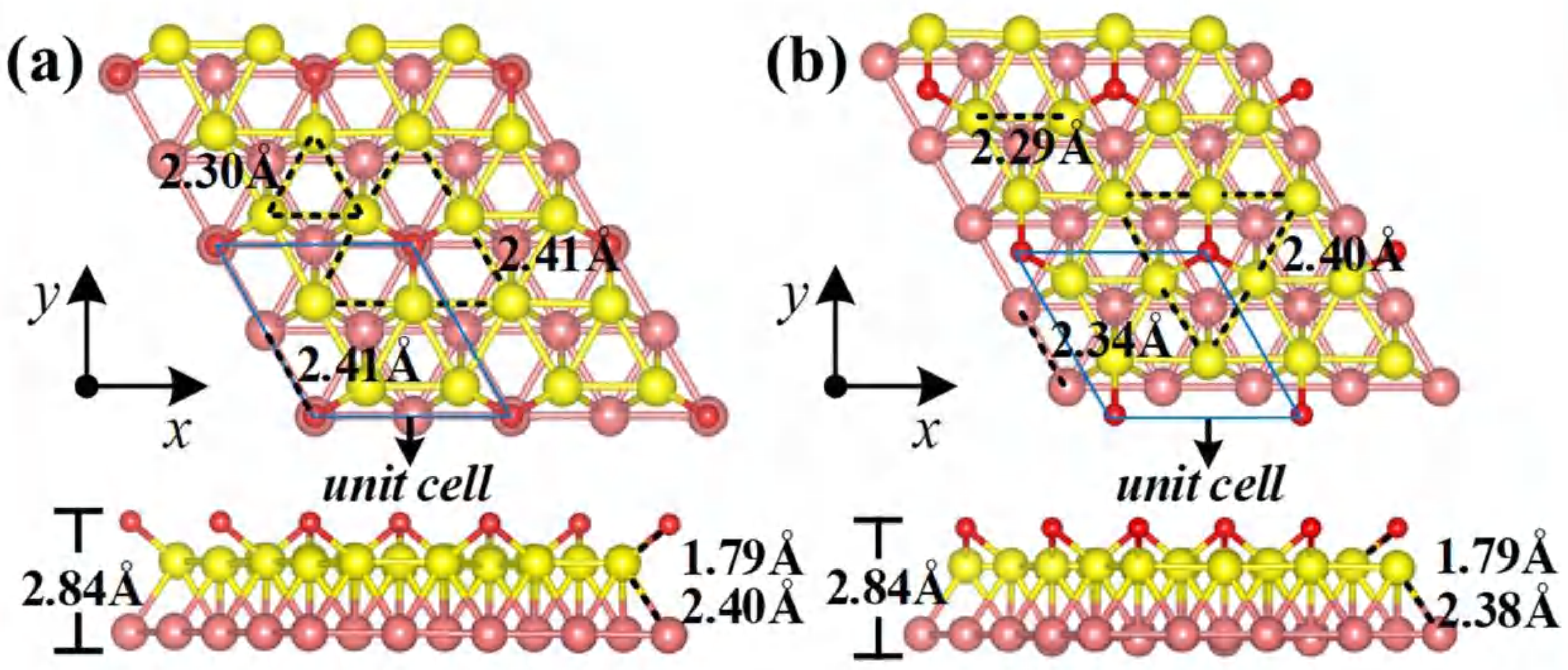

FIG 1. (a) Top and side views of 2 × 2 × 1 supercell of Fe_8N nanosheet: (a) H-Fe_8N and (b) B-Fe_8N. The yellow spheres are Fe atoms in the first layer; the pink spheres are Fe atoms in the second layer, and the red spheres are N atoms in Fe_8N.

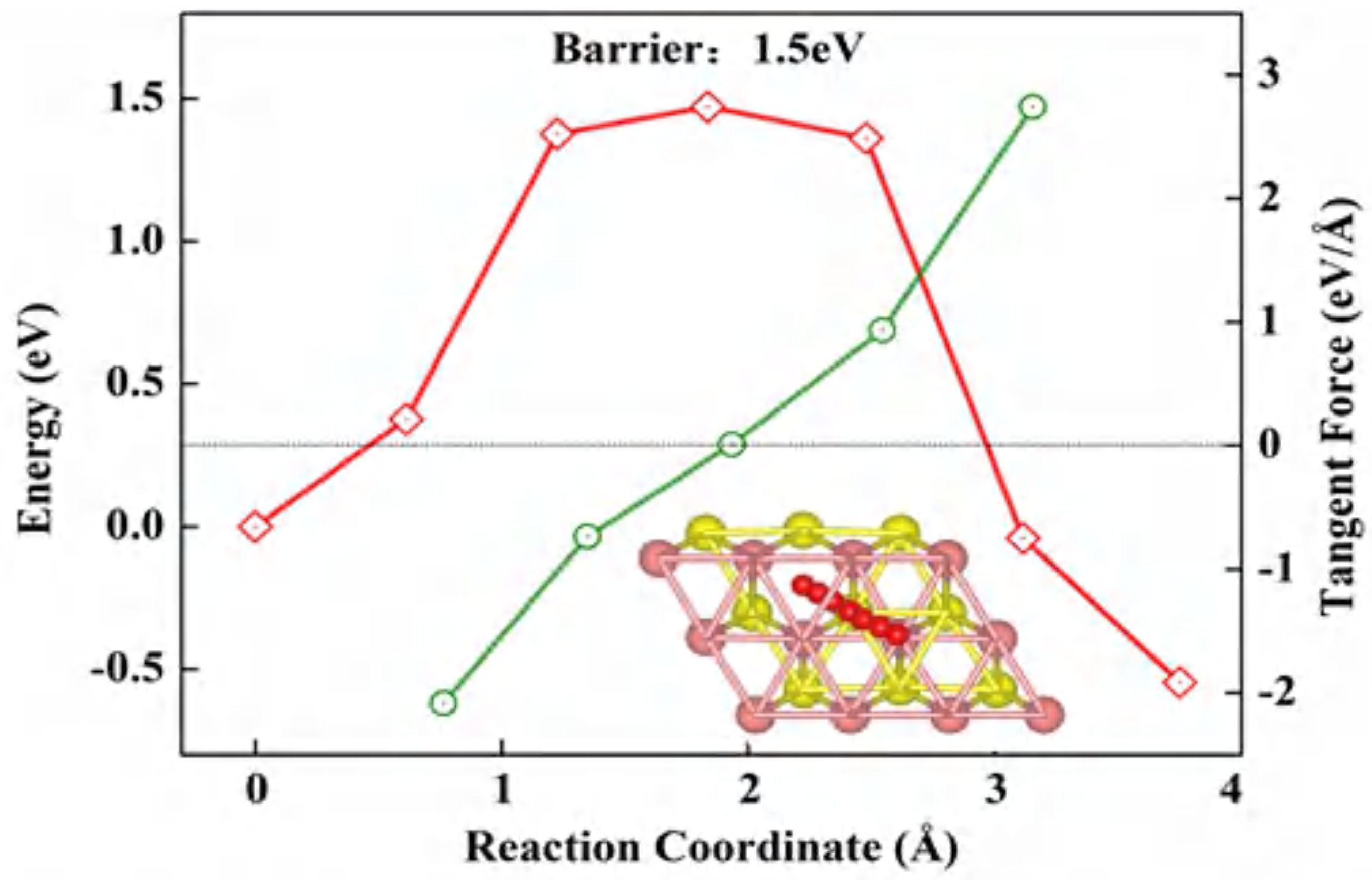

FIG 3. Minimum-energy paths of N atom penetration for B-Fe_8N. The red and green lines represent the energy barrier and tangent force of nitrogen penetration on Fe nanosheets, respectively.

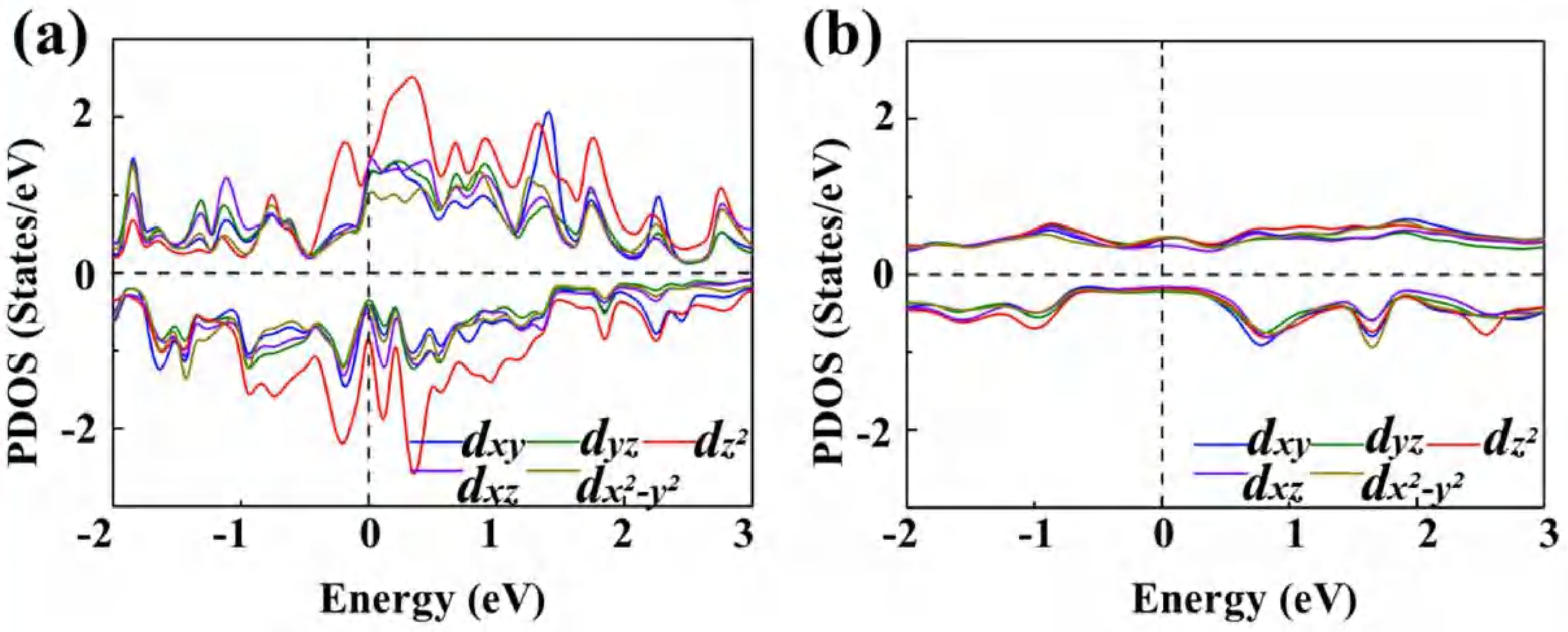

FIG 2. (a) PDOS of Fe *d* orbitals of Fe_8N nanosheets calculated by HSE06 functionals: (a) H-Fe_8N and (b) B-Fe_8N.

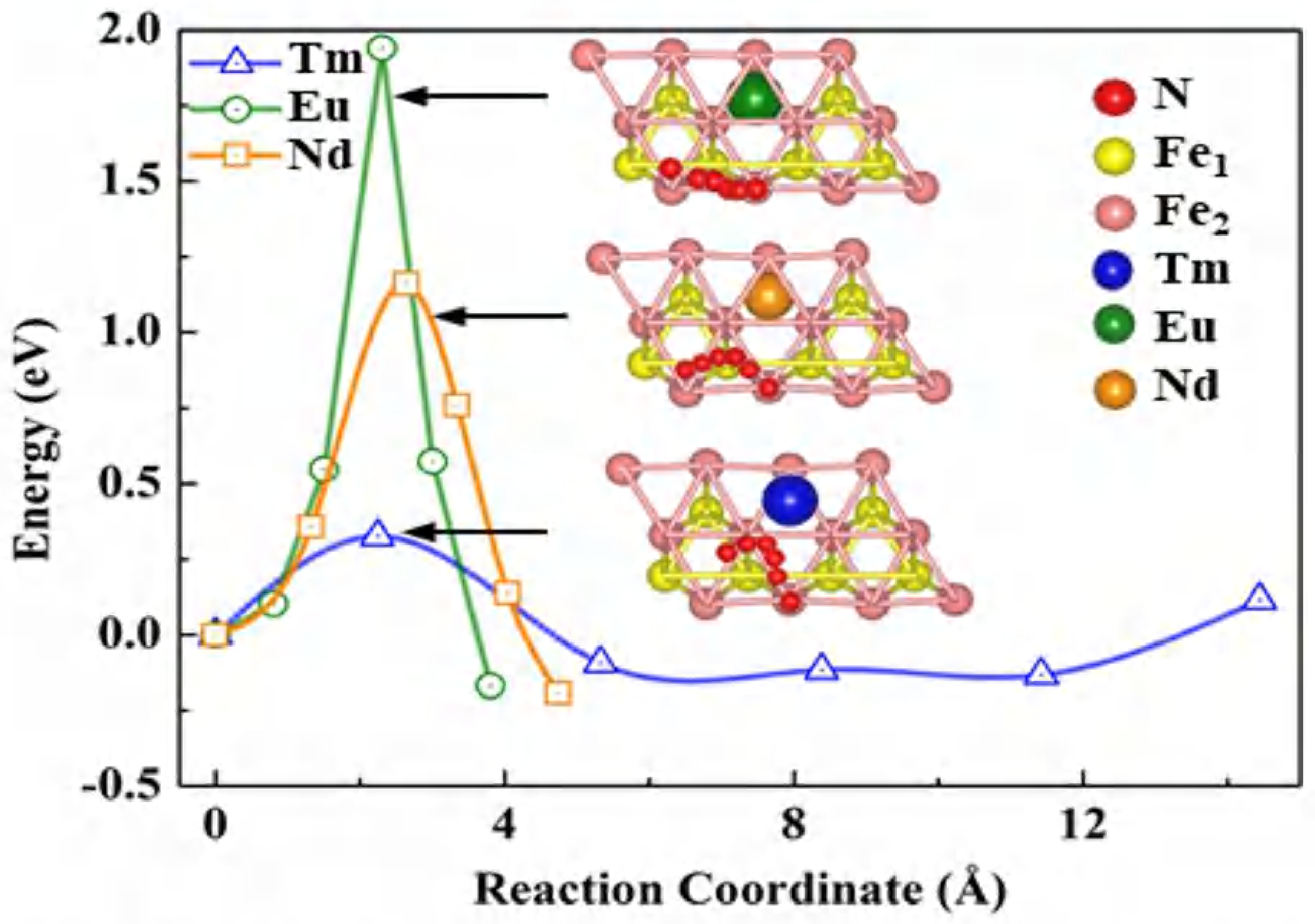

FIG 4. Minimum-energy paths of N atoms penetrated for V_{Fe} defects. The energy of 1.5 eV represents the energy barriers of nitrogen penetration on Fe nanosheets.

CONCLUSION

In summary, we have performed a comprehensive structural search of 2D Fe_8N monolayers and found two ferromagnets: a ground-state H-Fe_8N and a metastable B-Fe_8N. The metastable B-Fe_8N monolayer tends to transform into H-Fe_8N by changing the N positions after molecular dynamics simulation at room temperature. Interestingly, the change of N position causes the high-spin to low-spin transition of the magnetic state in the Fe_8N monolayer. The spin transition results from the symmetric change of 3*d* orbitals of Fe atoms. Our results show that the V_{Fe} vacancy is the dominant defect in the Fe_8N monolayer. Fifteen kinds of RE atoms are doped into V_{Fe} defects to effectively regulate the diffusion barrier, indicating that the Tm atom is an excellent monatomic catalyst for the Fe_8N monolayer. These findings offer insights for understanding the electronic and magnetic behaviors of 2D Fe_8N monolayers, which may also provide crucial information for design and synthesis of novel functional materials.

REFERENCE： Jiafei Pang, Wenyuan Jin, Xiaoyu Kuang,* and Cheng Lu. * J. Phys. Chem. Lett. 2021, 12, 8453−8459.

Electronic address: [a] scu_kuang@163.com (Xiaoyu Kuang), [b] lucheng@calypso.cn (Cheng Lu).

Acknowledgements: This work was supported by the National Natural Science Foundation of China (Nos. 12111530103, 11874043, 12174352).

Computational Screening of Bimetallic Ordered Catalysts for Nitrogen Reduction Reaction

Jing zhou, Xiayong Chen, Wangyu Hu, Bowen Huang, Dingwang Yuan*

College of Materials Science and Engineering, Hunan University, ChangSha 410082, China

ICM^3 - 2022

Introduction

Ammonia gas is an important chemical substance. The Haber process currently used for its industrial production has the disadvantages of high energy consumption and greenhouse gas emission, which prompts people to look for new catalysts. In this work, we use high-throughput calculation method to study the catalytic capacity of binary intermetallic compound A3B for NRR. We first analysis how geometric and electronic dominant adsorption behaviors. Then, the disturbance of the scaling relation is discussed. Finally, volcano plot is constructed to evaluate the activity and selectivity for this system.

Workflow

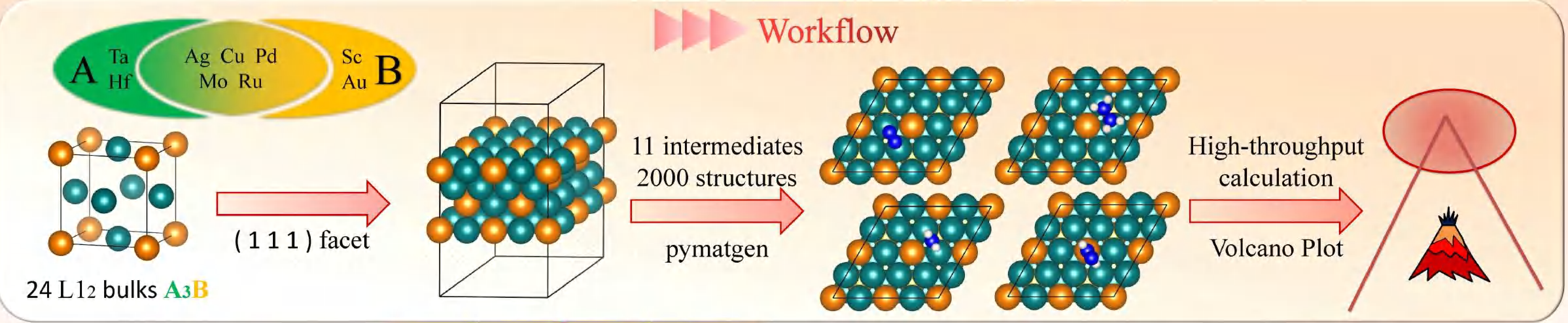

Geometric effect

- When active element change from A to B, adsorption site turn from ‘AAA’, ‘AA’ to ‘AAB’ or ‘AB’.
- Valency rule and whether N-N bond is activated decide adsorption configuration of NH_x and N_2H_x respectively.

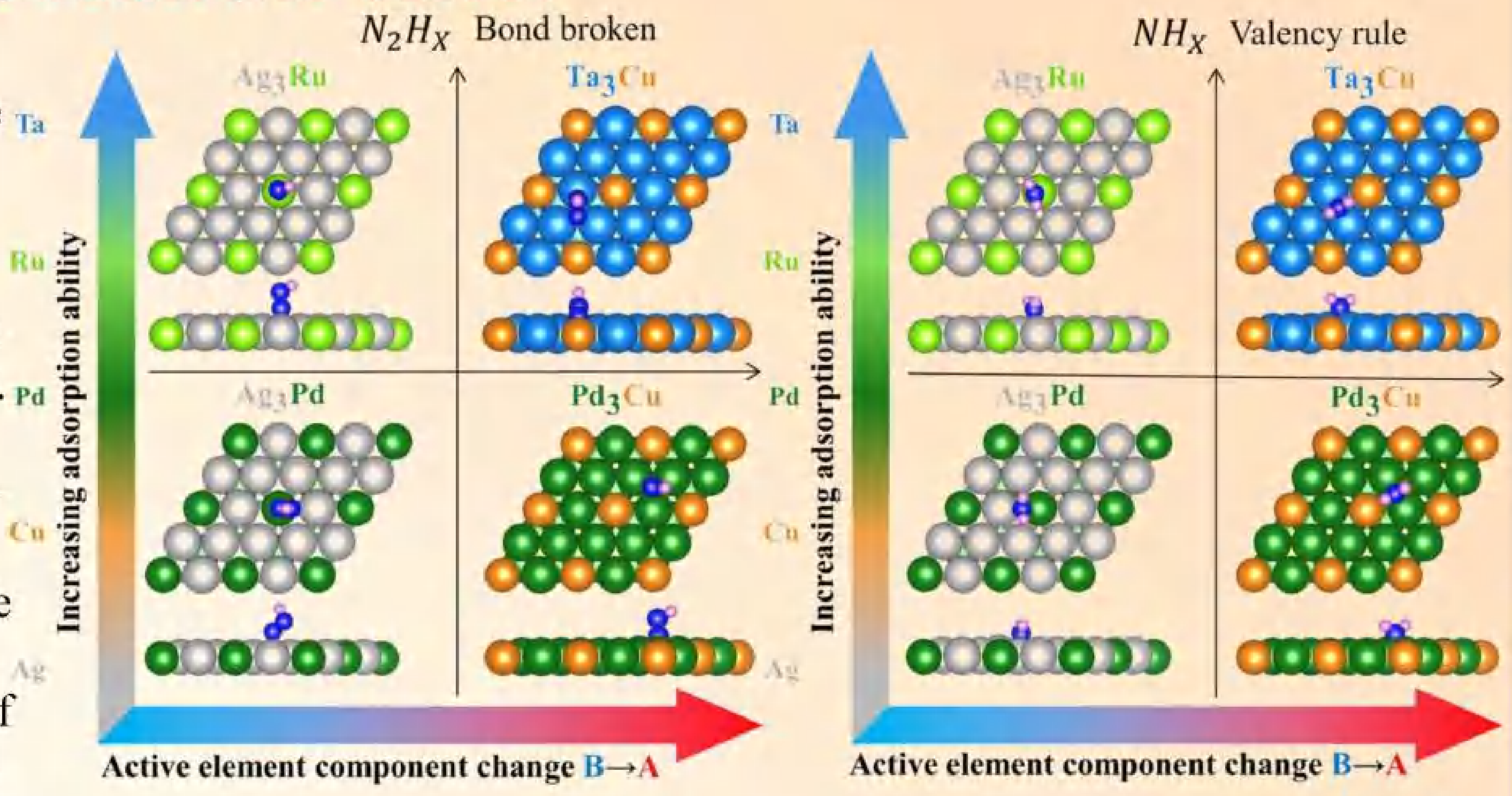

Electronic effect

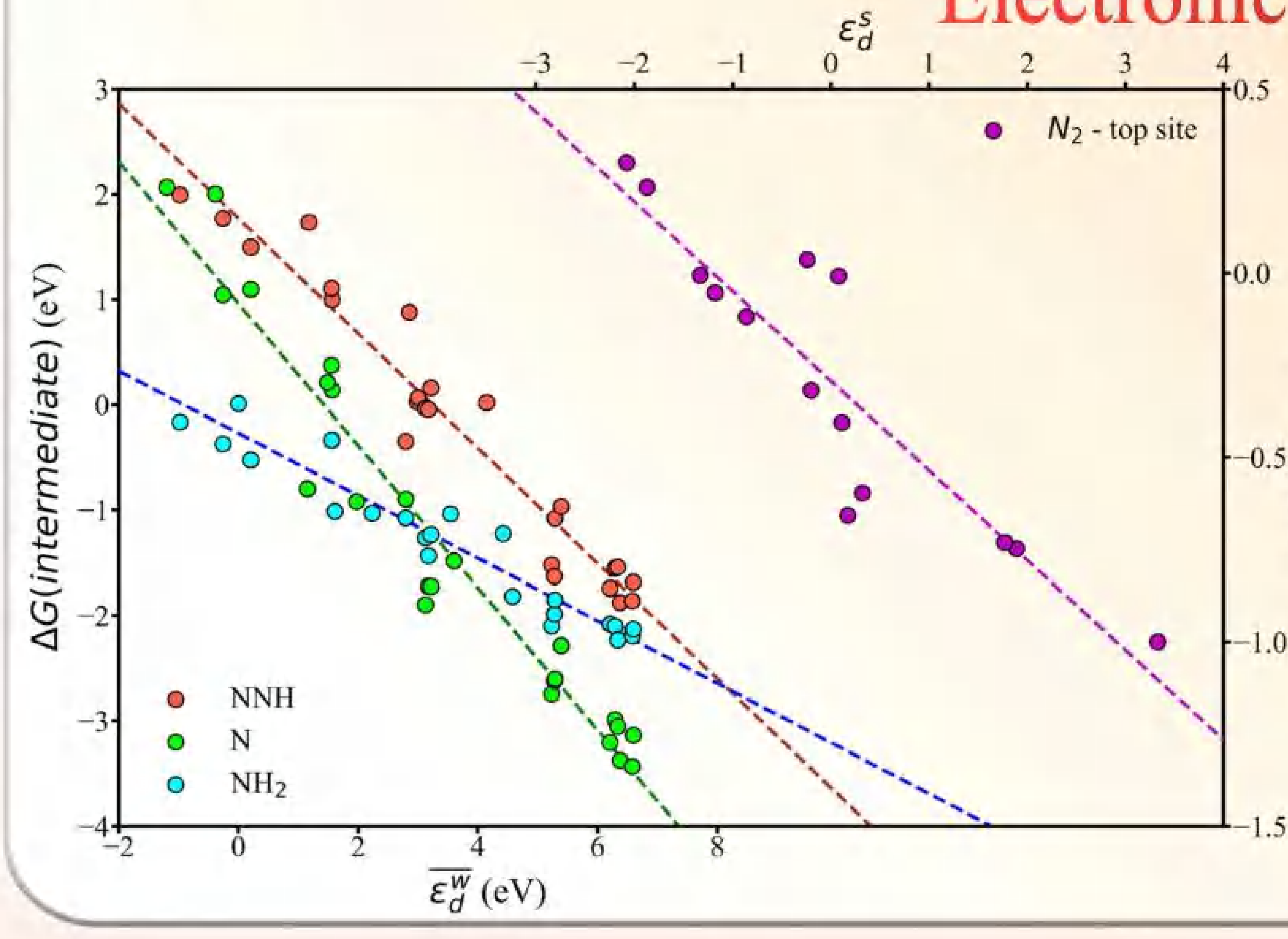

ε_d: d-band center

W_d: d-band width

S_F: Fermi softness

$$\overline{\varepsilon_d^w} = \varepsilon_d + \frac{1}{2} W_d$$

$$\varepsilon_d^s = \varepsilon_d + S_F$$

We use $\overline{\varepsilon_d^w}$ and ε_d^s to describe trend on adsorption energy in different situations.

Opposite trend between N2 and N

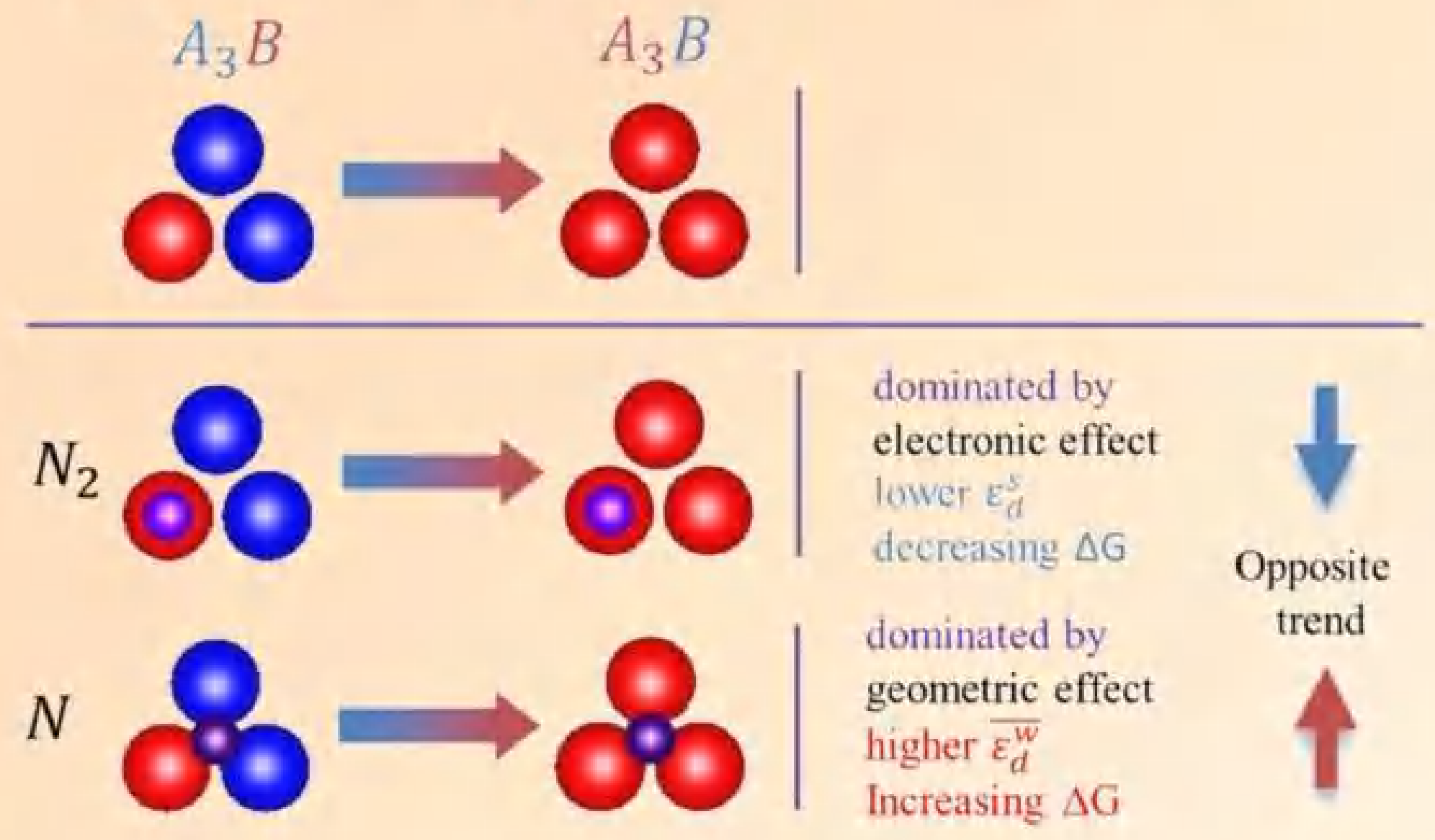

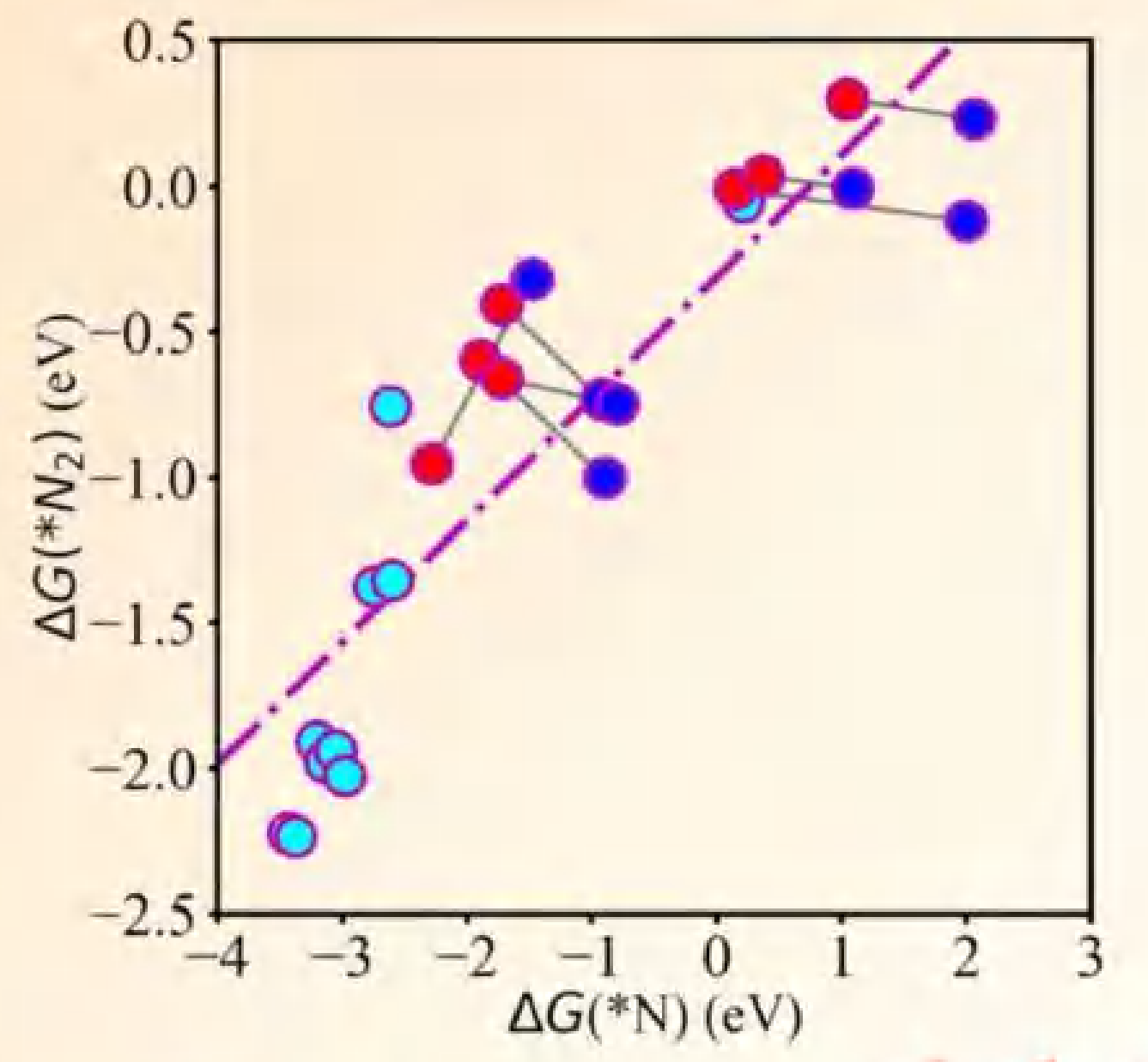

Horizontal NNH increase activity

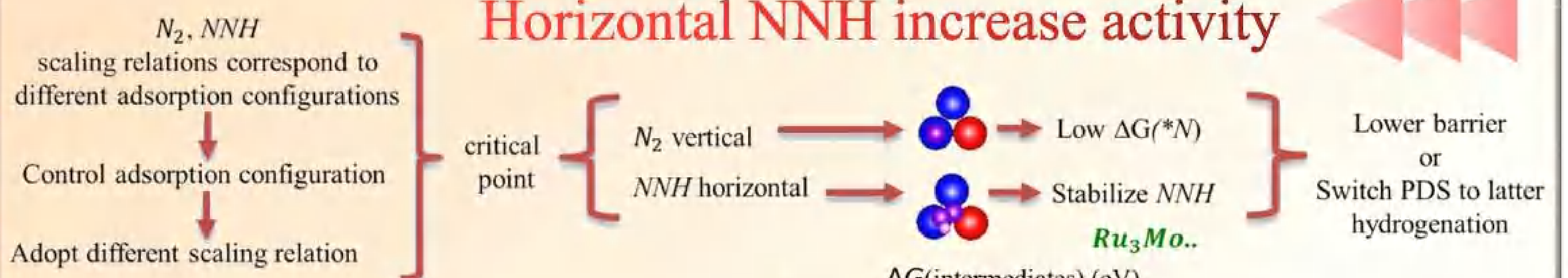

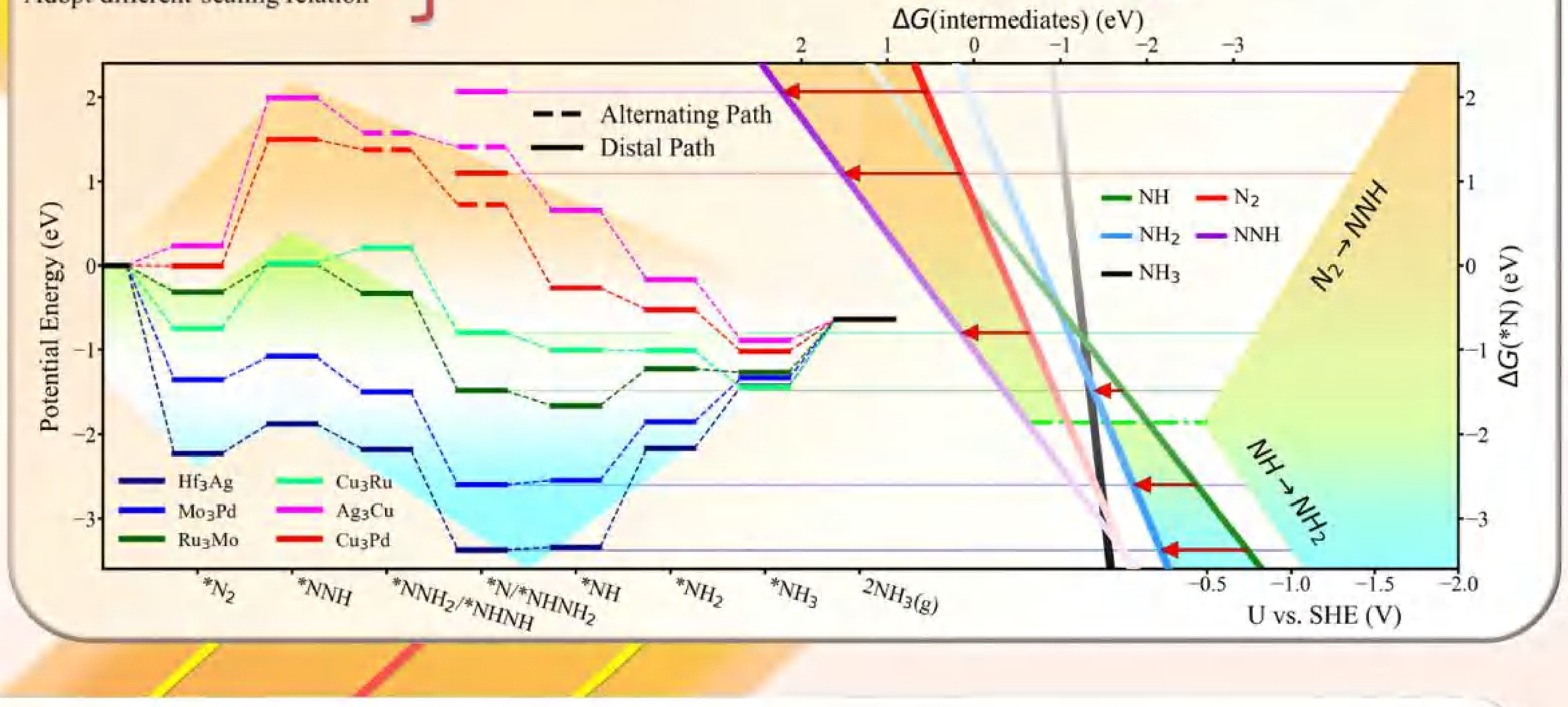

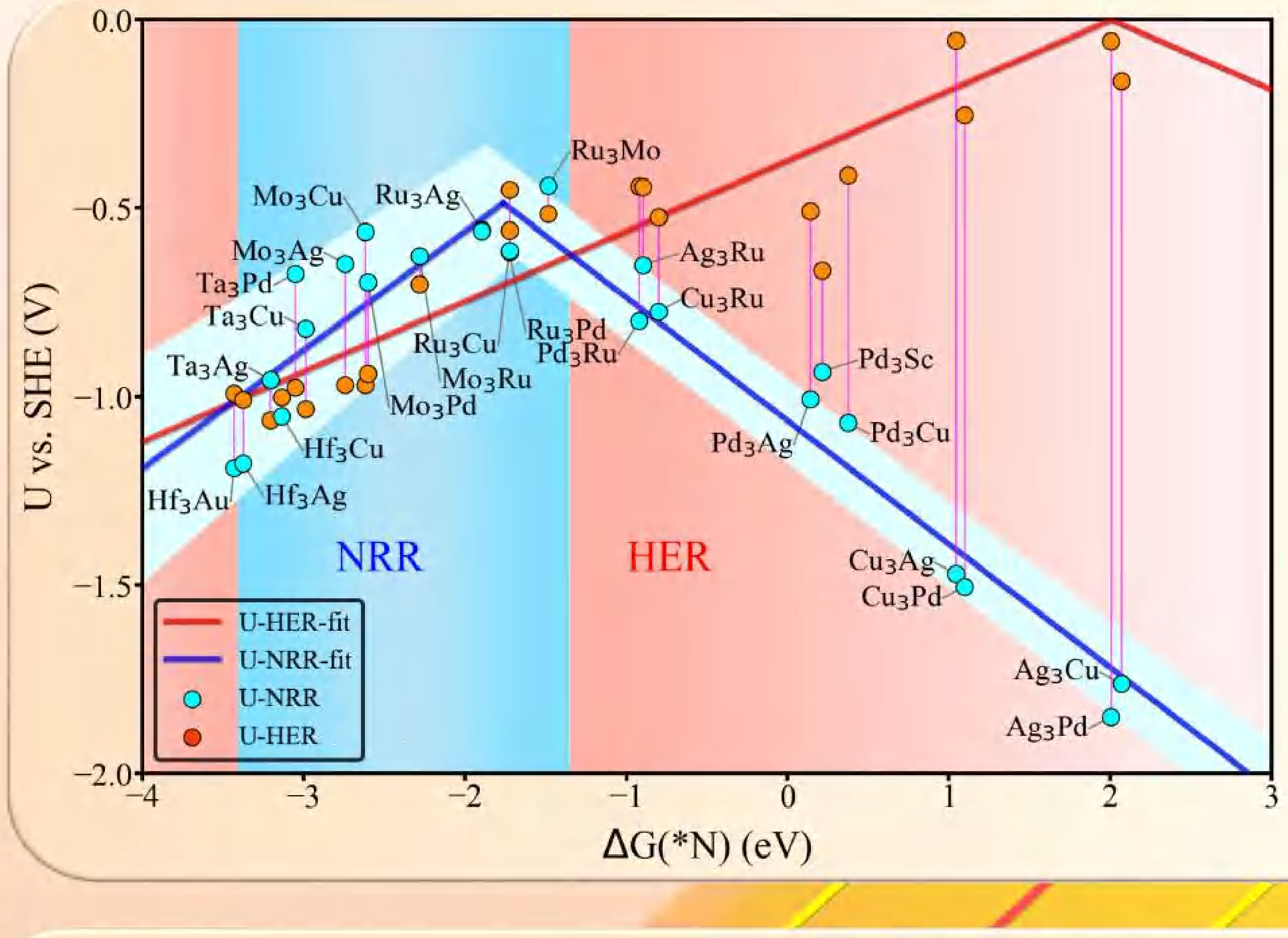

Activity

- With a proper ΔG(*N) near -1.9 eV, the (111) facet of L1₂ alloy can reach the best performance with a limiting potential around -0.4 V and be able to suppress HER.
- Amount the 24 alloys, Ru₃Mo has the lowest limiting potential of -0.44V.

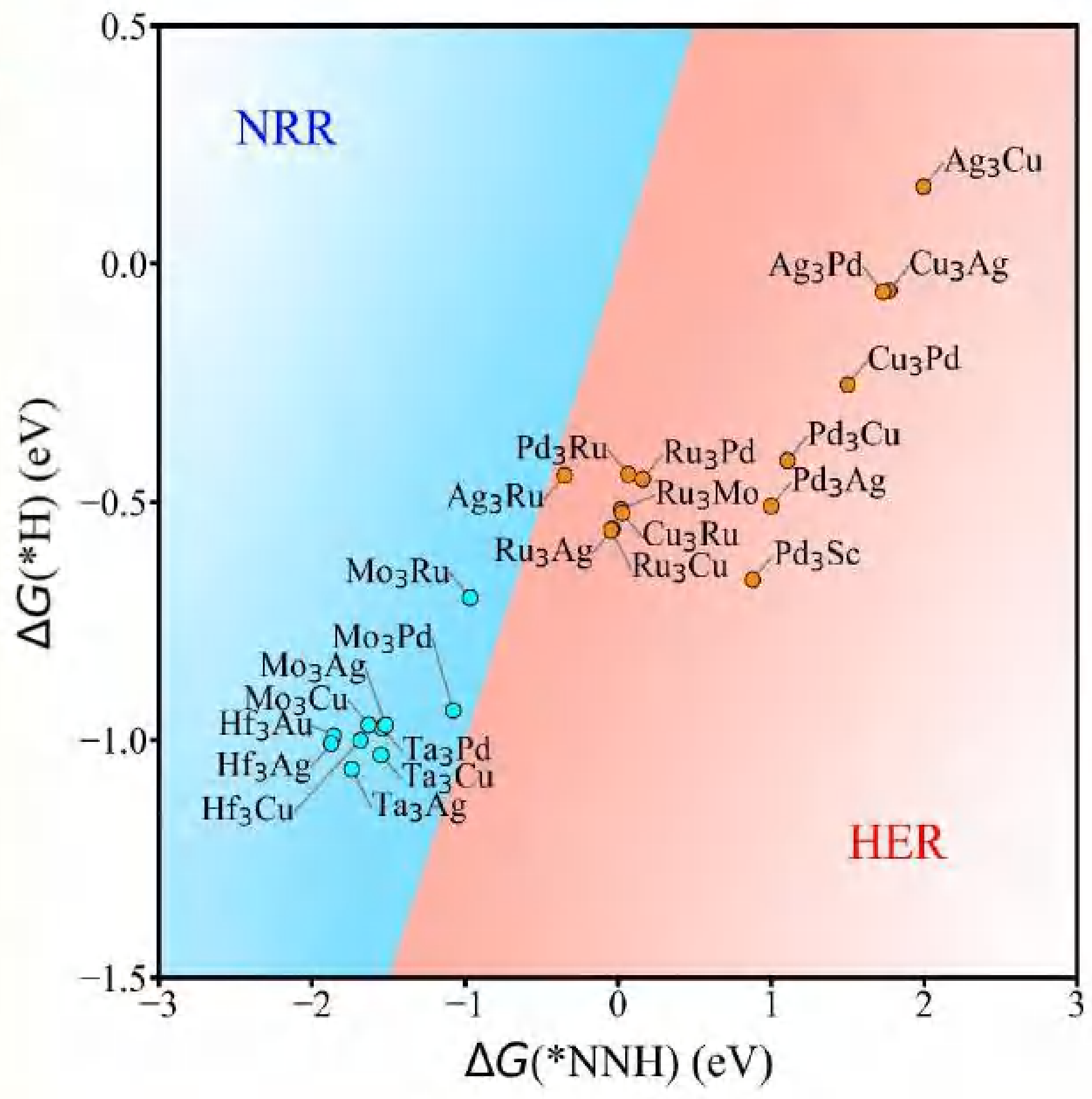

Selectivity

- To evaluate the selectivity, we compare the limiting potential of NRR and HER as well as the ΔG of NNH and H.
- Ru₃Mo has ΔG(*NNH)> ΔG(*H) and show low selectivity.
- Instead, Mo₃B shows high selectivity in both aspects.

Conclusion

- Free atom like structure in L1₂ alloys induce distribution to scaling relation resulting in destabilize N₂ and stabilize NNH that increase activity.
- According to the volcano plot, the activity and selectivity can be fulfill at the same time in L1₂ system. Ru and Mo based alloys are the potential catalysts with the lowest limiting potential approach -0.4 V.

Acknowledgements

- National Natural Science Foundation of China, Grant no.12074113.
- National Key Research Project of China, Grant No. 2018YFB0704000

Contact

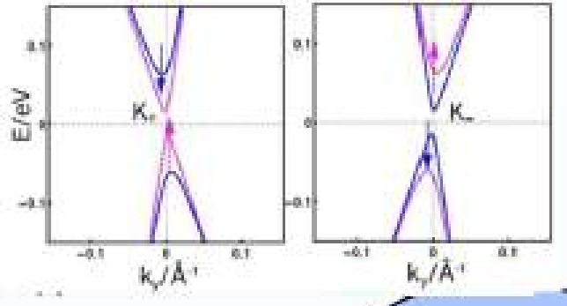

Longitudinal Optical Conductivities for Tilted Dirac Material in (1+d)-dimensional spacetime

Jiantong Hou(侯鉴桐)
(cooperated with Chao-Yang Tan, Hao-Ran Zhang, Zhiqiang Li, ect.)
CTP-SCU, College Of Physics，Sichuan University
870024031@qq.com

研究对象

我们计算了1+d维时空里无质量各向异性的*倾斜*狄拉克材料（tilted Dirac materials,参见式(1)与图①）在零温与有限化学势下（掺杂）的纵向光电导（LOC, longitudinal optical conductivity）$Re\ \sigma_{jj}(\omega,\mu;d)$,

$$(1)\quad H_\kappa(\boldsymbol{k}-\mathrm{K}_\kappa)=\kappa\boldsymbol{v_t}\cdot(\boldsymbol{k}-\mathrm{K}_\kappa)\mathbf{1}+\boldsymbol{v_F}\otimes(\boldsymbol{k}-\mathrm{K}_\kappa)\cdot\boldsymbol{\gamma}$$

其中$t=\frac{|\boldsymbol{v_F}\cdot\boldsymbol{v_t}|}{\boldsymbol{v_F}\cdot\boldsymbol{v_F}}$被称为材料的倾斜参数,向量组γ满足于Clifford代数。

若$\boldsymbol{v_F}$各向同性，平行于$\boldsymbol{v_t}$的方向叫做倾斜方向，以后角标记作jj=∥；垂直于$\boldsymbol{v_t}$的方向叫做倾斜方向

对于t的不同取值，相应的被称作：类石墨烯（untilted, 无倾斜,t=0），欠/亚倾斜（undertilted, 第I类, 0<t<1），过/超倾斜（overtilted, 第II类,t>1）与临界倾斜（critical tilted, 第III类,t=1）

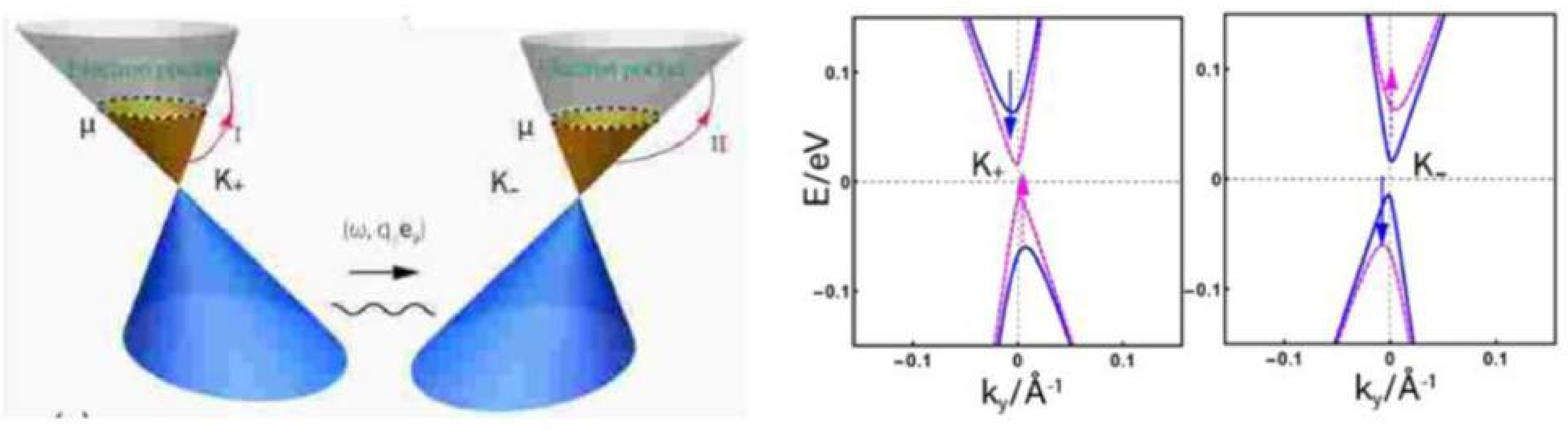

图①：2 维倾斜材料狄拉克点附近能带（左），左图为其沿 kₓ=const.的横截面

工作概要

·d=2,3之LOCs见图②。电中性(μ≈0)材料，$Re\ \sigma_{jj}=$各向异性常数。

·带间跃迁（interband）

光电导$Re\ \sigma(\omega,\mu;d)$有统一标度律：$c(d)\sigma_0 v_F^{d-2}\omega^{d-2}$, (c(d)是维数d的数量函数且c(1)=0),

且对于任意方向皆有一阶相变点(Lifshitz相变)：$\hbar\omega_\pm=\frac{2|\mu|}{1\mp t}$,

定义$\Gamma_{jj}^{IB}(\omega)=\frac{Re\ \sigma_{jj}(\omega;d,\mu)}{Re\ \sigma_{jj}(\omega;d,\mu=0)}$, 对于t=0其结果回到类石墨烯体系，

t≠0有如图③所示结果。

·带内跃迁（intraband）

光电导$Re\ \sigma_{jj}(0,\mu;d)$有统一标度律：$c'(d)\sigma_0 v_F^{d-2}|\mu|^{d-1}\delta(\omega)$,

$\delta(\omega)$可以由带宽为η的DOS峰近似代替：$\frac{\eta/\pi}{\omega^2+\eta^2}$，本质是一个Drude峰的因倾斜的极化

定义$\Gamma_{jj}^{D}(\omega)=\frac{Re\ \sigma_{jj}(0;d,\mu,t)}{Re\ \sigma_{jj}(0;d,\mu,t=0)}$对于t=0, 其值为1，对于t≠0有方程组(3)所示结果。

·任意维度d的电子态密度（DOS）与带内跃迁光电导、联合态密度（JODS）与带内跃迁光电导的奇异性具有一一对应关系。

·纵向光电导的对于与倾斜方向的夹角依赖性：

$$\mathrm{Re}\sigma_{nn}=\cos^2\theta\mathrm{Re}\sigma_{\parallel}+\sin^2\theta\mathrm{Re}\sigma_{\perp}$$

·1维是有奇性的。$\boldsymbol{v_F}$与$\boldsymbol{v_t}$的关系只能平行，这导致了1维带间跃迁光电导为零。

可视化图例与公式

以type-I，d=1,2,3为例

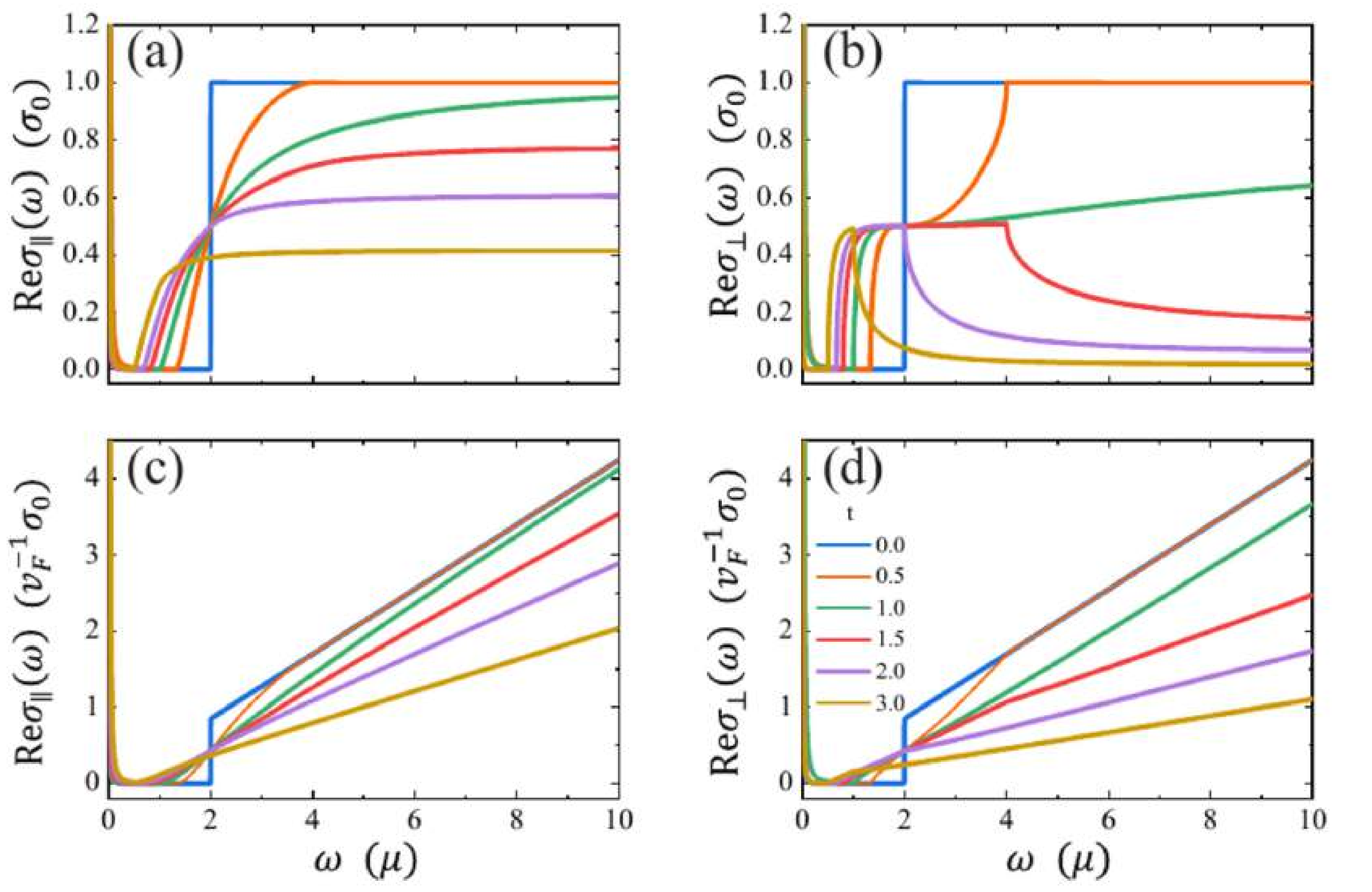

图②. 以$|\mu|/\hbar$为单位的入射光频率的纵向光响应示意图。d=2,3. (上)d=2; (下)d=3.

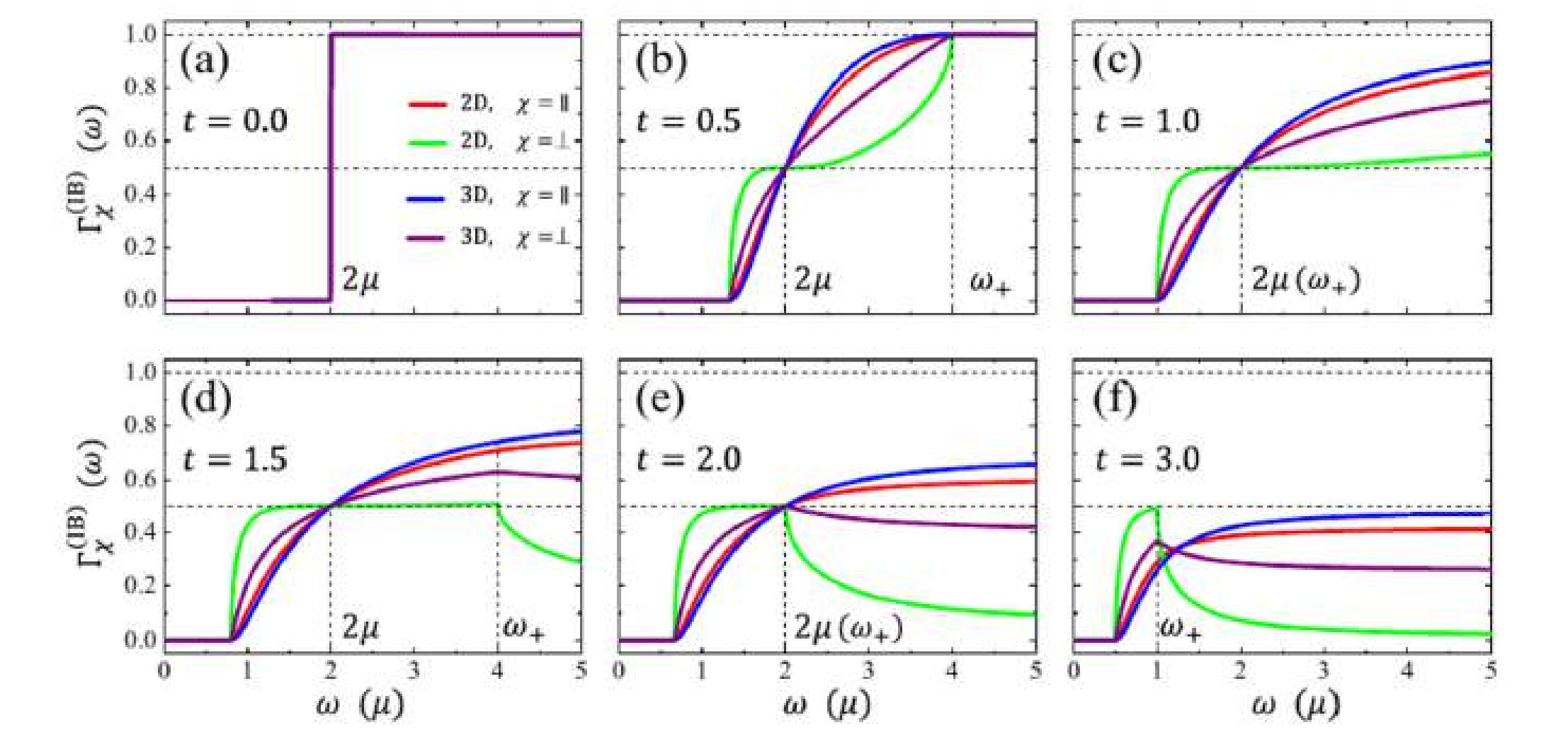

FIG. 2: The dependencies for each type of gamma scalar on optical frequency across dimensions. The thick, dashed, piecewise line is the gamma scalar for graphene-like Dirac material, i.e. $\Gamma_\chi^{\mathrm{IB}}(\omega)=\Theta(\omega-2|\mu|)$, for $\chi=\parallel,\perp$ and $d=2,3$. Top panel: the gamma scalar along tilted-tilted direction with $\mu=1$; from left to right, $t=1/3$, $t=1$, $t=1.5, t'=3.0$. Bottom panel: the gamma scalar along untilted-untilted direction, of which the parameters (μ,t,t') and colors are in the same setting with the corresponding top one. In the picture posited in the right column function $\omega_\pm(t)=\frac{2|\mu|}{t\mp1}$.

图③：带间光电导跨维度无量纲比较示意图(图中展示 d=1,2,3)

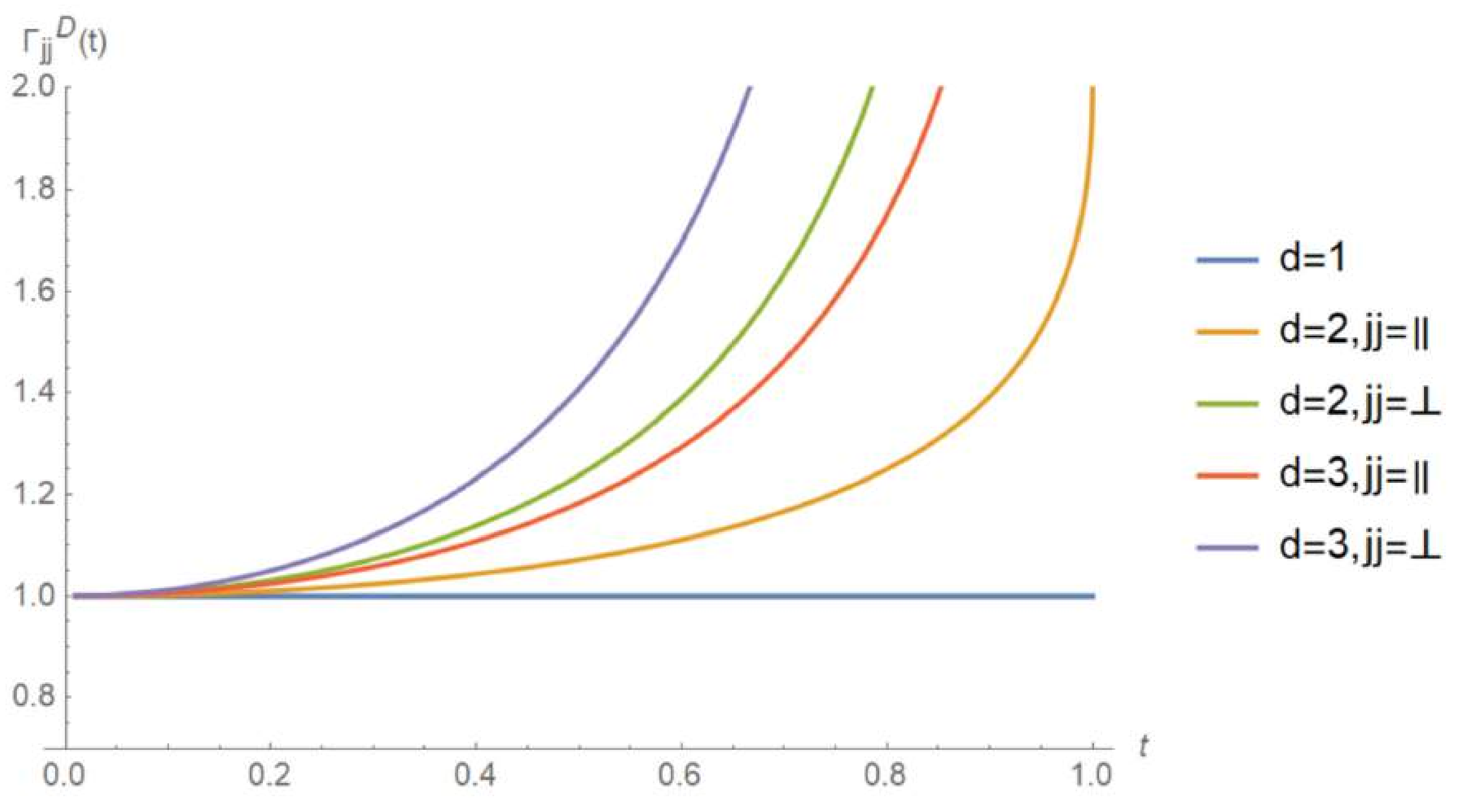

图④：对于 d=123 带间跃迁 Drude 峰关于 t 的极化后的相对高度(0<t<1)，对于无倾斜极限 1(t→0)

$$\mathcal{G}_{\parallel}^{(d)}(x)=Z^{(d)}xF(x^2;\frac{1}{2},\frac{1-d}{2},\frac{3}{2}),$$
$$\mathcal{G}_{\perp}^{(d)}(x)=Z^{(d)}xF(x^2;\frac{1}{2},\frac{3-d}{2},\frac{3}{2})-\frac{1}{d-1}\mathcal{G}_{\parallel}^{(d)}(x),$$
$$\Gamma_{\chi}^{\mathrm{IB}}(\omega;d,\mu,t)=\mathcal{G}_{\chi}^{(d)}(\tilde{\zeta_+})+\mathcal{G}_{\chi}^{(d)}(\tilde{\zeta_-}),\ \chi=\parallel\text{ or }\perp.$$

方程组(2)， Interband$\Gamma_{jj}(\omega,d)$的一般解析式。

$$\Gamma_{\parallel}^{(\mathrm{D})}(d=1;|\mu|/\Lambda,t)=1,$$
$$\Gamma_{\parallel}^{(\mathrm{D})}(d=2;|\mu|/\Lambda,t)=2\frac{1-\sqrt{1-t^2}}{t^2},$$
$$\Gamma_{\perp}^{(\mathrm{D})}(d=2;|\mu|/\Lambda,t)=2\frac{1-\sqrt{1-t^2}}{t^2\sqrt{1-t^2}},$$
$$\Gamma_{\parallel}^{(\mathrm{D})}(d=3;|\mu|/\Lambda,t)=\frac{3}{2t^3}\left[\ln\frac{1+t}{1-t}-2t\right],$$
$$\Gamma_{\perp}^{(\mathrm{D})}(d=3;|\mu|/\Lambda,t)=\frac{3}{4t^3}\left[\frac{2t}{1-t^2}-\ln\frac{1+t}{1-t}\right].$$

$$\Gamma_{\chi}^{\mathrm{DC}}(t;\frac{\Lambda}{\mu})=\frac{Z^{(d)}}{t^d(d-1)!}\left.\frac{\partial^{d-1}}{\partial s^{d-1}}\right|_{s=\frac{1}{t}}\left[X_\chi(s)Y_n(s)\log\frac{s+1}{s-1}\right]$$

$$\Gamma_{\chi}^{\mathrm{DC}}(t;\frac{\Lambda}{\mu})=\frac{Z^{(d)}\pi}{t^d}\left\{\frac{1}{2}X_\chi''(0)(-1)^{n-1}-\frac{1}{(d-1)!}\left.\frac{\partial^{d-1}}{\partial s^{d-1}}\right|_{s=\frac{1}{t}}\left[\frac{X_\chi(s)Y_n(s)}{\sqrt{s^2-1}}\right]\right\}$$

方程组（3）：左，对于 d=123 的解析式。右：（0<t<1)任意维数（区分奇偶）Drude 峰相对高度的一般形式

Direct *d-d* hybridization mechanism for strong anisotropic carrier transport in layered Mo_2SBr_2

Haijun Liao, Ye Xiao, Yibin Yang, Le Huang*, Huafeng Dong, and Fugen Wu
School of Materials and Energy, Guangdong University of Technology, Guangzhou 510006, China
huangle@gdut.edu.cn

PHYSICAL REVIEW B **105**, 195427 (2022)

Introduction

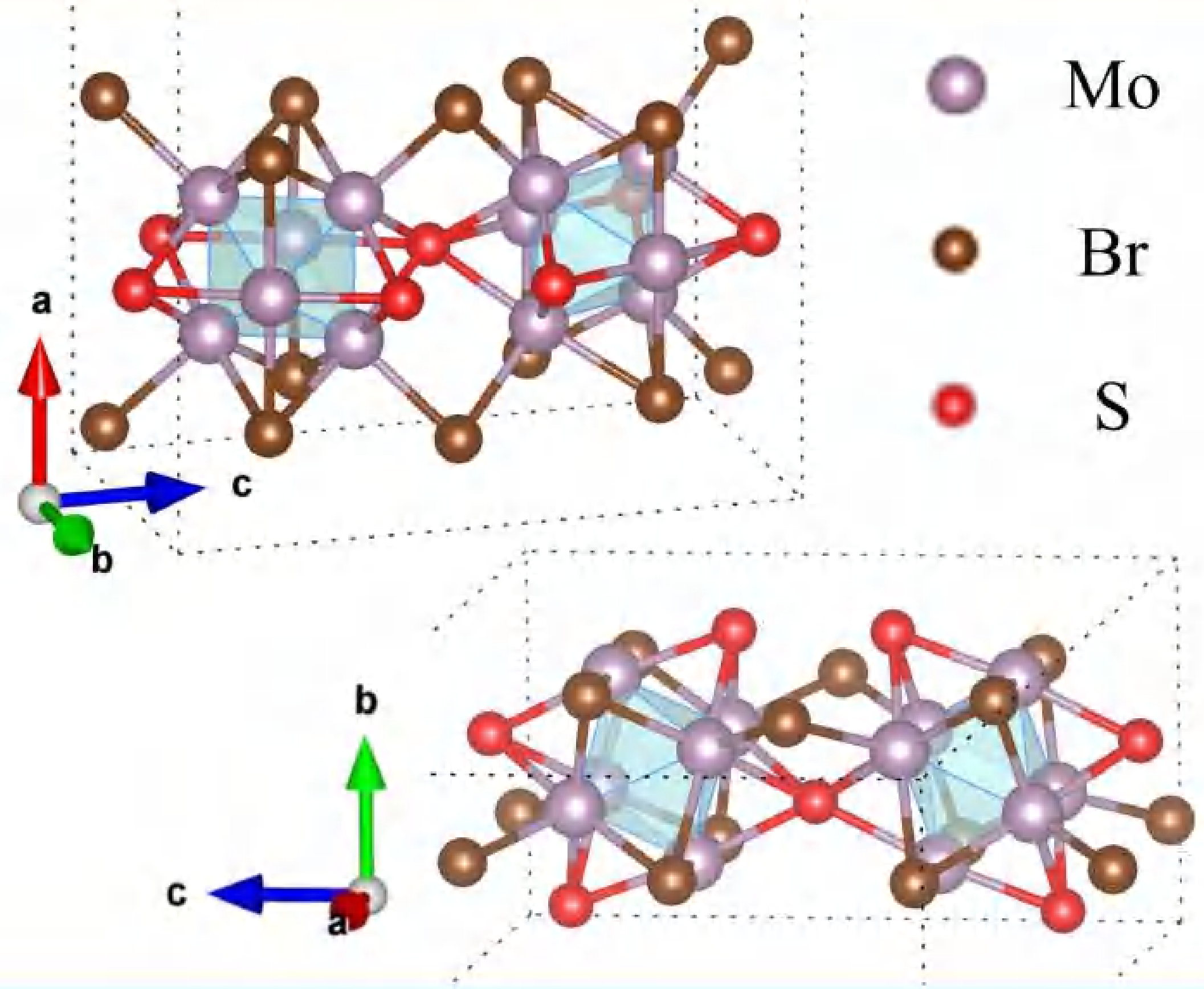

It is found that Mo_2SBr_2 experimentally exhibits obvious in-plane anisotropy in its electronic structure and photoelectric properties in 2019, which endows it with great application potential for polarized detection. The mechanism of the anisotropy, however, is far from clearness. Herein, theoretical calculations are performed to explore the physics of anisotropic properties of monolayer Mo_2SBr_2.

Results & Discussion

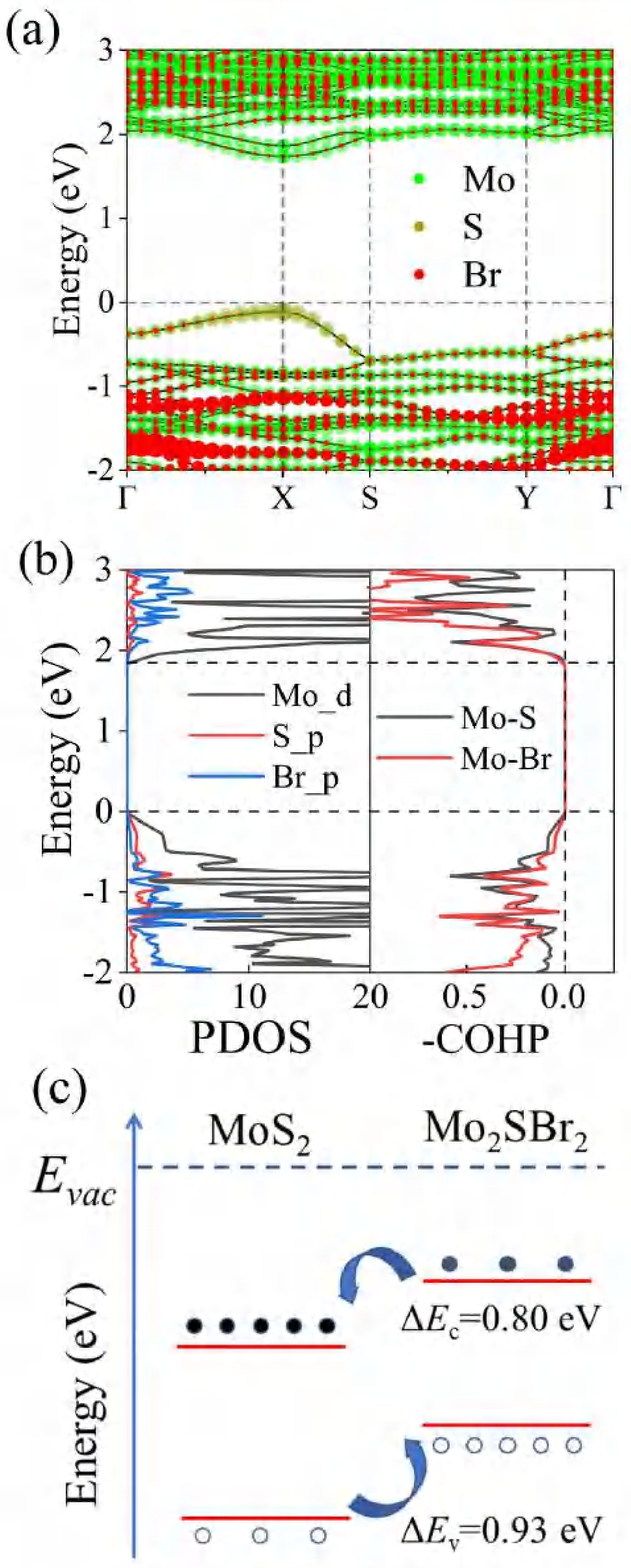

Fig. a, b and c show the figures of PBAND, PDOS -COHP and band-alignment, respectively. The VBM and CBM are formed by the anti-bonding of Mo-S and Mo-Br bond. The direct *d-d* coupling pushes the VBM and CBM of monolayer Mo_2SBr_2 upward.

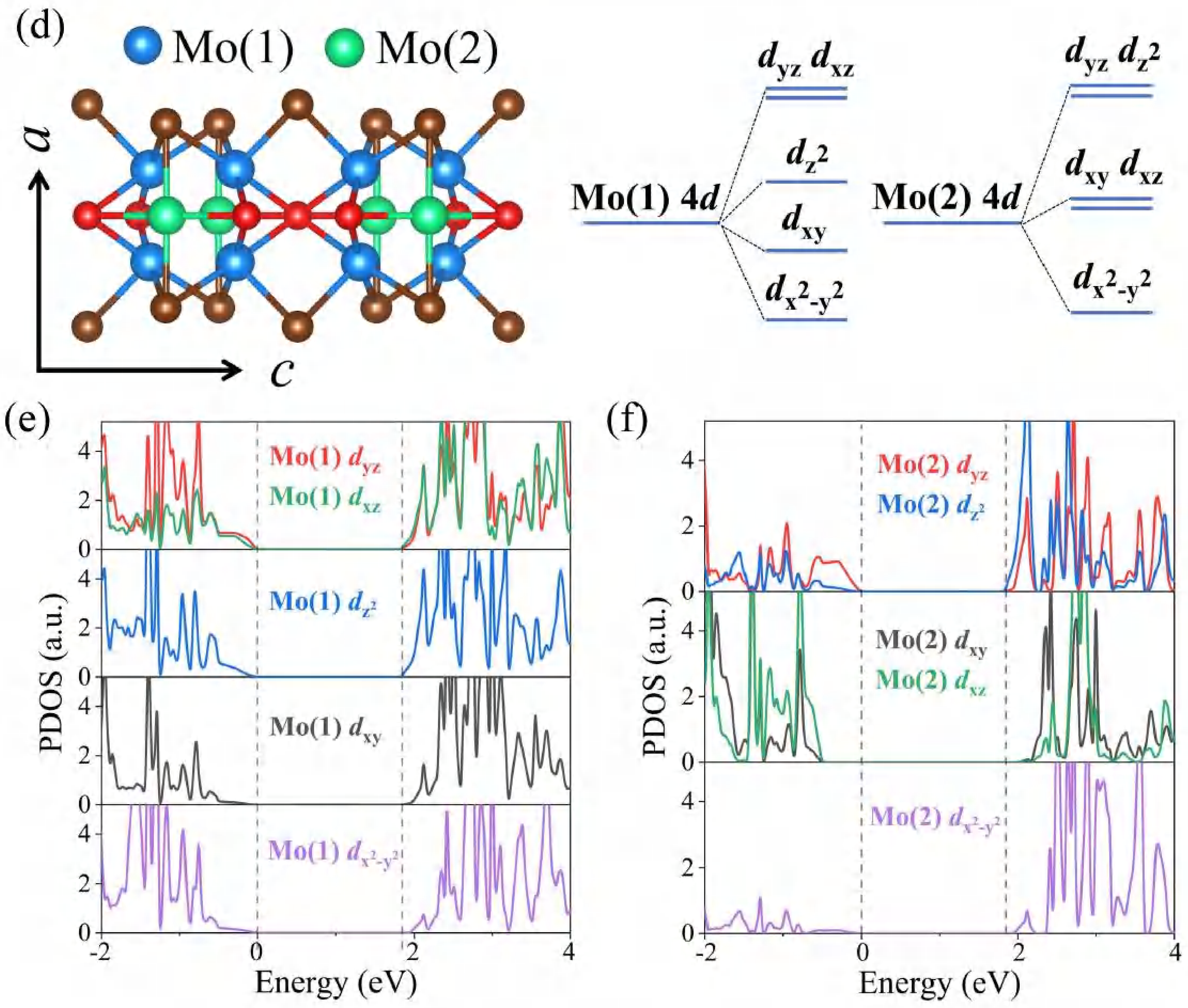

Fig. d shows two chemical environments of Mo atoms which are called as Mo(1) and Mo(2).

Fig. e and f give two PDOS images of Mo(1) and Mo(2). The orbitals of d_{yz} in Mo(1) form the direct *d-d* coupling which is benefited to carrier mobility transport.

The direct *d-d* coupling decreases effective mass along *c* direction by opening a carrier transport channel. Thus the hole effective mass along the *c* direction ($0.23\ m_c^*/m_0$) is much smaller than that of mobility along the *b* direction ($1.19\ m_b^*/m_0$). More evidences are shown in the Fig. g and h.

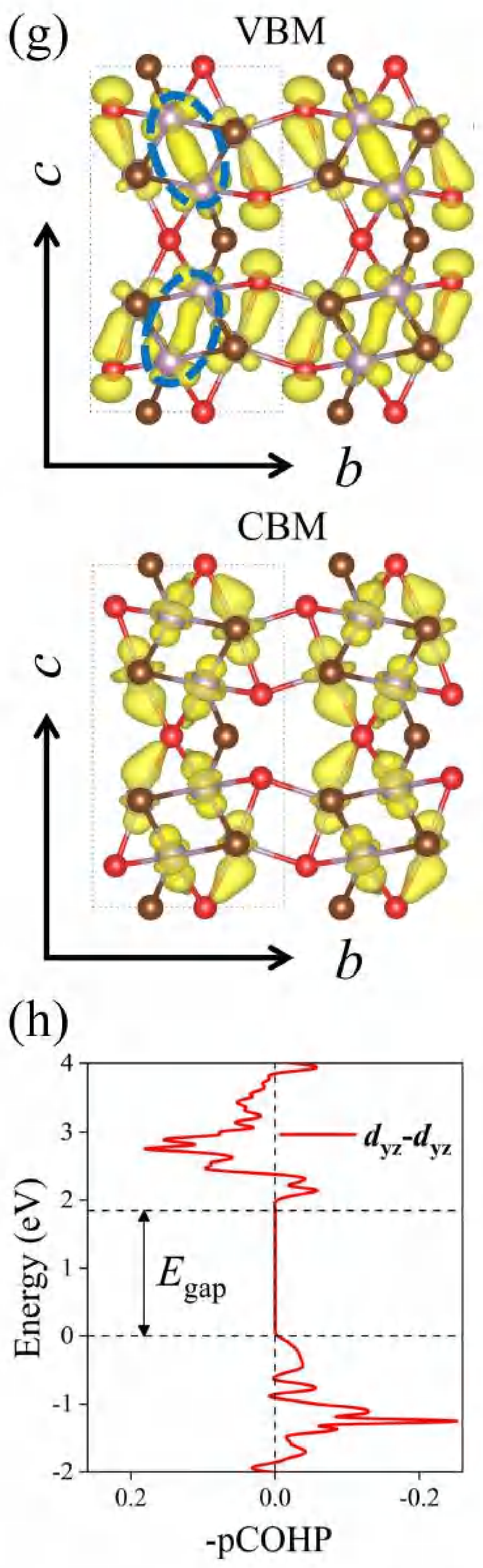

(g) Images of band decomposed charge density in VBM and CBM. It is obvious that direct *d-d* coupling is shown in the VBM.
(h) Image of -pCOHP between Mo d_{yz}-d_{yz}. The direct *d-d* coupling is actually existed in VBM.

Conclusion

- Monolayer Mo_2SBr_2 exhibited revealed strong anisotropies in its mechanical and electronic properties in our calculation. It is found that monolayer Mo_2SBr_2 demonstrates obvious anisotropy in its electron mobility, μ_e, with an extremely high μ_e of 10356.08 $cm^2 \cdot V^{-1} \cdot s^{-1}$ along the *b* direction. This strong anisotropy is attributed to the unique characters in the orbital coupling.
- Further studies show that direct *d-d* coupling between the nearest-neighboring Mo atoms plays a critical role in the unique carrier transport properties and strong anisotropy. Direct *d-d* coupling provides a fast hole transport channel along the *c* direction.

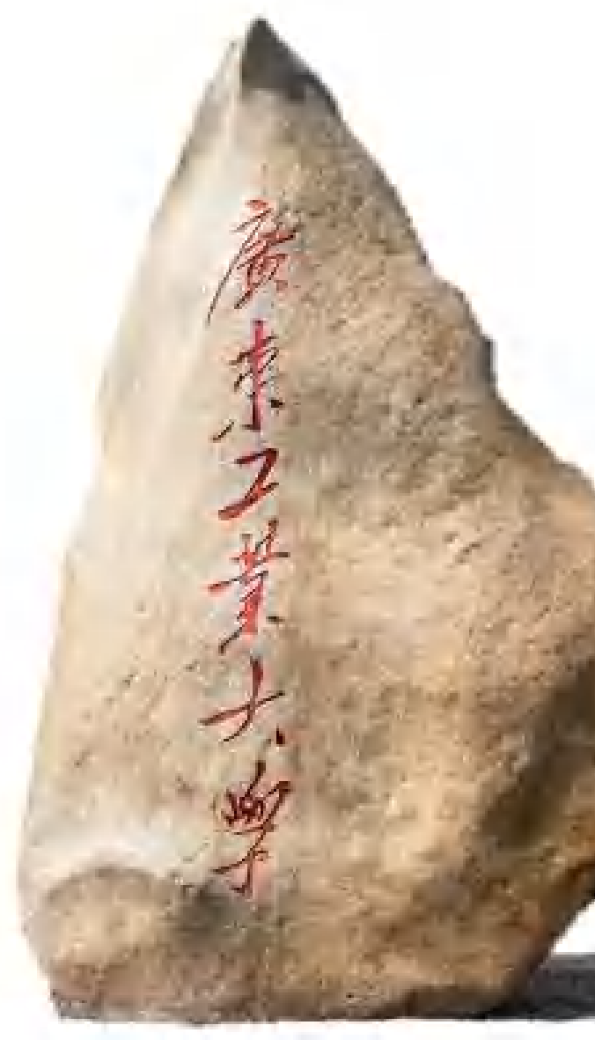

First Principle Study of Electronic Polaron in $CoCl_2$

Li Yao[1], Aolei Wang[1] and Jin Zhao[1,2,3*]

[1]Department of Physics, University of Science and Technology of China, Hefei, Anhui 230026, China
[2]Department of Physics and Astronomy, University of Pittsburgh, Pittsburgh PA 15260, United States
[3]CAS Center for Excellence in Quantum Information and Quantum Physics, University of Science and Technology of China, Hefei, Anhui 230026, China

I. Introduction

Polaron is a composite quasiparticle derived from an excess carrier trapped by local lattice distortion, and has been studied extensively for decades both theoretically and experimentally. The conventional mechanism of polaron formation is through electron-phonon coupling where the charge is dressed with a lattice distortion, leading to carrier localization. In principle, a purely electronic effect where a spontaneous ordering of electrons breaks the crystal symmetry. Via a purely electronic mechanism, would constitute a fundamentally new type of polaron, dubbed an **electronic polaron**. In recent years, polaronic physics in **two-dimensional** strongly-correlated systems has attracted considerable attention. Here, we demonstrate the presence of three electron polarons in monolayer $CoCl_2$ and the formation and transition.

II. Polaron Properties

- Structure distortion

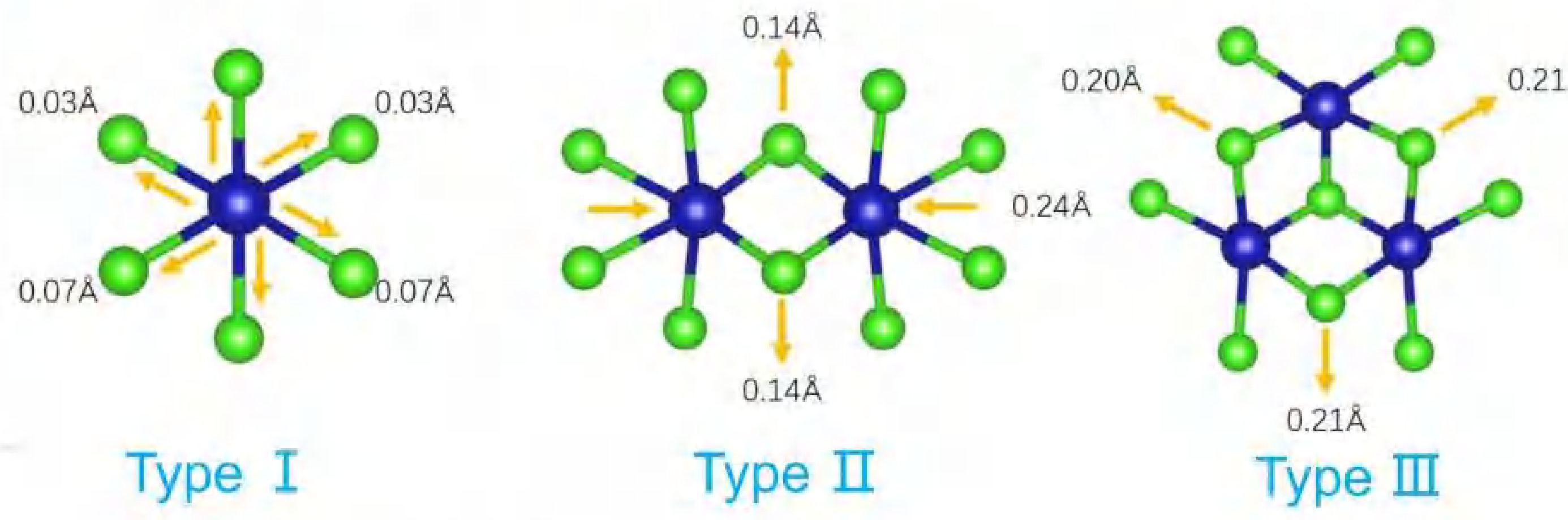

- Density of states (DOS)

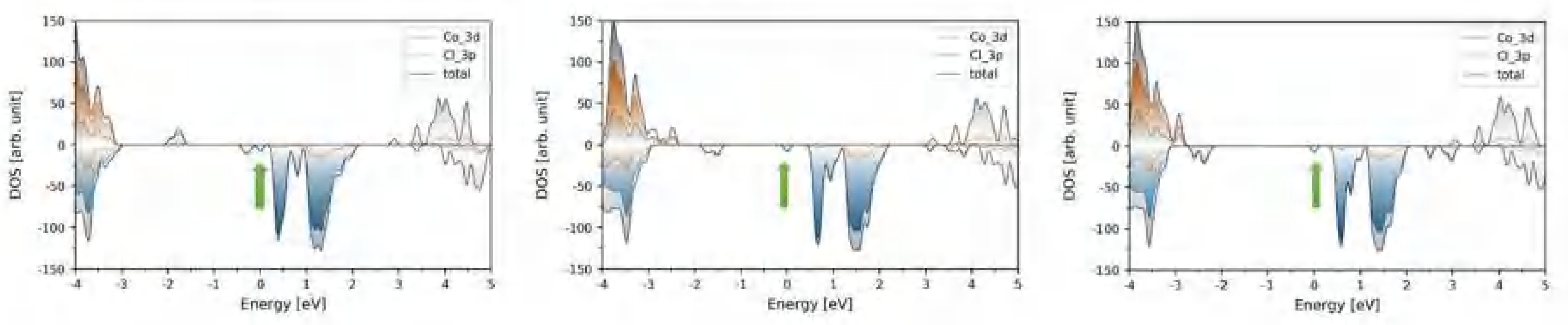

- Wave function of CBM (green arrow in DOS)

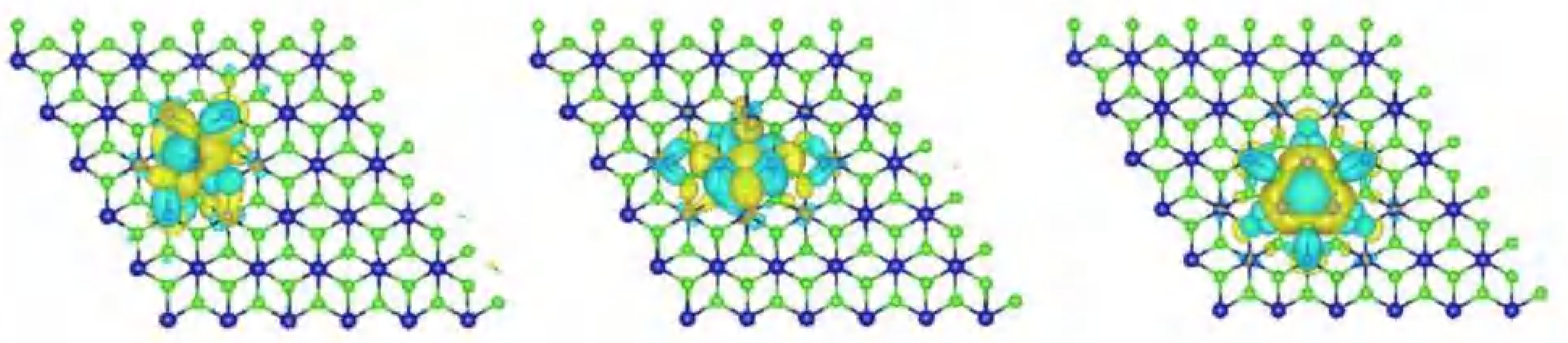

By injecting electron into $CoCl_2$, three type of polarons can be formed, which are localized on 1, 2 and 3 Co atoms, respectively. Type Ⅰ has the highest total energy and type Ⅲ hsa the lowest.

- Magnetic moment variation of Co atoms in polarons
  - Black line represents magnetic moment of pristine cell
  - Blue: type I Orange: type II Green: type III
  - Top: perpendicular to the plane Below: in the plane

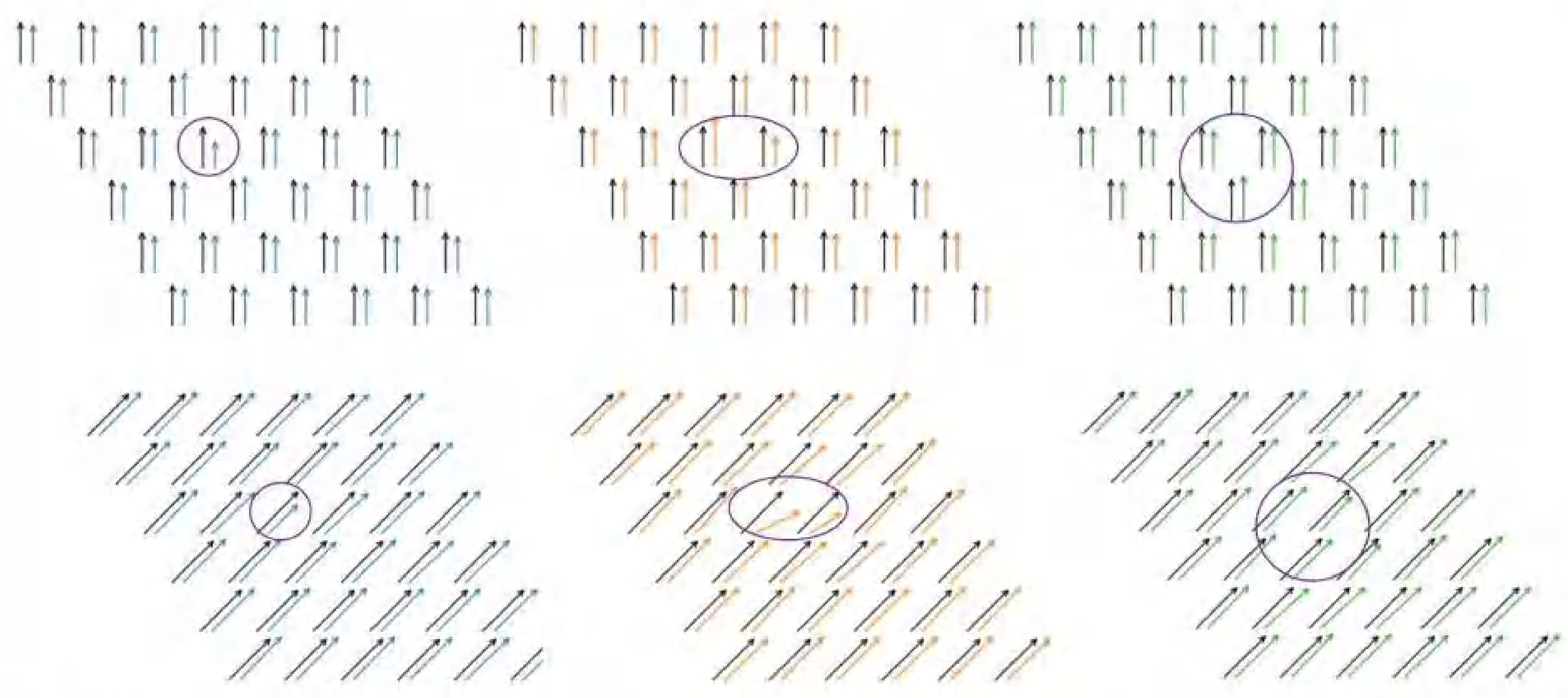

When the polarons forms in $CoCl_2$, the magnetic moment of the Co atoms at the structural distortion changes.

III. Polaron Dynamics

- Energy level evolution with time
  - Red line: polaron formation
  - Purple line: transition
  - Blue line: type II
  - Green line: type III

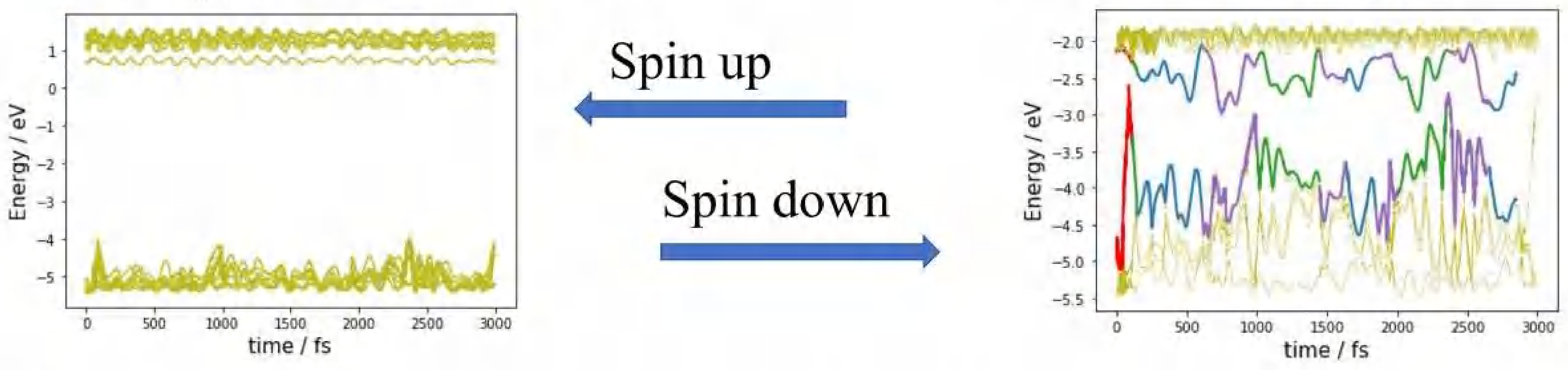

- Snap shots of wave function of polaron during MD

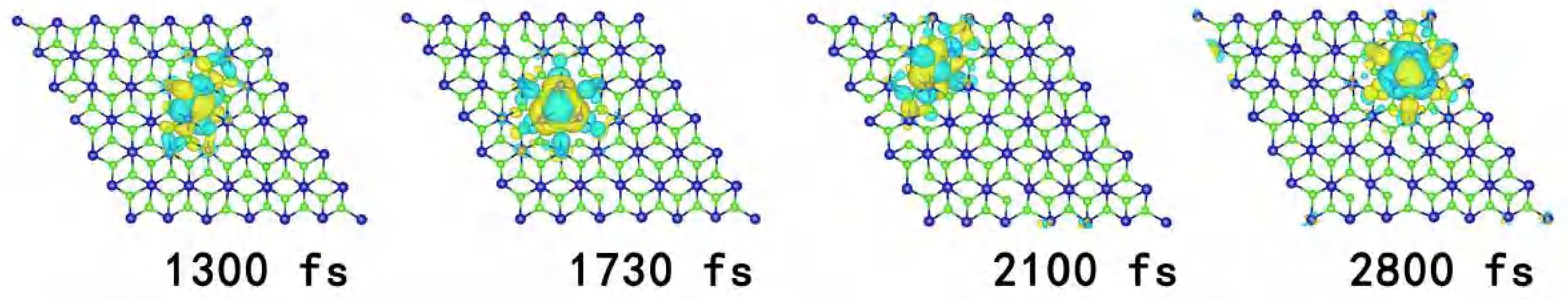

3 ps adiabatic molecular dynamics (MD) trajectories in the microcanonical ensemble are obtained with a 1 fs atomic time step. Firstly, type II polaron formation at about 100 fs. Then, the polaron transfer between type III and type II. Since type 1 polaron has the highest energy, it does not appear in the entire MD.

- Excited carrier recombition of spin up and spin down:
  Spin up: > 100 ps Spin down: 1.9 ps

The lifetime of the carriers in different spin channels are calculated using the Hefei-NAMD method.

IV. Conclusions

- We show the positions of the three polarons as well as their magnetic moment changes due to structural distortion .
- During MD, electronic polaron can transition between different types.
- The lifetime of the spin-down carrier is smaller due to the larger non-adiabatic coupling vector as well as the lower energy difference(CBM-VBM) of spin down.

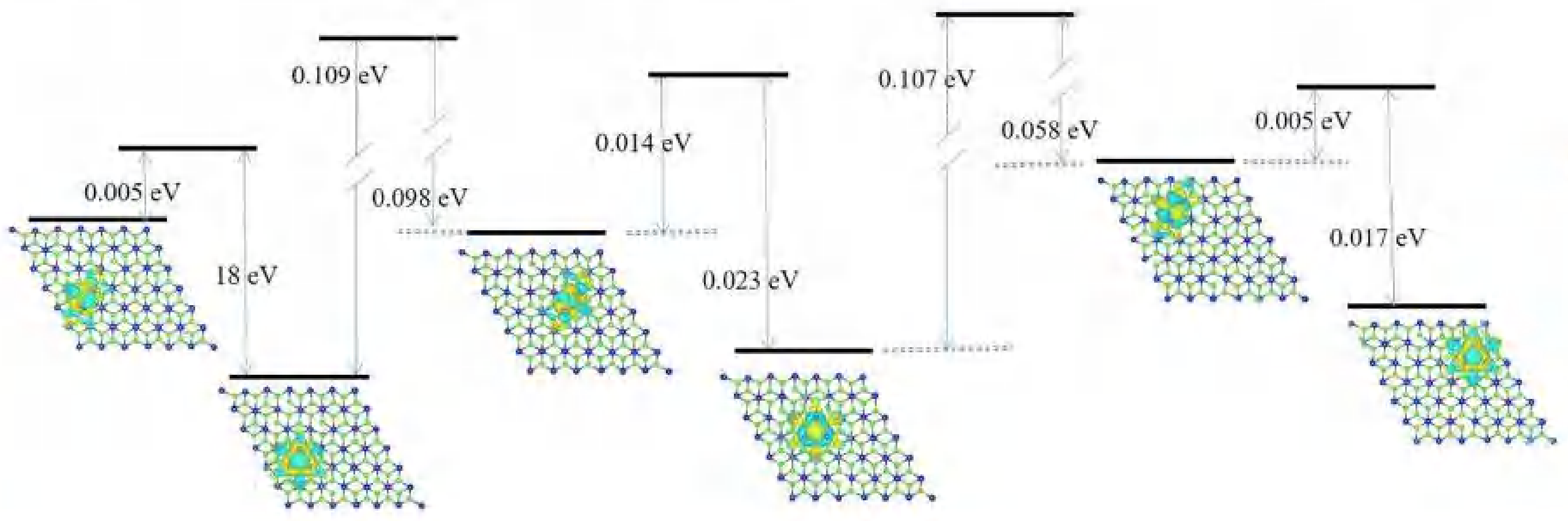

- Barrier diagram of polaron transition and migration

Electronic and optical properties of WTe_2/Sb heterostructure by first principle study

Wang fanfan , Yuan jun , Zhou jun*

School of Physical Science and Technology, Ningbo University, Ningbo 315211, Zhejiang, P. R. China

Introduction

Heterojunctions of two-dimensional materials have attracted great interest from researchers because they could present some novel properties, in which retain some nature of each layer. We established WTe_2/Sb heterojunctions and explored theirs optoelectronic properties based on DFT by Quantum-ATK software package.

Results and discuss

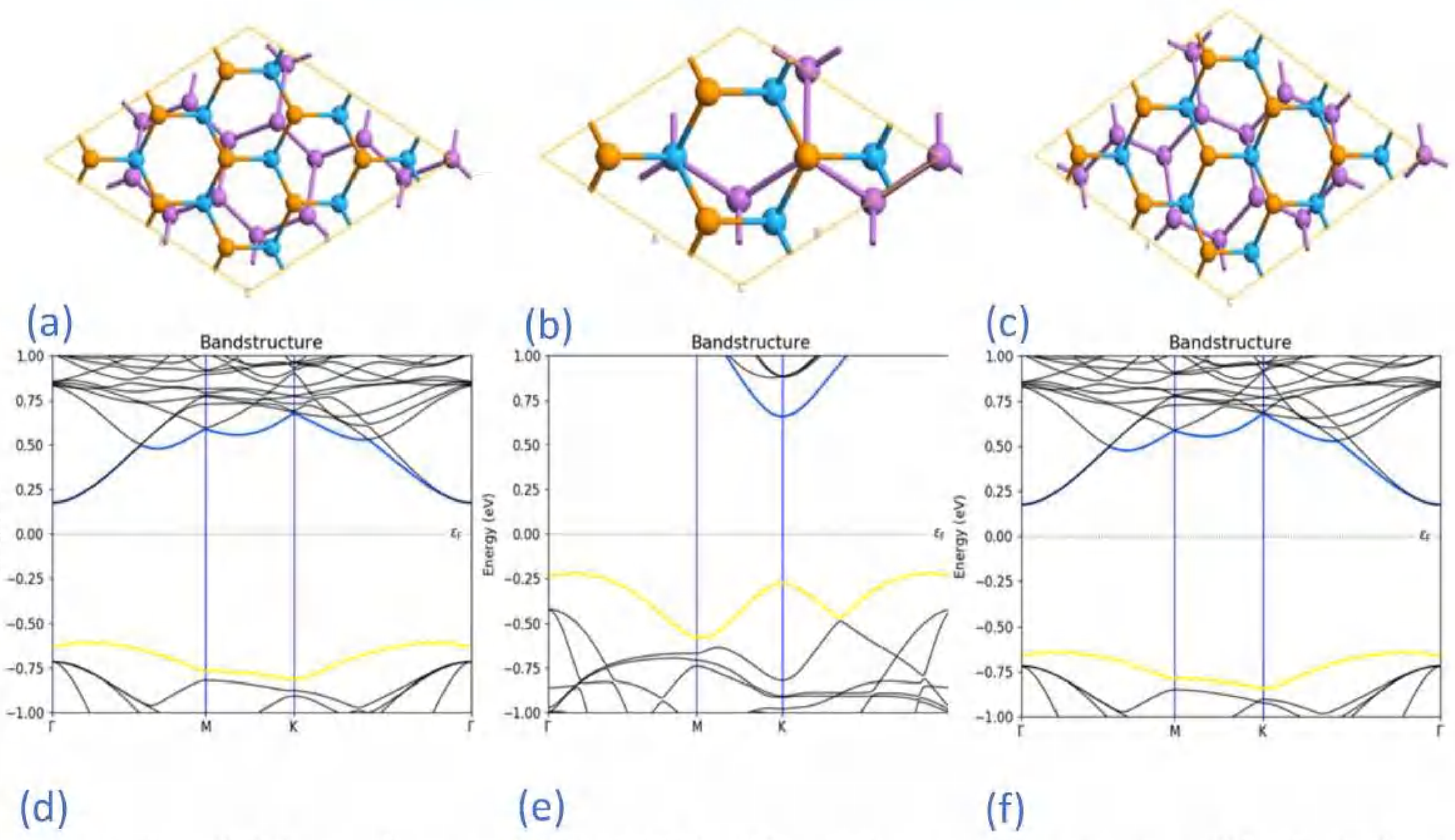

Figure 1 (a-c) Top view of the WTe_2/Sb bilayer structure with interlayer rotation of 19.11°, 30° and 40.89°, respectively. (d-f) The bandstructure of WTe_2/Sb bilayer with interlayer rotation of 19.11°, 30° and 40.89°, respectively.

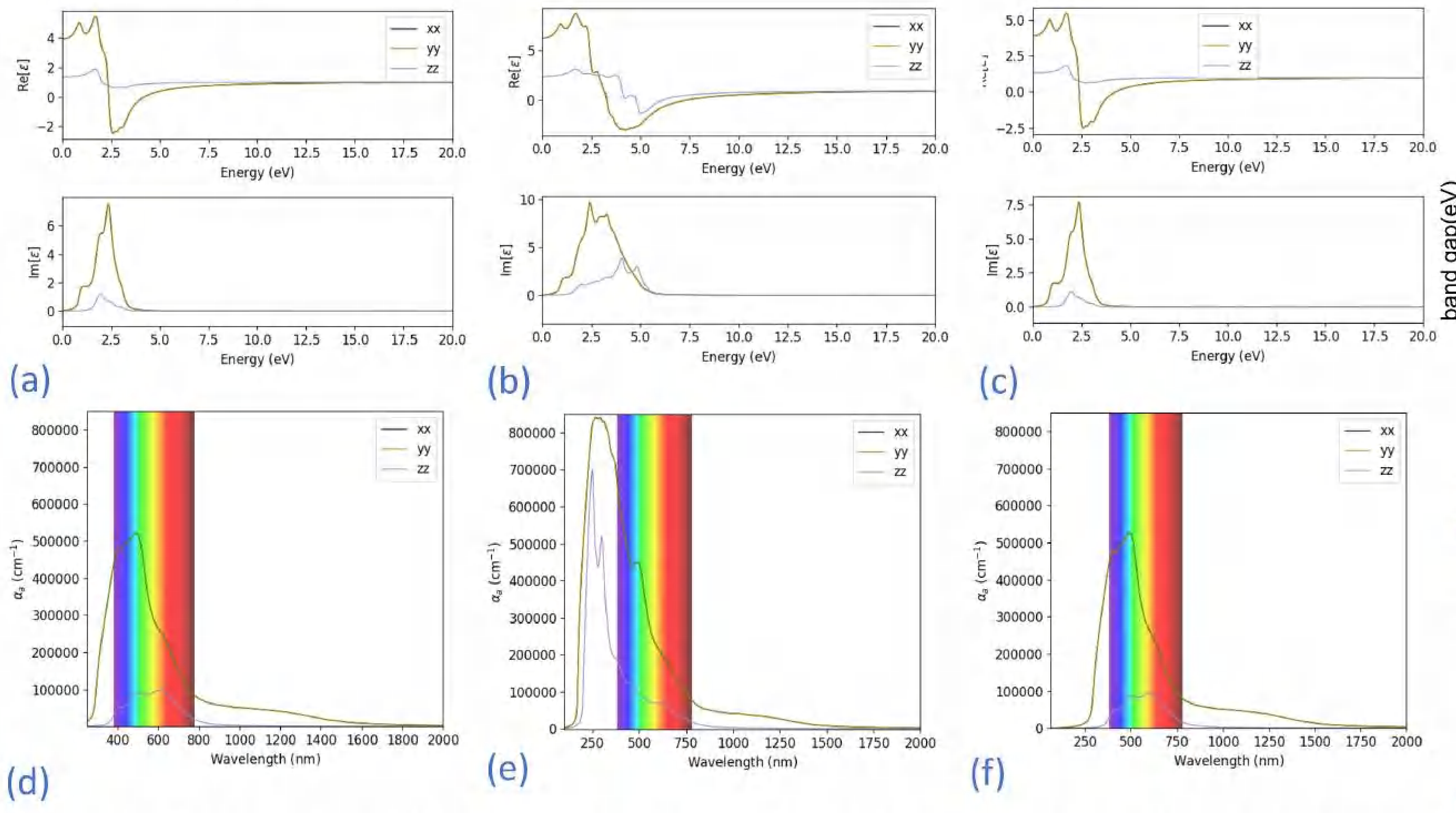

Figure 2 Dielectric coefficient *of the* Sb/ WTe_2 heterostructure with rotation angles of (a) 19.11°, (b) 30° and (c) 40.89° . Absorption coefficient *of the* WTe_2/Sb heterostructure with rotation angles of (d) 19.11°, (e) 30° and (f) 40.89° .

Dielectric coefficient	$\varepsilon(\omega)=\varepsilon_1(\omega)+i\varepsilon_2(\omega)$
Imaginary part formula	$\varepsilon_2(\omega)=\frac{2e^2\pi}{\Omega\varepsilon_0}\sum_{k,v,c}\left\|\psi_k^c\right\|u.r\left\|\psi_k^c\right\|^2\delta\left[E_k^c-E_k^v-E\right]$
Absorption coefficient	$\alpha=\sqrt{2}\omega\left(\sqrt{\varepsilon_1^2(\omega)+\varepsilon_2^2(\omega)}-\varepsilon_1(\omega)\right)^{\frac{1}{2}}$

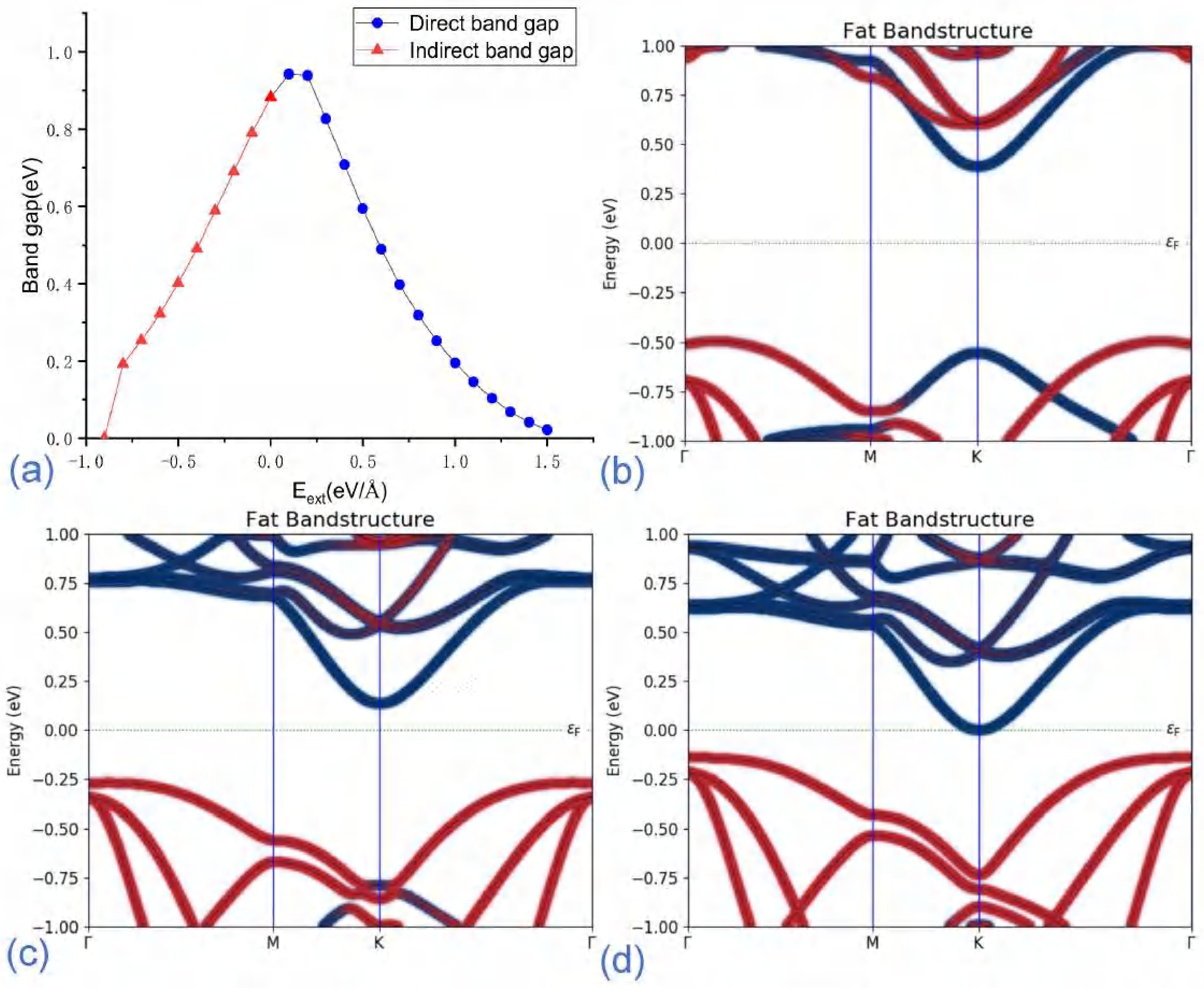

Figure 3 (a) The variation curves of band gap with applied voltage for heterojunction with interlayer rotation angle of 30°. The fat bandstructures of the 30° twisted interface at applied voltages of (b) +0.5V, (c) -0.5V and (d) -0.9V.

Under different external voltages, the bandgap of the structure not only exhibits regular changes, but also the direct and indirect band gaps can be tuned. In addition, the direct band gap exhibits type-I band edge alignment and the indirect band gap exhibits type-II band edge alignment.

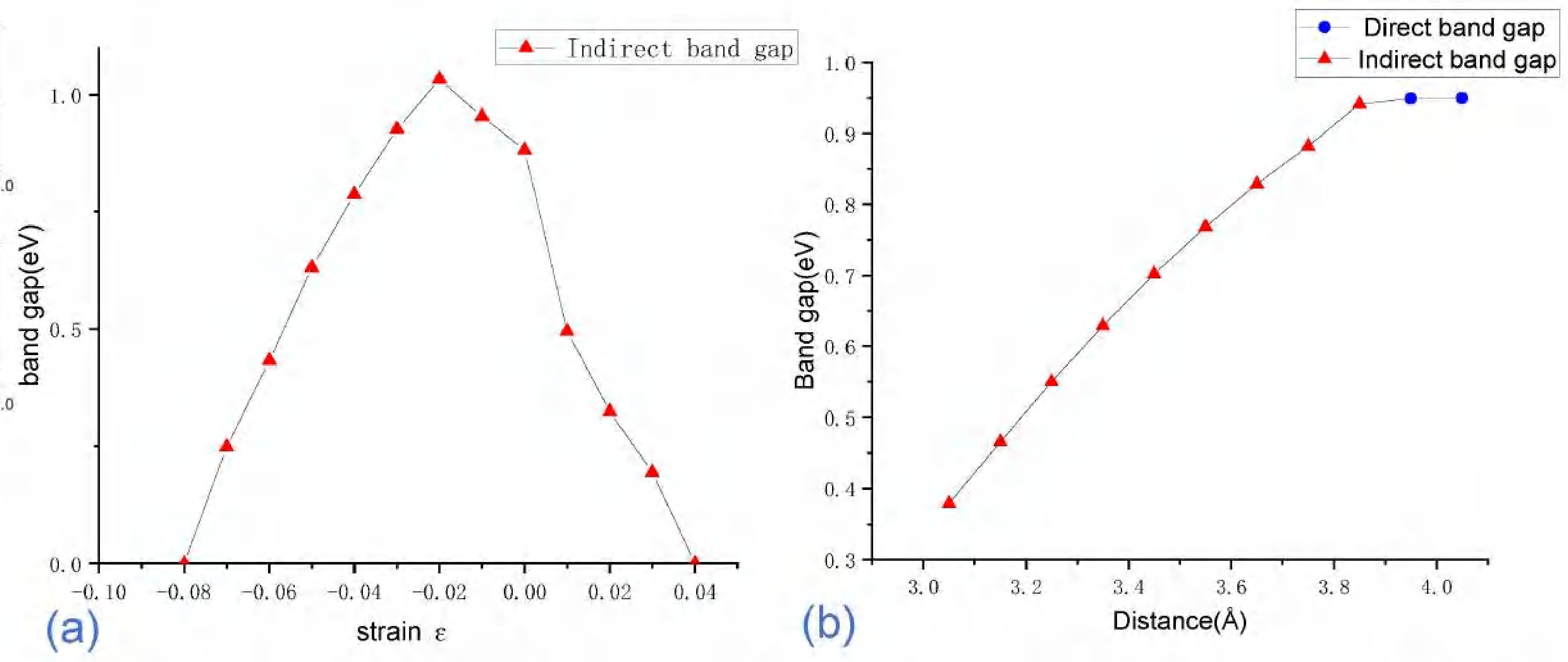

Figure 4 Band gap values of heterostructure with interlayer rotation of 30° as a function of (a) biaxial strain and (b)layer spacing.

Conclusion and Prospect

We calculated the bandstucture and optical spectrum of the WTe_2/Sb heterojunctions and tuned the bandgap by applying external voltage, biaxial strain, and vertical strain . We will also further explore its application potential for photocatalytic decomposition of water and solar cells.

Orbital Dependence in Single-Atom Electrocatalytic Reactions

Yanan Wang[1,2], Yingzong Liang[1,2], Tao Bo[1,2], Sheng Meng*[1,2], Miao Liu*[1,2,3]

[1]Songshan Lake Materials Laboratory, Dongguan, Guangdong 523808, China
[2]Beijing National Laboratory for Condensed Matter Physics and Institute of Physics, Chinese Academy of Sciences, Beijing 100190, China
[3]Center of Materials Science and Optoelectronics Engineering, University of Chinese Academy of Sciences, Beijing 100049, China

ABSTRACT: Transition metal single-atom catalysts supported on N-doped graphene (TM−N−C) could serve as an ideal model for studying orbital dependence in electrocatalytic reactions because the atom on the catalytic active site has discrete single-atom-like orbitals. In this work, the catalytic efficiency of Fe−N−C for the oxygen evolution reaction (OER) under a small structural perturbation has been comprehensively investigated with density functional theory calculations. The results suggest that the subtle local environment of a single atom can significantly modulate the catalytic reactivity. Further analysis demonstrates that the energy level of the TM d_{z2} orbital center, rather than the d-band center, is responsible for the OER catalytic efficiency as the d_{z2} orbital participates mainly in the reactions. Essentially, the d-band theory can be extended to the sub-d orbital level, and a small perturbation of the crystal field, induced by lattice strain or z-direction displacement of the TM atom, can prominently change the sub-d orbital associated with the reaction and in turn affect the catalytic activity.

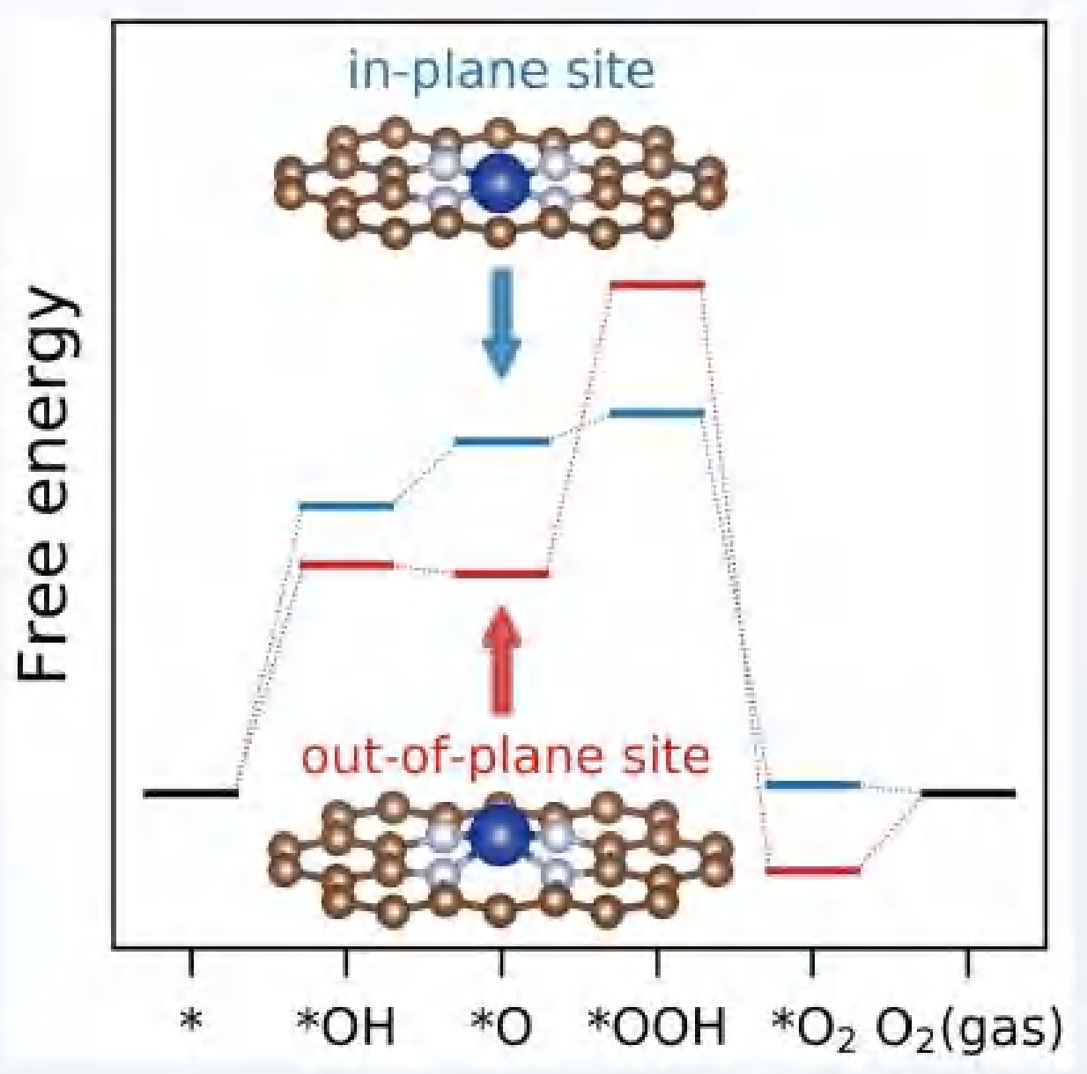

RESULTS

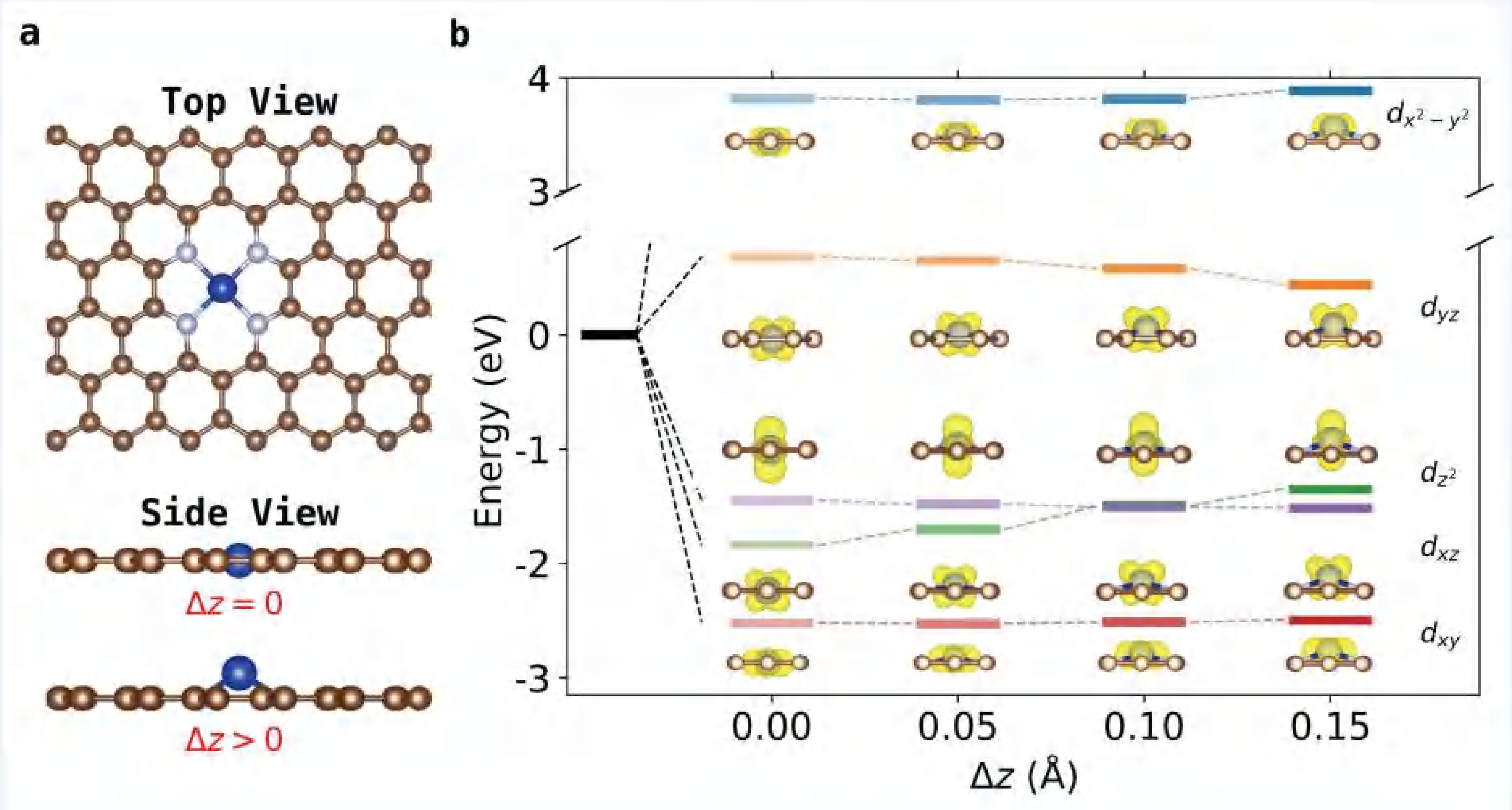

Figure 1. Atomic structure and d-band splitting diagram of TM−N−C. (a) Top and side views of the atomic structure of TM−N−C. (b) d-Band splitting of TM−N−C when there is a small displacement along the z-direction.

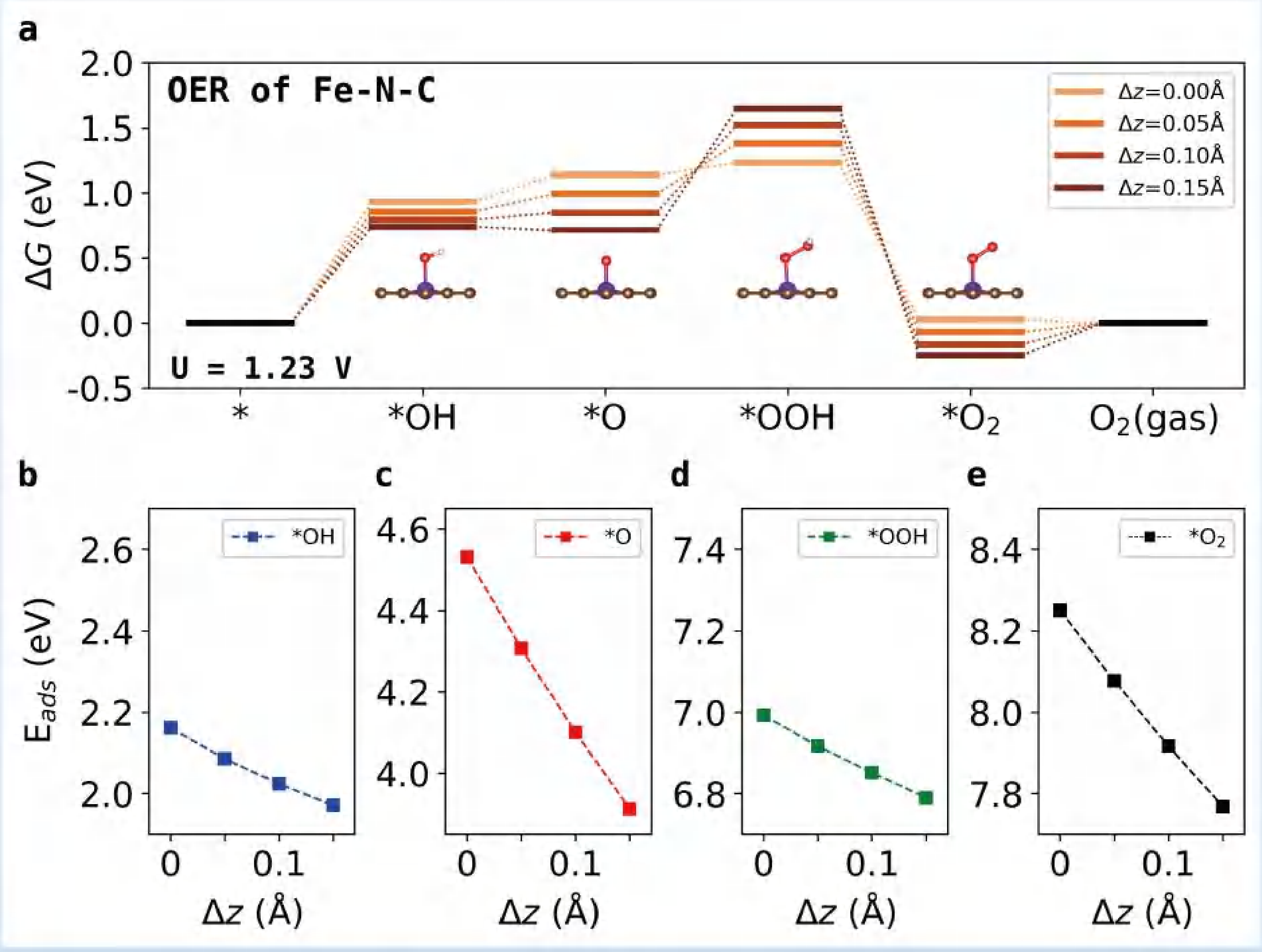

Figure 2. Catalytic efficiency of Fe−N−C regulated via vertical displacement. (a) Free energy diagram of Fe−N−C with Δz in the range of 0−0.15 Å. (b−e) E_{ads} values of four intermediate states that vary with the Δz of Fe−N−C.

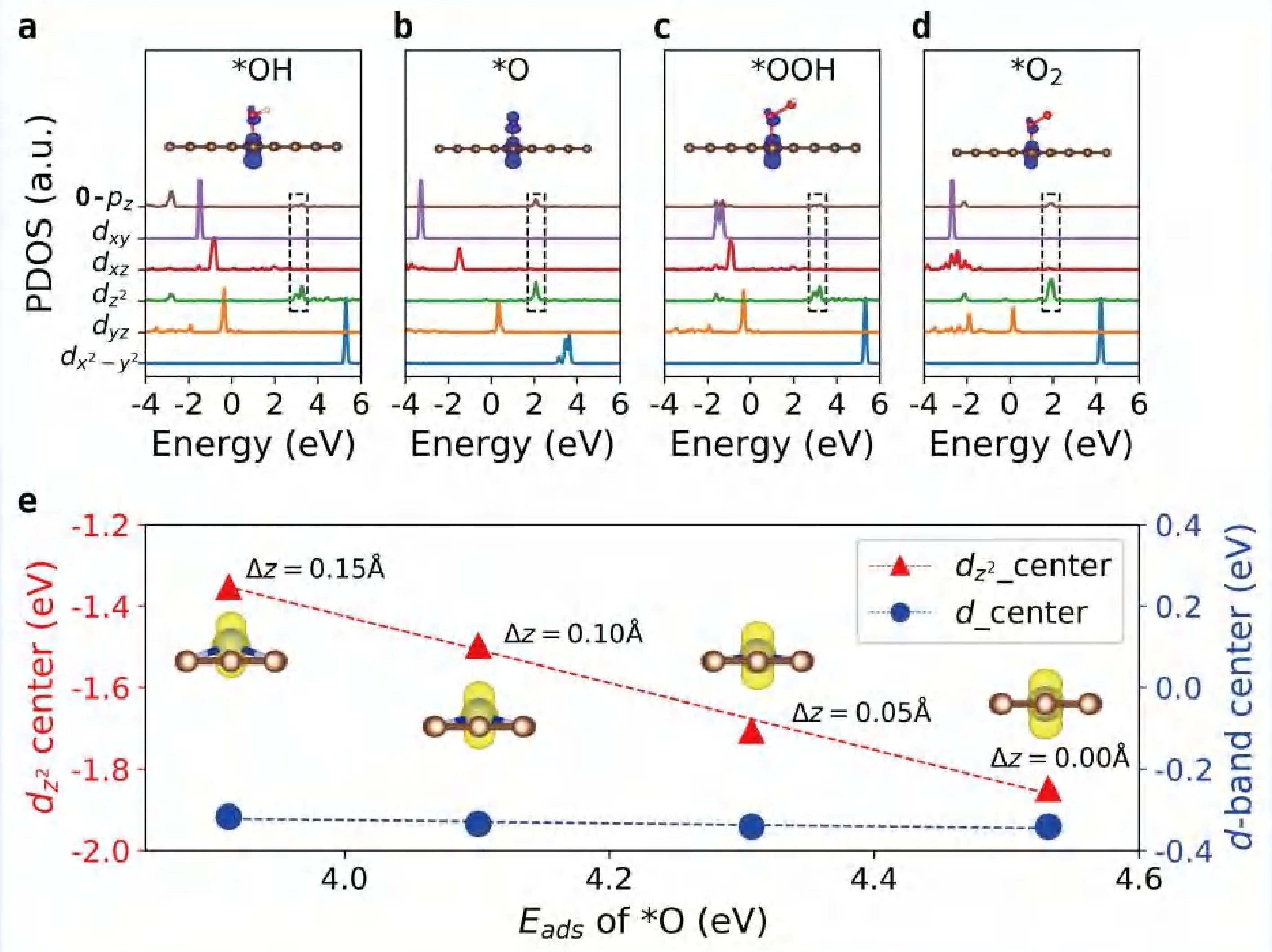

Figure 3. Only the d_{z2} orbital participates in the OER. (a−d) Partial density of states (PDOS) and orbital hybridizations of the four intermediate states in the OER process of Fe−N−C. (e) O atom adsorption energies correlate with the Fe d_{z2} orbital center and the d-band center as Δz of Fe−N−C gradually increases from 0 to 0.15 Å.

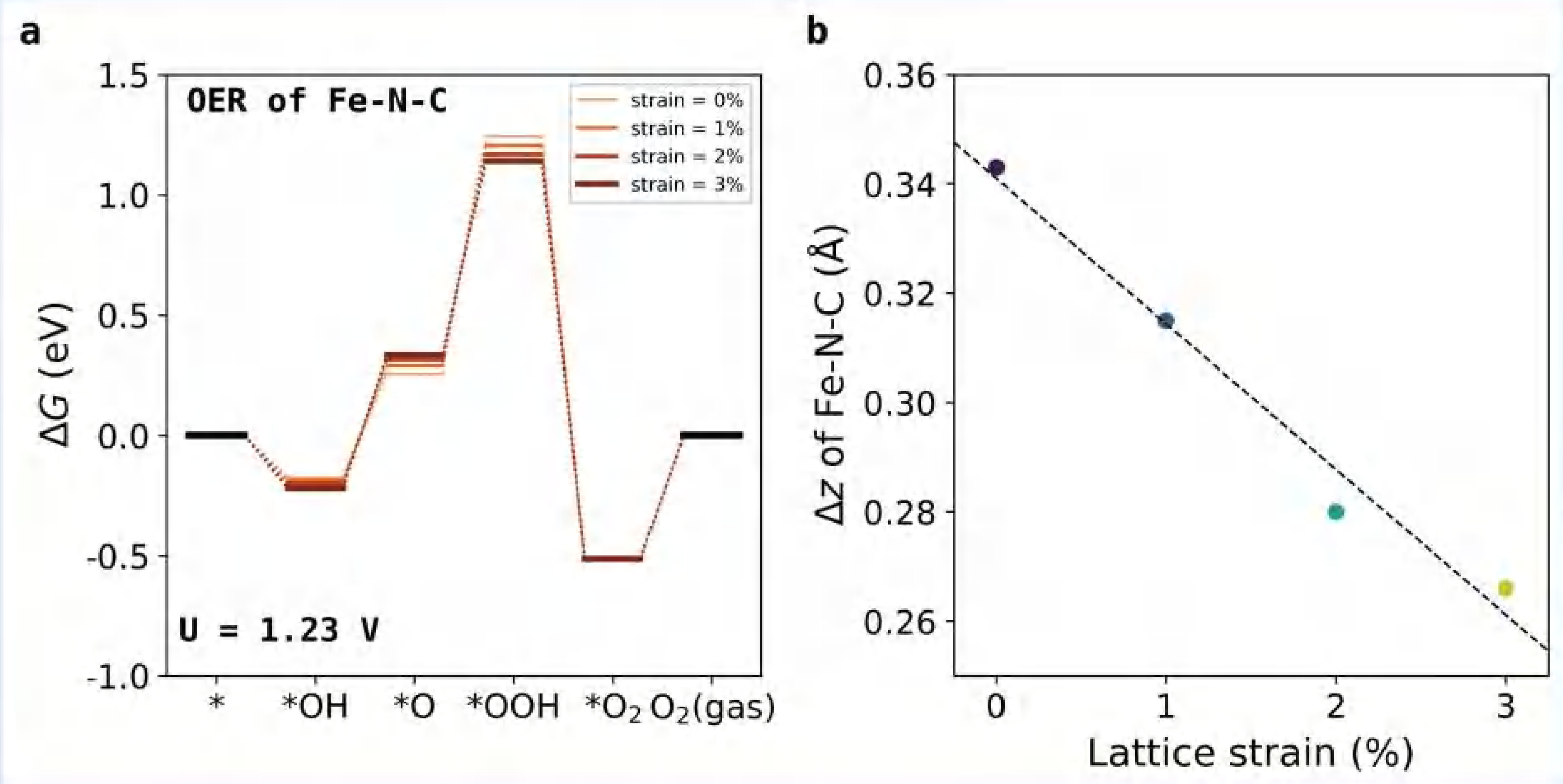

Figure 4. Lattice strain regulates the OER catalytic reactivity of Fe−N−C. (a) OER catalytic efficiency of the Fe−N−C system with change in strain from 0% to 3%. (b) Relationship between lattice strain and Δz of the *O step.

CONCLUSION: We propose that TM−N−C can be used as an ideal model system to study the orbital dependence in the water splitting catalytic reaction and provide a strategy for adjusting the electrocatalytic activity by changing the z-direction displacement between the TM single atom and N-doped graphene substrate. The DFT results show that the OER catalytic reactivity can be significantly modified with the variation of the z-direction displacement, and such modification breaks the “scaling relations” in catalytic chemistry. We have also investigated the microscopic mechanism behind the regulation of the OER catalytic activity. It is found that only the d_{z2} orbital of the TM single atom participates in the reaction, and the energy position of the d_{z2} orbital center can be used as a good indicator of OER reactivity. In addition, our calculations also indicate that lattice strain can be used as a good way to tune the z-direction displacement and thus regulate the catalytic activity. The results are expected to be generally applicable to other TM SACs, which provide an efficient way to tune the catalytic efficiency and achieve their applications in industrial catalysis.

This work has been published on J. Phys. Chem. Lett. 2022, 13, 5969-5976.

Control of Polaronic Behaviors and Carrier Lifetimes via Metal and Anion Alloying in Chalcogenide Perovskites

Qiao-qiao Li[1], LuoYan[1], Weibin Chu[2], Junjie He[3*], Huanbo Luo[4],
Thomas Frauenheim[5], Sergei Tretiak[6], Liujiang Zhou[1*]

Corresponding Authors: junjie.he.phy@gmail.com; ljzhou86@uestc.edu.cn

Background:

1. Transition metal perovskite chalcogenides have emerged as lead-free alternatives to lead-halide perovskites.
2. $BaZrS_3$ demonstrates superior moisture stability, direct band gap of 1.73-1.85 eV, high photon absorption, defect tolerance, and is suitable for optoelectronic devices.
3. For band gap regulation, whether alloying can facilitate the delocalization of polaron spatial distribution and carrier lifetimes remains to be investigated.

Polaronic Behaviors

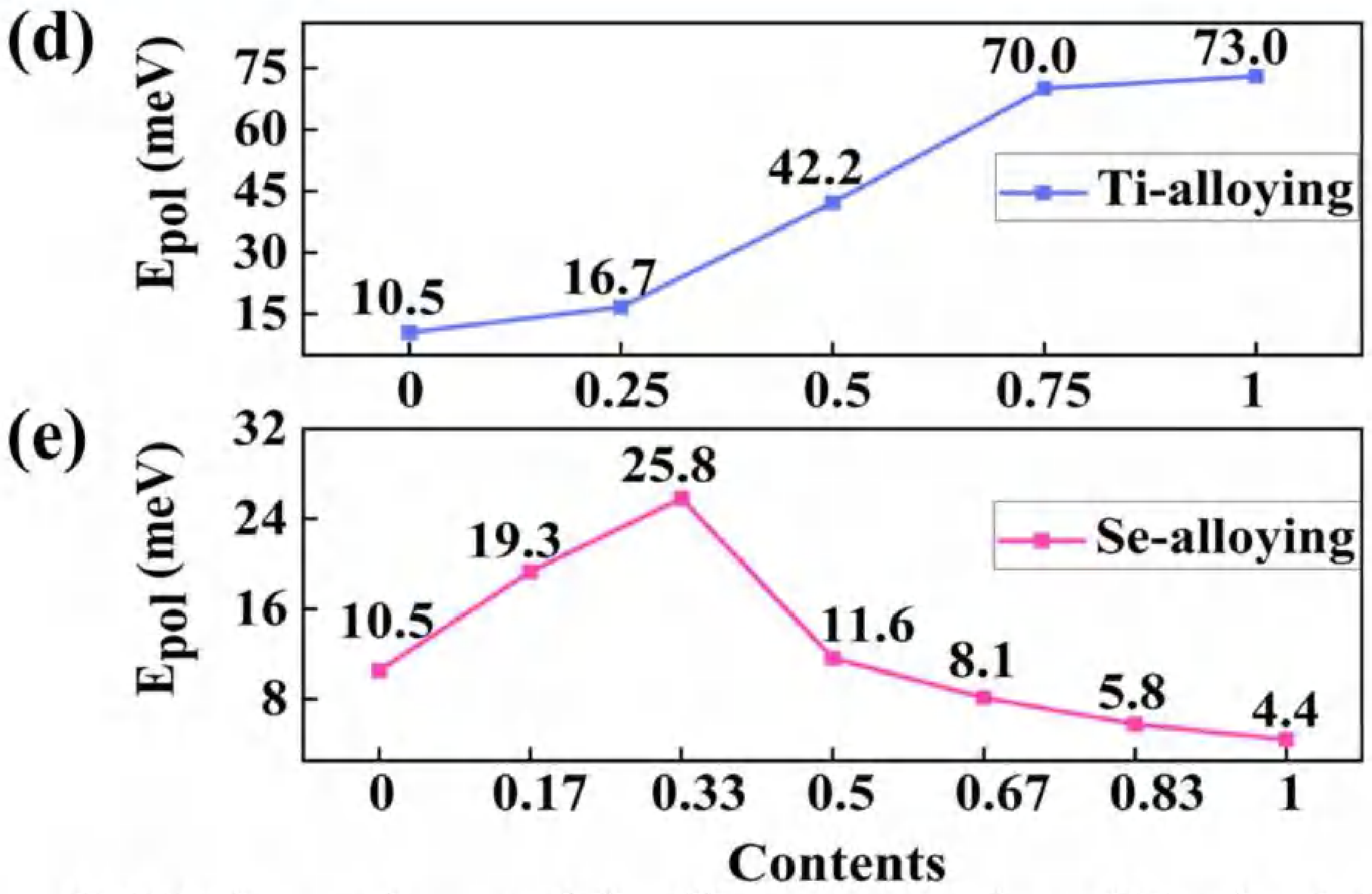

Fig. 2 Hole polaron binding energies (E_{pol}) rising in (d) $BaZr_{1-x}Ti_xS_3$ and reducing in (e) $BaZr(S_{1-x}Se_x)_3$.

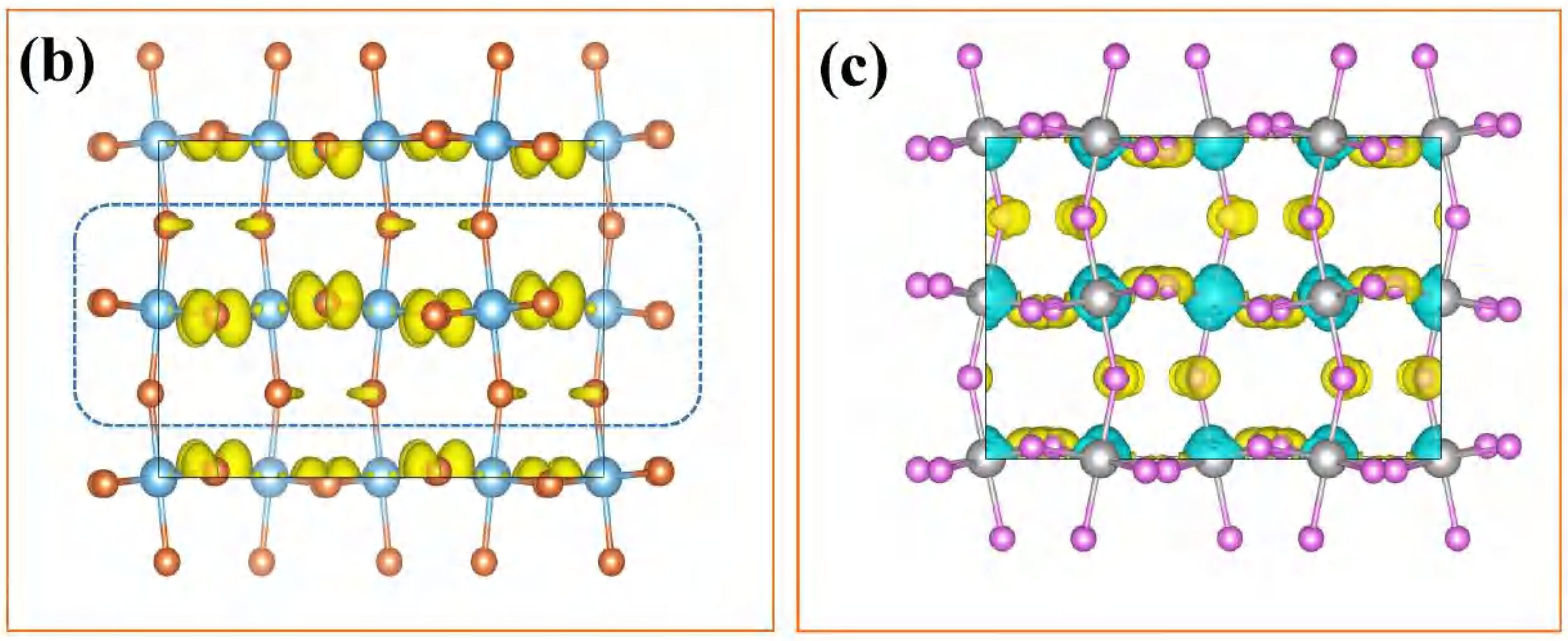

Fig. 3 Localized hole polaron distributions in $BaTiS_3$ (b) , and delocalized hole polaron in $BaZrSe_3$ (c).

Nonadiabatic Molecular Dynamics

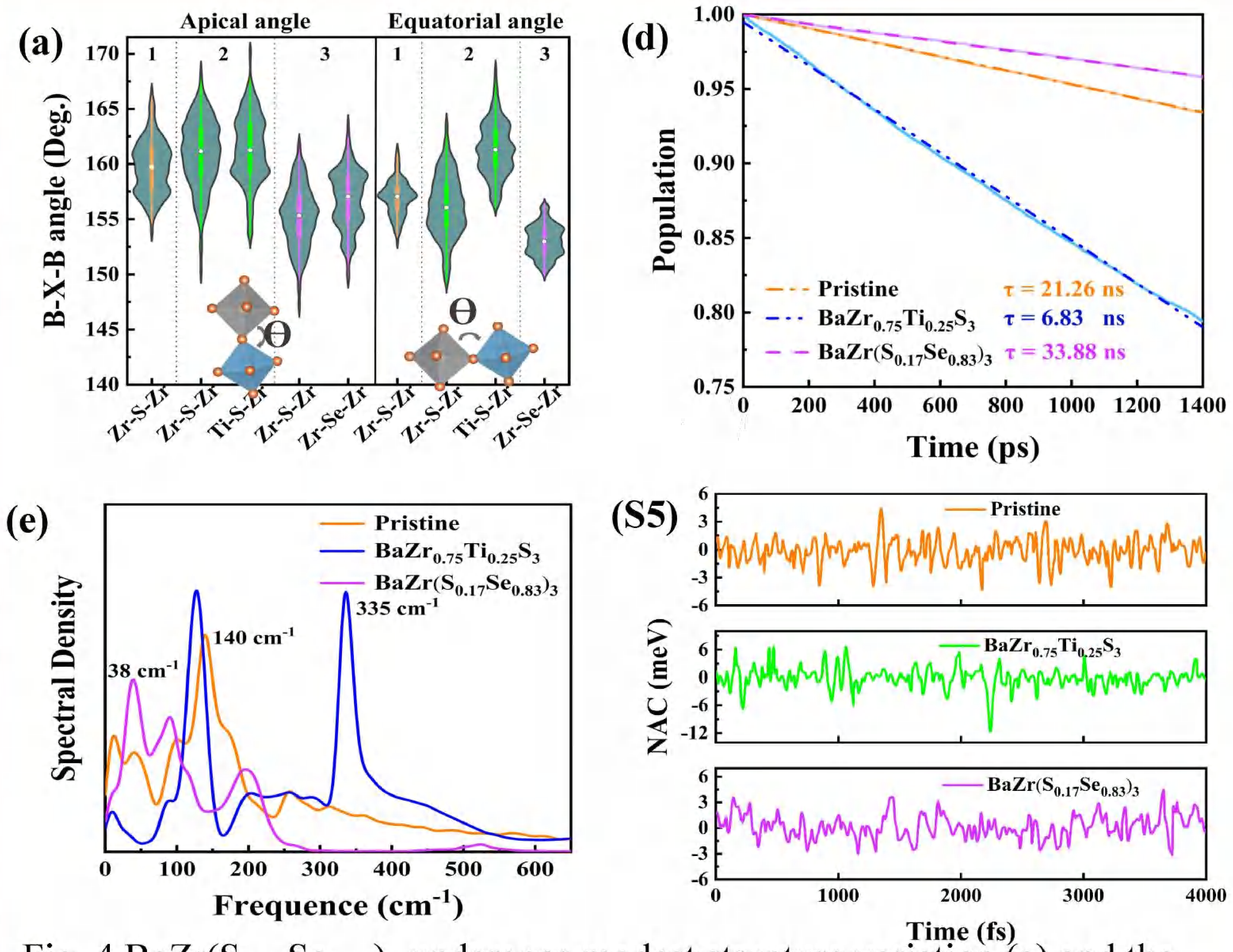

Fig. 4 $BaZr(S_{0.17}Se_{0.83})_3$ undergoes modest structure variation (a) and the longest e-h recombination lifetime (d) for the low frequency e-p coupling (e) and modest nonadiabatic coupling (S5).

Method

PWMAT

Polaronic Behaviors

Nonadiabatic Molecular Dynamics

Conclusion

1. S/Se alloying systems presenting delocalized large polarons, Ti enhances electron-phonon coupling ultimately leading to the localized small polaron limit.
2. Se substitution in $BaZr(S_{0.17}Se_{0.83})_3$ weakens electron phonon coupling as well as alleviating nonadiabatic coupling. This reduces *e-h* recombination rate prolongs the carrier lifetime by about 60% compared to the pristine $BaZrS_3$.

Relevant Publication: J. Phys. Chem. Lett. 2022, 13, 22, 4955–4962. *https://doi.org/10.1021/acs.jpclett.2c00880*

Topological defects and their induced metallicity in monolayer semiconducting γ-phase group Ⅳ monochalcogenides

Shengfeng Zeng, Xiaolong Zou*
Tsinghua-Berkeley Shenzhen Institute and Tsinghua Shenzhen International
Graduate School, Tsinghua University, Shenzhen 518055, China
*E-mail: xlzou@sz.tsinghua.edu.cn

Introduction

- A new predicted phase of group Ⅳ monochalcogenides (MX), γ-MX, possesses the more favorable energy than common α and β phases.[1]
- γ-GeSe was synthesized by chemical vapor deposition (CVD), but exhibiting metallicity rather than predicted semiconducting behaviors.[2]
- Structural defects formed during the CVD process have key impacts on electronic properties, including dislocation cores (DCs) and grain boundaries (GBs).[3]

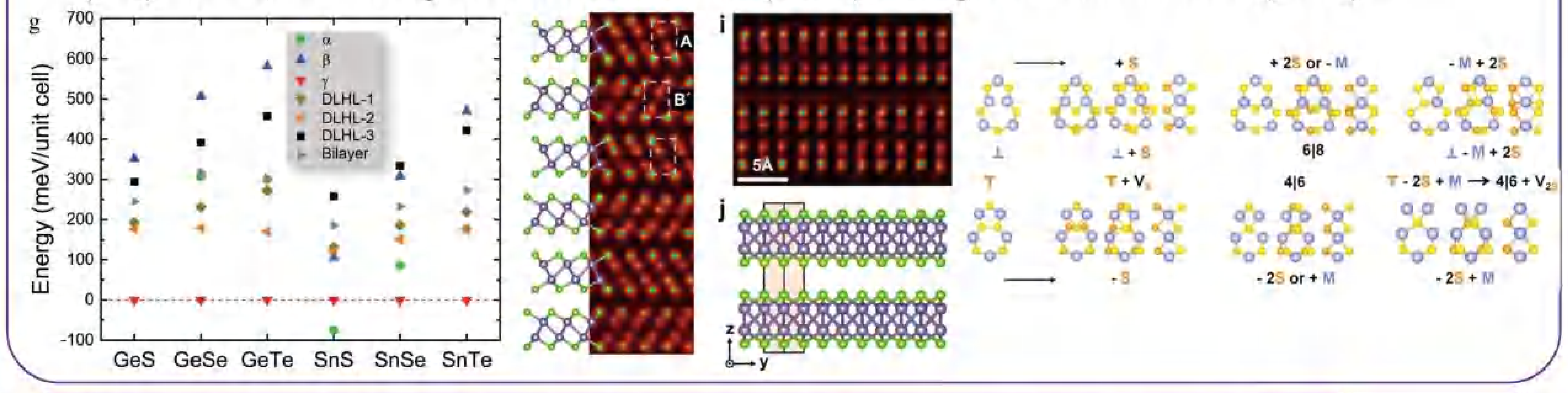

Structures and thermodynamic energies of DCs

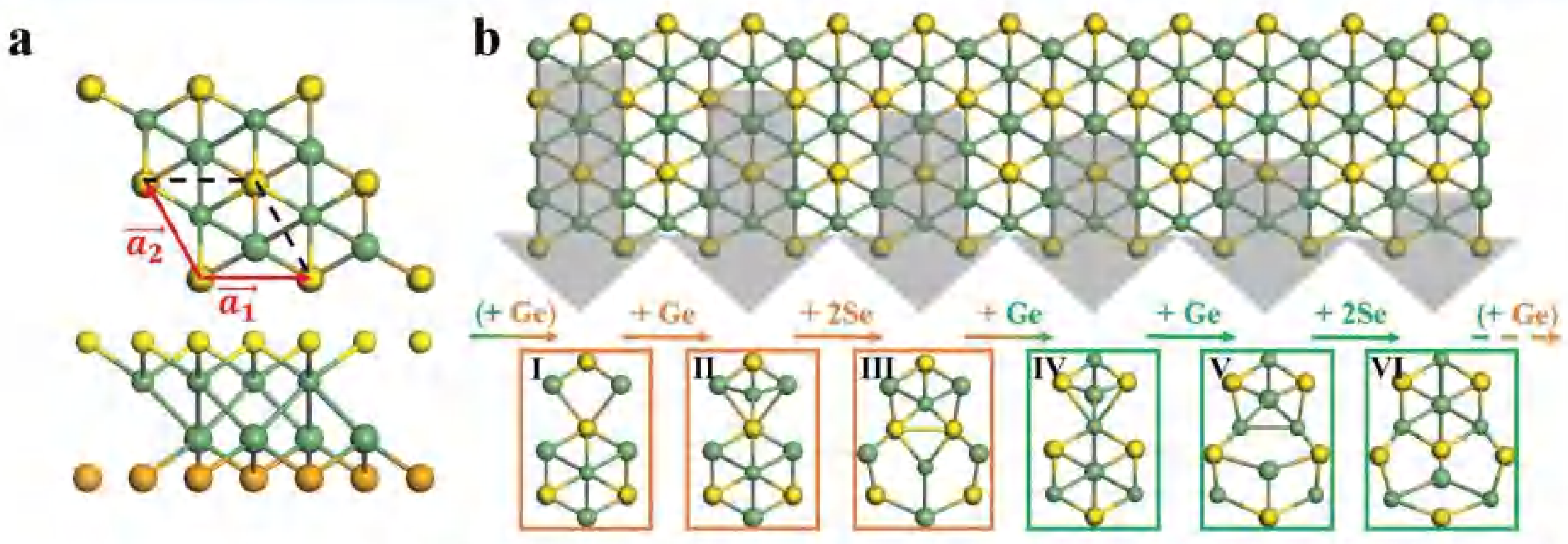

The hexagonal lattice of γ-GeSe makes it feasible to construct DCs in the same way as adopted in monolayer MoS_2, categorized into Se- and Ge-oriented types.

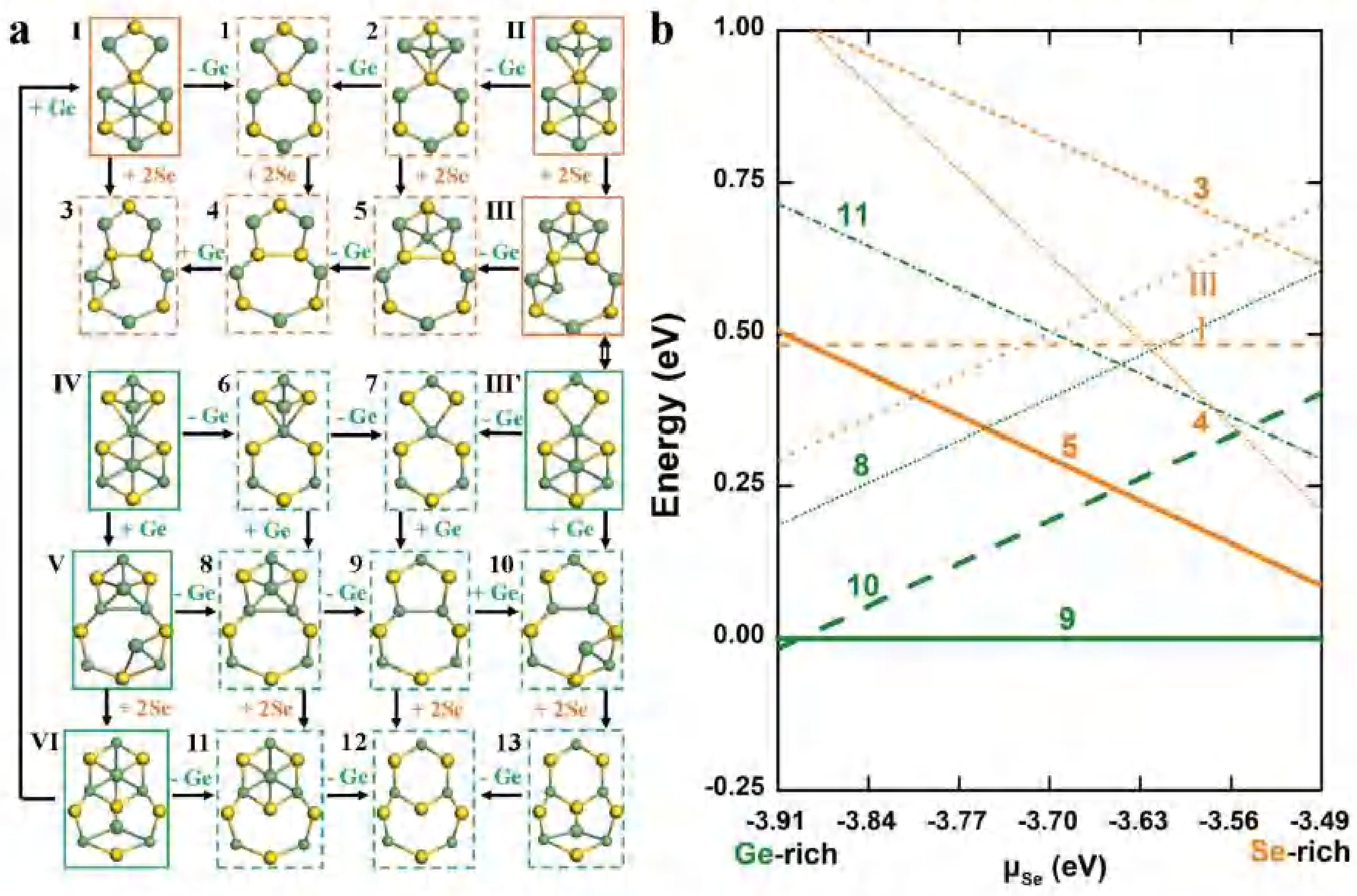

By interacting with some point defects, derivative DCs and their energies are obtained.

Evolution and energies of GBs versus tile angle α

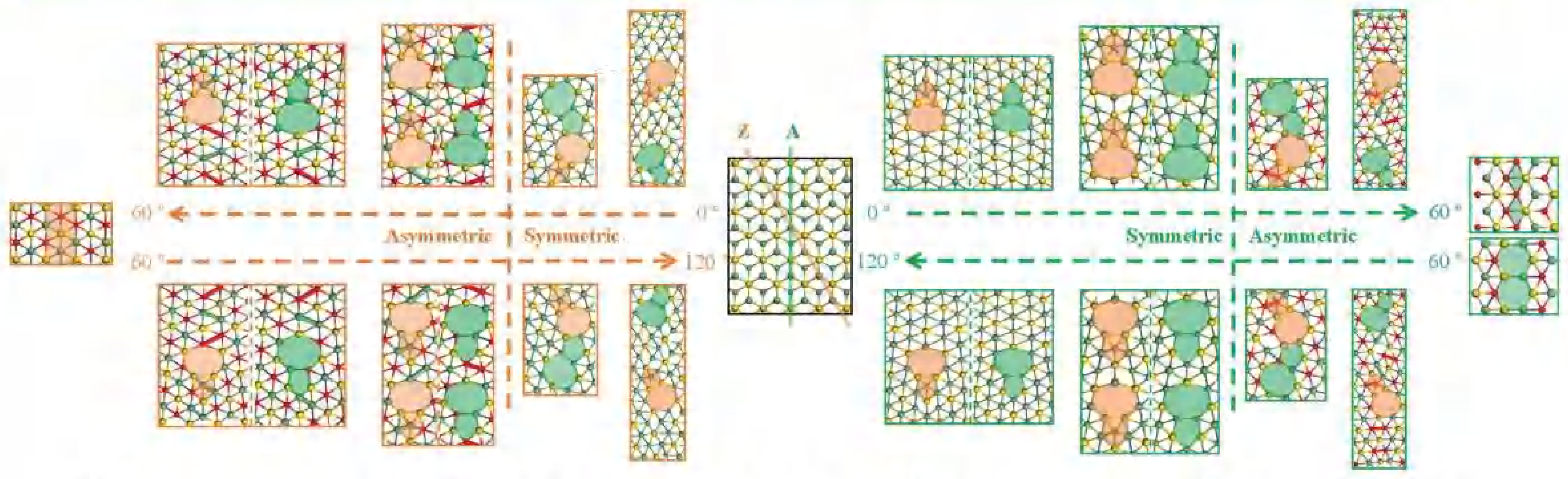

GBs are constructed by low-energy DCs, with two types of GBs emerged.

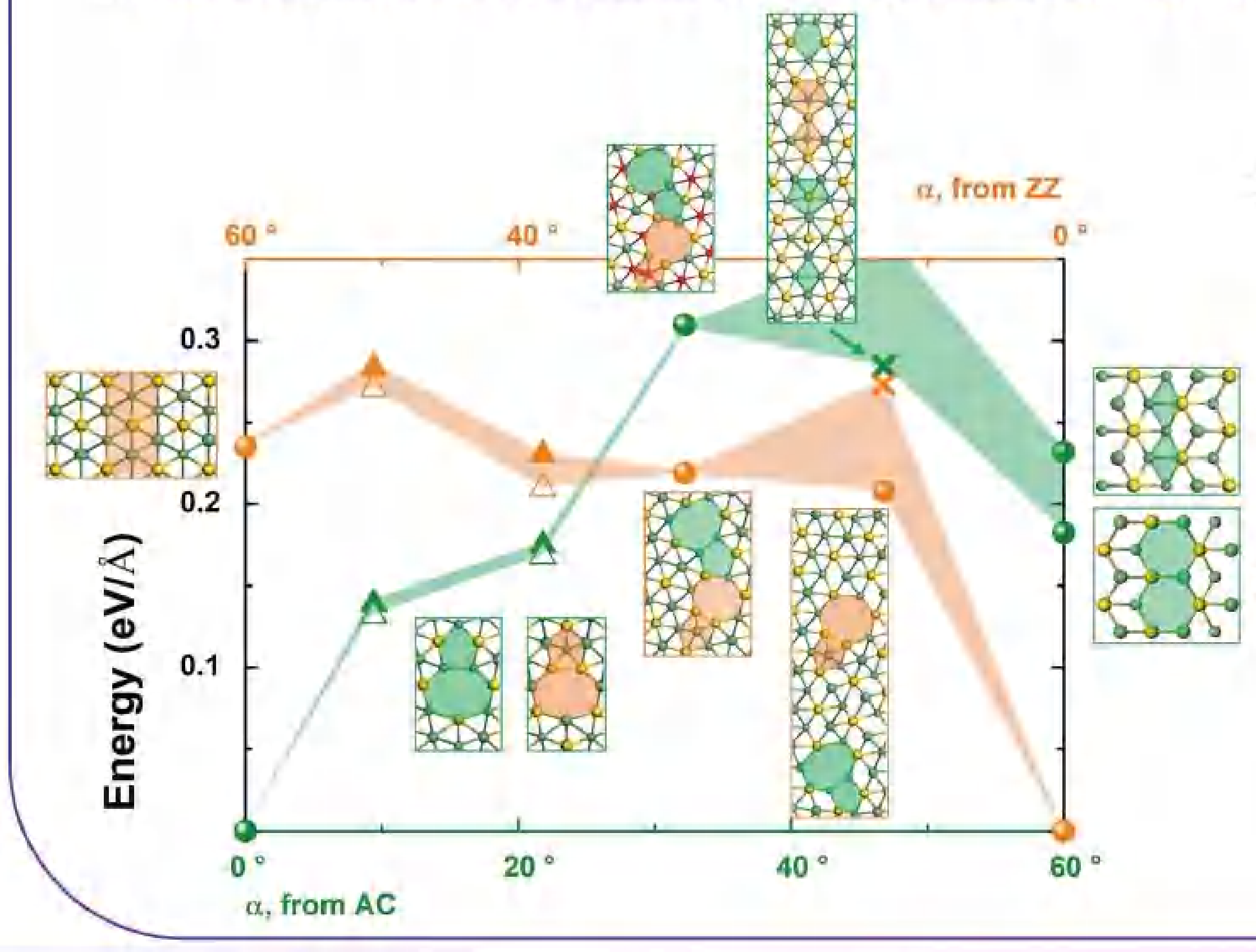

- Starting from armchair direction, GB energy increases with α as dislocation density grows first, then experiences a notable decrease when reaching 60°.
- Starting from zigzag direction, a similar trend of GB energy is observed.

A full set of 60° twin GBs and their stabilities

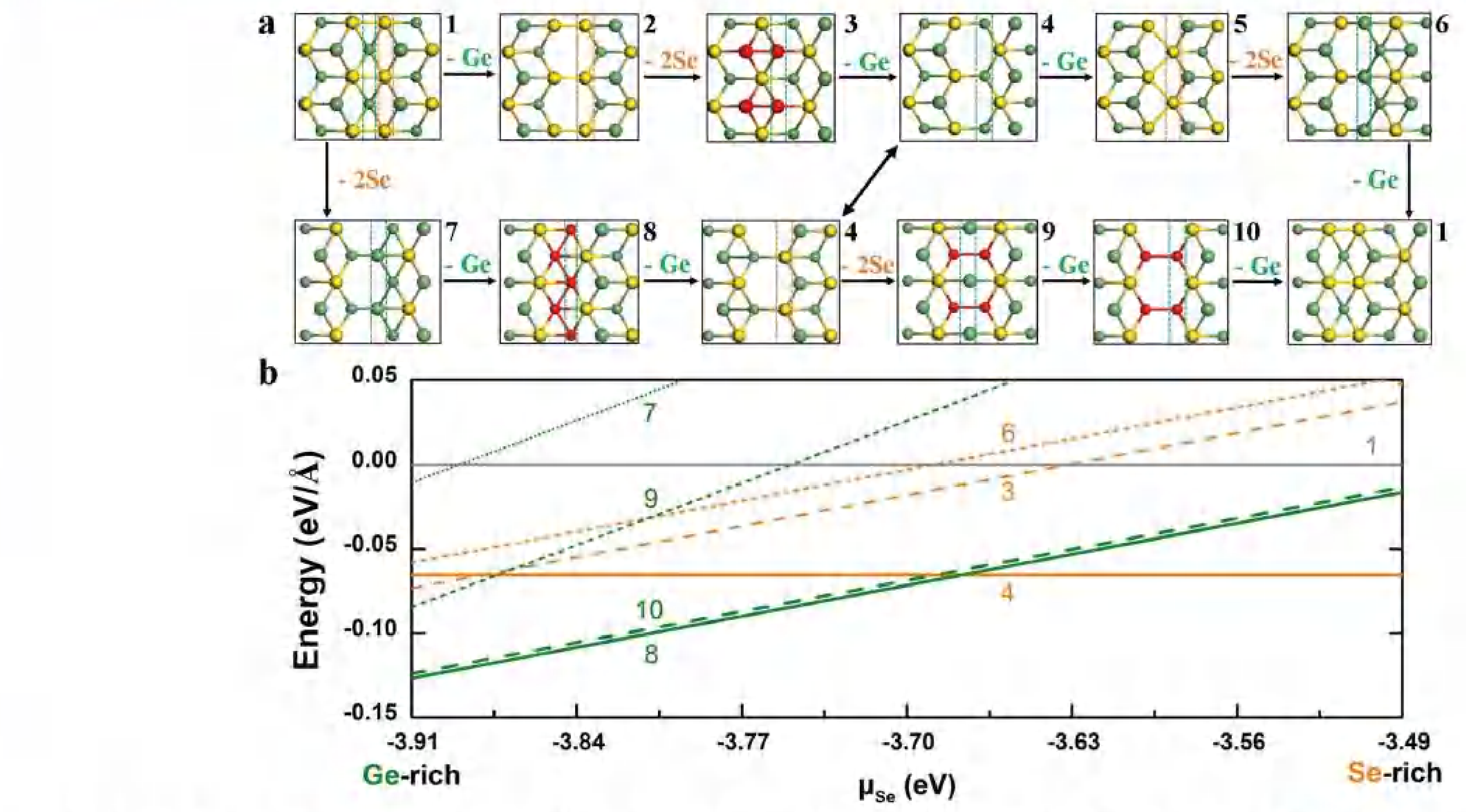

60° GBs are expected to be dominant in polycrystalline samples. The closed loop of evolution guarantees all configurations are searched.

Induced metallicity in low-energy GBs

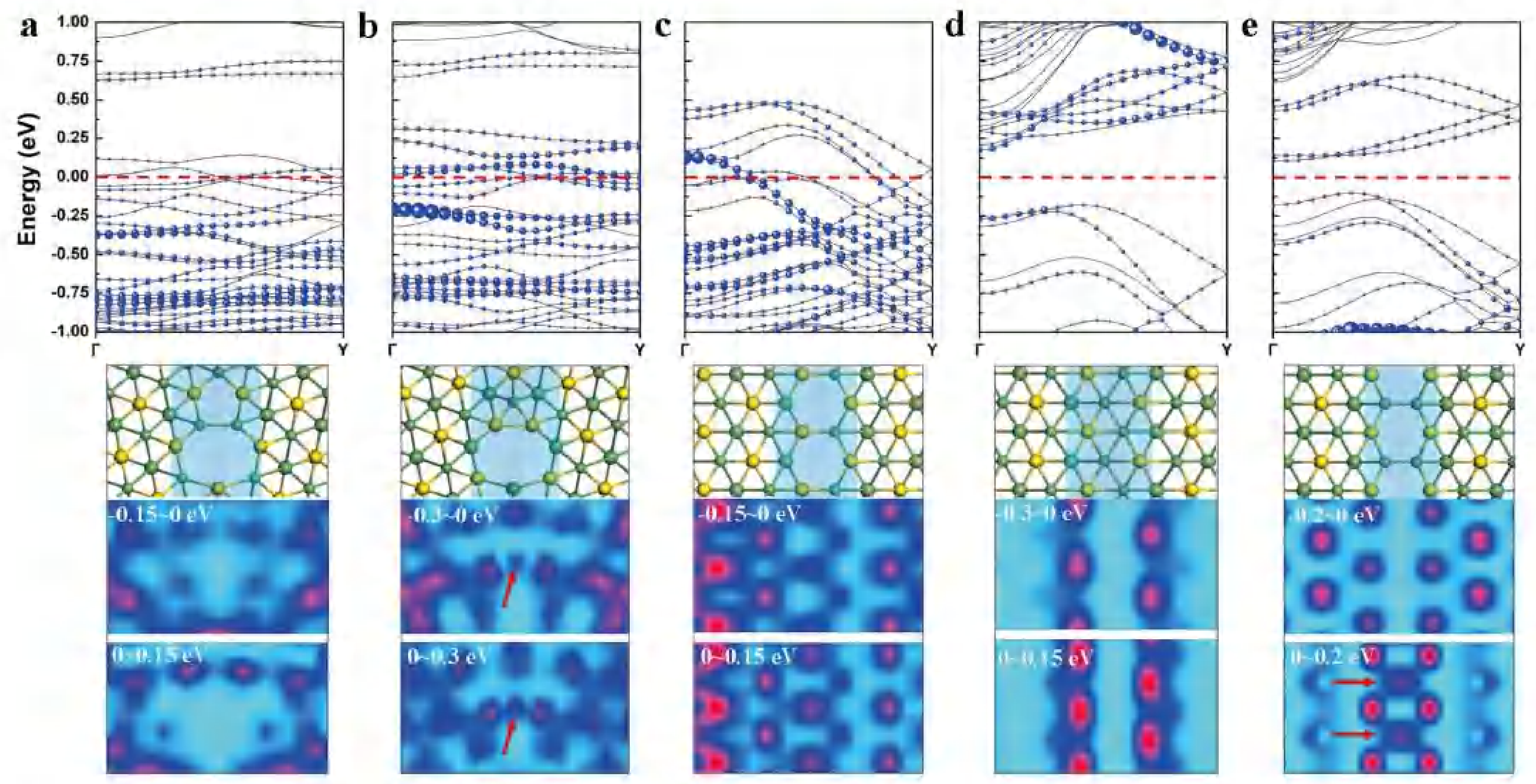

- The resonance effect between defect and bulk states renders most systems metallic, while some 60° GBs show semiconducting behaviors.
- The simulated STM images show characteristic current features around E_F.

Conclusion

- DCs in pentagon-heptagon 5|7 shape are generally more favored than others.
- The GBs assembled by an array of low-energy DCs could undergo significant structural relaxations, leading to different GB energies in various tilt angles.
- 21.8° GBs generally induce a strong resonance effect between dislocation and bulk states, giving rise to metallic features.
- 60° GBs exhibit both semiconducting behaviors with greatly reduced band gap and resonance-induced metallicity.
- All GBs possess distinct STM features, beneficial to be identified in practice.

Acknowledgements

This work was supported by the National Natural Science Foundation of China and Guangdong Innovative and Entrepreneurial Research Team Program.

Shengfeng Zeng

Prof. Xiaolong Zou

Contact

Wechat profile

References

1. Luo N, Duan W, et al. Adv Funct Mater, 2020, 30: 2000533.
2. Lee S, Jung JE, et al. Nano Lett, 2021, 21: 4305-4313.
3. Zou X, Liu Y, et al. Nano Lett, 2013, 13: 253-258.

Submitted

A Novel Monoclinic Phase and Tunable Magnetism of van der Waals Layered Magnet $CrTe_2$

Qidi Ren, Kang Lai, Jiahao Chen, Xiaoxiang Yu*, and Jiayu Dai*

Department of Physics, National University of Defense Technology, Changsha 410073, China

* (email: X. Y. xxyu@nudt.edu.cn; J. D. jydai@nudt.edu.cn)

INTRODUCTION

The van der Waals (vdW) layered magnetic materials are gaining wide attention due to their low-dimensional electrical and magnetic properties and flexible fabrication, especially beneficial for the development of next-generation spintronic devices[1,2]. Here, we report a novel monoclinic structure of vdW layered 1T-$CrTe_2$, which is one of the popular vdW magnets normally exhibiting a pristine trigonal structure. This new monoclinic phase emerges from a switchable magnetic state between ferromagnetism and antiferromagnetism through changing hole doping concentration, which suggests a practical approach to obtain such structure.

COMPUTATIONAL METHODS

We performed first-principles calculations of bulk 1T-$CrTe_2$ using density functional theory (DFT) [14,15] in the generalized gradient approximation (GGA) for the exchange-correlation function implemented in the Vienna ab initio simulation package (VASP) [16,17]. To consider the van der Waals interaction between layers, the projector augmented-wave method was employed with the Perdew-Burke-Ernzerhof (PBE) [18] optB88-vdW [19] for describing the exchange-correlation potential. The energy cutoff of the plane-wave basis was set at 650 eV. The atomic positions in the unit cell were fully relaxed until the force on each atom was smaller than 0.01 eV/Å. Phonon dispersions were calculated using the density functional perturbation theory (DFPT) method as implemented in the PHONOPY package [20]. The monkhorst-pack method was used to sample spatial integrals using the Gamma-centered grids of $12\times12\times8$ for electronic structure calculations and $5\times5\times5$ for phonon dispersion calculations. We used $2\times2\times1$ supercells and fixed the spin directions of Cr atoms to realize the AFM state. In the calculations, hole doping was realized by reducing the total number of electrons. Meanwhile, charge correction was considered by compensating the background of the opposite charge to realize the charge neutral. The value of doping concentration denotes the reduced number of electrons in a primitive unit cell including one Cr atom and two Te atoms. The unit of doping concentration is $e^+/CrTe_2$. The maximum doping concentration is 0.5 $e^+/CrTe_2$, corresponding to a carrier density of 1.6×10^{21} cm^{-3}.

Results & Discussion

1. Crystal structure

We compare two crystal structures of tr-$CrTe_2$ and m-$CrTe_2$. Both structures have a 1T-phase, namely, one Cr atom is surrounded by six Te atoms octahedrally, as shown in Fig (a, b, d, e). The space groups of the trigonal and monoclinic structure are $P3\bar{m}1$ and C2/m respectively. The interlayer distance of m-$CrTe_2$ is larger than that of tr-$CrTe_2$, while the length of a (or b) of m-$CrTe_2$ is smaller than that of tr-$CrTe_2$. The values of α (or β) and γ of m-$CrTe_2$ are 90.96 and 61.98, respectively, which are different from 90 and 120 of tr-$CrTe_2$. Due to the changes in lattice parameters are too small, the differences in atomic structure in Fig are not obvious. Different from tr-$CrTe_2$, the adjacent layers show slight planar sliding in m-$CrTe_2$. Moreover, as denoted by pink solid lines in Fig (a, d), the hexagon formed by three Te atoms and three Cr atoms and centered by a Te atom is regular in tr-$CrTe_2$ but irregular in m-$CrTe_2$. To confirm the lattice stability, we calculate the phonon dispersion. As given in Fig (c, f), all phonon modes are stable for tr-$CrTe_2$ and m-$CrTe_2$. Besides, the magnetic state of m-$CrTe_2$ is the AFM state.

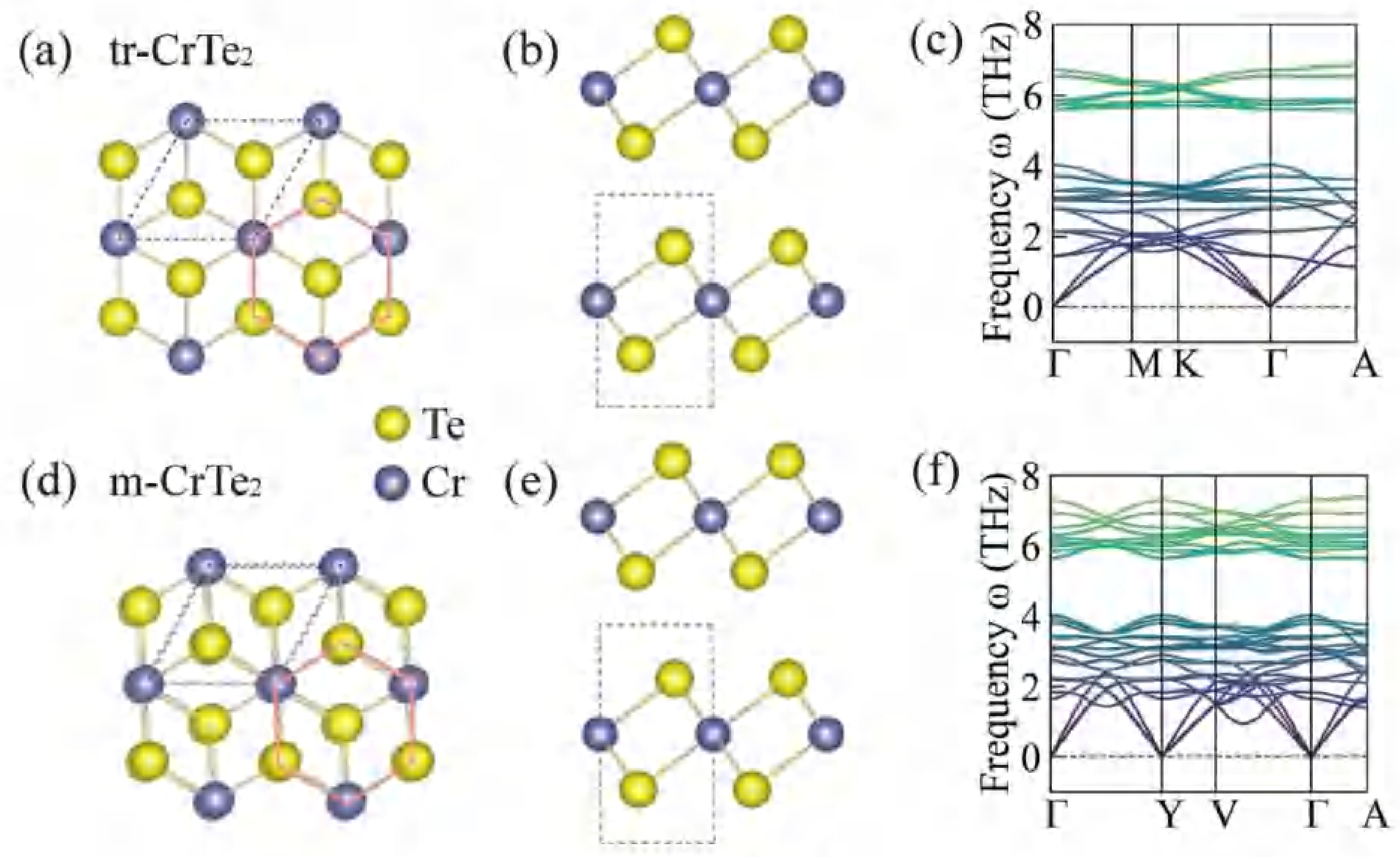

REFERENCE

[1] M. Gibertini, M. Koperski, A. F. Morpurgo, and K. S. Novoselov, Nat. Nanotechnol. 14, 408 (2019).

[2]X. Jiang, Q. Liu, J. Xing, N. Liu, Y. Guo, Z. Liu, and J. Zhao, Applied Physics Reviews 8, 031305 (2021).

[3]P. Hohenberg and W. Kohn, Physical Review 136, B864 (1964).

[4]J. Dai, J. Yuan, and P. Giannozzi, Applied Physics Letters 95, 232105 (2009).

[5]G. Kresse and J. Hafner, Physical Review B 47, 558 (1993).

[6]G. Kresse and J. Furthmüller , Physical Review B 54, 11169 (1996).

[7]J. P. Perdew, M. Ernzerhof, and K. Burke, The Journal of Chemical Physics 105, 9982 (1996).

[8]J. Klimeš, D. R. Bowler, and A. Michaelides, Journal of Physics: Condensed Matter 22, 022201 (2009).

[9] A. Togo and I. Tanaka, Scripta Materialia 108, 1 (2015).

2. Phase engineering (hole-doping)

Electrical method is a feasible tool to modulate the structural phase and magnetic properties. We investigate the effect of hole doping on binding energy, phonon dispersion, and crystal structure. The energy difference between tr-$CrTe_2$ and m-$CrTe_2$, which is expressed by $\Delta E = E_m - E_{tr}$. The energy difference decreases from positive to negative as the doping concentration increases. In the case without doping, tr-CrTe2 is more stable than m-$CrTe_2$, indicating that the new m-$CrTe_2$ is a metastable structure. When the hole doping concentration is larger than 0.25 $e^+/CrTe_2$, $\Delta E < 0$, suggesting that m-$CrTe_2$ becomes more stable than tr-$CrTe_2$.

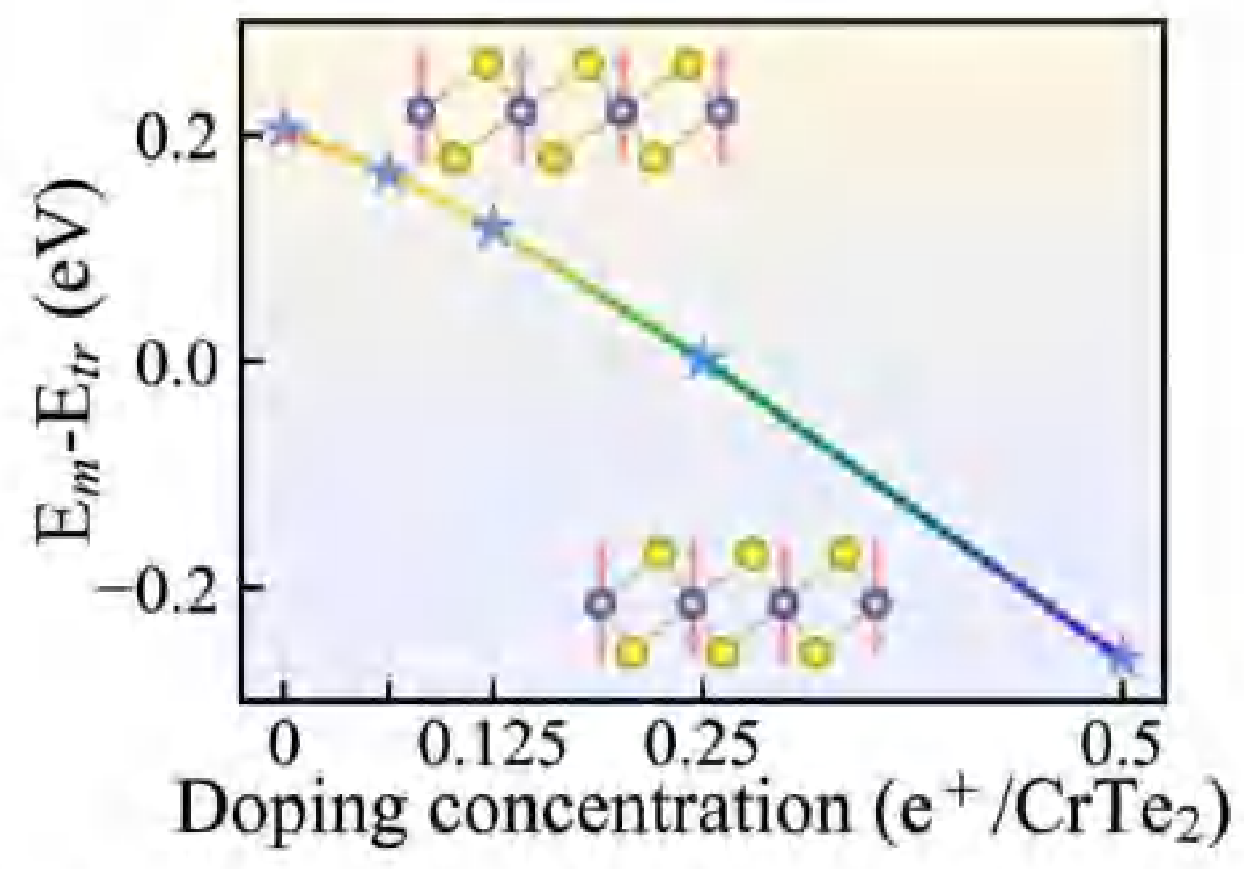

Except for the energy stability, one also needs to confirm the lattice stability via phonon dispersion. As the doping concentration increases, all phonon modes of m-$CrTe_2$ remain stable and show hardening. For tr-$CrTe_2$, most phonon modes show hardening. However, when doping concentration reaches 0.25 $e^+/CrTe_2$, two phonon modes Γ_1 and A_1 become unstable. As doping concentration increases to 0.5 $e^+/CrTe_2$, there are three unstable phonon modes: Γ_1, M_1, and A_1. These unstable phonon modes are stabilized by interlayer sliding and intralayer displacive distortion. Therefore, the results imply that hole doping could be a possible approach to accessing the novel m-$CrTe_2$ structure.

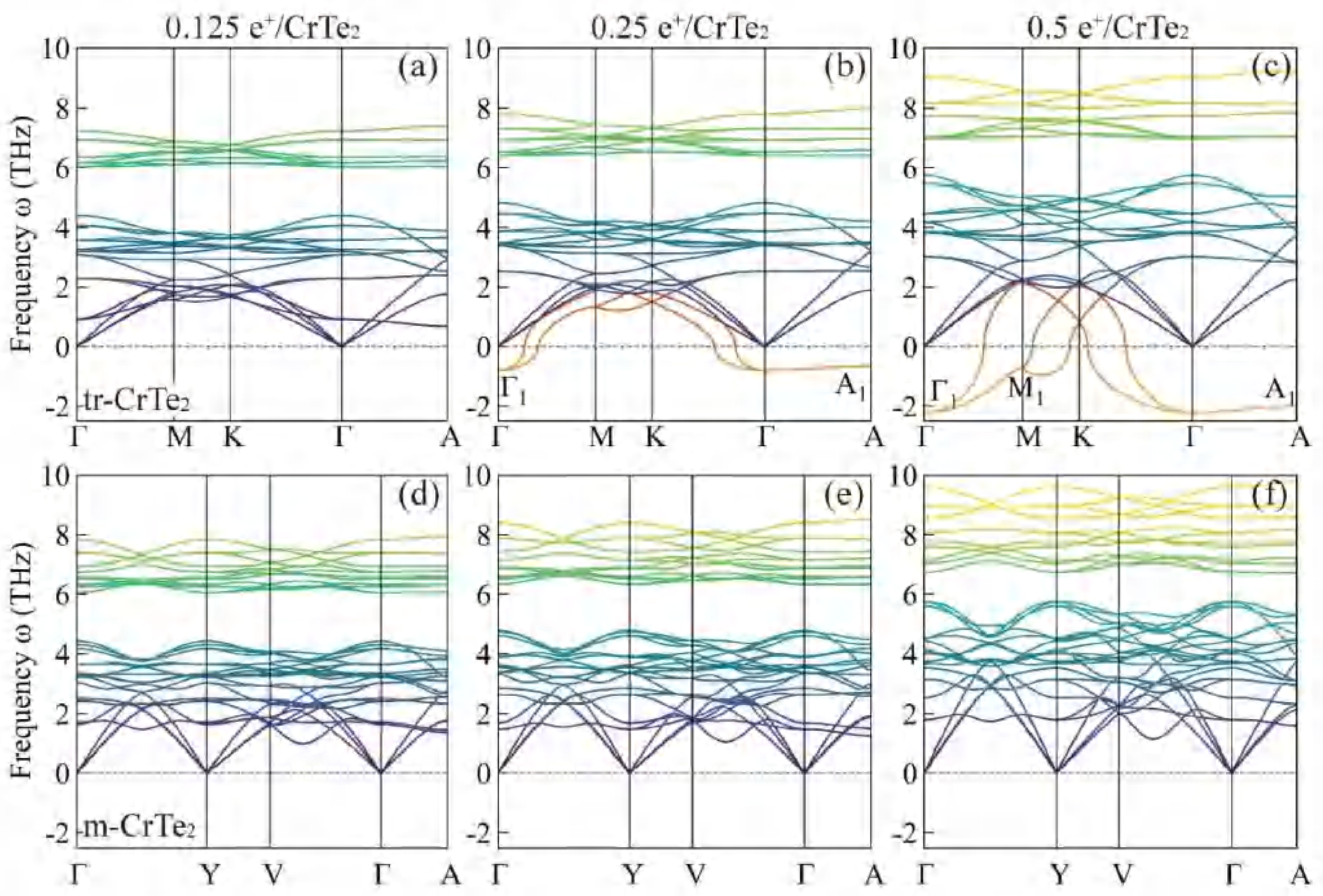

3. Phonon softening

To shed light on the mechanism of phonon softening in hole-doped tr-$CrTe_2$, we calculate the electronic band structures of tr-$CrTe_2$ with different doping concentrations. The anomalous phonon softening is attributed to the hole-doping-induced phonon Kohn anomaly. As the doping concentration increases, the spin-up and spin-down electron states of the Cr atoms shift towards the Fermi level. The energy shifts of electron states of the Te atoms are relatively small. For tr-$CrTe_2$ in hole doping of 0.5 $e^+/CrTe_2$, there are more electronic bands near Fermi level compared with undoped one. The high symmetry points of unstable phonon modes (Γ_1, M_1, and A_1) are consistent with the reciprocal-space positions where the electronic bands near the Fermi level locate. The increase of electron occupation near the Fermi level leads to enhanced electron screening and electron-phonon coupling, thus weakening the interatomic interactions and softening phonon modes at corresponding specific high-symmetry points.

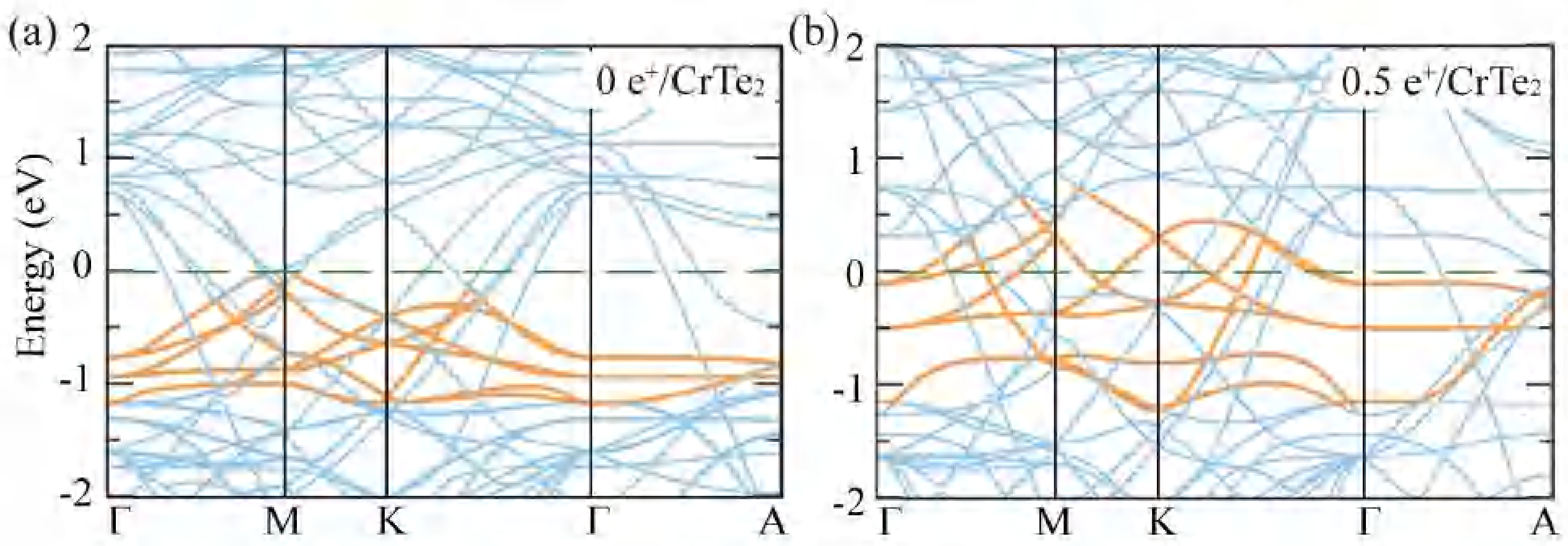

Conclusion

We predict a new monoclinic structure of vdW layered magnet CrTe2. Distinct from the conventional trigonal structure with ferromagnetism, the new structure exhibits a C2/m space group and antiferromagnetism, which emerges when exerting the hole doping. We verified the stability of the new phase through phonon dispersion and energy calculation. As hole-doping concentration increases, several phonon modes of tr-CrTe2 become unstable, while those of m-CrTe2 remain stable. We calculate the electronic structures to reveal the mechanism of this phase instability. We find that the hole-doping-induced phonon Kohn anomaly is responsible for the instability of certain phonon modes. Furthermore, the volume and other lattice parameters change with increasing hole-doping concentration.

第一性原理计算研究铁素体钢中金属合金元素的晶界平衡偏聚行为

杨梦梦，张瑶，董自成，王皞*（haowang7@usst.edu.cn）
上海理工大学，材料科学与化学学院/增材制造研究院

引言

合金元素在晶界上的偏析在多种合金体系中普遍存在。与非平衡偏聚不同，基于热力学平衡的平衡偏聚在材料的加工、制造、使役过程中几乎是无法避免的。并且平衡偏聚的结果往往对非平衡偏聚产生深远影响。因此，我们基于第一性原理的计算结果，结合Voronoi analysis得到的原子体积，分析了平衡偏聚过程中局部应变能最小化与局部化学能最小化各自的作用。相关结果可以加深科研人员对D.Mclean理论的理解，指导合金成分设计与晶界工程。

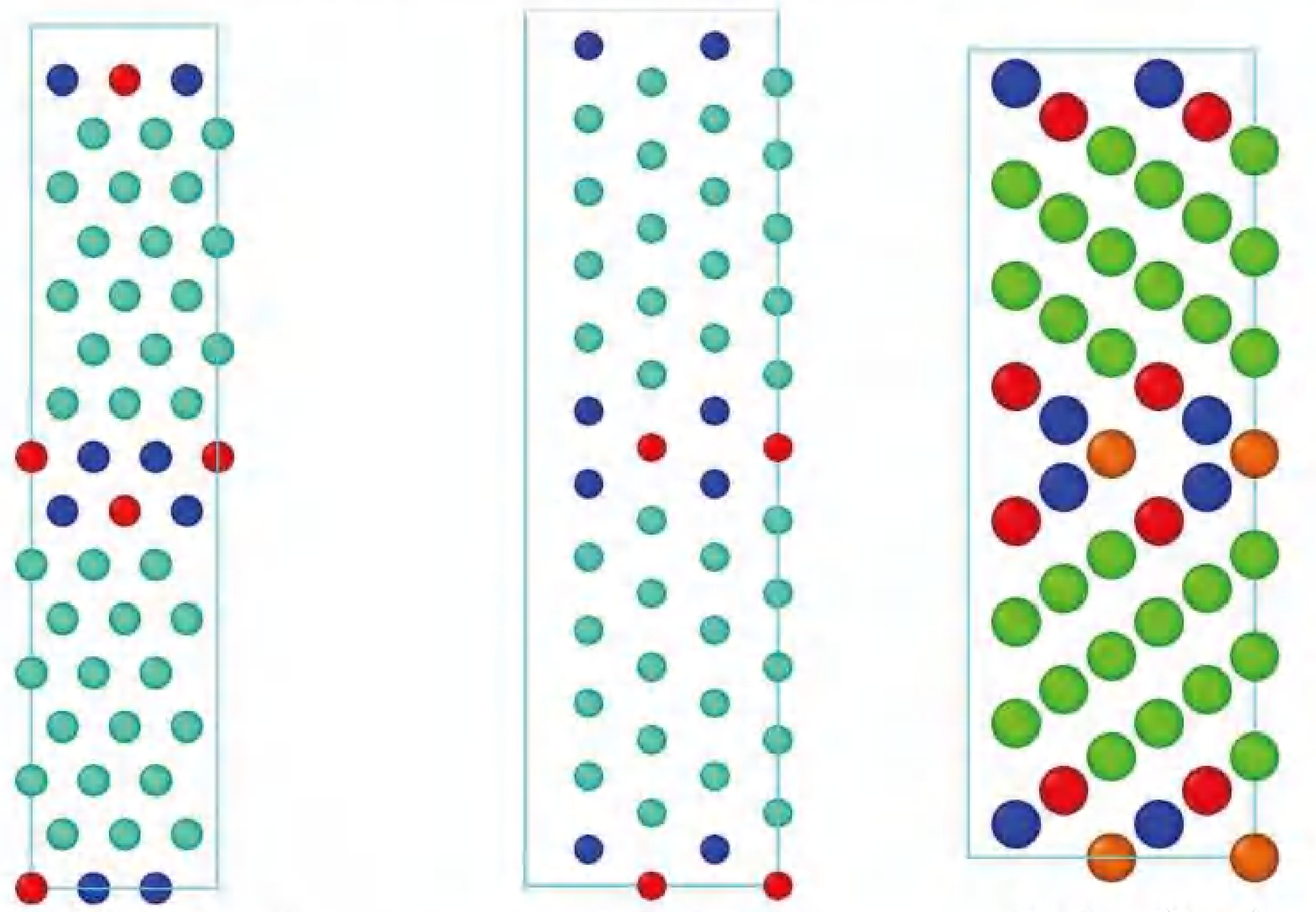

<111>（110） <111>（112） <110>（111）

11.28——11.4（点位体积） 11.23——11.35 10.29——12.23

图1 对称倾斜晶界模型及其相应原子占据的点位体积

如图1所示，在不同的晶界上，受几何因素影响，晶界原子的配位数（与化学能有关），点位体积（与应变能有关）等因素存在差异。这解释了之前一些实验中，合金元素在同一材料的不同种类晶界上展现出不同程度的偏析。

计算模型

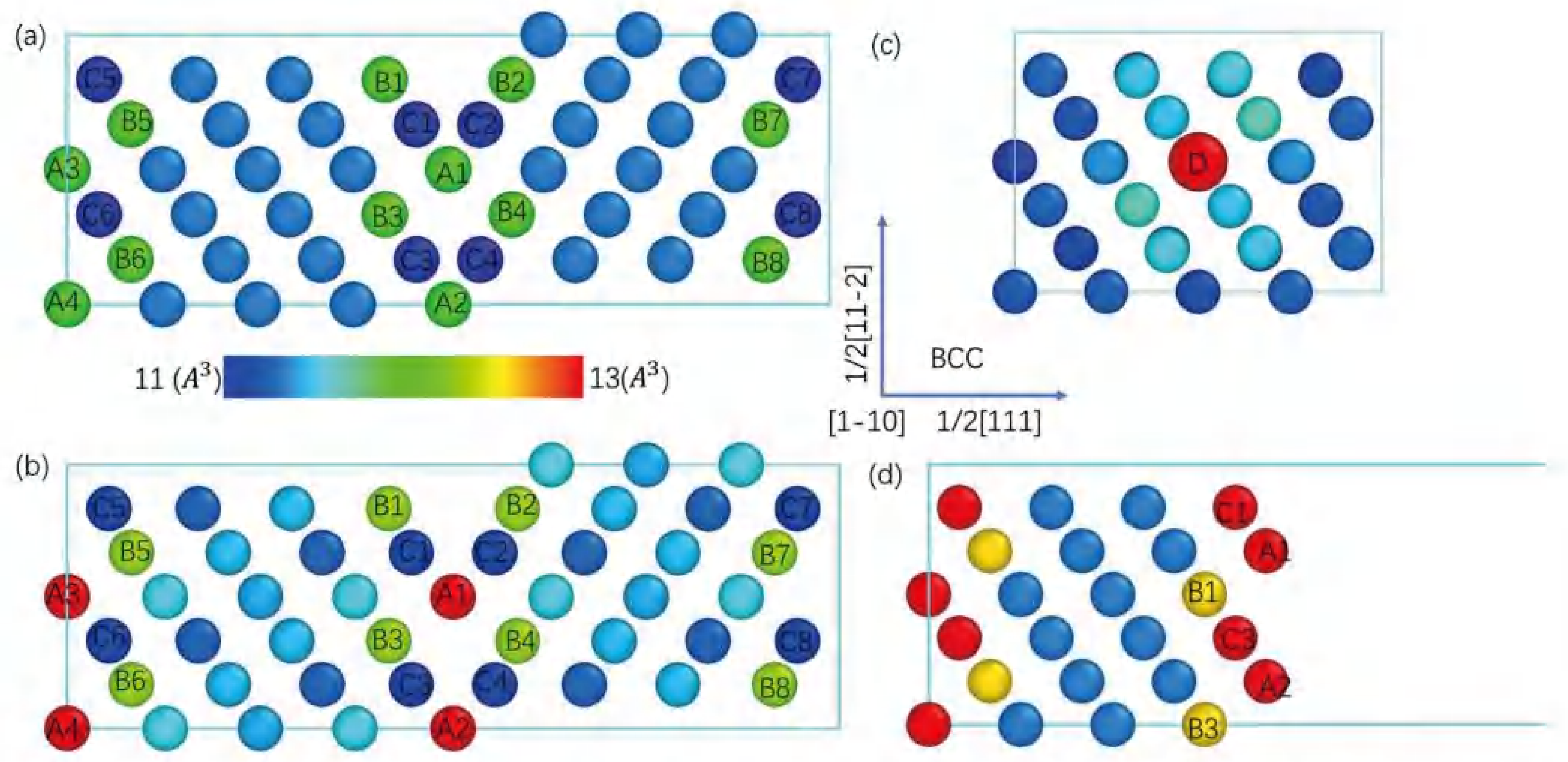

图2 （a）、(b)弛豫前后<110>(111)对称倾斜晶界的晶界模型及各原子所占据的点位体积；（c）合金原子D固溶后对局部原子所占据的点位体积的影响；（d）（111）表面模型；所有模型均为体心立方晶格。

点位体积差与晶界偏聚能

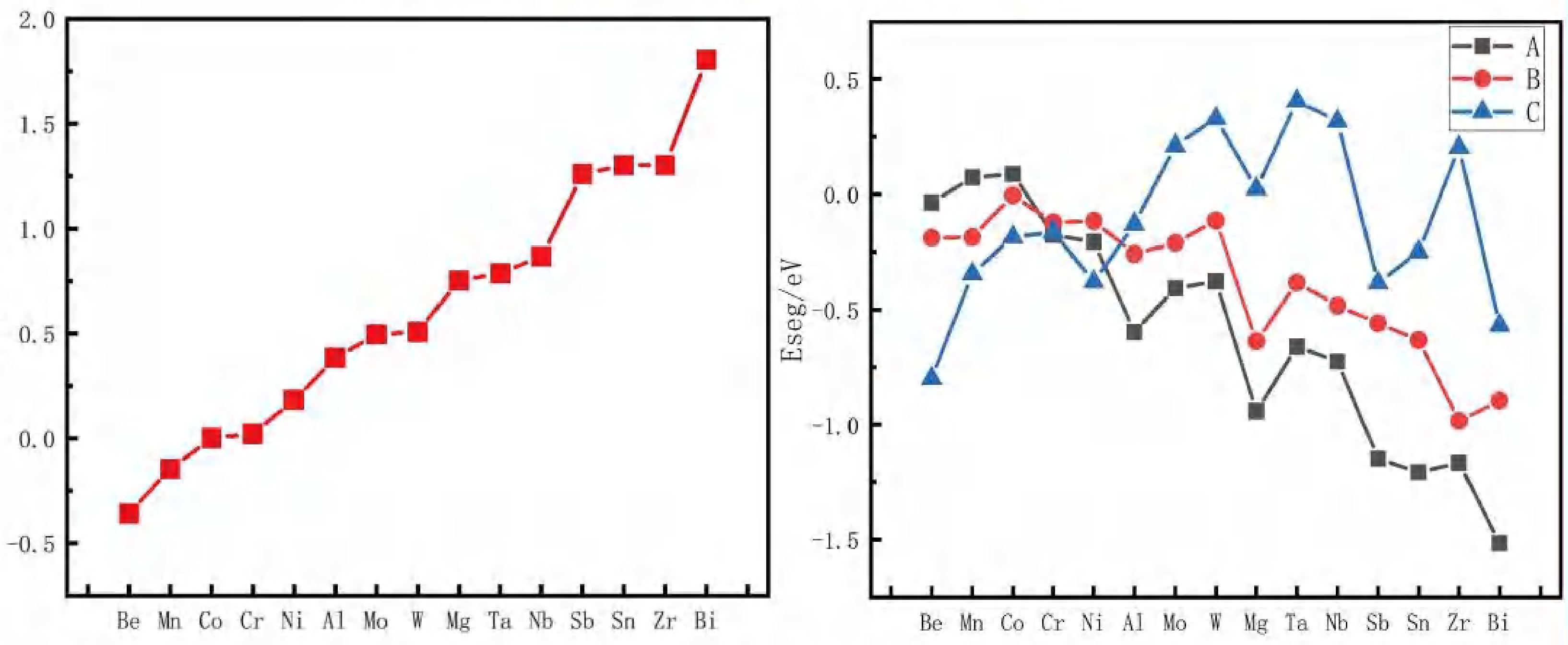

图3 左：在晶内固溶X（X=Be、Mn…）原子后，原子占据的点位体积(V_X)与基体中铁原子占据的点位体积（V_Fe）的差（△V=V_X-V_Fe）；
右：固溶原子X在如图2所示的A、B、C三类点位上的偏聚能。

根据D.Mclean理论（只考虑应变能作用），结合图2（b）可知，晶界上的A、B两类位点可提供比晶内更大的原子点位体积，因此在应变能最小化的驱动下，在晶内倾向占据更大原子点位体积的原子如Bi、Zr、Sn等会容易在这两类点位上偏聚；反之如Be,则倾向于往C类点位偏聚。值得注意，与Zr、Nb、Ta等不同，Bi、Sn、Sb向在理论上不利于应变能最小化的C类点位偏聚时偏聚能也为负。很显然，这是由于D.Mclean理论中未纳入考虑的化学能的影响。而局部化学能最小化对于Bi、Sn、Sb成为钢中的易偏析元素也很重要。

偏聚能的分解

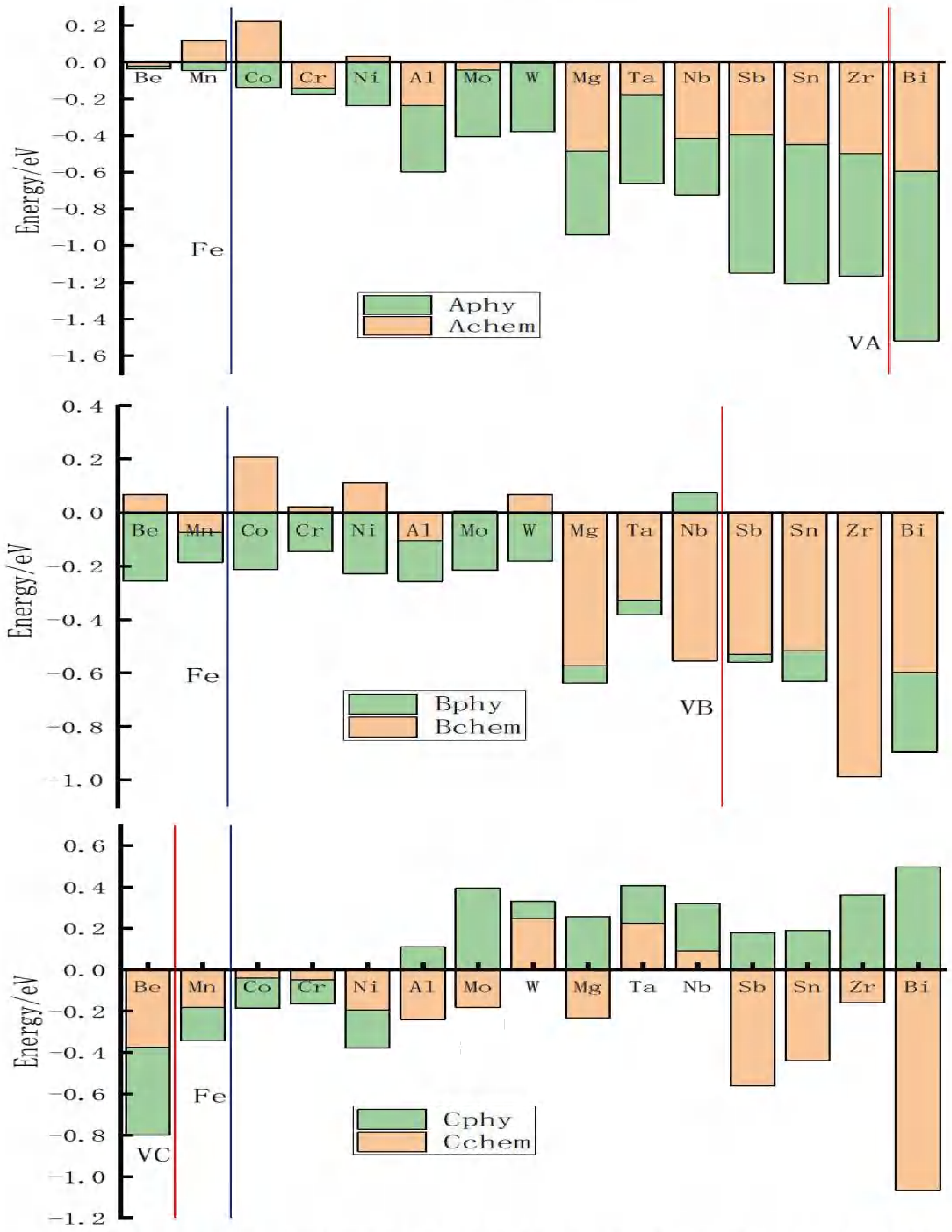

图4 将偏聚能分解为化学能和应变能的贡献，元素按其在晶内固溶后占据的点位体积排序，蓝线为晶内铁原子占据的点位体积，红线为晶界A、B、C三类点位上铁原子占据的点位体积。

对于晶界上易偏析的原子，以Bi为例，当晶界提供的原子点位体积大于晶内点位体积时，根据D.Mclean理论，在局部应变能最小化的驱动下，Bi原子自发的向A、B两类点位偏聚;而在C点位上，应变能阻碍Bi原子偏聚。实际情况是，由于在C点位化学能起主导作用，总的偏聚能依旧为负，原子仍可向C点位偏聚。显然，对于成为钢中的易偏析元素，化学能的影响很重要，因为晶界上总存在着一定比例的不符合D.Mclean理论的晶界点位，而只有化学能起主导时，这些点位才适合偏析。

局部差分电荷分析

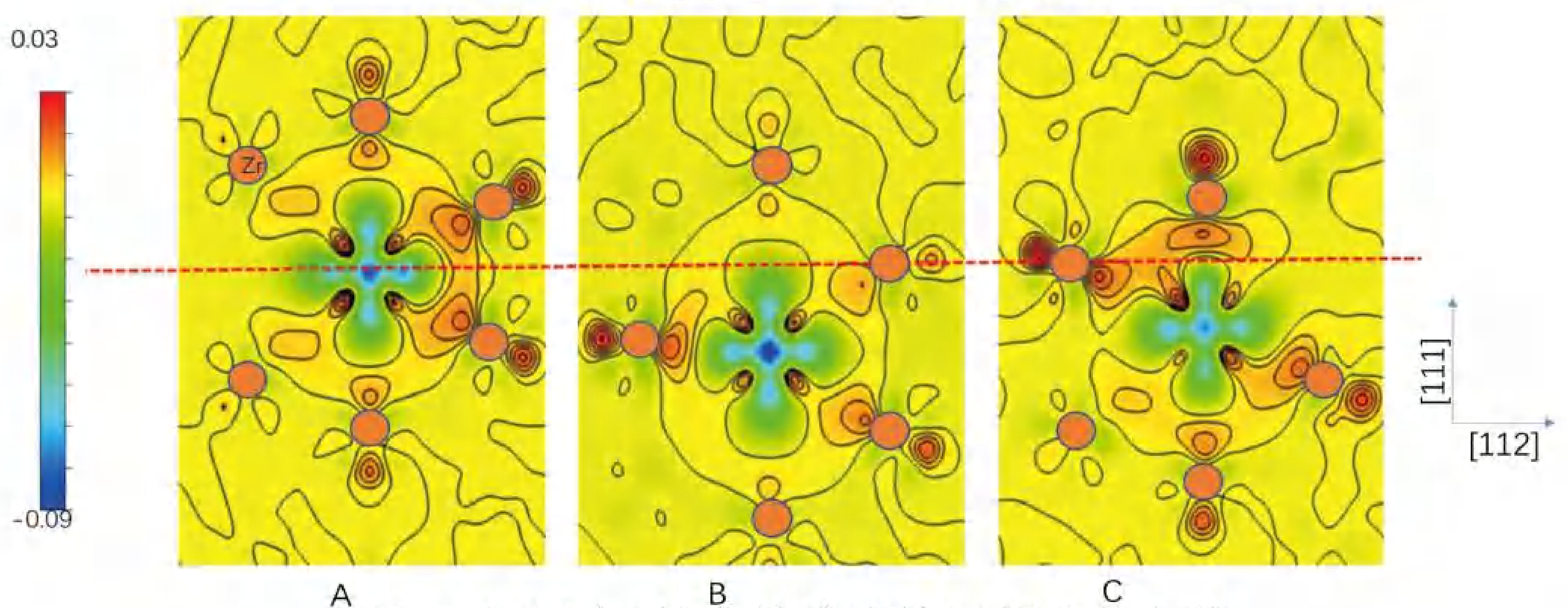

图5 Zr原子在3处点位偏聚的局部差分电荷

化学能的贡献主要来自于固溶原子与周围基体原子在不同环境中成键的电荷转移差异，电荷转移量差异越大，局部化学能最小化在偏析中的贡献越大。

结论

1. **同种材料同种合金元素在不同晶界上平衡偏析的差异受晶界原子点位体积的影响；**
2. **钢中易偏析元素在界面上不利于应变能最小化的点位处的偏析是受到化学能的驱动；从化学能方面分析，Bi、Sn、Sb等残余元素皆不喜待在钢的BCC晶格中，偏向于界面处的原子环境；**
3. **局部电荷转移的差异是影响偏析过程中化学能贡献大小的主要因素。**

四川大学 高分子科学与工程学院
College of polymer science and engineering, Sichuan University

高分子材料工程国家重点实验室（四川大学）
State Key Laboratory of Polymer Materials Engineering

Exploring Water Dissociation Pathways on Ruthenium Materials with Complex Catalytic Sites in Alkaline Electrolytes

Chengdong Yang,[1] Zihe Wu,[1] Zhenyang Zhao, Yun Gao, Tian Ma, Xikui Liu, Xianglin Luo, Shuang Li,* Chong Cheng,* Changsheng Zhao,*
College of Polymer Science and Engineering, State Key Laboratory of Polymer Materials Engineering, Sichuan University, Chengdu 610065, China
*Correspondence to: Prof. Chong Cheng, chong.cheng@scu.edu.cn

Introduction

Electrochemical water splitting has attracted dramatically increased attention due to its important role in the production of green hydrogen (H_2), which provides a carbon-neutral alternative to solve the environmental crisis[1,2]. Recent studies have disclosed that Ru-based catalysts can serve as promising alkaline HER electrocatalysts which surpass the state-of-the-art Pt catalysts[3]. However, the profound influences and roles of diverse Ru species (including clusters and single atoms) on water dissociation pathways and reaction principles remain ambiguous, which is of great importance to be discovered for the future design of optimal Ru catalysts. Here we overcome this challenge by creating complex Ru catalysts with well-defined metallic nanocluster and cationic single-atom sites to explore the adsorption-desorption behaviors of intermediates. Combining the theoretic calculation of reaction paths and experimental designing of active site poison, it can be concluded that the nanocluster Ru determines the major water dissociation activity and the single-atom Ru plays a cooperative role for the complex catalysts to achieve optimal performance in alkaline electrolytes. The proposed alkaline HER pathway will give guidance for future HER catalysts designing and also other electrochemical catalysts.

Key concepts and new discoveries

- Electrochemical studies have demonstrated that the Ru_n-Ru_s/NC exhibits the best catalytic activities. Meanwhile, the metallic Ru_n determines the major HER activity while the cationic Ru_s plays the cooperative role.
- DFT results validate that the Ru_n prefers to adsorb the OH* while Ru_s site prefers the H*. Then our study proposed a new three-steps alkaline HER pathway for the complex Ru catalytic sites.

Results-*experiment*

Structural and spectroscopic characterization of complex Ru catalysts

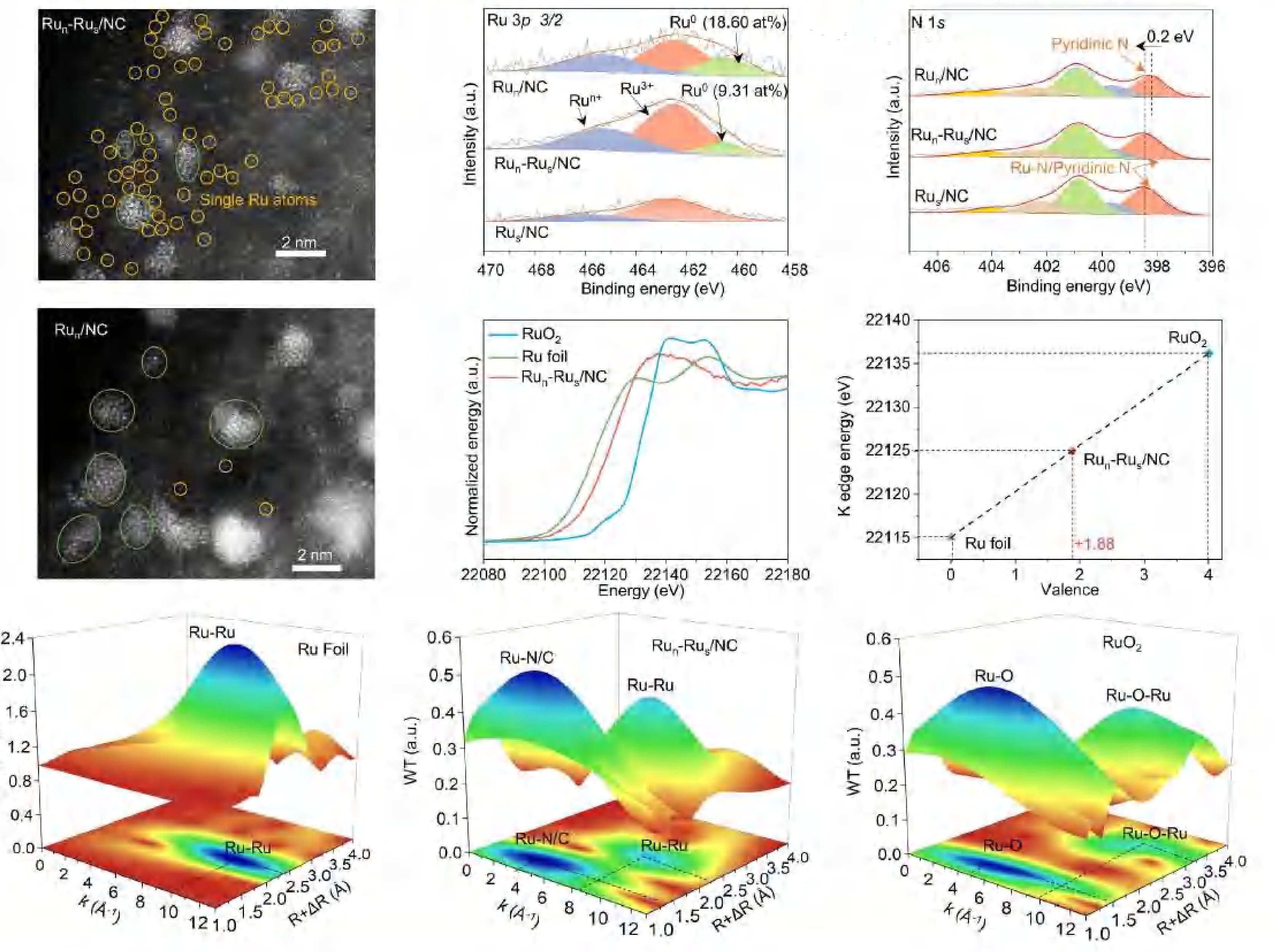

Electrocatalytic HER performances of the catalysts in 1 M KOH

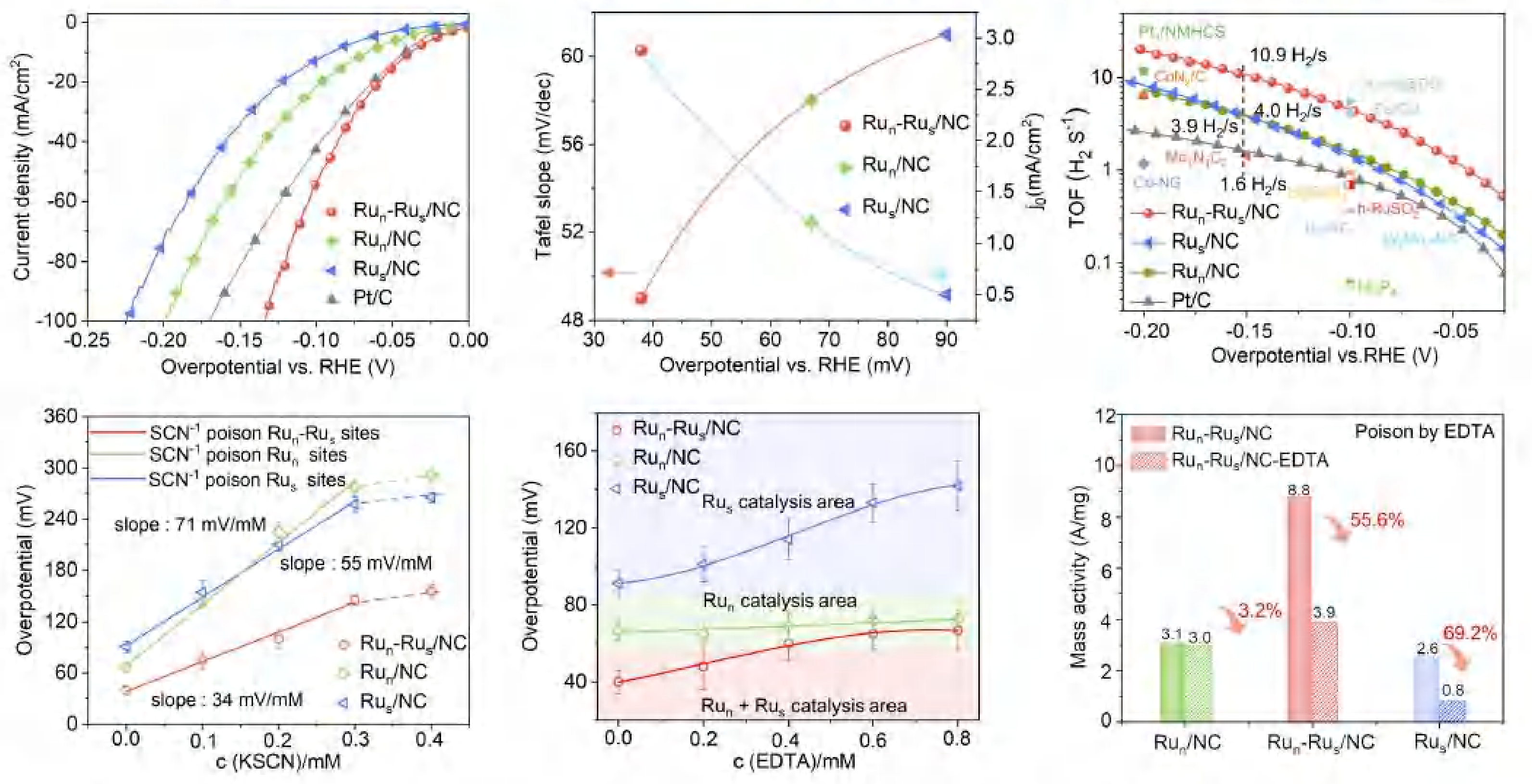

- ➢ Successful preparation of Ru_n-Ru_s/NC (characterized by STEM, XPS and XANES).
- ➢ The Ru_n-Ru_s/NC exhibits the fastest reaction kinetics and highest intrinsic catalytic activity (overpotential of 37 mV at 10 mA cm^{-2}, the highest Tafel slope and TOF value).
- ➢ The active site poisoning-assisted electrocatalytic tests have revealed that the metallic Ru_n determines the major HER activity while the cationic Ru_s plays the cooperative role for the complex Ru catalysts.

Results-*computation*

Bader charge distribution and various adsorption sites on different models

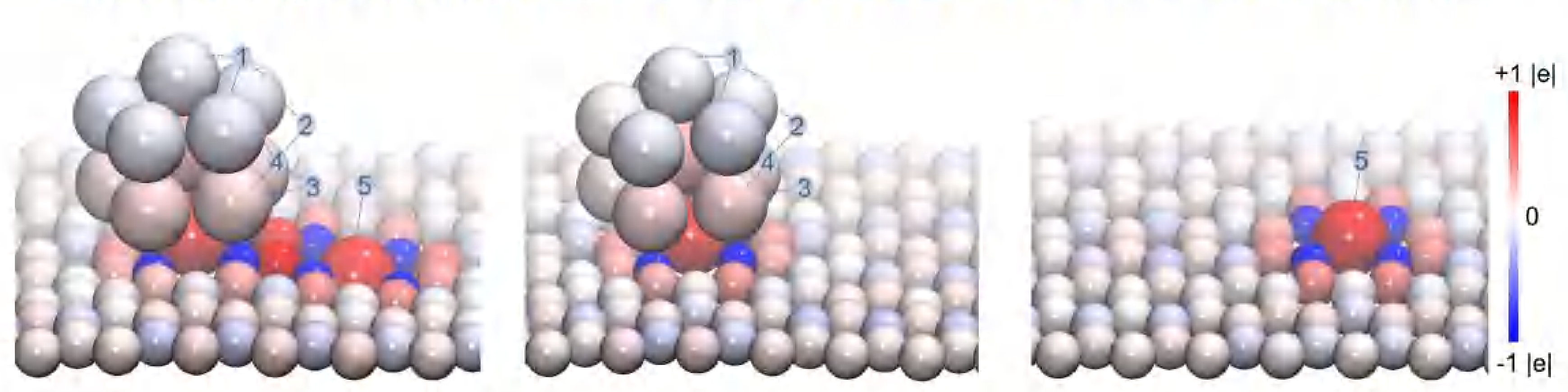

Screening of adsorption energy for H and OH species at different sites

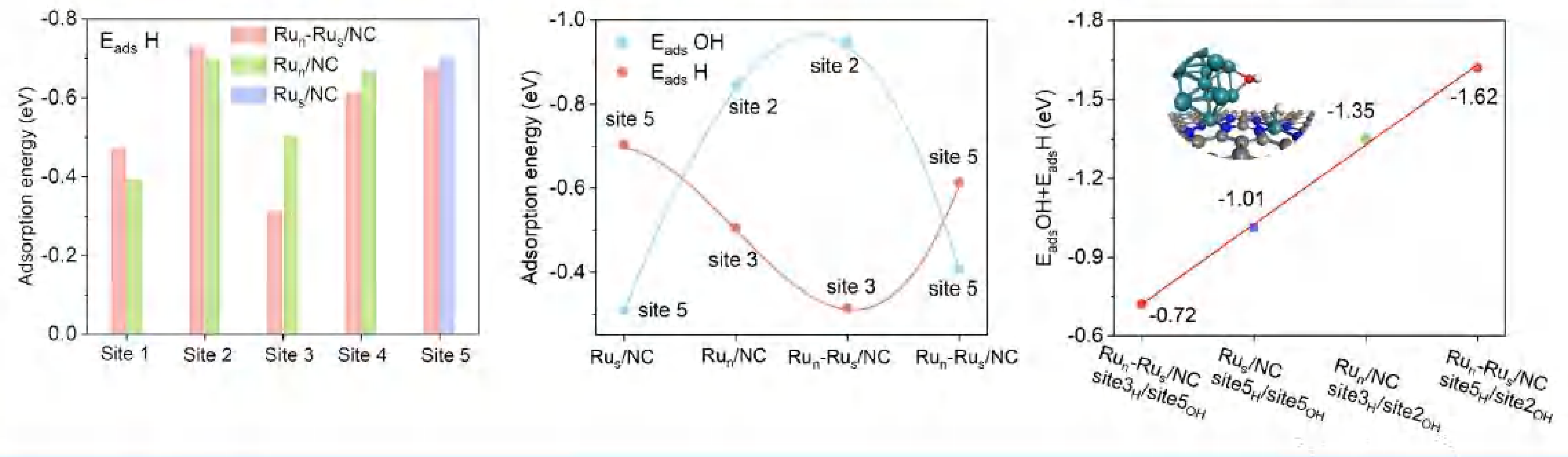

Water dissociation pathways on complex Ru sites

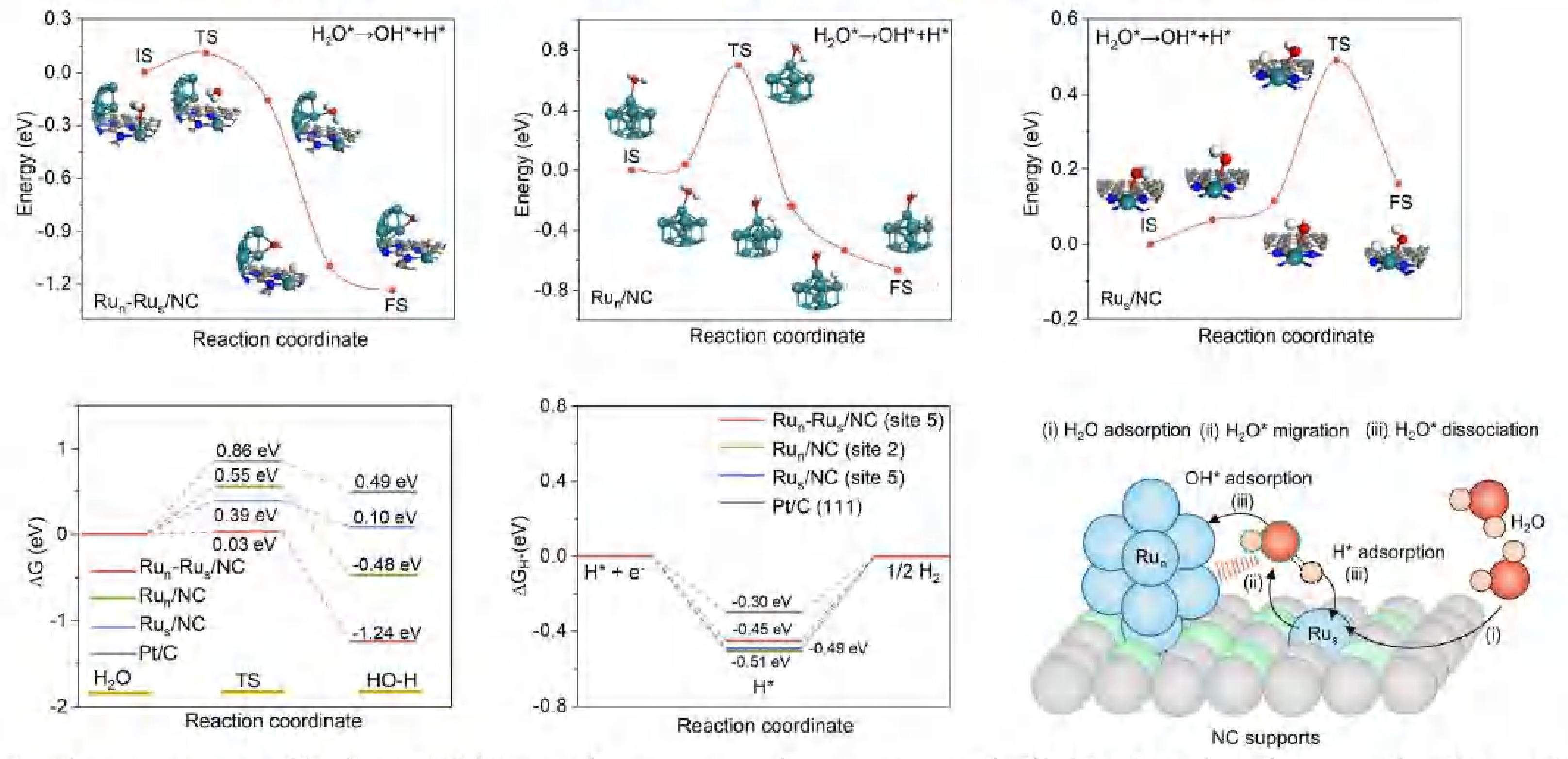

- ➢ A three-steps alkaline HER pathway can be proposed: i) H_2O adsorbs on the Ru_s site adjacent to Ru_n; ii) H_2O* migrates from Ru_s site to the interface between Ru_n and Ru_s; iii) the synergy binding effects of Ru nanocluster (prefers to adsorb OH*) and single-atom (prefers to adsorb H*) sites promote the fast split of HO-H bond.

Conclusion

In combination with theory and experiment, the water dissociation pathways of complex Ru catalysts with well-defined nanocluster and single-atom sites in alkaline HER have been systematically investigated to explore the profound influences of diverse Ru species on water splitting. Our study proposed a new alkaline HER pathway for the Ru complex sites with three steps: fast H_2O adsorption on Ru_s site adjacent to Ru_n, facile H_2O* migration from Ru_s site to the interface between Ru_n and Ru_s, and favorable synergy binding effects of complex sites to promote the fast split of HO-H bond. These findings offering a new strategy to design efficient and durable catalysts for practical production of H_2 in alkaline simulated seawater.

References

[1] Y. Shi, et al. *Nat. Commun.* 2021, 12, 3021.
[2] K. Deng, et al. *Adv. Mater.* 2022, 34, 2110680.
[3] J. Mahmood, et al. *Nat. Nanotechnol.* 2017, 12, 441.

Authors

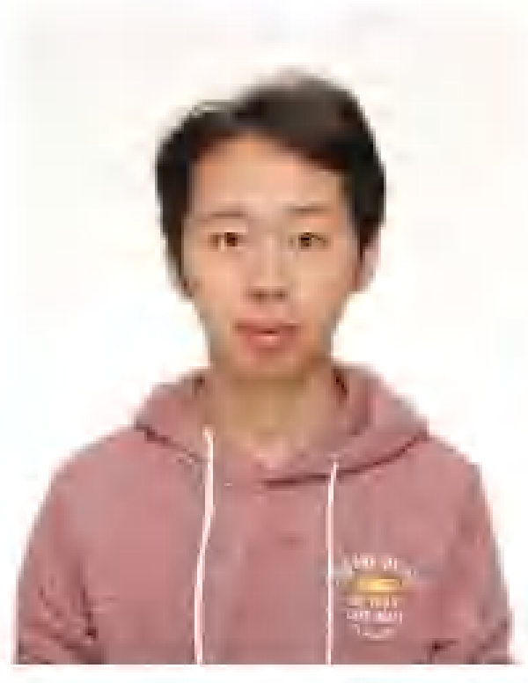
Chengdong Yang


Zihe Wu


Prof. Chong Cheng

This work was financially supported by the by the National Key R&D Program of China, Fundamental Research Funds for the Central Universities, National Natural Science Foundation of China, State Key Laboratory of Polymer Materials Engineering, and 1000 Youth Talent Plan.

Structural Phase Transitions and Quantum Dots Regulation of Perovskite Stannates

Miao Yu, [†,∥] **Xiaoyu Kuang,** [†,∥] **Hao Tian,** [*,‡,¶] **Zhangyao Xing,** [†] **Jiasi Qiu,** [†] **Yingqi Cui,** [‡,¶] **and Aijie Mao** [*,†]

† Institute of Atomic and Molecular Physics, Sichuan University, Chengdu 610065, China
‡ School of Physics and Electronic Engineering, Zhengzhou Normal University, Zhengzhou 450044, China
¶ Department of Materials Science and Engineering, Nanjing University, Nanjing 210093, China

First-principles calculations in conjunction with the CALYPSO structure search method are performed to investigate the structural phase transitions of the perovskite stannates $ASnO_3$ (A = Ca, Sr, and Ba) under hydrostatic pressure up to 100 GPa. Two reconstructive phase transitions appear in $CaSnO_3$, that is, from a perovskite state (Pv-*Pnma*) to a novel state that belongs to the post-perovskite family (pPv-*Cmcm*) and then undergoing another reconstructive transition to the so-called post-post-perovskite state (ppPv-*Pnma*) at higher pressure. In contrast, $SrSnO_3$ directly changes from Pv-*Pnma* phase to ppPv-*Pnma* phase under high pressure. However, $BaSnO_3$ only retains the ideal cubic perovskite structure up to 100 GPa without a phase transition. Subsequently, based on time-dependent density functional theory (TDDFT), quantum dots (QDs) fabricated by the pressure-induced stable structures of $ASnO_3$ interacting with ultrafast laser pulses are investigated. Strikingly, compared with traditional perovskite QDs fabricated by simple structure ($Pm\bar{3}m$), pPv-QDs based on the stable phase pPv-*Cmcm* of $CaSnO_3$ occur an obvious insulator-metal transition within a wide range of laser wavelengths and show enhanced optical absorption through size adjustment. In particular, $CaSnO_3$ pPv-QDs under high-intensity lasers exhibit nonvolatile memory characteristics, which demonstrates the potential applications for memory units and data storage devices.

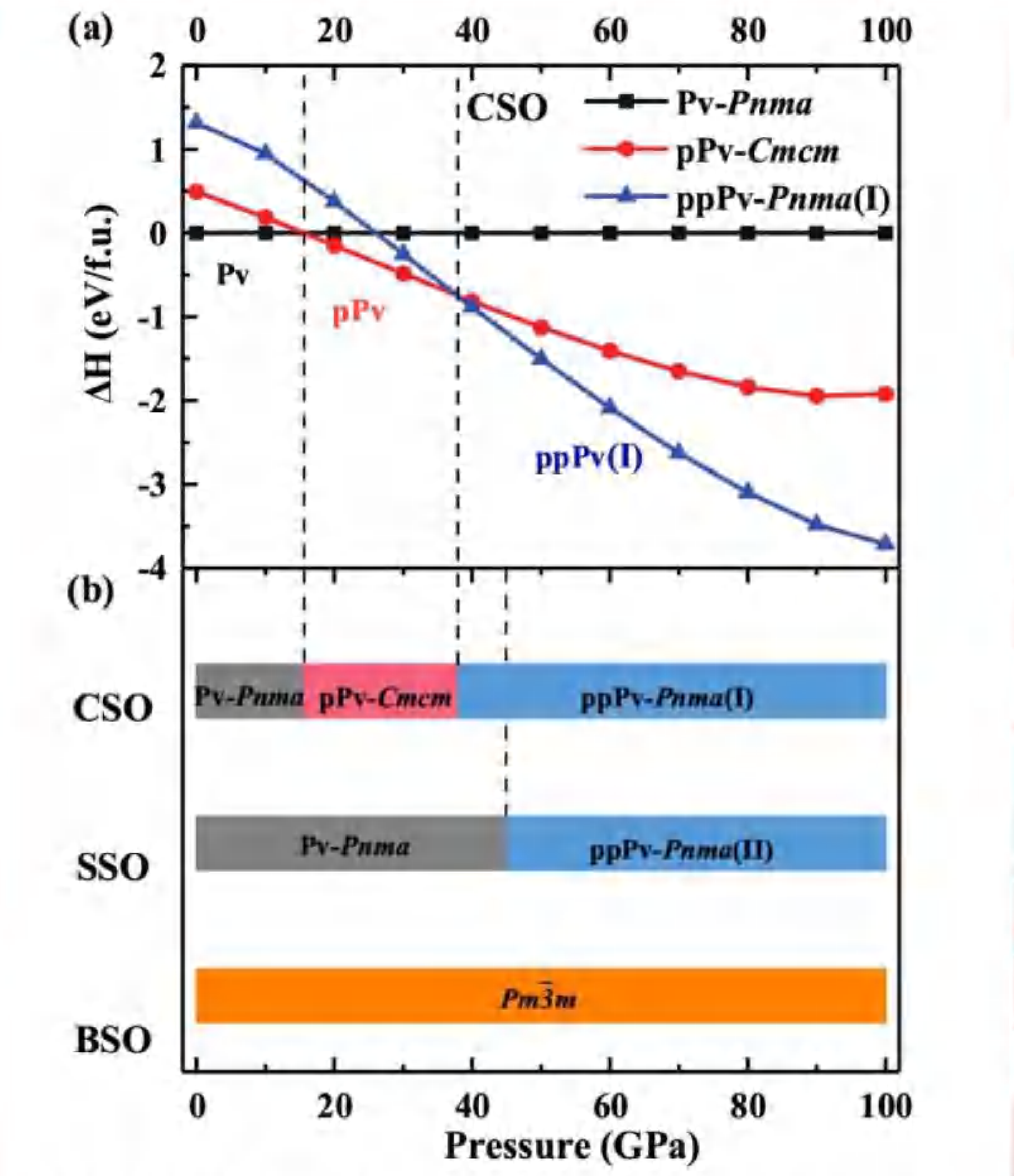

FIG 1. (a) The enthalpies of the predicted structures of $CaSnO_3$, (b) Stable phases of $ASnO_3$(A = Ca, Sr, and Ba) under hydrostatic pressure of 0–100 GPa.

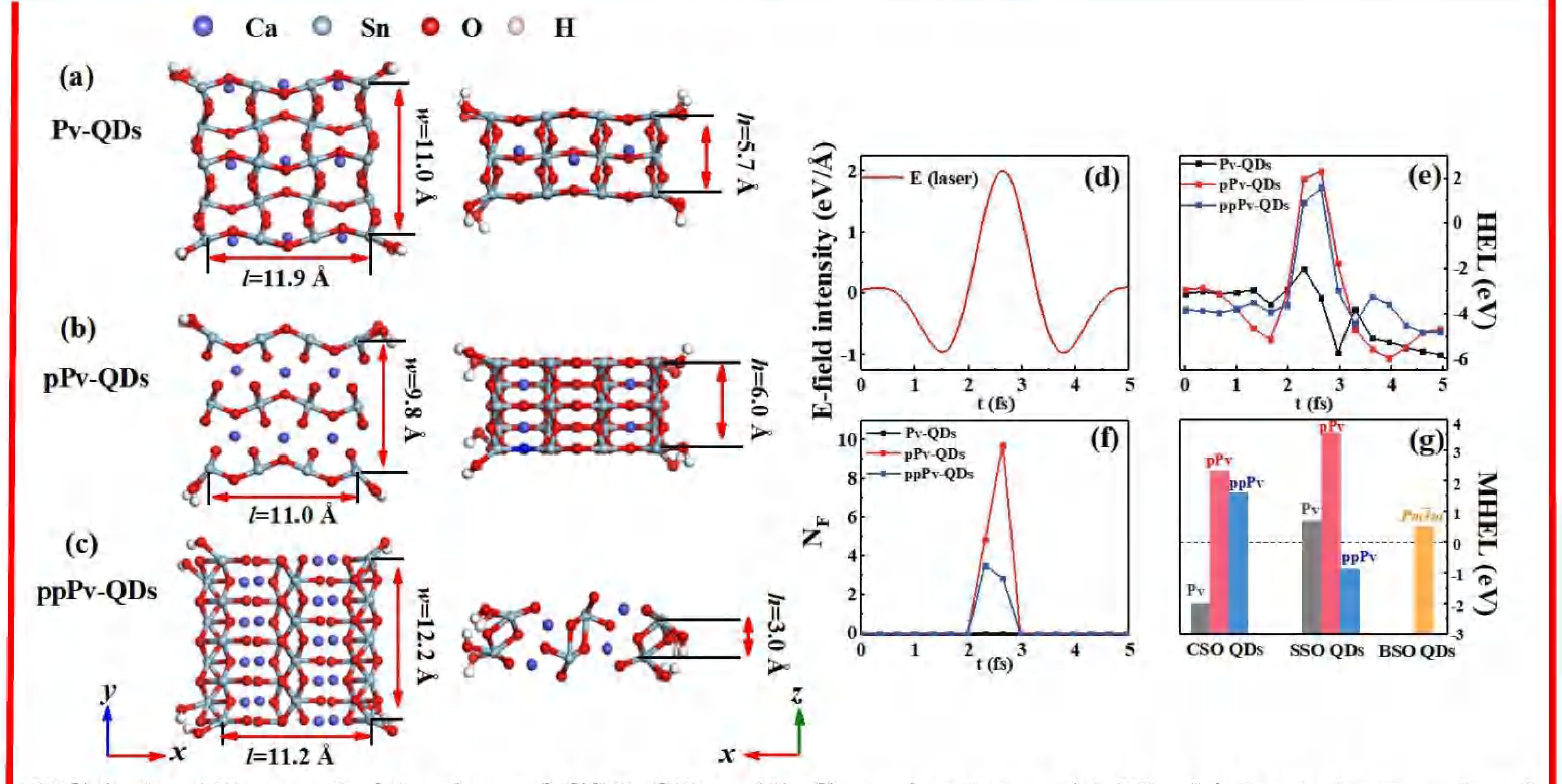

FIG 2. (a-c)Top and side view of CSO QDs, (d) Gaussian laser, (e) The highest electron level (HEL) of CSO QDs, (f) The number of electrons that across the Fermi surface (N_F) in CSO QDs, (g) The maximum values of the HEL (MHEL) for $ASnO_3$-based QDs under the ultrafast laser.

FIG 3. (a) Gaussian lasers, the wavelengths are 792, 654, 531, 476, and 355 nm. (b) Themaximum values of the HEL (MHEL) for CSO QDs under different wavelengths of ultrafast lasers.

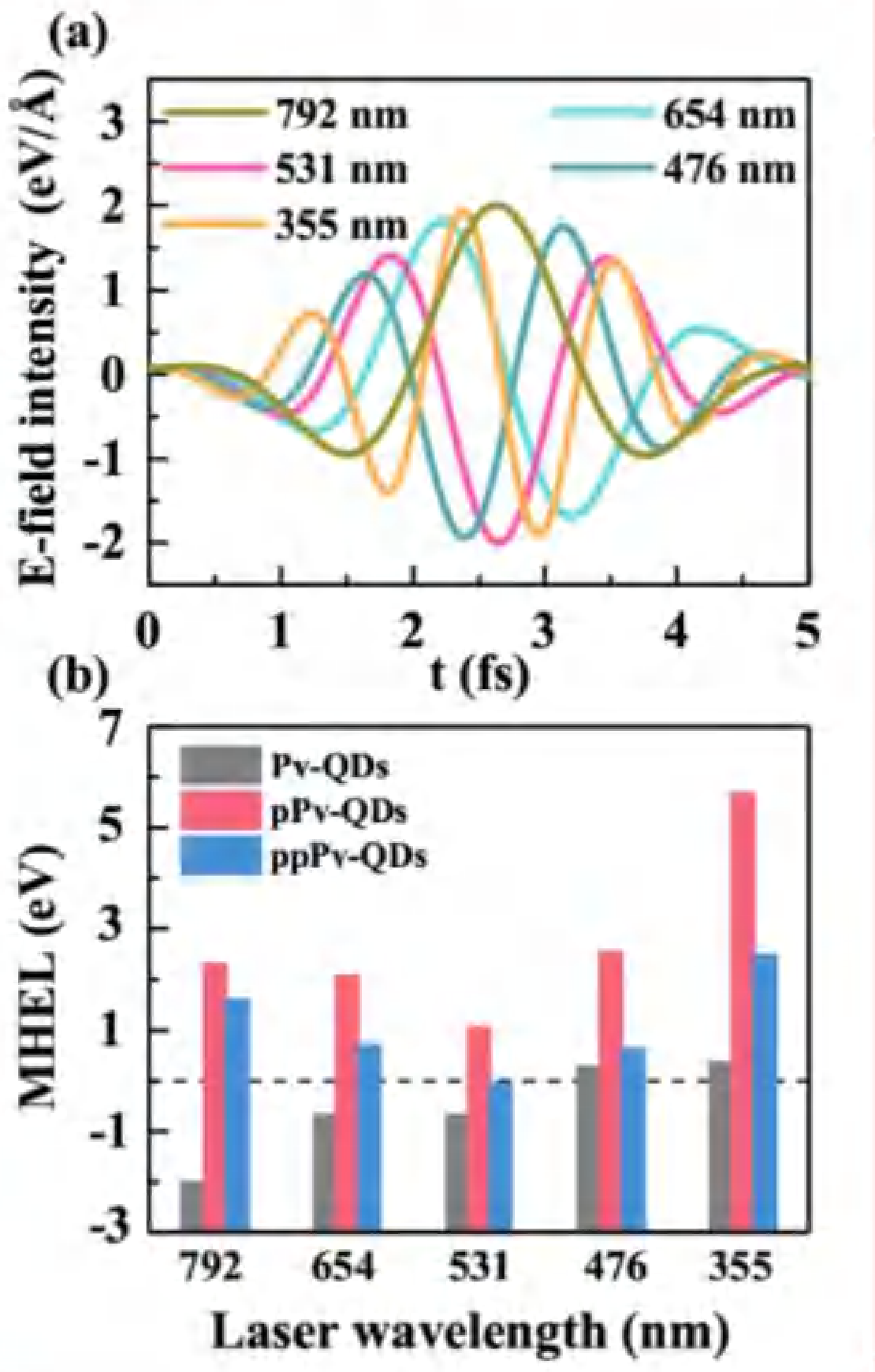

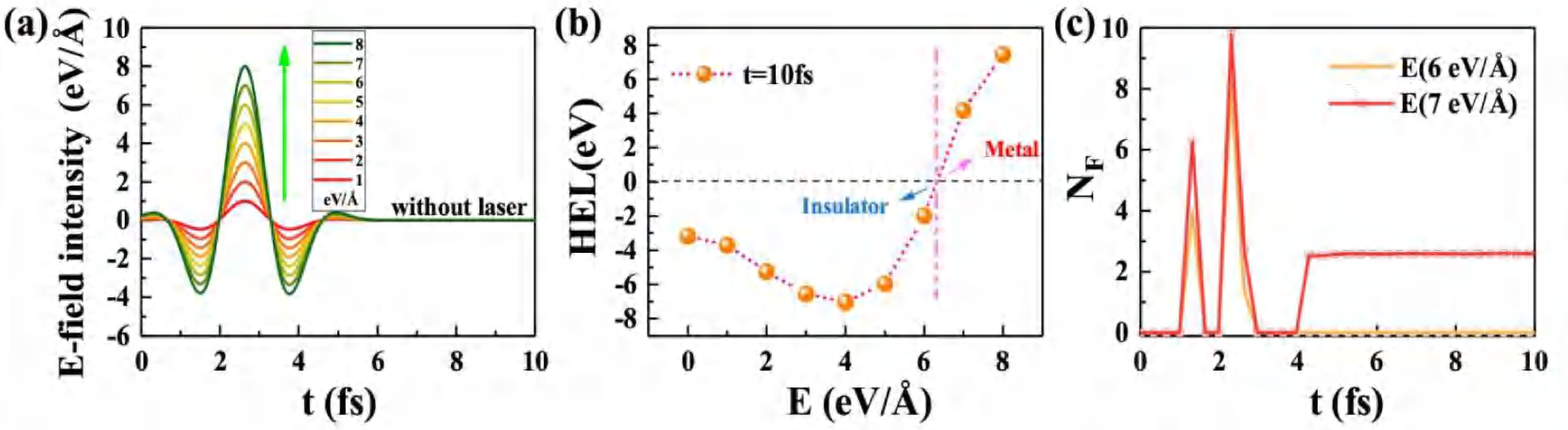

FIG 4. (a) Gaussian lasers with the wavelength of 792 nm and the maximum intensities range of 1.0–8.0 eV/Å. (b) The HEL of CSO pPv-QDs(III) at t = 10 fs under 1.0–8.0 eV/Å intensities of the laser. (c) The N_F of CSO pPv-QDs(III) under 6 eV/Å and 7 eV/Å intensities of the laser.

CONCLUSION

In conclusion, we have theoretically predicted the phase transitions of perovskite stannates ($ASnO_3$; A = Ca, Sr, and Ba) and made a comprehensive study of the optical properties of $ASnO_3$-based QDs. Under hydrostatic pressure of 0-100 GPa, we have identified two reconstructive phase transitions in $CaSnO_3$: from Pv-*Pnma* to pPv-*Cmcm*, as well as from pPv-*Cmcm* to ppPv-*Pnma*(I) at 15 and 38 GPa, respectively, and one reconstructive phase transition in $SrSnO_3$: from Pv-*Pnma* to ppPv-*Pnma*(II) at 45 GPa. Compared with $CaSnO_3$ and $SrSnO_3$, $BaSnO_3$ kept its ground state (*$Pm\bar{3}m$*) structure at the whole pressure range of 0–100 GPa. Meanwhile, the $ASnO_3$-based QDs fabricated by the pressure-induced stable structures presented different optical responses under ultrafast laser pulses. When the laser intensity was 2 eV/Å, $CaSnO_3$ pPv-QDs exhibited relatively stronger optical absorption compared with Pv-QDs and ppPv-QDs and experienced insulator-metal transitions under various wavelength lasers. The thinning and enlargement operations on pPv-QDs of $CaSnO_3$ could work together to further improve the optical absorption. Besides this, pPv-QDs(III) of $CaSnO_3$ exhibited nonvolatile properties under high-intensity lasers, which therefore implied the potential applications in developing data storage devices. Our investigations demonstrated that the optical responses of perovskite QDs could be effectively modified by applying pressure to change the bulk structures or adding different laser forms, and these two methods could act simultaneously for further practical quantum control.

Reference: M. Yu, X. Y. Kuang, H. Tian, Z. Y. Xing, J. S. Qiu, Y. Q. Cui, and A. J. Mao, J. Phys. Chem. C, 2022, 126, 4132-4139.

Electronic address: [a]tiao2007@126.com (H.Tian), [b] scu_mij@126.com (A. J. Mao)

Acknowledgements:This work is supported by the Central Government Funds of Guiding Local Scientific and Technological Development for Sichua Province (No. 2021ZYD0026), the National Natural Science Foundation of China (Nos. 11874043 and 11904328), the China Postdoctoral Science Foundatio (No. 2018M642205) and the Jiangsu Planned Projects for Postdoctoral Research Funds (No. 2019K249).

Realization of the Square-Root Higher-Order Topological Insulator in Electric Circuits

Lingling Song, Huanhuan Yang, Yunshan Cao, Peng Yan*

School of Electronic Science and Engineering and State Key Laboratory of Electronic Thin Films and Integrated Devices, University of Electronic Science and Technology of China, Chengdu 610054, China.

lily.song0215@foxmail.com

Introduction

The schematic plot for different types of topological insulators

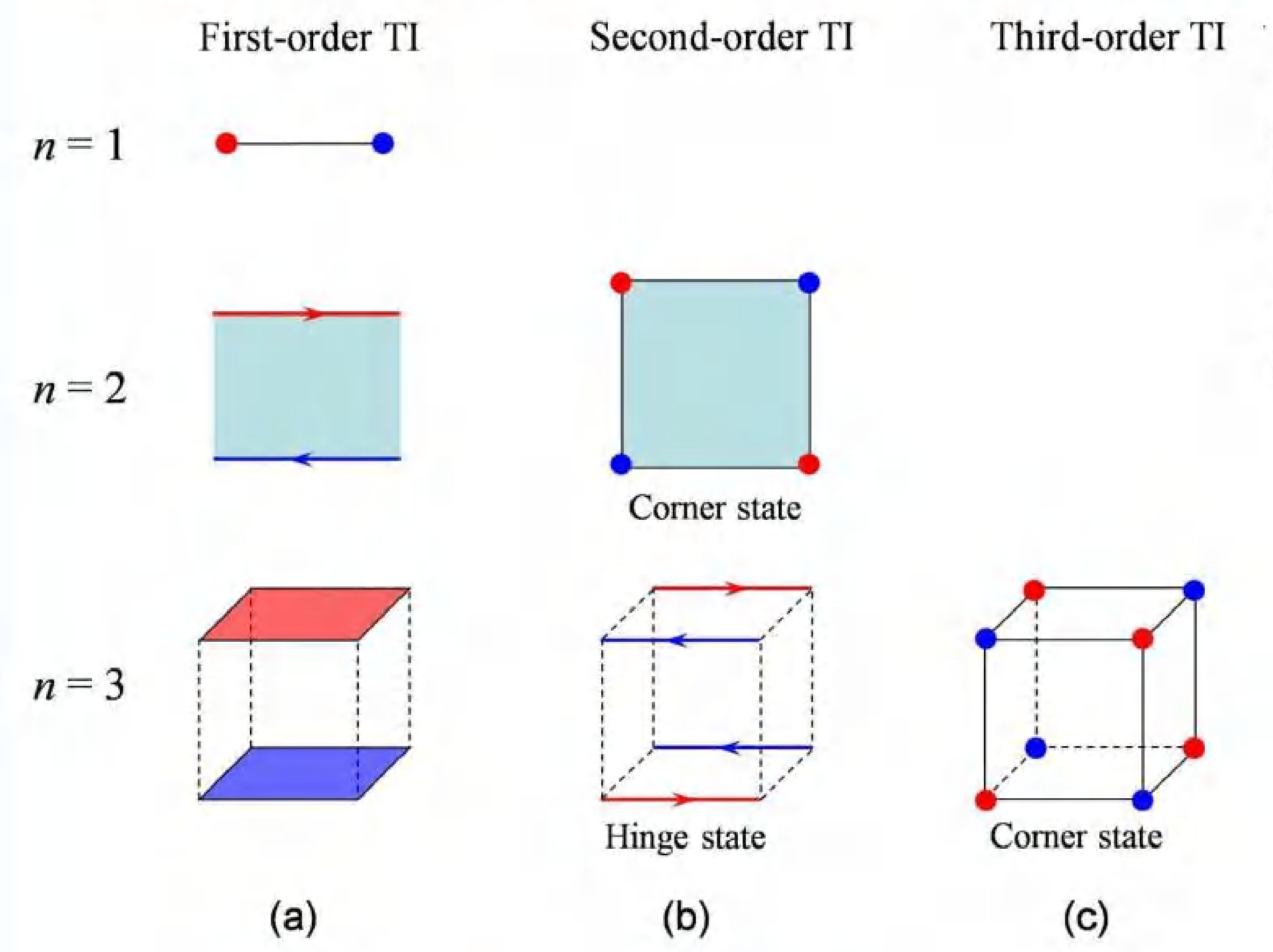

Physics Reports **915**, 1 (2021)

Square-root topological insulator

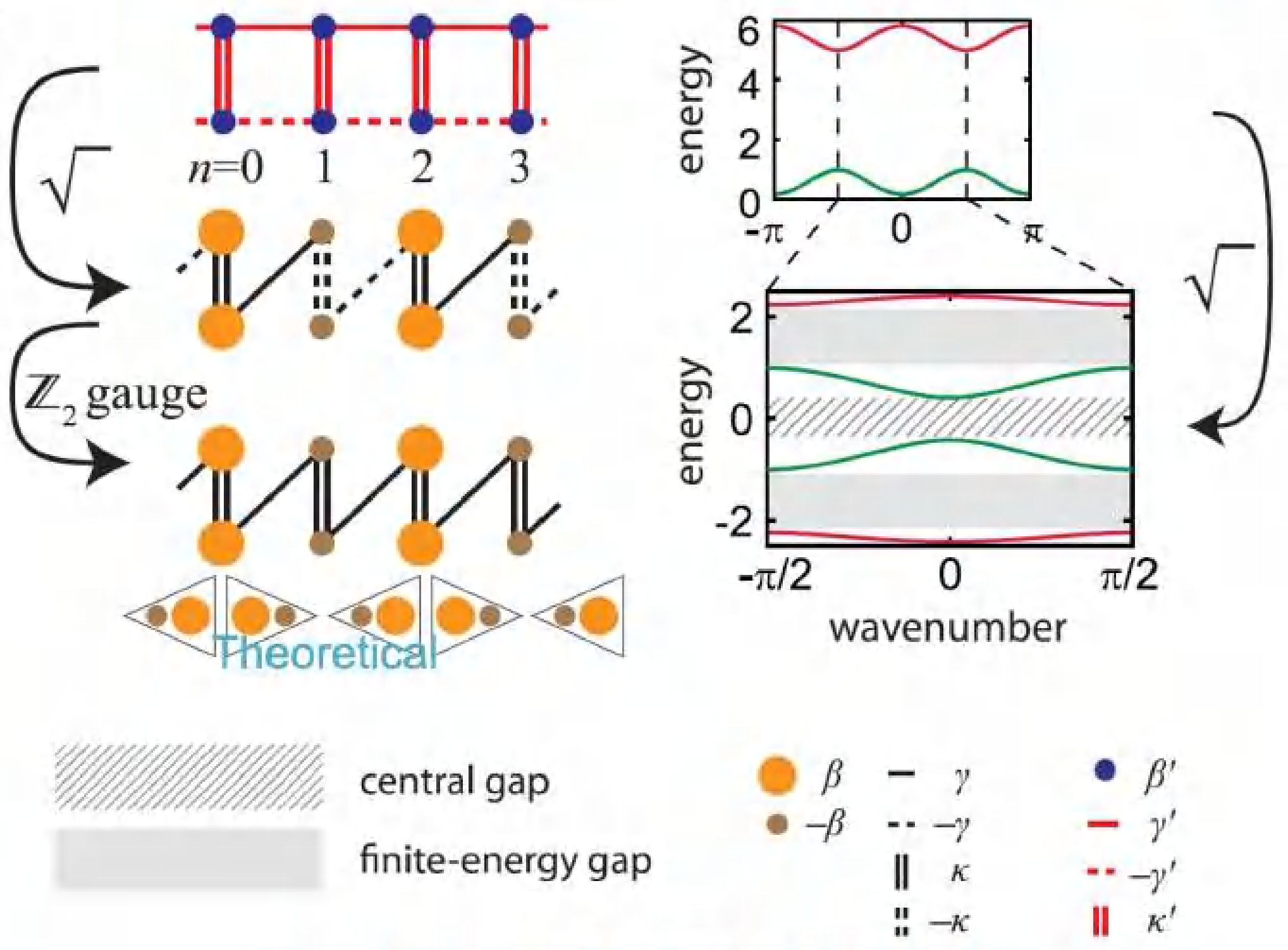

Phys. Rev. B **95** 165109 (2018)

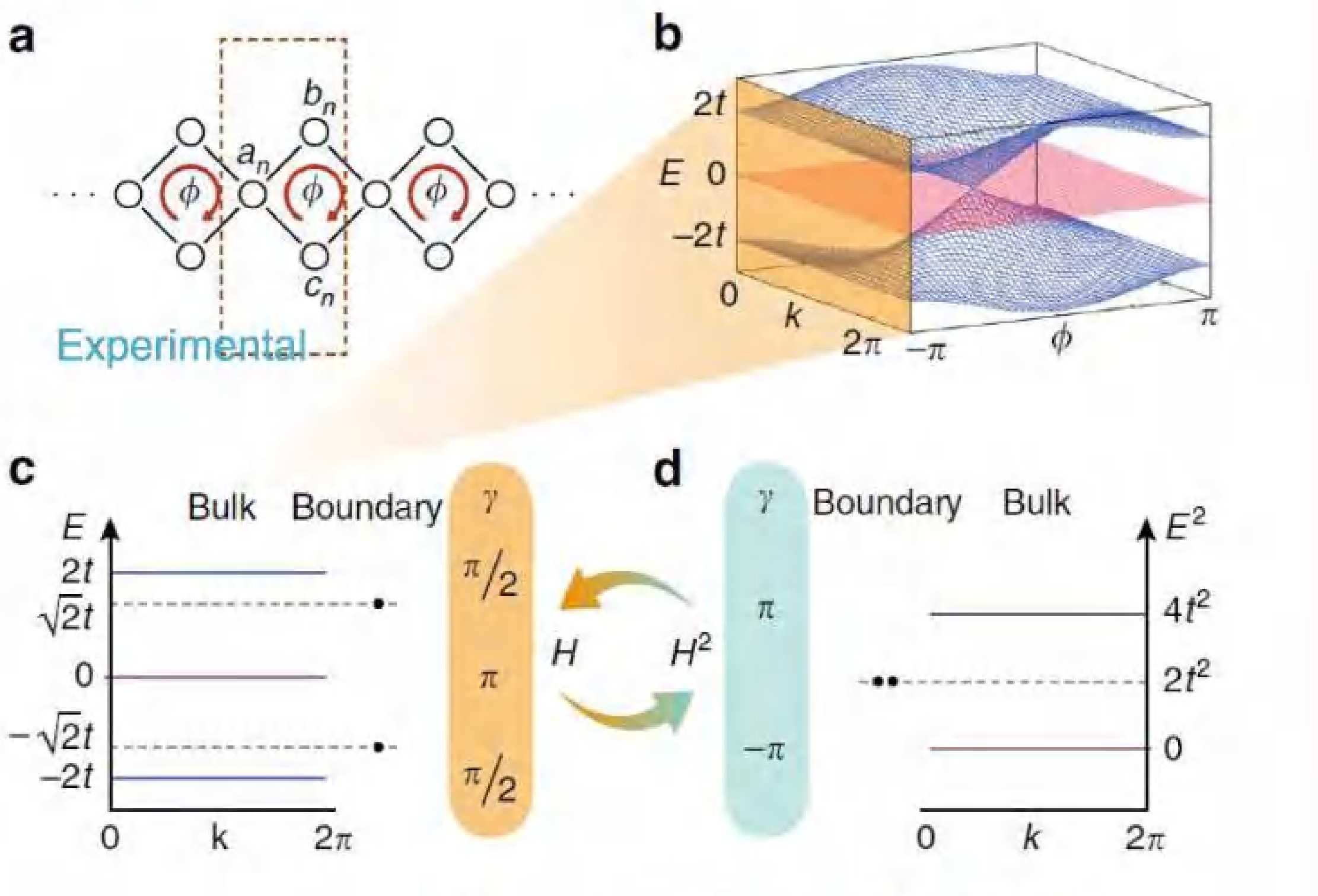

Nat. commun. **11**, 907 (2020)

Dirac (1928) $E = \pm\sqrt{m^2c^4 + p^2c^2}$

+ electron with spin up and down

– positron with spin up and down

I. Honeycomb-Kagome Electrical Circuit

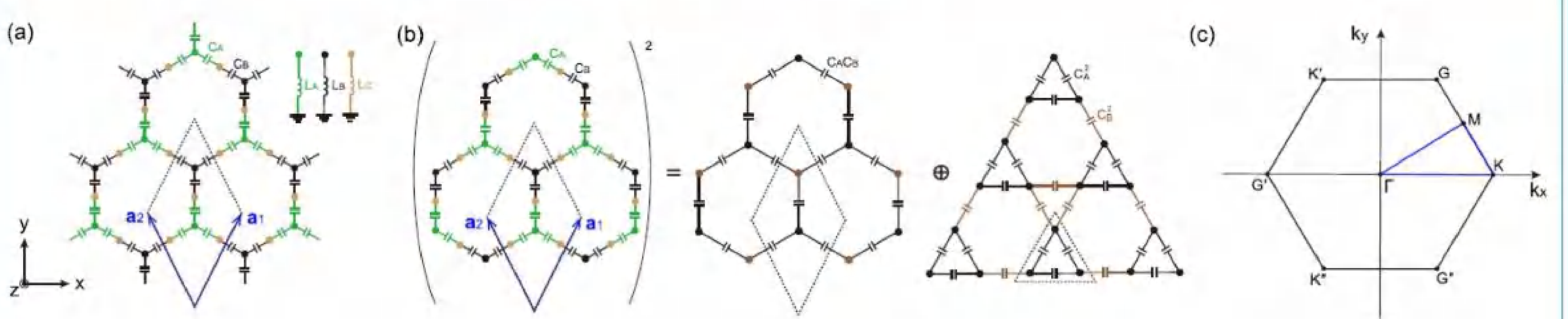

$$\mathcal{H} = \begin{pmatrix} Q_{11} & 0 & Q_1 & Q_1 & Q_1 \\ 0 & Q_{22} & Q_2 & Q_3^* & Q_4^* \\ Q_1 & Q_2 & Q_{33} & 0 & 0 \\ Q_1 & Q_3 & 0 & Q_{44} & 0 \\ Q_1 & Q_4 & 0 & 0 & Q_{55} \end{pmatrix}$$

$$[\mathcal{H}]^2 = \begin{pmatrix} h_{\mathbf{k}}^H & O_{2,3} \\ O_{3,2} & h_{\mathbf{k}}^K \end{pmatrix} \quad h_{\mathbf{k}}^{\mathrm{H}} = \Phi_{\mathbf{k}}^\dagger \Phi_{\mathbf{k}} \quad h_{\mathbf{k}}^{\mathrm{K}} = \Phi_{\mathbf{k}} \Phi_{\mathbf{k}}^\dagger$$

$$\Phi_{\mathbf{k}} = \begin{pmatrix} Q_1 & Q_2 \\ Q_1 & Q_3 \\ Q_1 & Q_4 \end{pmatrix}$$

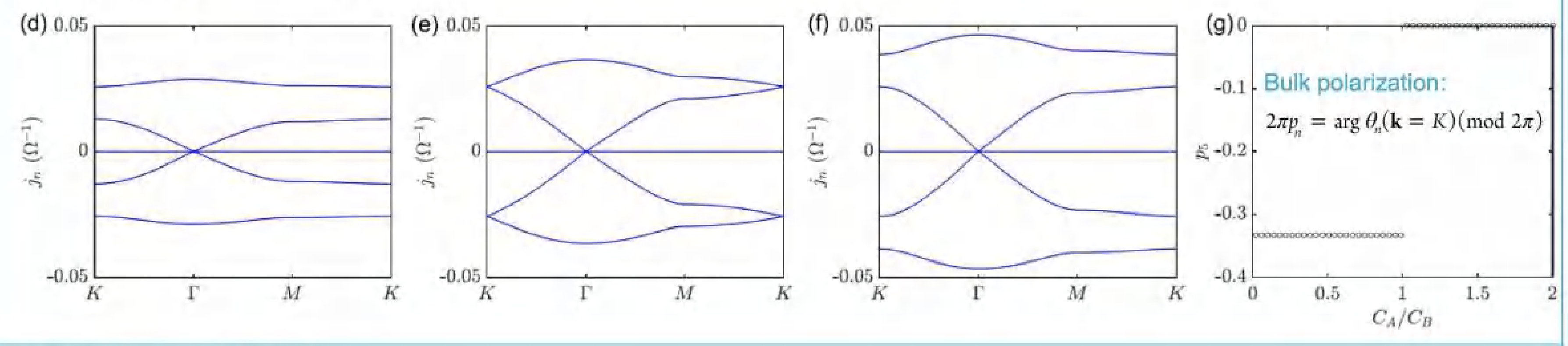

II. Corner States

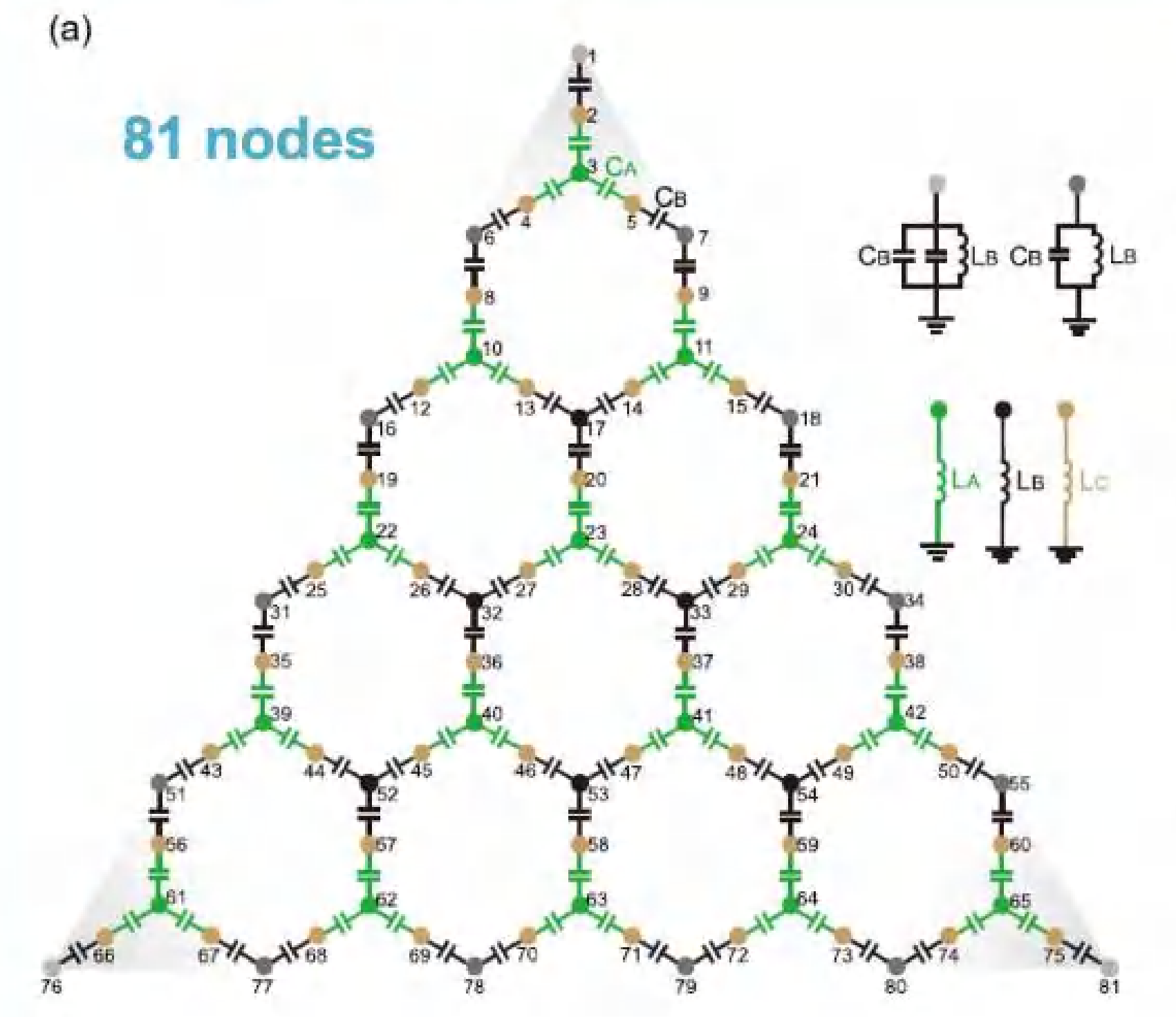

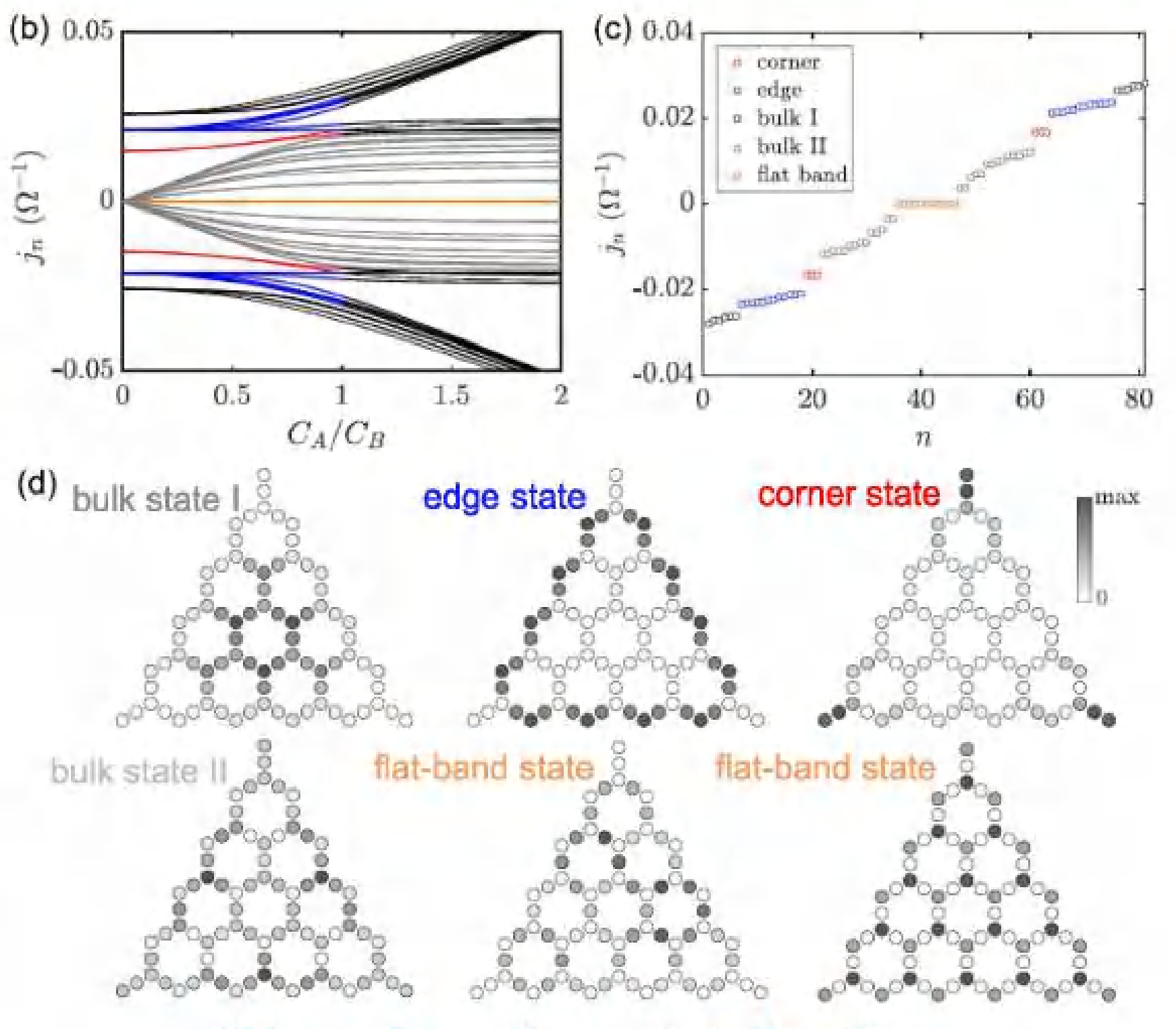

Wave function distribution

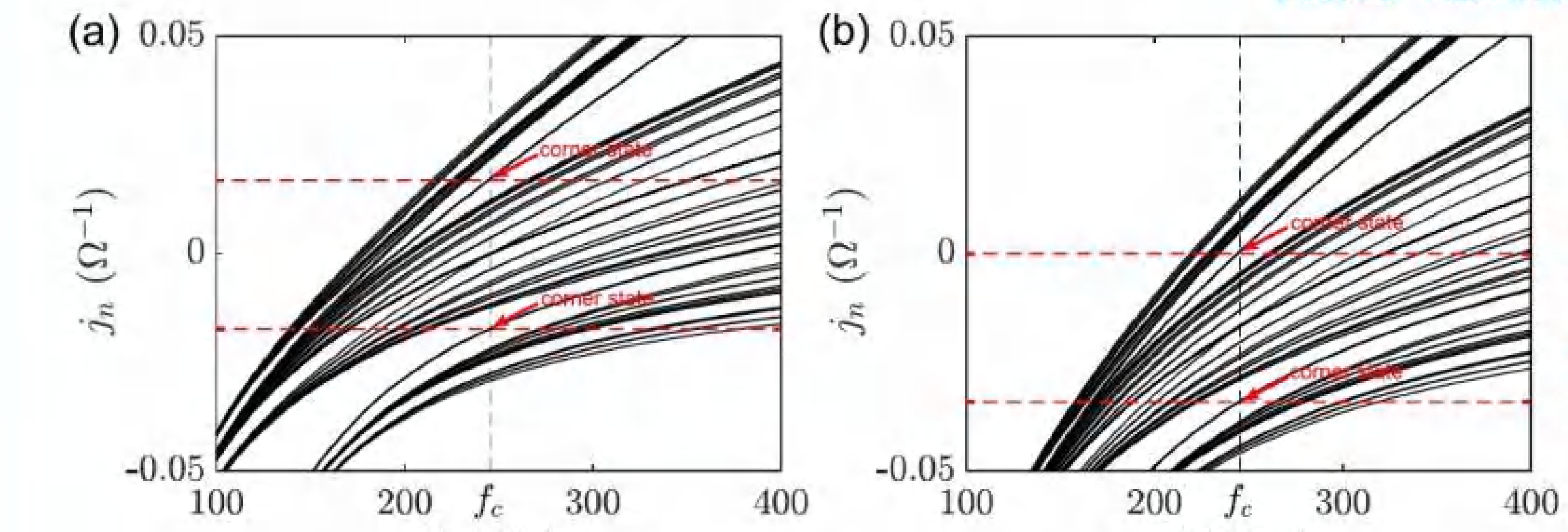

Theoretical spectrum of J(ω) depending on the frequency without (a) and with (b) grounded inductors L_G

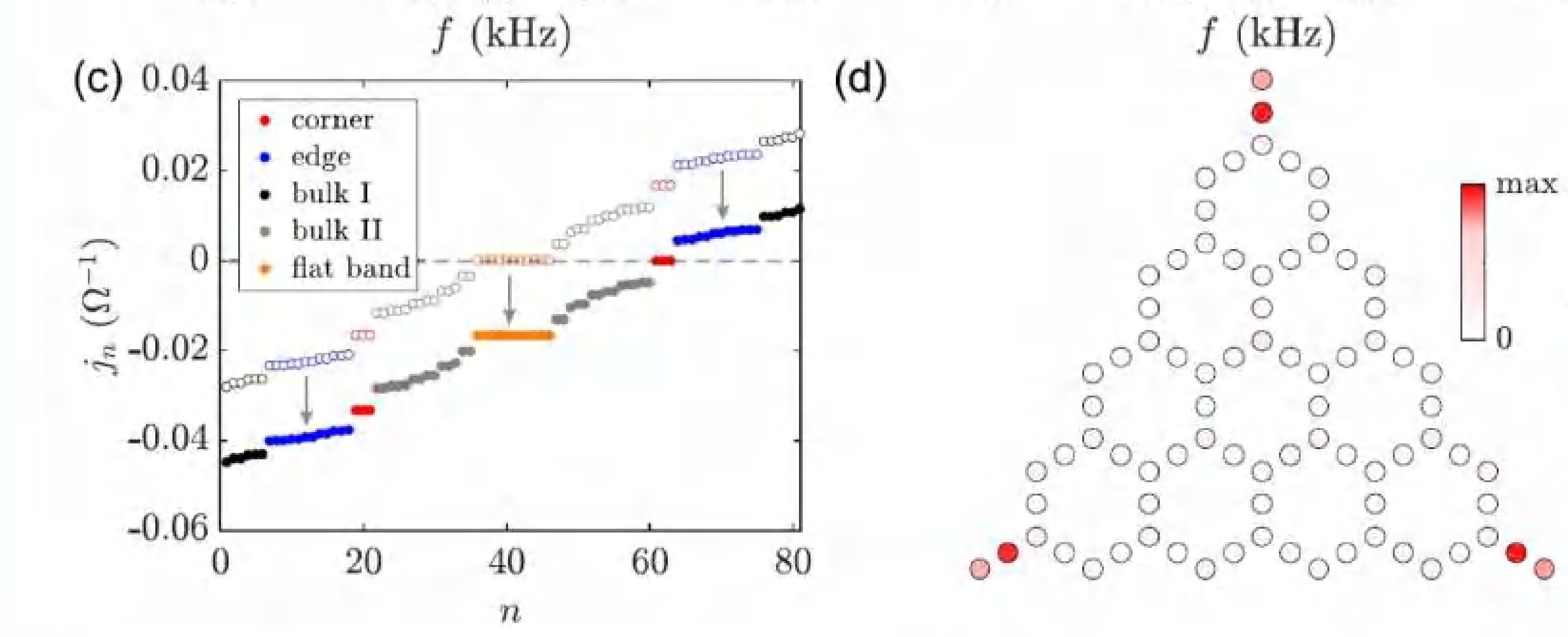

Theoretical impedance

$$Z_{ab} = \frac{V_a - V_b}{I_{ab}} = \sum_n \frac{|\psi_{n,a} - \psi_{n,b}|^2}{j_n}$$

III. Experimental Observation

Honeycomb-Kagome LC circuit board

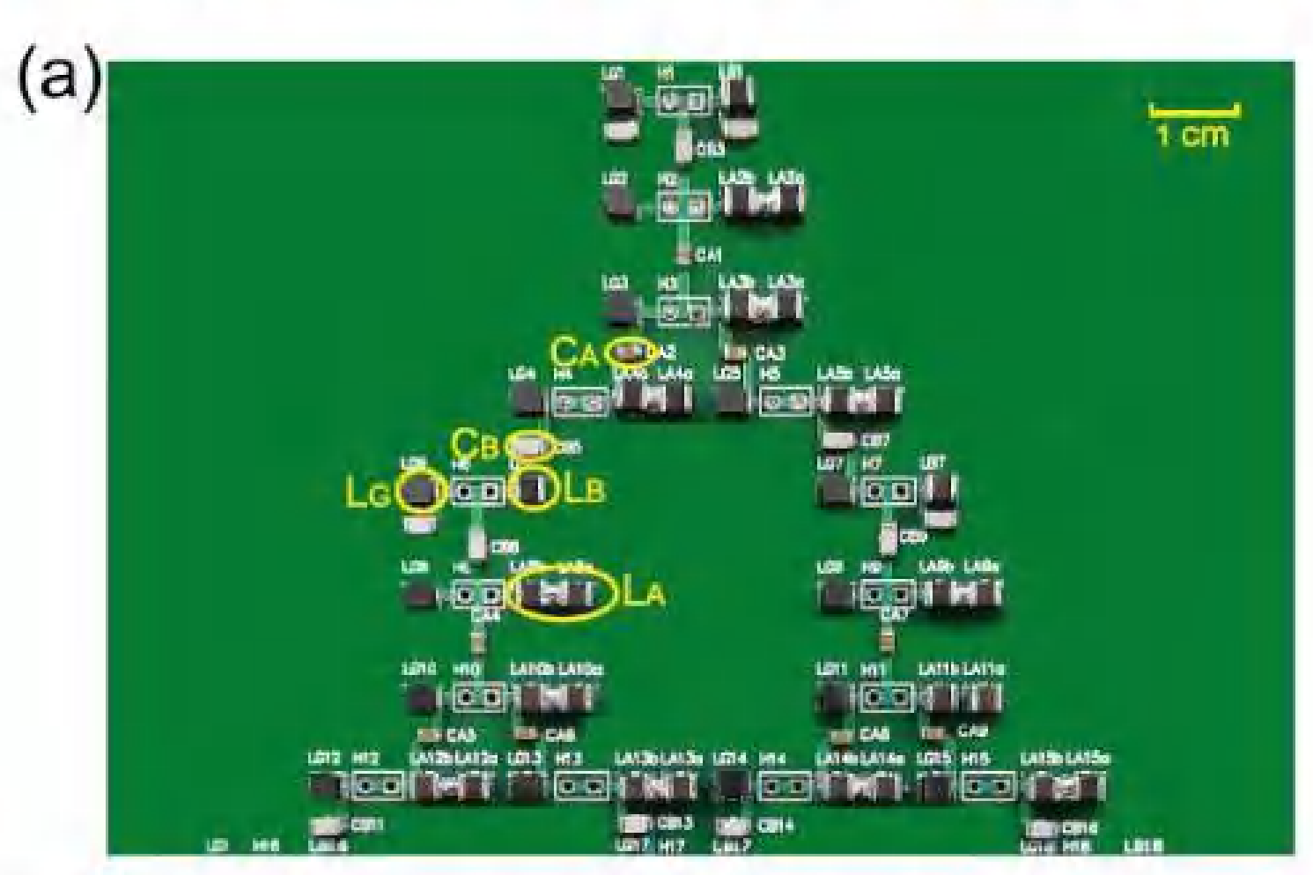

$C_A = \frac{C_B}{2} = 5\ \mathrm{nF}, L_A = 2L_B = L_A = 30\ \mu\mathrm{H}, L_G = 40\ \mu\mathrm{H}$

(b) Measured impedance

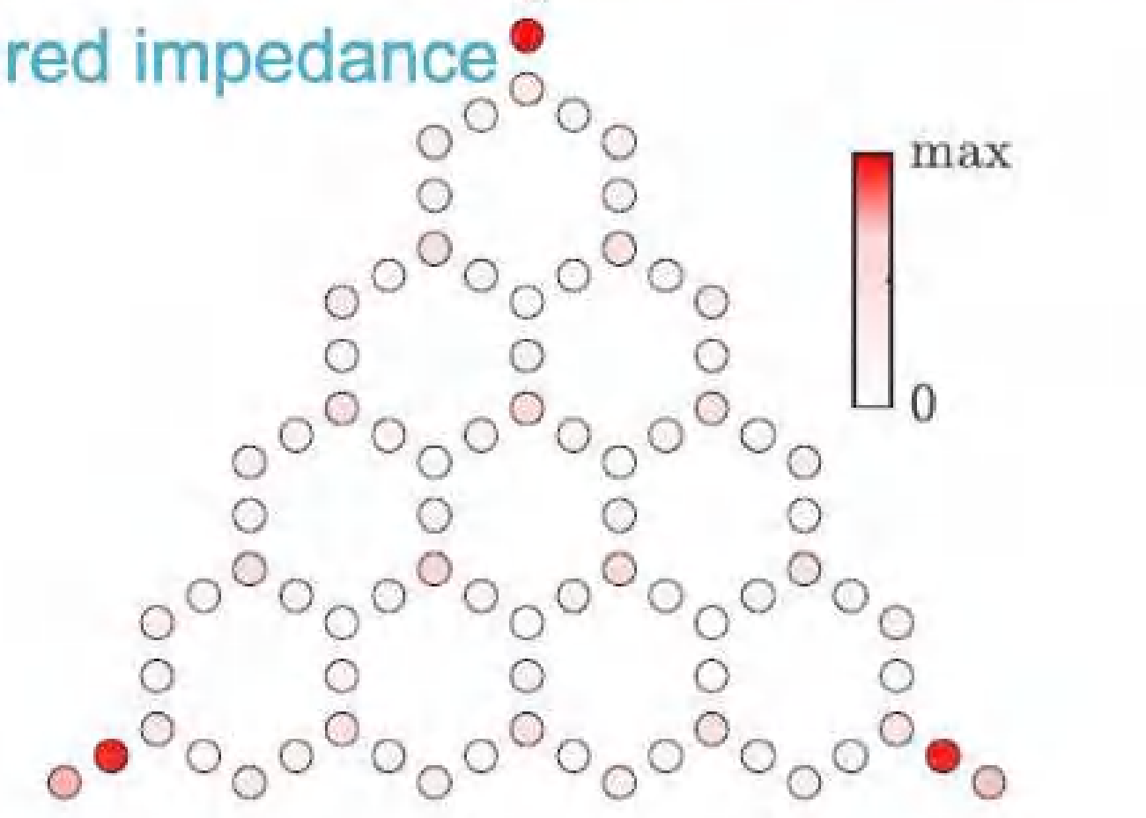

Impedance vs the driving frequency

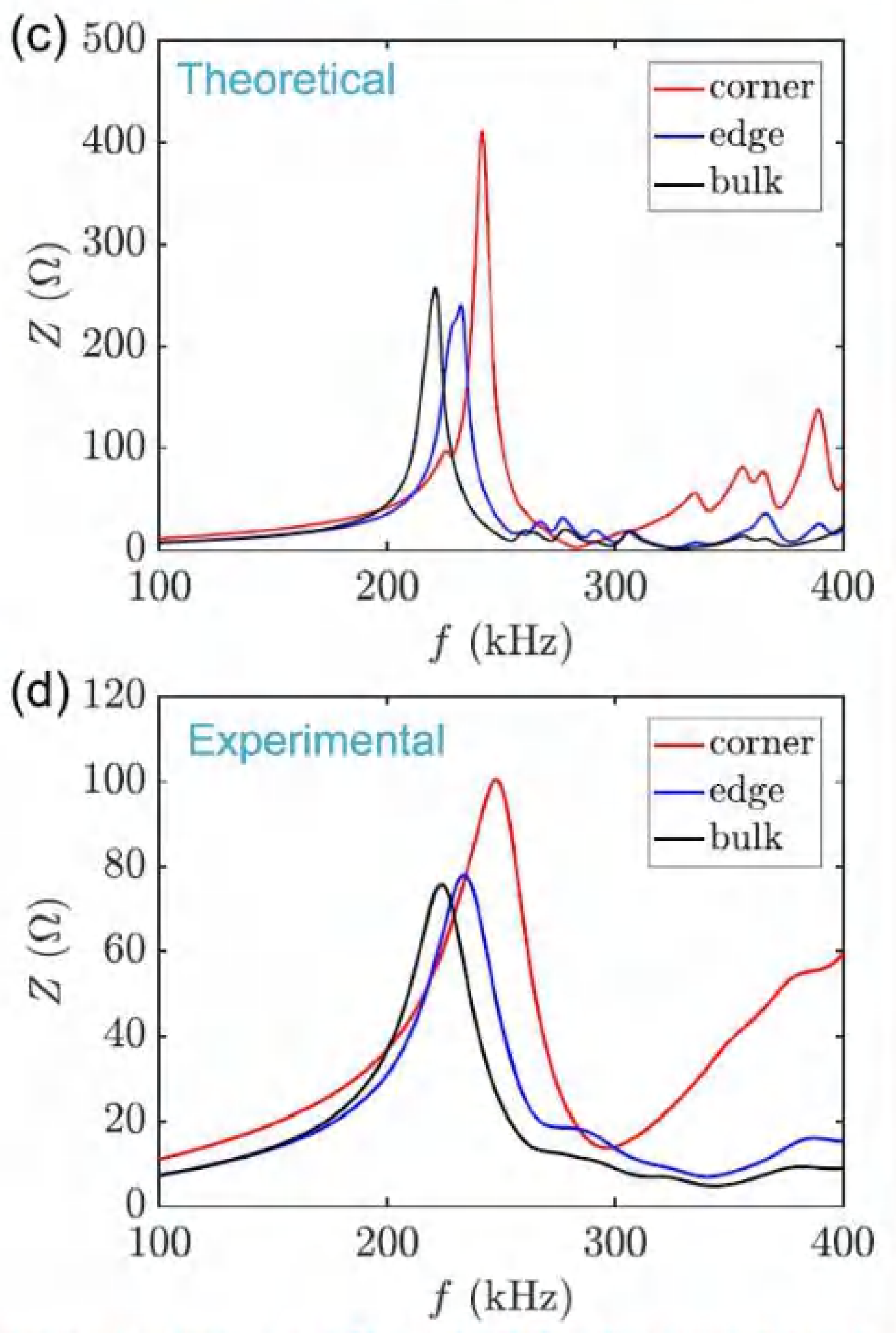

Break generalized chiral symmetry

Conserve generalized chiral symmetry

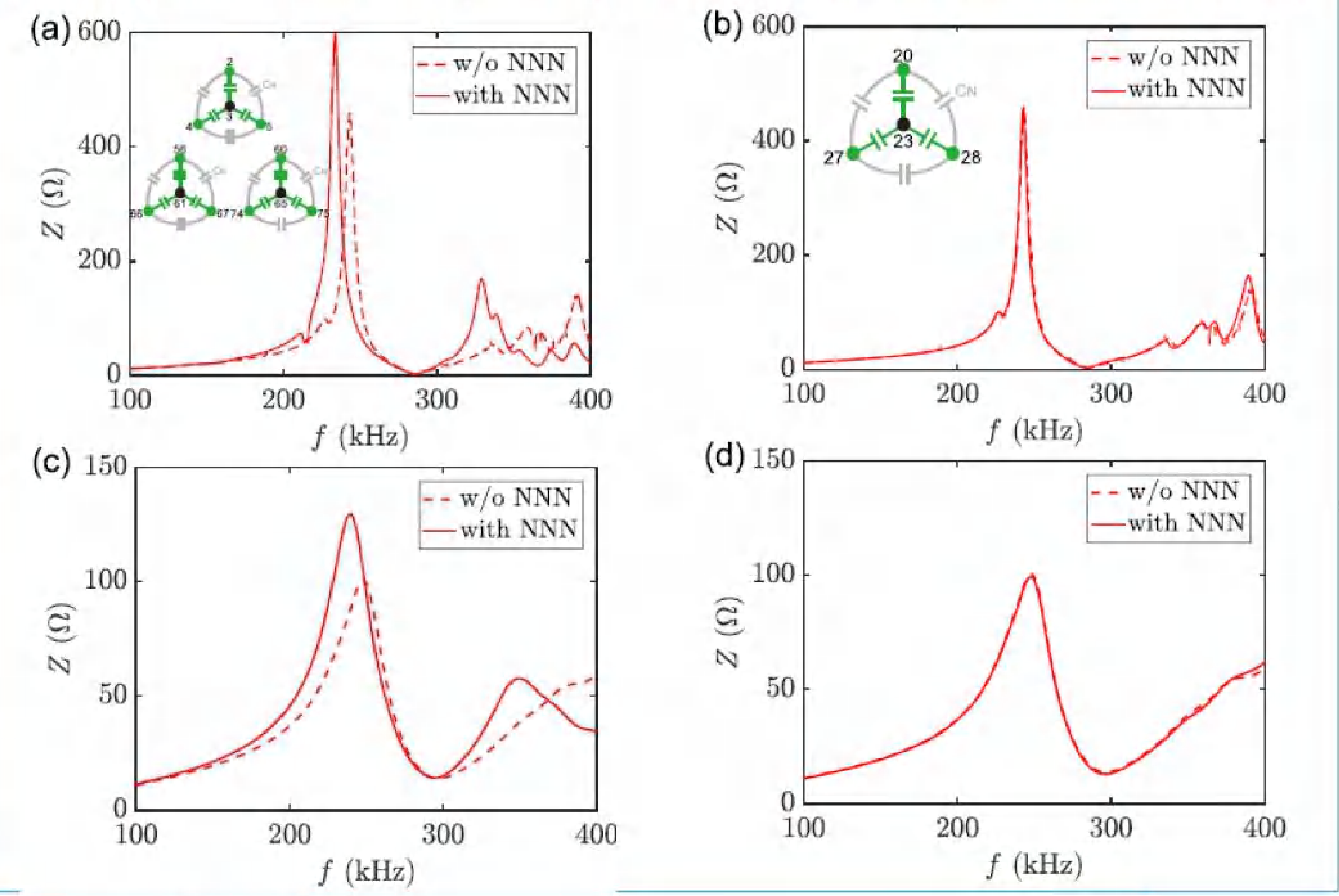

Conclusion

1. We predict the square-root HOTI in electrical circuit, which inherits the feature of wave function from its parent with corner states pinned to nonzero energies.

2. To experimentally observe the nonzero mode, we shift them to "zero energy" by introducing extra grounded inductors to each node but without affecting their spatial distributions.

Learn more about our team

Reference

Lingling Song, et al. "Realization of the Square-Root Higher-Order Topological Insulator in Electric Circuits." Nano Lett. **20**, 7566(2020).

2022材料多尺度计算模拟国际会议
International Conference of Multi-scale Modeling and Simulation of Materials (ICM3-2022)

Bi_2Te_3(111)和Al_2O_3(0001)衬底对Bi(111)双原子层的电子结构及拓扑性质的影响

孙海明（2019级本科生），陈明星
湖南师范大学，物理与电子科学学院

摘要：晶体铋沿（111）面方向的双原子层及薄膜具有新奇的拓扑性质.在实验生长或者实际应用中,其必然与衬底接触.本文采用紧束缚近似方法与第一性原理计算研究了Bi双原子层及其与Bi_2Te_3和Al_2O_3衬底形成的异质结的电子结构.计算结果表明,Bi双层是具有0.2 eV的半导体.当其与具有拓扑表面态的Bi_2Te_3形成异质结时,两者电子态之间有很强的杂化,不利于Bi(111)双层拓扑电子态的观测.将其放在绝缘体Al_2O_3(0001)时,导带与价带与衬底电子态杂化较小,并且展现出巨大的Rashba自旋劈裂.这是由于衬底诱导Bi(111)双原子层中心反演对称性破缺和自旋-轨道耦合共同作用的结果.进一步采用紧束缚近似计算得到的结果发现,衬底Al_2O_3(0001)对Bi(111)双层的作用等效于一个约为0.5～0.6 V/Å的外电场.此外,Bi(111)双原子层与衬底Bi_2Te_3电子态之间的强杂化会导致其发生拓扑相变--由二维拓扑绝缘体转变为平庸的绝缘体.

I. 引言

- 晶体铋具有层状结构，沿其(111)方向，层与层之间相互作用较弱，有利于人们从其块体相获得少层及薄膜结构．理论预言Bi(111)双原子层及薄膜是二维拓扑绝缘体.
- 实验通过分子束外延生长在拓扑绝缘体Bi_2Se_3以及Bi_2Te_3等表面得到了1BL-Bi，ARPES实验结果可能存在拓扑边缘态。
- Al_2O_3(0001)诱导表面1BL-Bi中出现Rashba自旋劈裂。

II. 1BL-Bi的电子结构

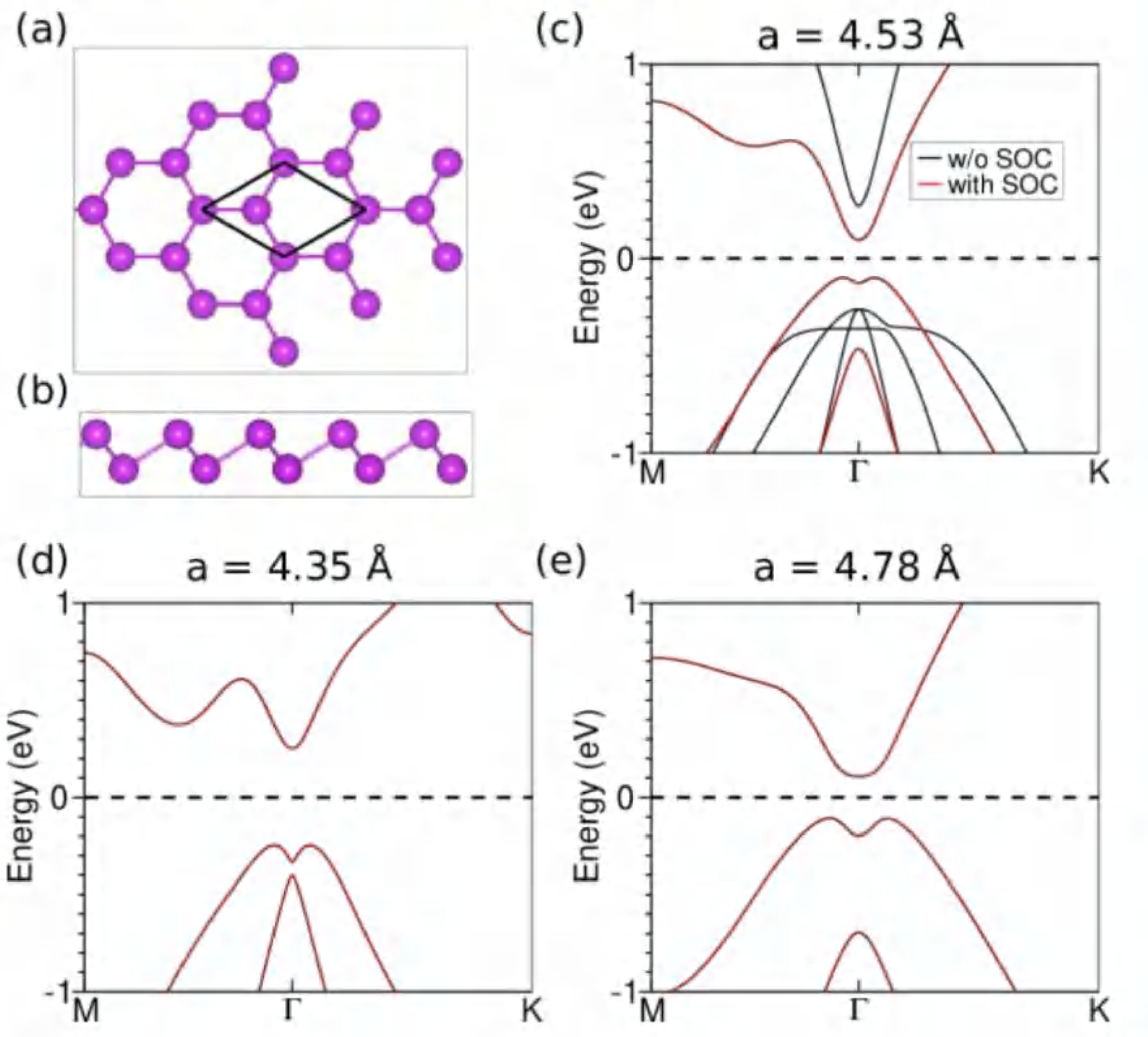

III. Bi/Bi_2Te_3(111)的能带与拓扑性质

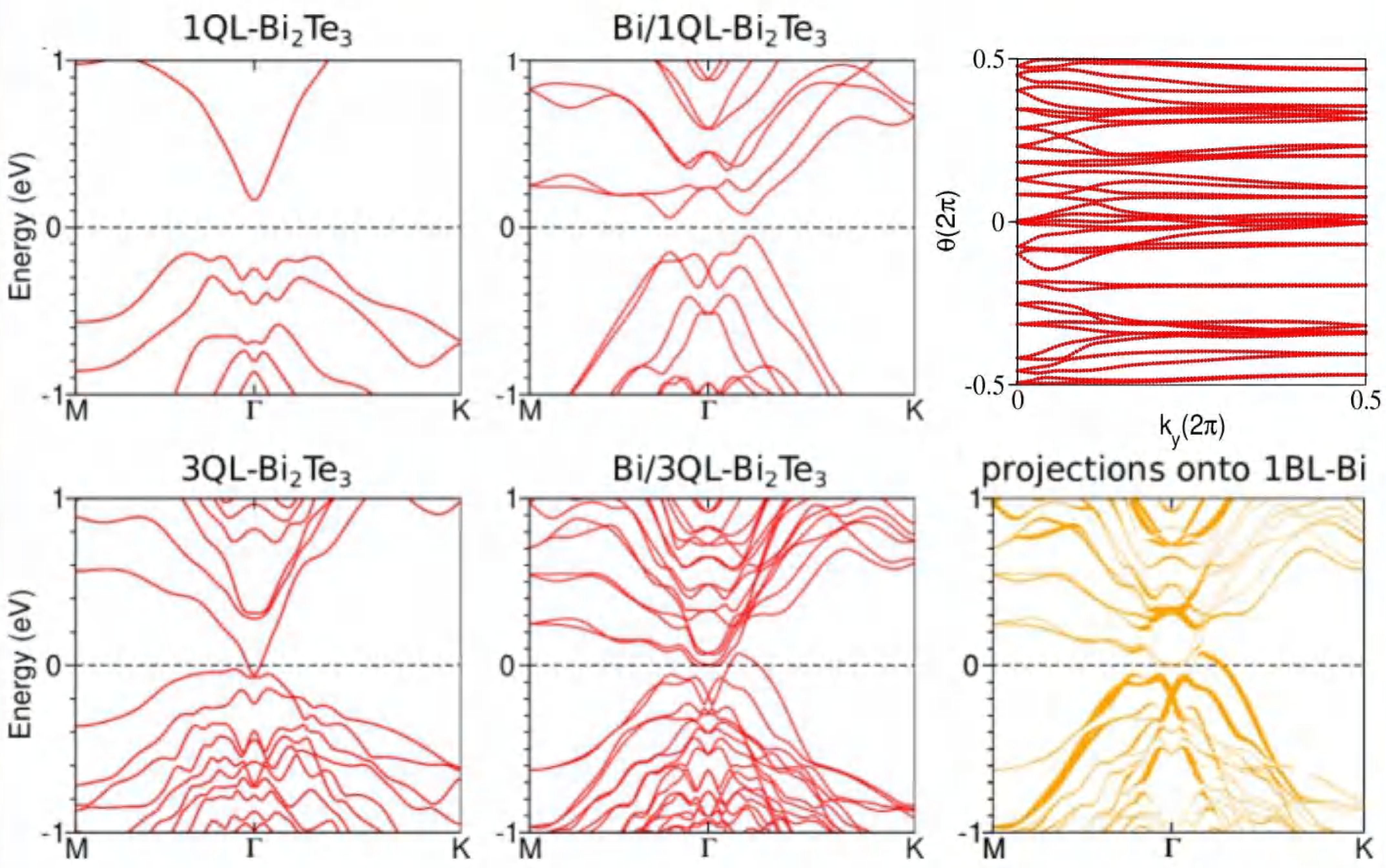

IV. Bi/Al_2O_3(0001)的能带及界面效应

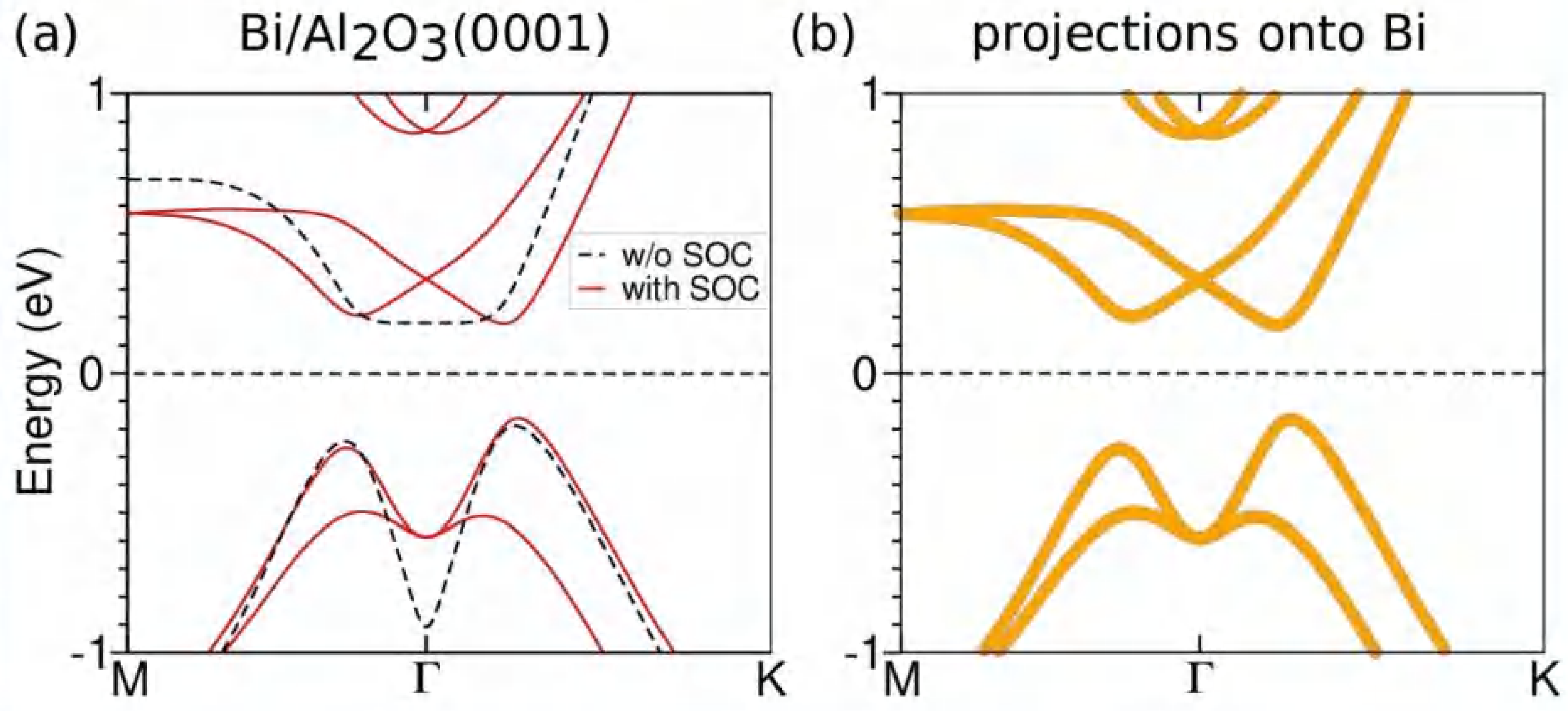

V. 紧束缚近似计算

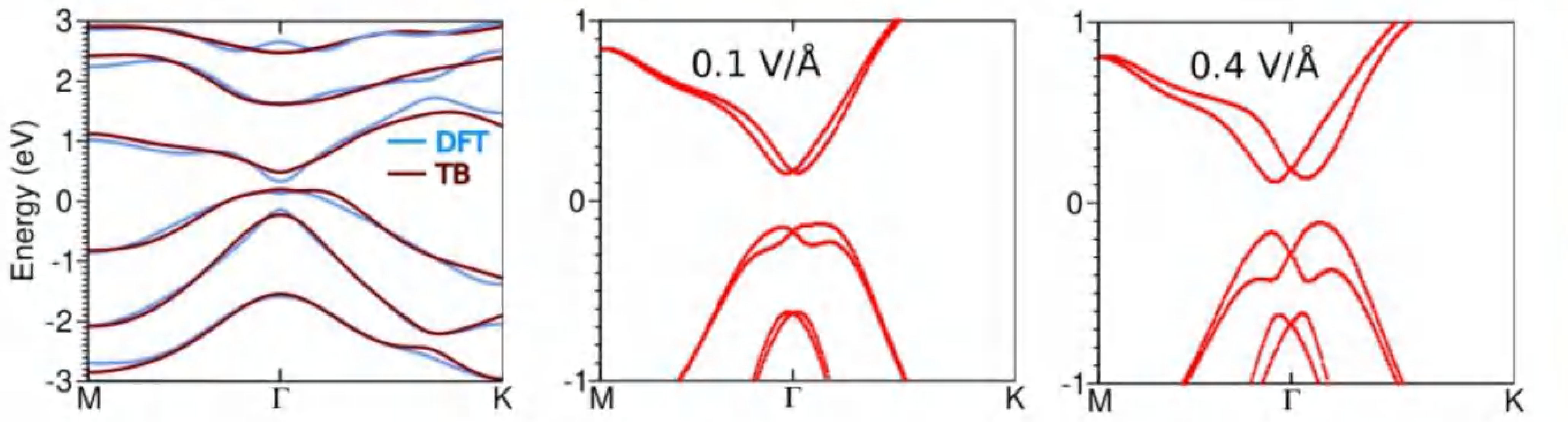

On-site (eV)				
	ε_s	ε_{px}	ε_{py}	ε_{pz}
	-9.477	-1.383	0.624	-0.154
Hopping (eV)				
	$V_{ss\sigma}$	$V_{sp\sigma}$	$V_{pp\sigma}$	$V_{pp\pi}$
1st NN	-0.455	1.439	1.718	-0.646
2nd NN	0.001	0.315	0.168	-0.013
3rd NN	0.019	0.278	0.162	-0.123
4th NN	-0.112	-0.096	0.162	-0.067
5th NN	-0.046	0.037	0.000	0.028

VI. 结论

- 1BL-Bi与Bi_2Te_3与电子态有严重的杂化，没有明显的Rashba劈裂，并且转变为平庸的绝缘体.
- 1BL-Bi与Al_2O_3(0001)形成异质结时，在费米能级附近的能带出现很大的Rashba劈裂.
- 紧束缚近似计算发现，Al_2O_3(0001)衬底对1BL-Bi电子结构的影响可以等效于一个约为0.5~0.6 V/Å的外电场.

References

1. 孙海明，物理学报（已接收）

Acknowledgement 湖南师范大学大学生创新实验项目（项目号：2022208）

Robust Dirac spin gapless semiconductors in a two-dimensional oxalate based organic Honeycomb-Kagome lattice

Jianpei Xing[1](邢健沛), Xue Jiang[1]*(蒋雪), Zhifeng Liu[2], Yan Qi[3] and Jijun Zhao[1](赵纪军)

[1]Key Laboratory of Material Modification by Laser, Ion and Electron Beams (Dalian University of Technology), Ministry of Education, Dalian 116024, China
[2]School of Physical Science and Technology, Inner Mongolia University, Hohhot 010021, China
[3]School of Physics and Materials Engineering, Dalian Minzu University, Dalian 116600, China

DOI: 10.1039/D1NR07076B (Paper) *Nanoscale*, 2022, **14**, 2023-2029

A family of 2D oxalate-based metal-organic frameworks (MOFs) which host intrinsic and robust spin-polarized Dirac cone are designed using comprehensive *ab initio* calculations. These 2D oxalate-based MOFs may be assembled by oxalate ions ($C_2O_4^{2-}$) and two homo-transition metal atoms. We demonstrate that 2D MOFs of $Ni_2(C_2O_4)_3$ and $Re_2(C_2O_4)_3$ are intrinsic Dirac spin gapless semiconductor with linear band dispersion, low energy dissipation and high electron carrier velocity. As robust ferromagnets, they also possess large magnetic moments, large perpendicular magnetic anisotropy, and high Curie temperature, e.g. 208 K for $Ni_2(C_2O_4)_3$. In particular, spin-orbit coupling triggers a topologically nontrivial band gap of 143 meV in $Re_2(C_2O_4)_3$, which is promising to realize quantum anomalous Hall effect at high temperature.

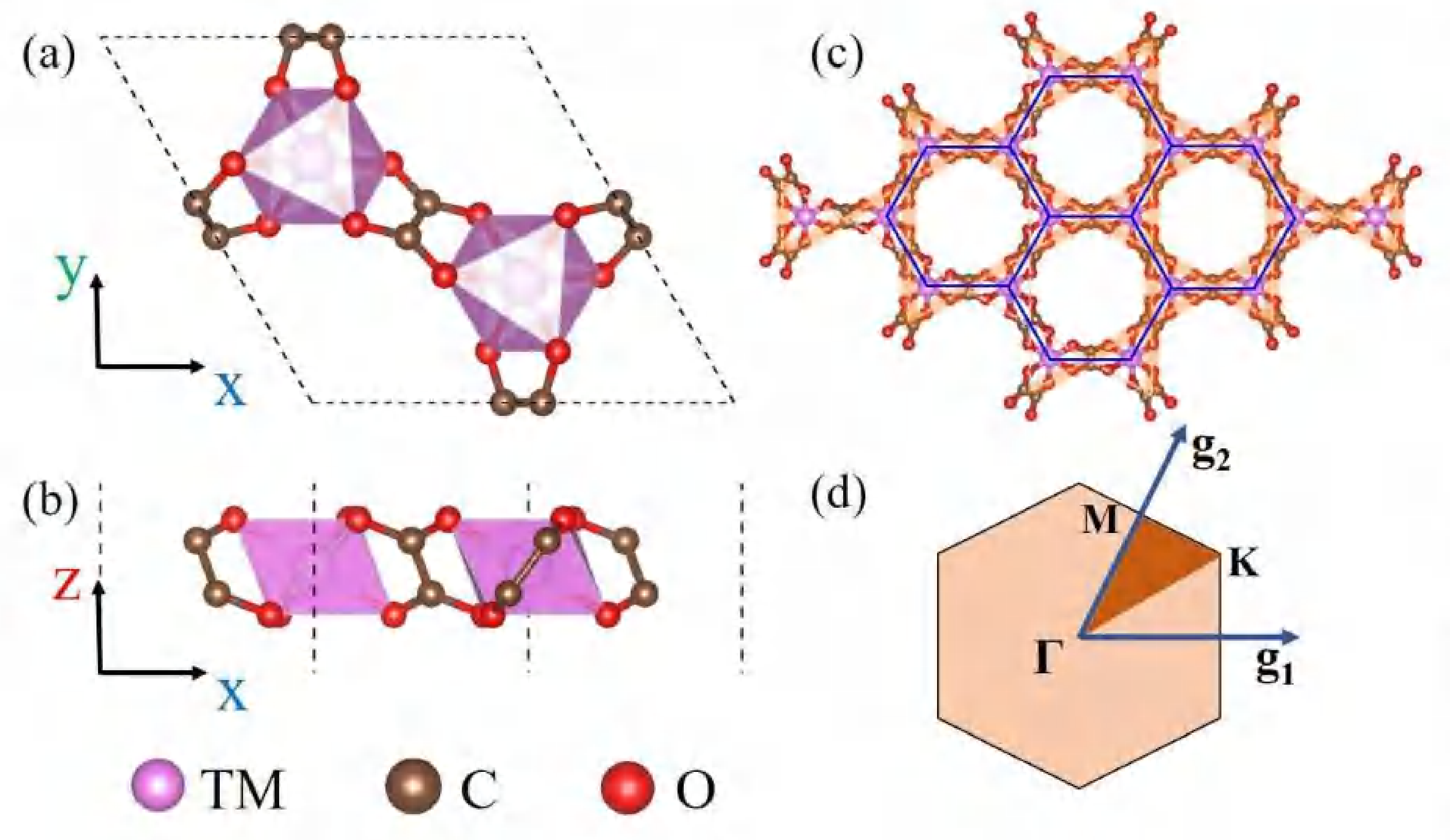

Fig.1 (a) Top view and (b) side view of $TM_2(C_2O_4)_3$ unit cell. (c) HK lattice. (d) Brillouin zone of $TM_2(C_2O_4)_3$. In (c), orange dotted line and blue full line highlight the Kagome lattice and honeycomb lattice, respectively.

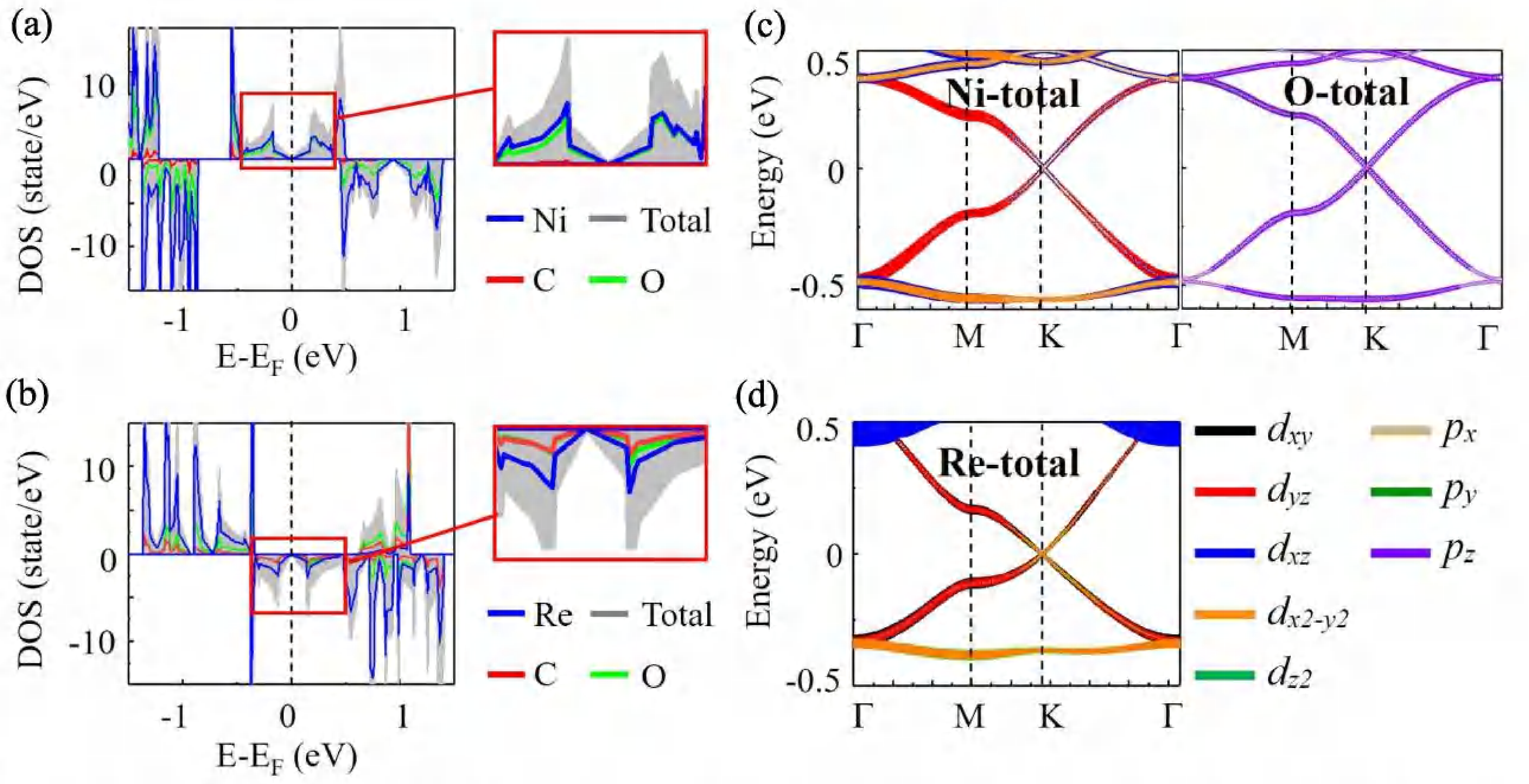

Fig. 3. PDOS of (a) $Ni_2(C_2O_4)_3$ and (b) $Re_2(C_2O_4)_3$. Projected bands of (c) Ni and O atoms in $Ni_2(C_2O_4)_3$ and (d) Re atom in $Re_2(C_2O_4)_3$.

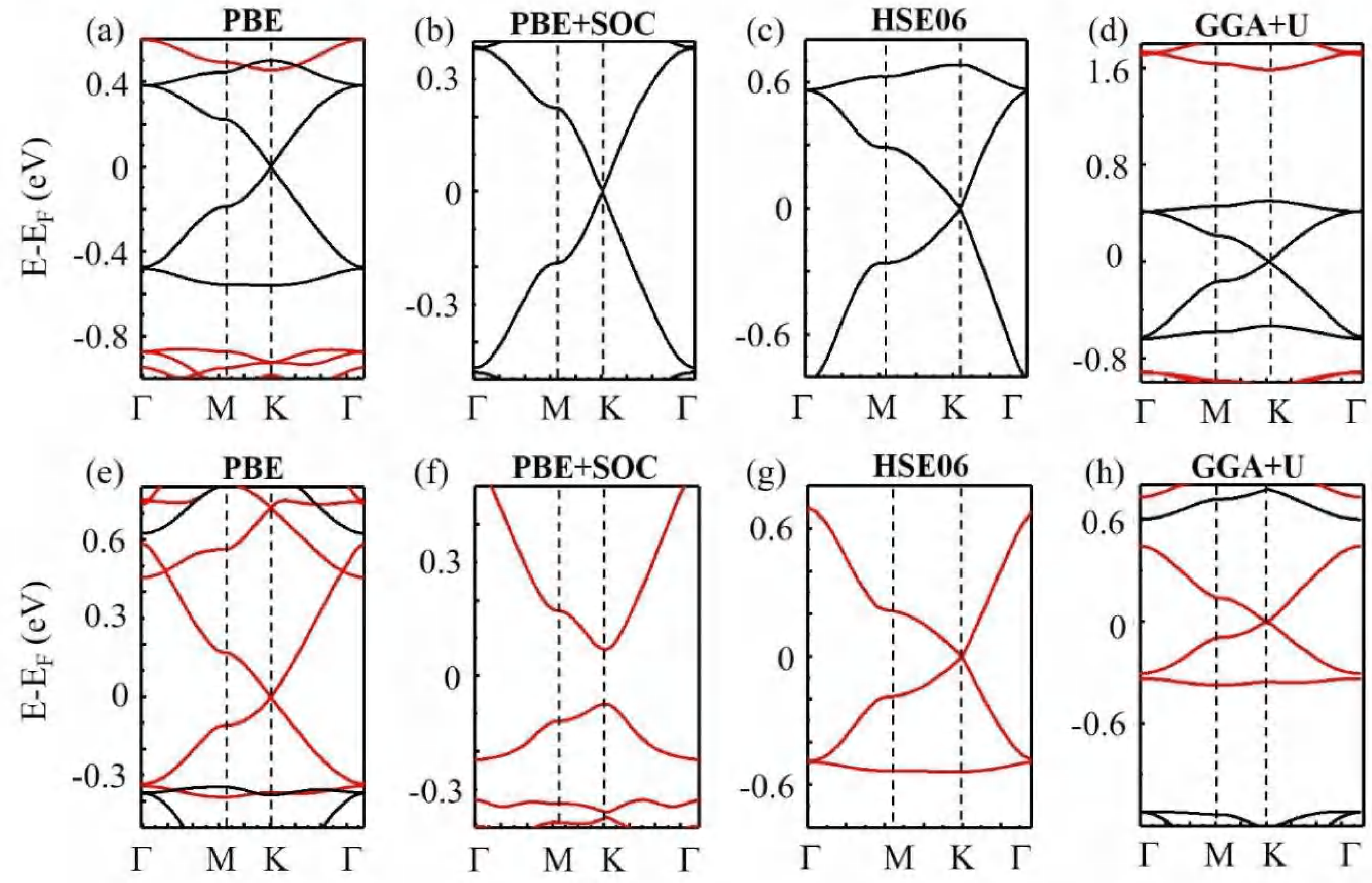

Fig. 2. The band structures of $Ni_2(C_2O_4)_3$ and $Re_2(C_2O_4)_3$ calculated with PBE function, PBE with SOC, HSE06 function, and Hubbard correction (PBE+U). The Fermi level is set to zero.

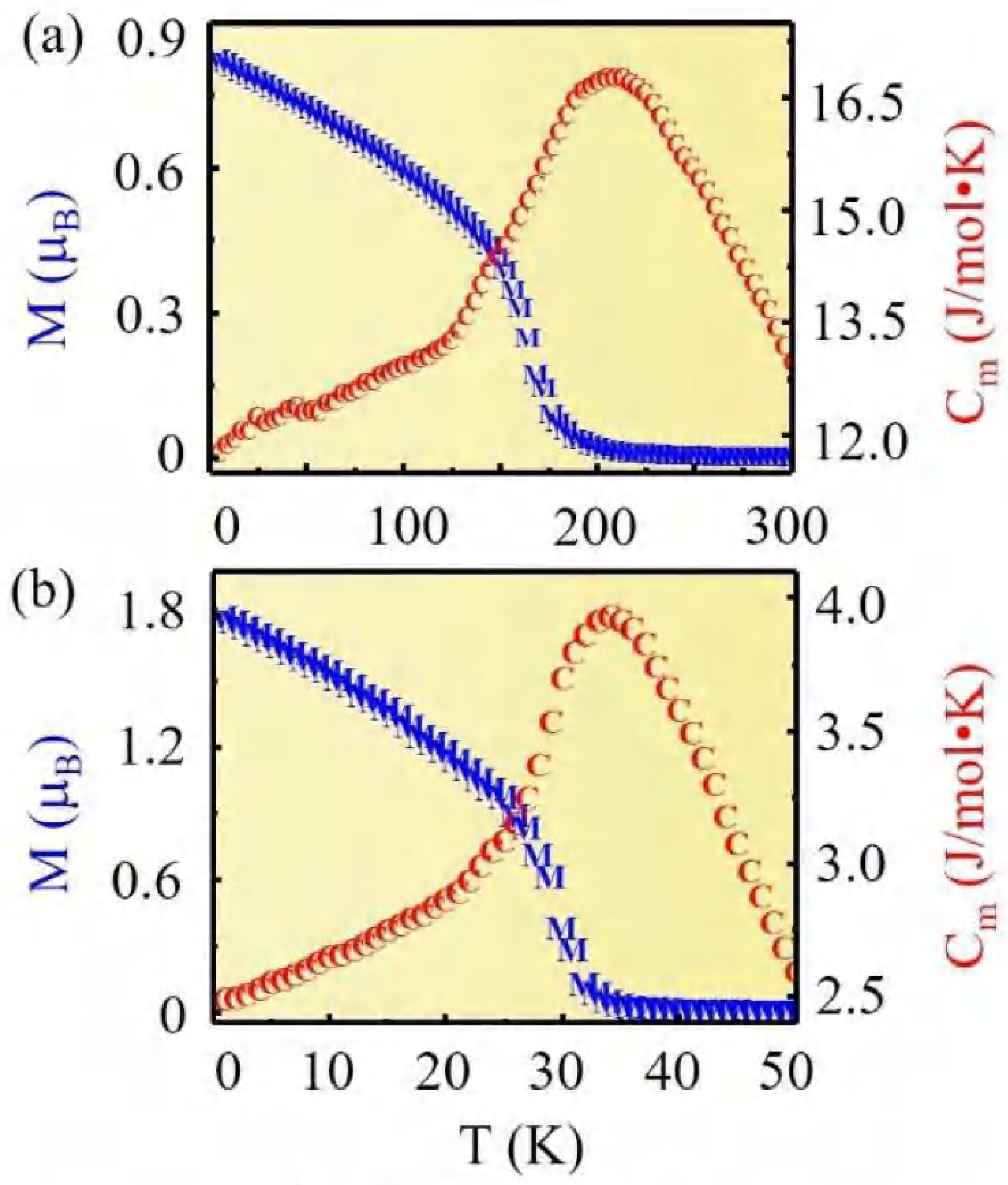

Fig. 4. Magnetic moment (M) and magnetic specific heat capacity (C_m) of $Ni_2(C_2O_4)_3$ and $Re_2(C_2O_4)_3$ (b) as a function of temperature from MC simulation.

- **$Ni_2(C_2O_4)_3$ and $Re_2(C_2O_4)_3$ systems are spin-gapless semiconductors with spin-polarized Dirac cone and linear energy dispersion in one spin channel, resulting in dissipation-less transport properties with Fermi velocity up to 2.78 x 10^5 m/s and 2.58 x 10^5 m/s ;**
- **Intrinsic FM with high T_C up to 208 K and large perpendicular magnetic anisotropy (up to 80 μeV/atom);**
- ***SOC triggers a topologically nontrivial band gap of 143 meV, which is beneficial to realize QAH effect at high temperature.***

Elastic stability and electronic structure of tantalum boride investigated via first-principles density functional calculations

Haihua Chen [1] , Yajie Yu [1] , Zhengang Zhang [1,2]

[a] Laboratory for Shock Wave and Detonation Physics Research, Institute of Fluid Physics, Chinese Academy of Engineering Physics, Mianyang 621900, China

[b] College of Physical Science and Technology, Sichuan University, Chengdu 610064, China

Abstract

The elastic properties, electronic structure and thermodynamic behavior of the TaB have been investigated for the first time in this work. Using first-principles plane-wave ultrasoft-pseudopotential density functional theory (DFT), the ground state properties and equation of state of TaB have been obtained. The average zero-pressure bulk modulus of TaB is 302 GPa. By analyzing the elastically anisotropic behavior and the relative structure parameters of TaB, we found that the crystal cell along the b-axis was more compressible than along the a and c axes. The calculated ratio of bulk modulus and shear modulus (*B/G*) for TaB is 1.58, demonstrating that TaB is rather brittle. From the elastic stiffness constants, we found that TaB in the Cmcm phase is mechanically stable. The calculated hardness of TaB is 28.6 GPa which is close to the previous data. Moreover, using the Gibbs 2 model, the thermodynamic properties such as the thermal expansion and Debye temperature of TaB have been obtained firstly. At the ambient temperature, the Debye temperatures of TaB are 792 K and 845 K from GGA calculation and LDA calculation, respectively.

Structure and elastic properties

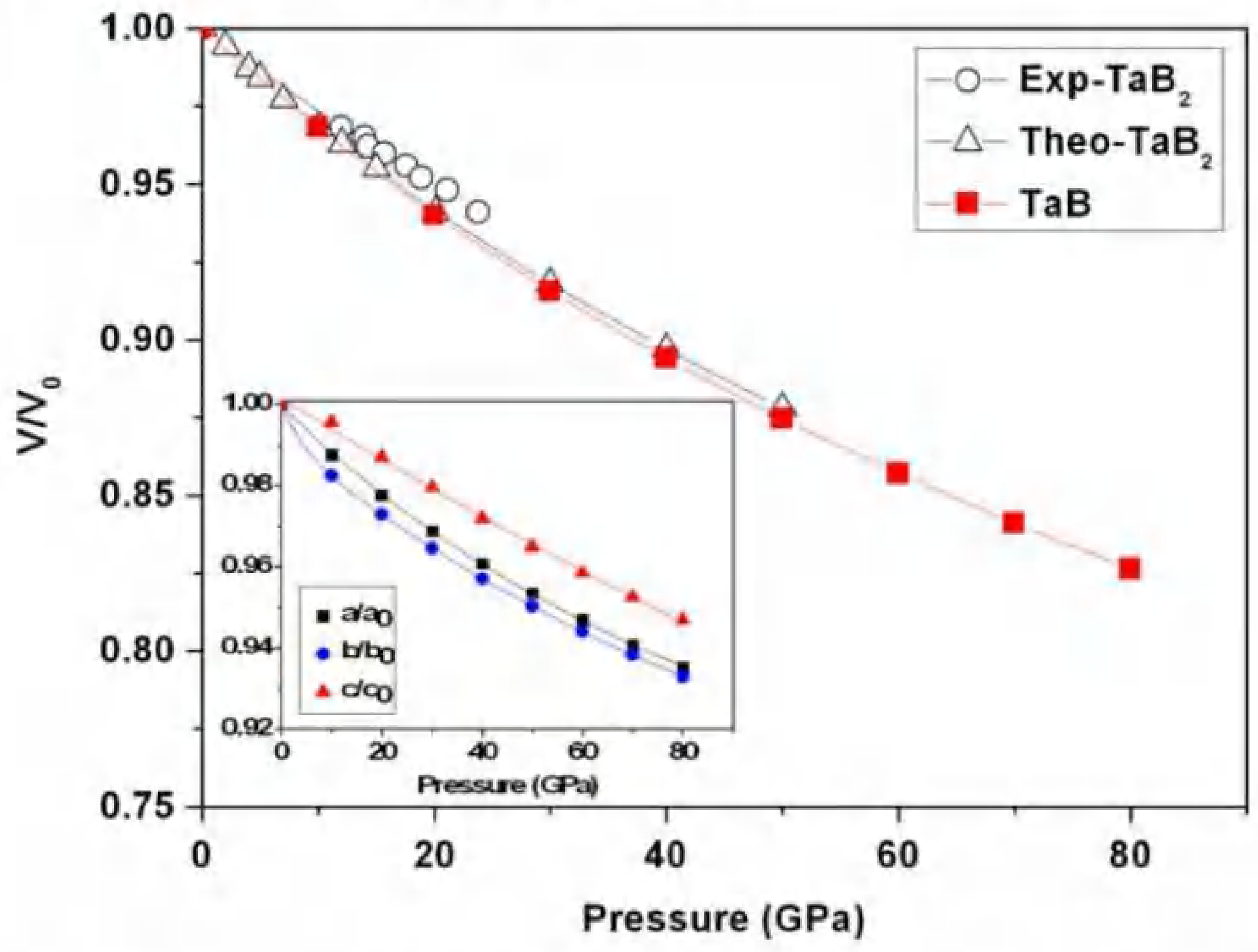

The relative volumes vis pressures of TaB by using GGA methods up to 80 GPa. The solid lines are the Birch–Murnaghan equation fits to the data. The open circles and triangles are the data of TaB_2 obtained by Winkler et al. The variations of lattice constants with pressure by GGA calculations are shown in the inset.

Electronic structure and hardness

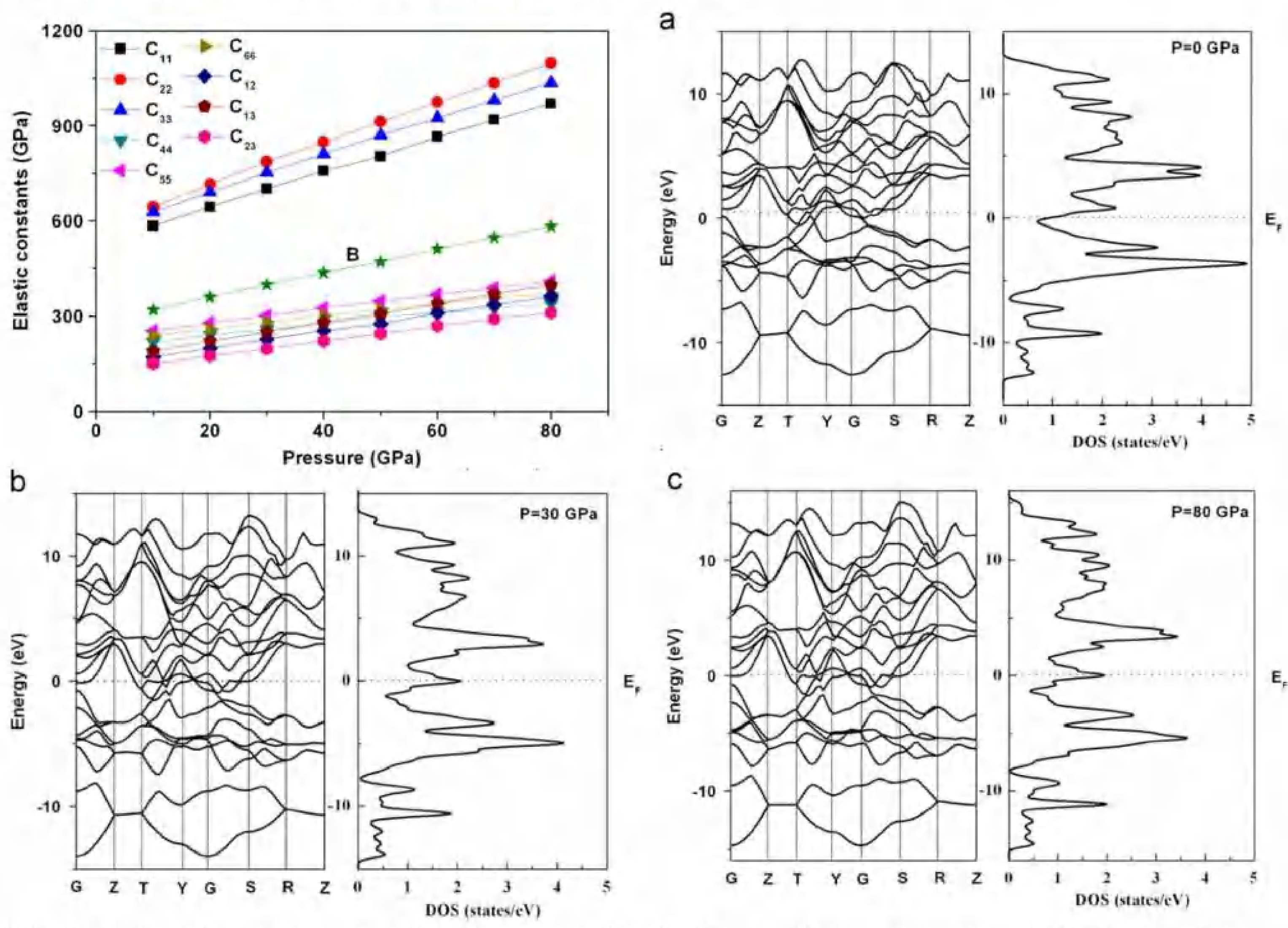

(1)The elastic constants by GGA calculations vis pressures of TaB under pressure.(2)Band structures and total density of states of TaB at pressure of 0 GPa (a), 30 GPa (b) and 80 GPa (c) at zero temperature.

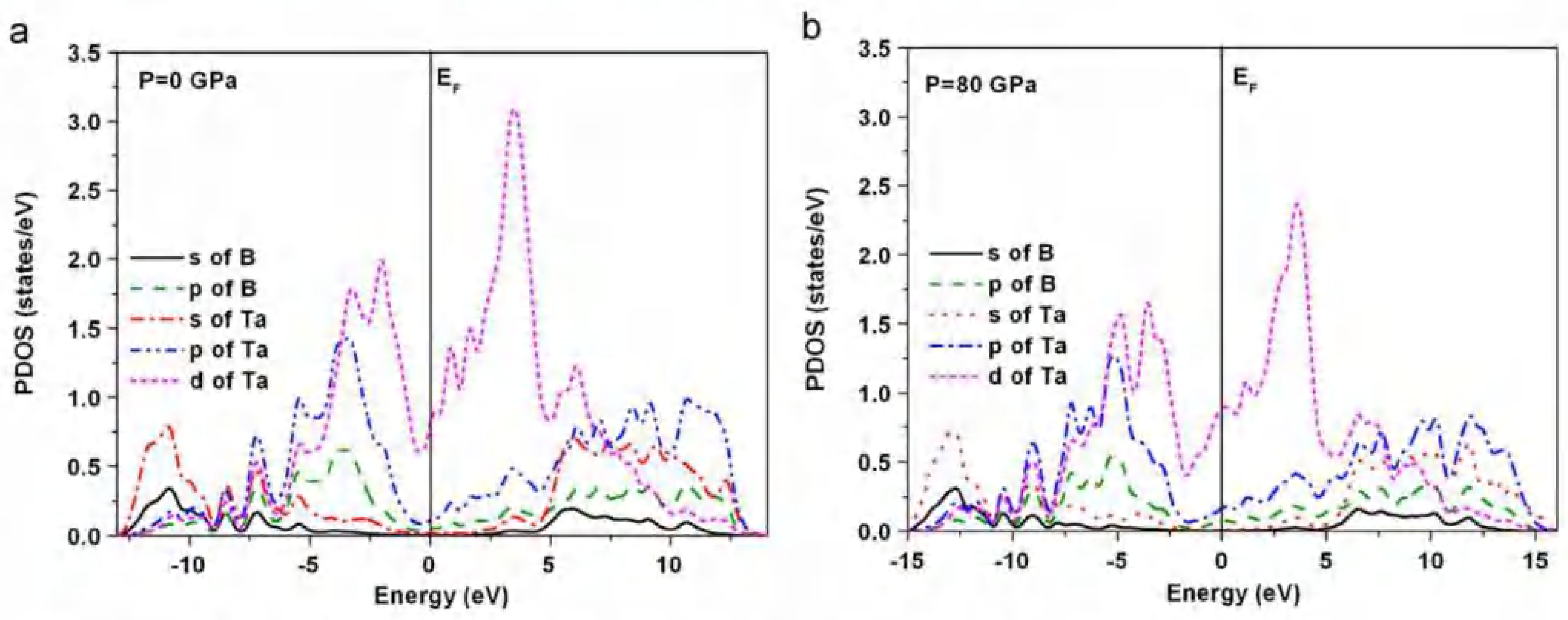

The partial DOS of s, p and d electrons of Ta and s and p electrons of *B* at pressure of 0 GPa (a) and 80 GPa (b).

Thermodynamic properties

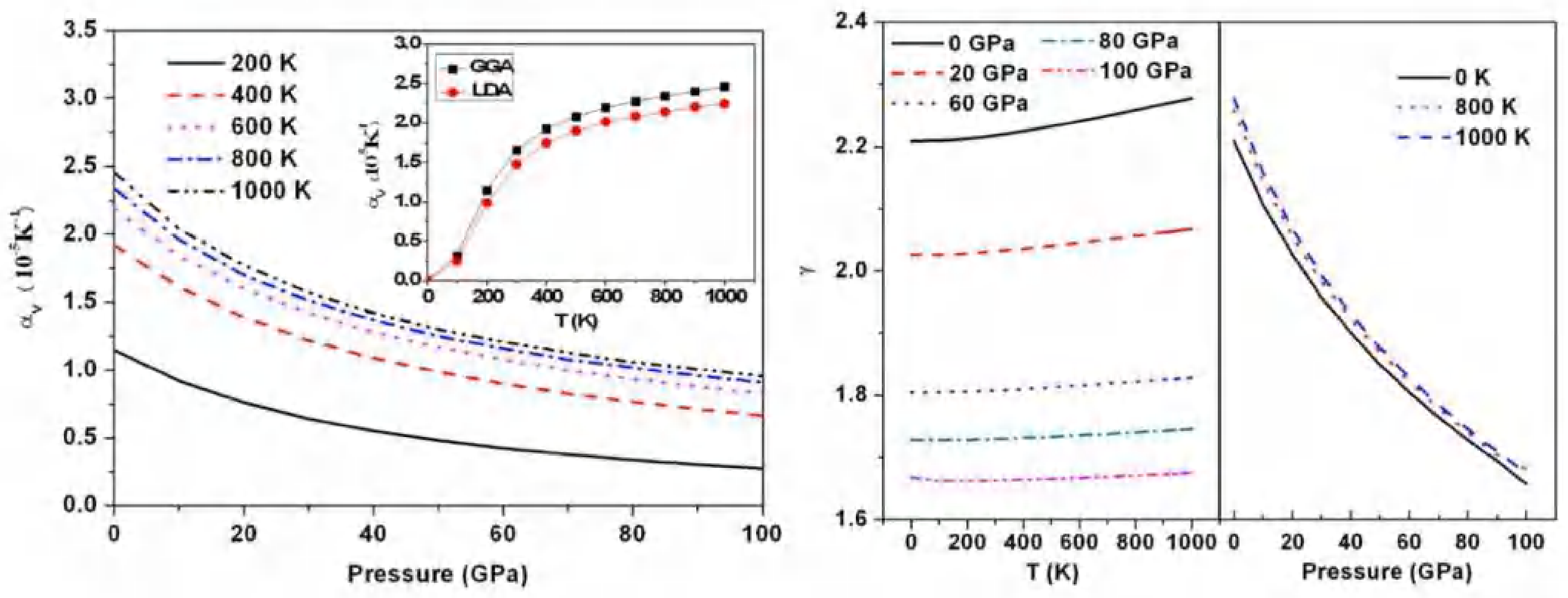

(1)The coefficients of thermal expansion α_V of TaB with different pressures. The inset shows α_V as a function of temperature. (2) Pressure (right) and temperature (left) dependences of the Grüneisen parameter γ for TaB.

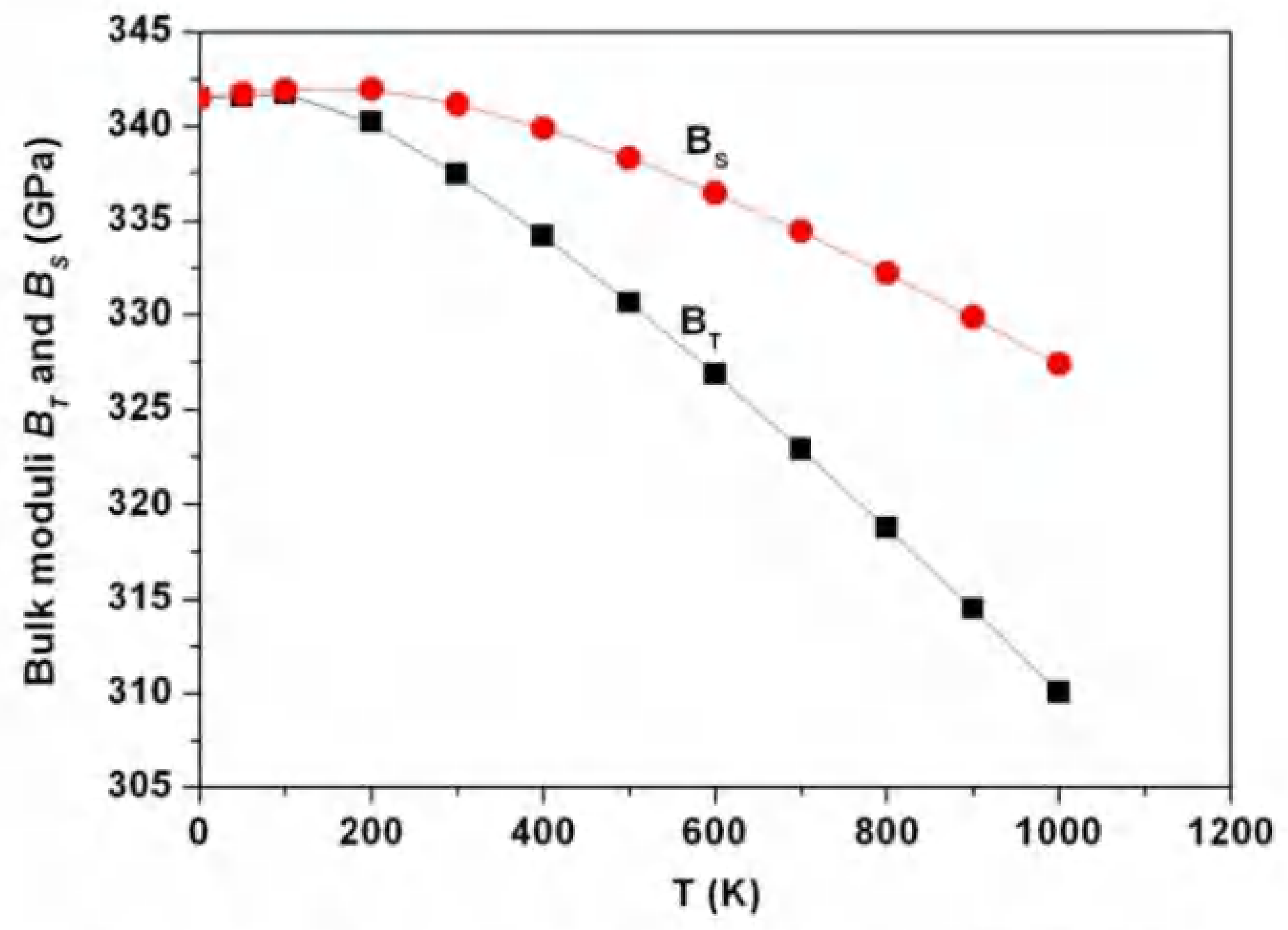

Temperature dependence of isothermal (B_0) and adiabatic (B_S) zero-pressure bulk modulus for TaB.

Conclusion

In summary, the elastic properties, electronic structure and hardness of the TaB under pressure have been investigated by first-principles calculations for the first time. The ground-state properties and equation of state of TaB have been obtained, which is close to the previous data. By analyzing the relative structure parameters and the elastically anisotropic behavior of TaB, we found that the crystal cell along the b-axis was more compressible than along a and c axes. Furthermore, from the relationship between the bulk modulus and shear modulus of TaB, we calculated ratio *B/G* for TaB is 1.58, which is indicating that TaB is rather brittle. The calculated hardness of TaB agrees with previous experimental results. Using the Gibbs 2 models, we firstly obtained the thermodynamic properties of TaB such as the thermal expansion and Debye temperature. At the ambient temperature, the Debye temperatures of TaB are 792 K and 845 K from GGA calculation and LDA calculation, respectively.

Spin Hall Conductivity and Anomalous Hall Conductivity in Full Heusler Compounds

姬一民　王小超　张文旭

电子薄膜与集成器件国家重点实验室
电子科技大学　成都，611731

ABSTRACT

The spin Hall conductivity (SHC) and anomalous Hall conductivity (AHC) in about 120 full Heusler compounds are calculated using the density functional theory in a high-throughput way. Our results show that the mechanism under the SHC or AHC is related to the very details of the electronic structures, which can only be obtained by calculations. A high-throughput calculation is efficient to screen out the desired materials. According to our present results, Rh_2MnAl and Cu_2CoSn, as well as Co_2MnAl and Co_2MnGa are candidates in spintronic materials regarding their high SHC and AHC values.

Methods

- Code

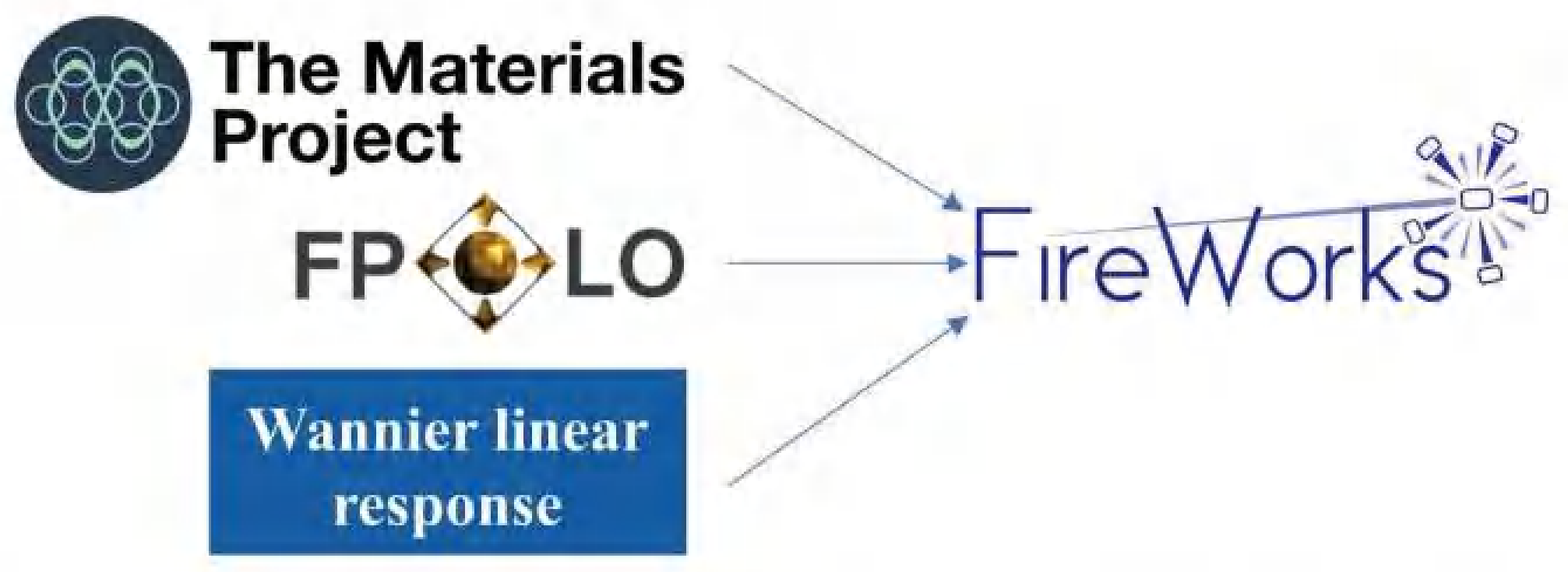

The Materials Project

FPLO

Wannier linear response

FireWorks

Fig.1 The code used in high-throughput framework

- Workflow

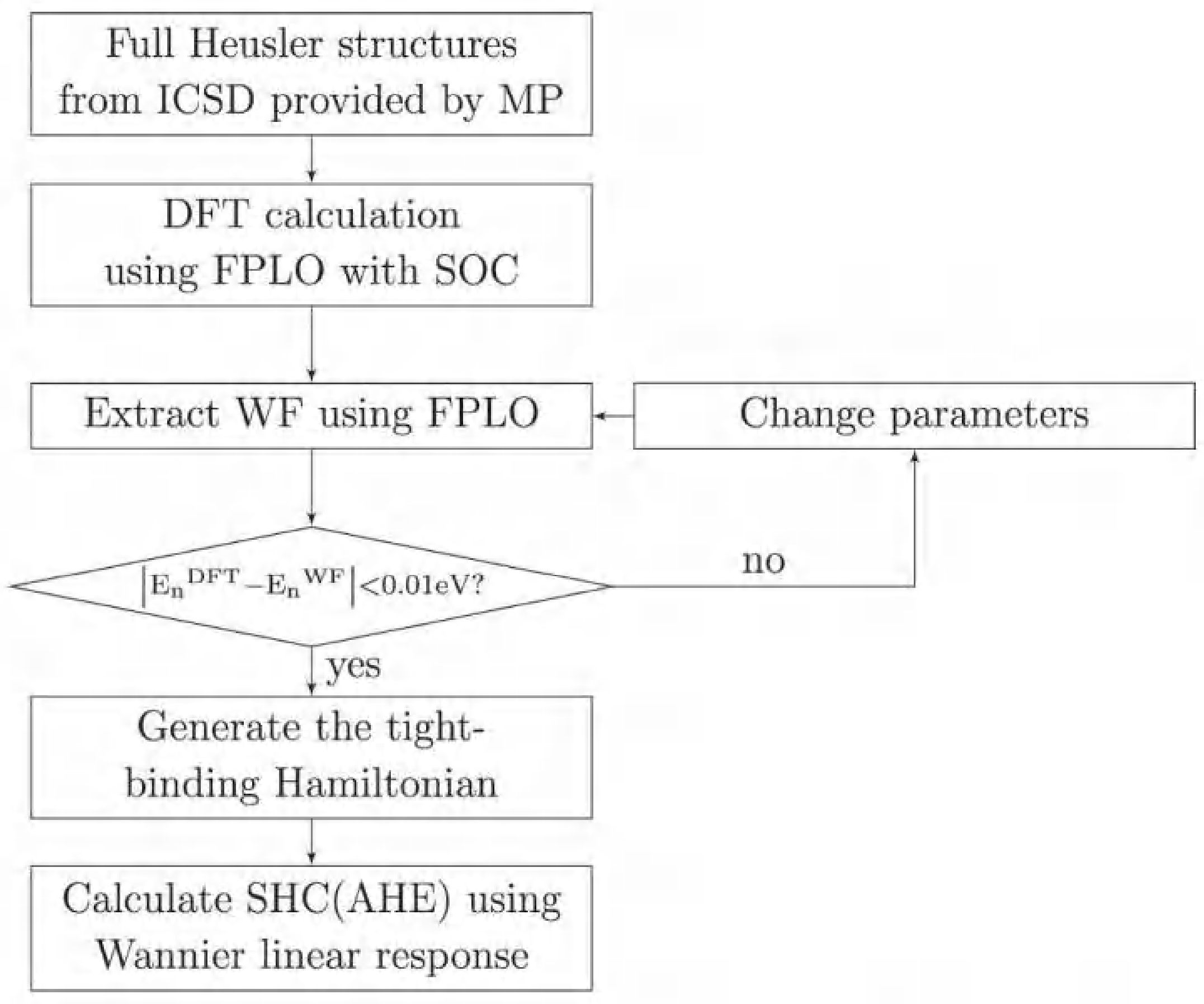

Full Heusler structures from ICSD provided by MP

DFT calculation using FPLO with SOC

Extract WF using FPLO

Change parameters

$|E_n^{DFT} - E_n^{WF}| < 0.01eV?$

no

yes

Generate the tight-binding Hamiltonian

Calculate SHC(AHE) using Wannier linear response

Fig.2 Workflow for the high-throughput

Results

- SHC and AHC around the Fermi level

The results show that the value of SHC reaches its maximum when the number of the valence electrons N_v is 26. The largest value in the nonmagnetic compounds is about 400 $\hbar/e\ (\Omega^{-1}cm^{-1})$ in Ni_2LiSn. In the ferromagnetic compounds, the maximum value is above 700 $\hbar/e\ (\Omega^{-1}cm^{-1})$ in Rh_2MnAl. The maximum of AHC obtained is 1649.21 $(\Omega^{-1}cm^{-1})$ in Rh_2MnAl.

- The maximum of SHC and AHC within ±5.0 eV

We calculated the maximum of the SHC and AHC absolute values within ±5.0 eV around the Fermi level achievable in the candidate compounds. Generally, a larger AHC also leads to a larger SHC. We fitted the data for Y = V and Mn respectively.

- Hints for the large SHC and AHC values

The mixing of the pairs of $\{d_{xz}, d_{yz}\}$ or $\{d_{xy}, d_{x^2-x}\}$orbitals due to the SOC is the main underlying mechanism for the anomalous velocity. The values of SHC and AHC depend on the electronic band structures, and the wave functions as well.

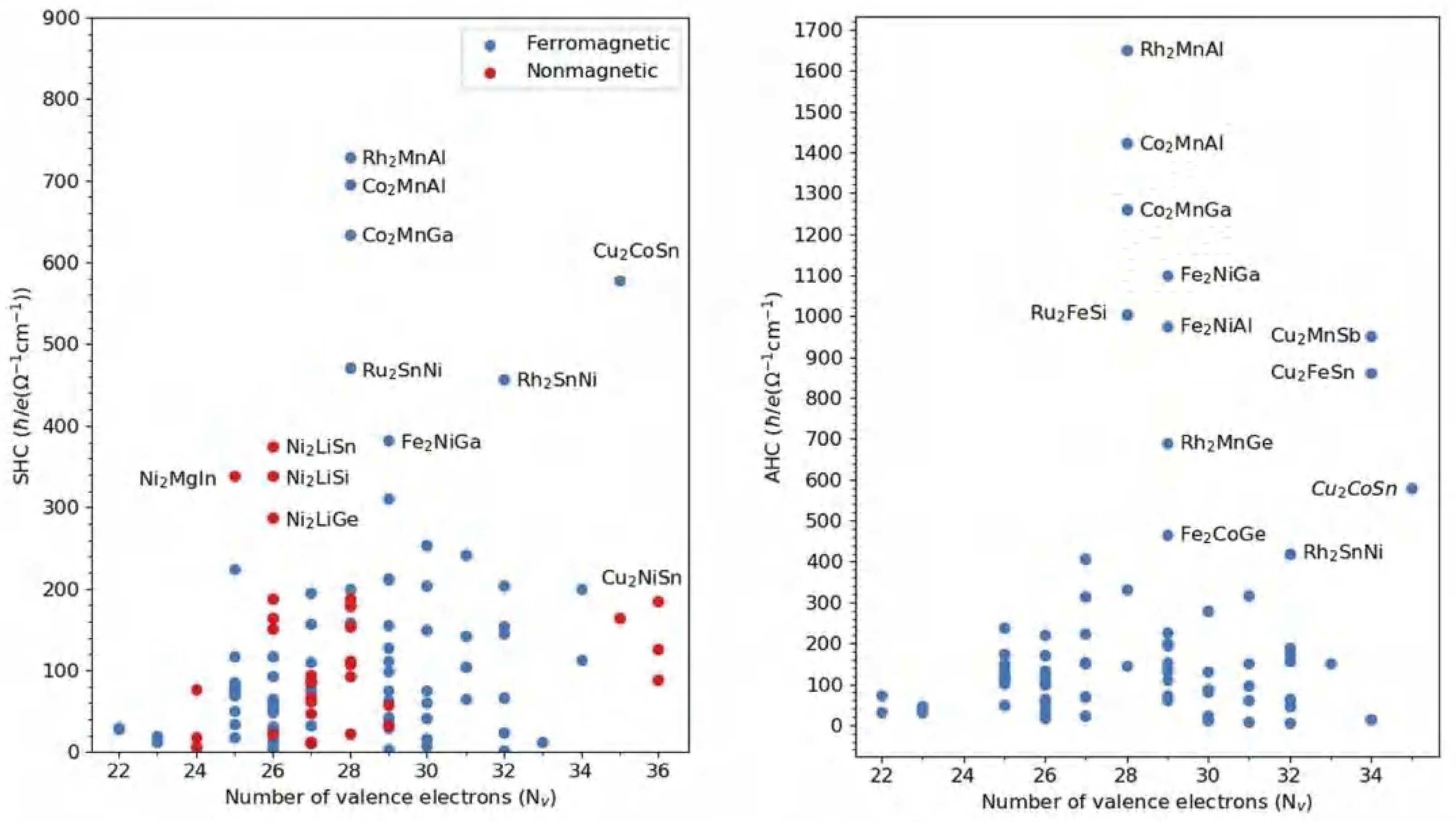

(a) SHC at the Fermi energy　(b) AHC at the Fermi energy

Fig.3 SHC and AHC at the Fermi level of the Heusler compounds vs the valence electron numbers

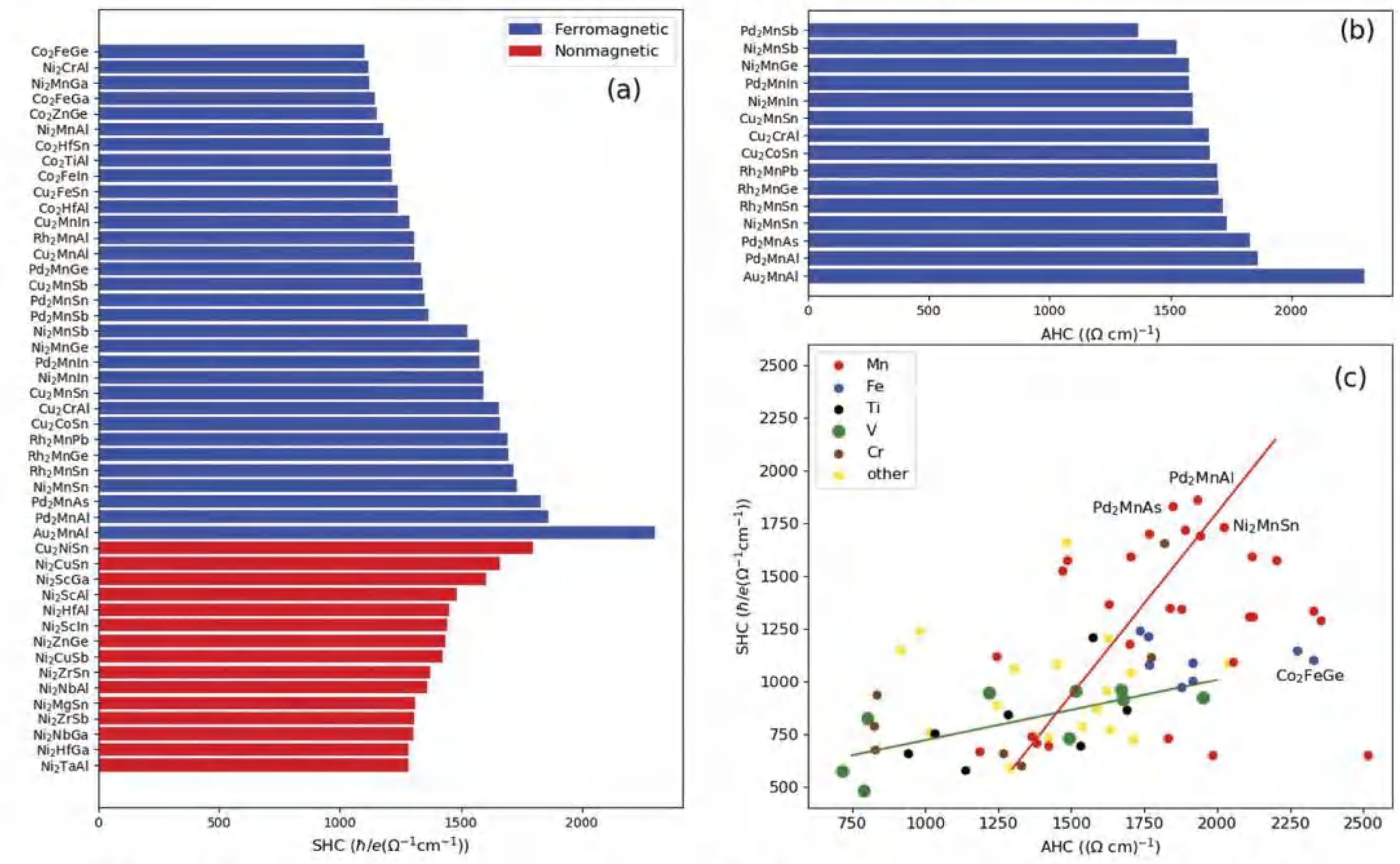

Fig.4 The leading maximum of SHC (a) and AHC (b) of the compounds within ±5 eV around the Fermi level

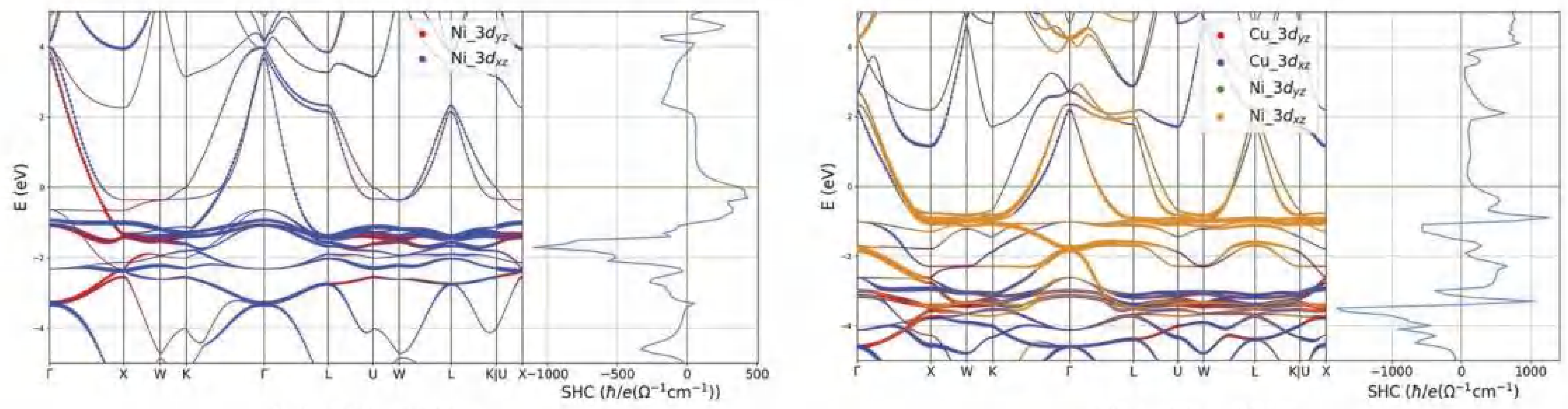

(a) Ni_2LiSn　(b) Cu_2NiSn

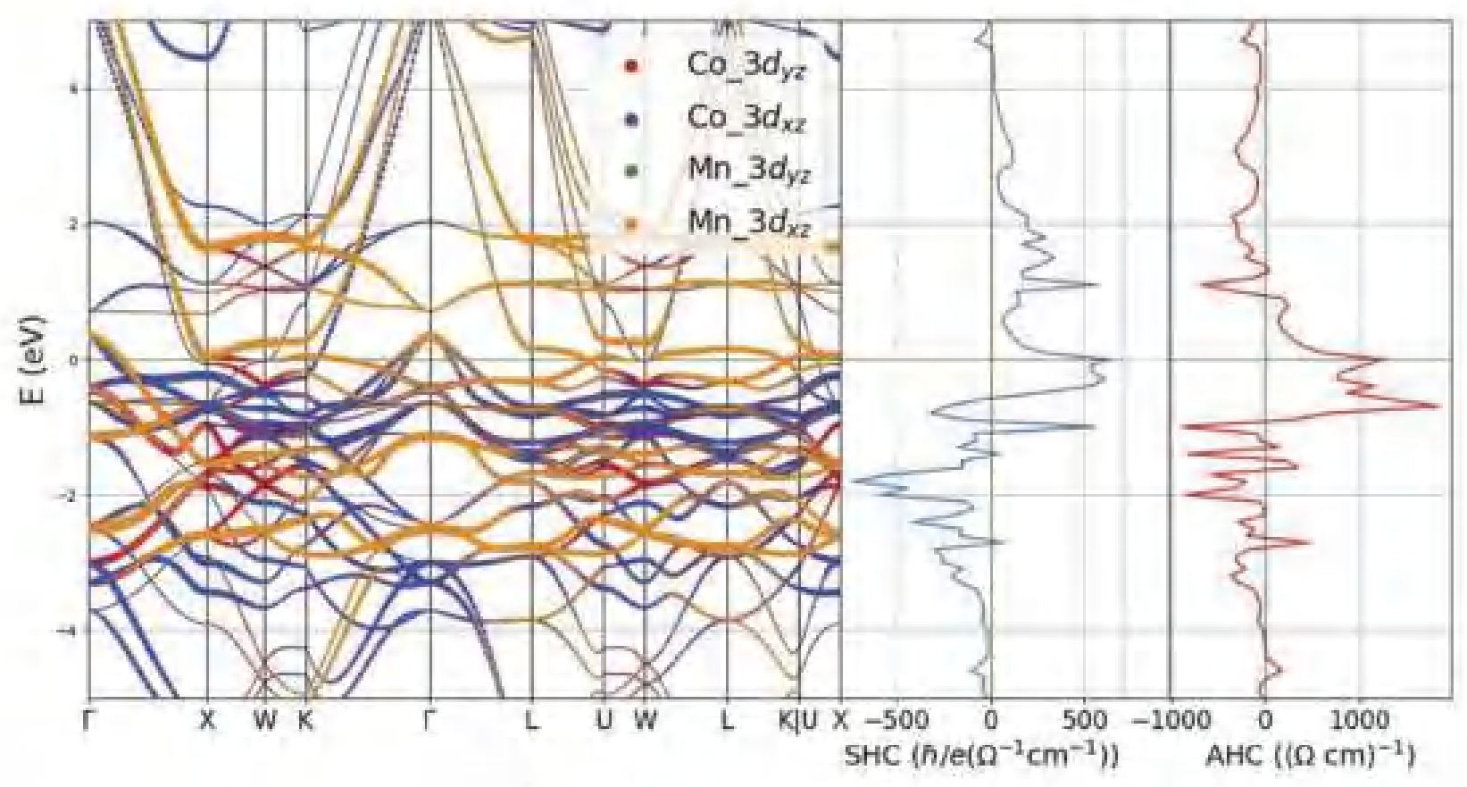

(c) Co_2MnGa

Fig.5 The electronic band structures with corresponding SHC and AHC

CONCULSION

We calculated the SHC and AHC in about 120 full Heusler compounds, both in nonmagnetic and ferromagnetic states. We find that the electronic states formed by the t_{2g} and e_g representations of the cubic symmetry play the determinant role of the properties. Tuning the Fermi level can be a possible way to obtain the high values of AHC or SHC when the largest values are not right at the Fermi level. The Heusler compounds, due to their vast element combinations and varieties of properties, may find more applications in modern spintronic devices.

2022材料多尺度计算模拟国际会议

International Conference of Multi-scale Modeling and Simulation of Materials (ICM^3-2022)

Microstructure, mechanical properties, and thermal stability of γ-Nb_5Si_3 under high temperature and high pressure

Zhengang Zhang[1,2], Jianyi Ma[1], Haihua Chen[2]

[1] Institute of Atomic and Molecular Physics, Sichuan University, Chengdu 610065, P. R. China

[2] Department of Basic Education, Qinghai University, Xining 810016, P. R. China

Abstract

Study on the effect of pressure and temperature on the structural and mechanical properties of materials is very difficult for current experimental techniques. Here, we have synthesized the γ-Nb_5Si_3 compound with remarkable quality by high pressure and high temperature (HPHT) technology. The effects of high pressure and sintering temperature on its microstructure, mechanical properties, and oxidation resistance of are discussed. The Vickers hardness and density of the γ-Nb_5Si_3 sample at 5.5 GPa and 1100 ℃ are 8.67 GPa and 5.73 g/cm³, respectively. It is shown that the HPHT behavior not only improves sample's compactness and microstructure, but also makes γ-Nb_5Si_3 to have a strong respond on the Vickers hardness and related density. Besides, some calculation for γ-Nb_5Si_3 are proformed to support the experimental results.

X-ray diffraction patterns of the sintered powder and calculated results

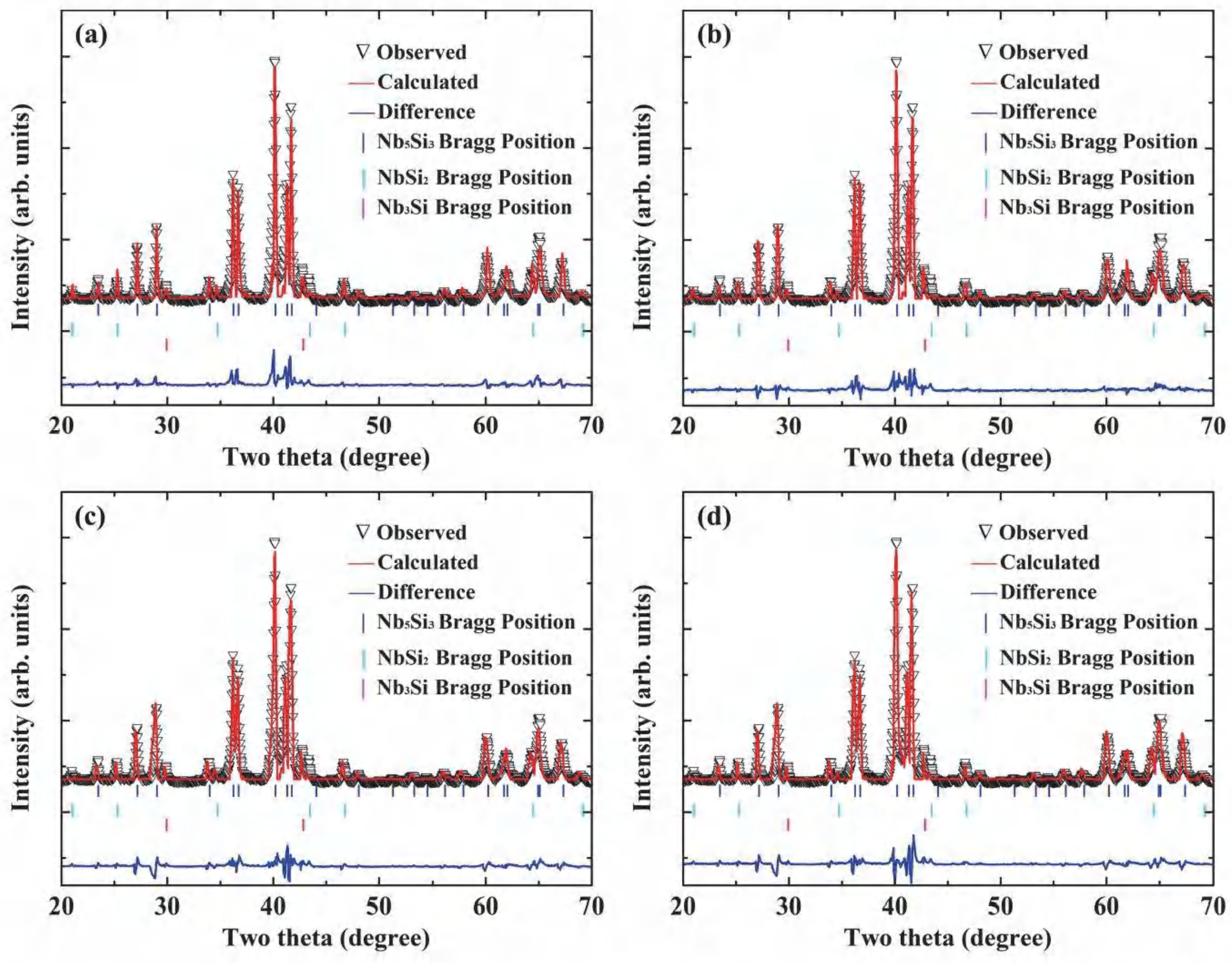

(a) Rietveld refinement XRD patterns (λ=1.5406 Å) of original Nb_5Si_3 powder, (b)-(d) are corresponding with the bulk Nb_5Si_3 sample at at 5.5 GPa/900 ℃, 5.5 GPa/1100 ℃, and 5.5 GPa/1300 ℃.

X-ray diffraction pattern information and analysis

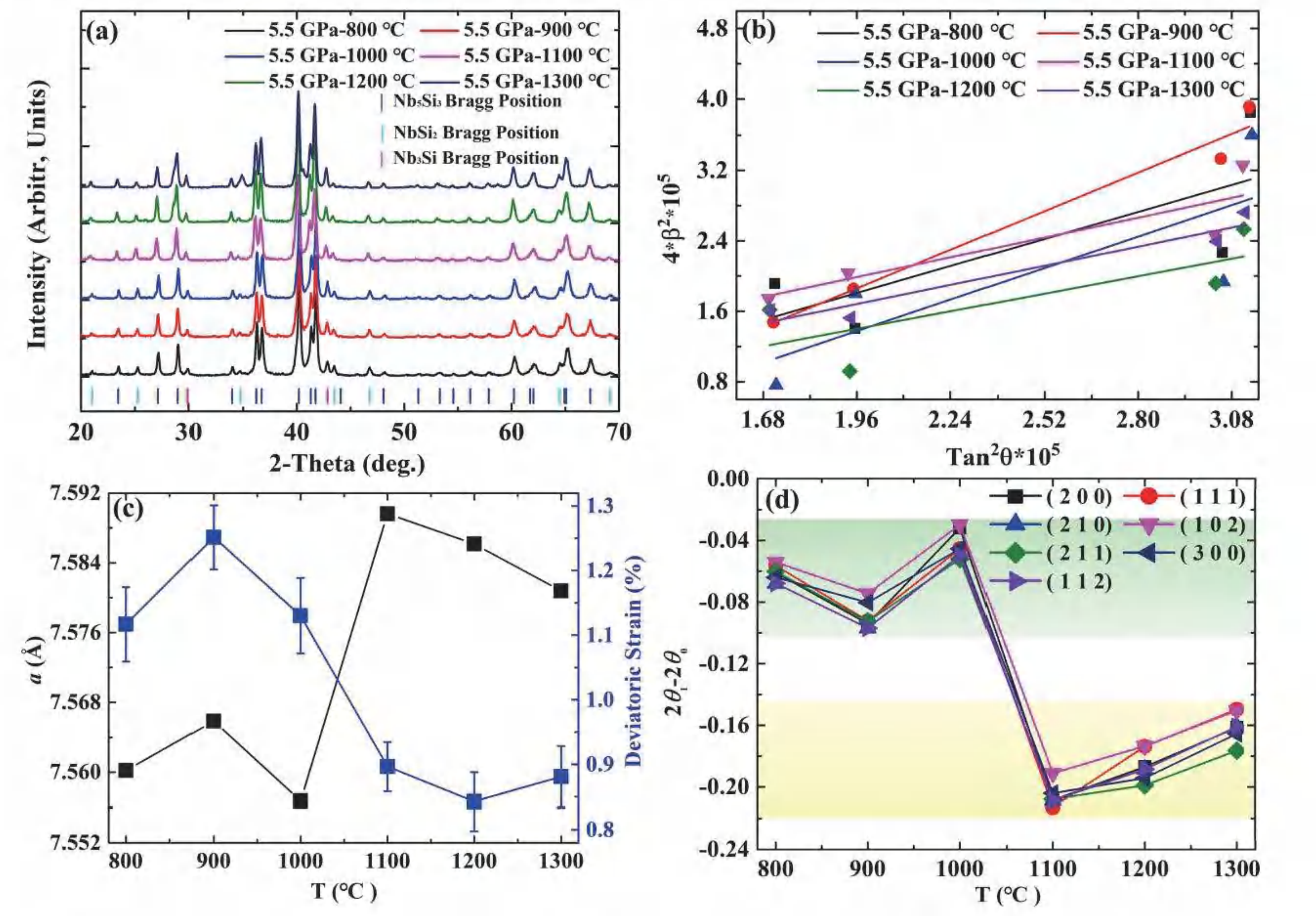

The linear fitting relationships between Bragg angle and FWHM for each bulk Nb_5Si_3 ceramic. Microscopic deviatoric strain and the lattice parameter (a) of Nb_5Si_3 at different sintered temperatures. The difference value of 2θ (Bragg position) between original and bulk sample.

SEM and EDS pictures of γ-Nb_5Si_3

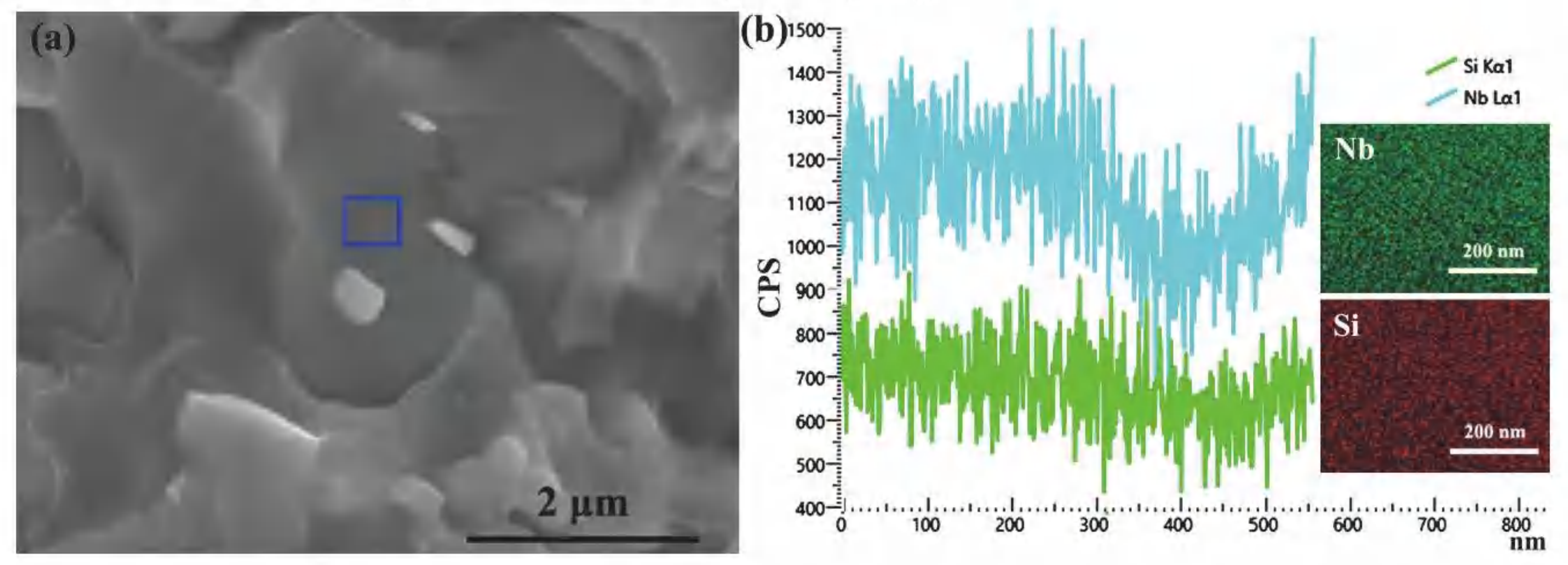

(a) The magnified SEM image of fractured surfaces of Nb_5Si_3 at 5.5 GPa/1100 C. (b) The EDS results of the blue region in (a). Two insets in (b) are respectively distribution diagram for Nb and Si atom.

DOS results of γ-Nb_5Si_3

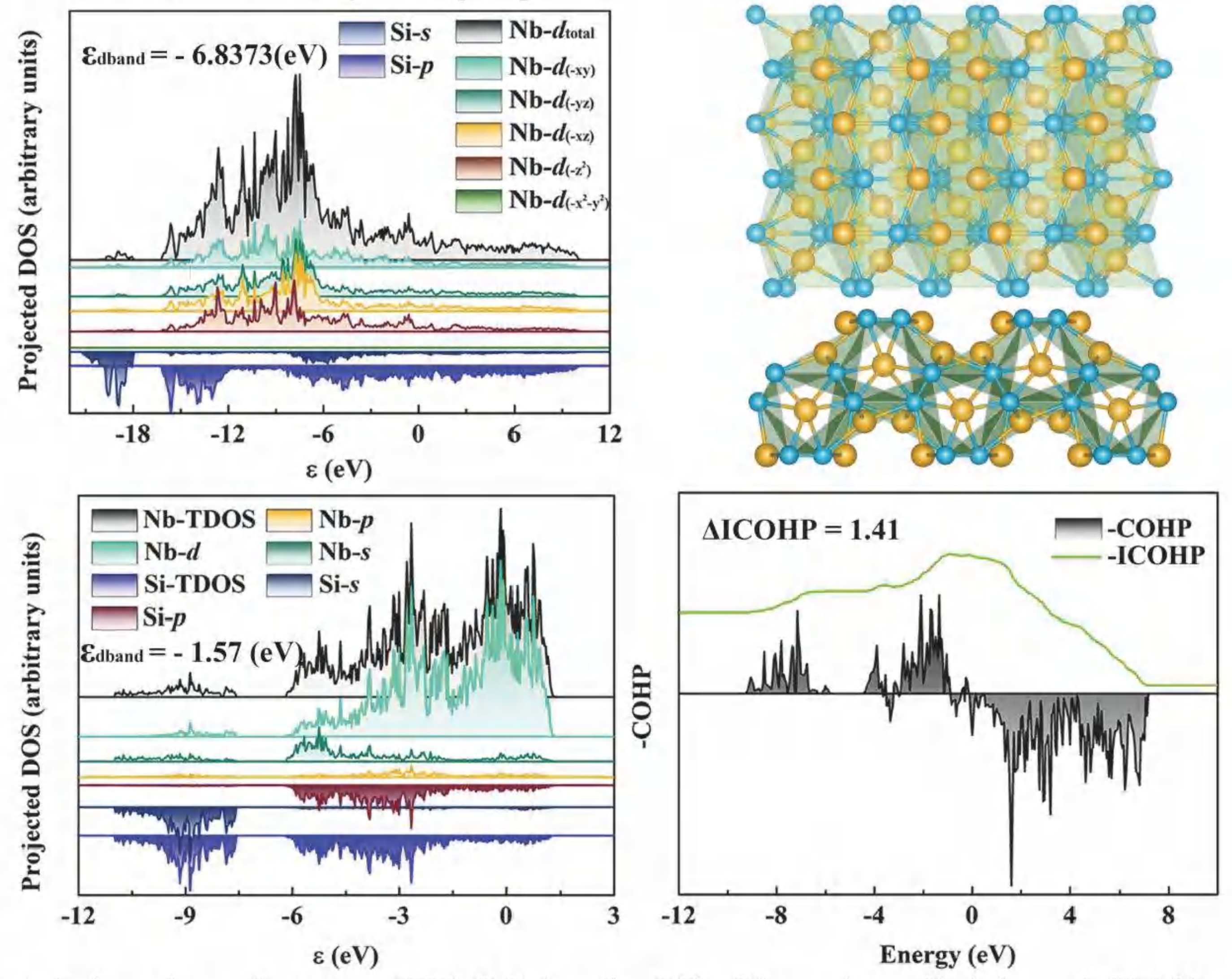

Total density of states (TDOSs) of γ-Nb_5Si_3 unit cell (a) and (300) slab modlue (c). (b) The (300) slab modlue. (d) Projected crystal orbit Hamiltonian population (COHP) and integrated COHP value (ICOHP) of the (300) slab.

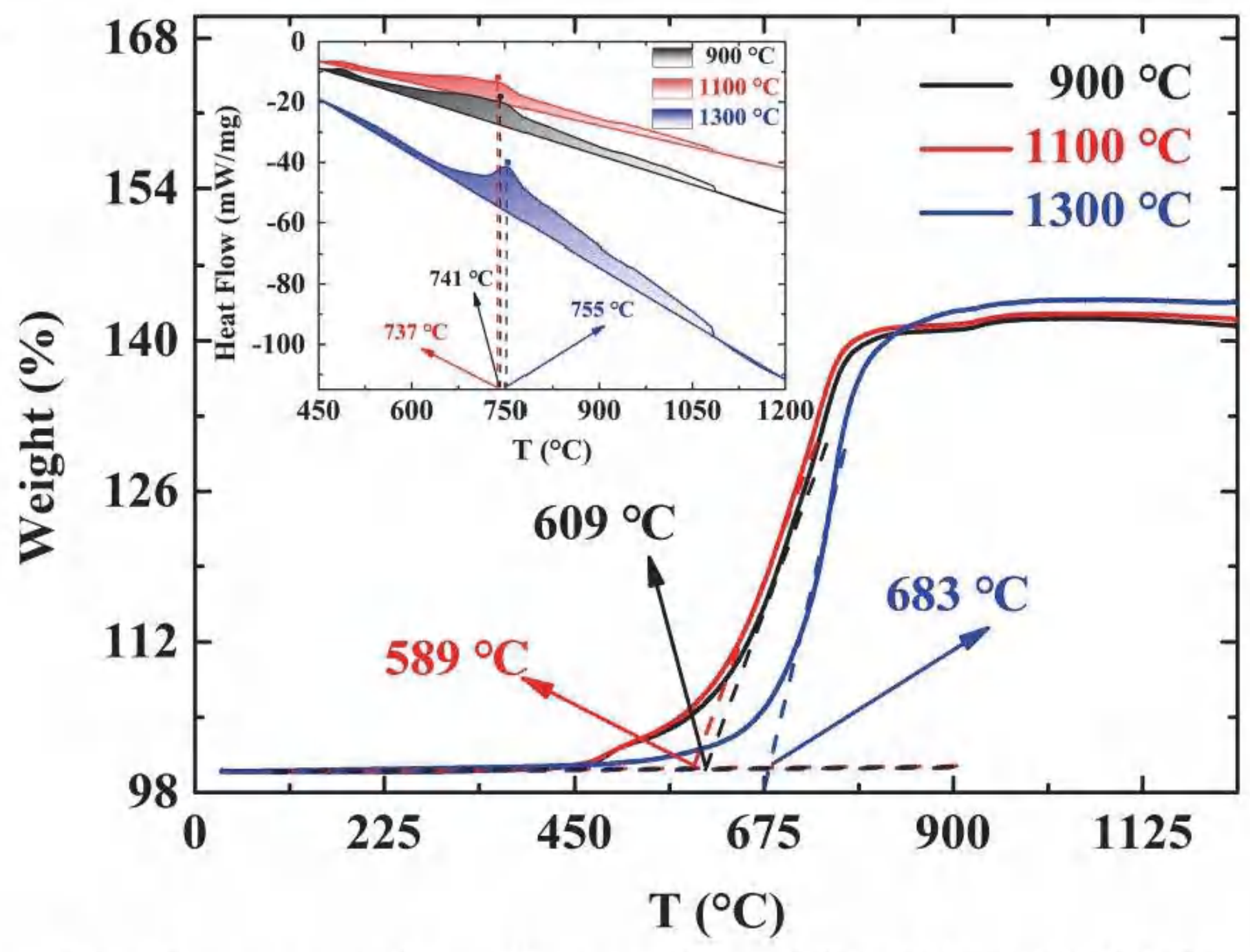

TGA curves for the samples sintered at 900 °C, 1100 °C, and 1300 °C. The inset is a corresponding DSC curve picture.

Conclusion

In summary, the HPHT sintering experiments and relevant characterizations of γ-Nb_5Si_3 sample are performed through XRD, SEM, and TGA-DSC techniques. The results show that the microstructures, including pore distribution, compactness, and bonding degree, play major factors in the mechanical properties and thermal stability of γ-Nb_5Si_3 sample. The Vickers hardness, density, and oxidation resistance of the bulk γ-Nb_5Si_3 at different sintered temperatures are reported, which clear indicate that the suitable temperature of γ-Nb_5Si_3 is 1100 ℃. The Vickers hardness and density of the γ-Nb_5Si_3 sample at 5.5 GPa and 1100℃ are 8.67 GPa and 5.73 g/cm3, respectively. The present results provide inspiration for synthesis and design novel high-temperature structural materials.

Intrinsic multiferroic in VNI monolayer

Ying Zhao [1], Qinxi Liu [1], Xue Jiang [1*], Jijun Zhao [1*]

Key Laboratory of Materials Modification by Laser, Ion and Electron Beams (Ministry of Education), Dalian University of Technology, Dalian 116024, China

E-mail: zy2123@mail.dlut.edu.cn, jiangx@dlut.edu.cn

Abstract: Two-dimensional (2D) multiferroic materials, exhibiting both ferromagnetism and ferroelasticity, have promising applications in the miniaturization of quantum devices, such as high-density data storage and spintronic devices. Using first-principles calculations, we propose a new type of 2D material, a ternary, vanadium-nitride-halide compound VNI. Its dynamic, mechanical, and thermal stabilities are confirmed by phonon spectrum, elastic modulus, and molecular dynamics simulations. The VNI monolayer is a robust ferromagnetic metal with a sizable in-plane magnetic anisotropic energy (150 μeV per V atom). Meanwhile, the monolayer has a moderate ferroelastic switching barrier of 100.66 meV/atom, which would facilitate the fast ferroelastic dynamics under external stress. Notably, the magnetic anisotropy axis of the VNI monolayer can be adjusted from the a-axis to the b-axis through reversible ferroelastic strain, exhibiting the characteristics of magnetoelastic coupling. These results shed light on the design of nonvolatile memory devices.

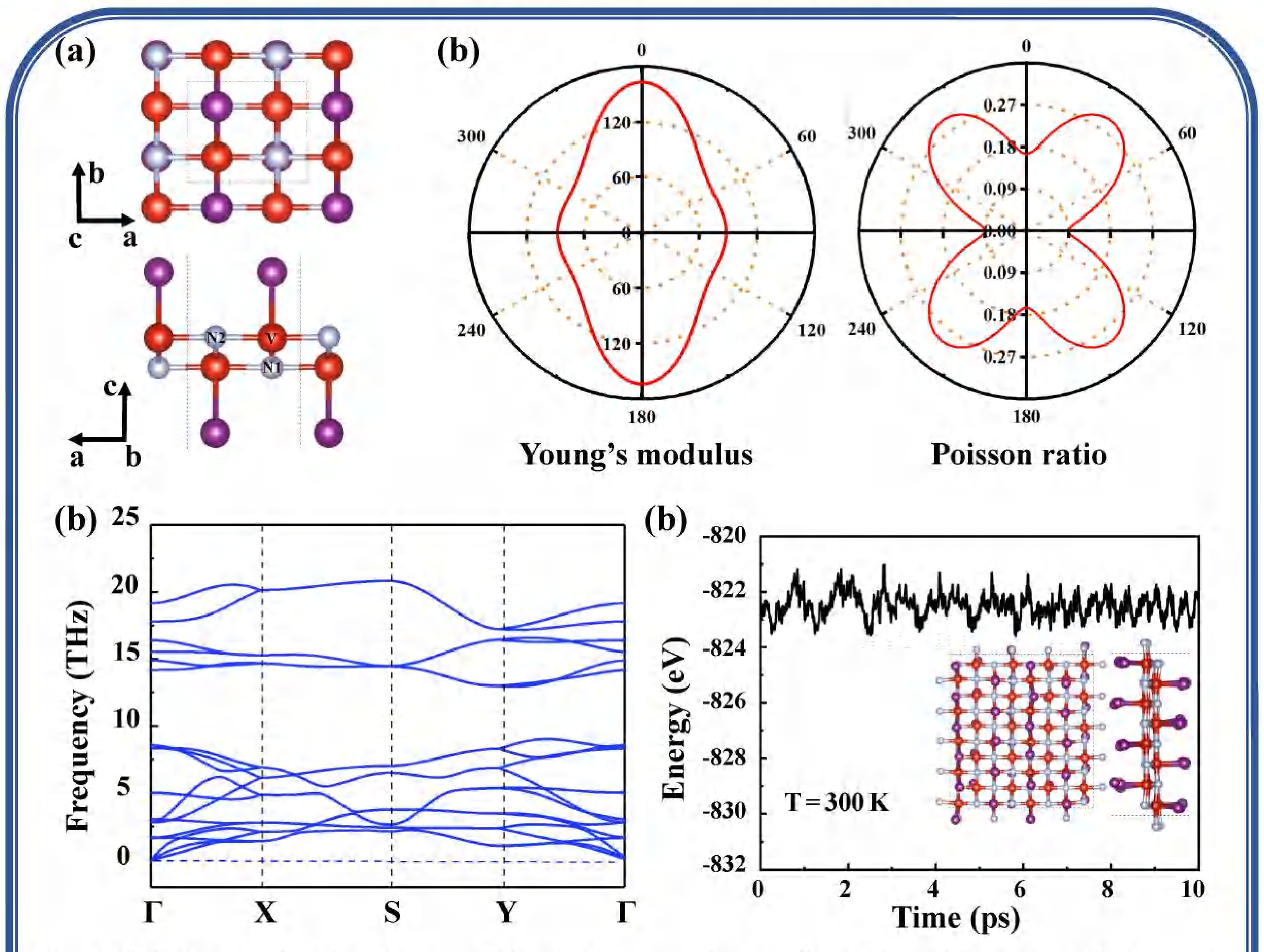

Fig. 1 (a) Top and side views of the VNI monolayer. (b) Polar diagrams of Young's modulus and Poisson ratio of the VNI monolayer. (c) Phonon dispersion spectrum. (c) Energy profile for the VNI monolayer at 300 K from AIMD simulations. The insets are snapshots structure at the end of 10 ps.

- ➢ VNI monolayer has excellent mechanical, dynamic and thermal stability.

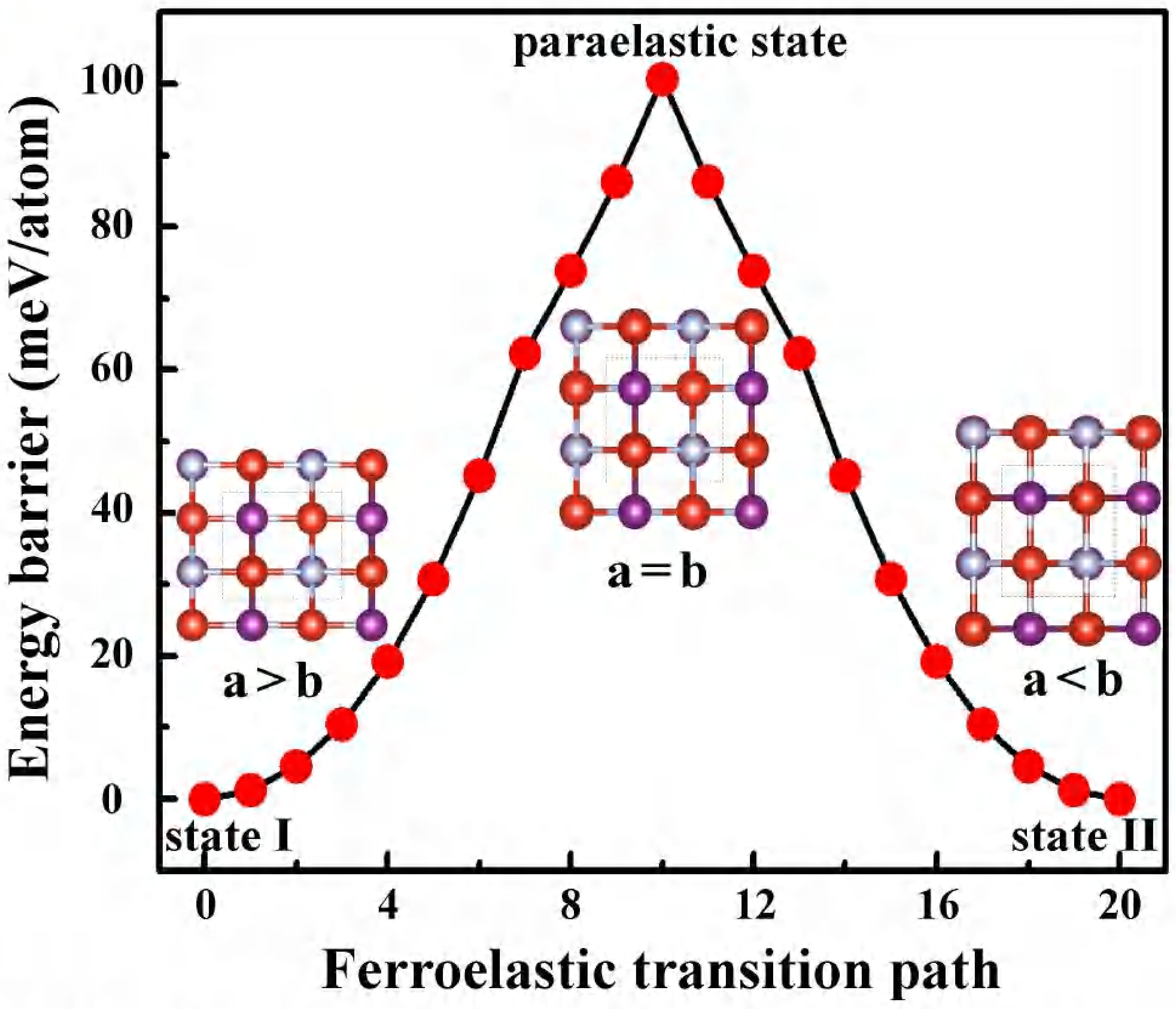

Fig. 2 Energy barrier of ferroelastic switching as a function of step number in the CI-NEB calculation for the VNI monolayer. The inset graphs represent structures for the ground states (state I and II) and the paraelastic state, respectively.

- ➢ VNI monolayer is an itinerant ferroelastic material, has a moderate ferroelastic switching barrier (100.66 meV/atom) with a reverse strain of 17.66 %.

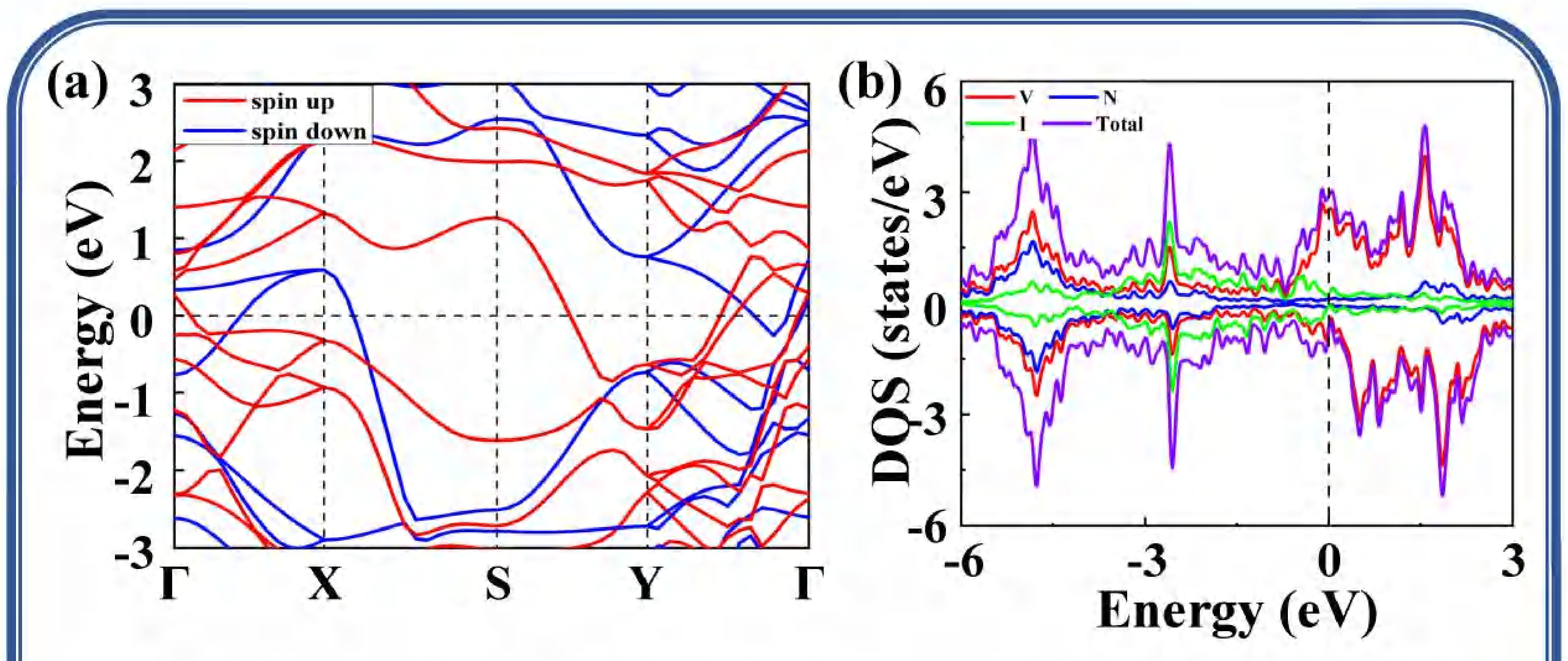

Fig. 3 (a) Spin-polarized band structures of VNI monolayer. (b) Total and partial density of states of the VNI monolayer. The Fermi level (dashed line) is set to zero.

- ➢ VNI monolayer has metallic properties and is derived from V-3d orbital.

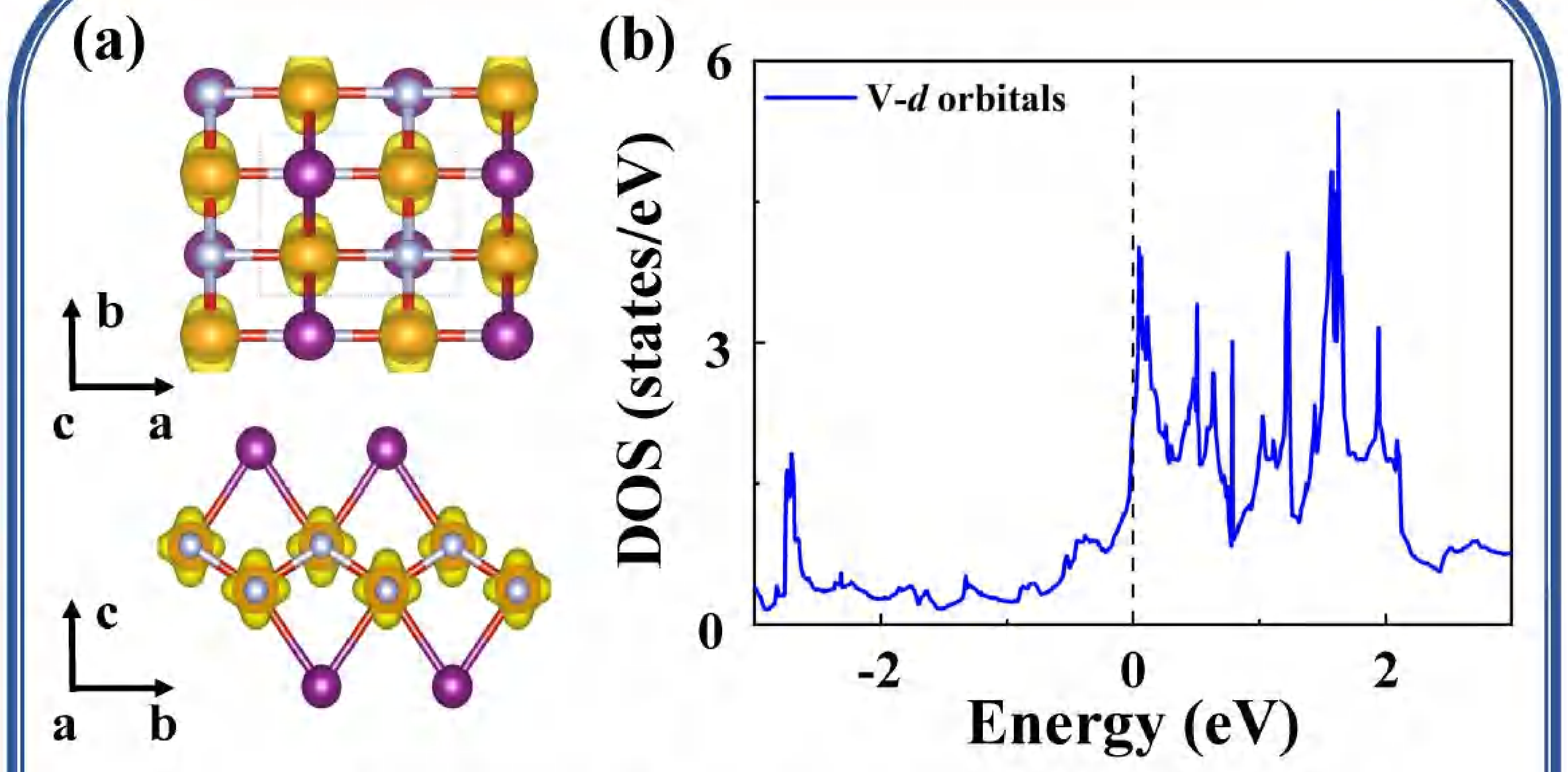

Fig. 4 (a) Spin density of the VNI monolayer with isosurface value of 0.015 a.u. The dashed lines represent a unit cell. (b) Electronic density of states for V d orbitals in the non-spin-polarized system in units of states/eV per V atom.

- ➢ VNI monolayer is an itinerant ferromagnetic material with a sizable in-plane magnetic anisotropic energy (150 μeV per V atom), and the origin of ferromagnetic ordering can be explained by Stoner model.
- ➢ The direction of the easy-magnetization axis changes from the in-plane a-axis to b-axis by applying ferroelastic strain, revealing a strong magnetoelastic coupling effect

Conclusion:

- ➢ **The VNI monolayer is an itinerant multiferroic metal with coexisting ferromagnetic and ferroelastic ordering. The origin of the ferromagnetic ordering can be explained by Stoner model and it exhibits moderate ferroelastic switching barrier (~100.66 meV/atom).**
- ➢ **VNI monolayer has a sizable in-plane magnetic anisotropic energy (150 μeV per V atom), and the direction of the easy-magnetization axis changes from the in-plane a-axis to b-axis by applying ferroelastic strain, revealing a strong magnetoelastic coupling effect.**

中国石油大学（北京）
CHINA UNIVERSITY OF PETROLEUM

Strain-controlled graphdiyne membrane for CO_2/CH_4 separation: First principle and molecular dynamic simulation

Xin Zheng[a], Shuai Ban[a,b,*], Bei Liu[a,*], Guangjin Chen[a]

[a] State Key Laboratory of Heavy Oil Processing, China University of Petroleum, Beijing 102249, China
[b] College of New Energy and Materials, China University of Petroleum, Beijing 102249, China

*Corresponding authors: banshuai@cup.edu.cn, liub@cup.edu.cn

Abstract

Tensile strain of porous membrane materials can broaden their capacity in gas separation. In this work, using van der Waals corrected density functional theory (DFT) and molecular dynamics (MD) simulations, the performance and mechanism of CO_2/CH_4 separation through strain-oriented graphdiyne (GDY) monolayer were studied by applying lateral strain. It is demonstrated that the CO_2 permeance peaks at 1.29×10^6 gas permeation units (GPU) accompanied with CO_2/CH_4 selectivity of 5.27×10^3 under ultimate strain, both of which are far beyond the Robeson's limit. Furthermore, the GDY membrane exhibited a decreasing gas diffusion energy barrier and increasing permeance with the increase of applied tensile strain. CO_2 molecule tends to reoriented itself vertically to permeate the membrane. Finally, the CO_2 permeability decreases with the increase of the temperature from 300 K to 500 K due to conserving of rotational freedom, suggesting an abnormal permeance of CO_2 in relation to temperature. Our theoretical results suggest that the stretchable GDY monolayer holds great promise to be an excellent candidate for CO_2/CH_4 separation, owing to its extremely high selectivity and permeability of CO_2.

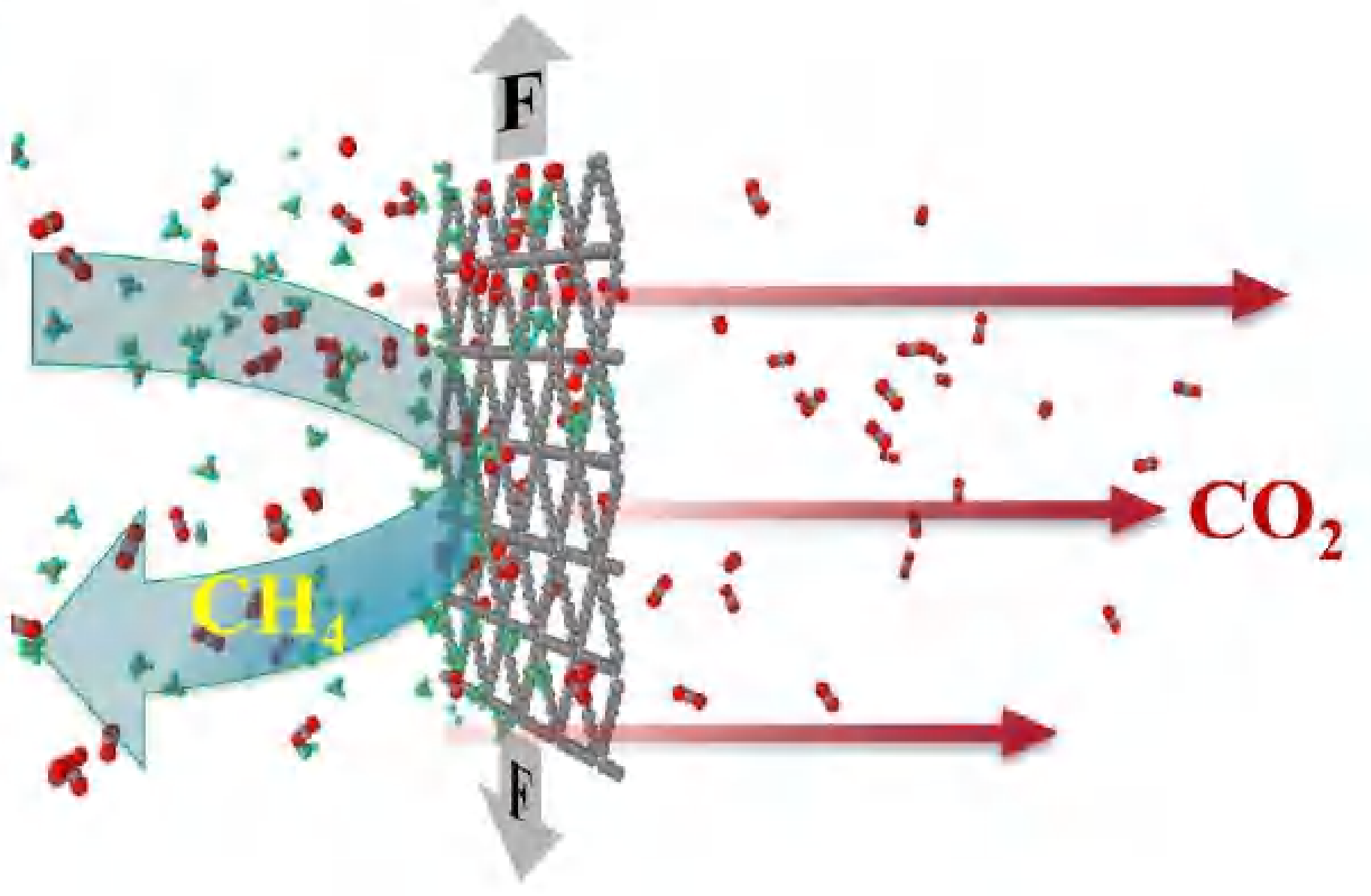

Issues & Challenges

- Graphene-like graphdiyne (GDY) with mechanical stability and periodically intrinsic uniform pores is only H_2-favorable.
- How to develop advanced technologies to efficiently achieve other mixture gases separation (CO_2/CH_4) using GDY membrane with fixed intrinsic pore size is still a challenge?

Coping strategies

- Regulating pore size through mechanical stretching based on GDY membrane with intristic uniform pores.

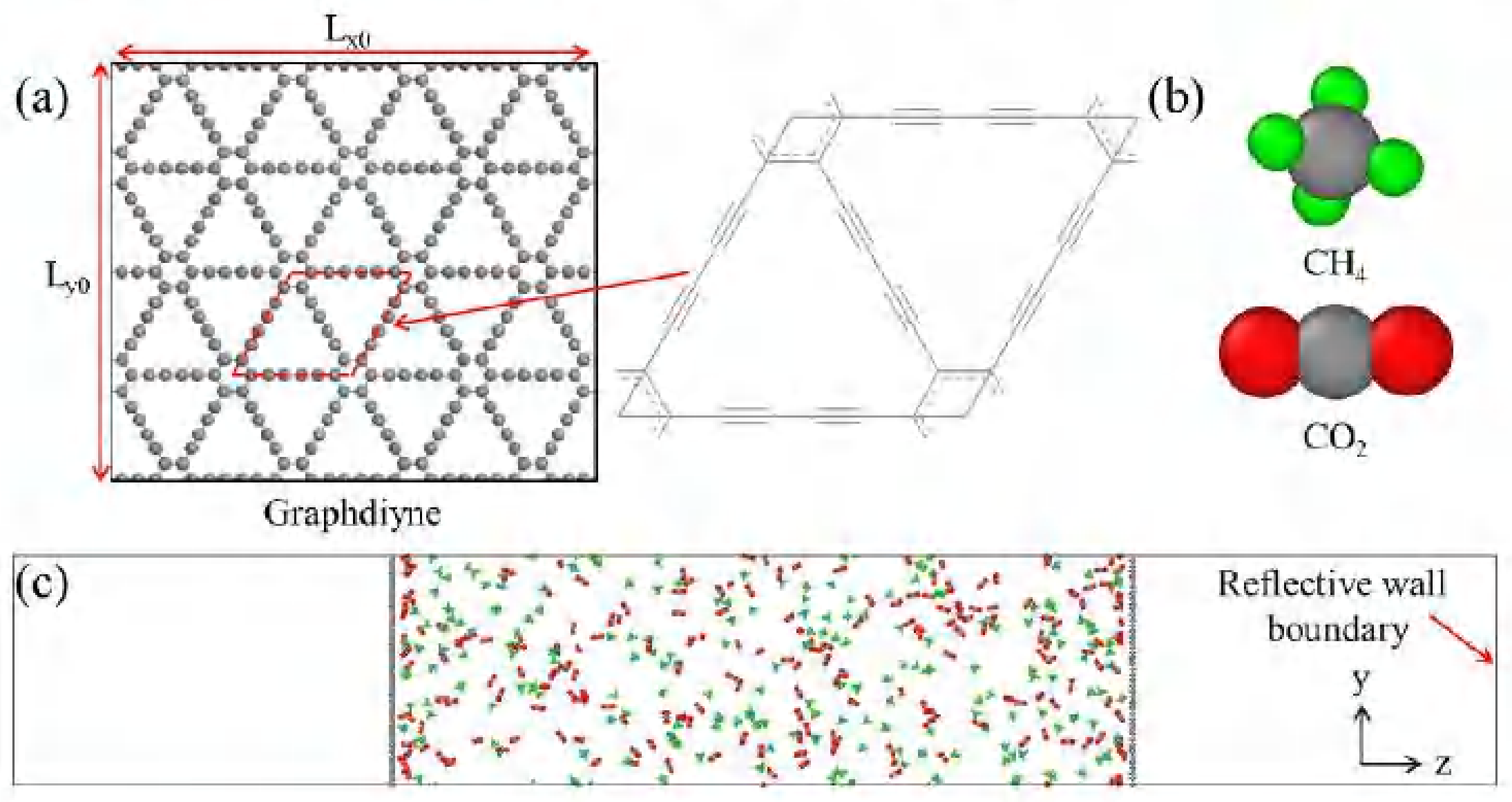

Results & Discussion

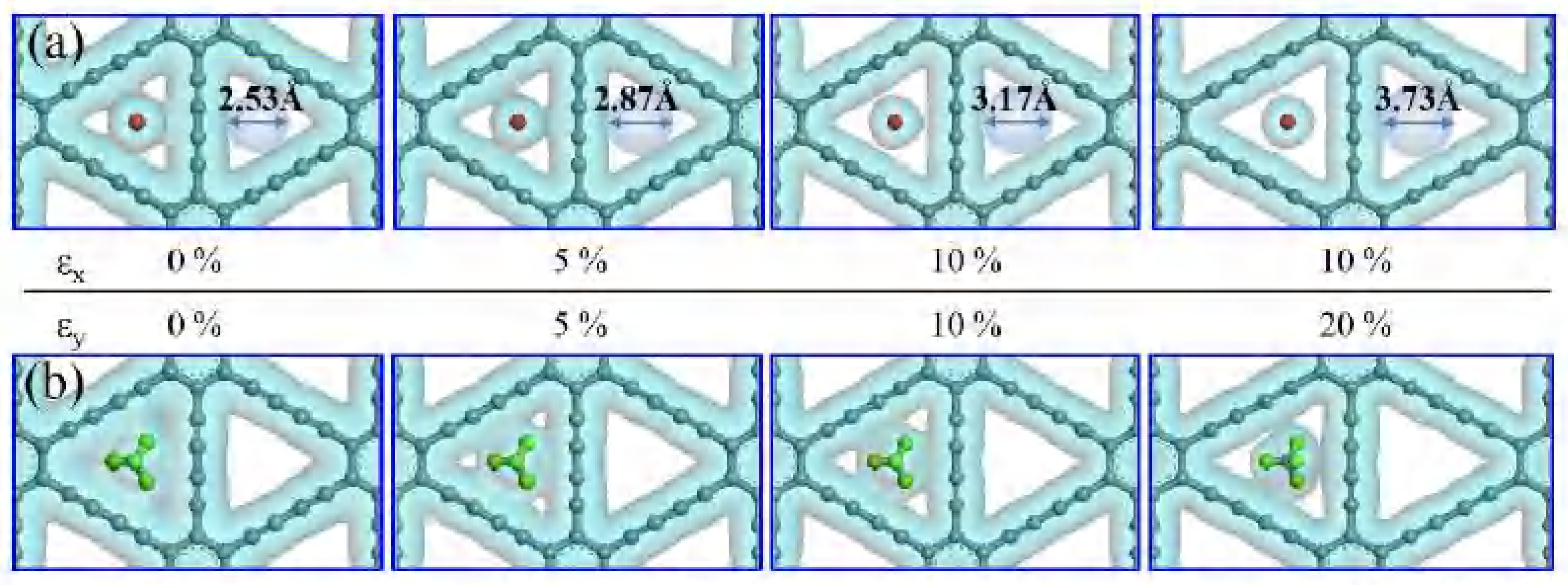

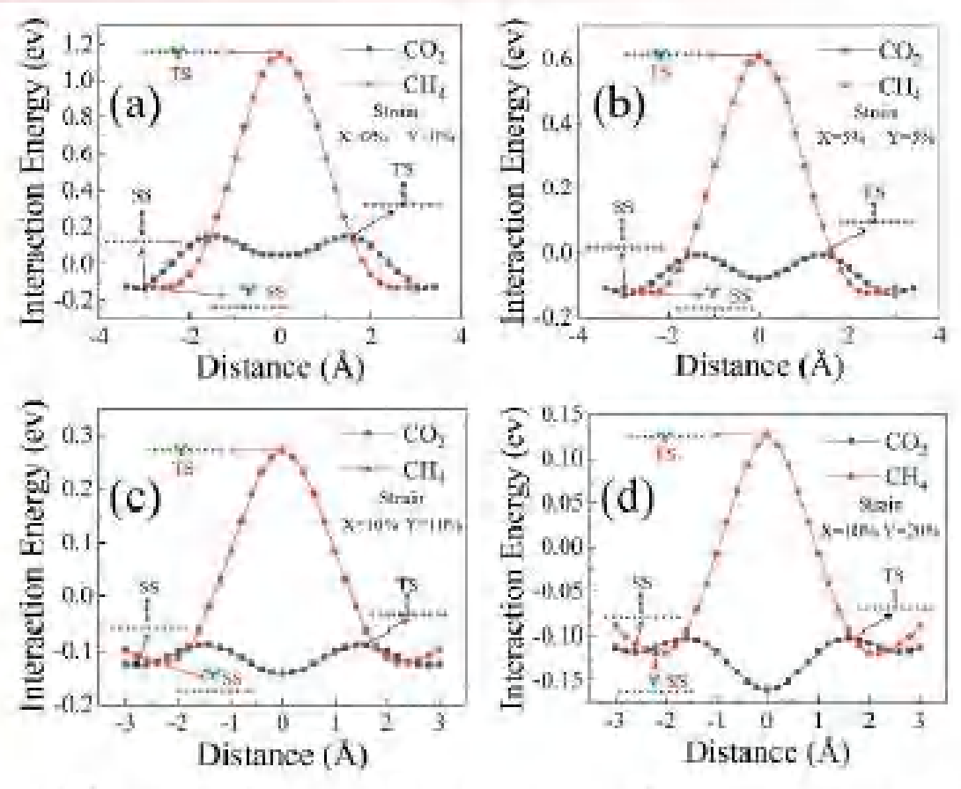

- The pronounced electron overlap of CH_4 with the triangle pore, resulting a higher energy barrier than that of CO_2 molecule.
- It is the electron density of the edge atoms of pore in the GDY network that hinders the gas molecules passing through the membrane.

Separation performance

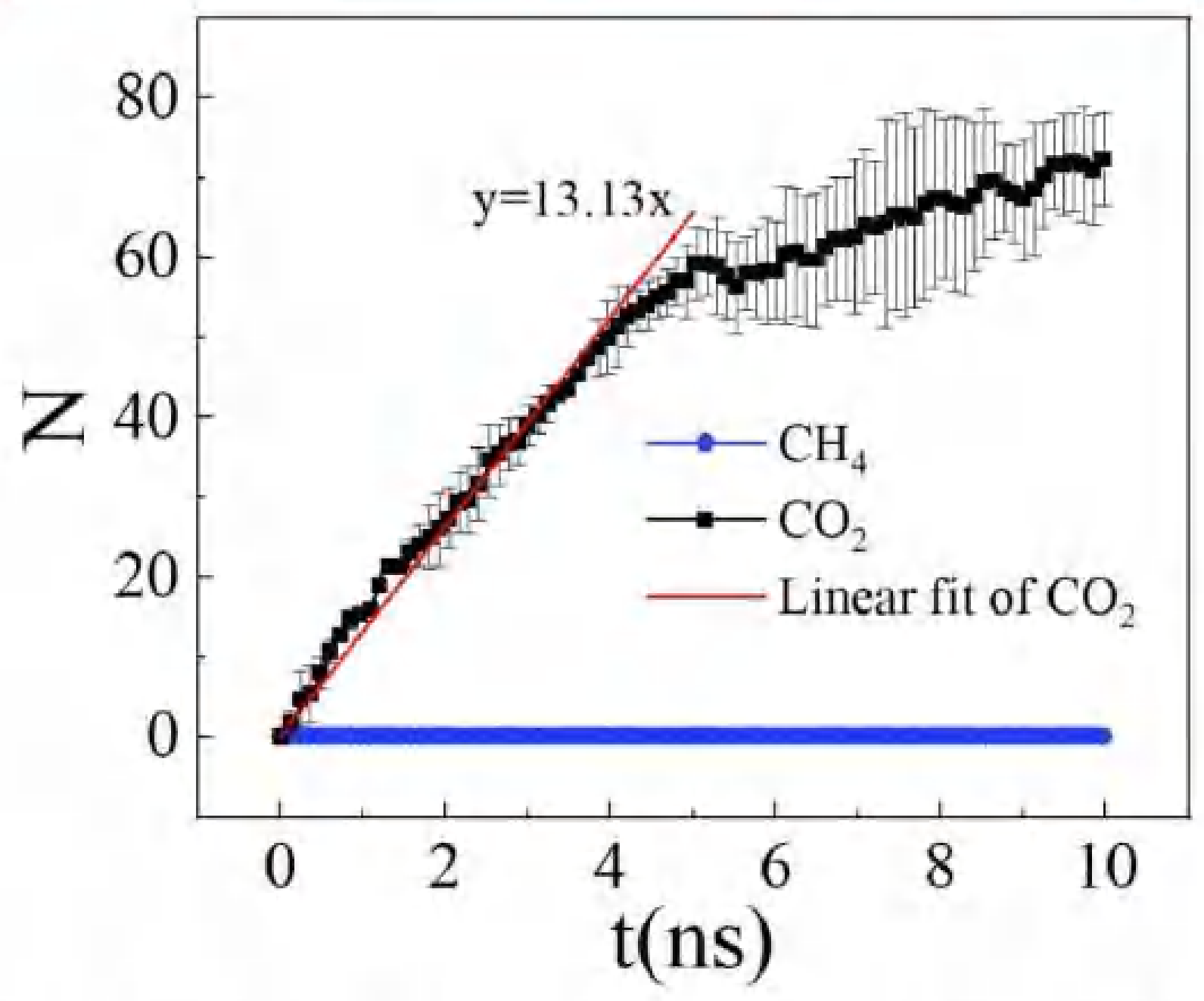

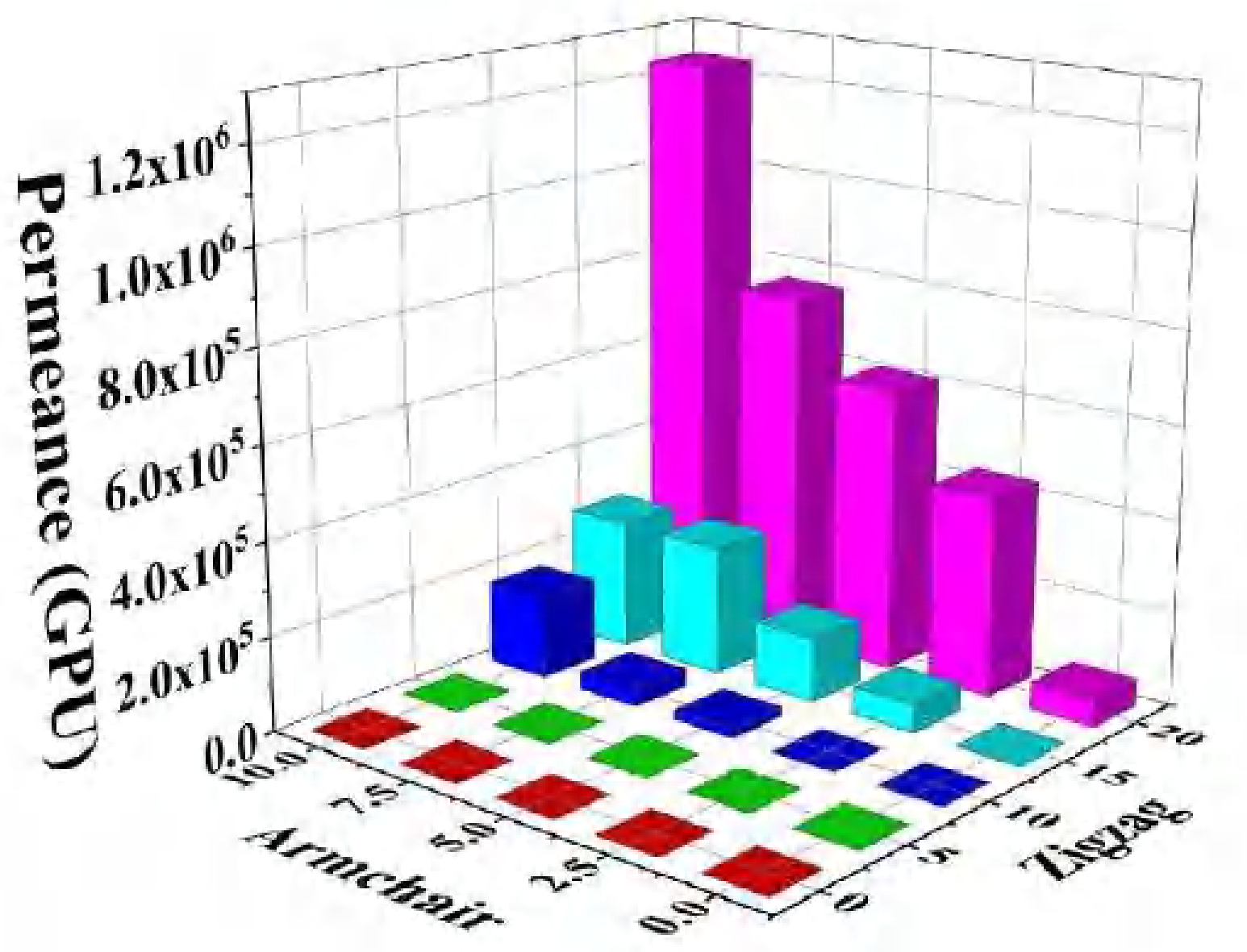

- CO_2 molecules preferentially pass through the stretched GDY membranes from feed chamber, whereas no CH_4 molecules could be detected in permeating areas after even 30 ns in MD simulations.
- The permeance of CO_2 increases as a function of GDY elongation.

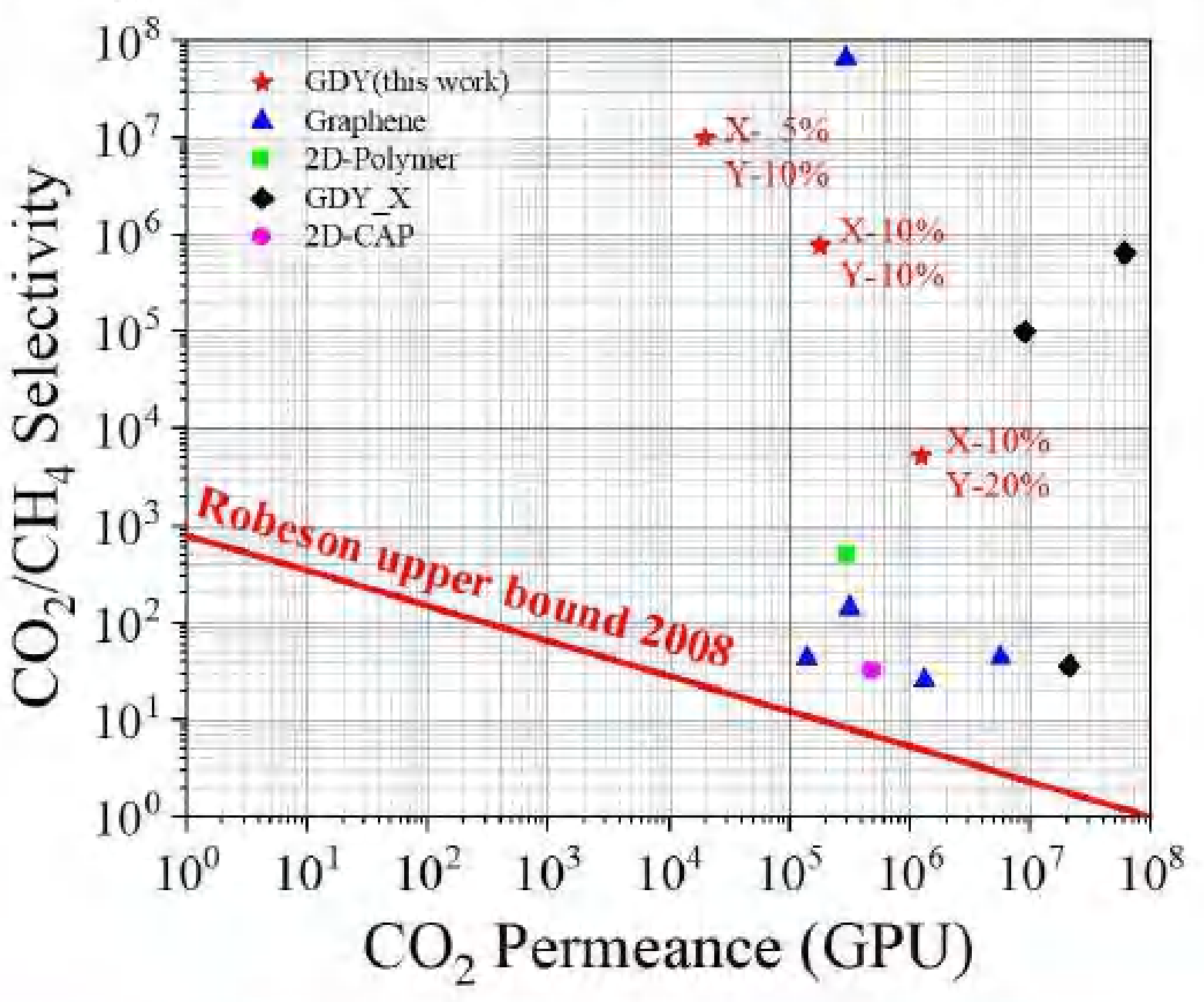

Conclusions

- MD and DFT results show that the permeance and selectivity of GDY towards CO_2 reach the magnitude of 1.29×10^6 GPU and 5.27×10^3 under ultimate-strain, surpassing the 2008 Robeson upper bound.
- A negative correlation between permeance and temperature has been found and elucidated for CO_2 owing to significant increase of rotational energy of CO_2 as temperature increases.

厚积薄发
开物成务

X. Zheng et al. / Chin. J. Chem. Eng. 28 (2020) 1898–1903

2022材料多尺度计算模拟国际会议
International Conference of Multi-scale Modeling and Simulation of Materials (ICM^3-2022)

Interface engineering of ferroelectricity in thin films of thiophosphate ABP_2X_6 (A = Cu, Ag; B = In, Bi, Cr, V; X = S, Se)

Guoliang Yu,[1] Anlian Pan,[2] and Mingxing Chen [1,*]
[1]Key Laboratory for Matter Microstructure and Function of Hunan Province, Key Laboratory of Low-Dimensional Quantum Structures and Quantum Control of Ministry of Education, School of Physics and Electronics, Hunan Normal University, Changsha 410081, China
[2]Key Laboratory for Micro-Nano Physics and Technology of Hunan Province, College of Materials Science and Engineering, Hunan University, Changsha 410082, China

Abstract

Two-dimensional ferroelectrics (FEs) are promising in the miniaturization of memory devices with ultra-high-density data storage and low power consumption. However, many thiophosphate monolayers, i.e., analogs of $CuInP_2S_6$ and referred to as ABP_2X_6, lose ferroelectricity and instead exhibit an antiferroelectric (AFE) or paraelectric ordering. We propose to tune the AFE ABP_2X_6 monolayers into the FE ordering through interface engineering. The mechanism is that there are couplings between the charge polarizations of the ABP_2X_6 monolayers and the local dipoles as well as the induced electronic polarizations in the substrate which have a tendency to stabilize the FE ordering. We further perform first-principles calculations for $CuInP_2Se_6$ and $CuCrP_2S_6$ monolayers and their van der Waals heterostructures. We find that an AFE $CuInP_2Se_6$ monolayer becomes FE as interfaced with graphene, MoS_2, and h-BN monolayers. In contrast, the $CuCrP_2S_6$ monolayer remains AFE since there is a large energy difference between the AFE and FE phases. Interfacing it with a $MoTe_2$ monolayer induces a metal-insulator transition for the heterostructure, whereas interfacing with a polar surface MgO(111) can drive it into FE. In particular, it is accompanied by an indirect-direct band-gap transition for the $CuInP_2Se_6$ monolayer. Our study offers an effective approach to tune the FE and electronic properties of ABP_2X_6 thin films for applications in electronics and optoelectronics.

A. Ferroelectricity of ABP_2X_6 monolayers

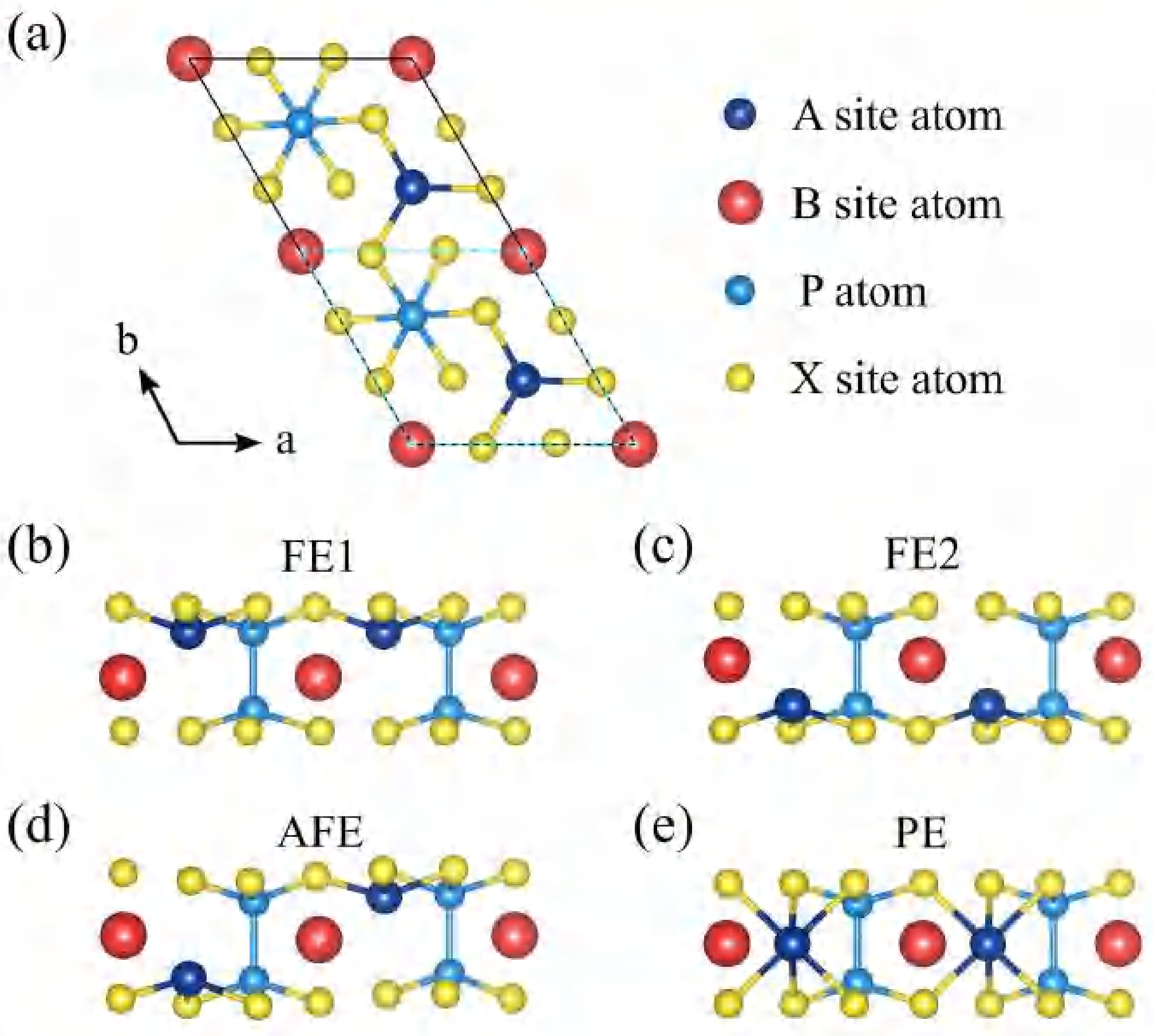

FIG. 1.Geometric properties of a ABP_2X_6 monolayer.

Systems	U_0 (meV)	U_1 (meV)	E (meV)	GS
$CuInP_2S_6$	218	242	24	AFE
$CuInP_2Se_6$	83	95	12	AFE
$CuBiP_2S_6$	269	272	3	AFE
$CuBiP_2Se_6$	121	104	−17	FE
$CuCrP_2S_6$	74	142	68	AFE
$CuCrP_2Se_6$	20	69	49	AFE
$CuVP_2S_6$	67	139	72	AFE
$CuVP_2Se_6$	−7	71	78	AFE
$AgInP_2S_6$	N/A	N/A	N/A	PE
$AgInP_2Se_6$	N/A	N/A	N/A	PE
$AgBiP_2S_6$	44	3	−41	FE
$AgBiP_2Se_6$	25	1	−24	FE

TABLE I. Energies of ABP_2X_6 monolayers. U_0 (U_1) denotes the energy difference between the PE and FE (AFE) phases, i.e., $U_0 = E_{PE} - E_{FE}$ ($U_1 = E_{PE} - E_{AFE}$). $\Delta E = E_{FE} - E_{AFE}$.

B. General concept

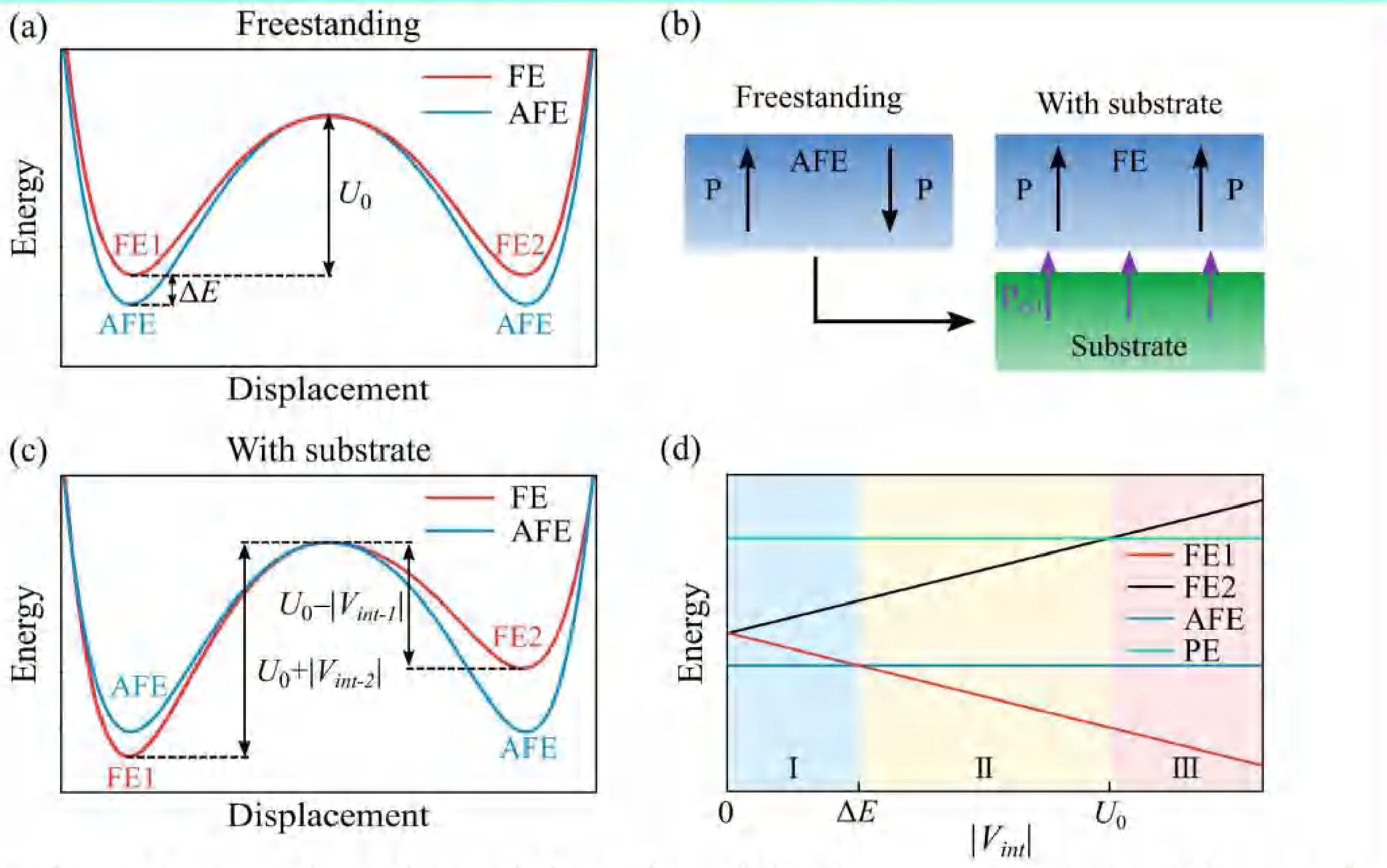

FIG. 2. Interface engineering of ferroelectricity in a monolayer with out-of-plane polarization.

C. $CuInP_2Se_6$-based heterostructures

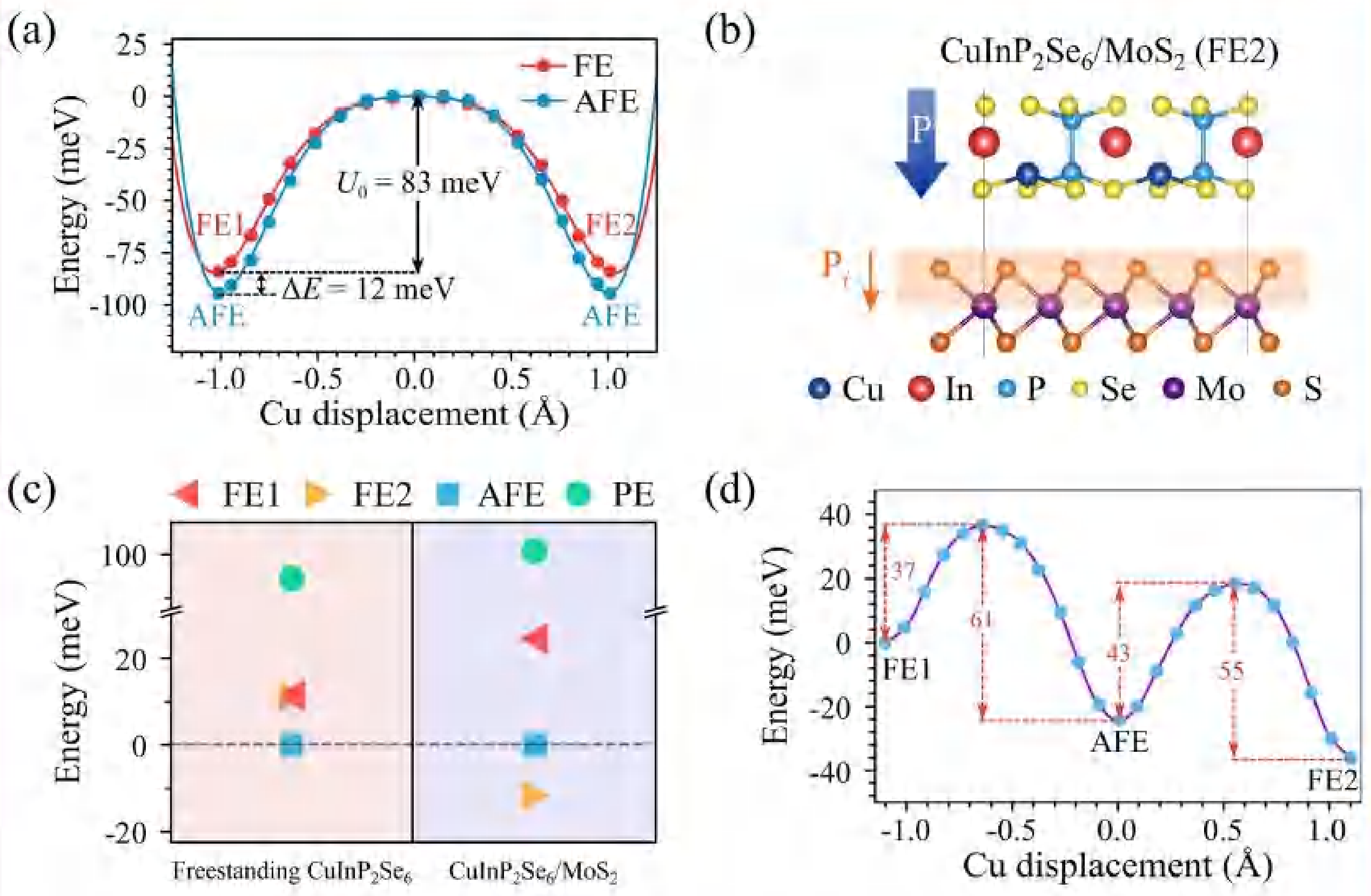

FIG. 3. vdW interface engineering of ferroelectricity in $CuInP_2Se_6$. (a) Potential energies of the FE and AFE phases of a free-standing $CuInP_2Se_6$ monolayer. (b) Structure of the FE2 phase for $CuInP_2Se_6/MoS_2$. (c) Effects of interfacing on energies of a $CuInP_2Se_6$ monolayer. (d) Kinetic pathway of the FE phase transform in $CuInP_2Se_6/MoS_2$.

D. $CuCrP_2S_6$-based heterostructures

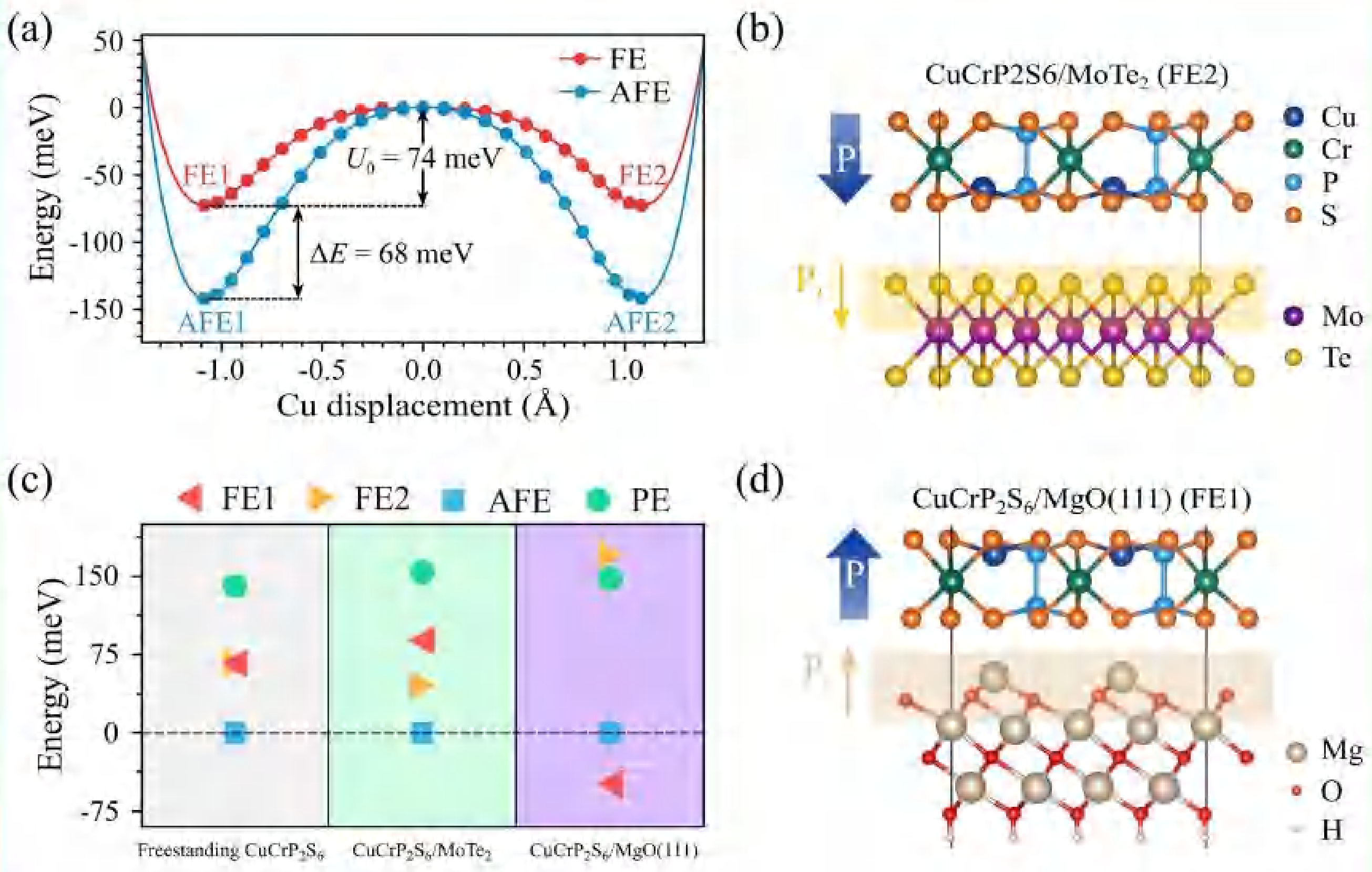

FIG. 4. Interface engineering of ferroelectricity in a $CuCrP_2S_6$ monolayer. (a) Potential energies a free-standing $CuCrP_2S_6$ monolayer. (b) Geometric structure of $CuCrP_2S_6/MoTe_2$ in the FE2 phase. (c) Effects of different substrates on the total energy of a $CuCrP_2S_6$ monolayer. (d) Geometric structure of $CuCrP_2S_6$/MgO(111) in the FE1 ordering, respectively.

E. Band structure

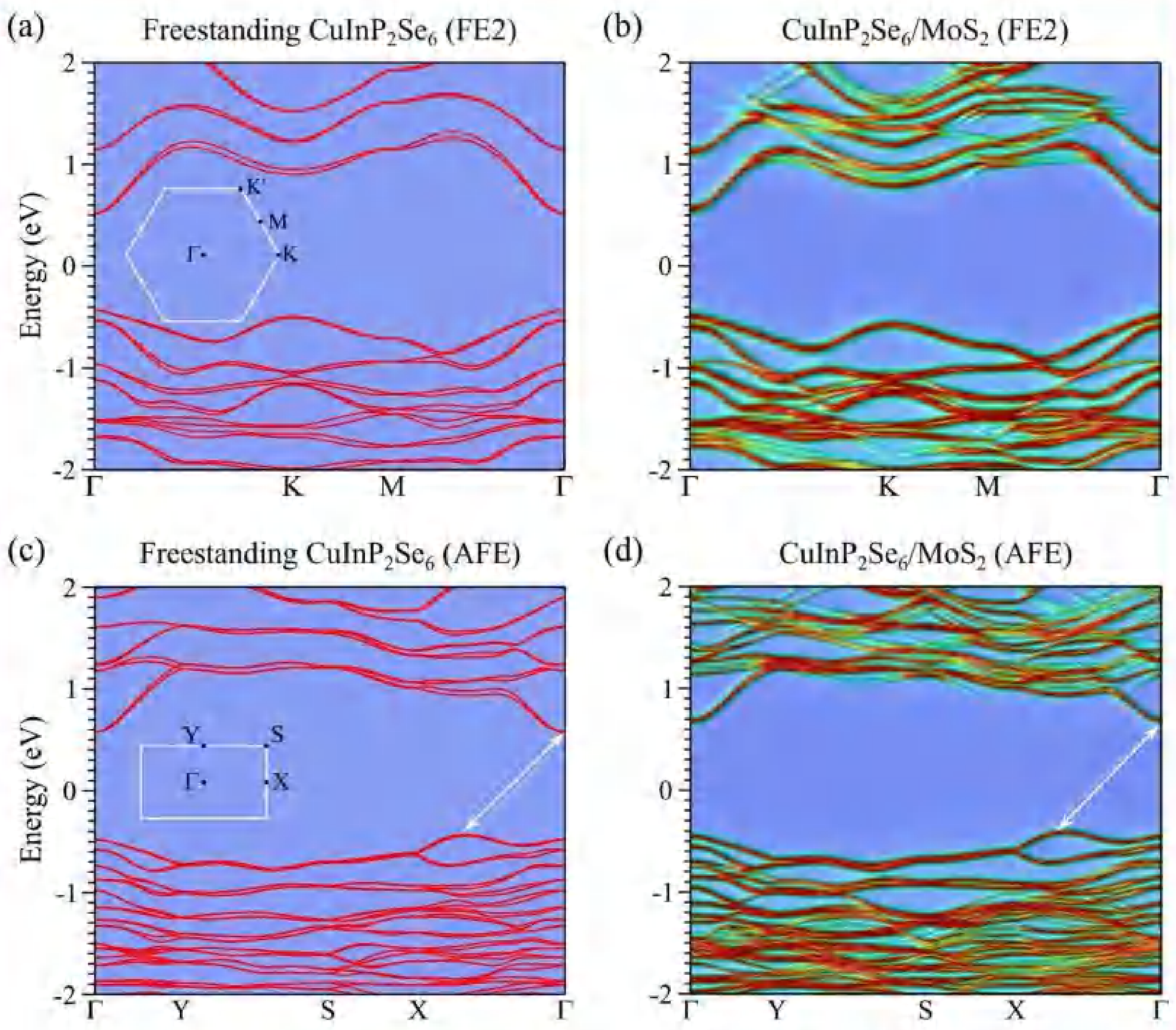

FIG. 5. Effects of a MoS_2 monolayer substrate on the band structure of a $CuInP_2Se_6$ monolayer.

F. Conclusions

- We find a number of ABP_2X_6 monolayers (A = Cu, Ag; B = In, Cr, V; and X = S, Se), lose ferroelectricity and exhibit an antiferroelectric (AFE) or paraelectric ordering.
- We propose to tune the AFE ABP_2X_6 monolayers into the FE ordering through interface engineering.
- We have applied the strategy to $CuInP_2Se_6$ and $CuCrP_2S_6$ monolayers and the interfacial interaction can drive an AFE-to-FE phase transition in these AFE monolayers.
- We further find a FE switching of electronic structures for $CuInP_2Se_6$- and $CuCrP_2S_6$-based interfaces.

G. Acknowledgment

This work was supported by the National Natural Science Foundation of China (Grants No. 11774084, No. 12174098, No. U19A2090, and No. 91833302).

Email:
mxchen@hunnu.edu.cn
guoliangyu@hunnu.edu.cn

Publication: G. L. Yu et al., Phys. Rev. B 104, 224102 (2021).

Origin of Bismuth-Rich Strategy in Bismuth Oxyhalide Photocatalysts

Yang Wang,[a] Jiazhi Meng,[a] Shaojie Jing,[a] Liyong Gan,*[a, b] and Xiaoyuan Zhou *[a, b, c]

a. Chongqing Key Laboratory of Soft Condensed Matter Physics and Smart Materials, College of Physics, Chongqing University, Chongqing 401331, China.
E-mail: ganly@cqu.edu.cn, xiaoyuan2013@cqu.edu.cn
b. State Key Laboratory of Coal Mine Disaster Dynamics and Control, Chongqing 401331, China
c. Analytical and Testing Center, Chongqing University, Chongqing 401331, China

Abstract: **Recently, the bismuth-rich strategy via increasing the bismuth content has been becoming one of the most appealing approaches to improve the photocatalytic performance of bismuth oxyhalides. However, insights of the mechanism behind the encouraging experiments are missing. Herein, we report the results of the theory-led comprehensive picture of bismuth-rich strategy in bismuth oxyhalide photocatalysts, selecting Bi_5O_7X (X = F, Cl, Br, I) as a prototype. First-principles calculations revealed that the strategy enables good n-type conductivity, large intrinsic internal electric field, high photoreduction ability and outstanding harvest of visible light, and particularly ranked the intrinsic activity of this family: Bi_5O_7F > Bi_5O_7I > Bi_5O_7Br > Bi_5O_7Cl. Designed experiments confirmed the theoretical predictions, and together these results are expected to aid future development of advanced photocatalysts.**

1. Introduction

❖**In this work, a combining theoretical simulations and experimental verifications method was used for thoroughly uncover the mystery behind the bismuth-rich strategy in bismuth oxyhalides photocatalysts.**

❖ First-principles calculations revealed that the strategy enables good n-type conductivity, large intrinsic internal electric field, high photoreduction ability and outstanding harvest of visible light, and particularly ranked the intrinsic activity of this family: Bi_5O_7F > Bi_5O_7I > Bi_5O_7Br > Bi_5O_7Cl.

❖ Designed experiments confirmed the theoretical predictions, and together these results are expected to aid future development of advanced photocatalysts.

2. Results and discussion

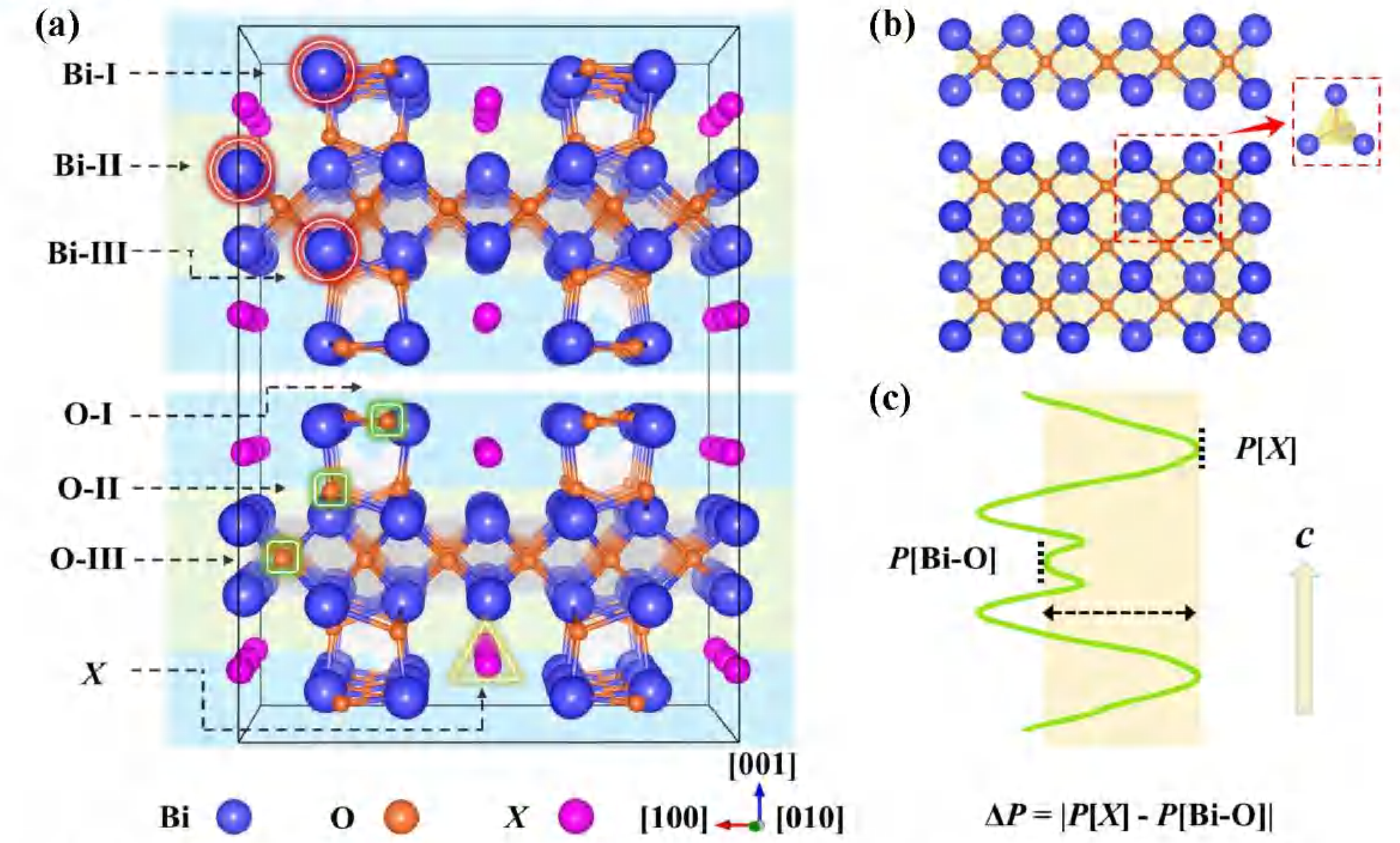

Fig. 1 (a) Crystal structure of Bi_5O_7X. The inequivalent Bi and O sites are marked by circles and squares, respectively. (b) Side (upper pannel) and top (lower pannel) view of the central [Bi-O] layer with the Bi_4O tetrahedron highlighted. (c) Electrostatic potential diagram of Bi_5O_7X.

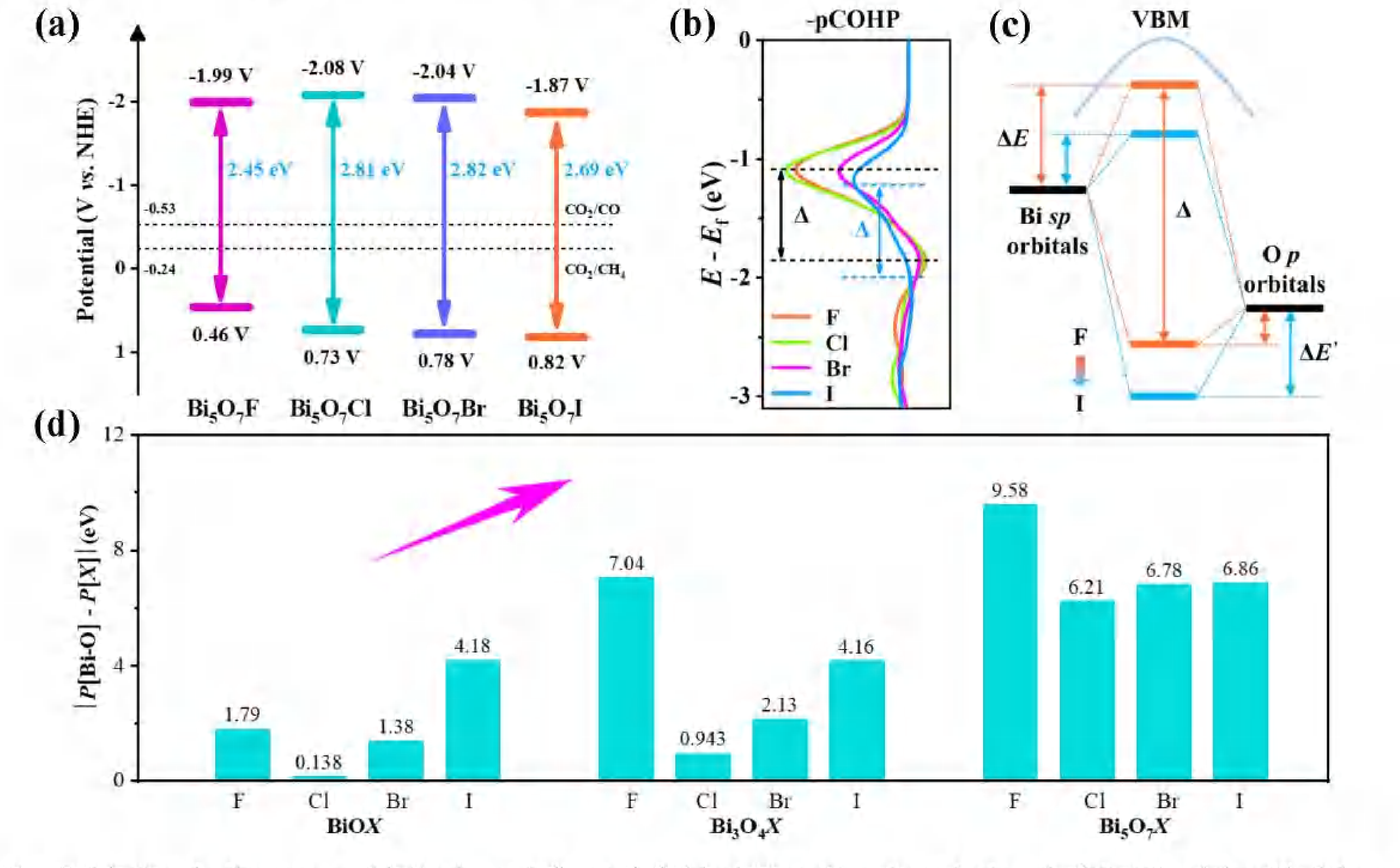

Fig. 2 (a) Band alignment. (b) Projected Crystal Orbital Hamilton Population (pCOHP) of the Bi-O bond that dominates the VBM. (c) Schematic illustration of the origin of VBM in Bi_5O_7X. (d) Electrostatic potential difference between the [Bi-O] and [X] layer in BiOX, Bi_3O_4X and Bi_5O_7X.

Bismuth-rich Strategy

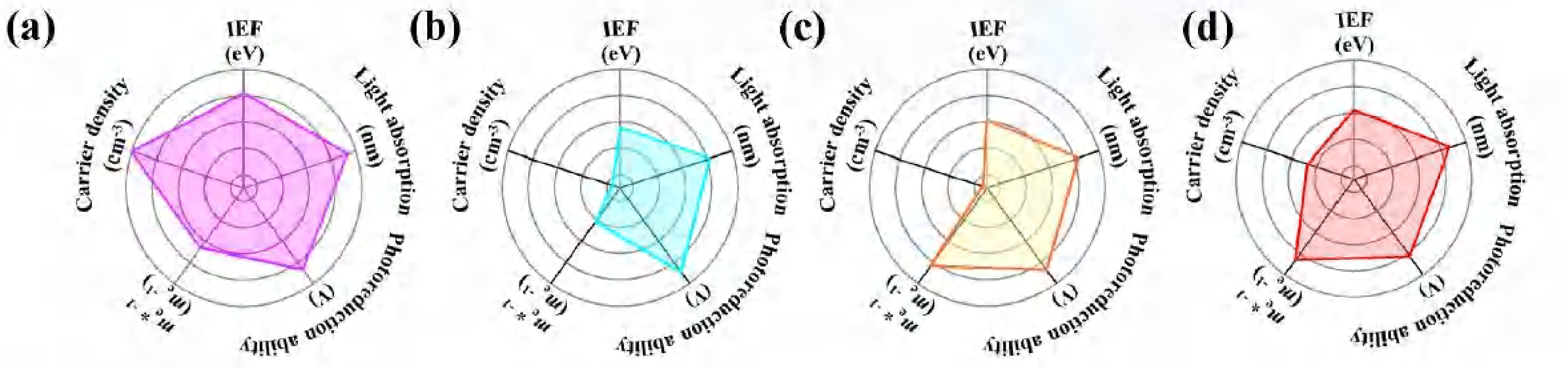

Fig. 3 Radar plots of the calculated photoreduction-related properties of (a) Bi_5O_7F, (b) Bi_5O_7Cl, (c) Bi_5O_7Br and (d) Bi_5O_7I.

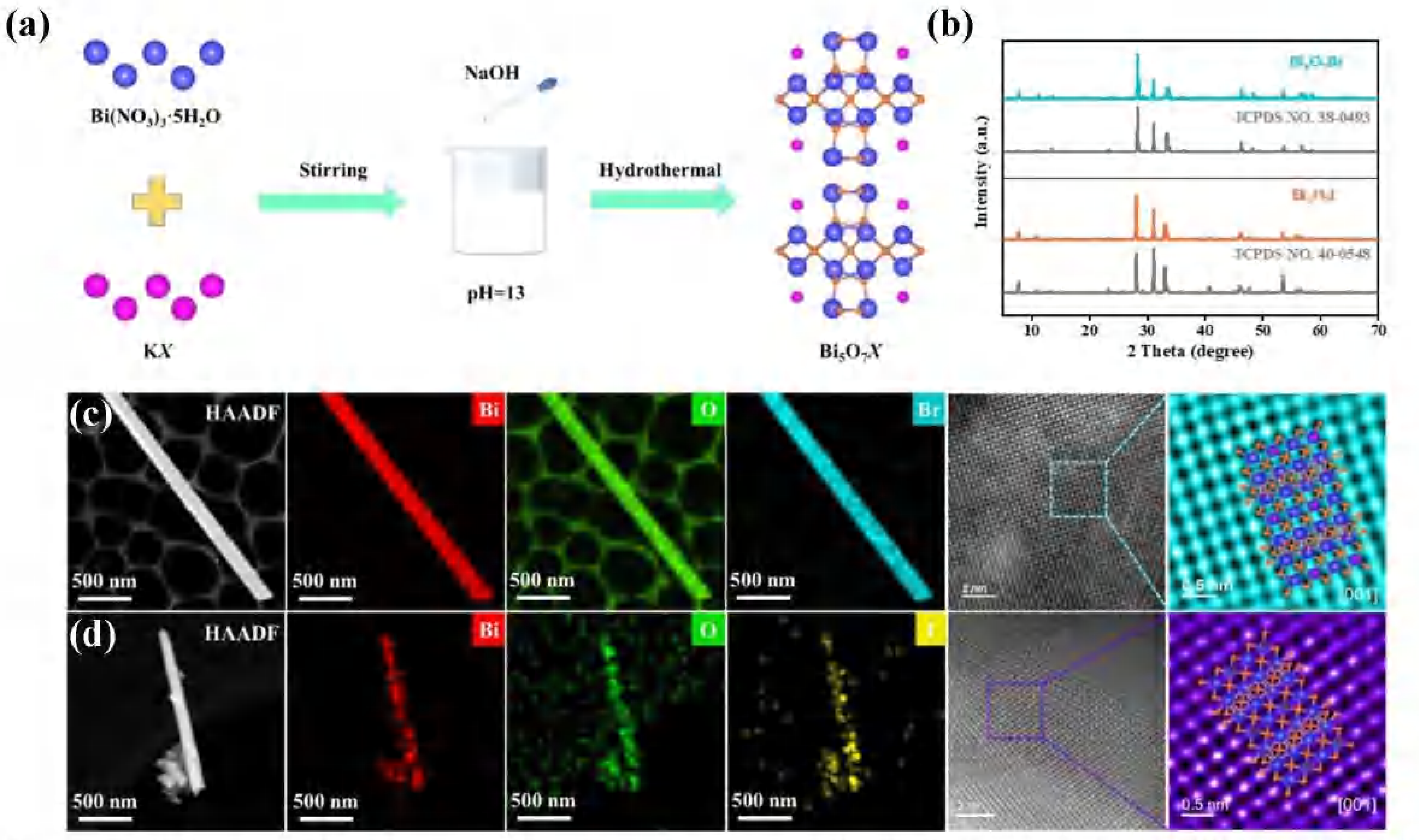

Fig. 4 (a) Schematic illustration of the preparation process for Bi_5O_7X nanorods. (b) XRD patterns of Bi_5O_7Br and Bi_5O_7I. (c, d) HAADF-STEM images and corresponding Bi, O, Br and I elemental mapping of Bi_5O_7Br and Bi_5O_7I.

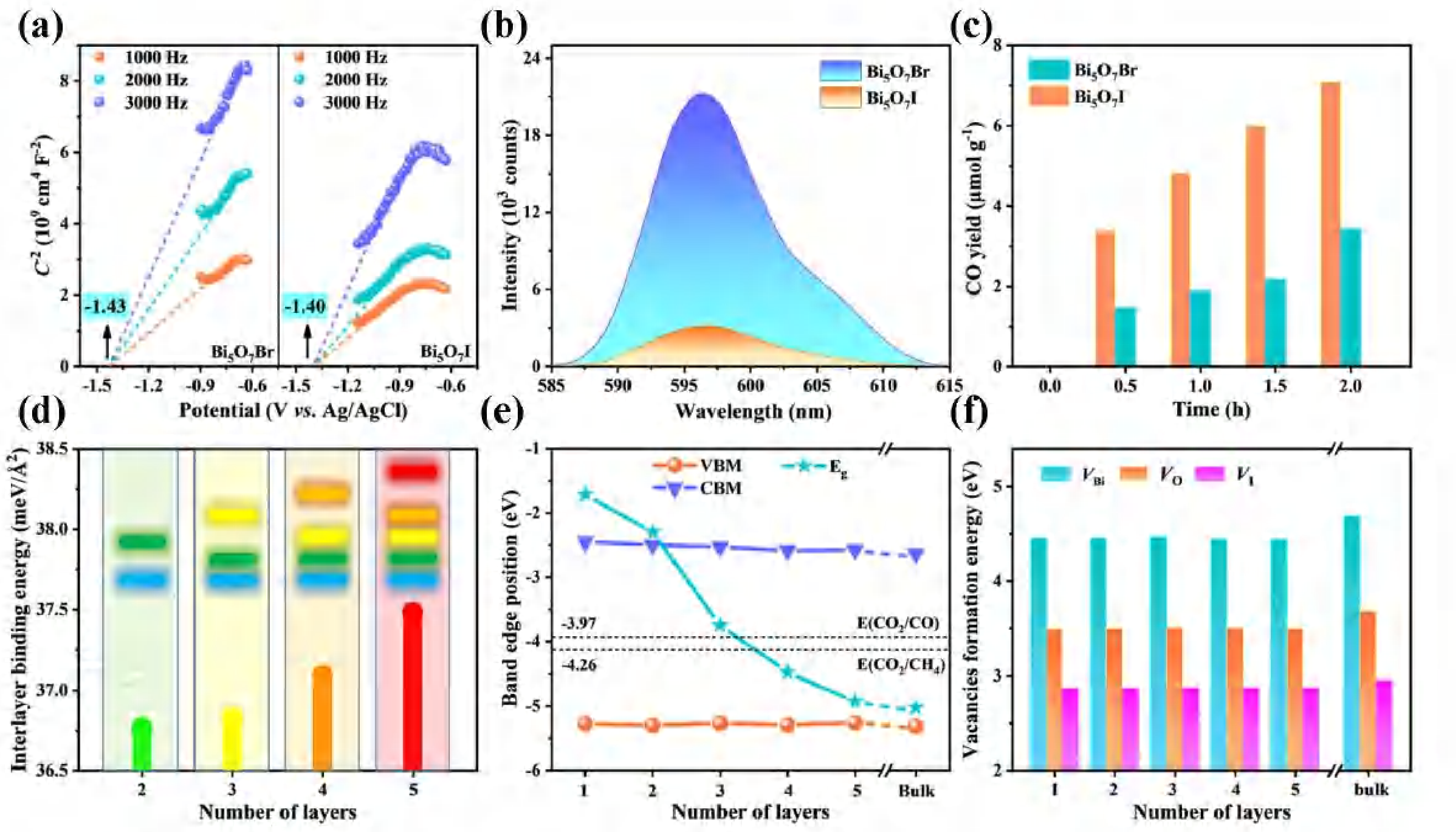

Fig. 5 (a) Mott-Schottky curves, (b) steady-state photoluminescence spectra, (c) yield of photocatalytic CO_2 reduction of Bi_5O_7Br and Bi_5O_7I. (d-e) Properties of Bi_5O_7I as a function of the number of layers, including interlayer binding energy, band edge position and vacancies formation energy of composition elements.

3. Conclusion

In summary, we have systematically studied the effects of bismuth-rich strategy on the bismuth oxyhalides Bi_5O_7X. The calculated results reveal that the strategy enables many advantages, such as good n-type conductivity, large IEF, considerably negative CBM and high harvest of visible light. These features collectively suggest a high CO_2 photoreduction ability. In particular, we identify an order for the intrinsic photocatalytic activity of this family: Bi_5O_7F > Bi_5O_7I > Bi_5O_7Br > Bi_5O_7Cl. Subsequent designed experiments are in excellent agreement with the theoretical predictions. Moreover, these photocatalytic properties can be further optimized upon tuning the thickness. Our results delivered a comprehensive picture of the bismuth-rich strategy, and are expected to aid future rational design of advanced bismuth-based photocatalysts. These results show the importance and potential of the theory-guided rational design of catalysts.

Acknowledgements

This work was financially supported from the National Science Fund for Distinguished Young Scholars (Grant No. 52125103) and the National Natural Science Foundation of China (Grant Nos. 52071041 and 12074048 and 12147102). This work was conducted at college of physics, Chongqing University and had been published in Energy & Environmental Materials (https://onlinelibrary.wiley.com/doi/10.1002/eem2.12432). We are very grateful to Profs. Cong Wang and Danmei Yu for their useful discussion. We also would like to thank Hanjun Zou, Bin Zhang and Chuanyao Yang at Analytical and Testing Center of Chongqing University for their assistance with XRD, TEM and PL analysis.

铁基合金中扭折晶界的成因及其对力学性能的影响

周嘉颖[1]，杨梦梦[1]，李勇[2]，李伟[2]，王皞[1,*]（haowang7@usst.edu.cn）
上海理工大学，材料科学与化学学院/增材制造研究院
上海交通大学，材料科学与工程学院

引言

研究人员通过轧制与热处理获得了具有扭折晶界的铁基合金试样。与传统的同成分试样相比，具有扭折晶界的试样在力学性能测试中表现出良好的低温强度与低温塑性。且具有扭折晶界的试样在低温拉伸测试中观察到了相当数量的刃位错。以上特性表明该材料具有在低温环境下的应用潜力，因此本工作基于分子动力学模拟揭示了扭折晶界的成因并探讨了其具有低温塑性的原因。

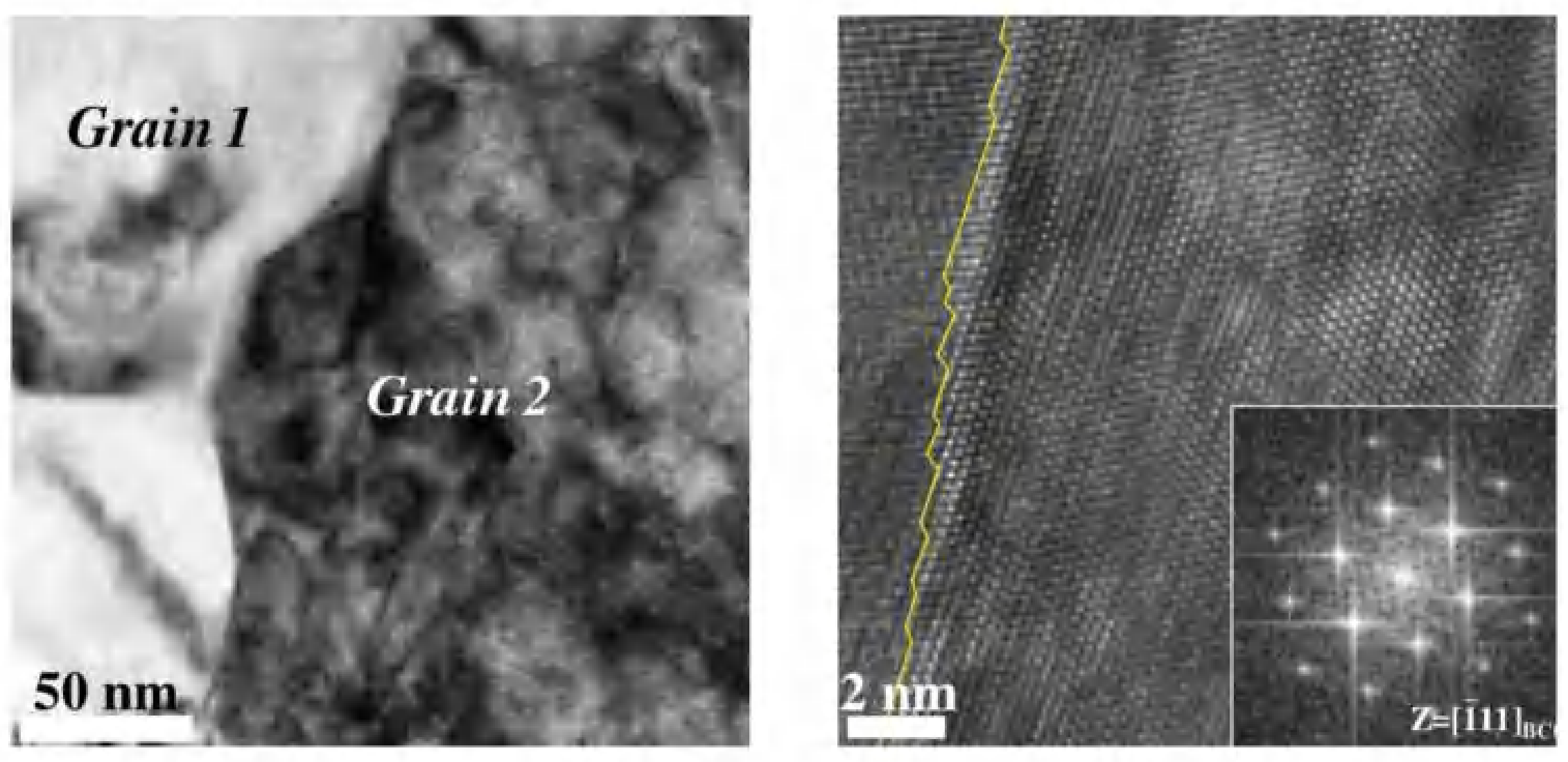

图1 实验中观察到的扭折状晶界

力学性能测试及晶界成分表征

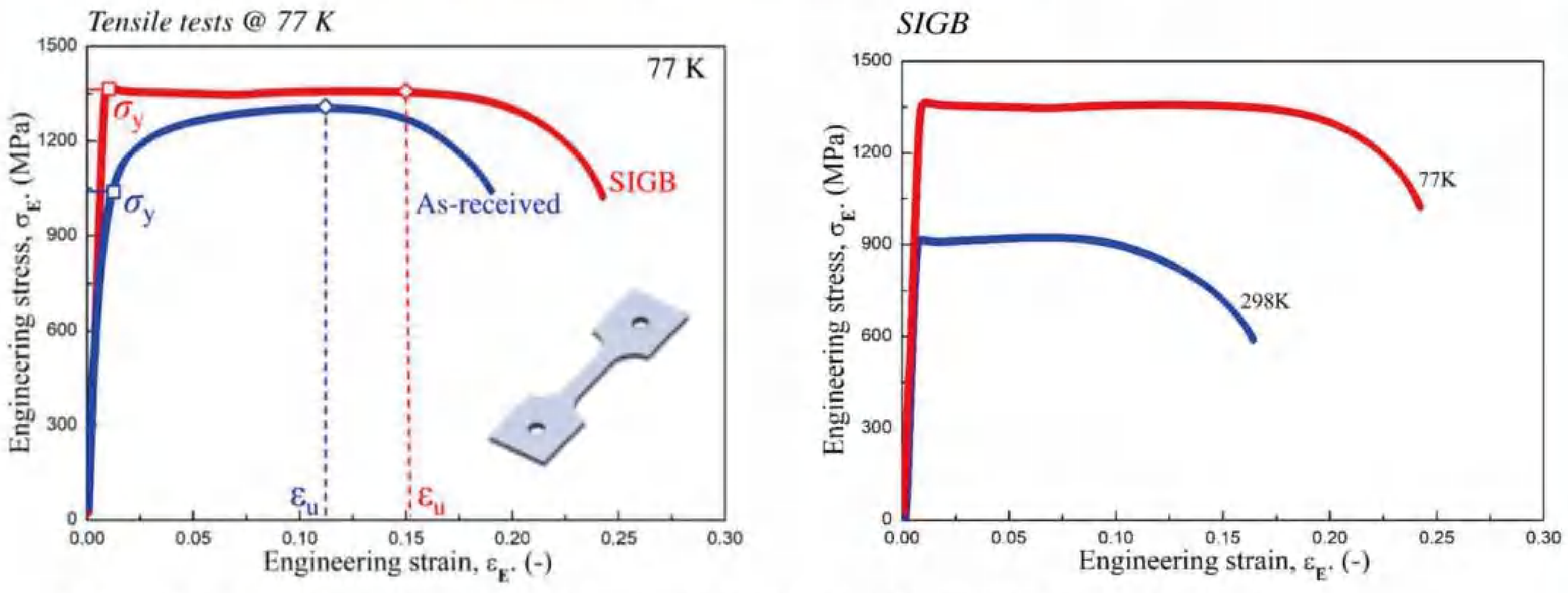

图2 扭折晶界试样（SIGB）与普通试样的低温拉伸测试（左）；
扭折晶界试样的低温与室温拉伸测试（右）

如图2所示，与以往的材料不同，具有扭折晶界的试样表现出反常的低温塑性，其强度和塑性都随着温度的下降增加。且在相同低温下，其强度和塑性也优于常规的具有平直晶界的试样。

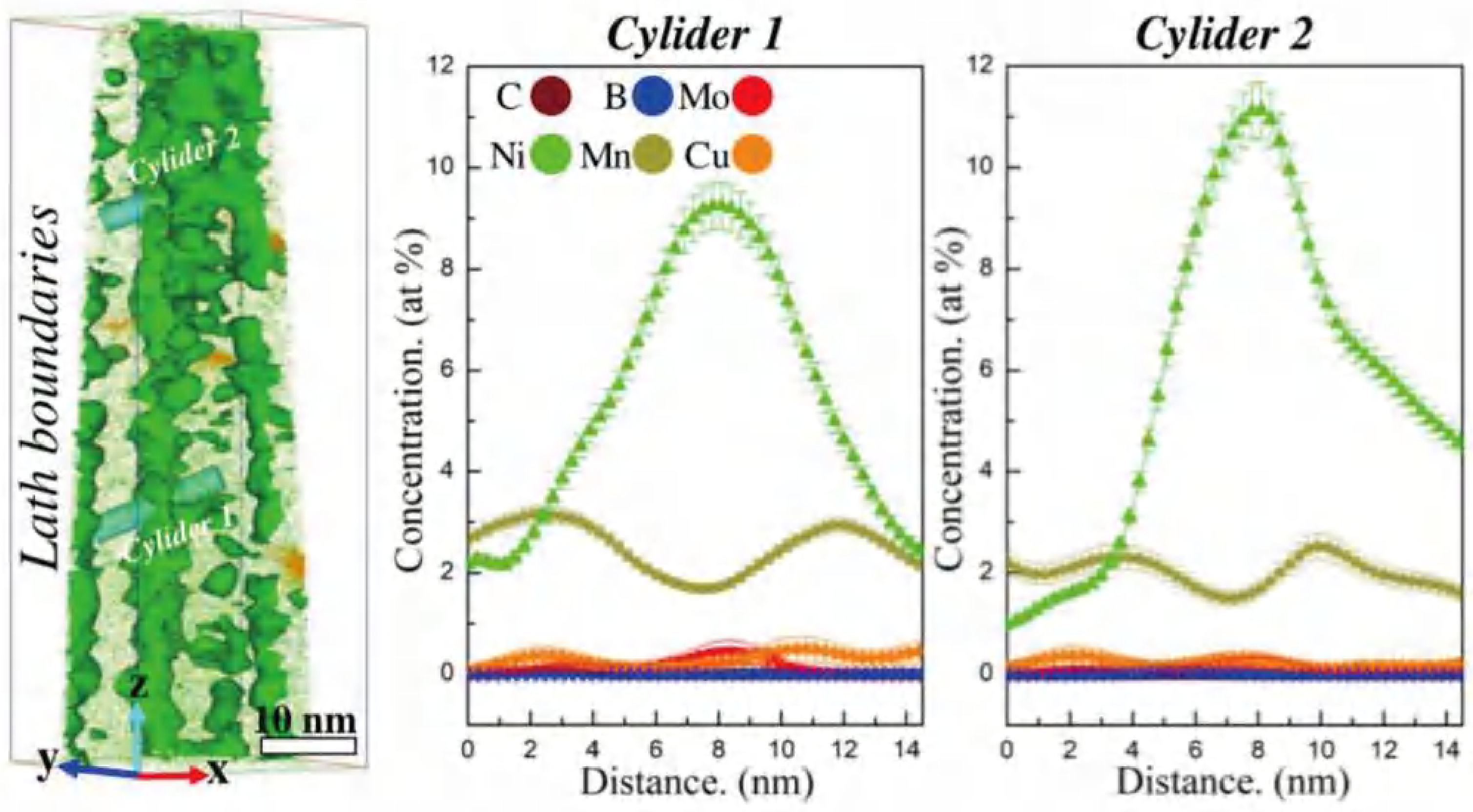

图3 晶界附近元素成分分析

如图3所示，晶界上出现了Ni的富集，在研究的初期，这被认为是促使晶界呈现扭折的原因

分子动力学模拟—扭折晶界成因

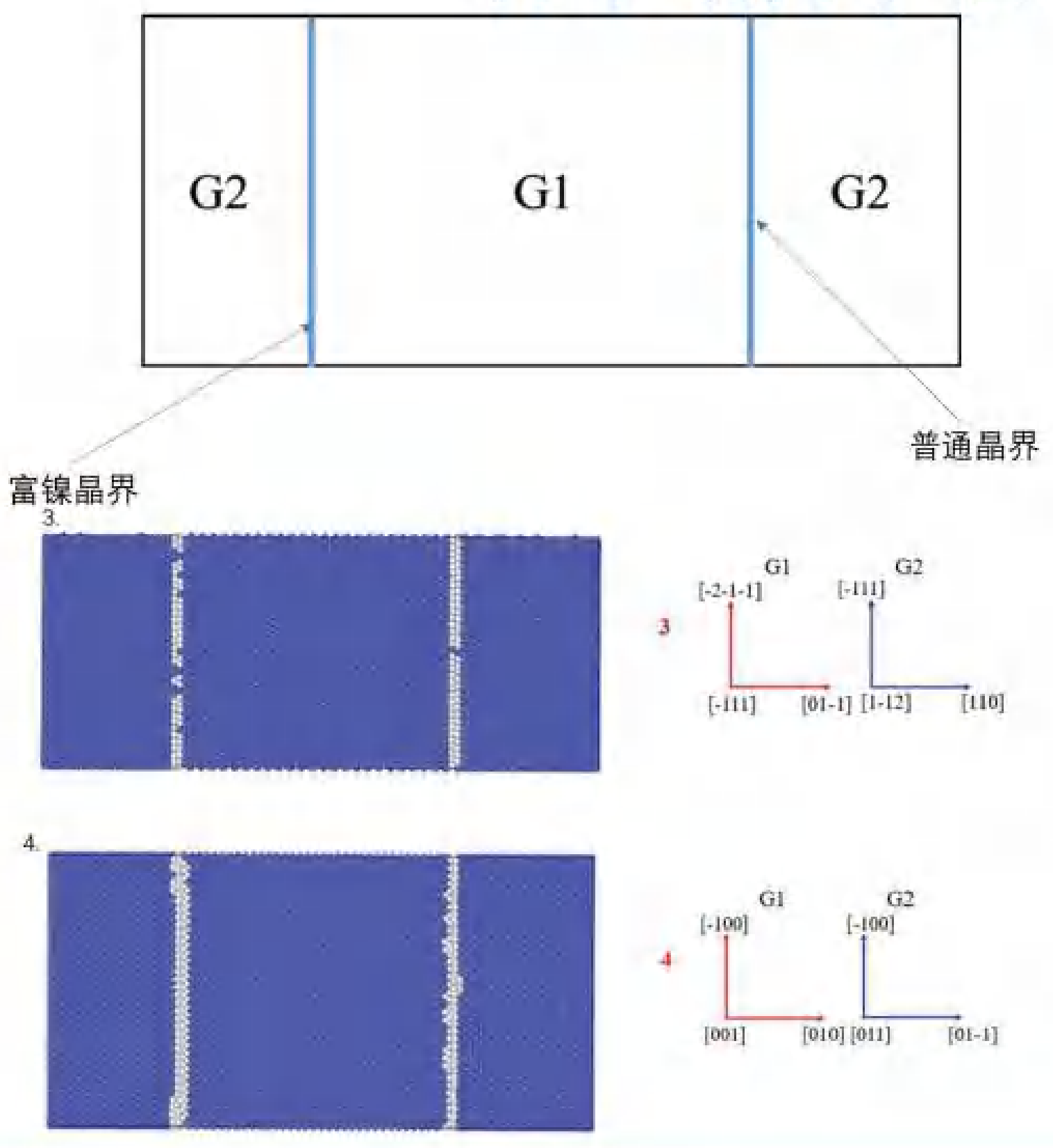

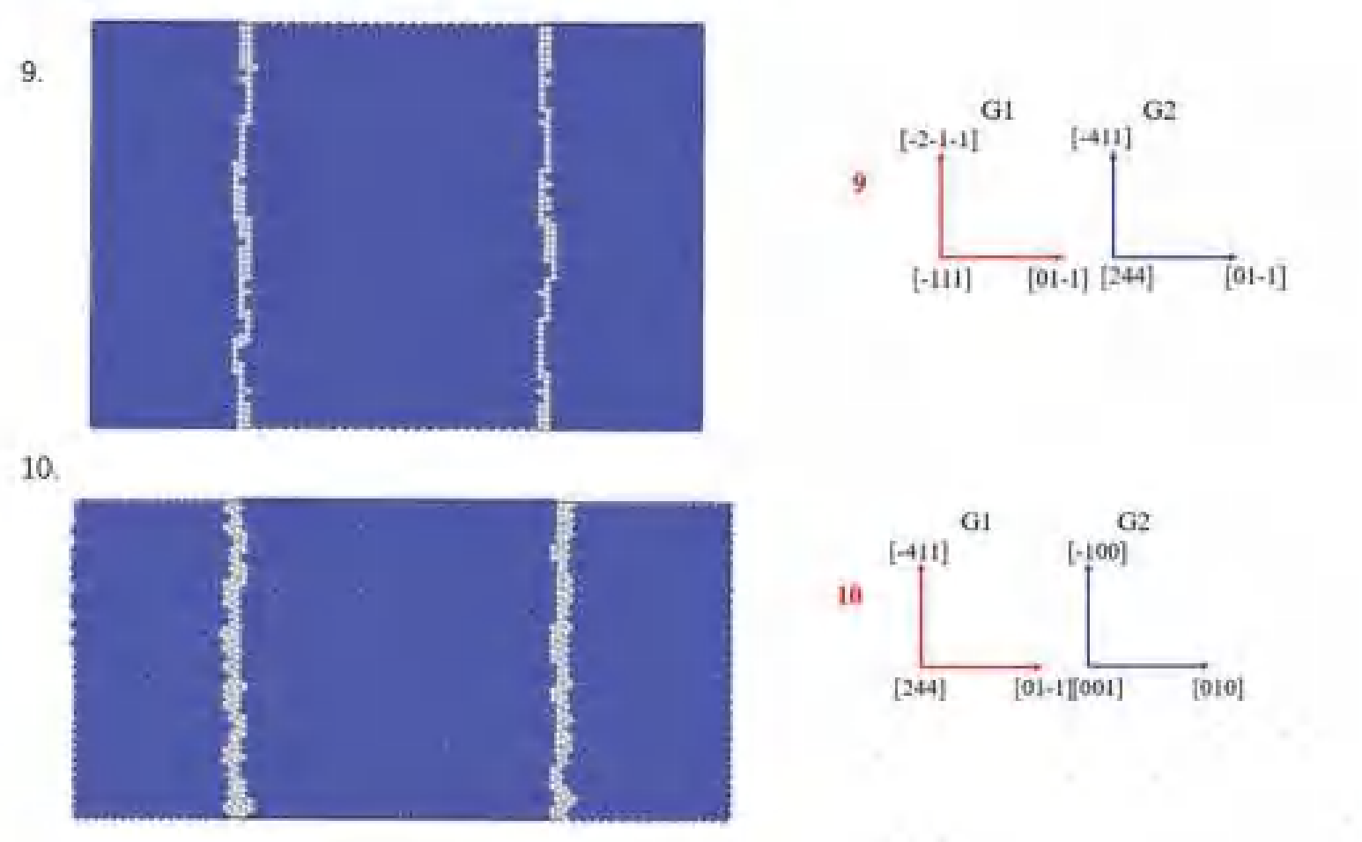

图4 选取了实验中常见15种(此处展示4种）晶粒取向组合分别设置贫镍与富镍晶界并进行弛豫，结果并未显示出扭折晶界与镍富集程度有关。

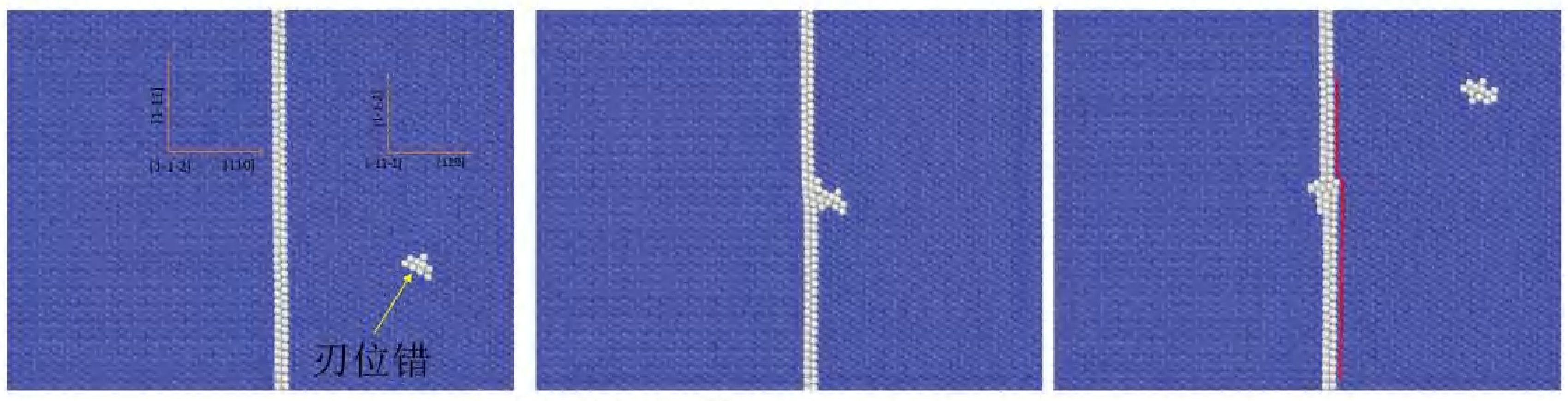

图5 阶梯状晶界的形成机制

材料中残留的刃位错在后续处理过程中运动到晶界形成一个台阶，这一过程还为晶界带来了一定量的合金原子，经此过程得到的台阶是较为稳定的。此外，相关研究表明，扭折也可由双相界面向单相晶界的演化过程中继承界面位错得到。

分子动力学模拟—富镍阶梯晶界的力学性能

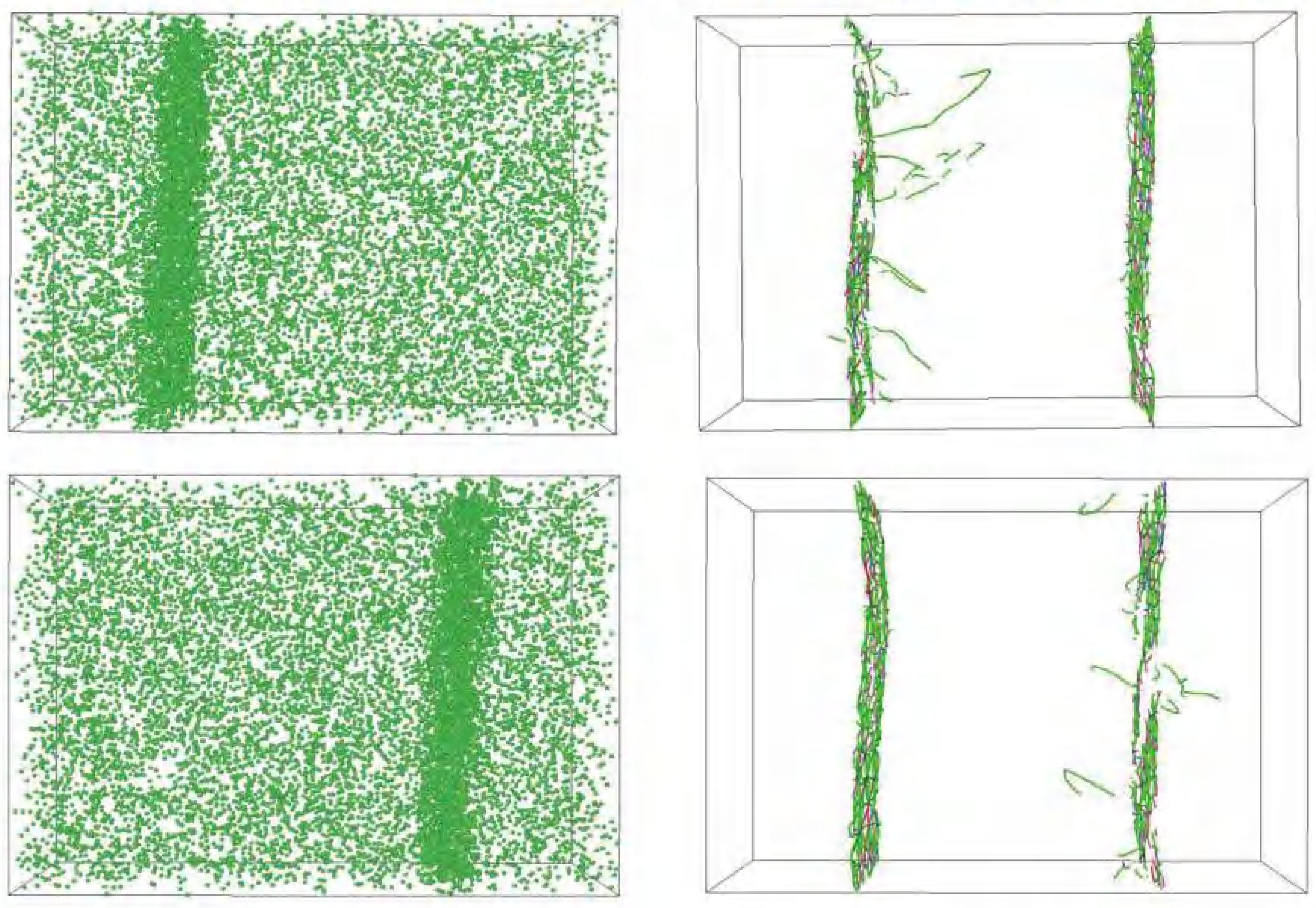

图6 镍偏聚对晶界位错发射的影响（图为合金中镍原子分布）；相同加载条件下，位错总先由富镍晶界处发射

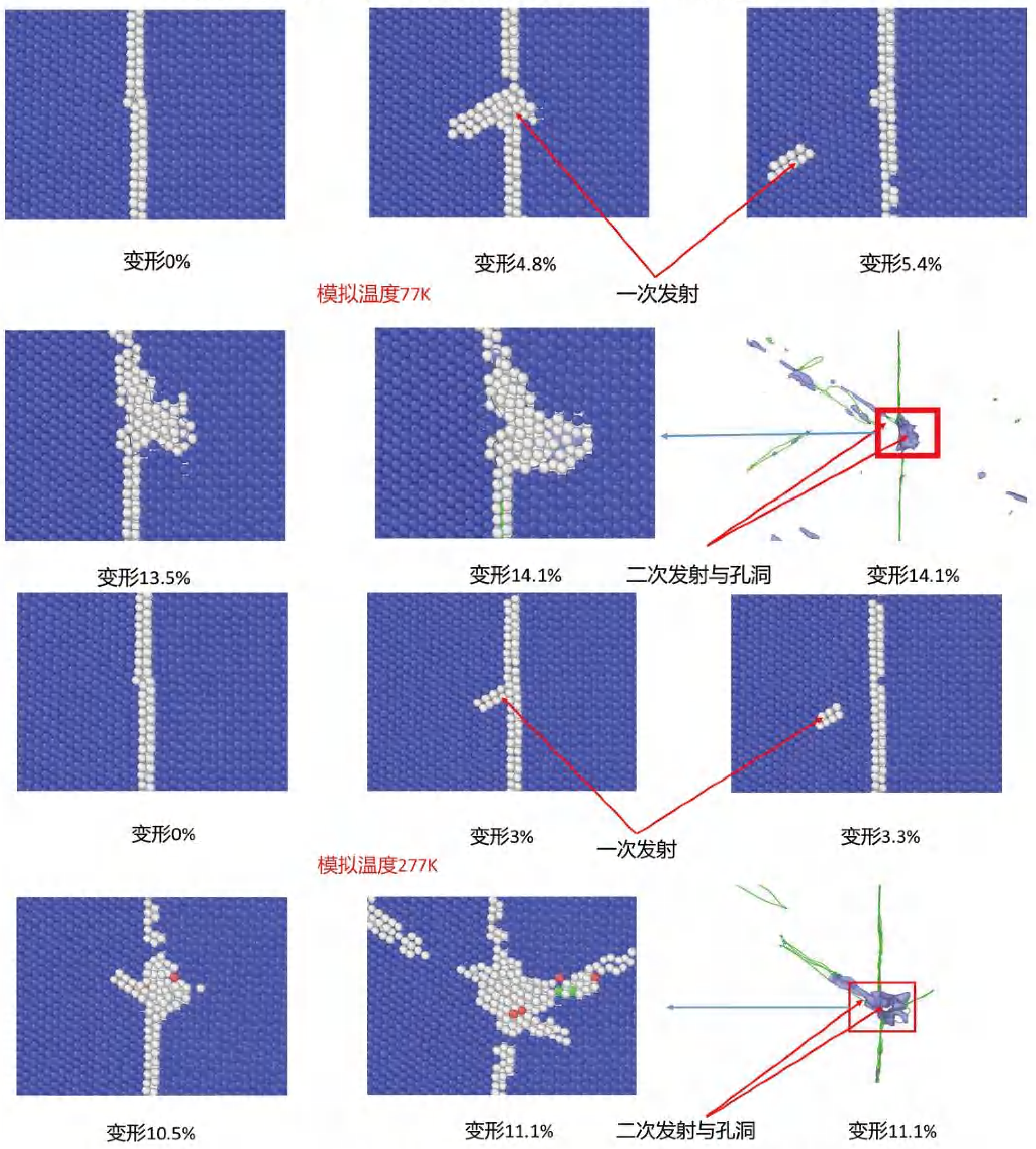

图7 温度对扭折晶界积存位错的发射和界面处孔洞形核的影响

结论

1. **材料中的刃位错能够在后续处理中运动、积存到晶界处形成扭折晶界，这一过程还为晶界带来了合金元素的偏聚；**
2. **镍在晶界处的偏聚增大了晶界处的平均原子体积，有利于晶界发射位错；**
3. **温度较高时，积存在扭折晶界上的位错在变形中容易从界面发射出去，温度较低时位错需要达到较大的局部应力（变形）才能从界面上发射出去。积存位错的延迟发射抑制了晶界孔洞形核，提高了材料的低温塑性。**

Effects of atomic site occupancy and compositional disordering on magnetic properties of Fe-Co-Cr alloys

Jing Zhang[1,2], Weiwei Sun[1,2], Pavel A. Korzhavyi[2]
1. School of Electronic Science and Engineering, Southeast University, 210096 Najing, China
2. Materials Science and Engineering, KTH Royal institute of Technology, SE-100 44 Stockholm, Sweden

Introduction

The FeCo alloys with B2 structure fall in the interesting category of ordered compounds. The compositional ordering has influence on the mechanical and magnetic properties and has therefore prompted a number of investigations. Fe-Co–Cr alloys developed for applications such as rotor or stator laminations in motors. However, the effects of atomic site occupancy of Cr and the corresponding chemical disordering still not clear. In this work, EMTO-CPA method was applied to investigate effect of Cr occupancy and compositional disordering on magnetic properties of Fe-Co alloys. The increase of chemical ordering will improve magnetic moment of Fe-Co alloys.

Computational methods

All calculations were conducted by using EMTO-CPA method. The exchange–correlation interactions were described by the PBE version of generalized gradient approximation (GGA); the full charge density technique (FCD) was used to calculate the total energies. The coherent potential approximation (CPA) implemented in EMTO software were used to treat chemical disordering of Fe-Co-Cr alloys.

Atomic site occupation

The atomic site occupancy has shown in Fig.1. The BCC (Fig1(a)) represents the fully disordered solid solution. Figure 1(b)-(f) represents Cr with varying concentrations at different sublattices.

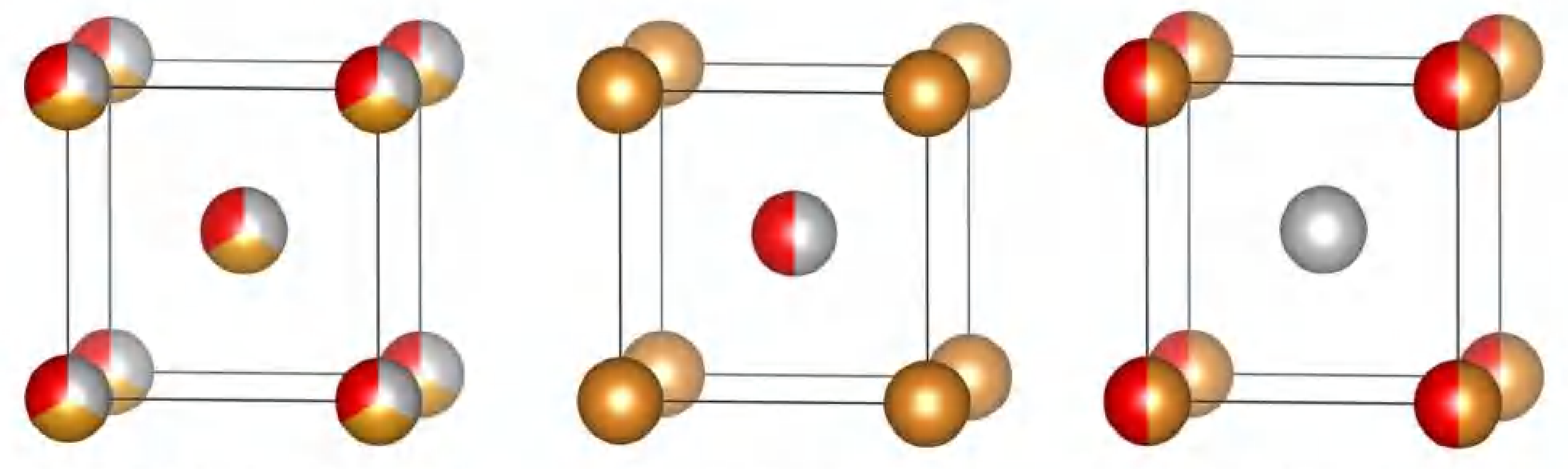

(a) FeCoX fully disordered (b) $Fe_{50}(Co_nX_{1-n})_{50}$ (c) $(Fe_nX_{1-n})_{50}Co_{50}$

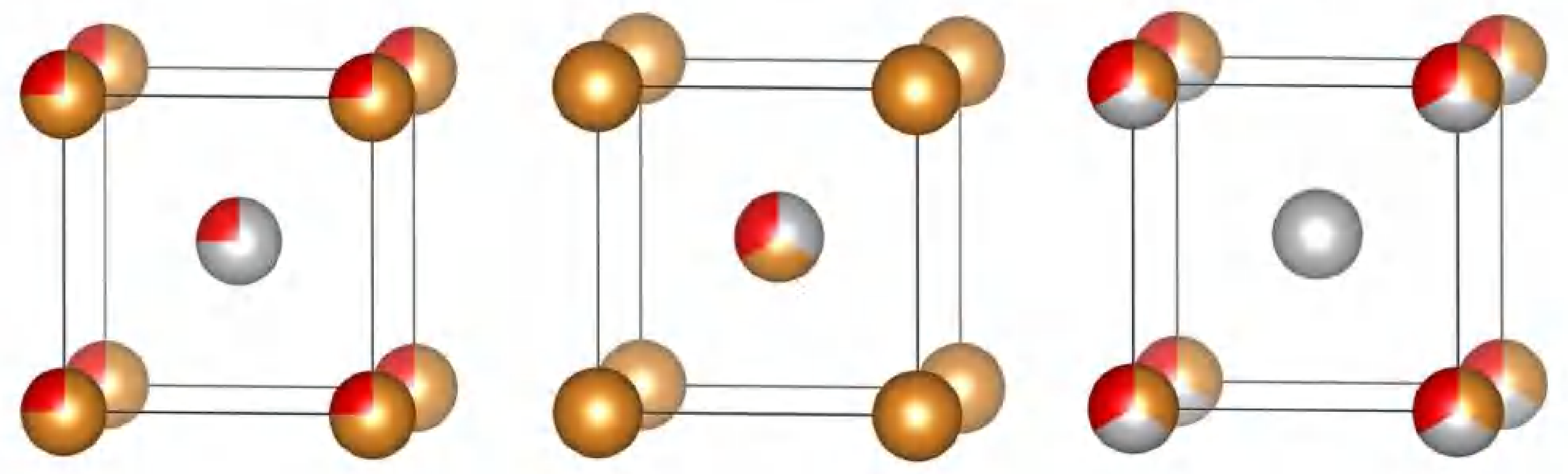

(d) $(Fe_nX_{1-n})_{50}(Co_mX_{1-m})_{50}$ (e) $Fe_{50}(Fe_{1-n-m}Co_nX_m)_{50}$ (f) $(Co_{1-n-m}Fe_nX_m)_{50}Co_{50}$

Fig.1 Atomic site occupations of Cr elements

Results

Fe-Co binary alloys

The mean atomic magnetic moments and saturation magnetization of Fe-Co alloys with BCC and B2 structures calculated by EMTO are compared with experiments in Fig.2. The difference of magnetic moments and saturation magnetization between BCC and B2 structures can be reproduce by the calculated results in this work.

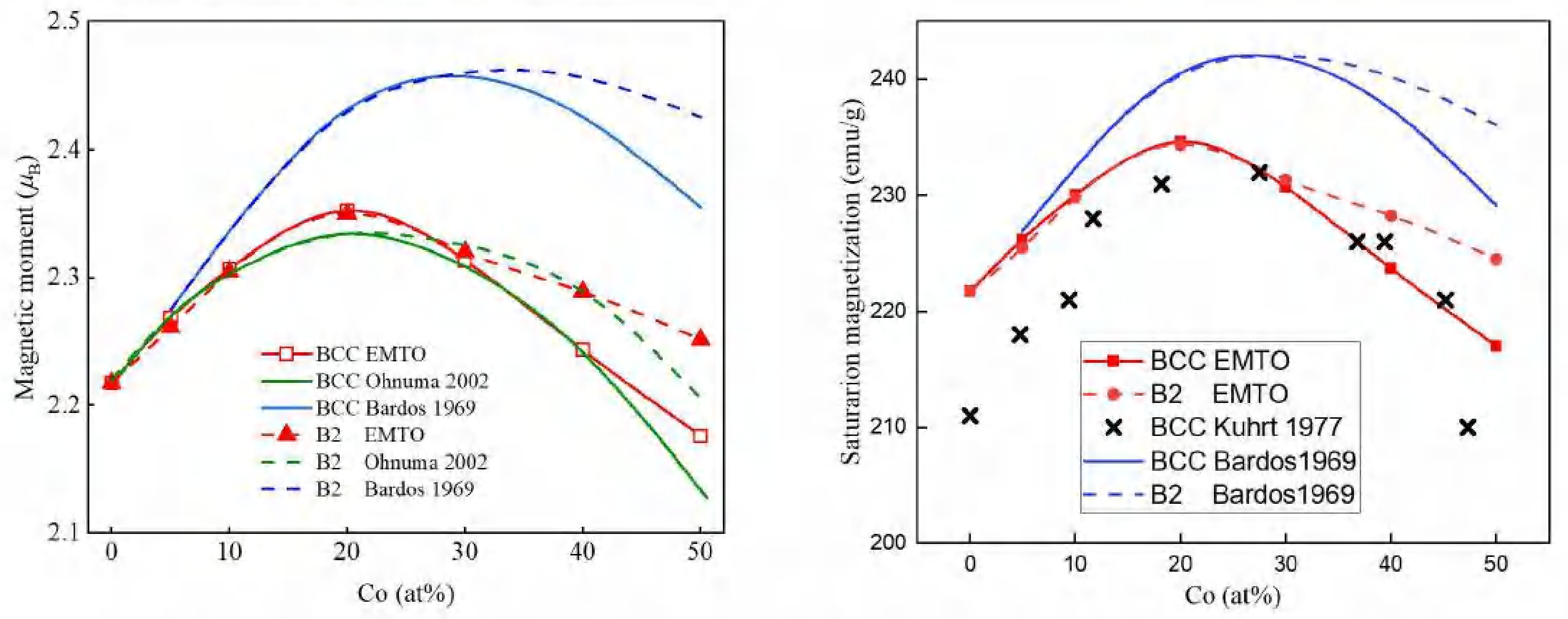

Fig.2 Magnetic moment and saturation magnetization of Fe-Co alloys

The mentioned difference can be correlated with chemical ordering which can be from configurational entropy S_{conf} as Fig.3 shows. The second-order derivative of S_{conf} over Cr content has the similar trend with mean atomic magnetic moments. This confirms the ordering of chemical composition has effect on magnetic properties of Fe-Co alloys. The increase of chemical ordering lead to improvement of magnetic properties.

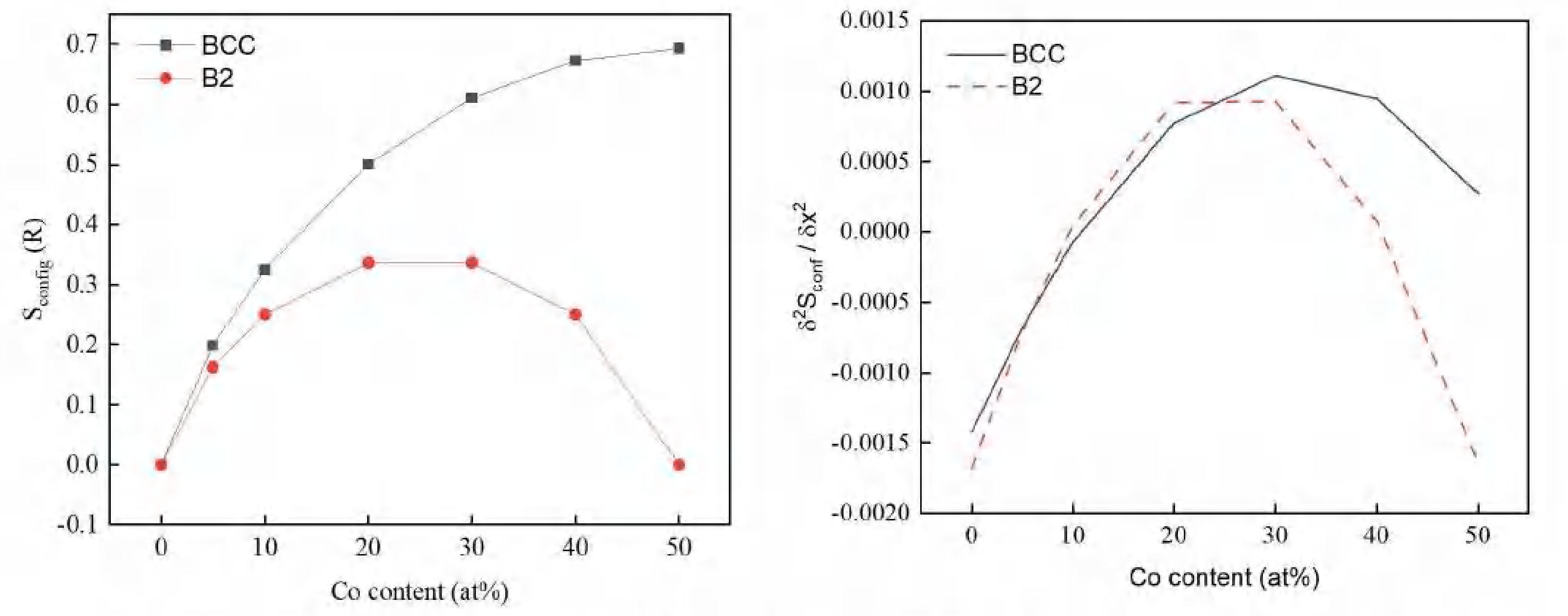

Fig.3 Configurational entropy and its second-order derivative of Fe-Co alloys

Fe-Co-Cr alloys

The mean atomic magnetic moments of Fe-Co-Cr alloys with BCC and B2 structures calculated by EMTO are compared in Fig.4. In Fig.4(d) the magnetic moment of BCC FeCoCr alloys were normalized by magnetic moment of pure Fe at 0K and the theoretical results are close to experimental data. Fig.4(e) indicates that the magnetic moments larger than other cases when Cr replace Fe atoms in B2 structure.

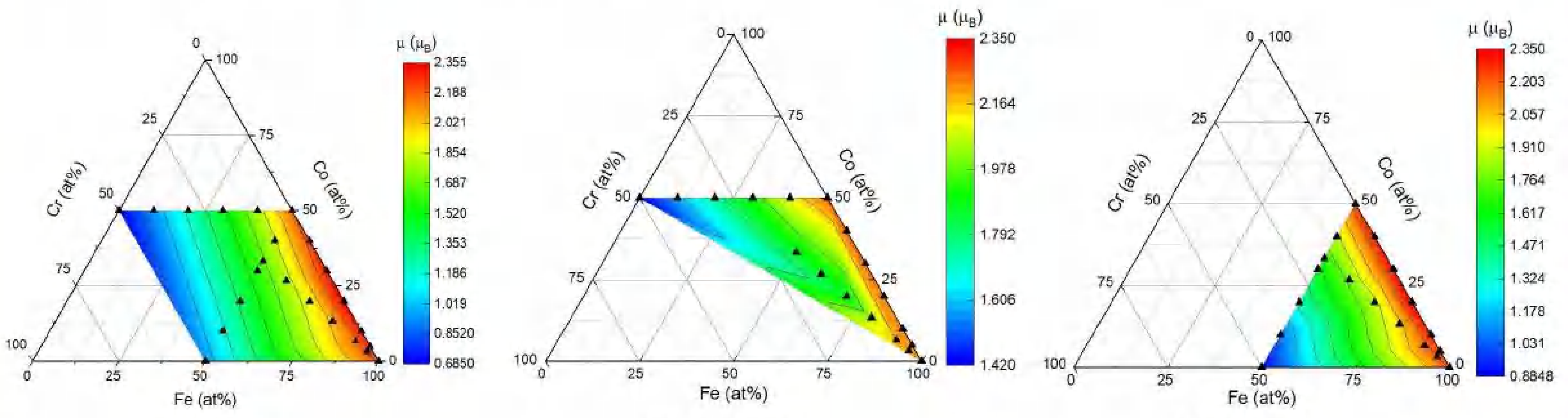

(a) FeCoCr (b) Fe(CoCr) (c) (FeCr)Co

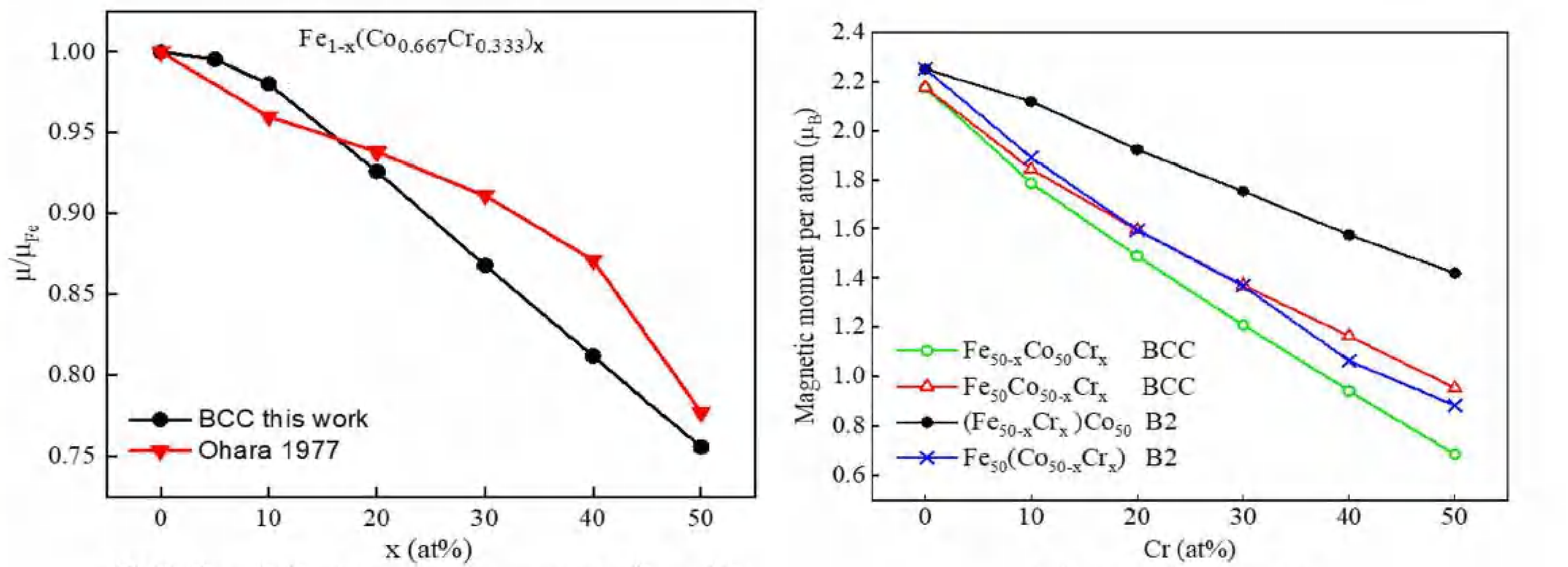

(d) Ratio relative to magnetic moment of pure Fe (e) magnetic moment

Fig.4 Magnetic moments of Fe-Co-Cr alloys. Triangles in (a)-(c) reprents calculated data points of this work.

References

Bardos D I. Mean magnetic moments in bcc Fe–Co alloys[J]. Journal of Applied Physics, 1969, 40(3): 1371-1372.

Ohnuma I, Enoki H, Ikeda O, et al. Phase equilibria in the Fe–Co binary system[J]. Acta Materialia, 2002, 50(2): 379-393.

Kuhrt C, Schultz L. Formation and magnetic properties of nanocrystalline mechanically alloyed Fe-Co and Fe-Ni[J]. Journal of applied physics, 1993, 73(10): 6588-6590.

Ōhara S, Komura S, Takeda T, et al. The Atomic Magnetic Moment in bcc Ternary Iron Alloys Fe (Co Mn) and Fe (Co Cr)[J]. Journal of the Physical Society of Japan, 1977, 42(6): 1881-1887.